THE UNIVERSITY OF HULL

THE ACOUSTIC MODELLING OF DISSIPATIVE ELEMENTS IN AUTOMOTIVE EXHAUSTS

being a Thesis submitted for the Degree of PhD

in the University of Hull

by

Raymond Kirby BEng

October 1996

Acknowledgements

I would like to express my sincere gratitude to my supervisor Professor Alan Cummings for all his help and guidance throughout the period of the research presented here and also during the preparation of this thesis. I would also like to thank Dr Keith Peat, who it was a pleasure working with during my time at Loughborough University. In addition, I wish to thank Dr Keshav Rathi for his help with the finite element programming carried out at Loughborough.

My thanks go to all my friends, especially my girlfriend Lisa for putting up with me during the preparation of this thesis, and my flatmates Jon, Lisa and Paul. I would also like to thank my parents for their continued support throughout my student career.

Finally, I would like to acknowledge the financial support for this work from the Department of Transport and an industrial consortium under LINK Research Grant, "Computer Aided Design Methods for Vehicle Silencers". In particular I would like to thank the members of the industrial consortium for supplying the test silencers, fibrous materials and perforate plates.

Abstract

The mathematical modelling and experimental testing of both dissipative silencers and catalytic converters is reported here, although dissipative silencers are of primary interest. The models examined are formulated with a view to introducing them into commercial software aimed at the acoustic design of automotive exhaust systems.

The porous materials which are commonly employed in dissipative silencers are examined first, and a semi-empirical model is formulated in order to predict the bulk acoustic properties of four different fibrous materials. Perforated tubes are also commonly employed in dissipative silencers separating the central channel from the absorbent, and the effects of both grazing flow and a backing layer of porous material upon the acoustic impedance of a perforate plate are examined.

Three different theoretical approaches to modelling dissipative silencers are reported, and the accuracy of each method is assessed in the light of experimental sound transmission loss data measured for five different dissipative silencers. Mean flow in the central channel is a feature of each model, in addition to the use of the new semi-empirical models for the perforated tube and the absorbent. A simple fundamental mode model is examined first, employing a straightforward analytical solution. More complex models are then investigated, incorporating finite element numerical methods. First, a fully general finite element model is examined and transmission loss predictions are obtained using both two and three dimensional meshes. A less complex eigenvalue solution, which also employs the finite element method, is examined next but this does not require such a high degree of computational effort. Predictions for finite length silencers are subsequently obtained using three different mode matching formulations. An examination of the accuracy of the predictions obtained using the different mathematical models is then carried out, from which conclusions are made concerning the future usefulness of each model in commercial design software. Finally, the effects of both mean flow and an axial temperature gradient upon the transmission loss of catalytic converters are examined. The relative influence the catalytic converter exerts sound attenuation, as compared to dissipative silencers, is also discussed.

Contents

Page

Page

Page

[All figures are located at the end of each chapter]

CHAPTER 1

GENERAL INTRODUCTION

Pollution is now an everyday aspect of the society in which we live. It is manifest in many different forms and, over recent years, society has become increasingly concerned about the impact pollution is having on our environment. Of particular interest in this thesis is environmental noise pollution. This differs from other forms of pollution because, although noise can undoubtedly damage the hearing, the environmental impact of noise seldom does any physical harm. To most people, noise pollution is simply an annoyance, the degree to which this is true being purely subjective, although very few people would consider aircraft or road traffic noise as anything other than noise pollution. Of increasing concern is the growing use of, and the reliance placed upon, the automobile and the associated effect this has had on both noise pollution and other forms of pollution. In recent years, public demand for controlling the growth of vehicular noise has increased and this is currently reflected in a broadening of Government legislation, designed to curb such pollution. The control of noise pollution emitted by automobiles forms the subject of this thesis.

To date, Government legislation has concentrated upon reducing the external noise emissions of vehicles by specifying a maximum noise level to which a "passer-by" is subjected from an individual vehicle. This is commonly enforced using "drive-by" tests, in which each new model of vehicle must pass a number of noise level criteria, measured in different positions remote from the vehicle. In a typical automobile, many different mechanisms of noise emission exist and, in order to meet the new noise criteria, manufacturers are being compelled to re-design their products with noise emissions in mind. The mechanisms which lie behind the generation of noise by automobiles are both numerous and complex, and the manner in which one re-designs new products in order to meet legislation is by no means straightforward. Indeed, it is still commonplace for companies to design the acoustic characteristics of their vehicles experimentally, employing a trial and error procedure. Clearly, this type of approach is rather unscientific and is expensive to undertake; additionally, one is not always guaranteed to obtain any improvement in the vehicle's performance, and the results are unlikely to be close to optimum. The continued introduction of increasingly more stringent noise legislation has forced automobile designers to depart from traditional methods and place greater emphasis on the use of predictive computer software for the overall noise emission from vehicles, before experimental validation takes place. Inevitably, to do this, one must resort to modelling the noise generation mathematically. Unfortunately, the mechanisms which lie behind noise emissions are numerous and a completely integrated mathematical model of an entire vehicle's noise emissions is, at present, impracticable. Consequently, one must focus on each mechanism individually, using a modelling procedure to refine the acoustic design of individual components before finally measuring the overall acoustic emissions from the vehicle experimentally. This is, at present, the only viable way of meeting the noise legislation, without resorting back to a purely experimental approach.

Of all the noise sources present in a typical automobile, the principal generator of environmental noise pollution is the engine, although as the acoustic design of both the engine and its exhaust system are improved, tyre noise is beginning to play a more significant role. The engine generally emits noise both from the inlet and exhaust and via structural vibration but, of these noise sources, the exhaust usually provides the major contribution to noise pollution. A typical exhaust system consists of an exhaust manifold, into which an internal combustion engine supplies gas flow and radiates noise. The exhaust gases are carried away from the exhaust manifold and are eventually communicated, along with the engine noise, to the environment via the tail pipe. To reduce the rate of emission of both the harmful exhaust gases and the radiated noise energy, passive elements are commonly employed in the exhaust system. The radiated engine noise is usually reduced by the use of a silencer, whilst the emission of harmful exhaust gases is controlled by a catalytic converter, although it is known that the catalytic converter can also alter the acoustic characteristics of the exhaust system. The catalytic converter is typically situated close to the outlet of the engine manifold, upstream of the silencer, in a part of the exhaust system known as the down pipe. This pipe is then joined, downstream of the catalytic converter, to the silencer. The tail pipe communicates both the exhaust gases and the radiated noise emitting from the silencer to the environment. The exhaust noise emitted by an automobile is usually quantified by measuring the externally radiated tail pipe noise. Therefore, to eliminate the costly experimental trial and error design process, one must produce mathematical models of the entire exhaust system, including the noise source (the engine), in order to predict the radiated tail pipe noise. Unfortunately, the engine provides a far from ideal sound source which is very difficult to model acoustically and therefore, at present, a fully integrated acoustic model of an exhaust system has yet to be realised. Consequently, research in this field has been concentrated on modelling components of the exhaust system individually, and this approach is also applied here. The research reported in this thesis is focused on acoustic modelling of the passive elements present in a typical automotive exhaust, namely the silencer and the catalytic converter. However, since the catalytic converter is not inserted into the exhaust for its acoustic characteristics alone, and subsequently the influence this has on noise emission is much smaller than that of the silencer - which is inserted specifically to reduce noise emissions - the bulk of this thesis is concerned with silencers.

The use of an exhaust silencer is the primary method available to the engineer for reducing exhaust noise emissions from the engine. Exhaust silencers have been in use nearly as long as automobiles themselves, although the design of these silencers has often been conducted on an *ad hoc* basis and it is only relatively recently, especially with the introduction of micro-computers, that the detailed mathematical modelling of silencers has taken place. Exhaust silencers are of two main types, reactive and absorptive (or dissipative). The reactive silencer typically consists of an expansion chamber in which each area discontinuity introduces an impedance mis-match which reflects a part of the incident sound energy back towards the engine. Interference effects between the incident and reflected waves cause a pronounced frequency dependence of the acoustic performance of expansion chamber silencers. The dissipative silencer typically contains a porous material which is capable of absorbing acoustic energy and hence only a part of this energy is either reflected or transmitted. In practice, however, silencers are neither completely reactive or completely dissipative. The use of both types of silencer is commonplace and, indeed, they are increasingly being employed together in the same silencer box, since the performance of each type can - with suitable design - complement that of the other. For instance, a complex reactive silencer can be constructed to be compact and acoustically efficient, but will tend to suffer from a high back pressure. On the other hand, the use of a simple dissipative silencer will provide low back pressure, but the low frequency performance of the silencer is poor. Consequently, the detailed acoustic modelling of both types of silencer is necessary in order to provide design tools for use in the acoustic design of the exhaust system as a whole. However, in practice, modelling reactive silencers mathematically has proved to be more straightforward than modelling dissipative silencers and consequently, at present, reactive silencer modelling is by far the more advanced of the two. Commercial PC-based software is now commonplace for use in the design of reactive silencers (see for example Peat [1]), and good agreement between prediction and experiment has been reported for complex multi-pass reactive silencer designs. This is not the case for dissipative silencers, the design of which is complicated by the introduction of porous sound absorbing materials. The relative dearth of effective models for dissipative silencers has meant that, in recent years, this type of silencer has received more attention, with a view to allowing its integration into current reactive silencer design software. However, at present, software aimed at the design of dissipative silencers is still not yet sufficiently advanced to allow this to take place. This thesis is therefore aimed at examining current dissipative silencer models with the object of either modifying existing models or introducing new ones in order to allow their incorporation into commercial software aimed at the acoustical design of automotive exhaust systems.

The study of dissipative silencers began as early as the 1930s, for instance Sivian [2] applied a simple plane wave approach to modelling a circular pipe lined with rock-wool. Sivian expressed the behaviour of the porous rock-wool in terms of its normal acoustic impedance and, in ignoring any axial wave propagation in the absorbent, treated the liner as "locally-reacting". Morse [3] also analysed a duct with a locally reacting liner, but extended Sivian's model to higher frequencies by including higher order modes. Scott [4] later realised that, in most practical situations, axial wave propagation occurs within the porous material (implying a so called "bulk-reacting" liner) and to describe the acoustic characteristics of the material, Scott employed two frequency dependent complex quantities: the propagation constant and the characteristic impedance. The early work of Scott et al. was hampered by the unavailability of computers and, in order to obtain a solution to the problem, it was often necessary to employ a number of approximations in order to make the problem tractable.

It was not until the advent of the computer that significant advances on the early dissipative silencer model were made. Bokor [5,6] verified Scott's model by comparing his predictions to experimental measurements made for the first mode of propagation only. Kurze and Vér [7], who - like Bokor - studied rectangular ducts lined on opposite walls, extended Scott's approach to include non-isotropic absorbing material, although Wassilieff [8] later corrected an error in Kurze and Vér's formulation. Wassilieff went on to solve the revised equations by using the Newton-Raphson method and obtained much closer agreement between prediction and experiment than had previously been observed. The effects of mean flow (the mean gas flow emanating from the engine in the case of automotive silencers) in the central channel, around which the absorbent material is usually packed, was introduced by Meyer et al. [9], and later by Ingård [10]. Tack and Lambert [11] also included mean flow and concluded that, in the low frequency region, the use of a uniform flow profile is adequate for most purposes. They were, however, unable to obtain a numerical solution to the problem. A study of both uniform mean flow and sheared flow was later conducted by Ko [12], who solved an eigenvalue equation by using an iterative numerical procedure. Peat [13] also included uniform mean flow in the central channel and employed a simple fundamental mode formulation in his investigation of a finite length axisymmetric silencer with a bulk reacting liner. However, for dissipative silencers, the inclusion of purely the fundamental mode is, perhaps, an over-simplification of the problem. Cummings [14], in a study of rectangular ducts lined on opposite walls, examined both higher order modes and the effects of a perforate facing situated between the mean flow in the central channel and the bulk reacting lining. A perforate was also included by Nilsson and Brander [15], who studied an infinite circular duct with mean flow in the central channel. Nilsson and Brander used both numerical and analytical techniques to solve the governing eigenequation for a number of modes. The models mentioned previously do not, however, fully account for the effects of mean flow in a finite length automotive silencer which also includes a bulk reacting lining.

Various investigations, in addition to Nilsson and Brander [15], have simplified the problem by assuming the silencer to be of infinite length. For instance, Cummings and Chang [16] developed an analytical eigenvalue formulation for an axisymmetric silencer with mean flow in both the central channel and in the absorbent, although the effects of a perforate were omitted. It is, however, not uncommon for the dissipative silencer to have a non-circular cross section; consider, for example, a typical oval shaped automotive exhaust silencer. Unfortunately this presents a number of additional problems and research concerning silencers of arbitrary cross section has again centred on the use of various types of eigenvalue formulation. For example, Astley and Cummings [17] used finite elements to study a silencer of arbitrary but uniform cross sectional shape, which included a bulk reacting liner and mean flow in the central channel. They obtained predictions for sound propagation in rectangular ducts lined on all four walls; circular silencers were later studied using this method by Rathi [18]. Glav [19] also employed numerical methods (the "null field" method and collocation) to examine silencers with an oval cross section, although mean flow in the central channel was omitted.

Unfortunately, eigenvalue solutions do not give much physical insight into the performance of a finite length silencer, and subsequently methods have been introduced whereby eigenvalue formulations are used to obtain performance predictions for finite length silencers. This clearly complicates the problem still further and hence the study of finite length dissipative silencers is less well researched. Nilsson and Brander [20, 21, 22] used the Wiener-Hopf method to study the duct discontinuities in a finite length axisymmetric dissipative silencer which contained both mean flow in the central channel and a perforate. Solutions for each duct discontinuity were then combined to provide predictions for a finite length silencer. Unfortunately this approach is very complex and it has yet to be applied to irregular cross sections. Cummings and Chang [23] utilised their original eigenvalue formulation [16] to implement a much simpler formulation which involved applying a mode matching method to the duct discontinuities. However, they ignored the effects of a perforate facing and, like Nilsson and Brander, they were restricted by their eigenvalue formulation to the study of axisymmetric silencers. Glav [19] later employed a mode matching approach in the study of silencers with arbitrary cross-sections, but omitted both mean flow in the central channel and a perforate facing.

The use of an eigenvalue formulation, in conjunction with an appropriate treatment of the duct discontinuities, to obtain predictions for a finite length silencer, has yet to be shown to be a completely satisfactory approach. For instance, predictions have yet to be obtained for silencers of arbitrary cross-section which includes both mean flow and a perforate. Furthermore, the use of an eigenvalue formulation restricts solutions to those silencers which have an axially uniform cross section. Recently an alternative to the use of an eigenvalue formulation has been applied. This approach has been based upon the well known finite element method, used in many other areas of engineering. Previously, Astley and Cummings [17] had used a finite element approach in an eigenvalue solution, although the finite element method can also be applied to finite length silencers, giving a more general formulation. The finite element method was employed by a number of authors (see for example Craggs [24] and Hobbeling [25]), although it was not until the study by Peat and Rathi [26] was carried out that a completely three dimensional finite element formulation was introduced, which also included mean flow in both the central channel and in the absorbent. Peat and Rathi did, however, omit the effects of a perforate facing and made numerical predictions for a circular silencer only. The approach of Peat and Rathi is, at present, the most general method for modelling dissipative silencers to appear in the literature. Unfortunately, a full finite element solution is very complex and the demand on CPU time is unavoidably large. However this does appear to reflect the complexity of the dissipative silencer problem and one must therefore expect to expend more CPU time on dissipative silencer design than on reactive silencer modelling. Only a brief background to the development of dissipative silencer modelling has been given here, and greater detail is given in the introduction to each individual chapter later in this thesis.

To date, a detailed quantitative assessment of the various dissipative silencer models described in the literature has yet to take place, and furthermore the practical application of such models in a commercial design environment has not been examined. The primary objective of this thesis is to examine dissipative silencer modelling in detail, with a view to enabling software to be written which will allow design engineers to optimise the acoustic design of an exhaust system. This inevitably means that, in addition to employing a modelling procedure which provides sufficiently accurate predictions, one must also consider the CPU time required to obtain these predictions.

The impetus behind the research described in this thesis was provided by funding from a combination of the Department of Transport and a number of industrial sponsors (the Motor Industry Research Association, Arvin Exhausts, Tenneco-Walker (U. K.) Ltd., Eminox Ltd., Perkins Technology and Ford Motor Company Ltd.). The research was initiated in response to demand from industry for the upgrading of existing design software. For instance, because of the reasons stated earlier, most commercial software aimed at the acoustic design of exhaust systems is limited to reactive silencers (see for example the LAMPS program described by Peat [1]). Consequently, most designers either omit any dissipative elements from their models, or account for the effects of the porous material by including a rather crude equivalent fluid representation, sometimes employing the somewhat heuristic formulae of Morse and Ingård [27]. Obviously, this approach to modelling dissipative silencers cannot be expected to provide accurate predictions and hence the demand for a more complete representation of the problem. The work reported here was begun with the eventual aim of extending the LAMPS program for reactive silencers to include dissipative elements (both silencers and catalytic converters), although the author is not concerned here with the actual writing of LAMPS style software. Consequently, since the work is aimed at use in a commercial environment, one must be continually aware of the demands of industry. Perhaps the most important demand to be made at the beginning of this research was the need to minimise the use of CPU time. Most of the industrial sponsors involved with this project are, with the exception of Ford, relatively small and they do not have access to large mainframe computers. Therefore, the software produced must be capable of running quickly and easily on a personal computer, in much the same way as the LAMPS software does. This criterion is not so easy to satisfy for dissipative silencers and inevitably places restrictions on the complexity of the models one can use; it also plays a large part in deciding the direction that the development of the modelling takes place. With regard to the dissipative silencers themselves, a number of initial criteria were also specified. It was decided that the model produced must be capable of accurately predicting the acoustic behaviour of a dissipative silencer over a frequency range of approximately 0-2kHz, accounting for a possible range of different absorbent materials in the process. The silencer should also have mean flow in the central channel, and the surrounding silencer box, in which the absorbent is placed, must be of arbitrary cross-sectional shape. A perforate may also be present, situated between the central channel and the absorbent. Finally, one must also be capable of accurately representing any dissipation of sound energy occurring in the catalytic converter.

The initial criterion introduced by the industrial sponsors at the inception of this research cannot, at present, be met by any of the current dissipative silencer models reported in the literature (see the earlier discussion). For example, at present, a perforate has yet to be included in a model which will accommodate silencers of arbitrary cross-section. In fact, the necessity of inclusion of a perforate in dissipative silencer modelling has currently not been firmly established. At present, it appears that most authors are content to leave the perforate out of their models, assuming that its acoustic effect is negligible. However, it appears that the acoustic influence of the perforate has not been examined in enough detail to allow for its exclusion. This is particularly true in the case of perforates backed by an absorbing material, a configuration which would often occur in a dissipative silencer. Indeed a perforate subjected to grazing flow and backed by a porous material has yet to be examined at all, and consequently this is studied in detail in Chapter 4 of this thesis. Subsequently, several theoretical models for dissipative silencers are derived, based upon some of the modelling procedures mentioned previously. In view of the requirement for computationally rapid solutions, the discussion of theoretical modelling begins in Chapter 6 with the simple fundamental mode model implemented by Peat [13]. The model is extended here to include the perforate, and also to remove the low frequency approximations employed by Peat, although the silencer geometry is still limited to being axisymmetric. To model silencers with an arbitrary cross-sectional shape it will be shown that one must resort to the use of numerical methods, and the implementation of a full three dimensional finite element model is described in Chapter 7. This is based upon the method used by Peat and Rathi [26], although the perforate is introduced into the model here, and also three dimensional solutions are obtained for the first time. Although the full finite element model in Chapter 7 provides a completely general approach to modelling dissipative silencers, completely satisfying the aforementioned criteria relating to modelling an individual silencer, it will be shown that, as one would anticipate, this model demands a considerable amount of CPU time. Consequently a method is investigated in which an attempt is made to balance the accuracy of the finite element approach with the speed of solution inherent in Peat's approximate method. Accordingly, a mode matching scheme is described in Chapter 9, which utilises a finite element eigenvalue formulation, described separately in Chapter 8. The finite element eigenvalue approach implemented by Astley and Cummings [17] is applied in Chapter 8, to allow the modelling of arbitrary cross sections and, in common with previous models, a perforate is introduced for the first time. Also, in Chapter 9, two new mode matching formulations are introduced, and the method of Cummings and Chang [23] is examined in detail. Finally, numerical predictions from each of the theoretical models described in this thesis are compared extensively to experimental measurements performed on a number of dissipative silencers, both with and without mean flow. The various silencers examined are all different, either in size, shape or type of absorbent material. This then provides a means of validating each of the theoretical models.

With the introduction of the features discussed earlier into the separate dissipative silencer models, an additional problem, common to all the modelling procedures described earlier, became evident. The performance of dissipative silencers is dependent upon the acoustic properties of the porous material employed in the silencer. It became apparent that, in most of the silencer models discussed previously, the use of experimental data obtained for the bulk acoustic properties of the absorbing material was in error when the data were extrapolated to sufficiently low frequencies. This effect was recognised by a number of authors, although the problem does not appeared to have been rectified satisfactorily. For instance, a theoretical microstructure model of the porous absorber has sometimes been employed at low frequencies, and used in conjunction with the experimental data at higher frequencies. However, this can incur a "jump" in material properties at the frequency of transition between the two methods, depending on the details of how the procedure is implemented. An alternative approach is to employ a single theoretical model over the entire frequency range, but this would normally lack the accuracy of the experimental data in the medium frequency range. At the beginning of this thesis (Chapters 2 and 3) this problem is rectified by employing a semi-empirical model for the bulk acoustic properties of the porous material which provides a continuous prediction across the frequency range of interest. The new model is then integrated into each dissipative silencer model that follows.

The research presented in this thesis is intended to be used as a design tool for the predictive modelling of dissipative elements employed in typical automotive exhausts. The integration of this work into a software design package useful in a commercial environment is left to others. In addition, the analysis of dissipative silencers is not yet sufficiently advanced to accommodate the dissipative elements that are sometimes used in complex multi-pass arrangements, with or without reactive elements. Consequently only "straight-through" dissipative silencers are considered in this investigation.

The acoustic analysis presented in this thesis is restricted to linear acoustics, and any non-linear effects caused by "high" sound pressure levels (above approximately 165dB) - such as are often present in an exhaust system - are ignored here. The treatment of non-linear effects in dissipative silencers, caused by high sound pressures, is extremely difficult and awaits further work. The effects of temperature gradients in dissipative silencers are also ignored, although the dissipative silencer models themselves should still be applicable at high temperatures, although this remains to be experimentally verified. Other approximations, on which the modelling is based, include the assumption of a rigid, isotropic, porous absorbent which contains no internal mean flow. The consequences of these assumptions about the porous medium are examined in Chapter 10. The mean flow in the central channel is assumed to have a Mach number of less than 0.3, so that the mean flow can be treated as incompressible. In addition the mean flow is also assumed to be uniform (see Tack and Lambert [11]) and therefore an infinitesimally thin boundary layer is assumed to be present adjacent to the walls of the central channel.

The work in this thesis can be split up into two parts. The first part, Chapters 2 to 5, is concerned with characterising the components which go to make up the dissipative silencers. This involves the introduction of new semi-empirical models for both the bulk acoustic properties of the absorbent and the acoustic impedance of the perforate (Chapters 2 to 4). In Chapter 5, experimental data, obtained for a number of dissipative silencers, are presented. The following part of this thesis, Chapters 6 to 9, is concerned with modelling the silencers theoretically, employing the data obtained in the first part. In Chapter 10, the performances of the various dissipative silencer models are compared to one another, and some observations are made concerning their future usefulness as predictive design tools. The modelling of catalytic converters is reported separately in Chapter 11. Finally, conclusions drawn from the results obtained in this thesis are presented in Chapter 12.

CHAPTER 2

SOUND PROPAGATION IN RIGID FIBROUS POROUS MATERIALS

Section 2.1

Introduction

Fibrous porous materials have long been used for their sound absorbing properties in exhaust silencers. The materials, in bulk form, are usually packed into a box surrounding the gas flow emitting from the exhaust. The fibres are often randomly packed, allowing interconnecting air spaces to permeate the material. The air spaces, or pores, lie in a random fashion forming irregular shapes throughout the absorbent. When a sound wave impinges upon the porous material it is propagated as a wave by the air, or gas, in the pores. In a rigid material the sound wave is dissipated due to irreversible losses in the viscous and thermal boundary layers close to the fibres. If the material is flexible, additional loss mechanisms can occur. This dissipation of sound energy is used to attenuate sound in numerous applications. This chapter is concerned with the study of sound attenuation in rigid porous media in order to understand their influence on the behaviour of dissipative silencers.

Sound dissipation in porous media was first studied by Rayleigh [28]. Rayleigh modelled a porous material as a solid matrix of capillary tubes with sound propagation in the axial direction. He approximated Kirchhoff's general theory [29] for sound propagation in tubes to narrow circular capillary tubes in order to model porous materials. Rayleigh went on to predict the absorption coefficient for porous media. The capillary tube approach of Rayleigh quickly became the favoured method for characterising porous materials.

Scott [4] used Rayleigh's approach to show that a porous material could be completely characterised by two frequency dependent complex quantities, the propagation constant and the characteristic impedance. In relating the properties of a single pore to those of a bulk material, Scott introduced the flow resistivity of the material (see also Carman [30]). This allowed Scott to compare experimental data to predictions obtained using the capillary tube theory and show that the viscous and thermal effects in the pores were frequency dependent.

The viscous and thermal effects present in a single axisymmetric pore were analysed separately by Zwikker and Kosten [31]. The increase in effective density of air in the pore was represented by the complex density, and the thermal effects by the bulk modulus. These two quantities were then combined to define the propagation constant and the characteristic impedance. Zwikker and Kosten stated that this method was an approximation of Kirchhoff's theory and exact only in the low and high frequency limits. A full account of a number of capillary tube models, all based on the theory of Kirchhoff, is reported by Tijdeman [32]. Subsequently, both Tijdeman and Stinson [33] noted that Zwikker and Kosten's model was in fact valid in a wider frequency range than first thought, incurring errors only in the intermediate frequency range. Zwikker and Kosten were the first to notice that the effective density of air in the bulk material was increased by the random alignment of the pores. This was said to be due to the sound wave undergoing a more tortuous path through the material, compared to that in a regular solid matrix. Zwikker and Kosten combined this frequency independent effect (later known as the tortuosity) with the frequency dependent viscous effects in the pores to give a frequency dependent structure factor.

The tortuous path of the sound wave was extended by Biot [34] to cover pores of different shapes. Biot used the limiting cases of circular pores and slit-like pores to show that the pore shape affected sound attenuation. He combined this effect with the tortuosity and called it the structural factor. The effect has later become separated from the tortuosity and become known as the pore shape factor (see Smith and Greenkorn [35]).

Alternatives to Rayleigh's approach were also examined, for instance both Zwikker and Kosten [31] and Biot [34] attempted to take account of frame motion. Biot predicted the existence of two dilatational waves and one rotational wave in a flexible material, which produced significant departures from the theory of rigid materials. Attenborough and Walker [36] derived a scattering theory, treating the material as a random array of parallel elastic fibres, where the fibres are either rigidly fixed or freely supported. The attenuation of wave energy occurs through viscous and thermal action on scattering at fibre boundaries. Burns [37] extended the capillary model to include fibres in a rigid hexagonal matrix; here, each fibre is within a "cylinder of influence", along which the sound propagation occurs. Mechel [38,39] also proposed a model similar to that of Burns. Cummings and Chang [40] extended Mechel's "parallel fibre model" to include the effects of mean flow in the material. It was shown that mean flow caused the material to behave anisotropically even if the medium was originally isotropic. Attenborough [41] gives a comprehensive review of the different theoretical models available for porous media.

The current thrust of work on porous material has centred on attempts to use a simple model, similar to Rayleigh's, but to account for the random nature of the material by the use of the tortuosity and/or the pore shape factor. Johnson et al. [42] produced interpolation formulae for a complex tortuosity (equivalent to the structure factor employed by Zwikker and Kosten [31]), based on limiting behaviour at zero and infinite frequency. They measured their tortuosity for inviscid flow (equivalent to using an infinite frequency in a viscous fluid), and used their formulae to extrapolate to lower frequencies. The tortuosity can be measured for effectively inviscid flow in a number of ways: electrical conductivity methods [30], using superfluid ^4He as the pore fluid [42], and air saturated ultrasonic wavespeed measurements [43]. The formula of Johnson et al. is extrapolated to lower frequencies by defining a characteristic length for each pore. Both Johnson et al. and Allard and Champoux [44] point out that this method is exact only at very high and very low frequencies, and also the characteristic length is difficult to measure accurately. It is evident that some confusion can exist due to the differing definitions for tortuosity. In this thesis, the tortuosity is separated from the complex density (unlike Johnson et al. [42]) but is still defined as frequency dependent. The pore shape factor has also been defined as both dependent and independent of frequency. For instance, Stinson and Champoux [45] showed that the Rayleigh type model implemented by Attenborough [46] must contain a frequency dependent pore shape factor if the model is to be correct in the limiting frequencies. However, they then went on to show how Biot's [34] viscosity correction function could be extended to include thermal conductivity effects, allowing the definition of a frequency independent pore shape factor. In a study on extreme ranges in pore size Champoux and Stinson [47] proposed that two pore shape factors were necessary. In the same paper, they also showed how experimental data can be used to obtain a "best fit" for the pore shape factor. To the best of the author's knowledge, a frequency dependent tortuosity has not been used together with a frequency dependent pore shape factor.

The use of microstructure models for predictive purposes has led to simplification of the models in order to reduce computational effort. Both Zwikker and Kosten [31] and Mechel [48] have introduced low frequency approximations for their microstructure models. This was done by using small argument approximations for the Bessel functions appearing in the models. However the models are only of use in conjunction with experimental data covering the middle to high frequency range. Chandler-Wilde and Horoshenkov [49] used Padé approximants to simplify both Attenborough's [46] and Stinson and Champoux's [45] models to cover the entire frequency range. Allard and Champoux [44] employed the tortuosity predictions of Johnson et al. [42] to produce a semi-empirical model, valid over the entire frequency range. However Allard and Champoux's model is restricted by the need to measure the characteristic length of Johnson et al.

In this chapter a theoretical model is developed specifically for fibrous materials, although it is likely that it will also be applicable to other materials such as foams. The intention of the model is to provide a simple means by which experimental data and low frequency theoretical predictions can be integrated to produce a continuous set of data which offers a higher degree of accuracy than the models discussed previously. The model is based on the parallel fibre model of Mechel [38,39] and Cummings and Chang [40], this closely resembles the physical characteristics of the fibrous absorbents. Simplification of the model is achieved by separating the viscous and thermal effects in the manner of Zwikker and Kosten [31]. The complex density and bulk modulus are derived for a single pore and then combined to give the bulk acoustic properties. The flow resistivity of the material is used to eliminate the fibre radius from the model, allowing the bulk acoustic properties to be written as a function of a dimensionless frequency parameter. The tortuosity and pore shape factor have both been included in the model and are defined as real frequency dependent quantities.

Section 2.2

Parallel Fibre Model

The parallel fibre model used here is identical to the geometrical model of Cummings and Chang [40]. However, since mean flow effects are not accounted for in this model, the discs used by Cummings and Chang to introduce inertial stresses have been removed. The model consists of a circular fibre, radius a, surrounded by a cylinder of influence, radius R. The fibres are assumed to be uniform along their length and lie in an hexagonal matrix as shown below in Figure 2.1.

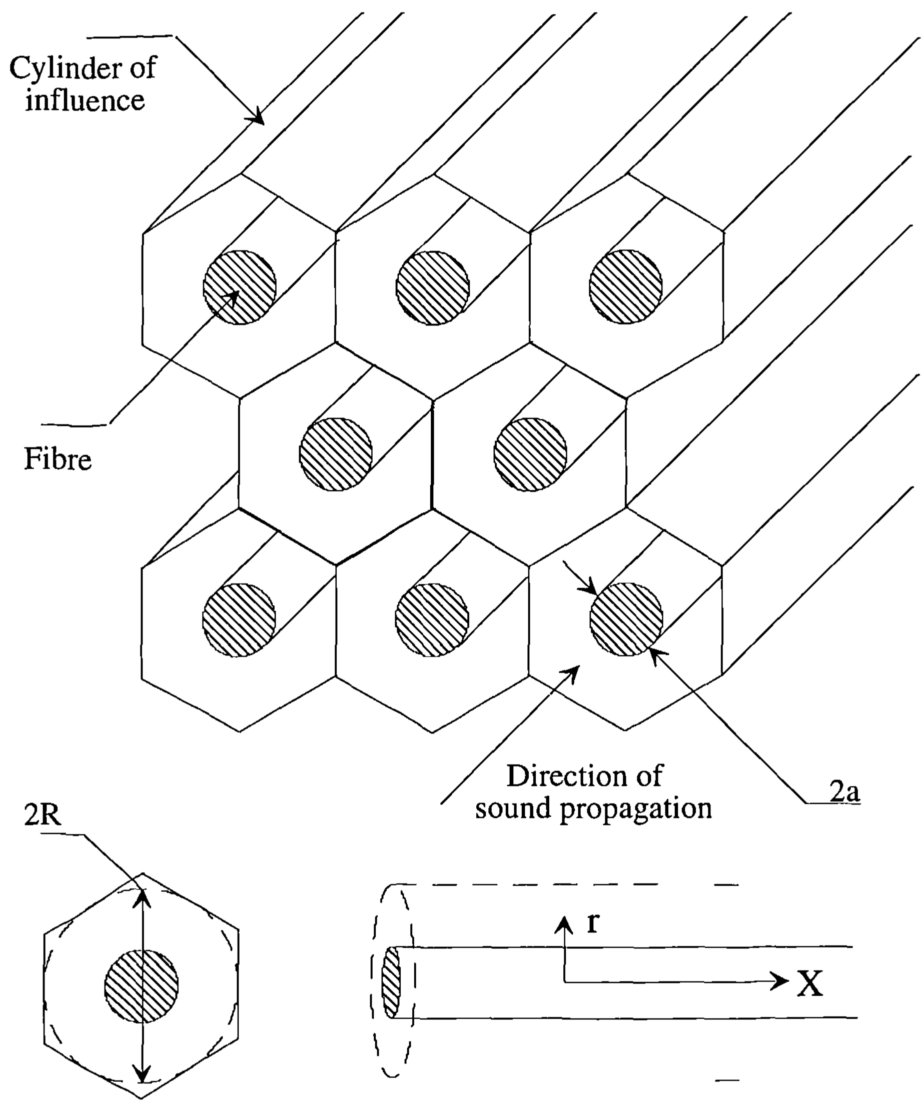

Figure 2.1. Geometry of parallel fibre model

In Figure 2.1 an hexagonal shape for the cylinder of influence is shown, this prevents any voids appearing in the model. However, in order to simplify predictions the cross sectional shape of the hexagonal cylinders of influence is to be approximated by a circle. In the parallel fibre model a hydraulic radius may be used to define the radius of each fibre. Glass fibres and mineral wools have approximately circular fibres and the hydraulic radius becomes simply the radius of the fibre. In the case of steel wools, the fibre cross sections tend to be irregular and an equivalent hydraulic radius has been assumed here. The volume porosity, Ω, of the material is given by $\Omega = 1 - a^2/R^2$.

Section 2.3

Complex Density

The complex density, first defined by Zwikker and Kosten [31], is a measure of the increase in effective density of the air in the pore, caused by the presence of a viscous acoustic boundary layer around each fibre. The linearized Navier-Stokes equation for a pressure drop in the x direction gives

$$\frac{\partial u'}{\partial t} = -\frac{1}{\rho_0}\frac{\partial p'}{\partial x} + \upsilon\left(\frac{\partial^2 u'}{\partial r^2} + \frac{1}{r}\frac{\partial u'}{\partial r}\right), \tag{2.1}$$

where u' is the axial acoustic velocity component, p' is the acoustic pressure, ρ_0 is the mean fluid density, t is time and υ is the kinematic fluid viscosity. In equation (2.1) the radial component of the velocity has been neglected. This is a valid approximation when the radius of the cylinder of influence is small in comparison with the wavelength and the axial velocity is much greater than the radial velocity (see Stinson [33] and Peat [50]). For a time dependence of $e^{i\omega t}$, where ω is the radian frequency and $i = \sqrt{-1}$, the Navier-Stokes equation can now be written as

$$i\omega u' = -\frac{1}{\rho_0}\frac{\partial p'}{\partial x} + \frac{\upsilon}{r}\frac{\partial}{\partial r}\left(r\frac{\partial u'}{\partial r}\right), \tag{2.2}$$

or

$$\frac{1}{\rho_0 \upsilon}\frac{\partial p'}{\partial x}=\left\{\frac{1}{r}\frac{\partial}{\partial r}\left(r\frac{\partial}{\partial r}\right)-i\frac{\omega}{\upsilon}\right\}u'. \tag{2.3}$$

Let $\zeta=\sqrt{-i\omega/\upsilon}$; then the general solution to equation (2.3) is

$$u'=\frac{1}{\rho_0 \upsilon \zeta^2}\frac{\partial p'}{\partial x}+A_1 J_0(\zeta r)+A_2 Y_0(\zeta r), \tag{2.4}$$

where J_n and Y_n are Bessel and Neumann functions respectively, of order n and A_1, A_2 are constants. The following boundary conditions apply:

at $r=R$, $du'/dr=0$, so

$$0=-\zeta A_1 J_1(\zeta R)-\zeta A_2 Y_1(\zeta R); \tag{2.5}$$

at $r=a$, $u'=0$, so

$$0=-\frac{1}{i\omega\rho_0}\frac{\partial p'}{\partial x}+A_1 J_0(\zeta a)+A_2 Y_0(\zeta a). \tag{2.6}$$

The constants are therefore given by

$$A_1=\frac{1}{i\omega\rho_0}\frac{\partial p'}{\partial x}\left\{\frac{Y_1(\zeta R)}{J_0(\zeta a)Y_1(\zeta R)-Y_0(\zeta a)J_1(\zeta R)}\right\}, \tag{2.7}$$

and

$$A_2=-\frac{1}{i\omega\rho_0}\frac{\partial p'}{\partial x}\left\{\frac{J_1(\zeta R)}{J_0(\zeta a)Y_1(\zeta R)-Y_0(\zeta a)J_1(\zeta R)}\right\}. \tag{2.8}$$

Equation (2.4) may now be written as

$$u'=-\frac{1}{i\omega\rho_0}\frac{\partial p'}{\partial x}\left\{1-\frac{J_0(\zeta r)Y_1(\zeta R)-Y_0(\zeta r)J_1(\zeta R)}{J_0(\zeta a)Y_1(\zeta R)-Y_0(\zeta a)J_1(\zeta R)}\right\}. \tag{2.9}$$

The complex density $\rho(\omega)$ is given by [31]

$$\rho(\omega) = -\frac{\partial p'/\partial x}{\partial\langle u'\rangle/\partial t}, \tag{2.10}$$

where $\langle u'\rangle$ is the space averaged velocity over the cross section and is given by:

$$\langle u'\rangle = -\frac{1}{i\omega\rho_0}\frac{\partial p'}{\partial x}\frac{1}{\pi\left(R^2-a^2\right)}\int_a^R\left\{1-\frac{J_0(\zeta r)Y_1(\zeta R)-Y_0(\zeta r)J_1(\zeta R)}{J_0(\zeta a)Y_1(\zeta R)-Y_0(\zeta a)J_1(\zeta R)}\right\}2\pi r dr, \tag{2.11}$$

i.e. $$\langle u'\rangle = -\frac{1}{i\omega\rho_0}\frac{\partial p'}{\partial x}\left\{1+\frac{2a}{\zeta\left(R^2-a^2\right)}\left[\frac{J_1(\zeta a)Y_1(\zeta R)-Y_1(\zeta a)J_1(\zeta R)}{J_0(\zeta a)Y_1(\zeta R)-Y_0(\zeta a)J_1(\zeta R)}\right]\right\}. \tag{2.12}$$

The complex density can now be written as

$$\rho(\omega) = \frac{\rho_0}{1+\dfrac{2}{\zeta a}\left(\dfrac{1-\Omega}{\Omega}\right)\left[\dfrac{J_1(\zeta a)Y_1(\zeta R)-Y_1(\zeta a)J_1(\zeta R)}{J_0(\zeta a)Y_1(\zeta R)-Y_0(\zeta a)J_1(\zeta R)}\right]}, \tag{2.13}$$

where a/R has been replaced by $\sqrt{(1-\Omega)}$.

Equation (2.13) defines the complex density for an axisymmetric pore. To account for pore shapes of irregular cross section the pore shape factor is introduced. The pore shape factor is introduced in the same manner as that of Biot [34] and Attenborough [46], hence ζ is redefined as

$$\zeta = s^2(\omega)\sqrt{-i\frac{\omega}{\upsilon}}, \tag{2.14}$$

where $s^2(\omega)$ is a real frequency dependent pore shape factor. The term ζa is a measure of the ratio of the viscous forces to the inertia forces. For small values of ζa (<1) then viscous forces are dominant and Poiseuille flow is present; for large values of ζa (>10) inertial forces dominate.

Section 2.4

Bulk Modulus

The bulk modulus is a measure of the thermal effects occurring in a pore. The compression and rarefaction of the air in the pore generate heat which is conducted between the air and the fibres. The density and pressure of the air during compression and rarefaction are not in phase and consequently the bulk modulus is complex. The bulk modulus is found by solving the energy equation relating the pressure and density fluctuations (see Tijdeman [32], and also Chapter 11). The linearized form of the energy equation gives

$$\rho_0 C_p \left(\frac{\partial T'}{\partial t} \right) = \lambda_h \left(\frac{\partial^2 T'}{\partial r^2} + \frac{1}{r} \frac{\partial T'}{\partial r} \right) + \frac{\partial p'}{\partial t}, \tag{2.15}$$

where T' is the temperature, C_p is the specific heat of air at constant pressure and λ_h is the thermal conductivity. Equation (2.15) is valid provided that the radial derivatives >> axial derivatives, for axisymmetric disturbances, and the particle velocity u' is purely axial (see Cummings and Chang [40]). This equation may be rewritten as

$$\frac{\lambda_h}{-i\omega\rho_0 C_p} \left\{ \frac{\partial^2 T'}{\partial r^2} + \frac{1}{r} \frac{\partial T'}{\partial r} \right\} + T' = \frac{p'}{\rho_0 C_p}, \tag{2.16}$$

for a time dependence of $e^{i\omega t}$. The general solution to equation (2.16) is

$$T' = \frac{p'}{\rho_0 C_p} + C_1 J_0(\alpha r) + C_2 Y_0(\alpha r), \tag{2.17}$$

where $\alpha = \sqrt{-i\omega N_{pr}/\upsilon}$, C_1 and C_2 are constants, and N_{pr} is the Prandtl number. The following boundary conditions apply:

at $r = R$, $dT'/dr = 0$, so

$$0 = -\alpha C_1 J_1(\alpha R) - \alpha C_2 Y_1(\alpha R); \tag{2.18}$$

at $r = a$, $T' = 0$, so

$$0 = \frac{p'}{\rho_0 C_p} + C_1 J_0(\alpha a) + C_2 Y_0(\alpha a). \tag{2.19}$$

The constants C_1 and C_2 are therefore given by

$$C_1 = -\frac{p'}{\rho_0 C_p}\left[\frac{Y_1(\alpha R)}{J_0(\alpha a)Y_1(\alpha R) - Y_0(\alpha a)J_1(\alpha R)}\right], \tag{2.20}$$

and

$$C_2 = \frac{p'}{\rho_0 C_p}\left[\frac{J_1(\alpha R)}{J_0(\alpha a)Y_1(\alpha R) - Y_0(\alpha a)J_1(\alpha R)}\right]. \tag{2.21}$$

Equation (2.17) can now be written as

$$T' = \frac{p'}{\rho_0 C_p}\left\{1 - \frac{J_0(\alpha r)Y_1(\alpha R) - Y_0(\alpha r)J_1(\alpha R)}{J_0(\alpha a)Y_1(\alpha R) - Y_0(\alpha a)J_1(\alpha R)}\right\}. \tag{2.22}$$

The bulk modulus $\kappa(\omega)$ is defined by Zwikker and Kosten [31] as

$$\kappa(\omega) = \frac{P_0}{\left(1 - R_G \rho_0 \langle T' \rangle / p'\right)}, \tag{2.23}$$

where R_G is the gas constant and $\langle T' \rangle$ is given by

$$\langle T' \rangle = \frac{p'}{\rho_0 C_p} \frac{1}{\pi\left(R^2 - a^2\right)} \int_a^R \left\{1 - \frac{J_0(\alpha r)Y_1(\alpha R) - J_1(\alpha R)Y_0(\alpha r)}{J_0(\alpha a)Y_1(\alpha R) - J_1(\alpha R)Y_0(\alpha a)}\right\} 2\pi r dr, \tag{2.24}$$

hence

$$\langle T' \rangle = \frac{p'}{\rho_0 C_p}\left\{1 + \frac{2}{\alpha a}\left(\frac{1-\Omega}{\Omega}\right)\left[\frac{J_1(\alpha a)Y_1(\alpha R) - J_1(\alpha R)Y_1(\alpha a)}{J_0(\alpha a)Y_1(\alpha R) - J_1(\alpha R)Y_0(\alpha a)}\right]\right\}, \tag{2.25}$$

where the previous substitution (see equation (2.13)) for a/R has been employed. Substituting equation (2.25) into equation (2.23) finally defines the bulk modulus as

$$\kappa(\omega) = \frac{\gamma P_0}{\left\{1 - \frac{2(\gamma-1)}{\alpha a}\left(\frac{1-\Omega}{\Omega}\right)\left[\frac{J_1(\alpha a)Y_1(\alpha R) - J_1(\alpha R)Y_1(\alpha a)}{J_0(\alpha a)Y_1(\alpha R) - J_1(\alpha R)Y_0(\alpha a)}\right]\right\}}. \tag{2.26}$$

The shape factor is introduced into the bulk modulus in the same manner as for the complex density, i.e. α is now redefined as

$$\alpha = s^2(\omega)\sqrt{-i\frac{\omega N_{pr}}{\upsilon}}. \tag{2.27}$$

Section 2.5

Extension to Bulk Material

The complex density and bulk modulus for the bulk material can now be predicted by using the expressions calculated for a single pore. This is done by equating the average particle velocity in the pore to the average velocity for the bulk material using the Dupuit-Forchheimer assumption (see Carman[30] and Attenborough [41]):

$$\langle u' \rangle = \frac{q^2(\omega)}{\Omega}\langle u_b' \rangle, \tag{2.28}$$

where $\langle u' \rangle$ is the average velocity in the pore, $\langle u_b' \rangle$ is the average velocity in the bulk material, and $q^2(\omega)$ is the frequency dependent tortuosity or dynamic tortuosity. Note that the dynamic tortuosity has only been introduced when bulk parameters are being considered. The complex density can now be found for the bulk material by the substitution of equation (2.28) into equation (2.10) to give

$$\rho_b(\omega) = \frac{q^2(\omega)}{\Omega}\rho(\omega). \tag{2.29}$$

The bulk modulus for the bulk material is found by substituting equation (2.23) into the continuity equation for a bulk material defined by Zwikker and Kosten [31] (see also Stinson and Champoux [45]). This gives

$$\kappa_b(\omega) = \frac{1}{\Omega}\kappa(\omega) \tag{2.30}$$

The subscript b denotes a bulk quantity.

It can be seen from equations (2.29) and (2.30) that the tortuosity only increases the effective density of the air in the bulk material. The bulk acoustic properties can now be written as a function of the bulk complex density and the bulk modulus by using the formulae of Zwikker and Kosten [31], hence

$$\Gamma = i\omega\left(\frac{\rho_b(\omega)}{\kappa_b(\omega)}\right)^{\frac{1}{2}} \text{ and } z_a = \left[\rho_b(\omega)\kappa_b(\omega)\right]^{\frac{1}{2}}, \qquad (2.31),(2.32)$$

where Γ is the propagation constant and z_a is the characteristic impedance. It is convenient to re-write equations (2.31) and (2.32) in terms of the properties of a single pore, i.e.

$$\Gamma = i\omega\left(q^2(\omega)\frac{\rho(\omega)}{\kappa(\omega)}\right)^{\frac{1}{2}} \text{ and } z_a = \frac{1}{\Omega}\left[q^2(\omega)\rho(\omega)\kappa(\omega)\right]^{\frac{1}{2}}. \qquad (2.33),(2.34)$$

By using equations (2.13) and (2.26), one may express the bulk acoustic properties as

$$\frac{\Gamma}{k_0} = i\left\{q^2(\omega)\frac{\left[1-\frac{2(\gamma-1)}{\zeta a\sqrt{N_{pr}}}\left(\frac{1-\Omega}{\Omega}\right)\frac{S_1(\alpha)}{S_0(\alpha)}\right]}{\left[1+\frac{2}{\zeta a}\left(\frac{1-\Omega}{\Omega}\right)\frac{S_1(\zeta)}{S_0(\zeta)}\right]}\right\}^{\frac{1}{2}}, \tag{2.35}$$

and

$$\frac{z_a}{\rho_0 c_0} = \frac{1}{\Omega}\left\{q^2(\omega) \Bigg/ \left[1+\frac{2}{\zeta a}\left(\frac{1-\Omega}{\Omega}\right)\frac{S_1(\zeta)}{S_0(\zeta)}\right]\left[1-\frac{2(\gamma-1)}{\zeta a\sqrt{N_{pr}}}\left(\frac{1-\Omega}{\Omega}\right)\frac{S_1(\alpha)}{S_0(\alpha)}\right]\right\}, \tag{2.36}$$

where

$$\frac{S_1(\zeta)}{S_0(\zeta)} = \frac{J_1(\zeta a)Y_1\left(\zeta a/\sqrt{1-\Omega}\right) - Y_1(\zeta a)J_1\left(\zeta a/\sqrt{1-\Omega}\right)}{J_0(\zeta a)Y_1\left(\zeta a/\sqrt{1-\Omega}\right) - Y_0(\zeta a)J_1\left(\zeta a/\sqrt{1-\Omega}\right)} \tag{2.37}$$

and

$$\frac{S_1(\alpha)}{S_0(\alpha)} = \frac{J_1(\zeta a\sqrt{N_{pr}})Y_1\left(\zeta a\sqrt{N_{pr}/(1-\Omega)}\right) - Y_1(\zeta a\sqrt{N_{pr}})J_1\left(\zeta a\sqrt{N_{pr}/(1-\Omega)}\right)}{J_0(\zeta a\sqrt{N_{pr}})Y_1\left(\zeta a\sqrt{N_{pr}/(1-\Omega)}\right) - Y_0(\zeta a\sqrt{N_{pr}})J_1\left(\zeta a\sqrt{N_{pr}/(1-\Omega)}\right)}. \tag{2.38}$$

The expressions derived for the bulk acoustic properties above are identical to those of Mechel [38, 39], with the exception of the introduction of a tortuosity and pore shape factor in the present analysis. The bulk acoustic properties have been written in terms of the fibre radius, however, since a value for the average fibre radius is extremely difficult to measure, it is desirable to re-write the bulk acoustic properties in terms of something more readily measurable. In the next section the fibre radius is related to the steady flow resistivity of the bulk material, a quantity which is easily measured by using non-acoustical means.

Section 2.6

Flow Resistivity

The flow resistivity of a porous material depends upon the velocity profile present within the pores and is therefore frequency dependent. Cummings and Chang [40] showed that the flow resistivity comprised both a viscous and inertial component. Since the mean flow in the material is taken to be negligible, only the viscous flow resistivity is to be considered here. The viscous flow resistivity has been widely used for the prediction of the bulk acoustic properties by obtaining values in the low frequency limit. At very low frequencies, where Poiseuille flow is present, the viscous flow resistivity becomes a purely real quantity, independent of frequency, and is equal to the steady flow resistivity. The steady flow resistivity is defined as the ratio of the pressure gradient across the sample to the average flow velocity through the sample at low flow velocities where viscous forces dominate (see Carman [30]). The steady flow resistivity is easy to measure using non-acoustical means [30], and is therefore an attractive quantity to use for eliminating the fibre radius from the model.

For Poiseuille flow in a single pore, the Navier-Stokes equation for steady flow with a pressure drop in the x direction (see White [51]) gives

$$\frac{1}{\mu}\frac{d\bar{p}}{dx}=\frac{1}{r}\left\{\frac{d}{dr}\left(r\frac{d\bar{u}}{dr}\right)\right\}, \tag{2.39}$$

where $\bar{u}$ denotes the velocity in the pore, μ is the dynamic fluid viscosity and the bar denotes a time average value. Solving for $\bar{u}$ gives

$$\bar{u}=\frac{r^2}{4\mu}\frac{d\bar{p}}{dx}+B_1\ln r+B_2, \tag{2.40}$$

where B_1 and B_2 are constants. Introducing the boundary conditions:

at $r=a$, $\bar{u}=0$ and $d\bar{u}/dr=0$ at $r=R$ yields

$$\bar{u}=-\frac{1}{4\mu}\frac{d\bar{p}}{dx}\left\{a^2-r^2+2R^2\ln\frac{r}{a}\right\}. \tag{2.41}$$

Averaging the velocity over a pore cross section gives

$$\langle\bar{u}\rangle=\frac{a^2}{4\mu\Omega(1-\Omega)}\frac{d\bar{p}}{dx}\left[\ln(1-\Omega)+\Omega+\frac{\Omega^2}{2}\right]. \tag{2.42}$$

The average velocity for a single pore can now be related to that of the bulk material by using the Dupuit-Forchheimer assumption (see equation (2.28)). However, since Poiseuille flow is being considered, the dynamic tortuosity at vanishingly low frequencies assumes a constant value i.e.

$$\lim_{\omega \to 0} q^2(\omega) \to q_0^2, \tag{2.43}$$

where q_0^2 is the steady flow tortuosity. The assigning of a steady value for the tortuosity at low frequencies will be discussed later. The Dupuit-Forchheimer assumption now becomes:

$$\langle \bar{u} \rangle = \frac{q_0^2}{\Omega} \langle \bar{u}_b \rangle, \tag{2.44}$$

and therefore

$$\langle \bar{u}_b \rangle = \frac{a^2}{4\mu q_0^2(1-\Omega)} \frac{d\bar{p}}{dx} \left[\ln(1-\Omega) + \Omega + \frac{\Omega^2}{2} \right]. \tag{2.45}$$

The dynamic viscous flow resistivity $\sigma_v(\omega)$ was defined by Zwikker and Kosten [31], by the use of a modified momentum equation,

$$-\frac{\partial \bar{p}}{\partial x} = \frac{q^2(\omega)\rho_0}{\Omega} \frac{\partial \langle \bar{u}_b \rangle}{\partial t} + \sigma_v(\omega) \langle \bar{u}_b \rangle, \tag{2.46}$$

where $\sigma_v(\omega)$ is the (frequency dependent) dynamic viscous flow resistivity. Therefore, for steady flow,

$$\lim_{\omega \to 0} \sigma_v(\omega) \to \sigma, \tag{2.47}$$

and

$$-\frac{\partial \bar{p}}{\partial x} = \sigma \langle \bar{u}_b \rangle, \tag{2.48}$$

where σ is the steady flow resistivity. Substitution of equation (2.48) into equation (2.45) gives

$$\sigma = -\frac{4\mu q_0^2}{a^2}\frac{(1-\Omega)}{\left[\ln(1-\Omega)+\Omega+\Omega^2/2\right]}. \tag{2.49}$$

Equation (2.49) gives a frequency independent expression for the steady flow resistivity in terms of the fibre radius. This allows the fibre radius to be eliminated from the expressions for the bulk acoustic properties, i.e.

$$(\zeta a)^2 = iq_0^2 s^2(\omega) 8\pi\xi \frac{(1-\Omega)}{\left[\ln(1-\Omega)+\Omega+\Omega^2/2\right]}, \tag{2.50}$$

where ξ is a dimensionless frequency parameter $(\xi = \rho_0 f/\sigma)$, f denoting frequency. Equation (2.50) can now be substituted into equations (2.35) and (2.36) to give the full expressions for the bulk acoustic properties.

Section 2.7

Low Frequency Model

The formulae derived so far can be used to predict the acoustic properties over a wide frequency range, with the limitations on accuracy in the intermediate range mentioned previously. The model involves the calculation of Bessel and Neumann functions, and whilst this does not cause any real problems, it is still desirable to simplify the model as far as possible in order to reduce computational effort. In this section, a low frequency model is derived using small argument approximations for the Bessel and Neumann functions. It will be shown that the low frequency approximation does not restrict the model since it is still valid over the entire frequency range of interest. Indeed the upper limit of the low frequency model will be shown to be coincident with the lower range of applicability of the parallel fibre model imposed because of the uncoupling of viscous and thermal effects.

The small argument approximations for Bessel and Neumann functions are listed by Abramowitz and Stegun [52]. The expressions given here are accurate to the fourth order in the argument:

$$J_0(z) = 1 - \frac{z^2}{4} + \frac{z^4}{64}, \tag{2.51}$$

$$J_1(z) = \frac{z}{2}\left(1 - \frac{z^2}{8}\right), \tag{2.52}$$

$$Y_0(z) = \frac{2}{\pi}\left\{\left[\ln\frac{z}{2} + \tilde{\gamma}\right] - \frac{z^2}{4}\left[\ln\frac{z}{2} + \tilde{\gamma} - 1\right] + \frac{z^4}{64}\left[\ln\frac{z}{2} + \tilde{\gamma} - \frac{3}{2}\right]\right\}, \tag{2.53}$$

$$Y_1(z) = -\frac{2}{\pi z} + \frac{z}{\pi}\left\{\left[\ln\frac{z}{2} + \tilde{\gamma} - \frac{1}{2}\right] - \frac{z^2}{8}\left[\ln\frac{z}{2} + \tilde{\gamma} - \frac{5}{4}\right]\right\}, \tag{2.54}$$

where z is complex and $\tilde{\gamma}$ is Euler's constant. Substituting the low frequency approximations into the expressions for $S_1(\zeta)/S_0(\zeta)$ and $S_1(\alpha)/S_0(\alpha)$ gives

$$\frac{S_1(\zeta)}{S_0(\zeta)} = \frac{-\frac{\zeta a}{2}\left\{\Omega - \frac{(\zeta a)^2}{4}\left[\ln(1-\Omega) + \frac{\Omega}{2}\left(\frac{2-\Omega}{1-\Omega}\right) - F_1(\Omega)\frac{(\zeta a)^2}{8}\right]\right\}}{(1-\Omega) + \frac{(\zeta a)^2}{4}\left[\ln(1-\Omega) + \Omega - F_2(\Omega)\frac{(\zeta a)^2}{8}\right]}, \tag{2.55}$$

and

$$\frac{S_1(\alpha)}{S_0(\alpha)} = \frac{-\frac{\zeta a\sqrt{N_{pr}}}{2}\left\{\Omega - \frac{(\zeta a)^2 N_{pr}}{4}\left[\ln(1-\Omega) + \frac{\Omega}{2}\left(\frac{2-\Omega}{1-\Omega}\right) - F_1(\Omega)\frac{(\zeta a)^2 N_{pr}}{8}\right]\right\}}{(1-\Omega) + \frac{(\zeta a)^2 N_{pr}}{4}\left[\ln(1-\Omega) + \Omega - F_2(\Omega)\frac{(\zeta a)^2 N_{pr}}{8}\right]}, \tag{2.56}$$

where

$$F_1(\Omega) = \left(\frac{2-\Omega}{1-\Omega}\right)\ln(1-\Omega) + \frac{2\Omega}{1-\Omega} + \frac{\Omega^3}{6(1-\Omega)^2}, \tag{2.57}$$

and

$$F_2(\Omega) = \left(\frac{3-2\Omega}{1-\Omega}\right)\ln(1-\Omega) - \frac{\Omega}{2}\left(\frac{\Omega-6}{1-\Omega}\right). \tag{2.58}$$

It is possible to asses the accuracy of the low frequency approximations by comparing equation (2.55) with equation (2.37). In Figure 2.2 such a comparison is made for $\Omega = 0.95$, and indicates that the low frequency model is accurate up to approximately $\xi = 0.2$. As the porosity decreases, the accuracy of the low frequency approximation decreases, and for a porosity of 0.5 the approximation is accurate up to $\xi = 0.05$. However, for a typical fibrous absorbent, the restrictions translate to an upper frequency limit of approximately 5kHz, which would normally be rather higher than the upper limit of the frequency range of interest. The upper limit for ξ also translates to the value of unity for ζa. The splitting of the viscous and thermal effects causes some degree of inaccuracy in the range $1 \le \zeta a \le 10$ (see Tijdeman [32]), hence the use of the low frequency model places no restrictions upon the accuracy of results available.

2.7.1 Low Frequency Complex Density for a Single Pore

The low frequency complex density will first be written as a function of ζa; the steady flow resistivity will be introduced later. Approximations to the fourth order are maintained for the complex density. Substituting equation (2.55) into equation (2.13) and simplifying gives

$$\frac{\rho(\omega)}{\rho_0} = \frac{\Omega}{\ln(1-\Omega)+\Omega+\dfrac{\Omega^2}{2}}\left\{\frac{[\ln(1-\Omega)+1+2\Omega]\ln(1-\Omega)+\Omega+\dfrac{3\Omega^2}{2}+\dfrac{\Omega^3}{3}}{\ln(1-\Omega)+\Omega+\Omega^2/2}+\frac{4(1-\Omega)}{(\zeta a)^2}\right\}. \tag{2.59}$$

2.7.2 Low Frequency Bulk Modulus for a Single Pore

To obtain accuracy comparable to the complex density it is only necessary to approximate the bulk modulus to the second order. This approach was also used by Zwikker and Kosten [31]. Hence, substituting equation (2.56) into equation (2.26) gives

$$\kappa(\omega)=P_0\left\{1+\left(\frac{\gamma-1}{\gamma}\right)\frac{N_{pr}(\zeta a)^2}{4\Omega(1-\Omega)}\left[\ln(1-\Omega)+\Omega+\frac{\Omega^2}{2}\right]\right\}. \tag{2.60}$$

2.7.3 Low Frequency Bulk Acoustic Properties

The low frequency values for the complex density and the bulk modulus can be combined to give the bulk acoustic properties in the same manner as Section 2.5. The propagation constant and the characteristic impedance are therefore given by:

$$\frac{\Gamma}{k_0}=i\sqrt{\gamma q^2(\omega)}\left\{\frac{\Omega[\ln(1-\Omega)+1+2\Omega]\ln(1-\Omega)+\Omega^2+\frac{3\Omega^2}{2}+\frac{\Omega^4}{3}}{\left[\ln(1-\Omega)+\Omega+\Omega^2/2\right]^2}-\left(\frac{\gamma-1}{\gamma}\right)N_{pr}-i\frac{\Omega}{2\pi\xi q_0^2 s^2(\omega)}\right\}^{\frac{1}{2}},$$

and

$$\frac{z_a}{\rho_0 c_0}=\sqrt{\frac{q^2(\omega)}{\gamma\Omega^2}}\left\{\frac{\Omega[\ln(1-\Omega)+1+2\Omega]\ln(1-\Omega)+\Omega^2+\frac{3\Omega^2}{2}+\frac{\Omega^4}{3}}{\left[\ln(1-\Omega)+\Omega+\Omega^2/2\right]^2}+\left(\frac{\gamma-1}{\gamma}\right)N_{pr}-i\frac{\Omega}{2\pi\xi q_0^2 s^2(\omega)}\right\}^{\frac{1}{2}}.$$

(2.61), (2.62)

Section 2.8

Discussion

A parallel fibre model for sound propagation in rigid fibrous porous materials has been derived in this chapter. The approximation of the model to low frequencies has simplified predictions and has been shown to be acceptably accurate over the frequency range of interest. The dynamic tortuosity and dynamic pore shape factor have been added to the model to account for the random nature of the bulk fibrous material. The model in this chapter will now be compared with other theoretical models in order to asses their relative merits. First, in order to allow a straightforward comparison between models, the tortuosity and pore shape factor are set equal to unity across the frequency range. The inclusion of these quantities will be discussed later.

The parallel fibre model of Section 2.5 produces similar expressions to those of Burns [37] and Mechel [38,39], this was expected due to the similarity in approach. However, the low frequency model produced in Section 2.7 is very different from the low frequency model of Mechel [48]. This is somewhat surprising considering similar models were used; it is possible that the differences arise from different approximations for the Bessel and Neumann functions. It is interesting to compare the predictions of Section 2.7 with the low frequency predictions of Mechel [48], and also those of Attenborough [46], who produced a low frequency model using Rayleigh's approach. The more complex microstructure models, such as Attenborough's scattering model [36], do not lend themselves to straightforward comparison and are not considered here. Mechel [48] gives approximate expressions for the propagation constant and the characteristic impedance:

$$\frac{\Gamma}{k_0} = i\sqrt{\gamma}\left\{\frac{1}{\gamma} - i\frac{1}{2\pi\xi}\right\}^{\frac{1}{2}}, \qquad \frac{z_a}{\rho_0 c_0} = \frac{1}{i\gamma\Omega}\frac{\Gamma}{k_0}, \qquad (2.63), (2.64)$$

and the Rayleigh model gives

$$\frac{\Gamma}{k_0}=i\sqrt{\gamma}\left\{\left[\frac{4}{3}-\left(\frac{\gamma-1}{\gamma}\right)N_{pr}\right]-i\frac{\Omega}{2\pi\xi}\right\}^{\frac{1}{2}}, \qquad \frac{z_a}{\rho_0 c_0}=\frac{1}{\Omega\sqrt{\gamma}}\left\{\left[\frac{4}{3}+\left(\frac{\gamma-1}{\gamma}\right)N_{pr}\right]-i\frac{\Omega}{2\pi\xi}\right\}^{\frac{1}{2}}. \qquad (2.65), (2.66)$$

It is apparent that the major difference between the models is the real part within the square root. This term is directly related to the complex density and hence the viscous forces present in the pores. In equation (2.61) the term is a function of porosity, whereas Mechel and Attenborough do not predict this. For typical values of $\gamma = 1.4$ and $N_{pr} = 0.702$, Mechel predicts the real part of the square root to be equal to 0.714, whereas Attenborough predicts 1.133. Equation (2.61) predicts values varying from 0.8 ($\Omega \to 1$), to 1 ($\Omega \to 0$). This indicates that all three models will differ in their predictions, especially in the medium to low frequency range where the real and imaginary parts within the square roots are of similar magnitude.

The differences in the predictions for the viscous forces present can be examined by looking at the real part of the complex density. Equation (2.59) indicates that for a single pore at low frequencies the complex density is dependent on porosity only. In Figure 2.3, the real part of the complex density is plotted against porosity. It can be seen that in the limit $\Omega \to 1$ then $\rho(\omega) \to \rho_0$, i.e. as the fibre radius approaches zero, the viscosity effects disappear. As the porosity decreases, the real part of the complex density first increases rapidly and then begins to level off, eventually reaching a limiting value of 1.2 as $\Omega \to 0$. It is also noticeable that as $\Omega \to 1$ the differences between the model presented in this chapter and those of Attenborough and Allard and Champoux [43] increase significantly. Attenborough predicts the real part of the complex density to be 1.33, whilst Allard and Champoux predict approximately 1.25. Values for a number of pore shapes based on a Rayleigh type model also differ considerably (see Craggs and Hildebrandt [53]). The differences again indicate that predictions using a parallel fibre model will differ significantly from those of a Rayleigh type model.

The real part of the complex density can also be used to show the limitations in the bulk theoretical models which assume the tortuosity to be constant. Equation (2.59) shows that at low frequencies the real part of the complex density is independent of frequency, and other models such as those of Attenborough [46], Allard and Champoux [44] and Champoux and Stinson [47], also predict the same behaviour. However, the experimental data of Delany and Bazley [54] show strong frequency dependence across the low to medium frequency range examined by the models above. This effect can also be observed in the experimental data of Mechel [55] and the data in Chapter 3. These observations have led to the defining of a frequency dependent tortuosity in an attempt to model the behaviour of the density of air at lower frequencies more closely.

A significant use of the model developed in this chapter is to infer frequency dependent values for the dynamic tortuosity and pore shape factor from experimental data on porous media. To date, the tortuosity has been defined as constant, thus removing viscous effects in order to give the tortuosity physical meaning. This allows values for the tortuosity to be measured at effectively infinite frequencies (i.e. zero viscosity). Although Johnson et al. [42] define a dynamic tortuosity, their definition is different to the one employed in the present study. This is because Johnson et al. use the tortuosity as a surrogate for the complex density, whereas here the tortuosity and complex density are separated. Consequently, in the context of the present study, the frequency dependence obtained by Johnson et al. can be ascribed to the frequency dependent complex density and this is used in conjunction with a constant value for the tortuosity. Johnson et al. pointed out that their definition of tortuosity is in error for medium to low frequencies and the measurement of the characteristic length of a pore is also very difficult for random fibrous materials, especially at lower frequencies. Furthermore, if non-acoustical methods are used to measure the characteristic length, errors can occur since the acoustic characteristic length can often be different, especially in materials of widely varying pore radii. Effort has been concentrated in this chapter on producing a model from where the dynamic tortuosity can be inferred from simple acoustic measurements.

In this chapter the tortuosity has been defined as a real frequency dependent quantity. Therefore the tortuosity is linked here to the viscous effects present in the pores. At very high frequencies, the flow is effectively inviscid and the velocity profile is almost flat with an extremely thin viscous boundary layer. As the frequency is reduced, the velocity profile gradually becomes more nearly parabolic as the viscous boundary layer grows. Hence the thickness of the viscous boundary layer, and therefore the effective density of the air, increase as the frequency is reduced. This turns out to cause a corresponding increase in tortuosity as the frequency is lowered, evidence for this will be shown in Chapter 3. Eventually, the viscous boundary layer will fill the pore, causing the viscous effects and hence the tortuosity to reach a maximum. At this point the dynamic tortuosity is taken to equal the steady flow tortuosity introduced in Section 2.6. The assumed form for the tortuosity employed here departs from previous work, thus loosing the physical definition of tortuosity first described by Zwikker and Kosten [31]. The dynamic tortuosity can be thought of here as a phenomenological variable, introduced in order to improve agreement between theoretical models and experimental measurement

Once the tortuosity has been defined as real and frequency dependent, the same definition for the pore shape factor follows. This will be shown in the next chapter, in addition to calculating the pore shape factor directly from values obtained from the dynamic tortuosity. A dynamic pore shape factor was shown by Stinson and Champoux [45] to be necessary for the Rayleigh model, based upon its limiting behaviour at low and high frequencies. However, pore shape factors do not appear to have been included in published work on parallel fibre models. Also, it may be noted that a dynamic tortuosity has never been used in conjunction with a dynamic pore shape factor, for any type of model. Consequently, new values for the dynamic pore shape factor will be generated by the present model, and whilst they cannot be directly compared to those for the Rayleigh model it is anticipated that the results will be similar.

Finally, the definition for the dynamic tortuosity allows a consistent definition for the steady flow resistivity (see equation (2.49)). The steady flow resistivity is used to eliminate the fibre radius from the model, and is measured experimentally at low flow velocities where viscous forces predominate. This occurs when the real part of the complex density is a maximum, and hence a frequency independent value for the tortuosity must be used in equation (2.49) to ensure that the steady flow resistivity is also independent of frequency.

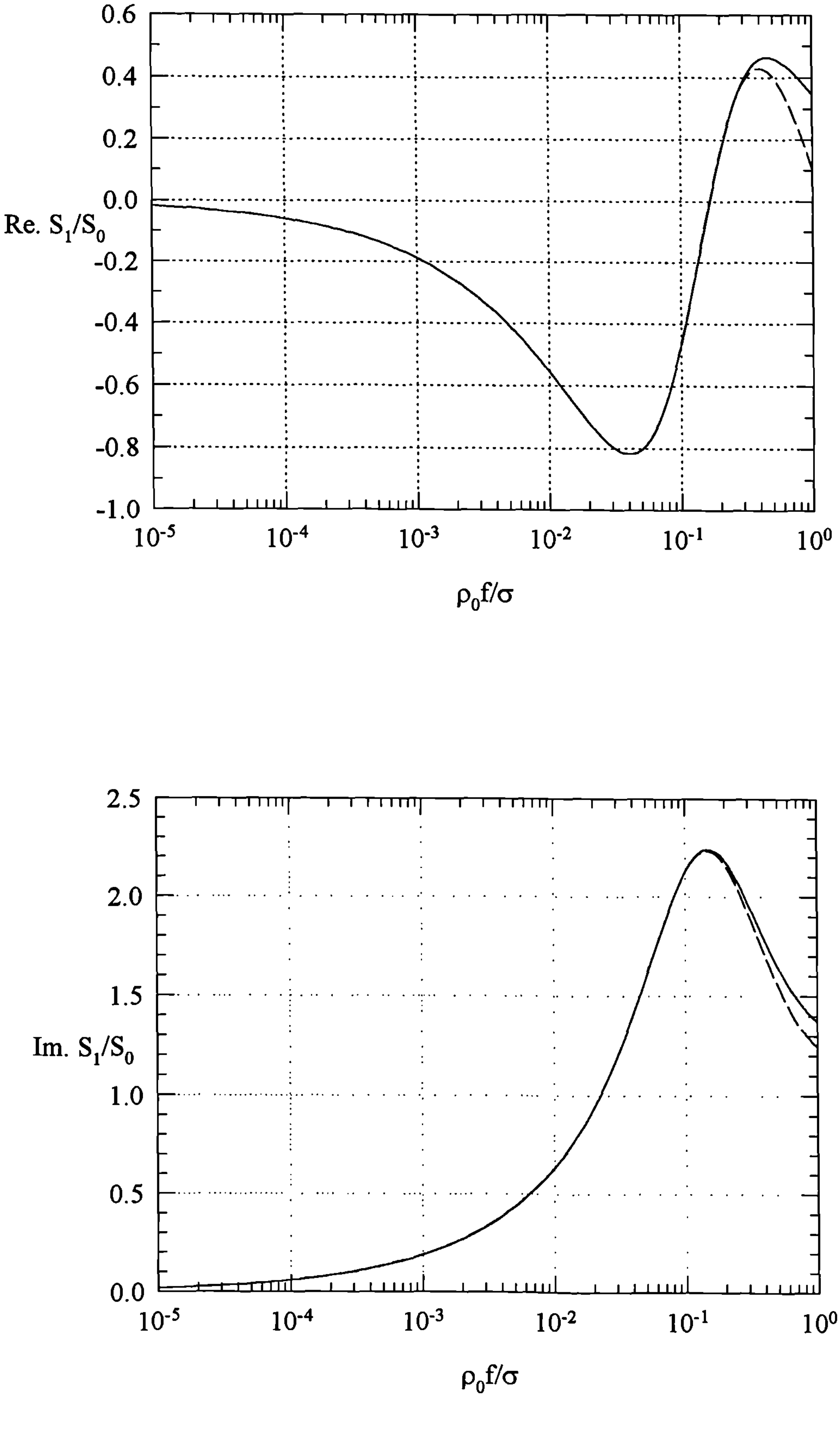

Figure 2.2. Comparison of approximate and exact expressions for S_1/S_0, for $\Omega = 0.95$.
—— , Full Bessel function expression; – – – , Low frequency approximation.

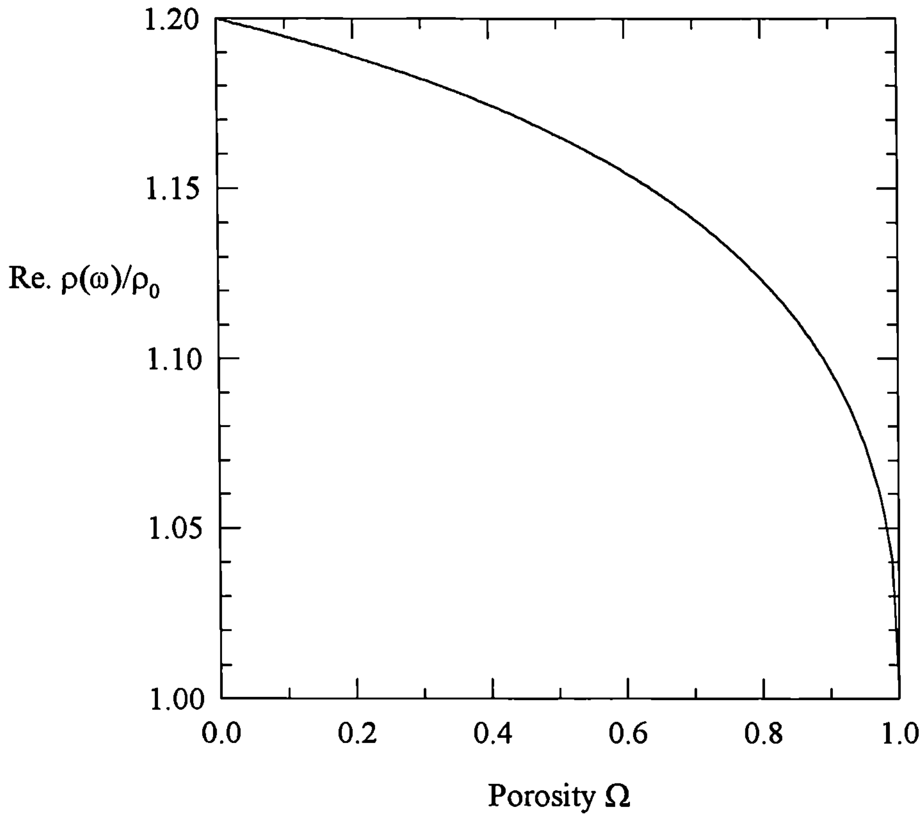

Figure 2.3. Complex density (Real) versus porosity.
——— , Complex density (real).

CHAPTER 3

MEASUREMENT OF THE BULK ACOUSTIC PROPERTIES OF RIGID FIBROUS MATERIALS, AND COMPARISON WITH EXPERIMENT

Section 3.1

Introduction

In the previous chapter a theoretical model was developed in order to predict the acoustic behaviour of porous materials. An alternative approach is to obtain predictions experimentally; this has the advantage of not being reliant upon the assumptions necessary in modelling of the microstructure of a porous material. However, it is not possible to extrapolate experimental data beyond that gathered by the experiment (see later discussion), and unfortunately the frequency range of data available solely from experiment is usually limited by the apparatus available. To overcome this problem, the experimental data obtained at the beginning of this chapter are used later on in this chapter to predict values for the dynamic tortuosity and dynamic pore shape factor (see previous chapter), and from here a full semi-empirical model is devised which provides predictions for the bulk acoustic properties over a much wider frequency range.

Early experimental measurements on porous materials concentrated on measuring the absorption coefficient. This allowed comparison with Rayleigh's theoretical predictions for the absorption coefficient [28]. However, as the use of impedance data became more important, effort began to concentrate on measurement of the surface impedance of porous materials, and these were performed by both Beranek [56] and Scott [57]. Scott proposed the use of a transmission line, or impedance tube, in which the porous material is positioned at one end of a closed tube. A plane sound wave, of discrete frequency, is set up at the other end of the tube, initiating a standing wave. The position and sound pressure level of the first maxima and minima are measured from the point where the surface of the material can be defined. From these measurements it is possible to infer the surface impedance of the material. A full description of the theory behind the impedance tube is given by Beranek [58]. Scott's method for measuring the surface impedance of a porous material quickly became widespread in use, and is still popular today.

Subsequent work has concentrated on measuring the more fundamental properties of a porous material, the propagation constant and the characteristic impedance. Scott's method has been used to calculate these properties directly (see Bies [59]) but this involves filling a long tube with material and assuming that no reflections occur from the rigid termination; the propagation constant and characteristic impedance are then measured by traversing a microphone within the sample. Obviously this method requires a large amount of material which is often unavailable; in addition, traversing the microphone within the material can often prove impracticable. Consequently, other methods have been devised which allow the bulk acoustic properties to be inferred from surface impedance measurements performed on small samples of material. Yaniv [60], following a suggestion by Zwikker and Kosten [31], first measured the surface impedance of a thin sample with a rigid backing, and then with a quarter-wavelength air gap behind the material. From the two sets of measurements the acoustic properties of the material were calculated. However, the method of Yaniv requires the air space depth to be changed at every discrete frequency, which can be a laborious task. Smith and Parrot [61] noticed that Yaniv effectively calculates the propagation constant and characteristic impedance by measuring two distinct impedances. They showed that the same results could be achieved by measuring two separate thicknesses of material, while Utsuno et al. [62] used two different air space depths behind the material. This removed the necessity to maintain a quarter-wavelength air gap behind the material and thus both methods have become popular for calculating the bulk acoustic properties.

The disadvantage of using discrete frequency measurements is the necessity to perform a number of measurements at each frequency. This is often a laborious and time consuming task. The advent of FFT analysers has allowed a method involving a broad-band random signal to be used; this allows data to be obtained quickly over a large frequency range. Seybert and Ross [63] first employed broad band noise using a special purpose impedance tube to perform the experiments. Chung and Blazer [64,65] also used a custom built tube and measured the transfer function between the acoustical pressure at two fixed locations in the tube. Fahy [66] later noticed that the standard impedance tube of Scott could be used to perform the broad-band tests of Chung and Blazer. This removed the need to build a special tube and also allowed the distance between the microphone positions to be altered, thus improving low and high frequency data. The broad-band noise tests offer a fast and accurate method of gathering surface impedance data, from which the acoustic properties are calculated in the same way as for the discrete frequency tests. However, the method does require expensive equipment, such as an FFT analyser, and also a PC.

Once the data for the porous materials have been measured, a method for plotting them is required. This is not a problem with surface impedance data as the impedance is simply normalised and plotted against frequency. However, although this method can be used for the acoustic properties (see Yaniv [60]), it is desirable to normalise the frequency axis as well. Delany and Bazley [54] used the steady flow resistivity of the material to normalise the propagation constant and characteristic impedance as a function of frequency divided by the steady flow resistivity. This allowed experimental data to be obtained for similar materials of differing densities, which can then be plotted on the same graph. Delany and Bazley found that data for different fibrous materials collapsed onto one curve, allowing the acoustic properties to be represented by simple power law relationships. The method of Delany and Bazley has become the most widely used method for presenting experimental data. Subsequent work has modified Delany and Bazley's approach to include the mean density of air by defining a non-dimensional frequency parameter ξ, (where $\xi = \rho_0 f / \sigma$, ρ_0 denoting mean fluid density, f denoting frequency and σ denoting steady flow resistivity). This corresponds to the frequency parameter in Chapter 2, thus allowing easy comparisons between theory and experiment to be made.

In order to present the acoustic properties in the manner of Delany and Bazley, one must measure the steady flow resistivity of the material. This is a simple and well established experiment (see Zwikker and Kosten [31] and Beranek [58]) and involves measuring the pressure drop across a known thickness of material for a range of flow rates. Before the advent of Delany and Bazley's method, the steady flow resistivity was measured for use in predictive theoretical models, but it has now become an important parameter for the presentation of experimental data as well.

This chapter concentrates upon measurement of the bulk acoustic properties of four fibrous materials commonly found in exhaust silencers; "E glass", "A glass", basalt wool and stainless steel wool. The experimental measurement of the acoustic properties is relatively straightforward and well understood, however it was pointed out by Delany and Bazley [54] that the curve-fitting method cannot be relied upon to provide predictions outside the range of measured data. Consequently, a semi-empirical model is developed later in this chapter which is intended to combine the best aspects of the theoretical and experimental approaches. The two approaches are linked through the use of the dynamic tortuosity and dynamic pore shape factor discussed in the previous chapter. This is done by using experimental data to predict the dynamic tortuosity and dynamic pore shape factor, and then substituting back into the theoretical model of Chapter 2, defining the acoustic properties in continuous form across a range of $0 \leq \xi \leq 1$.

Section 3.2

Experimental Method

Measurements of the propagation constant and the characteristic impedance were performed using an impedance tube similar to that used by Scott [57]. The surface impedance was also measured by using Scott's method because the apparatus required to perform broad-band measurements was not available at the time. In addition, Scott's method is well understood, and although tedious in implementation, a high degree of accuracy and confidence in the results is expected. The propagation constant and characteristic impedance of the material have been calculated by measuring the surface impedance of two distinct impedances; one where the material has a rigid backing, and the other with an arbitrary air gap behind the material. This is a combination of the methods of Yaniv [60] and Utsuno et al. [62]. Experience has shown that this method works best with relatively high flow resistivity materials such as fibre glass and mineral wools.

The standing wave tube used for the measurements is shown in Figure 3.1. The probe microphone is free to traverse the tube, its position being recorded by a ruler. The sound pressure level meter is used to determine the position of the maxima and minima of the standing wave; the FFT analyser then provides accurate readings for the frequency and sound pressure level. The size of the tube restricts the frequency bandwidth over which meaningful results can be obtained to approximately 150Hz to 2kHz. The bulk acoustic properties are given by

$$\Gamma = \frac{1}{2L} \ln\left\{ \frac{z_1/z_a + 1}{z_1/z_a - 1} \right\}, \tag{3.1}$$

and

$$z_a = \left[\rho_0 c_0 (z_2 - z_1) \coth(ik_0 l) + z_1 z_2 \right]^{\frac{1}{2}}, \tag{3.2}$$

where z_1 is the normal surface impedance of the sample with a rigid backing, z_2 is the normal surface impedance of the sample with an air space between the sample and the backing plate, L is the thickness of the sample and l is the depth of air space (note that l must avoid integer multiples of a half wavelength).

The air space behind the absorbent was achieved by locating the sample in a container with a retractable base (see Figure 3.1). Because of the bulk fibrous nature of the material it was found necessary to hold the sample in place with a wire gauze. The wire used in the gauze was approximately 0.5mm in diameter and the gauze had a percentage open area of approximately 45%, consequently the gauze used was effectively acoustically transparent. A small (1mm) step was machined into the inside wall of the container, allowing the wire gauze to be located. The acoustic effects caused by the area change in the container, whilst small, were included in the calculations. It was found by trial and error that optimum values for the thickness (or density) of sample and depth of air gap existed, outside which the surface impedance data suffered from large errors, especially at frequency extremes. A material thickness of 50mm was found to work well, along with air gaps ranging from approximately 25 to 40mm.

It is desirable to measure data over as wide a range of ξ as possible since this will improve the accuracy of the curve fitting formulae employed by Delany and Bazley [54]. Since the frequency range available for measuring data is limited by the size of the tube, it is necessary to use a range of values for the steady flow resistivity. This was carried out by manually compressing the samples in order to increase their density, a similar approach to that used by Delany and Bazley. Obviously there is a limit to how much it is possible to compress the material and an upper limit on the bulk density worked out to be approximately 180 kg/m^3. It was found that when different densities of material were used the experiment often shifted away from its optimum set up. This reduced the accuracy of the surface impedance results and the re-setting of the air gap was often found necessary in order to return to an optimum set up.

The steady flow resistivity was measured by passing a metered air flow along a tube (see Figure 3.2). The porous sample was located at one end with one side being open to atmospheric pressure. The pressure drop across the sample was measured using a manometer. The steady flow resistivity is given by the Ergun equation [30],

$$-\nabla\bar{p} = \sigma\bar{V} + \eta\bar{V}\left|\bar{V}\right|, \tag{3.3}$$

where $\nabla\bar{p}$ is the pressure drop across a sample of length L, V is the volume flow rate of air, σ is the steady flow resistivity, η is the steady inertial flow resistivity and the bar denotes a steady value. A plot of $\Delta\bar{p}/LV$ against V will give an intercept of σ and a slope of η. The samples were manually compressed in the same manner as the impedance tube tests, allowing the steady flow resistivity to be expressed as a function of the bulk density of the material.

Section 3.3

Experimental Results

The experimental data obtained for the four fibrous materials are given in this section. The bulk acoustic properties are plotted in the format of Delany and Bazley [54] since this method has been shown to be the most effective way of presenting the data, this will also allow straightforward comparisons to be made with other published data and theoretical predictions. It follows therefore that the steady flow resistivity must be measured first.

3.3.1 Steady Flow Resistivity

The steady flow resistivity, in units of Ns/m^4 (MKS rayls/m), is plotted against the bulk density of the material in Figure 3.3. A curve fitting procedure has been used in order to write the steady flow resistivity as a function of bulk density, i.e.

$$\sigma = A_1 \rho_b{}^{A_2}, \tag{3.4}$$

where ρ_b is the bulk density of the porous material and A_1 and A_2 are constants given in Table 3.1 below

Table 3.1. Regression Coefficients for the Steady flow resistivity

	A Glass	E Glass	Basalt Wool	Steel Wool
A_1	1.857	5.774	3.012	0.312
A_2	1.687	1.792	1.761	1.615

It is noticeable from Figure 3.3 that on a log-log scale, the empirical curve is a straight line, this relationship has also been observed by other authors [54,55,59,67].

The gradient of each curve also appears to be similar to that observed by other authors, for example, Bies [59] quotes a slope of 1.72 for steel wool and 1.67 for glass fibres. Mechel [55], in a study on numerous fibrous materials, quotes values ranging from 1.4 to 1.65. Both sets of results are close to the values of 1.615 for steel wool, 1.687 for A glass and 1.792 for E glass measured here. It is also evident that the empirical curves fit the experimental data well. The extrapolation of data outside the range of experimental values is possible for the steady flow resistivity, though in most cases this is not necessary.

It is of interest to study the effect of the fibre radius upon the steady flow resistivity. The measurement of an effective fibre radius for a random material such as those studied here is very difficult. Figure 3.4 shows the distribution profiles of the fibre diameters for each material quoted by the manufacturer [68], from which it is obvious that the fibre radius can vary quite significantly. This was confirmed by examining the materials under a scanning electron microscope; indeed an even wider range in fibre diameter than those quoted by the manufacturer was observed. This is the major reason for eliminating the fibre radius from theoretical models. However, even though an accurate value for the fibre diameter cannot be measured, the values shown in Figure 3.4 do indicate that the steady flow resistivity is dependent upon the fibre diameter. It appears that as the average fibre diameter decreases, the steady flow resistivity increases. This relationship was predicted by Bies and Hanson [67], who showed that for a material of uniform fibre diameter, the steady flow resistivity is directly related to the fibre diameter. Consequently, the variation of the steady flow resistivity with fibre diameter is an important aspect in the design of materials used in exhaust silencers, and explains why a wide range of material is used.

3.3.2 Bulk Acoustic Properties

The bulk acoustic properties can now be written as functions of the steady flow resistivity in the manner suggested by Delany and Bazley [54]. Delany and Bazley used the following empirical formulae to predict the propagation constant and characteristic impedance:

$$\Gamma = \alpha + i\beta, \qquad z_a = r_a + ix_a, \qquad (3.5), (3.6)$$

where

$$\frac{\alpha}{k_0} = a_1 \xi^{a_2}, \qquad \frac{\beta}{k_0} = 1 + a_3 \xi^{a_4}, \qquad (3.7), (3.8)$$

and

$$\frac{r_a}{\rho_0 c_0} = 1 + a_5 \xi^{a_6}, \qquad \frac{x_a}{\rho_0 c_0} = -a_7 \xi^{a_8}. \qquad (3.9), (3.10)$$

The dimensionless frequency parameter ξ is used here, where $\xi = \rho_0 f / \sigma$, and $a_1 .... a_8$ are the regression coefficients derived from the curve fitting process. The data obtained for A glass are shown in Figure 3.5 along with the empirical curves from equations (3.5) and (3.6). In order to reduce the amount of data plotted here, the experimental results for the other materials are included later, in conjunction with the final semi-empirical model. The regression coefficients measured for each material are given in Table 3.2 below.

Table 3.2. Regression Coefficients for the Bulk Acoustic Properties

	A Glass	E Glass	Basalt Wool	Steel Wool
a_1	0.2251	0.2202	0.2178	0.1540
a_2	-0.5827	-0.5850	-0.6051	-0.7093
a_3	0.1443	0.2010	0.1281	0.1328
a_4	-0.7088	-0.5829	-0.6746	-0.5571
a_5	0.0924	0.0954	0.0599	0.0877
a_6	-0.7177	-0.6687	-0.7664	-0.5557
a_7	0.1457	0.1689	0.1376	0.0876
a_8	-0.5951	-0.5707	-0.6276	-0.7609

The "quality" of data obtained for the bulk acoustic properties can be studied by measuring the coefficient of multiple determination (R_e^2) and the standard error of the estimate (σ_e), see Al-Khafaji and Tooley [69]. Table 3.3 gives these values for the four materials measured; a perfect fit occurs when $R_e^2 \to 1$ and $\sigma_e \to 0$.

Table 3.3. Quality of Fit for Regression Formulae

	A Glass		E Glass		Basalt Wool		Steel Wool	
	R_e^2	σ_e	R_e^2	σ_e	R_e^2	σ_e	R_e^2	σ_e
α/k_0	0.994	0.017	0.995	0.018	0.997	0.013	0.995	0.018
β/k_0-1	0.947	0.056	0.991	0.023	0.995	0.018	0.943	0.052
$r_a/\rho_0 c_0-1$	0.927	0.078	0.984	0.036	0.981	0.039	0.900	0.066
$-x_a/\rho_0 c_0$	0.981	0.029	0.989	0.026	0.994	0.018	0.976	0.042

The best correlation of data appears for the real part of the propagation constant (α), this is because α is the easiest quantity to measure accurately. The data for the imaginary part of the characteristic impedance (x_a) also exhibits a similar high degree of accuracy. The two quantities which suffer the most scattering of data are the imaginary part of the propagation constant (β) and the real part of the characteristic impedance (r_a). Both quantities have one subtracted from them before the log is taken, and this has the effect of exaggerating experimental errors which partially explains the higher degree of scatter. It is also known that r_a is inherently the most difficult quantity to measure accurately, and this fact leads to the largest errors occurring for this quantity. The trend in observed scatter for the data shown can also be seen in other published results such as those of Delany and Bazley. It is noticeable that the scatter in the data is more pronounced for materials of a lower flow resistivity, most notably steel wool. It is possible that this can be explained by the experimental procedure used. A material of low flow resistivity has a relatively large fibre diameter and consequently a flat surface is harder to achieve in the impedance tube, thereby introducing errors into the measurements. However, it is more likely that the method used, especially for steel wool, was not the most appropriate. More accurate results may have been possible by using two different thicknesses of material in order to calculate the acoustic properties. Unfortunately this would have involved rebuilding the material holder, and since steel wool is only of secondary importance, this was not carried out. However, the scattering of data for all the materials is relatively small and the curve fitting formulae of Delany and Bazley do provide satisfactory predictions.

Numerous experimental data exists for all types of porous materials. It is useful to compare the predictions in Table 3.2 with those of Delany and Bazley [54] and Mechel [55], since they both carried out extensive measurements on fibrous materials. The regression coefficients quoted by Delany and Bazley and Mechel are given in Table 3.4 below.

Table 3.4. Previously Published Regression Coefficients for Fibrous Materials.

	Delany and Bazley	Mechel		
		Rock Wool	Basalt Wool	Glass Fibre
a_1	0.189	0.235	0.231	0.199
a_2	-0.595	-0.578	-0.557	-0.615
a_3	0.098	0.123	0.103	0.095
a_4	-0.700	-0.669	-0.682	-0.720
a_5	0.057	0.044	0.047	0.020
a_6	-0.754	-0.763	-0.715	-0.928
a_7	0.087	0.135	0.137	0.104
a_8	-0.732	-0.636	-0.605	-0.701

The data in Table 3.4 show good correlation with the data in Table 3.2 . It should be noted that the data of Delany and Bazley were obtained for numerous different materials and collapsed onto one curve, whilst Mechel measured the materials individually. Consequently, direct comparison between the results of Delany and

Bazley and those of Table 3.2 is not advisable. This is principally due to the large number of materials measured by Delany and Bazley, allowing a larger envelope of ξ values to be used. Experience has shown that the curve fitting coefficients can vary significantly with changes in the range of ξ values measured. Unfortunately, as previously discussed, measurements can only be performed over a limited range of ξ for individual materials. Therefore, in order to achieve a more meaningful comparison with Delany and Bazley, all the experimental data for the four materials can be combined on to one plot and the regression coefficients calculated. This allows data to be plotted over a range of $0.0025 \leq \xi \leq 2$. The regression coefficients are given in Table 3.5 below.

Table 3.5. Regression Coefficients for Combined Data from the Four Materials	
$a_1 = 0.1742$	$a_2 = -0.6570$
$a_3 = 0.1344$	$a_4 = -0.6770$
$a_5 = 0.0847$	$a_6 = -0.6903$
$a_7 = 0.1039$	$a_8 = -0.7009$

It is apparent that the regression coefficients are now closer to those of Delany and Bazley. It is also evident that the results for an individual material are different to those for a combination of materials, although the differences observed are not large; it is felt however, that using data for individual materials is more representative of their actual behaviour. For each material, the comparison between the results in Table 3.2 and those of Mechel in Table 3.4 show good correlation and indicate that the experimental results obtained in this section are reliable. Consequently, for maximum accuracy the measurement of data for individual materials is necessary and it is not sufficient to rely on Delany and Bazley's data.

The major disadvantage associated with using the method of Delany and Bazley is that the formulae cannot be extrapolated outside the range of experimental data. This does not cause any problems in the high frequency range, since by varying the bulk density of the material data can be obtained up to approximately 5kHz. Problems occur at low frequencies, especially below about 120Hz, since varying the bulk densities of the material was not sufficient to provide experimental data for low values of ξ. The lack of data at small values of ξ becomes even more acute if the formulae are used to predict the acoustic properties at high temperatures. Christie [70] has shown that the steady flow resistivity increases with an rise in temperature, thus causing values of ξ for a similar frequency to fall well outside the range of measured data. Therefore, a method for predicting the bulk acoustic properties at low frequencies (or low values of ξ) is necessary in order to provide a full range of data. The next section will show how the theoretical model of Chapter 2 can be used in conjunction with the experimental data presented here to provide a full set of predictions for the bulk acoustic properties.

Section 3.4

Implementation of the Semi-Empirical Model

A model is described in this section which uses the theory of Chapter 2 in order to predict values for the dynamic tortuosity and dynamic pore shape factor using the experimental data shown previously. In order to do this it is helpful to split up the bulk acoustic properties into the complex density and bulk modulus, in the manner described in Chapter 2. This will also allow the problems associated with extrapolating experimental data to be clearly seen. The experimental predictions for the bulk complex density and bulk modulus are calculated by combining equations (2.32) and (2.33) to give

$$[\Gamma z_a]_{\mathrm{EXPT.}} = i\omega\rho_b(\omega) \quad \text{and} \quad [z_a/\Gamma]_{\mathrm{EXPT.}} = \kappa_b(\omega)/i\omega. \qquad (3.11), (3.12)$$

The bulk complex density and bulk modulus can now be written as

$$\frac{\rho_b(\omega)}{\rho_0} = -i\left[\frac{\Gamma}{k_0}\frac{z_a}{\rho_0 c_0}\right]_{\mathrm{EXPT.}} \quad \text{and} \quad \frac{\kappa_b(\omega)}{P_0} = i\gamma\left[\frac{k_0}{\Gamma}\frac{z_a}{\rho_0 c_0}\right]_{\mathrm{EXPT.}}, \qquad (3.13), (3.14)$$

from which the experimental values can be compared with the theoretical predictions of equations (2.29) and (2.30). The bulk complex density and bulk modulus calculated using the experimental data of Delany and Bazley [54] and also that obtained for the combination of four materials (see Table 3.5) are shown in Figure 3.6. Theoretical predictions for $\rho_b(\omega)$ and $\kappa_b(\omega)$ have also been included in Figure 3.6, employing the full Bessel functions in equations (2.13), (2.26) and (2.50) and a dynamic tortuosity and dynamic pore shape factor of one. The empirical formulae fitting the experimental data have been extrapolated to lower values of ξ in order to show why they cannot be relied upon at low frequencies. It is obvious from Figure 3.6 that the empirical predictions do not make any physical sense below about $\xi = 0.01$. This is apparent when the real part of the complex density and the imaginary part of the bulk modulus become negative. Obviously it is not possible to have an effective density of air in the pores less than the mean density of air. Furthermore, in the low frequency limit the bulk modulus must reach the isothermal value of P_0, which is a purely real quantity. These are strong physical reasons for not extrapolating experimental data and this leads to the requirement for theoretical predictions at low values of ξ.

The empirical predictions for the real part of the complex density are of particular interest here. An increase in the real part of the complex density occurs when the frequency is reduced, and this eventually reaches a maximum value. Such behaviour was also predicted in Chapter 2, based upon the behaviour of the viscous boundary layer in the pores of the material. Consequently it is assumed here that the empirically predicted data are invalid once the real part of the complex density attains a positive slope and at this point, the theoretical model must be used on its own.

The comparison between the theoretical and empirical predictions in Figure 3.6 show good correlation except for the real part of the complex density. This is also the case for the semi-empirical model of Allard and Champoux [44]. Chapter 2 described how the dynamic tortuosity can be used to improve the predictions for the bulk complex density. It is obvious from equation (2.29) that the dynamic tortuosity can be inferred from the bulk complex density and used to fit the theoretical model exactly to the experimental data. This semi-empirical approach can be used in the region of the experimental data, for frequencies below the point where the real part of the complex density becomes a maximum, beyond which the theoretical model is used on its own with the tortuosity set to a constant value. Values for the dynamic tortuosity can be calculated by multiplying equations (2.33) and (2.34) together to give

$$\frac{\Gamma}{k_0}\frac{z_a}{\rho_0 c_0} = i\frac{q^2(\omega)}{\Omega}\frac{\rho(\omega)}{\rho_0}. \tag{3.15}$$

The substitution of a theoretical expression for $\rho(\omega)$ into the right hand side of equation (3.15), and experimental data into the left hand side, allows the dynamic tortuosity to be inferred. Therefore, substituting the low frequency prediction for $\rho(\omega)/\rho_0$ from equation (2.59), and using equation (2.50), gives

$$\left[\frac{\Gamma}{k_0}\frac{z_a}{\rho_0 c_0}\right]_{\text{EXPT.}} = \frac{q^2(\omega)}{2\pi\xi q_0^2 s^2(\omega)} + iq^2(\omega)\left\{\frac{\left[\ln(1-\Omega)+1+2\Omega\right]\ln(1-\Omega)+\Omega+3\Omega^2/2+\Omega^3/3}{\left[\ln(1-\Omega)+\Omega+\Omega^2/2\right]^2}\right\}. \tag{3.16}$$

It is noticeable from equation (3.16) that the dynamic tortuosity has been separated from the dynamic pore shape factor in the imaginary part of the equation. This allows for the independent calculation of the dynamic tortuosity; values of the pore shape factor then follow from the real part of equation (3.16). This separation is only possible when the low frequency model is used because the pore shape factor is present within the argument of the Bessel functions in the full model, preventing separate explicit expressions being obtained. This is an important reason for using the low frequency model. Equating the real and imaginary parts of equation (3.16) gives

$$q^2(\omega) = \frac{\left[\left(1+a_3\xi^{a_4}\right)\left(1+a_5\xi^{a_6}\right)-a_1 a_7\xi^{(a_1+a_8)}\right]\left[\ln(1-\Omega)+\Omega+\Omega^2/2\right]^2}{\left[\ln(1-\Omega)+1+2\Omega\right]\ln(1-\Omega)+\Omega+3\Omega^2/2+\Omega^3/3}, \tag{3.17}$$

and

$$s^2(\omega) = \frac{q^2(\omega)}{2\pi\xi q_0^2} \frac{1}{\left[a_1\xi^{a_2}\left(1+a_5\xi^{a_6}\right)+a_7\xi^{a_8}\left(1+a_3\xi^{a_4}\right)\right]}, \tag{3.18}$$

where $a_1....a_8$ are the regression coefficients calculated in the previous section. Equations (3.17) and (3.18) are the principal results of this chapter. It is now possible to substitute the predictions for $q^2(\omega)$ and $s^2(\omega)$ into equations (2.61) and (2.62) to give a full description for the bulk acoustic properties.

In Chapter 2, the dynamic tortuosity and dynamic pore shape factor were assumed to be real and frequency dependent. Equations (3.17) and (3.18) show these assumptions to be correct. As mentioned in the previous chapter, this is in contrast to the work of Johnson et al. [42], who define a tortuosity which is independent of frequency. The difference between the two predictions occurs because different definitions for the tortuosity have been used, this is apparent in the differing form taken by the momentum equation in Chapter 2 compared to that used by Johnson et al.

The calculation of the dynamic tortuosity from equation (3.17) is relatively straightforward given the porosity of the material. The porosity is given by $\Omega = 1-\rho_s/\rho_b$, where ρ_s is the solid density of the fibre. The predictions for the dynamic tortuosity do however require the assignment of a maximum value at an appropriate point on the ξ axis. In Figure 3.6 the dynamic tortuosity is plotted on the same axes as the real part of the complex density and a maximum value can be seen to occur at approximately $\xi = 0.01$ for Delany and Bazley's formulae. At this point $q^2(\omega)$ is set equal to q_0^2, the steady flow tortuosity. Once this point has been manually defined, the dynamic pore shape factor can be found from equation (3.18). Again, at the same point on the ξ axis (see the real part of $\rho(\omega)$), the pore shape factor is set to a maximum value. Figure 3.7 shows how this method can be used to provide more accurate predictions for the complex density and the bulk modulus. It can be seen that the predicted values for the real and imaginary parts of the complex density exactly match Delany and Bazley's empirical formulae across the range of ξ measured by them. The values found for $q^2(\omega)$ and $s^2(\omega)$ which were used to achieve the new predictions are plotted on the same axes as the real part of the complex density. When the predictions shown in Figure 3.7 are compared with those in Figure 3.6, it is evident that the predictions for the bulk modulus have also been improved across the range of experimental data obtained by Delany and Bazley. It is also noticeable that in the low frequency limit the correct physical behaviour can be observed.

The method previously described can now be applied to the four fibrous materials measured earlier on in this chapter. The predictions for the bulk complex density and bulk modulus were calculated after assigning values to $q^2(\omega)$ and $s^2(\omega)$ for each material, the results of which are shown in Figures 3.8 to 3.11. As before, the values calculated for the dynamic tortuosity and dynamic pore shape factor are plotted on the same axes as the real part of the complex density. It is noticeable from Figures 3.8 to 3.11, that only the experimental data for steel wool reaches a maximum value for the real part of the complex density. This causes problems in assigning where the maximum values for the tortuosity should appear for the other materials. It is anticipated that this problem has occurred because data have not been obtained over a wide enough range of ξ to produce accurate regression formulae. It is noticeable that the data of Delany and Bazley and that of Table 3.5, both of which contain a wide range of data, do achieve maximum values. Also, there is a lack of data for low values of ξ (where the material was compressed as much as possible), causing errors in the curve fitting procedure in this region. It is also possible that at such values of ξ the experimental approach is inappropriate for the very high flow resistivities and low frequencies. It is expected that the problems encountered with the complex density are caused by the experimental procedure and that a maximum value for the real part of $\rho(\omega)$ does exist but has not been measured for every material. Indeed, the measurement of other individual materials not mentioned here, have shown maximum values for the real part of the complex density.

The point at which a maximum value for the real part of the complex density is assigned for the materials measured in this chapter has been based on Delany and Bazley's results, i.e. at approximately $\xi = 0.01$. However the results for steel wool do show that some consideration of the material's steady flow resistivity is also necessary.

Therefore, E glass has been assumed to reach a maximum at the highest value of ξ, next basalt wool and then A glass. A list of the values assigned to q_0^2, along with the point upon the ξ axis where $q^2(\omega) = q_0^2$, are given in Table 3.6 below.

Table 3.6. Values for the Steady Flow Tortuosity					
	Delany and Bazley	A Glass	E Glass	Basalt Wool	Steel Wool
ξ	0.011	0.025	0.005	0.0079	0.079
q_0^2	2.13	3.77	5.49	2.91	1.44

High gradients in the tortuosity have been avoided since this will lead to 'kinks' in the bulk modulus, and hence the bulk acoustic properties, when $q^2(\omega)$ is set equal to q_0^2.

The values obtained in Table 3.6 have been determined purely by inspection of the real part of the complex density. However, partial justification for the values determined for q_0^2 can be gained by examining the average fibre radius of the materials. Whilst it has been discussed how difficult it is to assign an average fibre radius to a material, it is interesting to see if the values predicted by equation (2.49) are close to the manufacturer's quoted range of fibre radii. Table 3.7 gives the range in fibre radius quoted by the manufacturer for each material (see also Figure 3.4), the steady flow resistivity for a typical bulk density of 130 kg/m^3 and the porosity.

Table 3.7. Average Fibre Radius for Materials			
	$a(\mu\mathrm{m})$	σ(rayls/m)	Porosity
E Glass	5-13	35,454	0.948
A Glass	18-26	6,839	0.948
Basalt Wool	6-18	15,904	0.954

The fibre radius is given by equation (2.49), i.e.

$$a^2 = -\frac{4\mu q_0^2}{\sigma} \frac{(1-\Omega)}{\left[\ln(1-\Omega)+\Omega+\Omega^2/2\right]}. \tag{3.19}$$

Substituting q_0^2 from Table 3.6 gives predictions for the fibre radii of

Table 3.8. Predicted Average Fibre Radii	
	$a(\mu m)$
E Glass	19.0
A Glass	36.6
Basalt Wool	19.2

The values predicted for the fibre radius are all of the correct order, but tend towards the high side of the measured radii. However, Attenborough [71], in examining his scattering theory also predicted a fibre radius that was too high. Attenborough pointed out that the larger fibre radii have lower contributions to the bulk attenuation, hence the distribution of the fibre radii is also important. This leads to the observation that the effective acoustic fibre radius is different to the measured mean fibre radius. Consequently, predictions from equation (3.19) cannot be expected to be close to the measurements, and even if an accurate value for the average fibre radius was known, it could not be used to predict q_0^2. However, when one takes into account this effect, the differences are not great and do seem to verify the approach used and the values obtained for q_0^2.

The assignment of where the real part of the bulk complex density reaches a maximum defines $q^2(\omega)$, q_0^2 and $s^2(\omega)$. This allows the full semi-empirical model to be implemented using equations (2.61) and (2.62). Figures 3.12 to 3.15 show the predictions obtained for the bulk acoustic properties using the semi-empirical model, compared with experimental data. These are the final results for the semi empirical model.

Section 3.5

Discussion

The semi-empirical model described in the previous section provides excellent agreement with the experimental data measured for all four materials. It is evident from Figures 3.12 to 3.15 that the predictions are virtually coincident with the regression formulae across the entire range of experimental data. Predictions have now been provided for lower values of ξ, and the correct physical behaviour is observed in the low frequency limit. The model also has the advantage of providing a continuous prediction across a range of $0 \leq \xi \leq 1$, removing the need to jump between experiment and theory.

It appears from Figures 3.12 to 3.15 that the semi-empirical model works best when the scatter of experimental data is small. This is apparent with the predictions for E glass, where all the curves are very smooth. Basalt wool, and especially A glass, suffer from a higher degree of scattering and A glass can be observed to have a definite kink in predictions. Steel wool does not suffer from a "kink" in predictions because the real part of the complex density reaches a maximum, however the curves are more undulating than for the other materials and tend not to fit the experimental predictions as well. Steel wool highlights the penalties associated with using the low frequency model outside its range of validity. It is evident from Figure 3.15 that although predictions for α and x_a are extremely good, problems occur in predicting r_a. The real part of the characteristic impedance shows the semi empirical model beginning to approach $-\infty$ as $\xi \rightarrow 2$. This cautions against using the model outside the range $0 \leq \xi \leq 1$. An alternative approach for $\xi > 1$ is to employ the full Bessel function model with $q^2(\omega) = s^2(\omega) = 1$. This avoids singularities in the middle range of ξ values, but will obviously suffer from the inaccuracies mentioned in Chapter 2. It is of course possible to revert back to using the regression formulae at higher values of ξ where the extrapolation of data is possible without introducing irrational predictions. However, the problems discussed here only occur for materials with a very low steady flow resistivity such as steel wool, and since steel wool is only of secondary importance, the semi empirical model does appear to be satisfactory.

A method for inferring the dynamic tortuosity and dynamic pore shape factor from acoustic measurements alone has been shown in this chapter. This is in agreement with Zwikker and Kosten [31], who first introduced the tortuosity and stated that it must be measured by acoustic means. Zwikker and Kosten went on to predict tortuosity values ranging from 3 to 7. A wide range of values for the tortuosity have since been quoted by numerous authors and a range of 1 to 10 appears to be representative for fibrous materials. Unfortunately, since all corresponding work has defined a frequency independent tortuosity, measured at effectively infinite frequencies, one cannot draw direct comparisons with previous work in the present study. Nevertheless, it appears that the values obtained for the tortuosity in Section 3.4 are acceptable. Comparing the results for the pore shape factor is more of a problem, since values depend upon the model used. The parallel fibre models mentioned in Chapter 2 [37,38,39] do not include pore shape factors, however for other models such as Allard and Champoux's [44], a range of 0.1 to 10 is quoted, whilst for the Rayleigh model values between 0.5 and 2 are thought to be acceptable [45]. In the literature, various arguments have been put forward for any number of different values for the tortuosity and pore shape factor. The values obtained in the previous section seem well within an acceptable range, however deciding what is not acceptable is almost as difficult.

The results in Table 3.6 indicate that a material of high porosity suffers from a high tortuosity. However, both types of glass wool have identical porosity but differing tortuosities, therefore the fibre radius must also be taken into account. This indicates that the tortuosity increases with a decrease in fibre radius. Beranek [72] predicted a variation of tortuosity with bulk density (or porosity), however the effects of the fibre radius were omitted.

The purpose behind producing the semi-empirical model has been to overcome the disadvantages present in previous models. The low frequency model of Mechel [48] has often been used to provide predictions outside the range of experimental data. However, even with the data of Delany and Bazley, a jump between the regression formulae and the predictions of Mechel is inevitable and this is obviously an undesirable aspect of the model. Mechel [73] attempted to remove the problems associated with jumping between experimental and theoretical formulae by modifying Delany and Bazley's regression coefficients until a smooth transition was ensured. Unfortunately this will result in the accuracy of the empirical formulae being reduced and it was noticeable that for the materials measured here the reduction in accuracy was often unacceptable. Allard and Champoux [44] also attempted to remove the problem of jumping from experiment to theory and they did this by employing a semi-empirical model, but as for Mechel's model, accuracy in the region where experimental data are available was sacrificed. This problem becomes more apparent when individual materials are examined. The method of Allard and Champoux can be improved by measuring values for their dynamic tortuosity, though this requires the measurement of the characteristic length of a pore which is very difficult.

To show the benefits of the new model, comparisons are made here with the models of both Allard and Champoux and Mechel. In order to provide a meaningful comparison between the low frequency predictions of Chapter 2 and those of Mechel (see equations (2.63) and (2.64)), the tortuosity and pore shape factor are both set equal to unity. Both models are compared in Figure 3.16 along with the regression formulae of Delany and Bazley, assuming a porosity of 0.95. The formulae of Delany and Bazley have been extrapolated in order to show how the predictions differ below $\xi = 0.01$. It is obvious from Figure 3.16 that although identical parallel fibre models were originally used, the two sets of predictions are different; this is particularly true at higher value of ξ. The biggest difference occurs for the real part of the characteristic impedance since Mechel's model predicts values tending to minus infinity as ξ approaches 0.1 whereas the new model is valid up to approximately 2. The differences are probably caused by the use of more accurate approximations for the Bessel functions in Chapter 2. The new model avoids singularities in the region $0 \leq \xi \leq 1$ and appears to be closer to experimental values across the frequency range. However, it is obvious that both models are not accurate enough to be used on their own and using either model in conjunction with experimental curves will involve a jump between the two.

The model of Allard and Champoux is capable of producing more accurate predictions than the low frequency models discussed previously. Allard and Champoux's model is compared with the full Bessel function predictions here ($q^2(\omega) = s^2(\omega) = 1$), since both models are valid over the entire range of ξ. Figure 3.17 shows a plot of both models alongside the formulae of Delany and Bazley. As before, the predictions at low values of ξ are very similar. At higher values of ξ, the predictions are still close to each other but Allard and Champoux offer a slight improvement as $\xi \to 1$ (the point where the theoretical model of Chapter 2 is in error). The accuracy has been improved over the low frequency models, though neither method is close enough to the empirical formulae to allow a complete substitution of the theoretical models in place of experimental data. As before, it is possible to use the predictions in conjunction with experimental data but a jump is again inevitable.

Finally, the inclusion of the dynamic tortuosity and dynamic pore shape factor into the model of Chapter 2 is shown in Figure 3.18. It is apparent that this approach provides the most accurate predictions. The results are very close to the data of Delany and Bazley across the entire range of experimental data. As the predictions are so close, the semi empirical model can be used to replace the regression formulae. It can also be seen that a smooth continuous curve has been obtained.

The extrapolation of the data of Delany and Bazley shows the difference in predictions obtained when the correct physical limits are applied at low values of ξ. It is evident that for the models described here, when the tortuosity and pore shape factor are included, the predictions differ significantly especially at low values of ξ; this places great importance the accurate measurement of these two quantities.

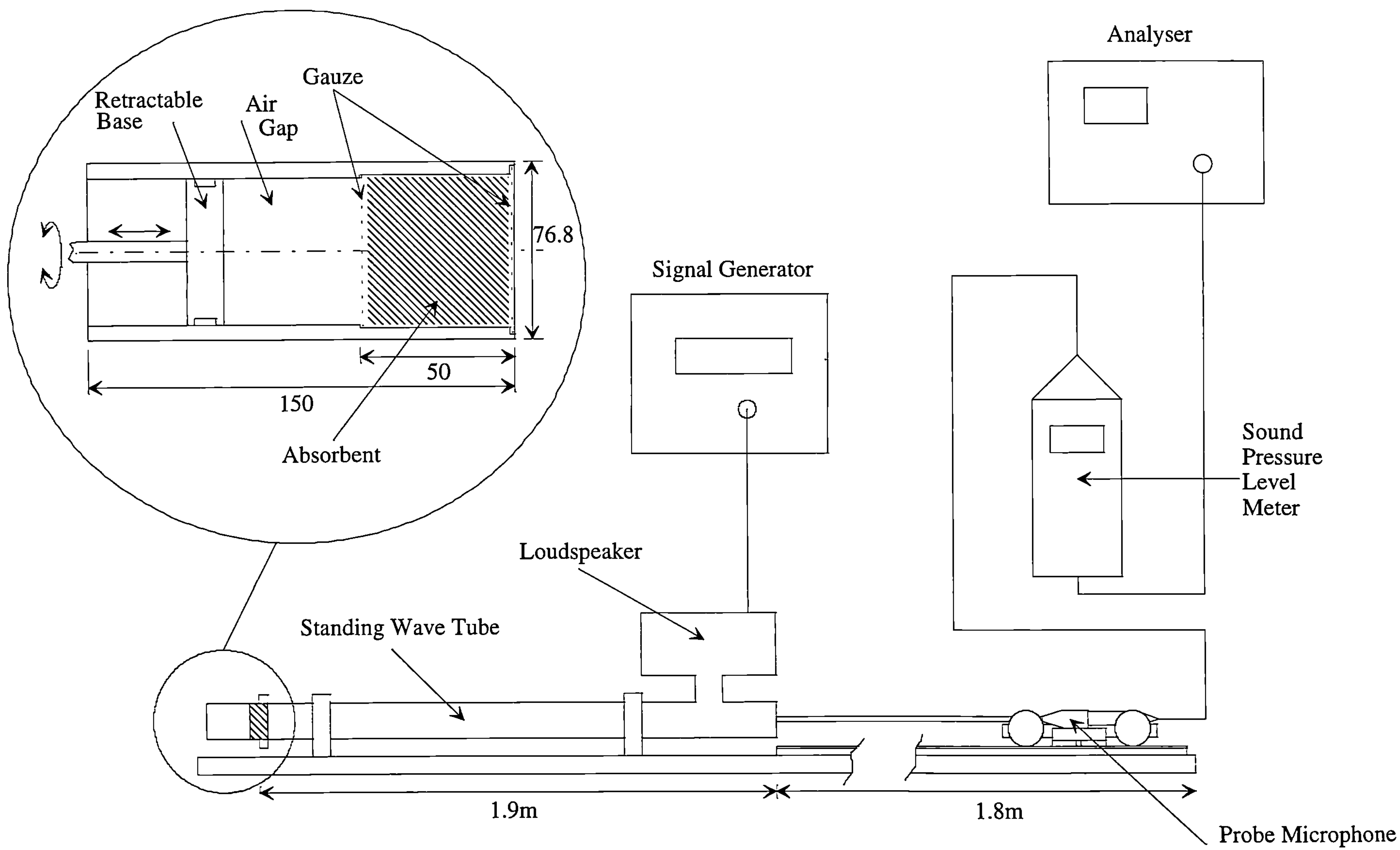

Figure 3.1 Standing Wave Tube Apparatus

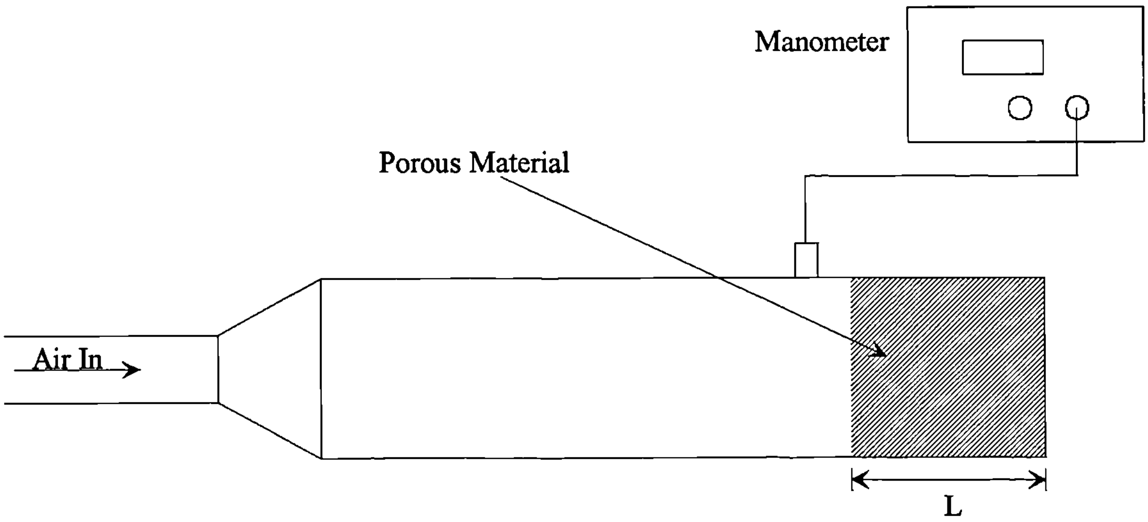

Figure 3.2. Flow Resistance Aparatus

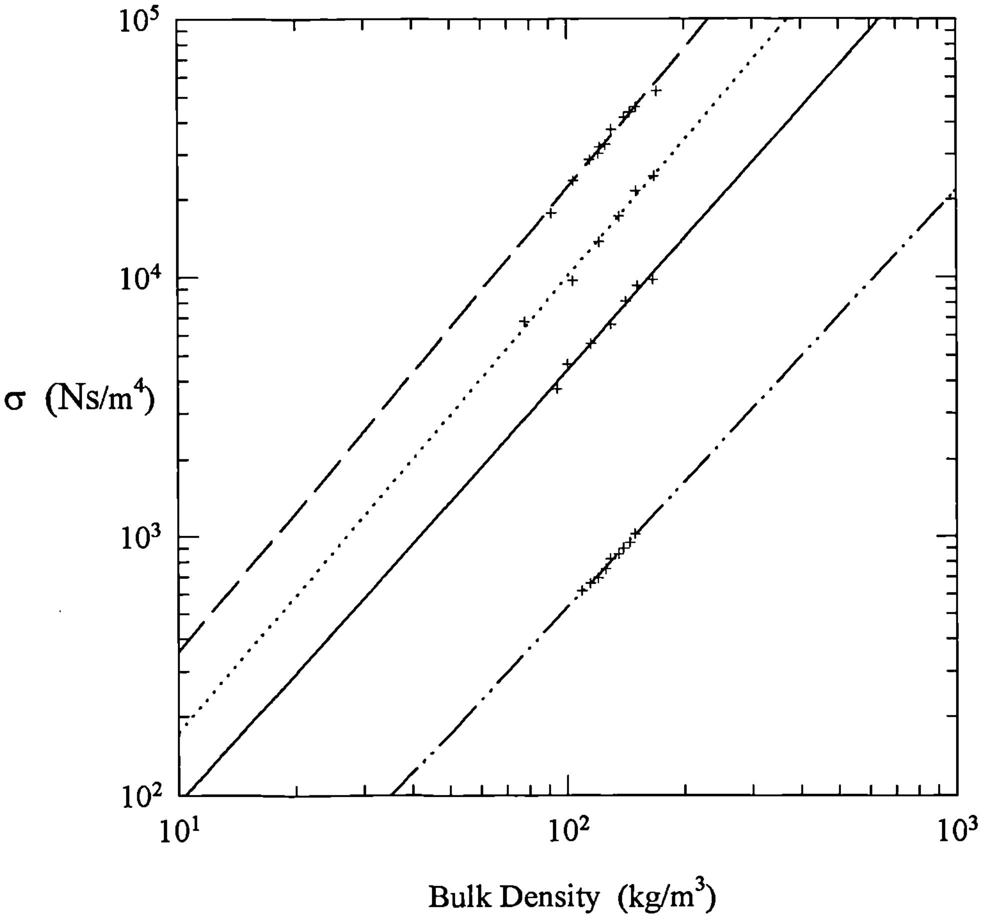

Figure 3.3. Regression curves for the steady flow resistivity.
+ , Experimental Data; ——— , A Glass; — — , E Glass; —·—·— , Steel Wool. ········ , Basalt Wool;

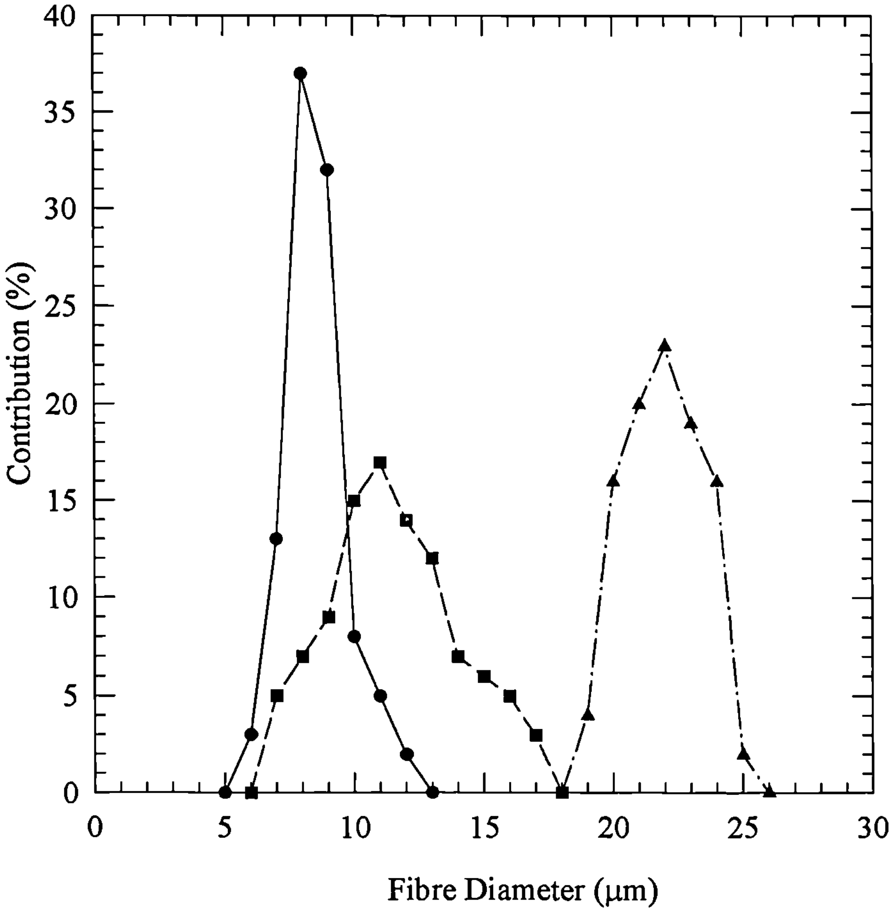

Figure 3.4. Fibre diameter distribution profiles. —●— , E Glass; —■— , Basalt Wool; —▲— , A Glass.

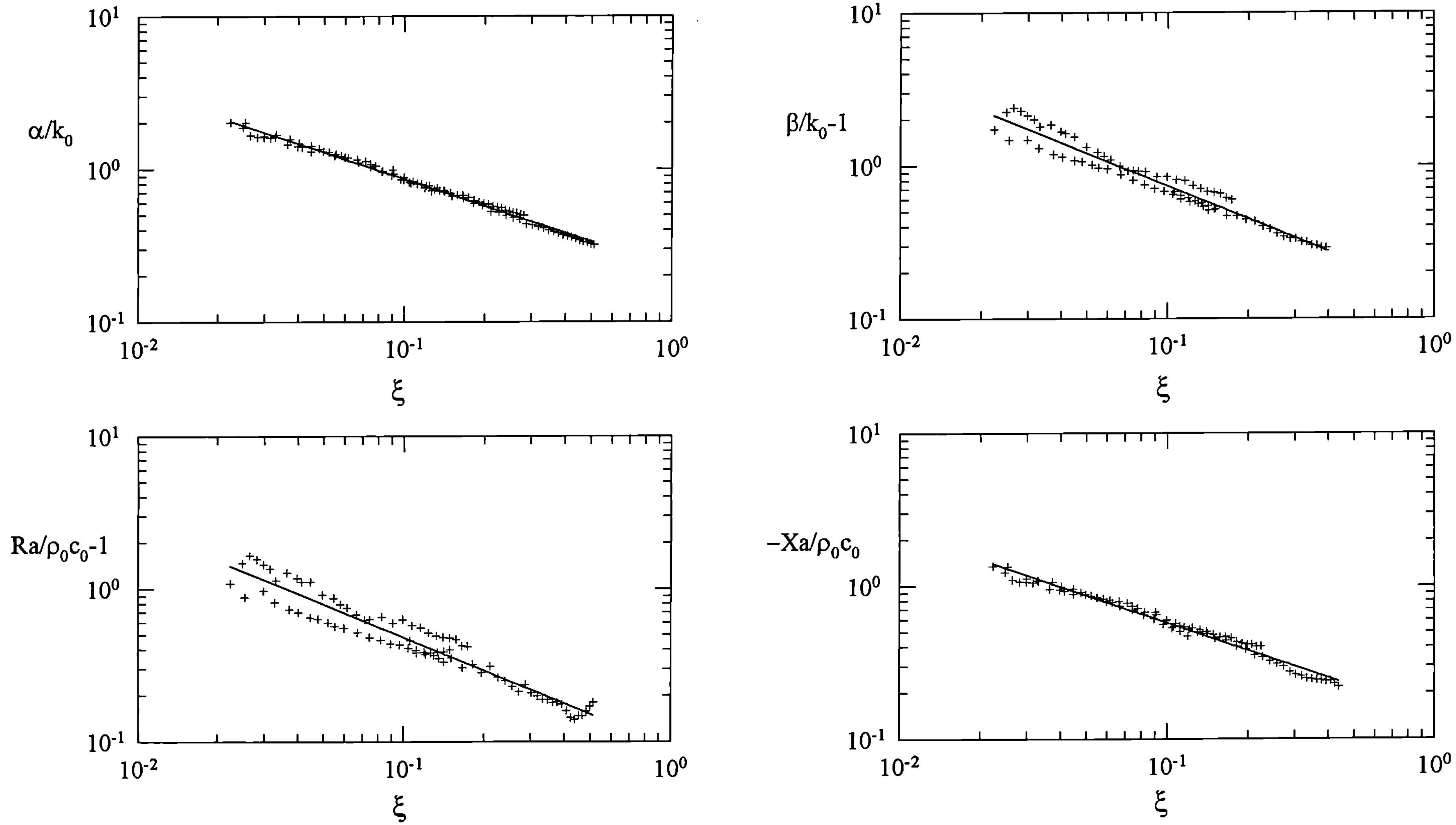

Figure 3.5. Bulk Acoustic Properties for A Glass. + , Experimental Data; —— , Delany and Bazley Formulae.

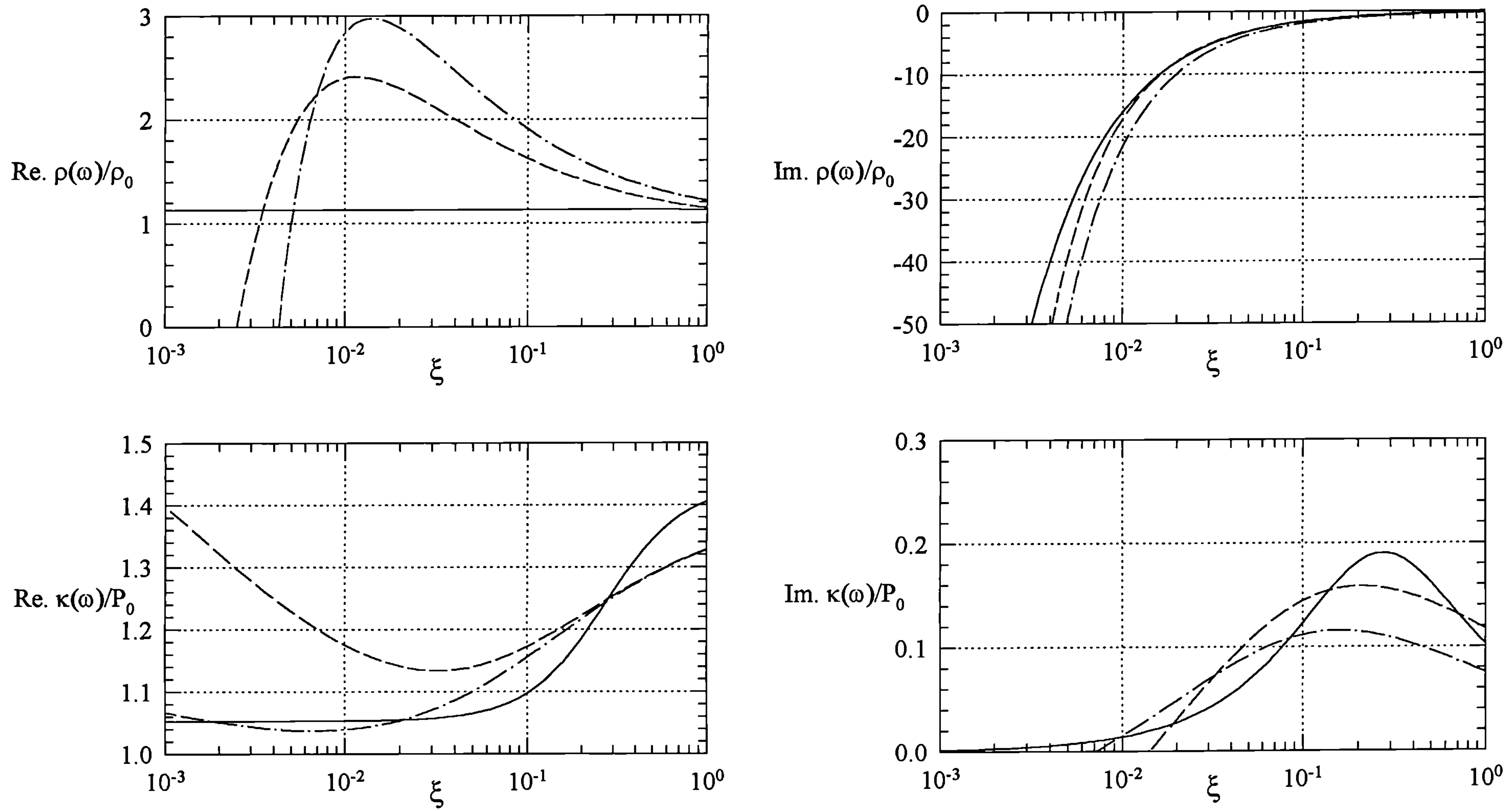

Figure 3.6. Bulk complex density and bulk modulus; — — —, Delany and Bazley data; —·—, Data from Table 3.5; ———, Full Bessel function model ($q^2(\omega) = s^2(\omega) = 1$).

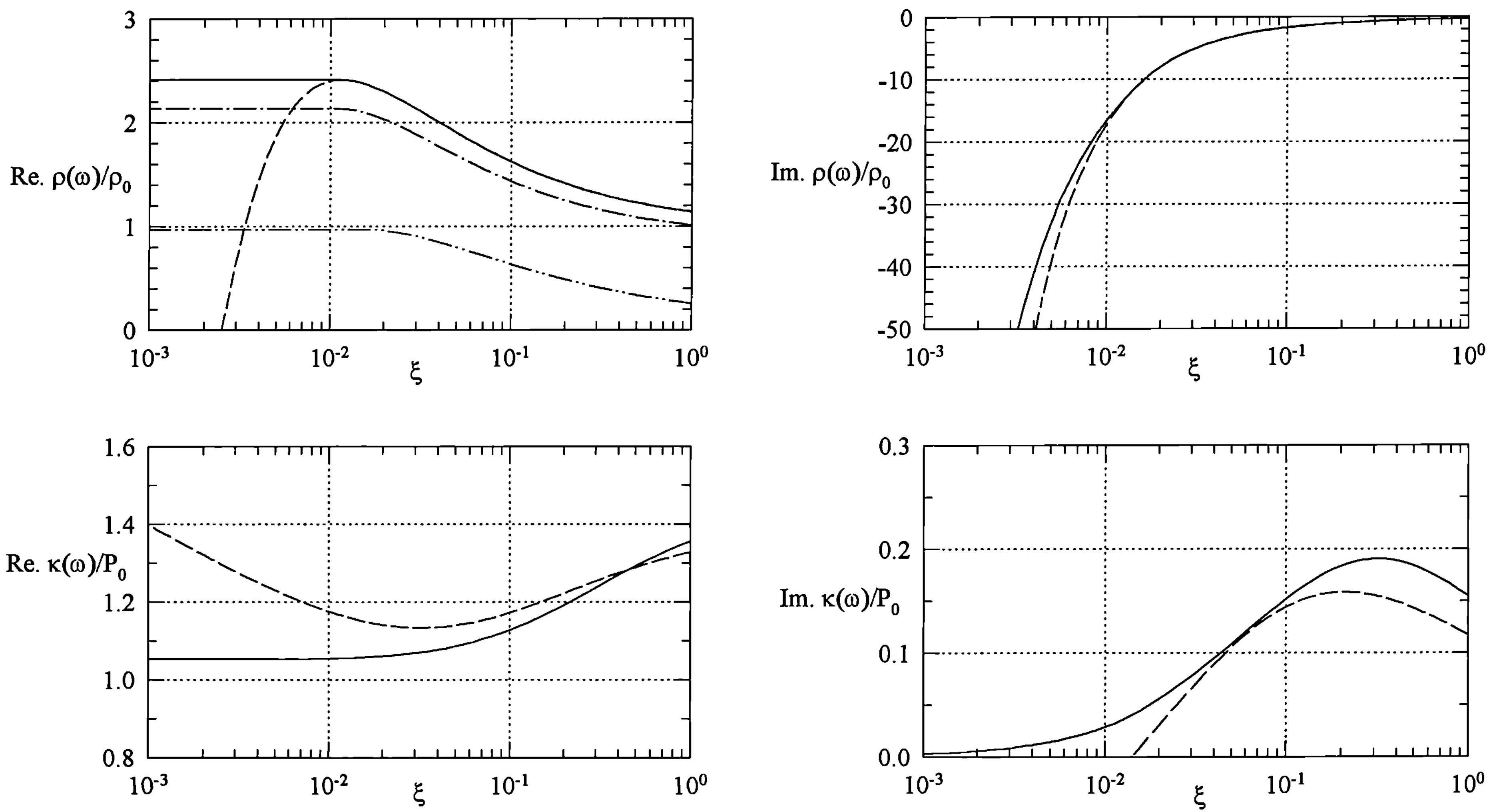

Figure 3.7. Predictions for the complex density and bulk modulus using $q^2(\omega)$ and $s^2(\omega)$. ——— , Theoretical predictions; – – – , Delany and Bazley predictions; —·— , Dynamic tortuosity; —··— , Dynamic pore shape factor.

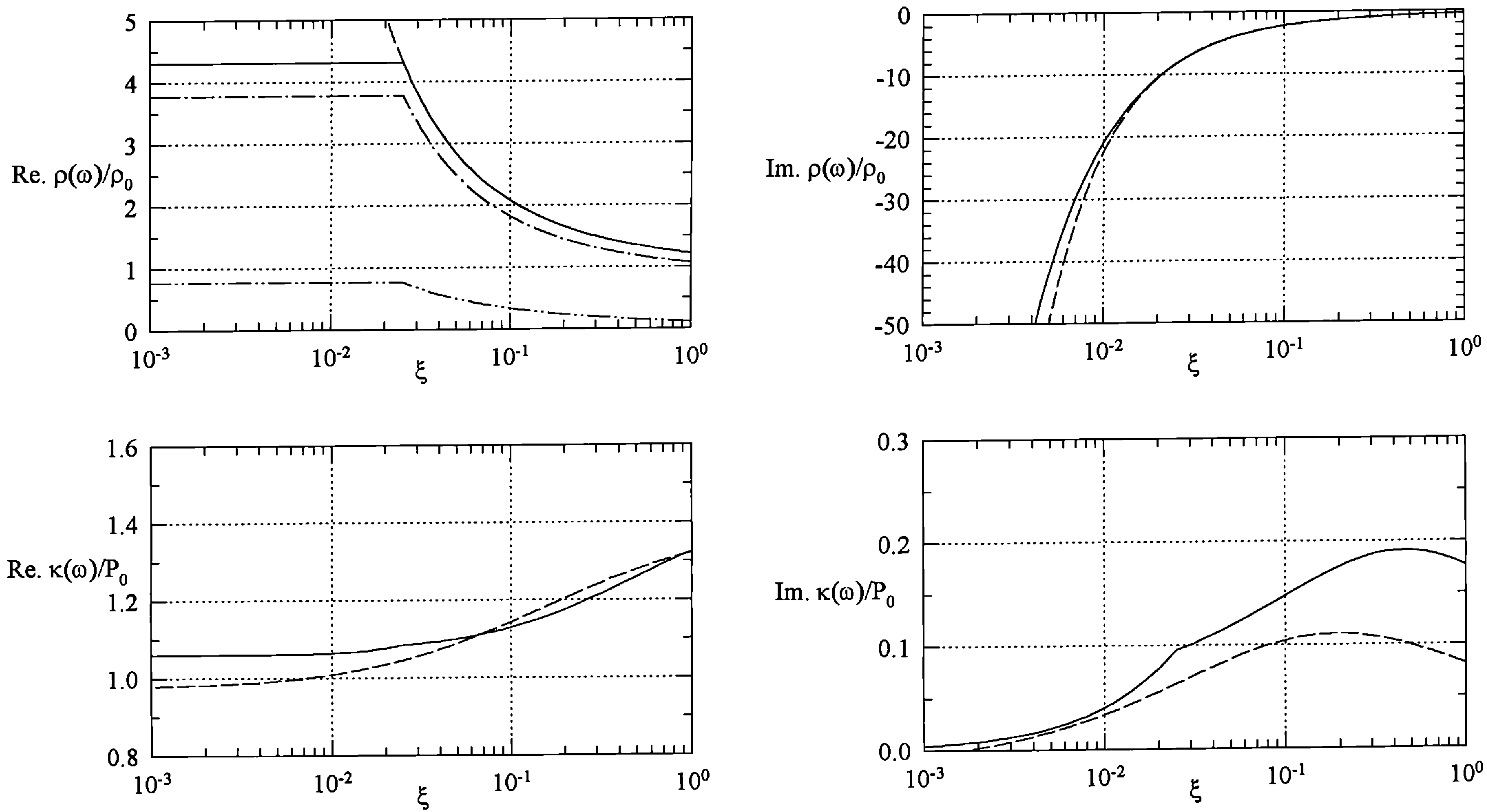

Figure 3.8. Bulk complex density and bulk modulus for A glass. — — —, Experimental data; ———, Theoretical predictions; —·—, Dynamic tortuosity; —··—, Dynamic pore shape factor.

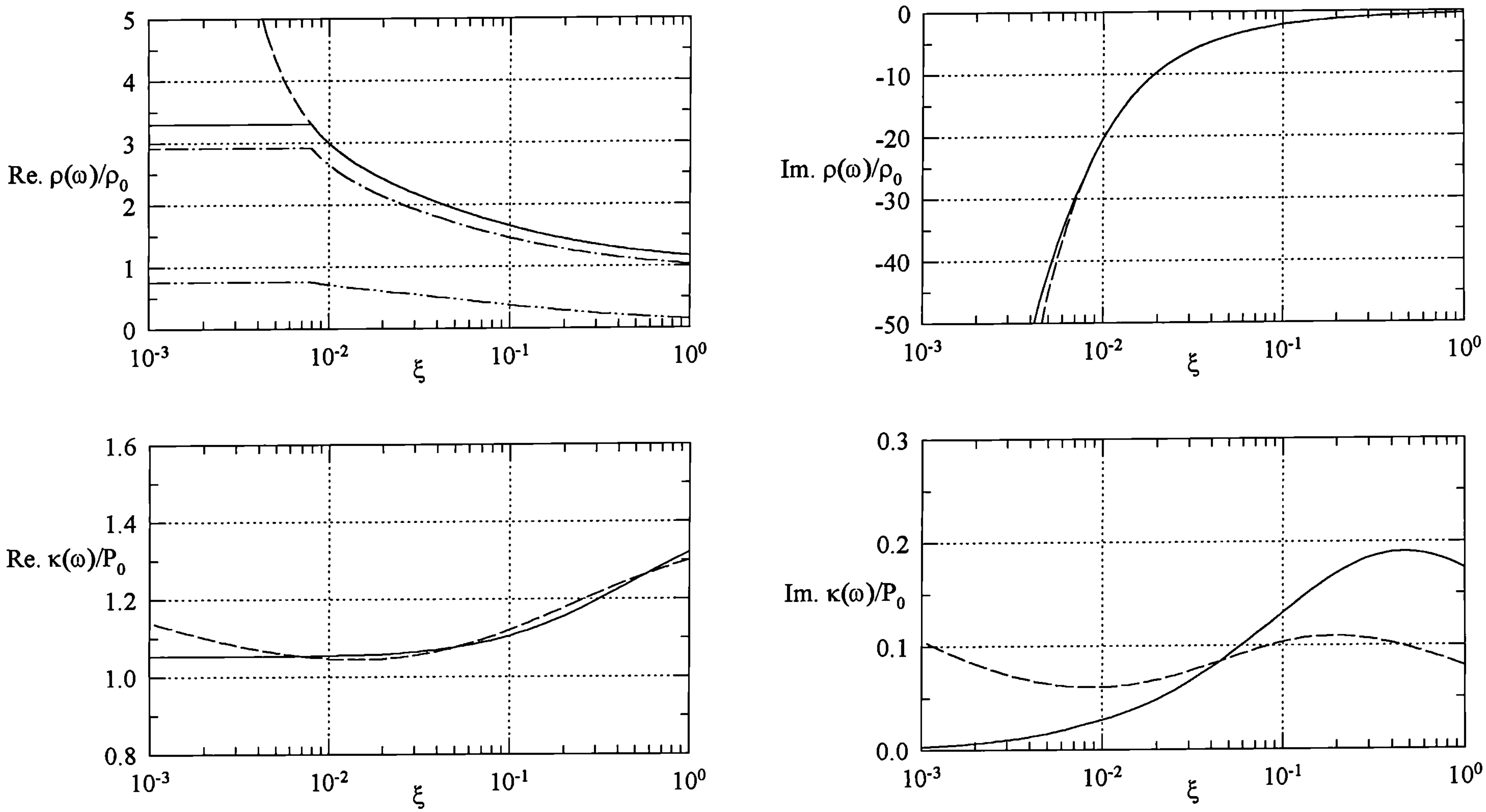

Figure 3.9. Bulk complex density and bulk modulus for basalt wool. — — —, Experimental data; ——, Theoretical predictions; —·—, Dynamic tortuosity; —··—, Dynamic pore shape factor.

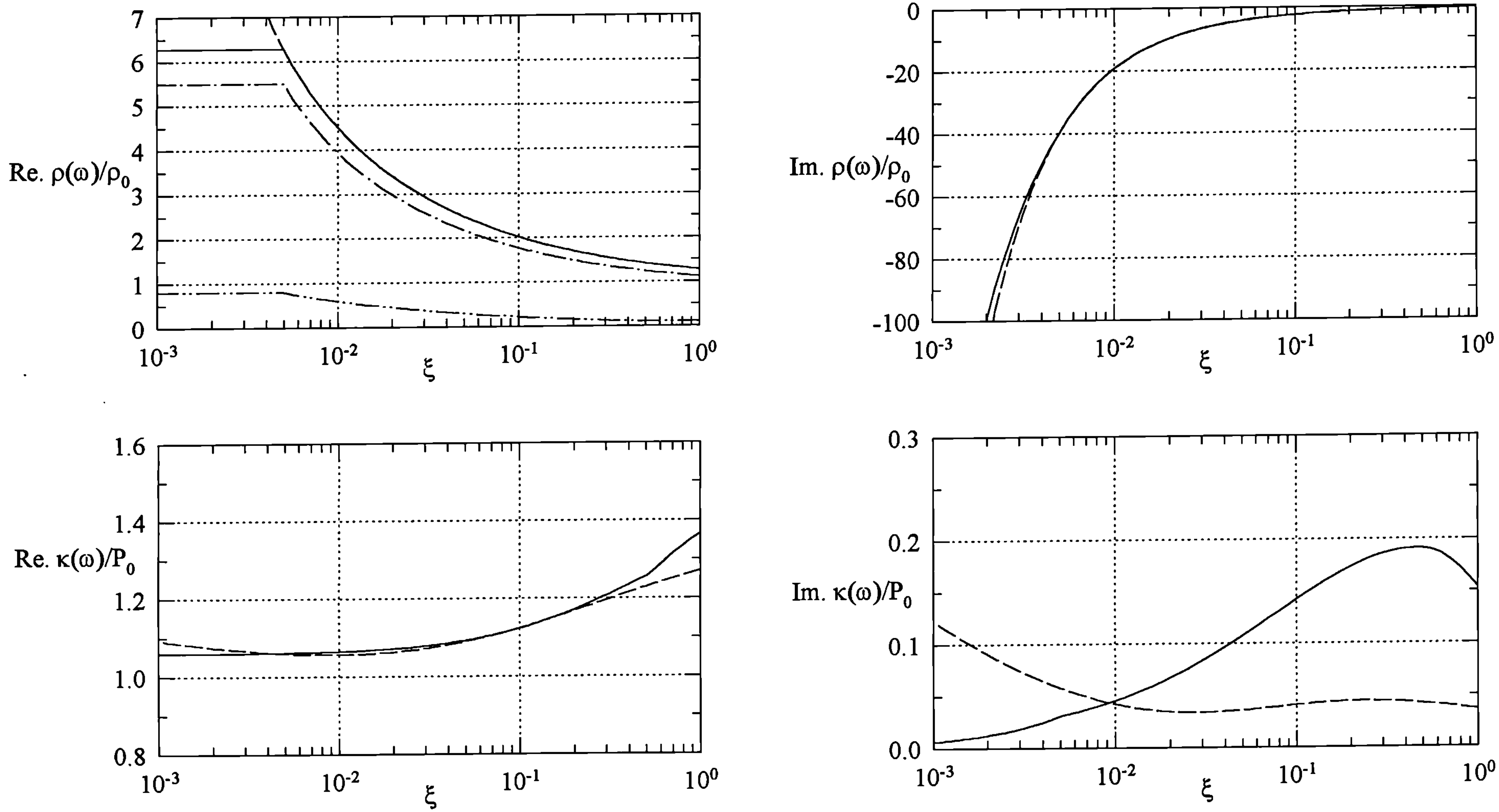

Figure 3.10. Bulk complex density and bulk modulus for E glass. — — — , Experimental data; ——— , Theoretical predictions; —·— , Dynamic tortuosity; —··— , Dynamic pore shape factor.

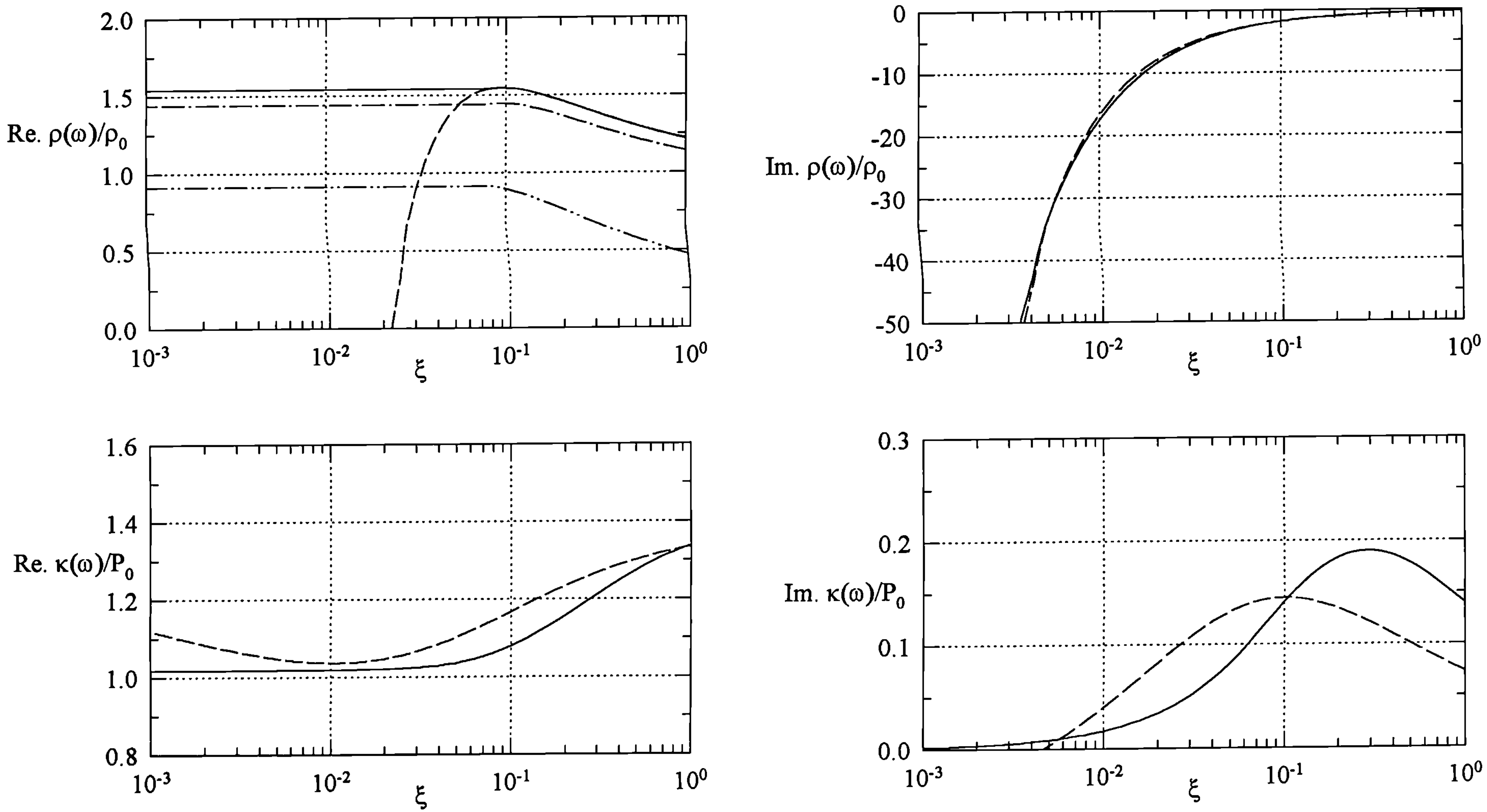

Figure 3.11. Bulk complex density and bulk modulus for steel wool. — — — , Experimental data; ——— , Theoretical predictions; —·— , Dynamic tortuosity; —··— , Dynamic pore shape factor.

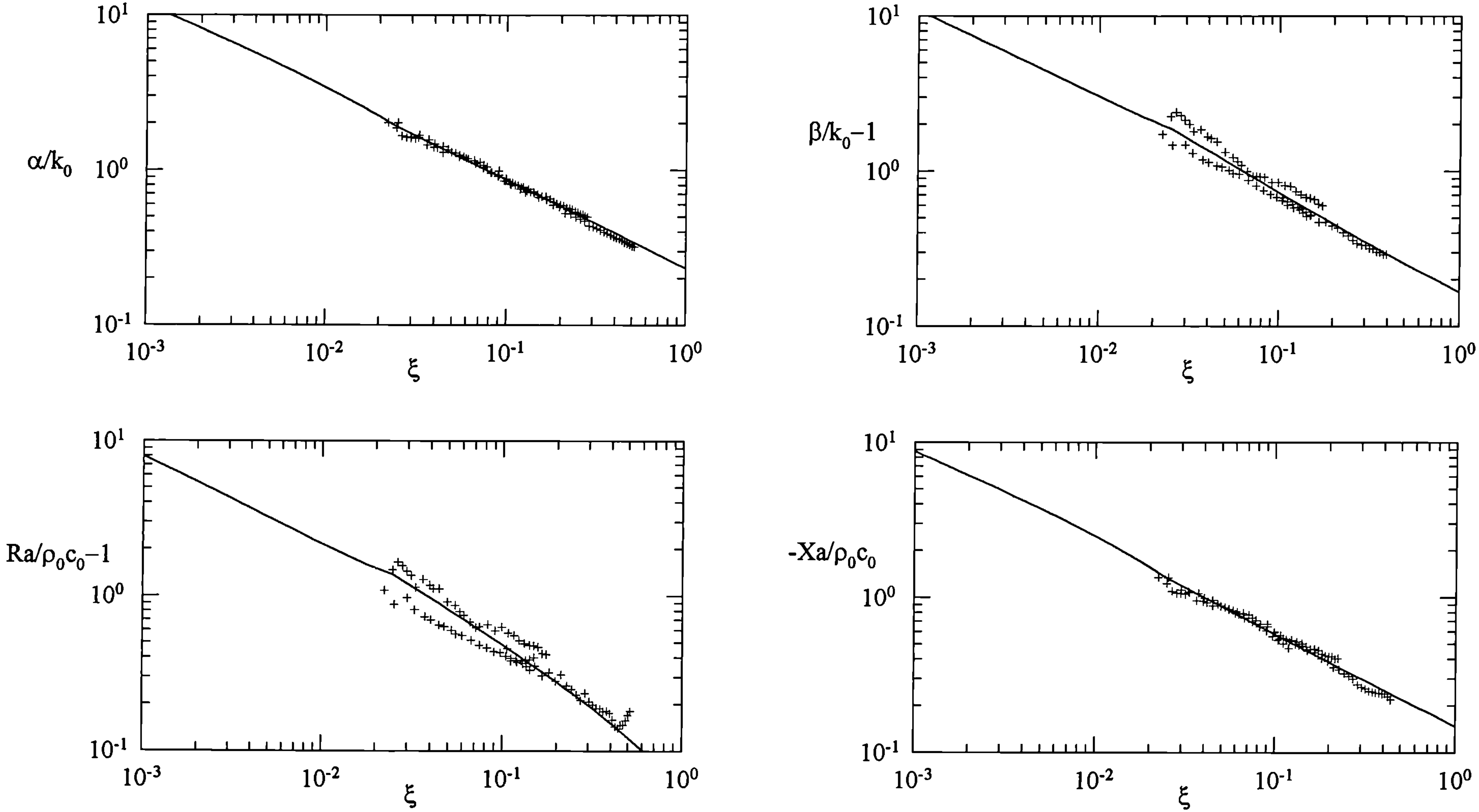

Figure 3.12. Semi empirical model for the bulk acoustic properties of A Glass. + , Experiment; —— , Semi empirical model.

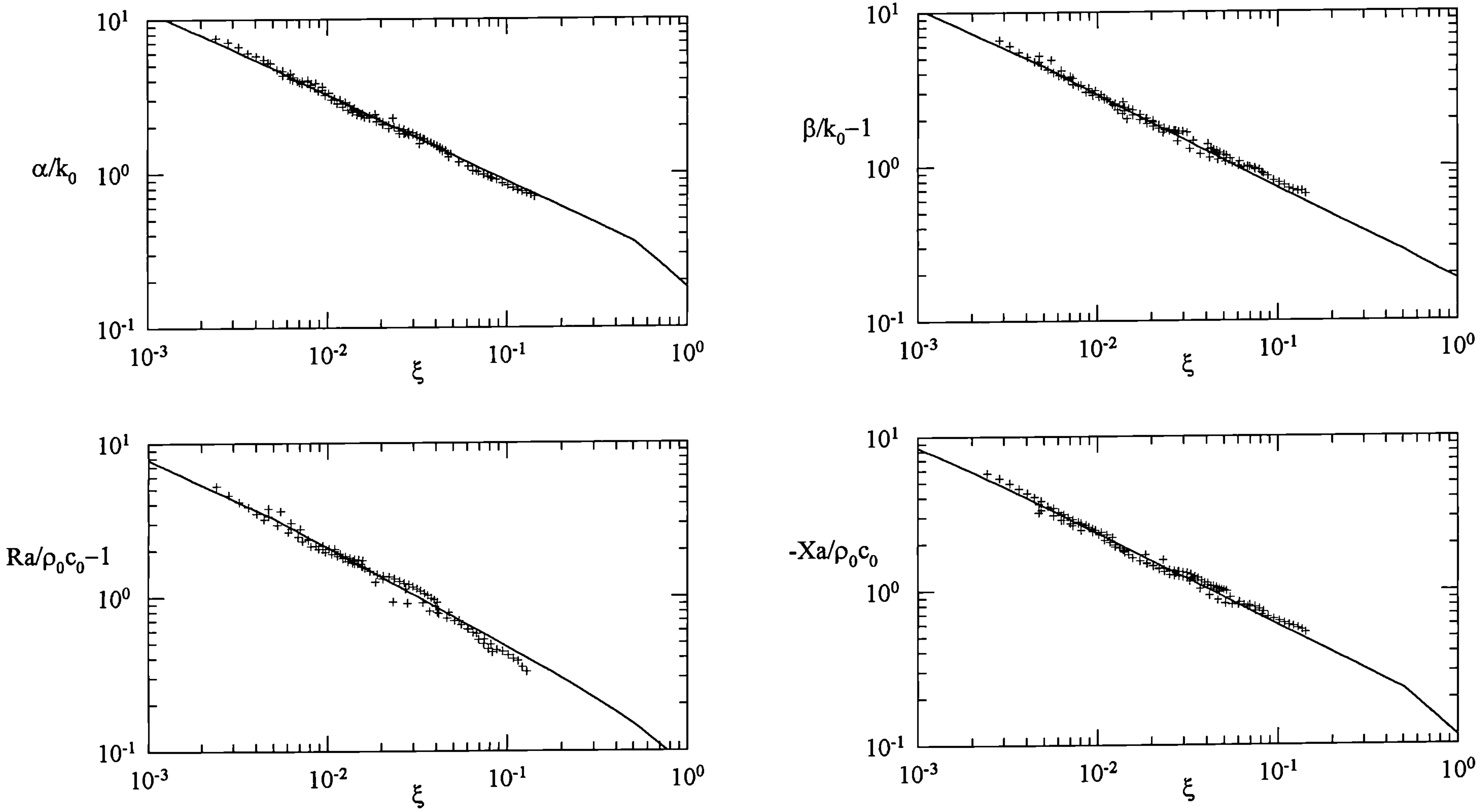

Figure 3.13. Semi empirical model for the bulk acoustic properties of E glass. + , Experiment; —— , Semi empirical model.

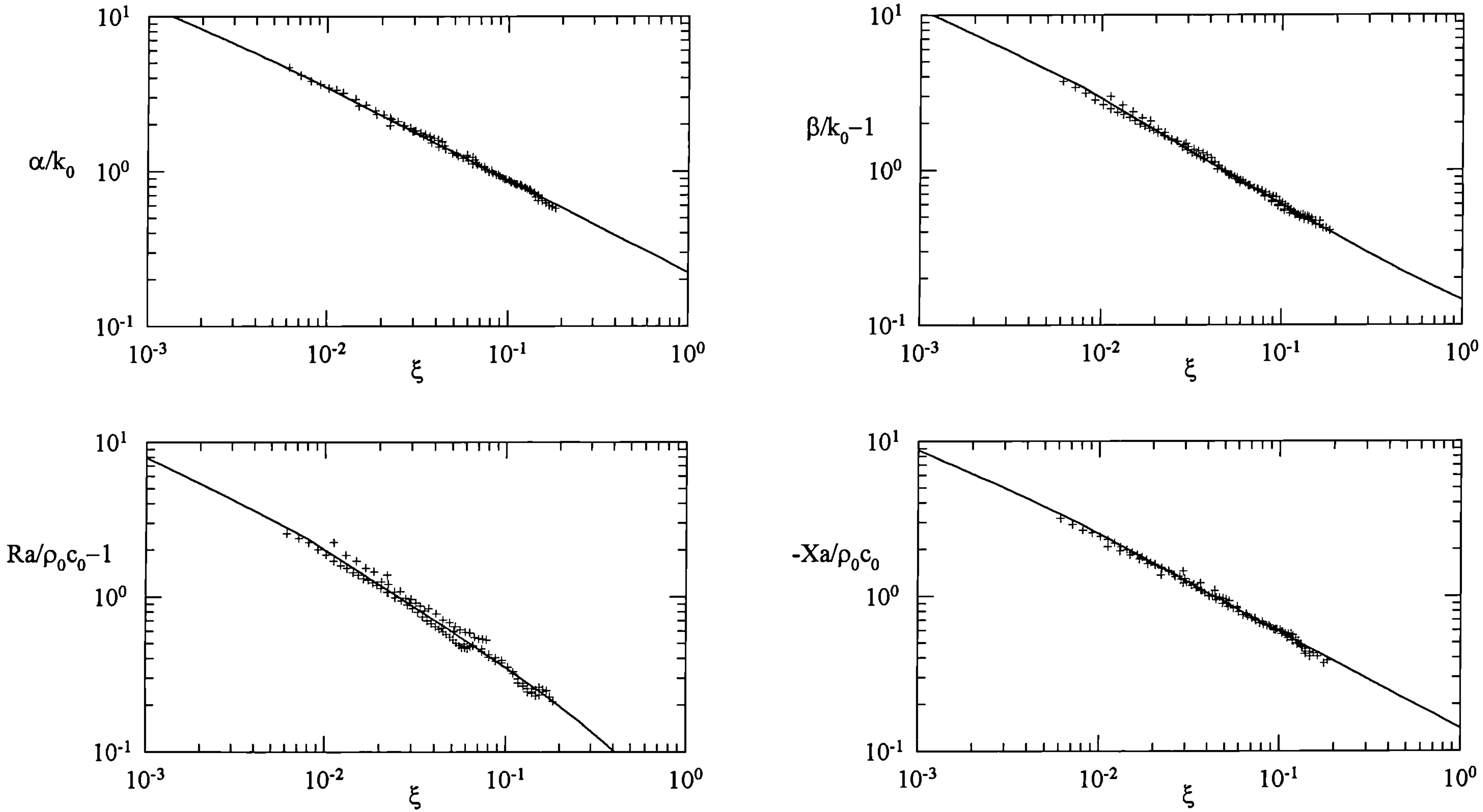

Figure 3.14. Semi empirical model for the bulk acoustic properties of basalt wool. + , Experiment; ——— , Semi empirical model.

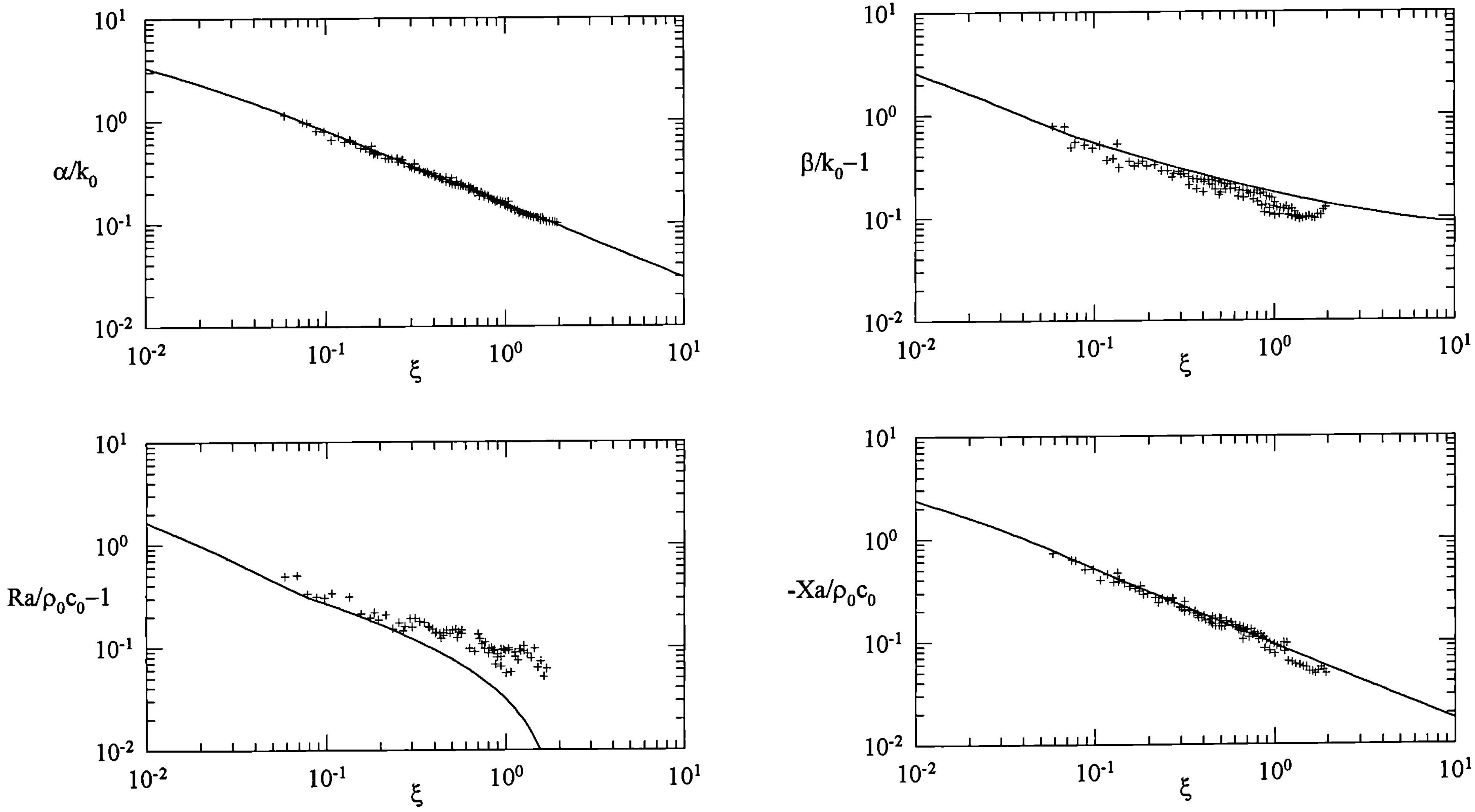

Figure 3.15. Semi empirical model for the bulk acoustic properties of steel wool. + , Experiment; —— , Semi empirical model.

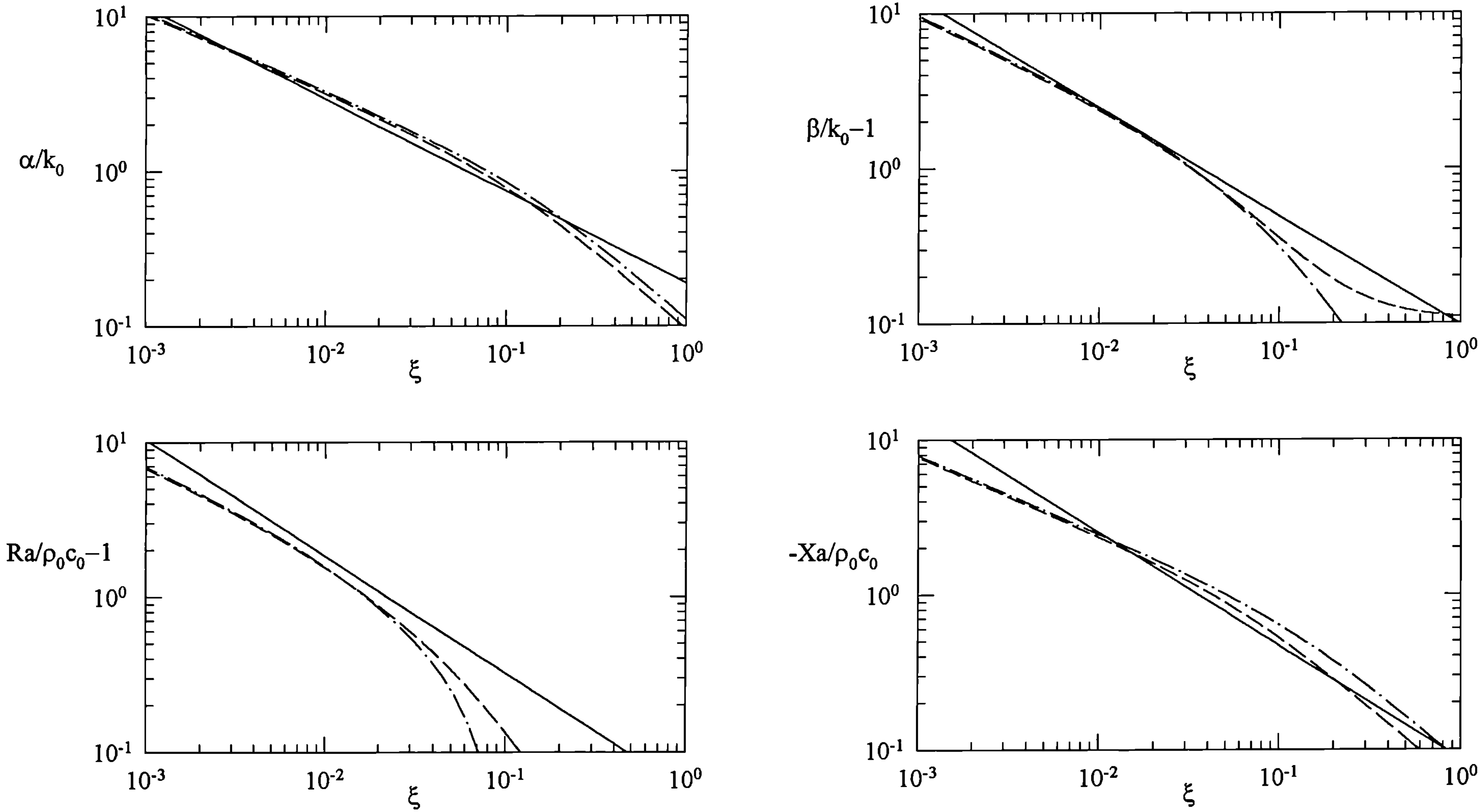

Figure 3.16. Comparison between theory and the expermental predictions of Delany and Bazley.
——, Experiment (Delany and Bazley); – – –, Low frequency model ($q^2(\omega) = s^2(\omega) = 1$); —·—, Predictions of Mechel.

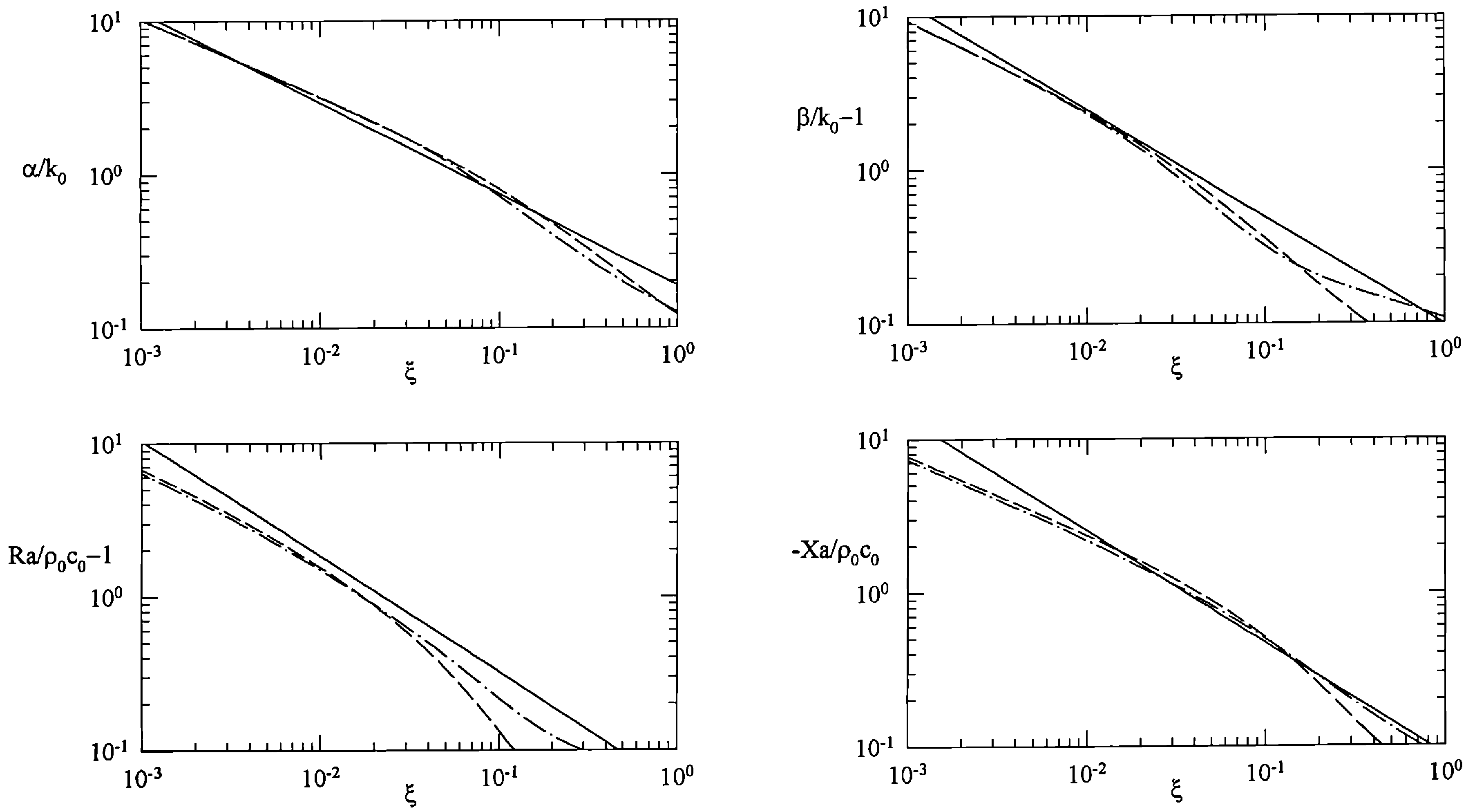

Figure 3.17. Comparison between theory and the experimental predictions of Delany and Bazley.
——— , Experiment (Delany and Bazley); – – – , Full parallel fibre model ($q^2(\omega) = s^2(\omega) = 1$); —·— , Model of Allard and Champoux.

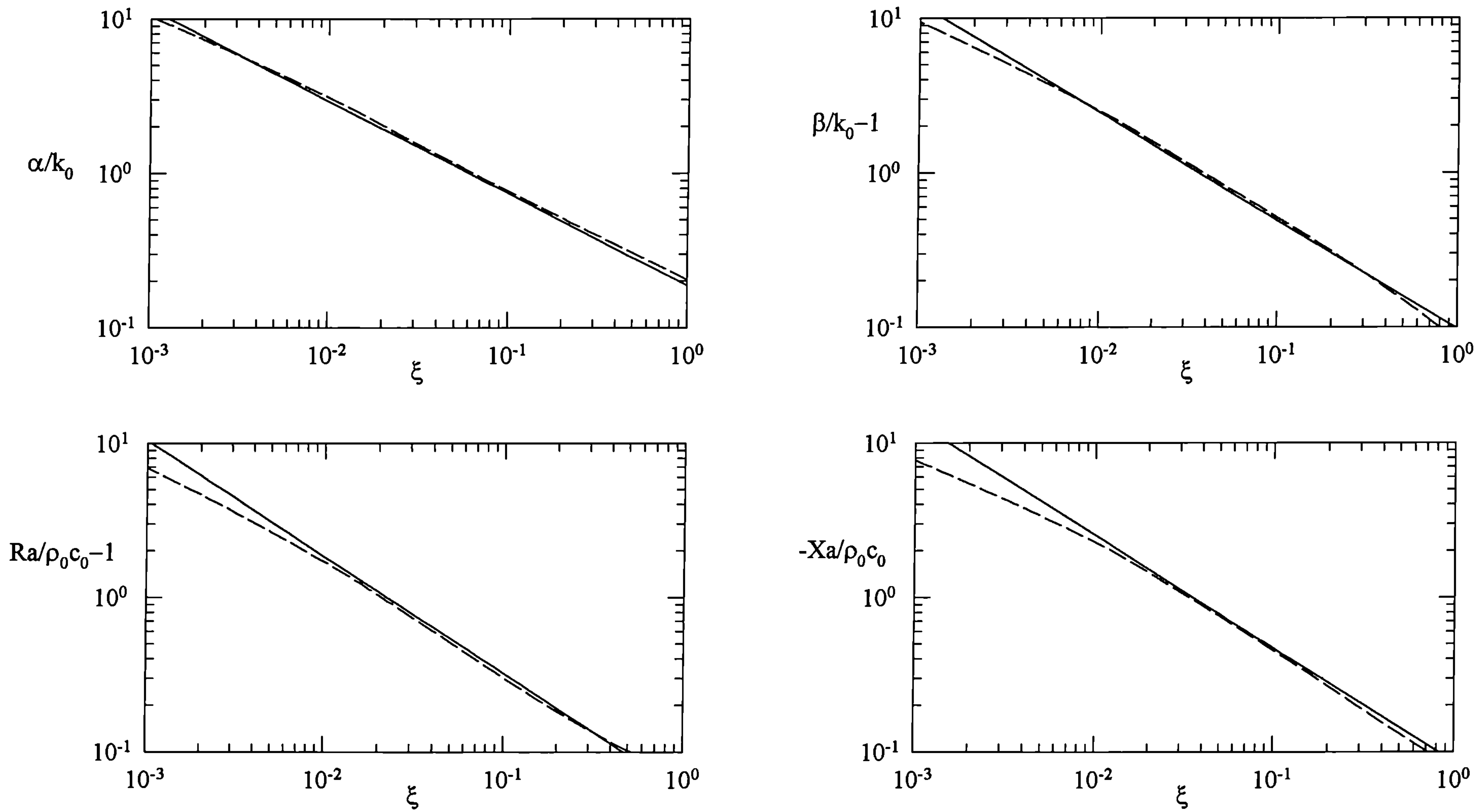

Figure 3.18. Comparison between the semi empirical model and the experimental predictions of Delany and Bazley.
——, Experiment (Delany and Bazley); – – –, Semi empirical model.

CHAPTER 4

THE IMPEDANCE OF PERFORATED PLATES

SUBJECTED TO GRAZING FLOW

Section 4.1

Introduction

The use of perforated plates is common in applications such as exhaust silencers and the duct linings for jet engines. The perforates usually surround the mean gas flow, but they are also known to effect the acoustic properties of the system. In exhaust silencers, perforates can be found in both reactive and dissipative elements. In dissipative silencers, which are of particular interest here, the perforate is commonly found in the form of a concentric tube which, in addition to altering the acoustic performance of the silencer, holds a porous material in a surrounding box, preventing loss of or damage to the material. In most cases the perforate is subjected to grazing flow by the exhaust gas from the engine. The study of the acoustic behaviour of perforates under such conditions is necessary in order to provide a complete understanding of silencer acoustics. In later chapters it will be shown that, especially when grazing flow is present, the acoustic impedance of perforates cannot be ignored in silencer design, and this applies even to perforates with a high percentage open area.

The mechanisms that lie behind the acoustic behaviour of perforates are very complex, and for the case of grazing flow, still not fully understood. However, it is possible to introduce many of the concepts behind the behaviour of perforates subjected to grazing flow by examining the simple case of the perforate behaving like an array of localised orifices without mean flow. The classical case of a single orifice in an infinite baffle was studied by Rayleigh [28] and later on by Morse [74]. Numerous studies on orifices have followed and it is now well known that if the plate thickness and orifice diameter are small compared to the incident wavelength, the air in a single orifice behaves as if it were a small piston. The motion of the plug of air is driven by the pressure differential across the orifice. Some of the air on either side of the orifice, adjacent to it, moves in synchronisation with the plug of air within the orifice and creates an "attached mass" effect that may be quantitatively described by "mass end corrections" that are added to the orifice depth to give the correct total effective mass of the air in the orifice. End corrections are required for both the resistive (real) and reactive (imaginary) components of the acoustic impedance of the orifice. The dissipation of sound (related to the resistive component) occurs because of irreversible loses in the viscous and thermal boundary layers close to the orifice. The reactance is governed by mass inertia effects in addition to viscous effects and is related to the mass end correction. The end corrections for a simple Helmholtz resonator in a baffle (an orifice with a backing cavity) are discussed in detail by Ingård [75] and Melling [76]. Ingård went on to study the effect of allowing the orifice to radiate into a tube; he also examined an array of Helmholtz resonators and looked at the effect of acoustic interaction between adjacent holes.

It has long been known that the presence of mean flow (grazing or incident) increases the resistance and decreases the mass end correction when compared to the no flow situation (see for example the experimental data of Ronneberger [77]). The mechanisms behind this observation have been the subject of considerable debate. In an effort to investigate the physical reasons behind the change in impedance, flow visualisation techniques and laser anenometry have been used by a number of authors in order to observe the flow patterns close to the orifice (see for example Baumeister and Rice [78] and Nelson et al. [79]). Efforts have concentrated on describing how the sound energy is absorbed in the orifice near field, from where theoretical models have been attempted. In examining grazing flow across a single orifice, Nelson et al. [80] deduced that the flow pattern immediately above the orifice was determined by the interaction of two perpendicular streams of outflow, one consisting of pressure fluctuations generated by the passage of vortices shed at the upstream lip of the orifice, and the other made up of pressure fluctuations associated with the reciprocating potential flow in the neck of the orifice. They predicted that a Coriolis force, due to the potential flow in the neck, accelerates the vortices in a streamwise direction and this extracts acoustic energy from the grazing flow. Howe [81] also noticed that the shed vortices establish a potential difference across the orifice, modifying the reciprocating potential flow causing the dissipation of acoustic energy. However, it appears that this explanation of the increase in acoustic energy loss is only applicable to low mean flow velocities and/or relatively large orifice radii. Other studies such as that by Ronneberger [82] show that at higher flow speeds, a free shear layer is set up above the orifice. The shear layer interacts with the reciprocating potential flow in the orifice neck so that at the trailing edge of the orifice the shear layer is periodically pumped into and blown out of the orifice. Ronneberger predicted that the dissipation of acoustic energy occurs due to the deflection of the outer flow. It is obvious from examination of the literature on the subject that several different mechanisms have been predicted, which can depend on parameters such as mean flow speed, boundary layer thickness, orifice diameter and perhaps orifice depth. It is evident that the problem is a very complex one and it is perhaps not surprising that a complete understanding of the absorption of acoustic energy has yet to be found.

The complexity of the problem has meant that only a small number of purely theoretical models have been attempted and in order to make the models tractable, the problem has generally been over-simplified. For instance, Howe [81] proposed a model based upon vortex shedding but did not include a mean shear layer in the model. This will obviously not be applicable for normal flow speeds where a free shear layer is known to exist. Howe recognised this problem and attempted to model a free shear layer with a vortex sheet but was unable to find a solution. Walker and Charwat [83] proposed a "hinged-lid" model in order to account for the influx and efflux of the free shear layer at the downstream edge of the orifice. However, the results depend largely upon where the flow separates and vortex shedding has been ignored. They did however obtain qualitative agreement with experimental results. Various other theoretical models have been attempted, generally based upon the behaviour of the free shear layer (see Ronneberger [77], Kaji et al. [84] and Hersh et al. [85]), but agreement with experiment has only been qualitative.

The difficulties apparent in the theoretical modelling of perforates subjected to grazing flow has resulted in a reliance upon data obtained experimentally. The experimental measurements on perforates has generally been restricted to measuring an individual orifice, from here it has been assumed that the results can be extrapolated to that for a perforate plate by using the knowledge of the percentage open area (or porosity) of the perforate. Ronneberger [77] measured the acoustic impedance of a single orifice under grazing flow and related the impedance to the reciprocal Strouhal number based upon the mean flow velocity U_0, orifice radius a and the radian frequency ω. However, Ronneberger used a very thin boundary layer; similar measurements under a thin boundary layer were also performed by Narayana Rao and Munjal [86]. It became apparent in later work (see Goldman and Panton [87]) that the thickness of the boundary layer affects the impedance of the orifice; this is particularly important in the study of exhaust silencers where, in most cases, fully developed turbulent flow is present. Consequently a method for quantifying the boundary layer thickness has become necessary. Goldman and Panton [87] measured the boundary layer thickness close to an orifice and were able to show that a young turbulent boundary layer was present. They proposed using the friction velocity u_* to characterise the boundary layer. This is a measure of the properties of the inner boundary layer (see Coles [88]), and was used by Goldman and Panton to replace the free stream velocity in the Strouhal number. Goldman and Chung [89] confirmed that the orifice impedance was only affected by the inner part of the boundary layer and concluded that the use of the friction velocity in the Strouhal number was correct. Kooi and Sarin [90], who also measured the friction velocity, re-defined the parameters used for the resistance and mass end correction. They wrote the resistance as a function of the inverse Strouhal number u_*/fd (where f is frequency and d the orifice diameter) and the mass end correction as a function of $u_*/f\,t$ (where t is the orifice depth). By studying a range of different plates, Kooi and Sarin found that the resistance could also be written as a function of t/d and they were able to derive simple algebraic expressions for both the resistance and mass end correction. Cummings [91], who also studied a number of different perforates, showed that the mass end correction could also be written as a function of t/d. This allowed general expressions to be derived which encompass a number of perforates thus eliminating the need to measure new perforates. Cummings studied the perforates under a fully developed turbulent flow and found systematic differences between his results and those of Kooi and Sarin, this was shown to be caused by Kooi and Sarin using a young turbulent boundary layer. Cummings concluded that boundary layer turbulence is an important parameter in the measurement of perforate impedance and it is necessary to measure them under similar conditions to those in which they are to be used. The method used by Cummings appears to be suited to the present investigation, provided the porosity of the plate is accounted for in the measurements. It is also assumed that any interaction between holes (see Ingård [75] and Flynn and Panton [92]) will be successfully accounted for using this method.

A feature of previous work on perforates subjected to grazing flow is that, to the best of the author's knowledge, the effect of a porous material backing the perforate has not been measured. The only work to be found combining a perforate with a porous material appears to be for locally reacting no flow situations, for example the investigations of Ingård and Bolt [93] and Davern [94]. This is surprising considering the frequent use of porous materials in exhausts. The aim of this chapter is to examine the effect of backing perforates with a porous material when they are subjected to grazing flow.

Section 4.2

Experimental Method

The acoustic impedance of six perforates, commonly used in silencers was measured experimentally. The perforate plates, supplied by Tenneco-Walker (U. K.) Ltd. and Eminox Ltd., consist of three "flat" plates and three louvred plates. The perforates were supplied by the manufacturer in the form of small off-cuts from pre-formed flat sheets. The flat plates are similar to those studied by previous authors, though despite louvres being common in automotive exhausts, the present investigation appears to be the first to include louvres.

The experimental arrangement used by Cummings [91] is appropriate here for the measurements both with and without absorbent. The experimental apparatus used is shown in Figure 4.1. A square section pipe has been used to carry the air flow from a variable speed air supply. The air supply was silenced by means of a large dissipative silencer close to its outlet. A square pipe was used to allow the small off-cuts of perforate to be mounted easily into the wall. The use of a square sectioned pipe does not present any problems so long as the perforate is located away from the corners of the pipe. Indeed, similar conditions to those encountered in circular pipes can be reproduced at the centre of the wall of a square pipe. The perforate is located approximately 2.5m from the air supply, and this allows time for a turbulent boundary layer to develop. A sinusoidal signal, fed via a power amplifier to a loudspeaker mounted near the air supply outlet, was used to supply the superimposed sound field.

The perforate, once it has been mounted flush into the pipe wall, is backed by a cavity to form a Helmholtz resonator. This was done by fixing a small flange to the perimeter of the perforate and locating the flange in a recess on the outside of the pipe wall. The cavity was then clamped onto the pipe, sandwiching the flange between the pipe wall and the cavity. This held the perforate flush with the grazing flow. Depending upon the tests performed, the cavity was either filled with porous material or left empty.

The acoustic measurements carried out on the perforates are based upon the two microphone method used by both Kooi and Sarin [90] and Cummings [91]. Measurements were taken from one microphone located in the cavity (note that the protective grille was left on the microphone because of the potential presence of a porous material) and from a microphone located in the pipe wall close to the perforate. The microphone in the pipe wall was located upstream of the perforate and the grille was removed to allow it to sit flush with the wall. The two microphones and the measuring amplifiers were phase-matched to within 0.5° over a range from 70Hz to 1kHz. To do this, the microphones were flush mounted close to each other in a steel plate and located at the far end of a standing wave tube. White noise was then use to calibrate the microphones across the frequency range required. To calculate the impedance of a perforate the only acoustic measurement necessary is the transfer function between the two microphones. This was performed for discrete frequencies and the transfer function was manually recorded from the analyser at regular intervals across a range of approximately 70Hz to 1kHz. To reduce the effect of flow noise the transfer function was averaged over a period of time. The lower frequency limit was set by the capability of the loudspeaker to generate sound pressure levels above those of the random (flow induced) noise. A mid-range acoustic driver was used for the tests here and this limited the available sound pressure levels at low frequencies. Above 1kHz the phase matching of the two microphones was deemed to be outside acceptable limits.

Once the transfer function has been recorded the acoustic impedance of the perforate can be inferred. Following Cummings [91], let the acoustic pressure at the microphone in the pipe be p_1, and the acoustic pressure in the cavity p_2. The transfer function p_2/p_1 can the be written in the form

$$\frac{p_2}{p_1} = r\,e^{i\phi}, \tag{4.1}$$

The measurements recorded from the FFT analyser are therefore the modulus r and the phase ϕ.

A detailed section of the perforate and cavity is shown in Figure 4.2. The total cross section of all the orifices in the wall is given by A_0, the cross sectional area of the cavity by A_c, the thickness of the plate by t (note that this is not the same as the thickness of the pipe wall) and the diameter of an individual orifice by d. Omitting time factor $e^{i\omega t}$, the acoustic pressure and the velocity in the cavity are given by

$$p_c(x) = P_0 \cos k_0 x, \tag{4.2}$$

and

$$u_c(x) = \frac{P_0}{i\rho_0 c_0} \sin k_0 x, \tag{4.3}$$

where p_c is the pressure in the cavity, P_0 is the pressure in the cavity at $x = 0$ (equal to p_2) and k_0 is the cavity wavenumber. Note that equations (4.2) and (4.3) assume that air is present in the cavity. If a porous material is present then k_0 is replaced by $-i\Gamma$ and $\rho_0 c_0$ replaced by z_a, where Γ and z_a are the propagation constant and characteristic impedance respectively for a porous material, see Chapters 2 and 3. The acoustic impedance of the perforate z_0 is given by

$$z_0 = \left(\frac{p}{u_0}\right)_{x=L}, \tag{4.4}$$

where L is the length of the cavity and u_0 is the acoustic velocity through the perforate. Therefore

$$z_0 = \frac{p_c(L) - p_1}{u_0}. \tag{4.5}$$

Continuity of volume velocity at $x = L$ gives

$$u_0 = \frac{A_c}{A_0}\frac{P_0}{i\rho_0 c_0}\sin k_0 L. \tag{4.6}$$

The acoustic impedance of the perforate can now be written as

$$z_0 = \frac{(P_0/p_1)\cos k_0 L - 1}{\dfrac{A_c}{A_0}\dfrac{(P_0/p_1)}{i\rho_0 c_0}\sin k_0 L}. \tag{4.7}$$

By substitution of $P_0 = p_2$ and using equation (4.1), z_0 can be re-written in terms of the experimental measurements,

$$z_0 = \frac{re^{i\phi}\cos k_0 L - 1}{\dfrac{A_c}{A_0}\dfrac{\sin k_0 L}{i\rho_0 c_0} re^{i\phi}}. \tag{4.8}$$

Simplifying equation (4.8) gives

$$z_0 = \rho_0 c_0 \frac{A_0}{A_c}\left[\frac{-\sin\phi + i(r\cos k_0 L - \cos\phi)}{r\sin k_0 L}\right]. \tag{4.9}$$

It is convenient to write the perforate impedance in the form

$$z_0 = r_0 + i\omega\rho\ell, \tag{4.10}$$

where r_0 is the resistance and ℓ is the effective orifice length, i.e.

$$r_0 = -\rho_0 c_0 \frac{A_0}{A_c} \frac{\sin\phi}{r \sin k_0 L} \tag{4.11}$$

and

$$\ell = \frac{A_0}{k_0 A_c} \frac{(r \cos k_0 L - \cos\phi)}{r \sin k_0 L}. \tag{4.12}$$

The mass end correction is found by subtracting the geometrical orifice length t from equation (4.12). Again, it should be noted that if a porous material is present in the cavity, $\rho_0 c_0$ is replaced by z_a and k_0 by $-i\Gamma$. Equations (4.11) and (4.12) are a simplified version of the expressions for the resistance and mass end correction used by Cummings [91].

When a viscous fluid flows in a pipe, the presence of the wall obviously has the effect of retarding the flow. Consequently the velocity of the fluid will vary from zero at the wall to the free stream velocity in the centre of the pipe, the region of sheared flow being known as the boundary layer. When turbulent motion is present in the boundary layer, the radial variation of the fluid velocity (the velocity profile) exhibits three distinct regions; one very close to the wall, one far away from the wall and an intermediate region. The region very close to the wall is dominated by viscosity and the velocity profile is linear, all turbulent flows are dynamically similar in this region. Close to the wall the functional dependence of the velocity profile upon parameters such as the wall shear stress and the fluid viscosity is known as "the law of the wall". The velocity profile in the outer region of the boundary layer must be referenced to the free stream velocity and the flow appears to be insensitive to wall roughness parameters. The functional dependence of the velocity in the outer region (given by Panton [95]) is known as the "velocity defect law". The third region in the boundary layer represents the link between the law of the wall and the velocity defect law. The velocity profile in this region has a largely logarithmic dependence. Coles [88] was able to show that the velocity defect law could be combined with the logarithmic region by introducing an additional functional dependence to the defect law, Coles called this the "law of the wake". Goldman and Chung [89] measured a number of boundary layer profiles and showed that these could be successfully represented by a combination of the law of the wall together with the law of the wake suggested by Coles. They were able to show that the perforate impedance was dependent solely upon the parameters governing the law of the wall. The law of the wall supposes that u/u_* is a function of yu_*/υ, where u is the velocity as a function of the distance y from the wall and υ is the kinematic viscosity. Consequently, the relevant parameter for grazing flow over a perforate plate when a turbulent boundary layer is present is the friction velocity u_*. This quantity was later used by both Kooi and Sarin [90] and Cummings [91].

The friction velocity can be written in terms of the wall shear stress τ_w [95],

$$u_* = \sqrt{\frac{\tau_w}{\rho_0}}. \tag{4.13}$$

Gessener and Jones [96] measured the wall shear stress vector for square pipes and found that, for a Reynolds number of $\mathrm{Re} = 3\times10^5$ (based upon the hydraulic diameter of the pipe), it was inclined at no more than 1° to the axis for the centre region of the pipe. This justifies the assumption that the experimental results measured here are also applicable to circular tubes. It is also known that τ_w varies around the perimeter of a square duct. For a square pipe, Fujita [97] predicts $\tau_w/\overline{\tau}_w$ to vary from 1 to 1.05 across the perforates used here ($\overline{\tau}_w$ being the perimental average of τ_w).

Two methods are available for measuring the friction velocity. Cummings [91] related the friction velocity to the mean pipe velocity by

$$u_* = \overline{u}\sqrt{\frac{f_r}{8}}, \tag{4.14}$$

where $\bar{u}$ is the mean velocity in the pipe and f_r is the friction factor for the pipe. The friction factor for turbulent flow in square ducts with smooth walls was found by Fujita [97] to be given by

$$f_r = 0.306\,\mathrm{Re}^{-1/4}, \tag{4.15}$$

for $10^4 < \mathrm{Re} < 10^5$ and this expression was employed by Cummings [91] in equation (4.14). This method has the disadvantage of requiring the mean velocity in the pipe to be measured. This can be a laborious task since it is necessary to take measurements at a number of locations over the cross section of the pipe. The method is also prone to errors due to the difficulty in measuring flow rates in the corners of the pipe where unsteady flow exists.

An alternative approach is to use a Preston tube, a full description of which given by Patel [98]. The method involves measuring the skin friction directly by placing a circular Pitot tube on the pipe wall. Patel provides a complete set of calibration curves for a number of Pitot tube diameters. He applied a curve fit to the acquired data and the following relationship was found:

$$x^* = y^* + 2\log_{10}\left(1.95y^* + 4.1\right), \tag{4.16}$$

where $x^* = \log_{10}\left(\dfrac{\Delta p d_p^2}{4\rho_0 \upsilon^2}\right)$ and $y^* = \log_{10}\left(\dfrac{\tau_w d_p^2}{4\rho_0 \upsilon^2}\right)$ for $5.6 < x^* < 7.6$.

Hence, Δp is the measured pressure difference between the Pitot and static pressures and d_p is the outside diameter of the Pitot tube (a Pitot tube 3mm in diameter was used here). Equation (4.16) can be solved to give τ_w and hence u_* at any individual position on the wall of the pipe. Consequently, the number of measurements is reduced compared to the more usual method of Cummings [91]; also the wall shear stress is measured directly and does not depend upon a relationship between f_r and Re.

Section 4.3

Experimental Results

The perforates measured in the previous section are separated here into two groups, one containing the "flat" perforates and one containing the louvres. The flat perforates are to be known here as "plates" and are numbered 1 to 3; the louvres are also numbered 1 to 3. Each perforate has a different t/d ratio. For the louvres, the diameter of a circle equivalent in area to that of the orifice has been used. The dimensions and porosity (fractional open area) of each perforate are given in Tables 4.1 and 4.2 below. A full description of the geometry of each of the three louvres is given in Figure 4.3. The dimensions quoted for the louvres in Figure 4.3 are only approximate since the dimensions of individual holes can vary due to discrepancies in the manufacturing process, therefore the values given in Table 4.2 were averaged over large sections of each louvre. It should be stressed here that the grazing flow passes underneath the louvre in the direction shown in Figure 4.3, this means that the section of the louvre that has been pressed out lies within the porous material.

Table 4.1. Dimensions of flat perforate plates

Plate	t / mm	d / mm	t/d	Porosity
1	1.5	3.1	0.484	0.210
2	1.5	2.8	0.536	0.205
3	1	3.5	0.286	0.272

Table 4.2. Dimensions of louvres

Louvre	t / mm	$d_{equiv.}$ / mm	t/d	Porosity
1	1	2.25	0.444	0.04
2	1	2.92	0.342	0.09
3	1	2.73	0.366	0.08

Plates 1 and 2 and louvres 1,2 and 3 were supplied by Tenneco-Walker (U. K.) Ltd. and plate 3 was supplied by Eminox Ltd.

4.3.1 Acoustic Impedance Without a Porous Backing

The experimental measurements for the acoustic impedance without a porous backing are presented here in the manner first proposed by Kooi and Sarin [90]. This method is used here because it has been shown to be a successful way of presenting data, furthermore it also allows a straightforward comparison to be made between the results obtained here and those of both Kooi and Sarin [90] and Cummings [91]. Kooi and Sarin's method involves non-dimensionalising both the resistance and the mass end correction. Therefore, in defining the normalised acoustic impedance ζ by

$$\zeta = \frac{z_0}{\rho_0 c_0} = \frac{r_0}{\rho_0 c_0} + i\frac{\omega \rho_0 \ell}{\rho_0 c_0} = \theta + i\chi, \tag{4.17}$$

equation (4.9) allows θ and χ to be written as

$$\theta = -\frac{A_0}{A_c}\frac{\sin\phi}{r\sin k_0 L}, \tag{4.18}$$

and

$$\chi = \frac{A_0}{A_c}\frac{\left(r\cos k_0 L - \cos\phi\right)}{r\sin k_0 L}. \tag{4.19}$$

The resistance of the orifice θ has two components, the resistance induced by the flow, θ_f, and the resistance attributable to the viscous boundary layer, $\theta_{\text{visc.}}$, where

$$\theta = \theta_f + \theta_{\text{visc.}}. \tag{4.20}$$

Now $\theta_{\text{visc.}} = \left(t/d^2\right)\sqrt{16\pi\upsilon/f}$ (see Kooi and Sarin [90]), therefore the flow induced resistance for the orifice is given by

$$\theta_f = -\frac{A_0}{A_c}\frac{\sin\phi}{r\sin k_0 L} - \frac{t}{d^2}\sqrt{\frac{16\pi\upsilon}{f}}. \tag{4.21}$$

For the total mass end correction δ, the orifice length t is subtracted from the effective orifice length ℓ, to give

$$\delta = \ell - t, \tag{4.22}$$

where $\ell = \chi/k_0$.

The resistance and mass end correction can now be non-dimensionalised in the same way as that used by Kooi and Sarin [90]. Therefore the resistance is presented in the form $\theta_f c_0/fd$ and the mass end correction as δ/δ_0, where δ_0 is the mass end correction without flow (equal to $0.849d$ for an isolated orifice with $d \ll \lambda$, λ being the wavelength). This value (also used by Cummings [91]) for δ_0 is used here even though some inter-orifice interaction effects must inevitably occur. If values for δ_0 calculated by Ingård [75] for the impedance of an orifice radiating into a tube are used here on the basis that each orifice has a surrounding "cylinder of influence", the results obtained produce radically different plots and it was found that these did not allow comparison with other published data. In accordance with Cummings [91] the resistance data are to be plotted against u_*/fd and the mass end correction against u_*/ft.

The friction velocity was measured by using the Preston tube method since this method allows the quick and easy measurement of τ_w (see equation (4.16)), from which u_* can be calculated. Values for τ_w were obtained, once values for Δp had been found, by solving equation (4.16) by using the Newton-Raphson method. The wall shear stress was measured at a number of places around the central region of the duct wall and the friction velocity was averaged over the region. The results were compared to the measurements obtained using the method of Cummings [91] (described earlier) and close agreement between the two methods was found (within 10%). Measurements for the acoustic impedance of the perforates were carried out for four different friction velocities, 0.476 m/s, 0.986 m/s, 1.626 m/s and 2.192 m/s. The last value corresponds to the maximum friction velocity obtainable from the equipment used in the tests. A full measurement of the boundary layer profile indicated that a developing turbulent boundary layer was present, though the profile was close enough to that of fully developed flow to allow the assumption of a fully developed turbulent boundary layer.

To correlate the data, the curve fitting method of Cummings [91] was tried. The method combines results for the resistance and the mass end correction into separate algebraic expressions. Cummings used this method exclusively for flat plates, it will be shown later that the method cannot be applied to louvres. The experimental results measured for plates 1 to 3 are shown in Figure 4.4 and the left hand side of Figure 4.5, also shown are the algebraic curve fitting formulae found by using the method of Cummings (solid line). The resistance is given by

$$\frac{\theta_f c_0}{fd} = \left\{ 26.16 \left(\frac{t}{d} \right)^{-0.169} - 20 \right\} \frac{u_*}{fd} - 4.055, \tag{4.23}$$

and the mass end correction by

$$\frac{\delta}{\delta_0} = 1, \quad \frac{u_*}{ft} \leq 0.18 \frac{d}{t},$$
$$\frac{\delta}{\delta_0} = \left(1 + 0.6 \frac{t}{d} \right) \exp \left\{ - \left[\frac{\frac{u_*}{ft} - 0.18 \frac{d}{t}}{1.8 + \frac{t}{d}} \right] \right\} - 0.6 \frac{t}{d}, \quad \frac{u_*}{ft} > 0.18 \frac{d}{t}. \tag{4.24}$$

The experimental results for the louvres are shown on the right hand side of Figure 4.5 and Figure 4.6. The louvres require a different method for correlating the data. Each louvre requires a different curve fitting formulae because it was found to be impossible to group them as a function of t/d. For the resistance

$$\frac{\theta_f c_0}{fd} = A_1 + A_2 \left(\frac{u_*}{fd} \right) + A_3 \left(\frac{u_*}{fd} \right)^2, \tag{4.25}$$

where $A_1 \ldots A_3$ are constants given in Table 4.3 below.

Table 4.3 Curve fitting constants for the resistance of the louvres			
louvre	A_1	A_2	A_3
1	1.424	1.128	0.303
2	-0.528	3.359	0.202
3	0.670	2.351	0.432

The mass end correction is given by

$$\begin{aligned} \frac{\delta}{\delta_0} &= B_1 + B_4, \quad \frac{u_*}{ft} \le \frac{B_2}{B_3}, \\ \frac{\delta}{\delta_0} &= B_1 \exp\left(B_2 - B_3 \frac{u_*}{ft} \right) + B_4, \quad \frac{u_*}{ft} > \frac{B_2}{B_3}. \end{aligned} \tag{4.26}$$

where $B_1 \ldots B_4$ are constants given in Table 4.4 below.

Table 4.4 Curve fitting constants for the mass end correction of the louvres				
louvre	B_1	B_2	B_3	B_4
1	0.7	0.629	0.286	0.2
2	0.9	0.413	0.250	-0.1
3	0.9	0.707	0.400	-0.1

4.3.2 Acoustic Impedance With a Porous Backing

The experimental method described earlier for measuring the impedance without a porous backing can also be applied to measurements with a porous backing. However, the normalised acoustic impedance must be re-defined to take account of the porous material, i.e.

$$\theta = -\frac{z_a}{\rho_0 c_0} \frac{A_0}{A_c} \frac{\sin\phi}{r \sin k_a L}, \tag{4.27}$$

and

$$\chi = \frac{z_a}{\rho_0 c_0} \frac{A_0}{A_c} \frac{(r \cos k_a L - \cos\phi)}{r \sin k_a L}, \tag{4.28}$$

where z_a is the characteristic impedance of the porous material and $k_a = -i\Gamma$, Γ being the propagation constant (see Chapters 2 and 3). Three porous materials were used in the experiments performed here: A glass, E glass and basalt wool. Each material was packed into the cavity to give a bulk density of approximately 120kg/m^3.

The resistance and mass end correction can be non-dimensionalised in the same manner as before. However, an examination of equations (4.27) and (4.28) indicates that, because k_a and z_a cannot be dependent upon u_*, it is not possible to plot the data as a function of the friction velocity. This means that the experimental results must be displayed for individual friction velocities and the frequency used for the abscissa. Obviously, in most applications, it is desirable to be able to represent the impedance as a function of the flow speed, thus avoiding the need to re-measure the impedance every time a new flow speed is encountered. Therefore, instead of correlating the experimental data as a function of frequency for individual friction velocities, an attempt is made here to predict the impedance as a function of the friction velocity as well as frequency. This is to be done by combining theoretical predictions of the effect of the porous material with the empirical formulae found when a porous material was not present. This will form a semi-empirical model which can then be compared to experimental results.

Predicting the effect of the absorbent material is possible by examining the mass end correction in the cavity. For a single orifice with no porous backing and no mean flow present, the normalised mass end correction is given by [28],

$$\chi = 0.4245 d k_0 i. \tag{4.29}$$

Now, the equivalent mass end correction when a porous material is present can be written as

$$\chi_{\text{abs}} = 0.4245d\frac{z_a}{\rho_0 c_0}\Gamma. \tag{4.30}$$

When the porous material is present, the mass end correction given by equation (4.29) must be removed and the mass end correction from equation (4.30) added. Obviously equation (4.29) contains both real and imaginary terms, therefore the acoustic impedance must be re-defined as

$$\frac{z_0}{\rho_0 c_0} = \zeta - 0.4245dk_0 i + 0.4245d\frac{z_a}{\rho_0 c_0}\Gamma. \tag{4.31}$$

The effect of the porous material on the impedance of the perforate may therefore be predicted by equation (4.31). The measurements obtained for the perforate without an absorbent present (ζ) and the values given for Γ and z_a from Chapter 3, can now be substituted into equation (4.31) to give the full semi-empirical predictions, i.e.

$$\frac{z_0}{\rho_0 c_0} = \theta_f + \theta_{\text{visc.}} + ik_0(\delta + t) + 0.4245dk_0\left[\frac{z_a}{\rho_0 c_0}\frac{\Gamma}{k_0} - i\right], \tag{4.32}$$

where θ_f and δ are given by equations (4.23) and (4.24) respectively. The known properties of the porous material are therefore used in an attempt to predict the behaviour of the perforate with a porous backing, solely by using the experimental measurements made without a porous backing. The effectiveness of the semi-empirical predictions can be observed by comparing predicted values to the measured impedance values with a porous material present. Experimental measurements were performed for the perforates backed by absorbent at three different friction velocities, 0.986 m/s, 1.626m/s and 2.192 m/s. The "flat" plates were measured first and plate 1 was backed by basalt wool, plate 2 by E glass and plate 3 by A glass. Figures 4.7 to 4.9 show the experimental results obtained for plates 1 to 3. A number of results are not shown here because of the large amount of data obtained, however the results for the highest friction velocity have all been shown since these are of most relevance to the work carried out later in this thesis. Figures 4.7 to 4.9 also include the predictions made by equation (4.32) (solid line), and the empirical formulae for the perforates without porous backing (see equations (4.23) and (4.24), dashed line). The formulae found when no absorbent was present have been included in order to show the effect of the porous material.

The louvred plates were next to be measured with a porous backing, but no difference between the results with and without the porous material were observed. The reasons for this will be discussed in the next section.

Section 4.4

Discussion

Experimental results have been obtained for the three "flat" perforate plates and the three louvres, both with and without a porous backing. The experimental method used by both Kooi and Sarin [90] and Cummings [91] has been shown to work both with and without the presence of a porous material. The method used by Cummings to correlate data has been found to work successfully for the flat plates but not for the louvres. Attempts were then made to predict the effect of the porous material upon the impedance of the perforate and compare this with measured data.

The experimental results obtained for the flat plates will be discussed first since these allow a straightforward comparison to be made with the published data of Goldman and Chung [89], Kooi and Sarin and Cummings. The correlation of data obtained without a porous material present agree qualitatively with the other published data. The resistance of the flat plates exhibit a linear relationship with u_*/fd, and for the mass end correction, decreasing values are observed as u_*/ft increases. A constant negative value for the mass end correction has been assumed at very high values of u_*/ft in accordance with the assumptions made by Cummings. The presence of grazing flow can be seen to increase the resistance of the perforate and removes the mass end correction at high values of u_*/ft. Figures 4.4 and 4.5 indicate that the method used by Cummings to correlate the experimental data works very well for the flat plates measured here, also the observed spread in experimental data is similar to that found by other authors. As expected, the spread in the resistance data is small; this is principally because the resistance can be measured accurately. The difficulties in measuring the mass end correction have been well documented and this is apparent in the large scatter of the data present in Figures 4.4 and 4.5. It is also apparent that, when compared to the data obtained by Cummings for a single orifice, the scatter present in the results for multi-orifice perforates has increased. This was confirmed by performing a number of experiments on single and multi-orifice perforates under identical conditions and comparing the results.

A comparison between the algebraic expressions given by equations (4.23) and (4.24) with those of Cummings show a systematic difference between the two once a value has been assigned to t/d. The resistance predicted by Cummings is far greater than that given by equation (4.23), especially for large t/d ratios. The results for the mass end correction do appear to be similar although the curves given by equation (4.24) do not appear to be as steep as δ/δ_0 approaches 1. The differences found are similar to those Cummings observed between his predictions and those of Kooi and Sarin. Cummings concluded that the differences between the two were down to differing levels of boundary layer turbulence. Whilst it is possible that differences between the present experiment and that of Cummings is due to the use of a less fully developed boundary layer in the present study, it appears unlikely that this is the only cause, especially as the resistance differs by so much at higher values of u_*/fd and this is found to be a function of t/d. One obvious difference between the results presented here and those of both Kooi and Sarin and Cummings is the range of data measured. In Figures 4.4 and 4.5, the resistance has been measured for values of u_*/fd from close to zero up to 10, while the mass end correction u_*/ft has been measured up to 6. For t/d ratios comparable to those used in the present tests, Cummings measured resistance values up to approximately 1.7 for t/d=0.488 and 0.42 for t/d=0.225. An examination of the experimental data obtained for the resistance in Figures 4.4 and 4.5 (especially plate 3 where t/d=0.286) indicates that the formulae used is very dependent upon the data obtained at high values of u_*/fd. Therefore, it is possible that, because Cummings only measured a small number of data over a very limited range, his predictions are not accurate enough for low t/d ratios. This might also caution against combining data over a large range of t/d ratios. It was also noticeable here that data obtained for plates with the lowest t/d ratios suffered from the highest degree of scatter, therefore a large amount of data is essential for low values of t/d. The differences found between the formulae calculated here and those of Cummings cannot be attributed to the acoustic interaction between holes in the present tests. Although the majority of the tests were performed with a section of the normal multi-orifice perforate, further tests were performed with only a single orifice present and also with 50% of the holes blocked. It was found that all the experimental data collapsed onto the curves shown in Figures 4.4 and 4.5. From this it can be concluded that single orifice data are valid for predicting the impedance of mulit-hole perforates and the effect of any acoustic interaction between the holes is small.

The experimental results obtained for the louvres without the presence of a porous material show the same qualitative behaviour as the flat plates, though they are quantitatively quite different from each other. The most obvious difference is that the resistance curves for the louvres have a non-linear shape. A quadratic curve was found to fit the resistance data very well for each louvre. For the mass end correction the louvres appear to attain higher values than the flat plates as u_*/ft increases, also they do not reach a maximum value of $\delta/\delta_0 = 1$ for lower values of u_*/ft. The reasons for the change in behaviour of both the resistance and the reactance are not entirely clear. Obviously the holes in the louvres are of a totally different nature from those in the flat plates since the orifice is oriented normal to the grazing flow and is not circular in shape. This seems the most likely reason behind why the behaviour of the louvres is so different, however a detailed knowledge of the flow pattern through the louvre's orifice would be necessary in order to pin-point any physical reasons behind this behaviour. The louvres do appear to show a similar degree of scatter in the experimental data, although the resistance data do exhibit less scattering at lower values of u_*/fd. Unfortunately it was found to be impossible to group the measured data for the louvres as a function of t/d. This is perhaps not surprising given the fundamental difference in orifice shape between the louvres. This means that the impedance must be measured experimentally when a new louvre is encountered.

The addition of a porous material behind the flat perforates can be seen to cause a large increase in the impedance. Figures 4.7 to 4.9 show that a systematic increase in both the real and imaginary parts has been measured, compared to the predictions for the perforates without a porous backing (dashed line). The size of the increase appears to depend upon the porous material backing the perforate since materials with a high flow resistivity, such as E glass, cause the largest increase in impedance. The measurements obtained for the resistance appear to exhibit a similar degree of scatter to those previously observed, but problems are apparent in the measurement of the mass end correction. A high degree of scatter can be observed in the mass end correction and it is noticeable that data below 450Hz was virtually unobtainable. The reason why this occurs when a porous material is added is not fully understood at present. It is also observed from the plots on which the frequency is the abscissa that measurements were unobtainable around 400Hz and 800Hz; it is possible that this problem was caused by the presence of a pressure node at the perforate and/or non-linearities caused by a resonance in the cavity.

When measurements were carried out with the flat plates backed by porous materials it was apparent that the results were very dependent upon the density of the material immediately adjacent to the holes. This indicates that the porous material has only a very localised effect upon the orifice impedance. The results shown in Figures 4.7 to 4.9 were obtained by using a regular, flat layer of absorbing material covering the near field of each orifice. Indeed it can be seen in the resistance data presented here that, especially at low friction velocities, different trends in the data occur. The reason for this is that slight inhomogeneity (or "layering") of the material was inevitable when separate measurements were performed. This localised effect was particularly obvious when measurements were performed on the louvres backed by a porous material. The alignment of the holes in the louvres means that bulk porous materials (in this case E glass) does not sit immediately adjacent to the orifice. Consequently it was found that the porous material had no measurable effect upon the acoustic impedance of the louvres. This appears to back up the observation that the absorbent material only affects the orifice near field. The consequence of this localised effect is important when using the data measured here to predict the behaviour of mass produced silencers. In commercial silencers the porous material is often randomly packed around the perforate tube, and therefore it can be expected that only a percentage of the material will lie evenly in the near field of the perforate. This will inevitably lead to the formulae presented here over-predicting the impedance. Obviously it will be very difficult to quantify the random nature of the absorbent packing. This problem will be discussed in greater detail later on in this thesis when comparisons between predictions made by using the formulae presented here and measurements on actual silencers can be compared (see Chapter 10).

The semi-empirical predictions for the impedance of the flat plates backed by absorbent (equation (4.32)) are also shown in Figures 4.7 to 4.9 (solid lines). It is evident that for the resistance, the measured values are very close to the predictions. This is especially true for higher friction velocities where the accuracy in measurement has probably been improved because there is more of an effect to measure. As before, the main problems seem to occur with the mass end correction. Figures 4.7 to 4.9 indicate that, in most cases, the mass end correction has been over-predicted. The reasons for this are not clear, however it is possible that experimental error is the cause. It is also possible that the predictions of equation (4.32) over-simplify the problem and that some additional mechanism is at work, which reduces the effect of the absorbent upon the mass end correction. A noticeable feature of the predictions is that at low frequencies a rise in the mass end correction is predicted; this is in contrast to falling negative values obtained when the absorbent is not present. Unfortunately the lack of experimental data at low frequencies does not allow any conclusions to be drawn concerning the accuracy of these predictions at low frequencies. However, the semi-empirical predictions do provide good agreement for the resistance and appear to be adequate for the mass end correction. Therefore, it appears that equation (4.32) is a useful method for estimating the effect of the porous material on the behaviour of a "flat" perforate. This is important because equation (4.32) allows the impedance to be written for any friction velocity and hence any mean flow speed. This removes the need to perform experiments upon perforates backed by a porous material, since experimental data for perforates without absorbent are all that is required.

The principal effect found when a flat perforate plate is backed by a porous material is a large increase in the acoustic impedance over plates without absorbent backing. The results show that, even for plates with a large percentage open area, the acoustic impedance of the perforates must be accounted for when modelling silencers. This is not so important with louvres since the porous material has no measurable effect upon their acoustic impedance, but it is still recommended that the values obtained with no porous backing are included in silencer modelling.

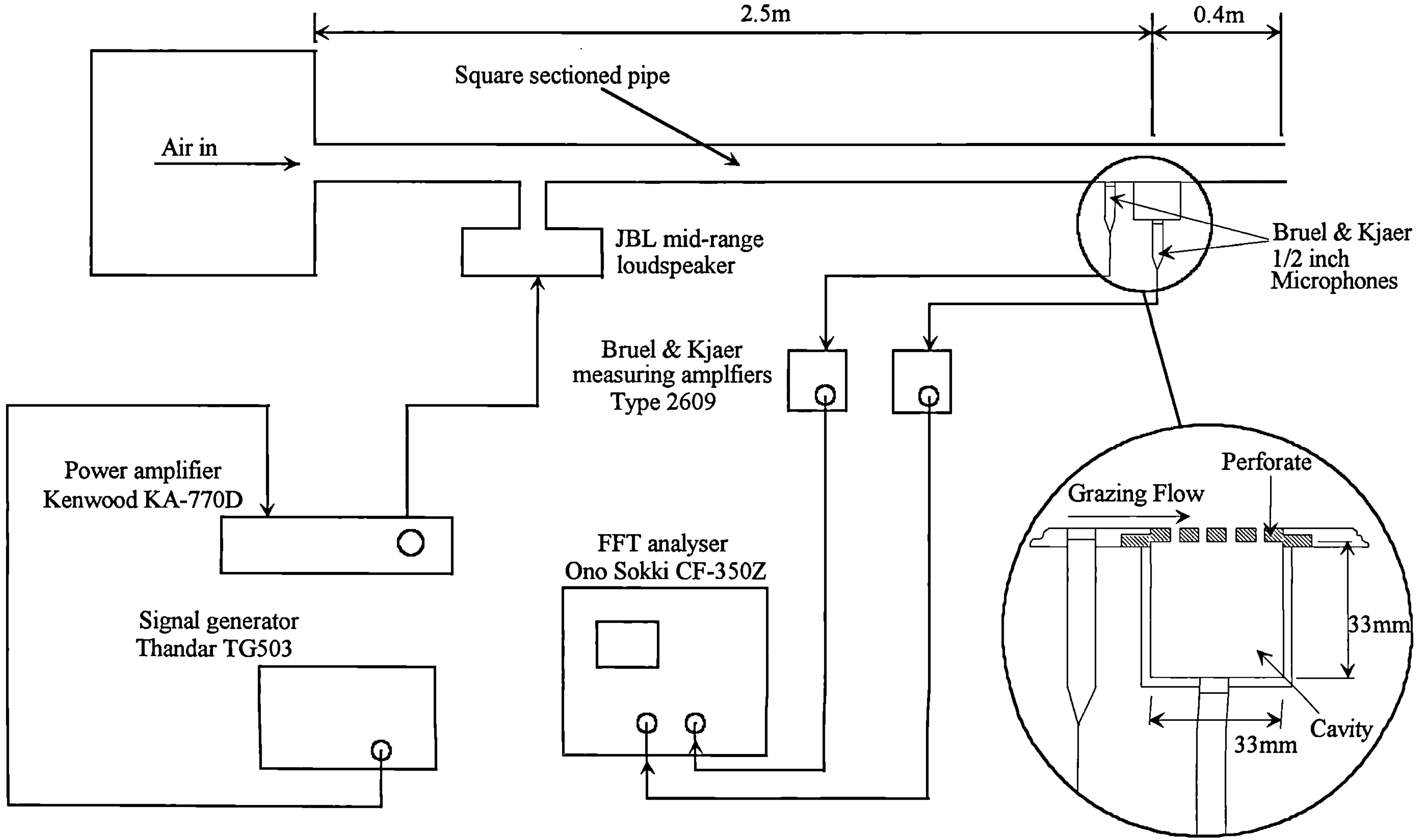

Figure 4.1. Apparatus for the measurement of the acoustic impedance of a perforate.

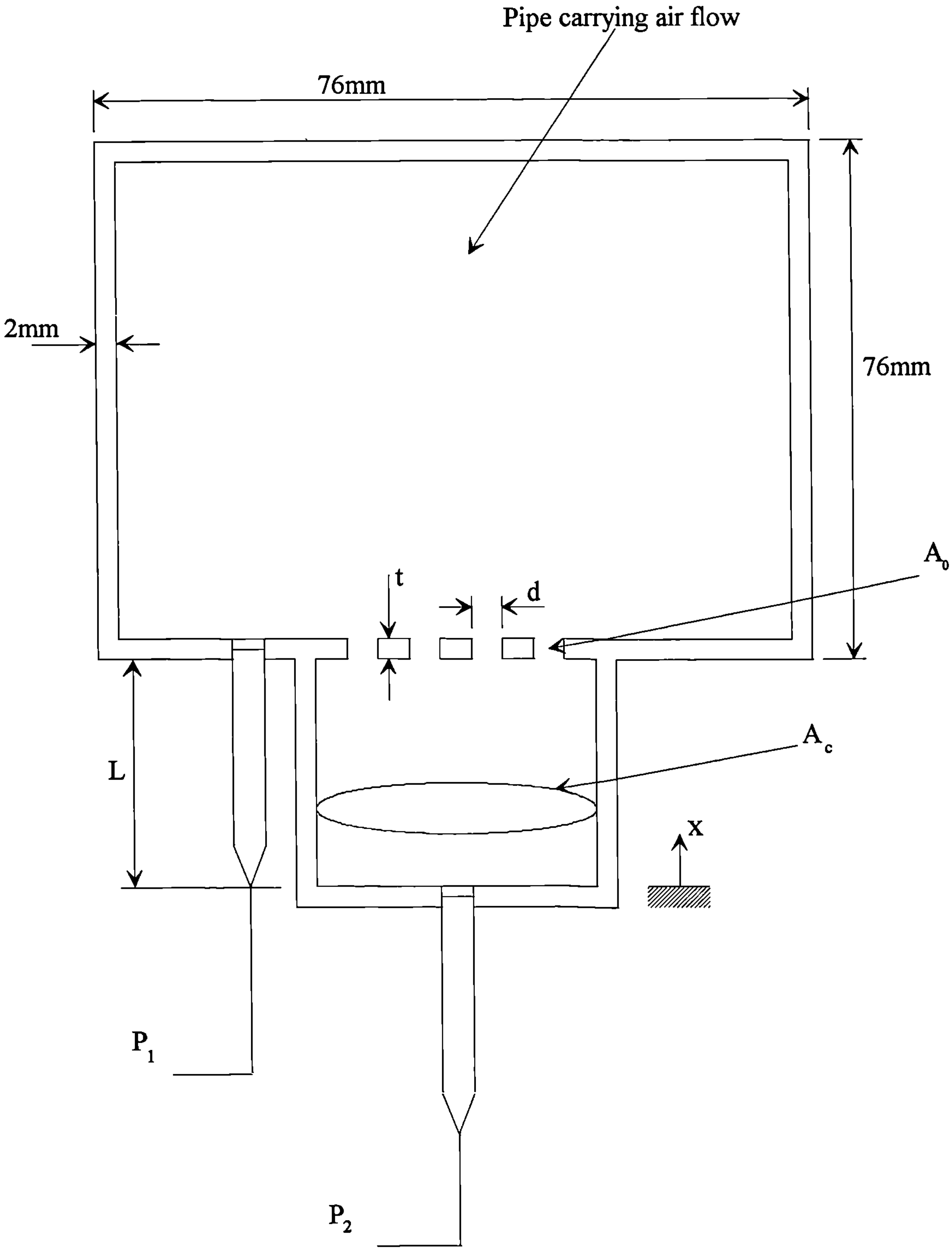

Figure 4.2. Cross section of pipe and cavity

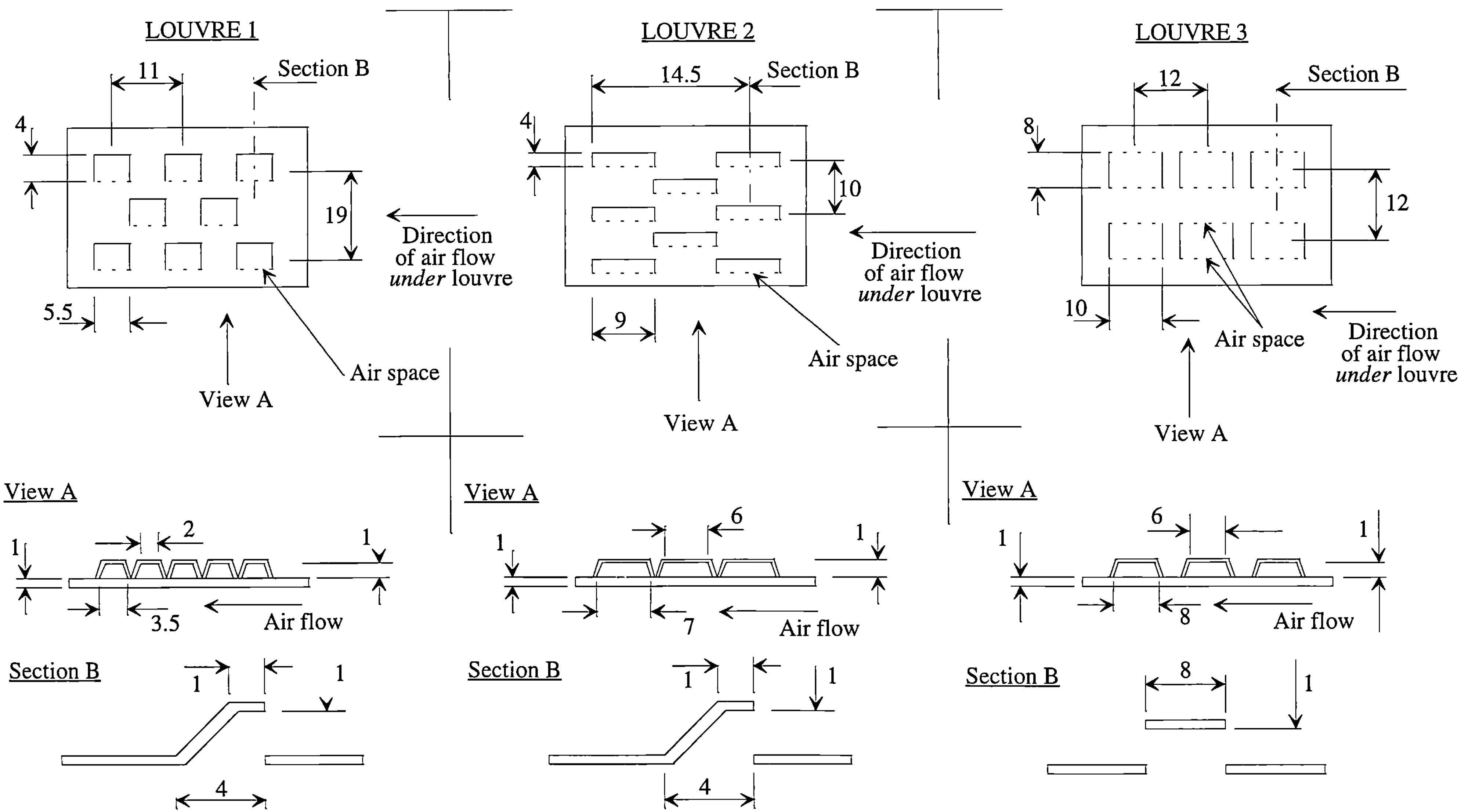

Figure 4.3. Geometry of louvres.

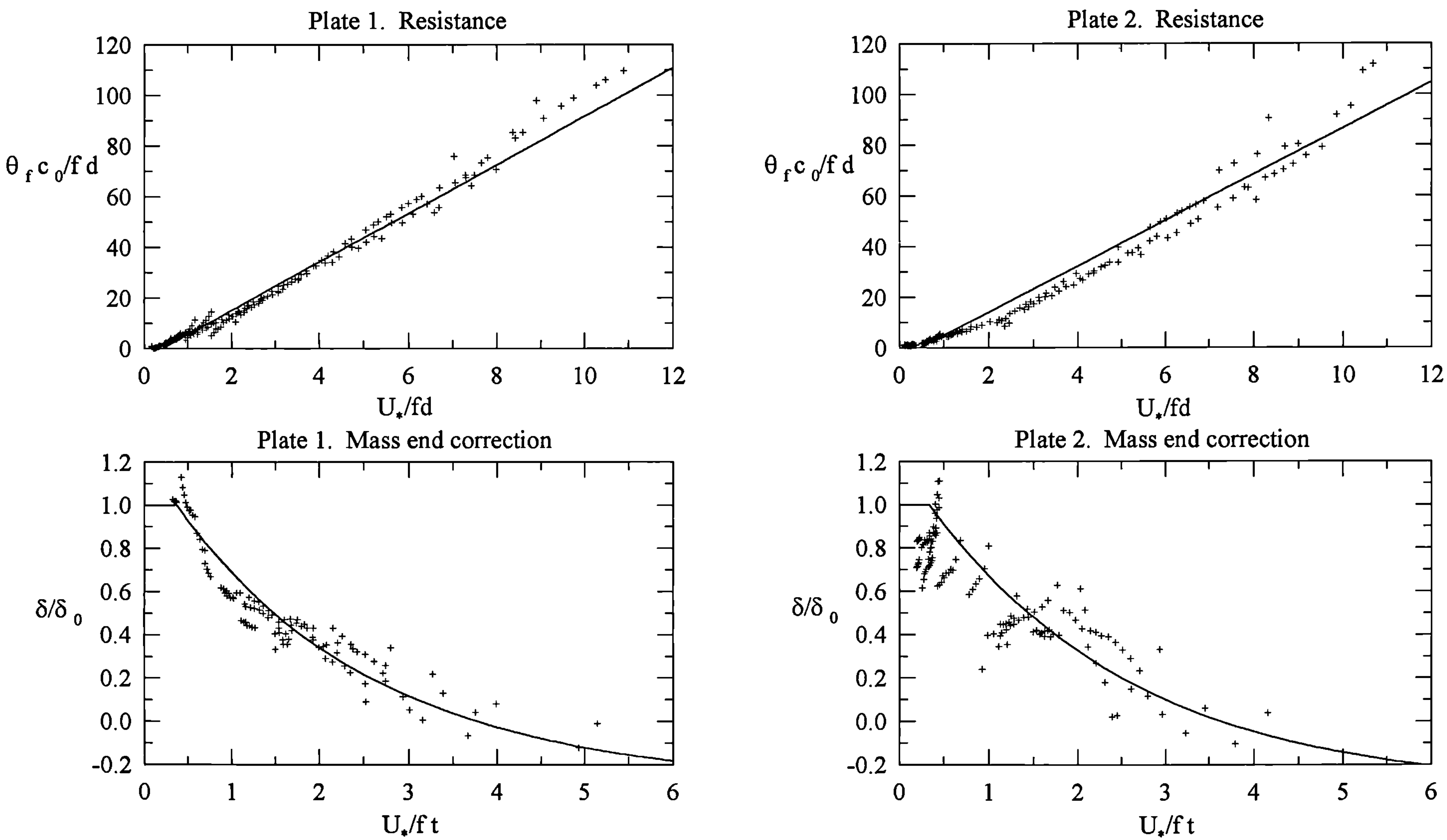

Figure 4.4. Acoustic impedance of plates 1 and 2. + , Experiment; —— , Curve fitting formulae.

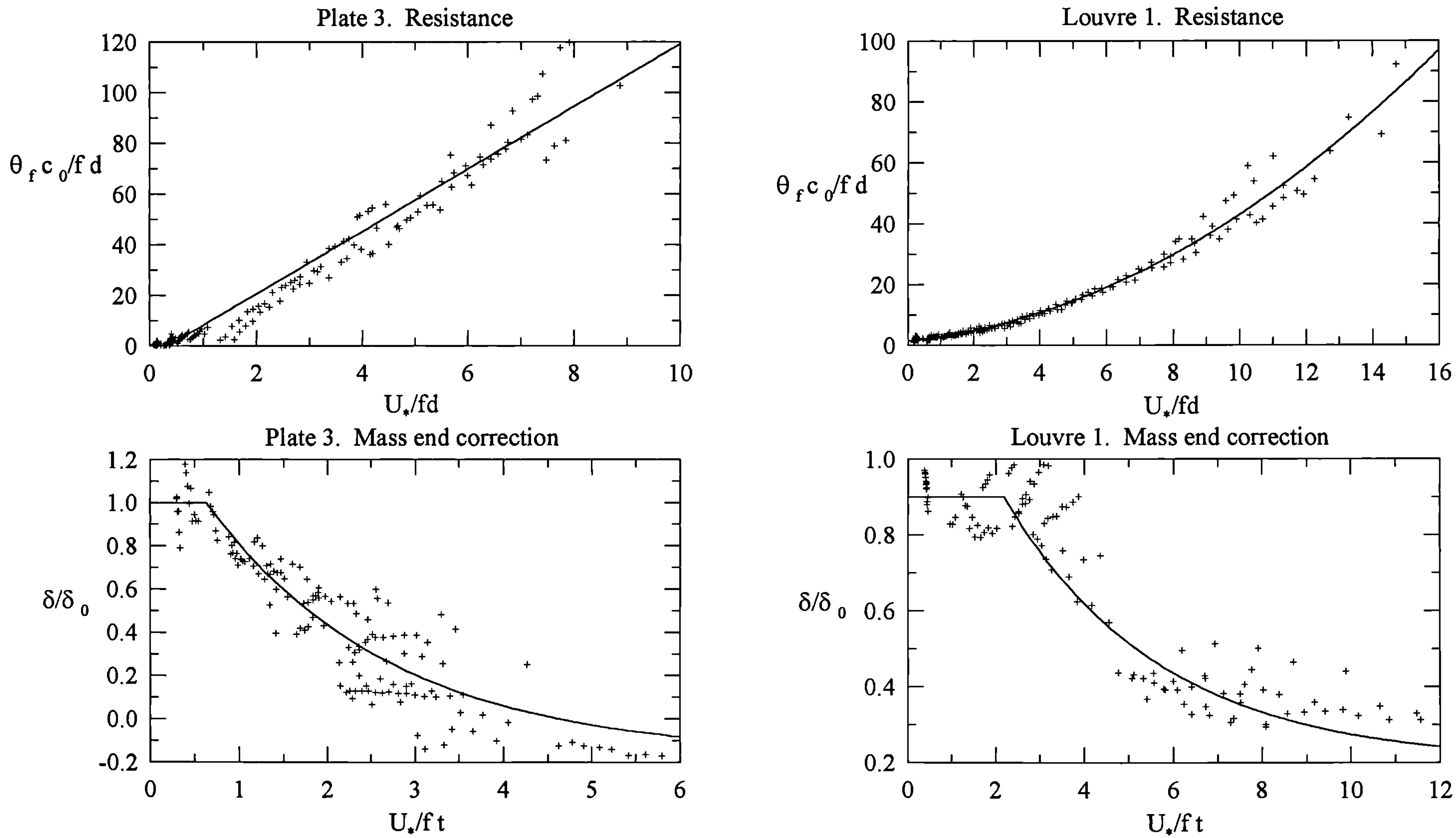

Figure 4.5. Acoustic impedance of plate 3 and louvre 1. + , Experiment; —— , Curve fitting formulae.

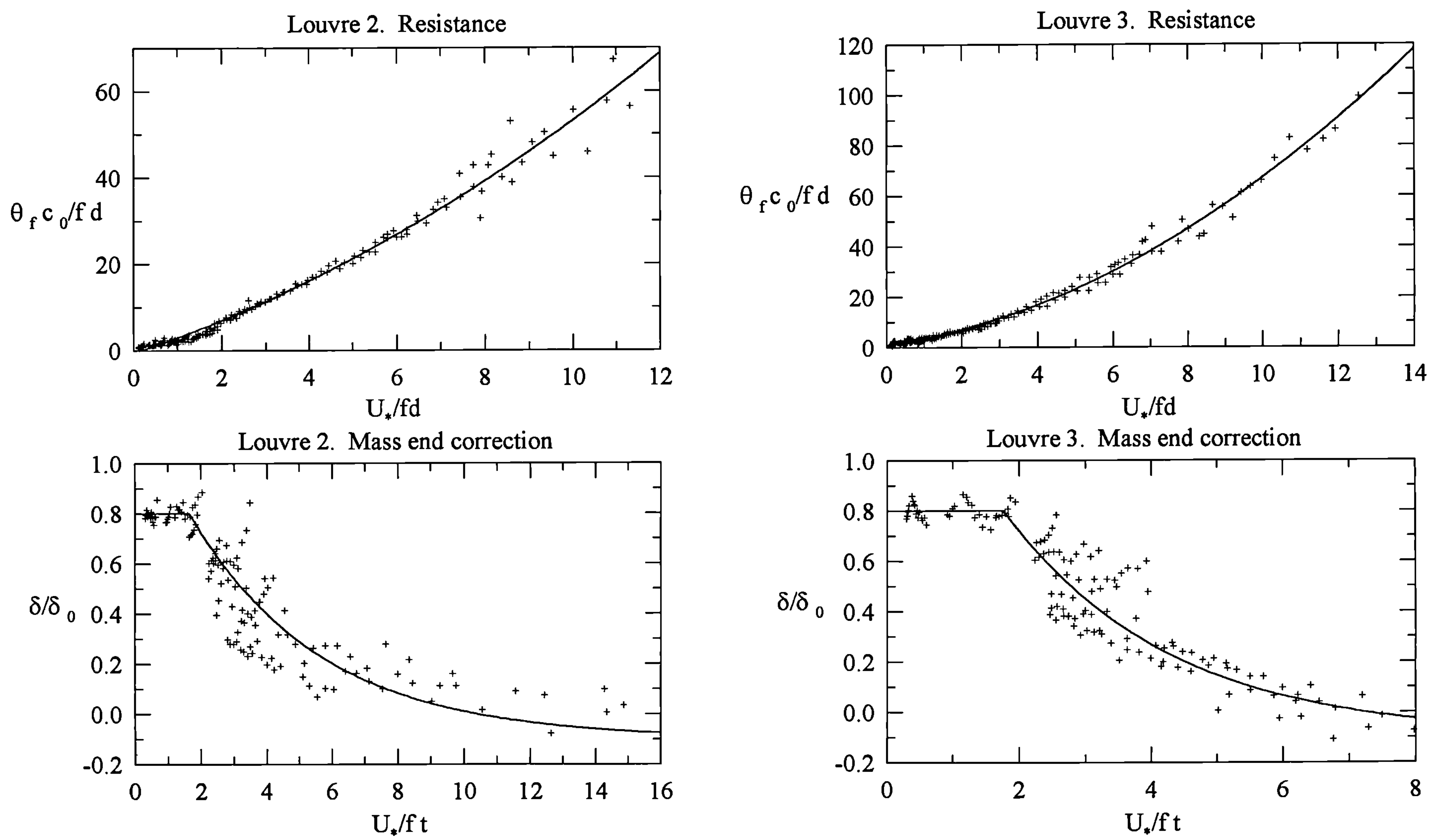

Figure 4.6. Acoustic impedance of louvres 2 and 3. + , Experiment; —— , Curve fitting formulae.

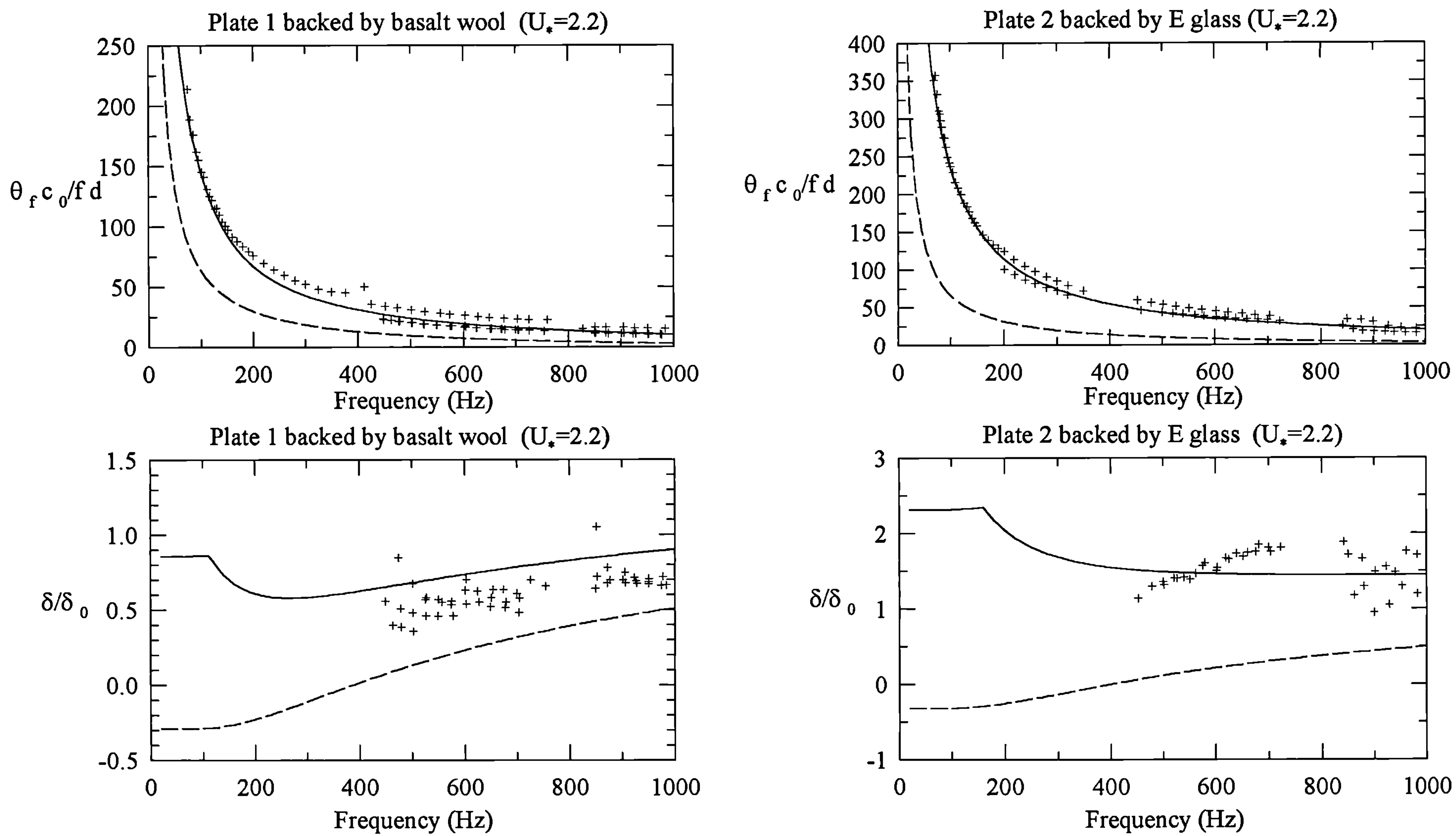

Figure 4.7. Acoustic impedance of perforates backed by a porous material.
+ , Experiment; ——— , Semi-empirical predictions; – – – , Formulae without absorbent.

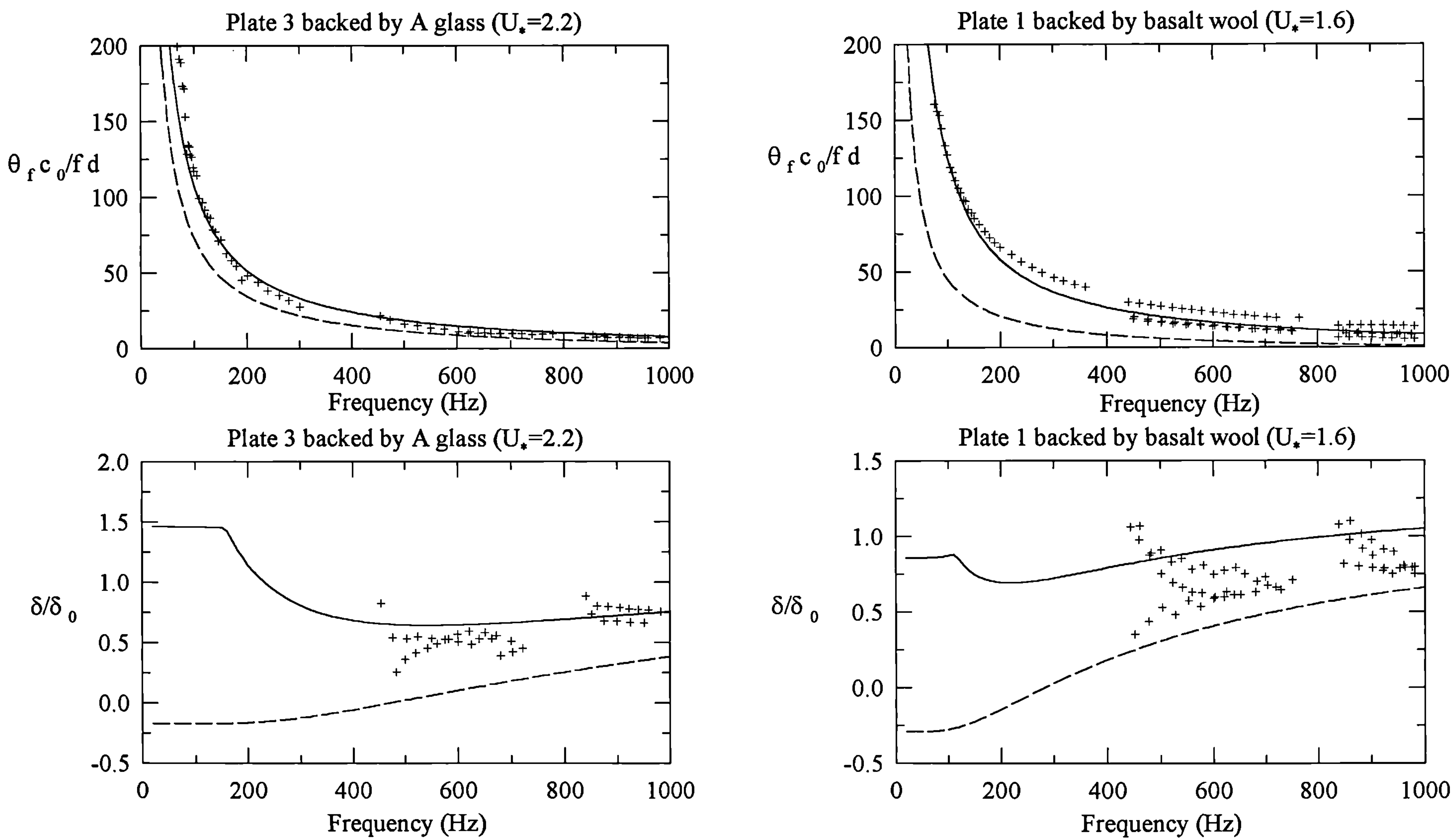

Figure 4.8. Acoustic impedance of plates 1 and 3 backed by a porous material.
+ , Experiment; ——— , Semi-empirical predictions; – – – , Formulae without porous backing.

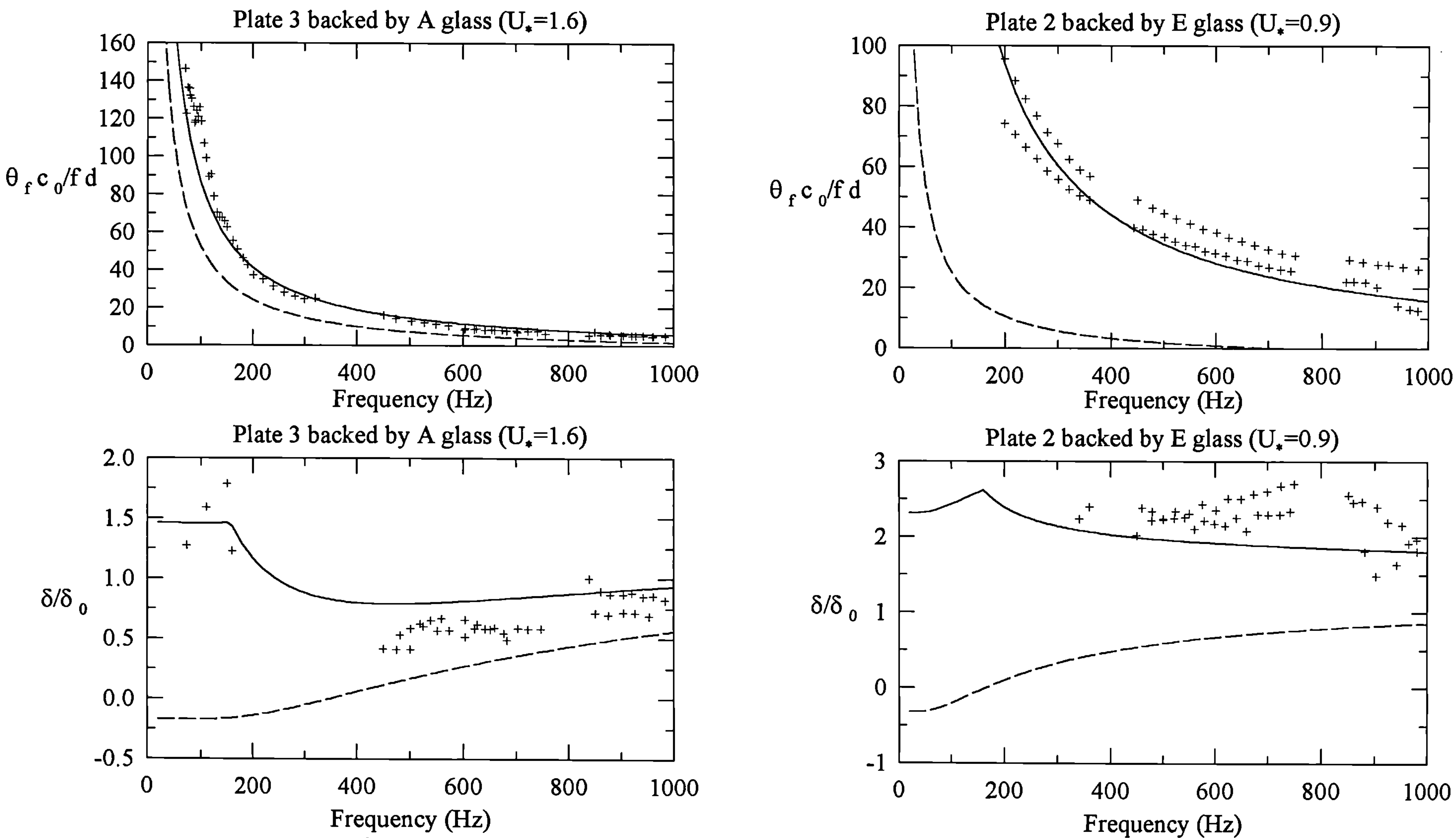

Figure 4.9. Acoustic impedance of plates 2 and 3 backed by a porous material.
+ , Experiment; ——— , Semi-empirical predictions; – – – , Formulae without porous backing.

CHAPTER 5

MEASUREMENT OF THE ACOUSTIC PROPERTIES OF DISSIPATIVE SILENCERS

Section 5.1

Introduction

The experimental measurement of exhaust systems is essential to allow comparisons to be made with theoretical models. This will then allow the accuracy of the theoretical models to be assessed. The experimental data obtained for silencers, taken by the methods described in this chapter, were used as the basis for deciding the route that modelling should take as the research proceeded. The experimental results presented for the silencers here will be extensively referred to in later chapters; however the measurements on catalytic converters, although performed by using the same methods, will be discussed separately in Chapter 11.

A silencer box is only a small component of the overall automotive exhaust system, which consists of an exhaust manifold into which an internal combustion engine supplies gas flow and radiates noise, and a more or less complex series of silencer elements (including catalytic devices) that ends in the tail pipe. The exhaust gases and noise are communicated to the environment by the tail pipe outlet. It is the effect of the silencer upon the tail pipe noise that is of interest here. Two distinct approaches are commonly used in order to test the effectiveness of a silencer experimentally. First, the effect of a silencer on an exhaust system can be measured by running the engine with the exhaust system in place and measuring the externally radiated noise. Secondly, the individual performance of the silencer can be measured by either removing the silencer from the exhaust system altogether, or measuring it in isolation whilst still on the exhaust.

Measuring externally radiated noise with the silencer as a part of the exhaust system is the most popular method, especially with commercial exhaust manufacturers. This is because such an approach is the only way to measure the true performance of a silencer. Two different measurements are commonly performed on the silencer system as a whole, insertion loss measurements and the measurement of the radiated sound pressure level. The measurement of the radiated sound pressure level involves measuring the sound pressure level at several locations remote from the tail pipe. This test is often the final test on an exhaust system since the type of results that are gathered are often those required by noise regulations. However, it is very difficult to assess the relative performance of an individual silencer from these measurements because so many other unknowns are present. If the measurement of the individual characteristics of a silencer is a priority (as it is here) then the insertion loss is usually measured. The insertion loss is calculated, like the radiated sound pressure level, from measurements of the sound pressure outside the tail pipe, however the measurements are usually taken much closer to the outlet of the tail pipe. Sound pressure level measurements are taken both with and without the silencer in place and the insertion loss is given by the difference between the two (the latter minus the former). The relative performance of a silencer can now be far more easily assessed and consequently this is the method most widely used in the empirical design of silencer boxes. An obvious advantage of measuring the performance of the silencer system as a whole is that only simple sound pressure level measurements are required outside the exhaust system.

The other experimental approach available to the designer is to measure the silencer in isolation from the rest of the exhaust system. This is of particular use when the acoustic characteristics of the silencer box alone are being studied since the method is capable of providing more direct information on the performance of an individual box than insertion loss data, which exhibit wave interference phenomena from the connecting pipework. On the other hand, measurements on an isolated silencer cannot be expected to provide detailed information on how the silencer will perform in insertion loss tests. Three different methods exist for measuring a silencer on its own: transmission loss, noise reduction and attenuation rate. The transmission loss of a silencer is defined as the fraction of acoustic power the silencer transmits from an incident wave into an anechoic termination downstream of the silencer. The noise reduction of a silencer is the difference between sound pressure levels upstream and downstream of the silencer, while the attenuation rate (in dB per unit distance) is the measurement of an "infinite" length of silencer transmitting the outgoing wave into an anechoic termination (this method is only of use with dissipative silencers). The attenuation rate of a silencer is usually measured for comparison with a theoretical eigenvalue analysis of a silencer and provides little physical insight into the potential performance of a silencer on-engine. Furthermore it only has any real physical significance for a single mode of sound propagation in the silencer duct, and the attenuation rate usually varies strongly between modes. It is usual for attenuation rate data to be given for the "least attenuated mode" but this is of limited relevance to the multimode sound field in a silencer of finite length. Consequently, the transmission loss and the noise reduction are the most common quantities to be measured when a silencer is studied in isolation. It is possible to study a silencer in isolation when it is still part of the exhaust system, but the measurements can be very difficult to perform because microphones must be located in the hot exhaust gases. Consequently transmission loss and noise reduction measurements are usually performed at room temperature under laboratory conditions. This has led to these experiments being most widely used in academic research.

A full description of the methods available for measuring silencers is given by Munjal [99], Sridhara and Crocker [100] and Prasad and Crocker [101]. The final testing of any silencer must be performed with the silencer as part of the entire exhaust system, this is because the impedance of the noise source (in this case an internal combustion engine) can influence the performance of a silencer. Consequently the insertion loss is the most important measurement for assessing the performance of a silencer. Unfortunately the insertion loss is not an attractive quantity to use for assessing the accuracy of theoretical predictions made for individual silencers. This is because the insertion loss is an extremely difficult quantity to predict accurately using theoretical models alone. The reason for this is that, in addition to predicting the performance of the silencer, it is also necessary to predict the engine (or source) impedance and also the tailpipe radiation impedance. Accurate prediction of the tailpipe radiation impedance is not too difficult, particularly if measurements are performed with the tail pipe radiating into an infinite baffle (see Munjal [99]). However predicting the source impedance presents large problems since the detailed theoretical modelling of the impedance of a multi-cylinder internal combustion engine is a formidable task and accurate models have yet to be obtained. Therefore, purely theoretical methods for predicting the insertion loss have been forced to assume that the source impedance is either zero (constant pressure), infinite (constant volume velocity) or characteristic. However, Prasad and Crocker [101] showed that only values obtained experimentally were satisfactory for predicting the source impedance of an engine. Since the source impedance has a large influence upon the insertion loss of a silencer, Prasad and Crocker found it necessary to resort to empirical measurements. This is obviously an undesirable approach to theoretical modelling. Since this thesis is concerned only with the modelling of silencer elements, it would seem to be unwise to draw conclusions from insertion loss measurements where uncertainty over predictions of the source and radiation impedance exists. This leads to the necessity of measuring a silencer in isolation where its performance is independent from the noise source.

The quantity most widely measured to characterise silencers in isolation is the transmission loss, this is because the noise reduction is not uniquely a characteristic of the silencer since it is affected by the geometry of the connecting pipes. Obviously, as previously discussed, it is not practicable to measure the transmission loss of silencers on-engine, therefore laboratory tests must be used. This does not allow measurements to be taken at high temperatures unless a hot gas flow facility is available, but on the other hand the tests are a very useful way of providing experimental data for comparison with theoretical predictions. The transmission loss tests reported in this chapter were used as the principal method for obtaining experimental data for comparison with theoretical predictions. The experiments were performed for a number of mean flow Mach numbers, which allowed the effect of flow on the theoretical predictions to be assessed.

It was also decided to perform insertion loss measurements on the silencers. The measurements of insertion loss presented in this chapter were performed by the industrial sponsors MIRA. The tests were carried out by MIRA because not all the relevant apparatus was available in Hull, most notably an anechoic chamber. MIRA carried out the measurements in an anechoic chamber by using a loudspeaker as the sound source and allowing the tail pipe to radiate into an "infinite" baffle; mean flow was not available. The experiment represents a rather idealised situation because the source impedance can be fairly accurately assumed to be infinite and the sound is radiated into an anechoic chamber. Consequently the results cannot be expected to shed much further light upon the accuracy of the theoretical modelling, though they do provide a set of independent experimental results for comparison to predicted data. Finally, it was proposed to perform insertion loss tests with the silencers on-engine in order to test the final predictions from the modelling. Unfortunately, even for insertion loss measurements, the experiment is very complicated, principally because the engine provides a far from ideal sound source. Although MIRA did perform on-engine tests the results were not of sufficient quality to be included here.

Section 5.2

The Test Silencers

The measurement of the transmission loss and insertion loss of six silencers was carried out in this investigation. Five of the silencers were dissipative silencers and the other silencer was an expansion chamber containing no sound absorbing material. The reactive silencer was included to allow the accuracy of the experimental method to be assessed since the acoustic performance of a plain expansion chamber is well understood and theoretical predictions are known to provide accurate correlation with experiment. The design of the dissipative silencers measured here was kept relatively simple; this is because the theoretical modelling reported in this thesis is not at a sufficiently advanced stage to be able to deal with complex multi-box silencers. Consequently each silencer has a simple "straight-through" design. Each silencer consisted of a simple box, constant in cross section along its length, surrounding a concentric perforated tube which is used to carry the air flow through the silencer. Three circular and two oval (approximately elliptical) cross section boxes were used. The elliptical boxes were included as an exercise in the modelling of non-circular cross section silencers. Three of the four materials discussed in Chapter 3 were used as acoustic absorbers in the silencers. Steel wool was not used because it is usually only employed as a "sock" surrounding the perforate, and it was felt that including a sock would unduly complicate the modelling. The three axisymmetric dissipative silencers are shown in Figure 5.1 and the two elliptical silencers in Figure 5.2. The reactive expansion chamber silencer is of the geometry shown in Figure 5.1, but contained no fibrous sound-absorbing material. Since the silencers were similar only one drawing has been shown for each type and the relevant dimensions are included in Table 5.1 below. The dimensions for the elliptical silencers refer to approximate dimensions of the major and minor axes of the ellipse.

Table 5.1. Dimensions of Test Silencers

Silencer	Length (mm)	Diameter (mm)	Absorbent
1	315	152.4	E glass
2	330	203.2	E glass
3	450	152.4	A glass
4	350	228.6×127	basalt wool
5	450	203.2×101.6	E glass
Expansion Chamber	315	152.4	N/A

Each silencer was fabricated by the industrial sponsors Eminox Ltd., who only stock one type of perforate plate (corresponding to plate 3 in Chapter 4, where the plate thickness is 1mm, the hole diameter 3.5mm and the percentage open area is 27.2%), and therefore each dissipative silencer uses the same perforate, note that the expansion chamber did not include a perforate. Eminox also uses mainly E glass in its silencers, hence its use in three of the five silencers; the other materials were supplied by other industrial sponsors. The silencers tested were intermediate in size between car and truck silencers. The inlet and outlet pipe sizes were chosen to fit the existing flow duct apparatus. The silencer sizes selected were advantageous in that the acoustic attenuation of all but the lowest frequencies is large enough to be measurable to acceptable accuracy.

Section 5.3

Experimental Method for the Measurement of the Transmission Loss

Early methods developed for measuring the acoustic performance of exhaust silencers centred around using standing wave tubes, similar to those used for measuring porous materials in Chapter 3. Gatley and Cohen [102] reviewed a number of alternative methods to the standing wave tube but concluded that the optimum method for measuring the transmission loss was to use a standing wave tube terminated by an anechoic chamber. It has subsequently been asserted by a number of authors (see for example Munjal [99]) that if transmission loss measurements are to be carried out using a standing wave tube then an anechoic chamber must be used. The method of Gatley and Cohen relied upon discrete frequency measurements which are laborious to perform, and it was not until broad-band measurements were introduced by Seybert and Ross [63] that results could be taken over a wide frequency range in a single test. Seybert and Ross found it necessary to modify the traditional standing wave tube by locating a third microphone downstream of the silencer, before the anechoic termination, in order to be able to obtain transmission loss results. The standing wave tube method has been shown to work successfully, though it does have a number of limitations. The transmission loss is calculated indirectly from measurements of the maxima and minima of the standing wave, and this often incurs errors in the final predictions, errors are usually most apparent in the low frequency region (between 100 and 150Hz). Problems can also occur in setting up and measuring standing wave patterns in a tube with superimposed mean flow since traditional standing wave tube apparatus do not allow the introduction of mean flow. Finally, a problem that is unique to the experiments performed here is the lack of an anechoic chamber, and this essentially precludes the use of the standing wave tube method for measuring the transmission loss.

The limitations present when using a standing wave tube to measure the transmission loss were considered by Singh and Katra [103]. They proposed using an impulse technique that involved measuring the transmission loss directly and was also capable of providing broad-band data. The method involves passing a pulse of short duration and large peak pressure through the silencer. The incident pulse is captured by a microphone upstream of the silencer and the transmitted pulse is captured by a microphone downstream. Singh and Katra captured both the incident and transmitted pulses at the same time. To do this they relied upon sufficiently large distances between the upstream microphone and the silencer and the downstream microphone and the end of the outgoing pipe to avoid reflected pulses. Cummings and Chang [23] modified this method by measuring the incident pulse and the transmitted pulse separately. They did this by using only one microphone to capture data, performing the experiment both with and without the silencer placed in the test rig. One advantage of this method is that acoustic reflections from the silencer do not appear in the signal at the microphone measuring the incident pulse. Another advantage of the method is that both the incident and the transmitted pulse are measured in approximately the same position.

The method used by Cummings and Chang [23] is the most appropriate method to use here. This is because an anechoic chamber was not available and the room that was available only had limited space, thereby precluding the use of Singh and Katra's method. The apparatus was arranged as shown in Figure 5.3. The acoustic source signal was a rectangular pulse initiated by the function generator which was fed via a power amplifier to a loudspeaker. The pulse travelled down 3.3m of circular cross section steel tubing before reaching the silencer. The microphone was situated as close by as possible to the downstream end of the silencer in order to eliminate any effects due to the piping between the microphone and the silencer. The additional length of pipe on the downstream side of the silencer was used in order to avoid reflections from the end of the pipe appearing back at the microphone too early. Ideally, steel pipe would have been used, but the laboratory was not of sufficient size to accommodate this; therefore a piece of flexible plastic tubing was used, and this appeared to introduce no adverse effects. The output of the microphone was fed, via a measuring amplifier, to an FFT analyser and measurements were recorded both with and without the silencer in place. When the silencer was removed, the short section of steel pipe, into which the microphone was inserted was connected by a flange to the steel pipe upstream. The mean flow was supplied by a variable volume flow compressed air supply, and this was silenced in order to reduce flow and compressor noise. The mean flow velocity was measured by the use of a Pitot tube at the outlet of the flexible pipe.

5.3.1 Data Acquisition

When the impulse technique is used to measure the transmission loss of a silencer, the choice of pulse and the way in which the pulse is captured is very important. In order to obtain accurate measured values for the transmission loss, it is desirable for the pulse that enters the silencer (the output pulse) to have a number of characteristics; these were given by Singh and Katra [103] to be: (i) the pulse spectrum must be adequately uniform over the desired frequency range, (ii) the pulse must have a relatively short time span to avoid excessive pipe lengths or an excessively long time window, (iii) the pulse should be wide enough to contain sufficient power spectral density to ensure a good signal to noise ratio, and (iv) the combined physical limitations of the loudspeaker and amplifier must not be exceeded. Unfortunately, the combined response of the power amplifier, loudspeaker and also the side branch, means that the acoustic signal found at the silencer (the output pulse) does not have a pulse similar in shape or spectral characteristics to that of the initial electronic signal (or input pulse) applied to the amplifier. It is possible to overcome this problem by synthesising the input pulse in order to obtain the desired characteristics in the output pulse. Singh and Katra [103, 104] synthesised a digital input pulse by means of trial and error in order to arrive at the desired output pulse. Salikuddin et al. [105] also used signal synthesis, but they measured the combined response of the amplifier and loudspeaker experimentally, from where a sharp output pulse with flat frequency response was obtained by feeding the convolution of the desired pulse and the inverse Fourier transform of the reciprocal of the amplifier plus loudspeaker response into the acoustic driver. Signal synthesis is undoubtedly capable of providing the desired output pulse, however it does require the re-calculation of the input pulse for each test condition, this can prove to be a laborious task. Furthermore, problems can arise if the acoustic driver cannot generate sufficient sound pressure levels at frequencies outside its own frequency band limits.

For the impulse tests performed here, it was decided that, in view of the extra effort involved in implementing signal synthesis techniques and the frequency limitations of the loudspeaker, a more straightforward method was necessary. Also, the tests performed on silencers here are relatively simple and it was anticipated that as long as the signal to noise ratio was large enough, no problems would be encountered. Therefore if synthesis of the input signal is not used, the only option is to use an input pulse with a flat frequency spectra, and this was obtained by varying the pulse length on the signal generator. The effect upon the output pulse caused by the combination of the amplifier, loudspeaker and side-branch is shown in Figure 5.4. It is evident that over a frequency range of 0-2kHz, a fall-off occurs in the pressure amplitude at high and very low frequencies. This effect upon the output pulse is unavoidable but does not present too many problems so long as high enough sound pressure amplitudes are used, although it does appear that at very low frequencies problems might occur. It should also be mentioned that pressure amplitudes should be kept low enough to avoid acoustic non-linear effects occurring in the silencer, since transmission loss is normally specified in the linear regime.

The selected input signal was fed from the signal generator to the power amplifier and then to the loudspeaker; the radiated acoustic signal was captured by the microphone which transmitted the signal, via the measuring amplifier to the analyser. This process was performed for a number of consecutive, identical, pulses. To allow time domain averaging (necessary for reducing the effects of flow noise, see Salikuddin [105]) the signal captured by the analyser was triggered by the signal generator. Once the data capture has been triggered and the pulse stabilised on the screen of the analyser the sampling parameters listed by Singh and Katra [103] must be set. The test parameters used here are given in Table 5.2 below.

Table 5.2. Sampling Parameters for Test Pulse	
Time window B	0.2 seconds
Number of data points N	400
Time resolution Δt	0.5ms
Sampling frequency f_s	2kHz
Maximum frequency of interest $f_{\max.}$	1kHz
Frequency resolution Δf	5Hz
Number of averages	128-4096

The test parameters are dependent upon each other in the following way

$$B = N\Delta t,\ \Delta t = 1/f_s,\ f_{\max.} = f_s/2 \text{ and } \Delta f = 1/B. \qquad (5.1...5.4)$$

The criteria were set up after discussion with the industrial sponsors, it was decided that the maximum frequency of interest was to be 1kHz. A high frequency resolution (5Hz) was also required because the results are to be displayed in the form of continuous frequency spectra. From these two criteria all the other factors can be set using equations (5.1) to (5.4) and it can be seen that, although transmission loss data were measured up to 2kHz, only measurements up to 1kHz were reliable.

Finally, the captured signal must be edited in the time domain in order to obtain results that are a function of the silencer's performance only and do not include "spurious" data. Such spurious data usually occur in the form of axial acoustic reflections that appear in the time window; for instance, once the signal passes through the silencer it continues on to the termination of the flexible pipe, from here it is reflected back along the pipe, eventually being captured by the microphone again. This effect can also occur when the input pulse is reflected back toward the source by the silencer, to the loudspeaker and then back down through the silencer again. "Editing out" of the reflected pulses is necessary in order to simulate the effects of anechoic terminations on both sides of the silencer. The lengths of piping between the microphone and the points at which the pulse is reflected determine the time it takes before reflections appear in the time window. The two lengths of pipe used in this investigation were made similar so that both the reflections arrived back at the microphone at approximately the same time. The reflections captured in the time window can be seen in the top left hand graph in Figure 5.5. The first signal is the incident pulse and the second is a combination of the reflected pulse emanating from the loudspeaker and that from the end of the flexible tube; the latter component probably dominates, since the second signal is almost the inverse of the first, with a diminution in peak pressure values, characteristic of an acoustic reflection, at low Helmholtz number, from an open tube termination. Subsequent reflections can be seen in the time window and these continue until eventually the great majority of their energy is dissipated. These reflections were edited out from the total signal before the data was transformed into the frequency domain. This was done by using the analyser's force window which allows the user to set data equal to zero, removing any spurious signals from the time window. The effect of employing the force window can be seen in the graph shown in the bottom left hand corner of Figure 5.5. The edited signal is now characteristic of the silencer in isolation. The undulations present after the initial spike are internal reflections associated with the silencer box. When time domain editing is carried out in this way it is very important to delay the arrival of the reflected pulses as long as possible in order to allow the internal reflections within the silencer to die away to a sufficient extent. The low frequency reflections inside the silencer will take the longest to die down, because they are less highly attenuated than the higher frequency components, and therefore these are the most prone to interference by external reflections. Unfortunately, it is impossible not to truncate some low frequency data due to the finite lengths of piping that must be used. For the measurements performed here, the low frequency limit is approximately 100Hz.

The pulses are ensemble-averaged in the time domain in order to remove - as far as possible - time dependent random flow noise. Depending upon the mean flow speeds used, it was found necessary to take between 128 and 4096 data samples in the time-averaging. It should, however, be noted that there is a practical limit to the number of samples that can be time averaged to advantage. As the number of samples is increased, the relative benefit derived from time averaging, in terms of the reduction of flow noise, diminishes. And furthermore, an excessively large number of samples can introduce a "flow jitter" effect, whereby large-scale turbulence or minor fluctuations in the mean flow speed can cause small variations in the arrival time of the test pulse at the microphone, relative to the triggering time. The result of this is a "blurring" of the time averaged signal and eventual loss of resolution in the data. A figure of 4096 samples was considered to be the maximum that could be usefully employed. The effect of time averaging a signal for a Mach number of 0.15 is shown on the right hand side of Figure 5.5. The graph in the top right hand corner shows the signal before time averaging and the graph in the bottom right hand corner shows the signal after averaging 2048 samples. It is evident that time averaging is capable of considerably smoothing the results.

The measurements described above need to be carried out in a similar manner both with and without a silencer. The analyser then captures each signal in the time domain and transforms it into the frequency domain by applying a discrete Fourier transform. The frequency spectra can then be downloaded to a PC, which is used to compute the transmission loss. The transmission loss (TL) is given by

$$\mathrm{TL} = 20\log\left|\frac{A_\mathrm{I}}{A_\mathrm{T}}\right|, \tag{5.5}$$

where A_I is the pressure amplitude of the pulse captured without the silencer present and A_T is the pressure amplitude of the pulse captured with the silencer present. The results obtained for the six test silencers are described in Section 5.5.

Section 5.4

Experimental Method for the Measurement of the Insertion Loss

The insertion loss measurements discussed here were performed in an anechoic chamber by the industrial sponsors MIRA. The tests constitute a rather idealised situation because a high impedance source has been used and the tail pipe radiated into an "infinite" baffle situated inside the anechoic chamber. Furthermore the tests were carried out at room temperature. It was not expected that this approach would provide any further insight into the validity of the theoretical models (over and above that furnished by the transmission loss data), but rather the purpose of the tests was to allow comparisons to be made between numerical predictions and two completely independent sets of measured data.

Since the author made no contribution to the experiments, only a brief description of the method used is given here. The apparatus used by MIRA is shown in Figure 5.6. The loudspeaker radiated into a small diameter tube in order to simulate a high impedance source, and this ensured that the output did not vary significantly with the load impedance. Obviously the use of a loudspeaker in such a manner does not allow the introduction of mean flow. The tail pipe was terminated by an effectively infinite baffle and sound pressure data were taken by means of a microphone located at the mouth of the tail pipe. As in the case of the transmission loss, sound pressure measurements were taken both with and without the silencer in place. The insertion loss was found by measuring the acoustic pressure p at the microphone and the supply voltage to the loudspeaker V. The insertion loss (IL) is then given by

$$\mathrm{IL} = 20\log\left|\frac{p_{\mathrm{I}}V_{\mathrm{T}}}{p_{\mathrm{T}}V_{\mathrm{I}}}\right|, \tag{5.6}$$

where p_I and V_I were measured without the silencer present and p_T and V_T were measured with the silencer present. The results obtained by MIRA for the insertion loss are shown in the next section.

Section 5.5

Experimental Results and Discussion

The experimental results obtained for both the transmission loss and the insertion loss are described in this section. For the transmission loss, measurements were obtained both with no mean flow and with mean flow Mach numbers of 0.05, 0.11 and 0.15. For the insertion loss, all the results were obtained with no mean flow. A large amount of data were obtained and, for the sake of brevity, only relatively few of the results are shown here. However, a larger number of the experimental data are discussed later on in this thesis, where they are used for comparison to theoretical predictions.

It was mentioned previously that a plain expansion chamber was fabricated in order to validate the experimental method. The results for both the transmission loss and the insertion loss without mean flow are shown in Figure 5.7. For both graphs the solid line represents the measured data and the dashed line the theoretical predictions. The theoretical predictions for the expansion chamber were supplied by Peat [106], and since this thesis is concerned only with the modelling of dissipative silencers, the theory behind the predictions is not given here. The theoretical method used to obtain the numerical predictions shown in Figure 5.7 has been extensively compared to other measured data for reactive silencers and shown to be accurate in the plane-wave frequency range. It is evident for both the transmission loss and the insertion loss that the predicted and measured data agree well. This is particularly true of the transmission loss, where good agreement can be observed between 100Hz and 1.6kHz. This represents a wider range of agreement than was expected after setting $f_{max.}$ to be 1kHz. The insertion loss data also show good agreement, especially at low frequencies, where prediction and measurement shows better agreement than is the case with the transmission loss data. This effect is probably attributable to the aforementioned higher "cut-off" frequency imposed by the impulse test technique used to obtain transmission loss data. The troughs present in the insertion loss data occur because of resonance effects in the pipes connected to the silencer, and the difference between the predictions and measurements are likely to be partly caused by errors in the measurement of pipe lengths and/or temperature. Nevertheless the insertion loss predictions agree closely with measured data up to 1.6kHz, with the main discrepancies occurring at the peaks in the data. The differences at the peaks are probably caused partly by the neglect of acoustic boundary-layer attenuation in the theoretical model and partly by a lack of sufficient sound energy in the test signal to ensure accurate measurement of the peaks. However, a comparison between measurement and prediction for both the transmission loss and the insertion loss indicates that both experimental methods give reliable data.

Once it was established that the experimental methods used were adequate, measurements were performed on the dissipative silencers. Figure 5.8 shows transmission loss plots for silencers 1, 2, 4 and 5. For silencer 1 (top left hand corner), results are shown for no mean flow and it can be seen that a relatively smooth curve has been obtained. It is noticeable that at frequencies up to 100Hz the data are negative, and this is attributable to the errors incurred when the reflections are filtered out of the time window. Although data are presented up to 2kHz, results above 1kHz should be treated with caution. For silencer 2 (top right hand corner), measurements for the highest obtainable Mach number (M=0.15) are shown. It can be seen that introducing mean flow causes the plots to become more irregular because of flow noise, the effects of which cannot be completely removed. Data are shown for silencer 4 in the bottom left hand corner, the lower curve for M=0.15 and the upper curve for M=0. It is evident that mean flow has brought about an overall drop in transmission loss. Indeed a systematic reduction in transmission loss occurs when the mean flow speed is increased and this can be seen in the measurements for silencer 5 (bottom right hand corner) where data for each flow speed have been plotted; the upper curve is for M=0 and successively lower curves are for M=0.05, 0.11 and 0.15. The insertion losses of silencers 1, 3, 4 and

5 are shown in Figure 5.9. All the plots shown are for zero mean flow and the curves do not show the undulations, caused by mean flow, that are evident in the transmission loss data. For both the insertion loss and the transmission loss, the problems occurring in the expansion chamber data are also evident for the dissipative silencers. With the transmission loss, inaccuracies in experimental data occur below 100Hz although, as for the expansion chamber, the data appear reasonable up to 1.6kHz. Clearly the introduction of mean flow decreases experimental accuracy and this is particularly true at the frequency extremes. The insertion loss measurements show better accuracy than the transmission loss data at low frequencies (below 100Hz), although it appears that 50Hz is the lowest frequency at which the results can be relied upon. At frequencies up to 1kHz, there is little to choose between the two methods in terms of accuracy, and at higher frequencies, rather better accuracy can be expected from the insertion loss technique.

It can be concluded that the transmission loss measurements do appear to be reliable, at least within the frequency range 100Hz to 1kHz. The insertion loss data can be used for comparison to theoretical predictions at the lower frequencies where predictions by transmission loss measurements are inaccurate. The transmission loss is the most straightforward quantity to predict theoretically, and therefore the bulk of comparisons between theory and experiment, made later in this thesis, will be made on the basis of transmission loss data.

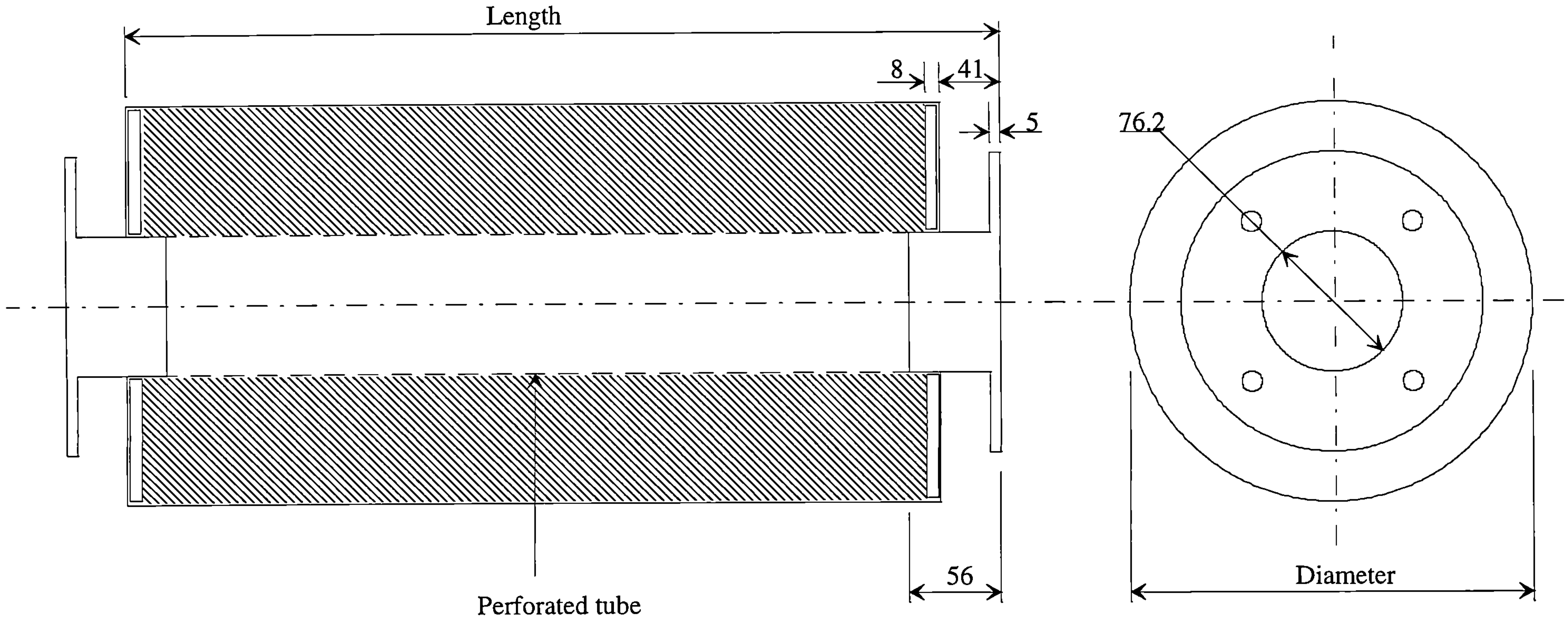

Figure 5.1. Dimensions for axisymmetric dissipative silencers.

All dimensions in mm.

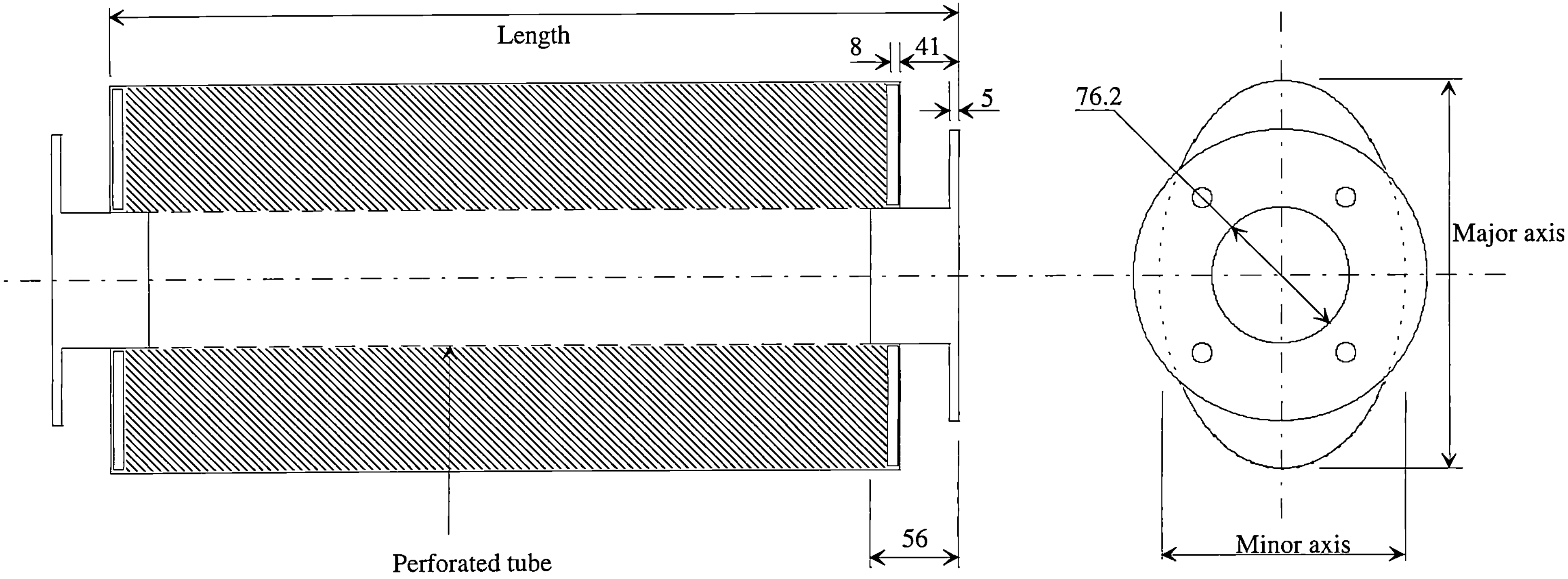

Figure 5.2. Dimensions for elliptical dissipative silencers.

All dimensions in mm.

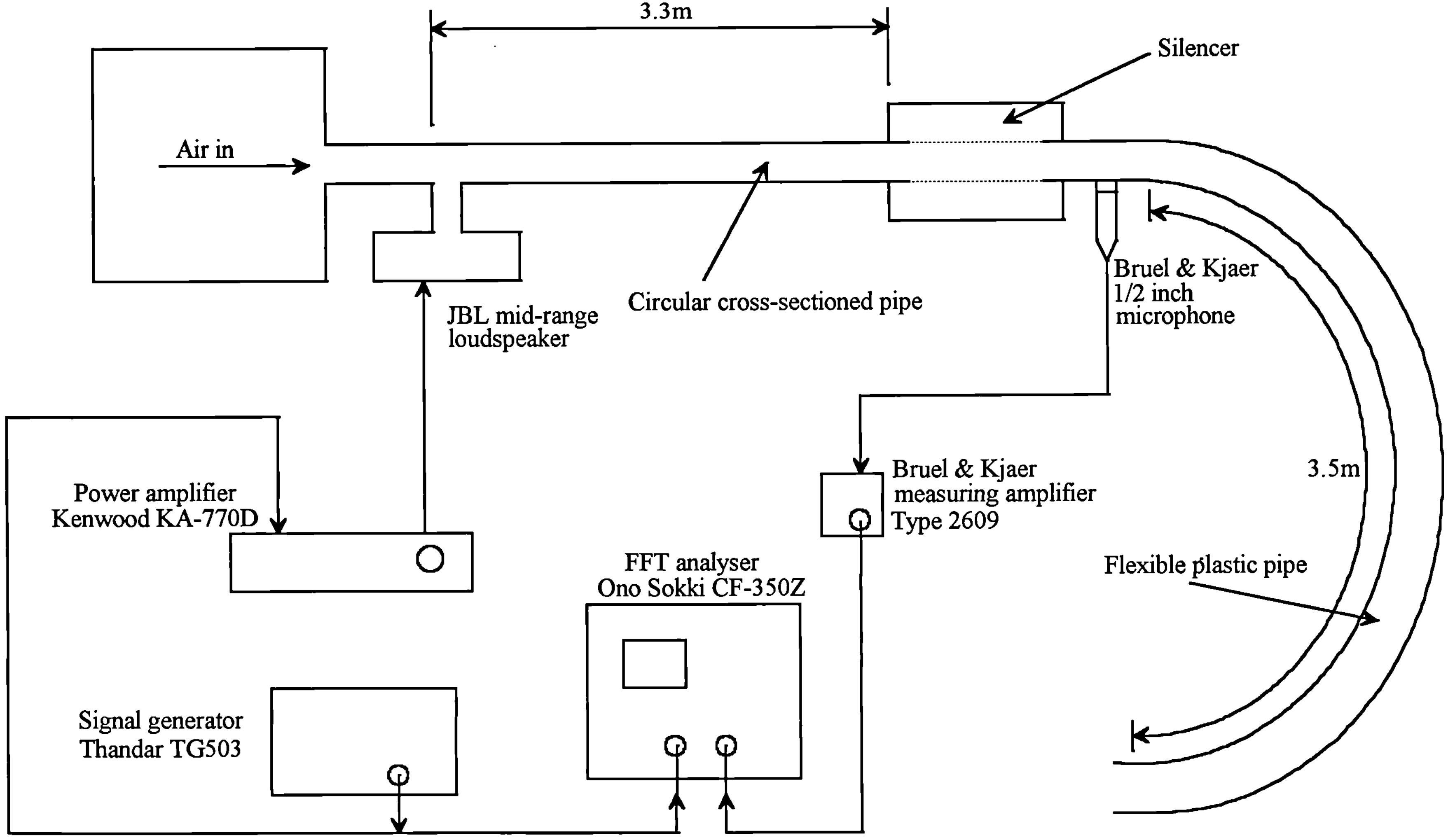

Figure 5.3. Experimental apparatus for measuring the transmission loss of a silencer

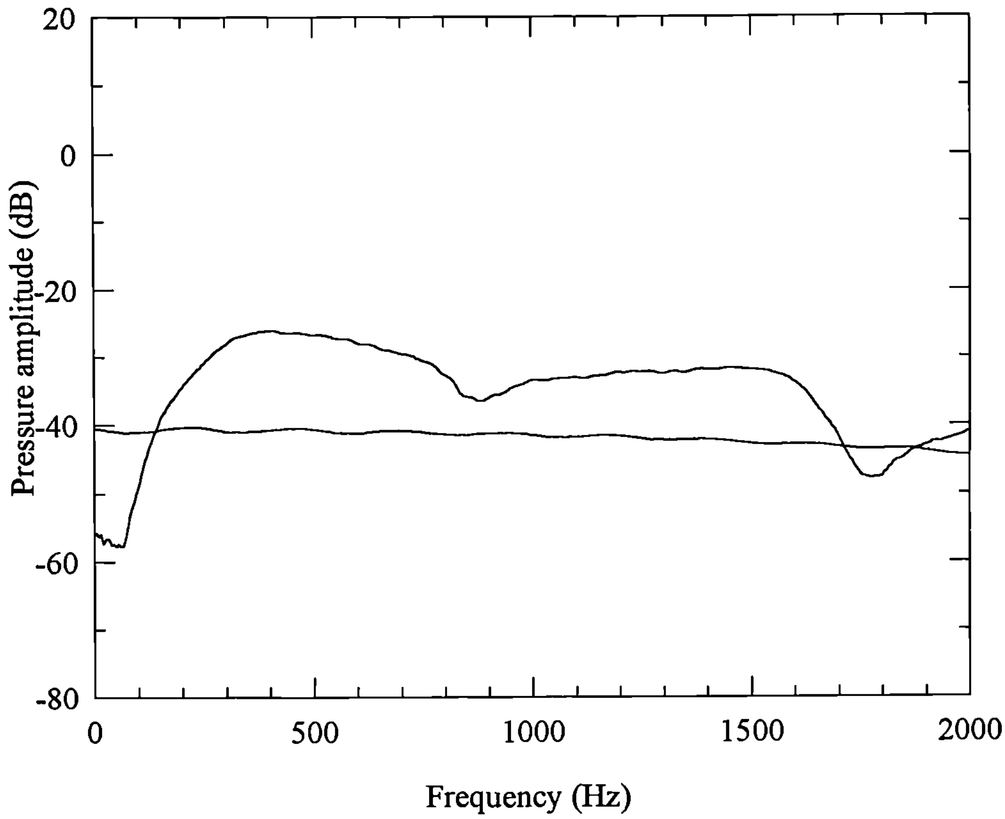

Figure 5.4. Frequency spectra for the pulse emitted by the signal generator (input pulse) and the pulse seen by the microphone (output pulse) with no silencer present.

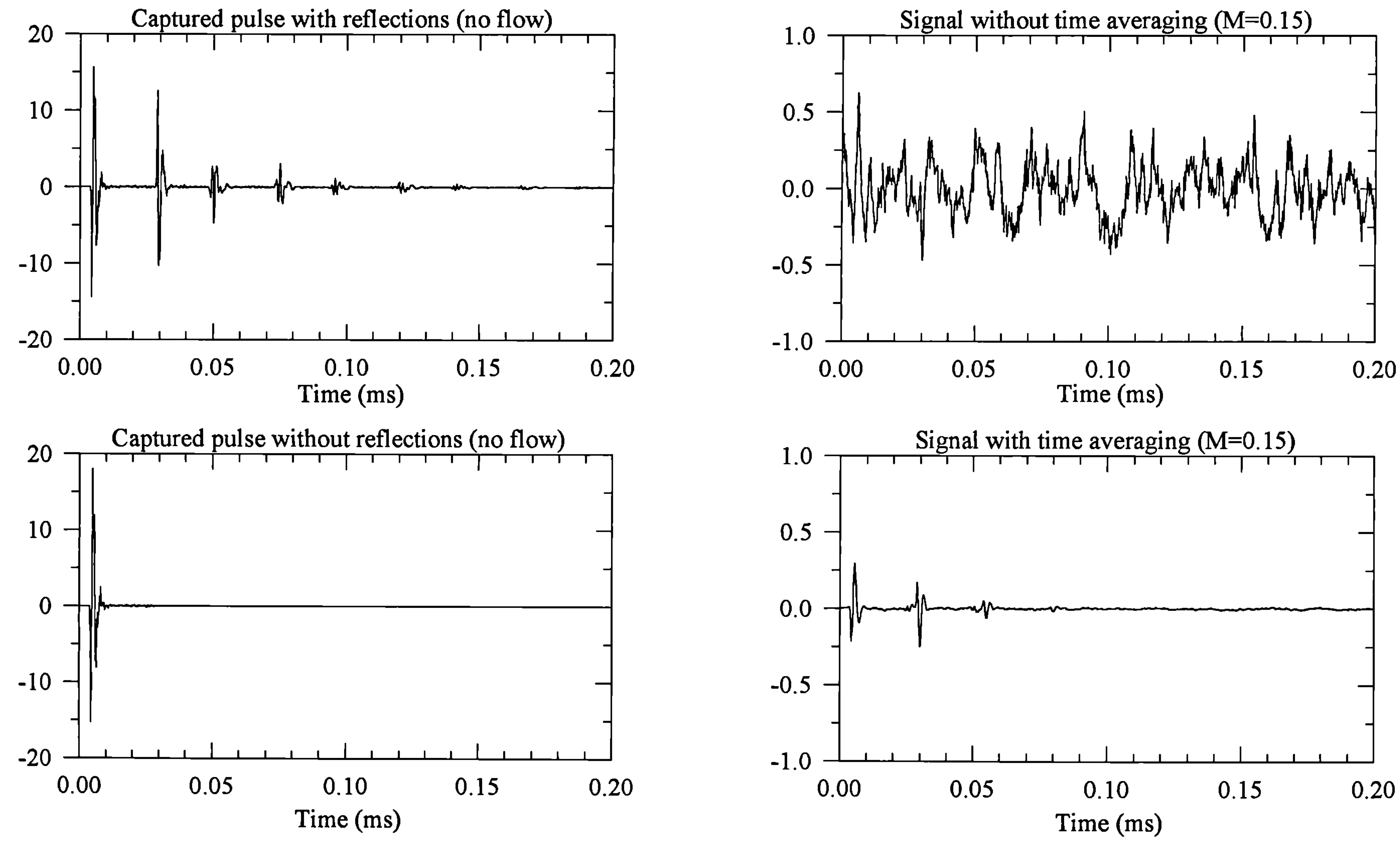

Figure 5.5. Acquisition of data and signal editing for transmission loss measurements.

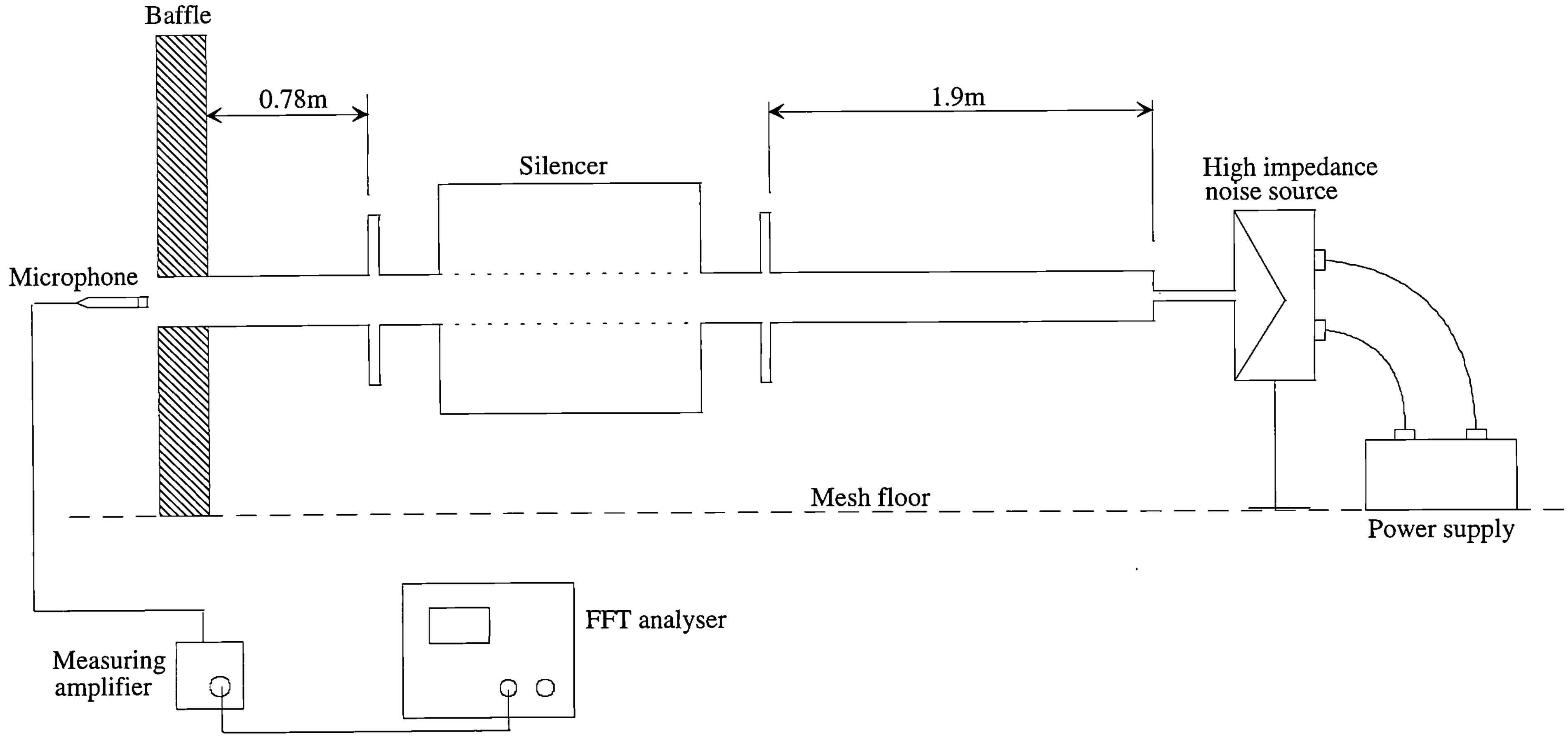

Figure 5.6. Experimental apparatus for measuring the insertion loss of a silencer.

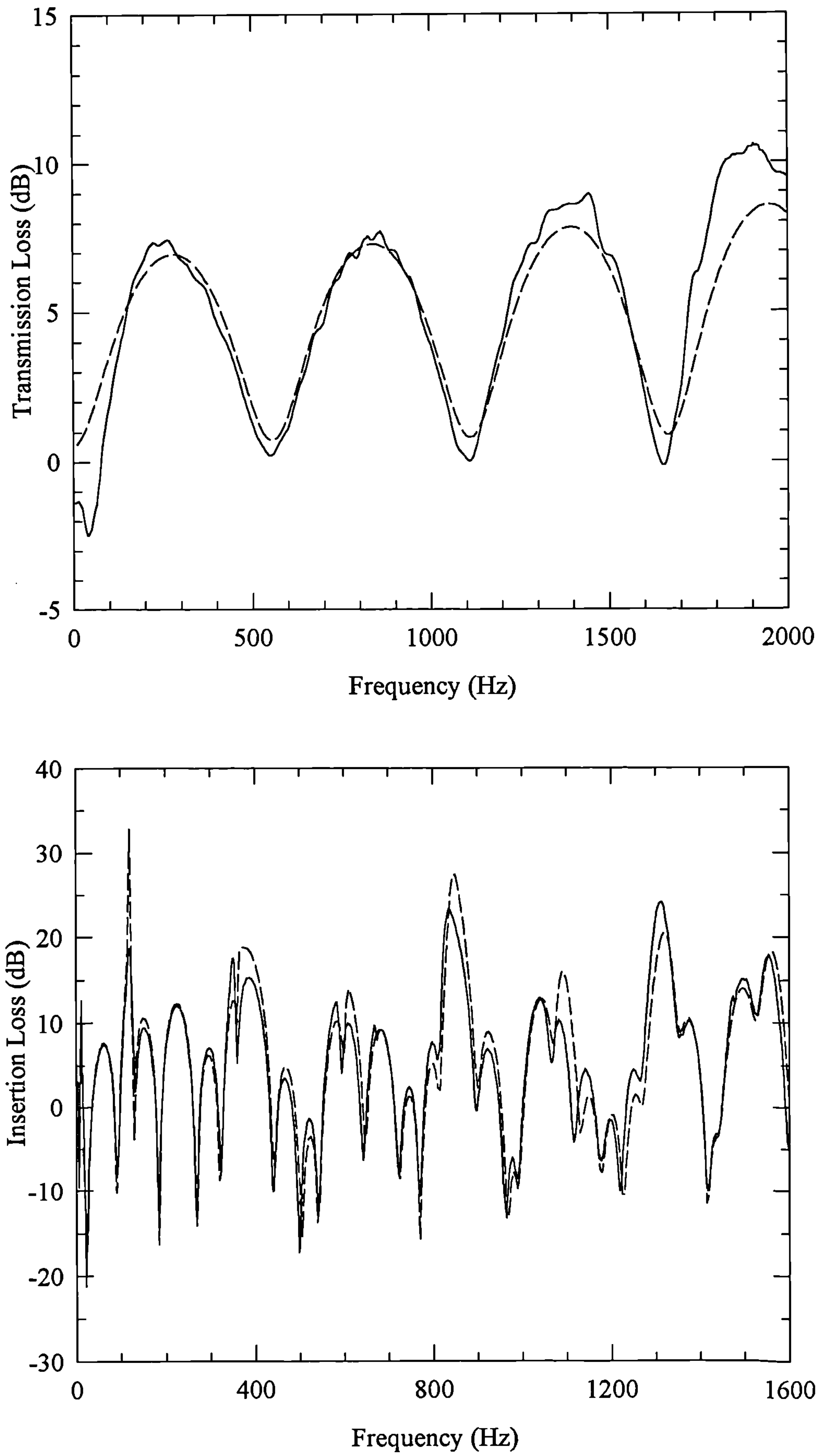

Figure 5.7. Transmission loss and insertion loss data for expansion chamber with M=0.
—— , Experiment; — — — , Theoretical predictions.

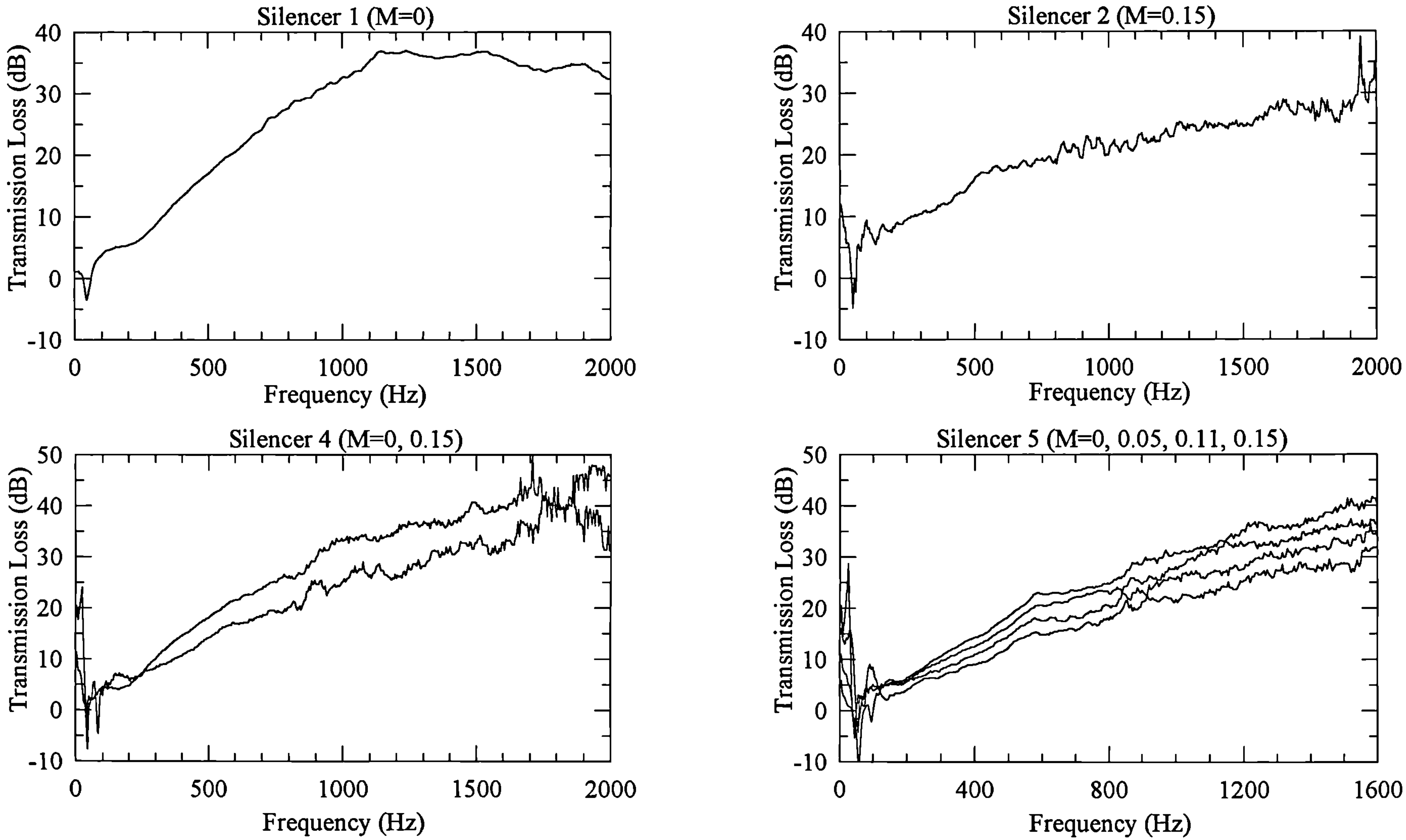

Figure 5.8. Experimental data obtained for the transmission loss.

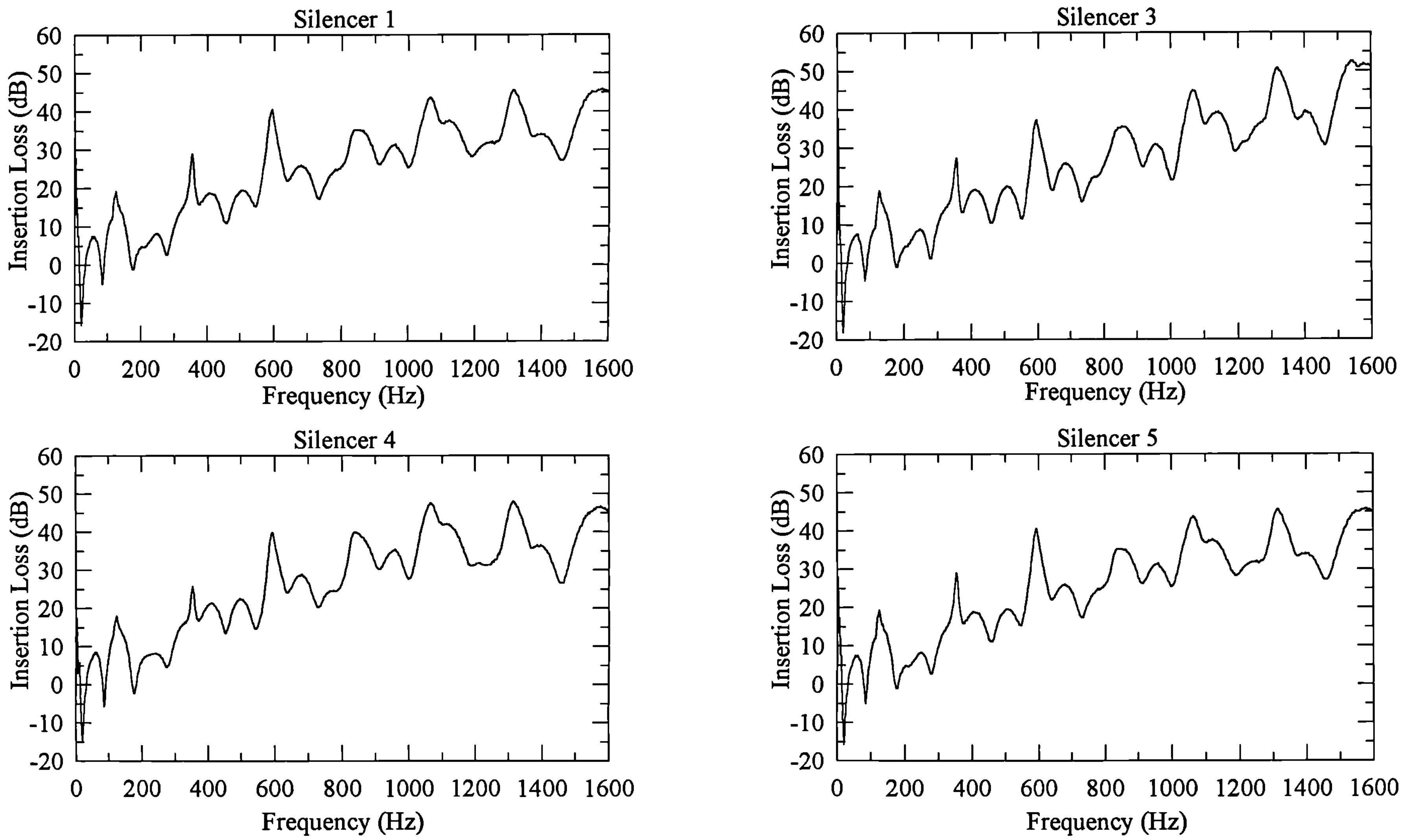

Figure 5.9. Experimental data obtained for the insertion loss.

CHAPTER 6

A FUNDAMENTAL MODE APPROACH TO MODELLING AXISYMMETRIC DISSIPATIVE SILENCERS

Section 6.1

Introduction

The next four chapters in this thesis will concentrate on modelling the acoustic behaviour of dissipative silencers theoretically. In Chapters 6 to 9 different methods will be developed in order to predict both the transmission loss and insertion loss of the five silencers measured in the previous chapter, and in Chapter 10 the relative merits of each approach will be compared. Once the theoretical modelling of silencers can be carried out it will become clear how important the bulk acoustic properties of the absorbent and the perforate impedance (see Chapters 2, 3 and 4) are to the final results - hence their inclusion early in the thesis. The most obvious place to start when modelling silencers is to employ the simplest method available. In general, when studying duct acoustics, the simplest approach available to the designer is to use a fundamental mode model.

To introduce the concept of a fundamental mode model for dissipative silencers, it is useful to first look at the case of a simple rigid walled pipe of circular cross section. The sound pressure field in a rigid walled cylindrical pipe is governed by the acoustic wave equation, which is a homogeneous second order partial differential equation. One method of solving the wave equation is to use the standard mathematical technique of separation of variables, and the general solution is obtained by writing the sound pressure as an infinite sum of eigenfunctions which form a complete set. The eigenfunctions are often known as modes of propagation. For hard-walled cylindrical pipes, the eigenvalues corresponding to the various modes lie either on the real or imaginary axes, but they are not complex. Depending upon variables such as excitation frequency, diameter of pipe and ambient temperature, each mode is either "cut-on" or "cut-off". The lowest mode propagates at all frequencies, whereas each higher mode has a well defined cut-off frequency, below which it is evanescent and above which it is propagating. At the cut-off frequency, the positive motion is normal to the pipe axis and the axial phase velocity is infinite. The lowest mode is easily identified because it has the smallest eigenvalue of all the modes. For circular pipes with no mean flow, the lowest eigenvalue is equal to the wavenumber of the gas contained in the pipe and is real valued. This first mode is known as the fundamental mode and its eigenfunction is independent of transverse position and equal to unity. Consequently the fundamental mode has a pressure distribution which is uniform across the radial dimension of the pipe and this has subsequently become known as a "plane-wave". Since the fundamental mode is the only plane wave solution to exist for a hard-walled pipe, models that include only the fundamental mode are known as plane wave models. The plane wave approach to modelling hard-walled pipes is used extensively because the exclusion of higher order modes does not appear to effect the accuracy of predictions for most applications.

The fundamental mode approach can also be applied to dissipative silencers, though the behaviour of the modes changes when a dissipative element is introduced into the pipe. It is still possible to represent the sound pressure field in a dissipative silencer as an infinite sum of eigenfunctions, although it has not been proved that these form a complete set (this will be discussed in later chapters). In a dissipative silencer, the dissipation of sound energy in the absorptive region causes the eigenvalues for each mode to become complex and the fundamental mode is no longer a plane wave. Furthermore, the "ordering" of modes becomes less clear-cut than it is in a rigid walled duct. There are, in general, no well-defined cut-off and cut-on phenomena, and higher order modes are capable of undergoing lower attenuations than the fundamental mode at the same frequency. The "fundamental mode" may therefore not necessarily be the least attenuated mode in a dissipative duct. The fundamental mode must be identified by examining the mode shape (or eigenvector) as well as the eigenvalues of each of a series of individual modes. By convention, the fundamental mode in a dissipative silencer is taken to be the plane wave like mode (see Cummings and Chang [23]) and this is usually less strongly attenuated than the first radial mode. The fundamental mode can usually be easily identified by examining solutions at very low frequencies since at this point the mode is usually very close to being a plane wave and is almost always the least attenuated mode.

In the literature, fundamental mode predictions have usually been performed by approximating full modal solutions. Full modal solutions usually take the form of an eigenvalue analysis of an infinite duct and this method has been widely covered in the literature. Eigenvalue solutions for silencers of general cross sectional shape will be discussed further in Chapter 8. The solution of particular interest here is the full modal solution performed by Cummings and Chang [16] who calculated the attenuation of a number of modes for an axisymmetric dissipative silencer. This solution is useful because a simple analytical formulation of the problem was found, from which eigenvalues were calculated numerically by using suitable initial guesses for the axial wavenumber of an individual mode. Cummings and Chang included mean flow in both the airway and the absorbent although they did not include a perforate and did not go on to calculate the transmission loss. The transmission loss of a finite length silencer was later calculated by Cummings and Chang by using a mode matching approach (see ref. [23] and also Chapter 9). The approach to solving the eigenequation found by Cummings and Chang was simplified by Peat [13] who studied only the fundamental mode solution to the general eigenequation. Peat was able to remove the requirement for an initial guess by using a low frequency approximation to the eigenequation, this allowed the derivation of an explicit expression for the fundamental mode. It was also shown, by using only the fundamental mode, that a simple expression for the transmission loss could be found. Peat went on to show good agreement between the fundamental mode predictions and the experimental data measured by Cummings and Chang [23] for the transmission loss of a circular silencer. The results were also included by Peat in a transfer matrix formulation, which potentially allows incorporation of predictions into a complete model of an exhaust system, allowing straightforward calculation of the insertion loss. Mean flow in the absorbent and the effect of a perforate were omitted by Peat.

The fundamental mode solution implemented by Peat [13] is essentially a quasi plane-wave approach to modelling dissipative silencers and this appears to be the most straightforward method to be found in the literature. Consequently this method is to be used here, especially since the results can be formulated as a transfer matrix, allowing both the transmission loss and insertion loss predictions to be found in a straightforward manner. The acoustic impedance of the perforate separating the airway from the absorbent is also included in the model here. In the fundamental mode model it is assumed that the cross-section of the silencer is axisymmetric, though, as previously mentioned, predictions for irregular shaped silencers are also reported in this thesis. In this chapter, the elliptical section silencers will be assumed to have a circular cross section with a cross sectional area equivalent to that of the ellipse, in order to allow comparisons between prediction and experiment to be made. This will provide a severe test of the feasibility of using a plane wave model to tackle silencers of a general shape. Furthermore, whilst Peat [13] compared predictions against experimental data for a "small" silencer, the comparisons made here for larger silencers should provide a more stringent test of the model.

Section 6.2

Governing Equations

The theoretical analysis presented here is based upon the fundamental mode solution implemented by Peat [13]. The solution is an approximation to the full modal solution presented by Cummings and Chang [16]. In this method, coupled modal solutions are sought for the sound field in both the airway and the absorbent, with a common axial wavenumber linking the two regions. This allows an eigenequation to be written as a function of the axial wavenumber for an individual mode, from which it is possible to write an analytical solution for the fundamental mode.

The geometry of the dissipative silencer to be studied in this chapter is given in Figure 6.1 below:

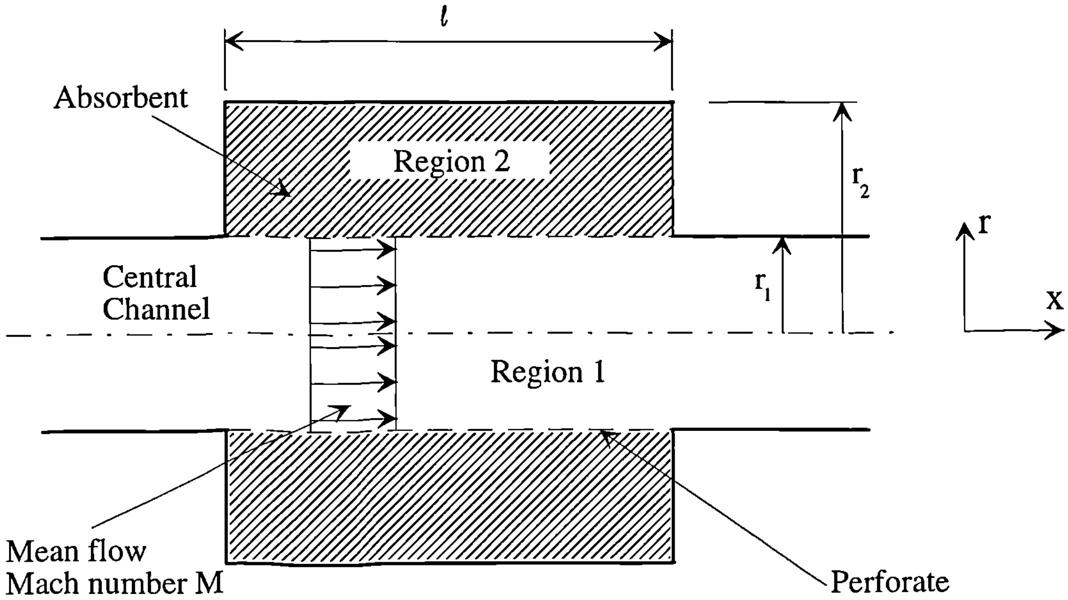

Figure 6.1. Geometry of dissipative silencer.

The dissipative silencer is assumed to be axisymmetric with a uniform mean flow of Mach number M in the central channel (region 1). A perforate liner is present between the central channel and the surrounding absorbing material (region 2). Mean flow in the absorbent is assumed to be negligible.

The solution proceeds by first finding the wave equations for regions 1 and 2, thus allowing a description of the sound pressure field throughout the silencer to be written. The two wave equations are solved by separation of variables, and hence the pressure fields are written as infinite sums of eigenfunctions. The two pressure fields are then linked together by their common axial wavenumbers to form an eigenequation.

6.2.1 Acoustic Wave Equation in the Central Channel (Region 1)

The linearised Euler equation for the sound field in region 1, with mean flow in the x direction only, is given by

$$-\frac{1}{\rho_0}\nabla p_1' = \frac{\partial \mathbf{u}_1'}{\partial t} + (\mathbf{U}\cdot\nabla)\mathbf{u}_1', \tag{6.1}$$

where $\mathbf{u}'$ is the acoustic velocity vector, $\mathbf{U} = (U_0, 0, 0)$ is the mean flow velocity vector (U_0 being the mean flow velocity in the x direction), ρ_0 is the mean fluid density, p' is the acoustic pressure and t is time.

The linearised continuity of mass equation, for mean flow in the x direction only, gives

$$\frac{\partial \rho_1'}{\partial t} + \rho_0 \nabla . \mathbf{u}_1' + (\mathbf{U} \cdot \nabla)\rho_1' = 0, \tag{6.2}$$

where ρ' is a perturbation in the fluid density. To derive the wave equation, we must first take the divergence of equation (6.1), i.e.

$$-\frac{1}{\rho_0}\nabla^2 p_1' = \nabla \cdot \frac{\partial \mathbf{u}_1'}{\partial t} + (\mathbf{U} \cdot \nabla)(\nabla . \mathbf{u}_1'), \tag{6.3}$$

and then differentiate equation (6.2) with respect to time, to give

$$\frac{\partial^2 \rho_1'}{\partial t^2} + \rho_0 \nabla \cdot \frac{\partial \mathbf{u}_1'}{\partial t} + (\mathbf{U} \cdot \nabla)\frac{\partial \rho_1'}{\partial t} = 0. \tag{6.4}$$

Multiplying equation (6.3) by ρ_0 and subtracting from it equation (6.4) gives

$$\nabla^2 p_1' - \frac{\partial^2 \rho_1'}{\partial t^2} + \rho_0 (\mathbf{U} \cdot \nabla)(\nabla . \mathbf{u}_1') - (\mathbf{U} \cdot \nabla)\frac{\partial \rho_1'}{\partial t} = 0. \tag{6.5}$$

Equation (6.2) can now be used to eliminate the particle velocity term from equation (6.5) to give

$$\nabla^2 p_1' - \frac{\partial^2 \rho_1'}{\partial t^2} - (\mathbf{U} \cdot \nabla)\left(\frac{\partial \rho_1'}{\partial t} + (\mathbf{U} \cdot \nabla)\rho_1'\right) - (\mathbf{U} \cdot \nabla)\frac{\partial \rho_1'}{\partial t} = 0, \tag{6.6}$$

and simplifying gives

$$\nabla^2 p_1' - \frac{\partial^2 \rho_1'}{\partial t^2} - 2(\mathbf{U} \cdot \nabla)\frac{\partial \rho_1'}{\partial t} - (\mathbf{U} \cdot \nabla)(\mathbf{U} \cdot \nabla)\rho_1' = 0. \tag{6.7}$$

If the fluid in the central channel is assumed to be non heat conducting and inviscid (consistent with the use of the Euler equation), the isentropic relationship between pressure and density holds, i.e.

$$\frac{\rho_1'}{p_1'}=\frac{1}{c_0^2}, \tag{6.8}$$

where c_0 is the isentropic speed of sound. Substituting equation (6.8) into equation (6.7) and re-writing gives

$$\nabla^2 p_1' - \frac{1}{c_0^2}\frac{\partial^2 p_1'}{\partial t^2} - 2\frac{M}{c_0}\frac{\partial^2 p_1'}{\partial x \partial t} - M^2\frac{\partial^2 p_1'}{\partial x^2}=0, \tag{6.9}$$

where the Mach number $M=U_0/c_0$. Equation (6.9) is the acoustic wave equation for the central channel with uniform mean flow in the x direction only. For a time dependence of $e^{i\omega t}$ this can be re-written in the form

$$k_0^2 p_1' - 2iMk_0\frac{\partial p_1'}{\partial x} + \left(1-M^2\right)\frac{\partial^2 p_1'}{\partial x^2} + \frac{1}{r}\frac{\partial p_1'}{\partial r} + \frac{\partial^2 p_1'}{\partial r^2}=0, \tag{6.10}$$

where $k_0 (=\omega/c_0)$ is the wavenumber in the central channel.

A separated solution to equation (6.10) is now sought. The solution for p_1' is assumed to be of the form of an infinite sum of eigenfunctions, i.e.

$$p_1' = \sum_{n=0}^{\infty} P_{i_1}^n \Psi_{i_1}^n e^{-ik_{x_i}^n x} + \sum_{n=0}^{\infty} P_{r_1}^n \Psi_{r_1}^n e^{-ik_{x_r}^n x}, \tag{6.11}$$

where P^n is the modal coefficient, Ψ^n is the transverse modal eigenfunction, k_x^n is the axial wavenumber and i refers to an incident wave, r to a reflected wave. For a single propagating mode, in this case the fundamental mode, equation (6.11) can be simplified to give

$$p_1' = P_{i_1}\Psi_{i_1}e^{-ik_{x_i}x} + P_{r_1}\Psi_{r_1}e^{-ik_{x_r}x}. \tag{6.12}$$

The pressure field, defined by equation (6.12), is now substituted back into equation (6.10) and, after simplifying, the wave equation becomes

$$\frac{\partial^2\Psi_1}{\partial r^2} + \frac{1}{r}\frac{\partial\Psi_1}{\partial r} + \Psi_1\left[k_0^2 - 2Mk_0k_x - \left(1-M^2\right)k_x^2\right] = 0, \tag{6.13}$$

where Ψ_1 is the transverse modal eigenfunction (region 1) and k_x the axial wavenumber for the fundamental mode for either the incident or the reflected wave. The general solution to equation (6.13) is

$$\Psi_1 = A_1J_0\left(k_{r_1}r\right) + A_2Y_0\left(k_{r_1}r\right), \tag{6.14}$$

where J_n and Y_n are Bessel and Neumann functions respectively, of order n, A_1 and A_2 are constants and k_{r_1} is the radial wavenumber in region 1 and is given by

$$k_{r_1}^2 = k_0^2 - 2Mk_0k_x - \left(1-M^2\right)k_x^2. \tag{6.15}$$

The pressure p_1' must be finite at $r=0$, and therefore $A_2 = 0$. A_1 is incorporated into the modal coefficient to give an expression for the incident wave of

$$p_1' = P_1J_0\left(k_{r_1}r\right)e^{-ik_xx}. \tag{6.16}$$

Equation (6.16) gives the pressure field for region 1; the same must now be found for region 2 which will then allow the two regions to be linked together.

6.2.2 Acoustic Wave Equation in the Absorbent (Region 2)

A modified linearized momentum equation for the propagation of sound in a bulk reacting porous material was given by Zwikker and Kosten [31] (see also equation (2.46)), i.e.

$$-\nabla p_2' = \frac{q^2(\omega)\rho_0}{\Omega}\frac{\partial \mathbf{u}_2'}{\partial t} + \sigma_v(\omega)\mathbf{u}_2', \tag{6.17}$$

where $q^2(\omega)$ is the dynamic tortuosity, $\sigma_v(\omega)$ is the dynamic viscous flow resistivity and Ω is the porosity of the material. All these quantities were introduced in Chapter 2 and they are assumed to be independent of material orientation.

The linearized continuity equation for a porous material was also given by Zwikker and Kosten as

$$\Omega\frac{\partial \rho_2'}{\partial t} + \rho_0 \nabla\cdot\mathbf{u}_2' = 0. \tag{6.18}$$

Proceeding in the same manner as for region 1, one may take the divergence of equation (6.17),

$$-\nabla^2 p_2' = \frac{q^2(\omega)\rho_0}{\Omega}\nabla\cdot\frac{\partial \mathbf{u}_2'}{\partial t} + \sigma_v(\omega)\nabla\cdot\mathbf{u}_2', \tag{6.19}$$

and the time derivative of equation (6.18) gives

$$\Omega\frac{\partial^2 \rho_2'}{\partial t^2} + \rho_0 \nabla\cdot\frac{\partial \mathbf{u}_2'}{\partial t} = 0. \tag{6.20}$$

Now $\mathbf{u}_2'$ is eliminated from equation (6.19) by substituting from equations (6.20) and (6.18) to give

$$\nabla^2 p_2' - q^2(\omega)\frac{\partial^2 \rho_2'}{\partial t^2} - \sigma_v(\omega)\frac{\Omega}{\rho_0}\frac{\partial \rho_2'}{\partial t} = 0. \tag{6.21}$$

The relationship between the pressure and density in a porous material is given by [31] as

$$\rho_2' = \frac{\rho_0 p_2'}{\kappa(\omega)}, \tag{6.22}$$

where $\kappa(\omega)$ is the bulk modulus of the porous material (see Chapter 2). Substituting equation (6.22) back into equation (6.21) and assuming a time dependence of $e^{i\omega t}$ gives

$$\nabla^2 p_2' + \frac{\rho_0 \omega^2 q^2(\omega)}{\kappa(\omega)} p_2' - \frac{i\omega\sigma_v\Omega}{\kappa(\omega)} p_2' = 0. \tag{6.23}$$

Equation (6.23) is the wave equation for a porous material, assuming that no mean flow is present within the material. The wave equation can be re-written in a simpler form by assuming a travelling wave solution of $p_2' \approx e^{-\Gamma x}$ (see for example Cummings and Chang [40]), where the propagation constant Γ (see Chapter 2) is defined by

$$\Gamma^2 = -\rho_0 \omega^2 \frac{q^2(\omega)}{\kappa(\omega)}\left[1 - i\frac{\Omega\sigma_v(\omega)}{\omega\rho_0 q^2(\omega)}\right]. \tag{6.24}$$

The wave equation for region 2 can now be written as

$$-\Gamma^2 p_2' + \frac{\partial^2 p_2'}{\partial x^2} + \frac{1}{r}\frac{\partial p_2'}{\partial r} + \frac{\partial^2 p_2'}{\partial r^2} = 0. \tag{6.25}$$

In accordance with the method used for region 1, a separated solution to equation (6.25) is sought. An incident wave containing only the fundamental mode is considered here, with the pressure field in the absorbent being given by

$$p_2' = P_2 \Psi_2 e^{-ik_x x}. \tag{6.26}$$

Substituting equation (6.26) into equation (6.25) and simplifying gives

$$\frac{\partial^2\Psi_2}{\partial r^2}+\frac{1}{r}\frac{\partial\Psi_2}{\partial r}-\Psi_2\left[\Gamma^2+k_x^2\right]=0. \tag{6.27}$$

The general solution to equation (6.27) is

$$\Psi_2 = B_1 J_0\left(k_{r_2} r\right)+B_2 Y_0\left(k_{r_2} r\right), \tag{6.28}$$

where B_1, B_2 are constants and k_{r_2} is the radial wavenumber in region 2 and is given by

$$k_{r_2}^2 = -\left[\Gamma^2+k_x^2\right]. \tag{6.29}$$

The boundary condition of zero normal particle displacement at the silencer walls therefore applies:
at $r=r_2$, $\partial\Psi_2/\partial r=0$, so

$$0=k_{r_2}\left[B_1 J_1\left(k_{r_2} r_2\right)+B_2 Y_1\left(k_{r_2} r_2\right)\right], \tag{6.30}$$

and therefore

$$\Psi_2 = B_1\left[J_0\left(k_{r_2} r\right)-\frac{Y_0\left(k_{r_2} r\right)J_1\left(k_{r_2} r_2\right)}{Y_1\left(k_{r_2} r_2\right)}\right]. \tag{6.31}$$

The pressure field in region 2 can now be written as

$$p_2' = P_2\left[J_0\left(k_{r_2} r\right)-\frac{Y_0\left(k_{r_2} r\right)J_1\left(k_{r_2} r_2\right)}{Y_1\left(k_{r_2} r_2\right)}\right]e^{-ik_x x}. \tag{6.32}$$

6.2.3 Boundary Conditions at the Perforate

The boundary conditions used to derive the two wave equations were zero normal particle displacement at the walls of the silencer and finite pressure at the centre of region 1. The remaining boundary conditions occur at the interface between the porous material and the central channel; this links together the two solutions for regions 1 and 2. As usual, an infinitesimally thin boundary layer is assumed to exist in the central channel, and therefore the appropriate boundary conditions at the perforate are continuity of pressure and continuity of normal particle displacement. A simple way of combining these two boundary conditions is to equate the "displacement impedance" on either side of the perforate. The displacement impedance was defined by Cummings [14] as

$$\varepsilon = p'/i\omega\xi\rho_0 c_0, \tag{6.33}$$

where ε is the displacement impedance, p' is the sound pressure, ρ_0 is the mean fluid density, c_0 is the speed of sound and ξ is the radial acoustic particle displacement component. The displacement impedances for regions 1 and 2 can therefore be written as

$$\varepsilon_1 = \frac{p_1'}{i\omega\rho_0 c_0 \xi_1'} \quad \text{and} \quad \varepsilon_2 = \frac{p_2'}{i\omega\rho_0 c_0 \xi_2'}. \qquad (6.34), (6.35)$$

The displacement impedances on either side of the perforate must now be related. Since the impedance of the perforate (ζ) is given by

$$\zeta = \frac{p_1' - p_2'}{i\omega\rho_0 c_0 \xi}, \tag{6.36}$$

where ζ corresponds to the term $z_0/\rho_0 c_0$ in Chapter 4, the relationship between ε_1 and ε_2 at $r = r_1$ takes the form of

$$\varepsilon_1(r_1) = \varepsilon_2(r_1) + \zeta. \tag{6.37}$$

Equation (6.37) is the boundary condition at the perforate which links solutions found in region 1 to those found in region 2. The assumption of an infinitesimally thin perforate is implicit in equation (6.37), this approximation is valid since, for the perforates studied here, the thickness of each perforate is very small compared to the dimensions of the silencers. In order to implement equation (6.37), values found in Chapter 4 for the perforate impedance are used and $\varepsilon_1(r_1)$ and $\varepsilon_2(r_1)$ are calculated in the following way:

6.2.4 Displacement Impedance for Region 1

In order to calculate the displacement impedance it is only necessary to consider the normal acoustic particle displacement. The Euler equation in the central channel (equation (6.1)) can be simplified to give

$$-\frac{1}{\rho_0}\frac{\partial p_1'}{\partial r} = \frac{\partial u_{1_r}'}{\partial r} + U_0\frac{\partial u_{1_r}'}{\partial x}, \tag{6.38}$$

where u_{1_r}' is the acoustic velocity component in the radial direction. The radial particle displacement ξ_1' is related to the radial velocity (see Cummings and Chang [16]) by

$$\frac{D\xi_1'}{Dt} = u_{1_r}', \tag{6.39}$$

where D/Dt is the substantive derivative and for region 1,

$$\frac{D}{Dt} = \frac{\partial}{\partial t} + U_0\frac{\partial}{\partial x}. \tag{6.40}$$

Substituting equation (6.39) into equation (6.38) and eliminating u_{1_r}' gives

$$-\frac{1}{\rho_0}\frac{\partial p_1'}{\partial r}=\frac{\partial^2\xi_1'}{\partial t^2}+2U_0\frac{\partial^2\xi_1'}{\partial x\partial t}+U_0^2\frac{\partial^2\xi_1'}{\partial x^2}. \tag{6.41}$$

If a time dependence of $e^{i\omega t}$ is assumed and $\partial/\partial x=-ik_x$, then

$$\frac{1}{\rho_0}\frac{\partial p_1'}{\partial r}=\xi_1'\left[\omega^2-2U_0\omega k_x+U_0^2k_x^2\right], \tag{6.42}$$

and re-writing gives a radial particle displacement of

$$\xi_1'=\frac{1}{\rho_0c_0^2\left[k_0-Mk_x\right]^2}\frac{\partial p_1'}{\partial r}. \tag{6.43}$$

The displacement impedance for region 1 is now found by substituting equations (6.43) and (6.16) into equation (6.34) to give

$$\varepsilon_1(r_1)=\frac{i(k_0-Mk_x)^2}{k_0k_{r_1}}\frac{J_0(k_{r_1}r_1)}{J_1(k_{r_1}r_1)}. \tag{6.44}$$

6.2.5 Displacement Impedance for Region 2

The derivation of the displacement impedance for region 2 proceeds along the same route as for region 1, except that the substantive derivative is given by

$$\frac{D}{Dt}=\frac{\partial}{\partial t}, \tag{6.45}$$

and therefore

$$\frac{\partial\xi_2'}{\partial t}=u_{2_r}'. \tag{6.46}$$

Substituting equation (6.46) into the momentum equation for a porous material (equation (6.17)) gives

$$-\frac{\partial p_2'}{\partial r}=\frac{\rho_0 q^2(\omega)}{\Omega}\frac{\partial^2 \xi_2'}{\partial t^2}+\sigma_v(\omega)\frac{\partial \xi_2'}{\partial t}, \tag{6.47}$$

which can be simplified to give

$$\frac{\partial p_2'}{\partial r}=\frac{\rho_0 \omega^2 q^2(\omega)}{\Omega}\left[1-\frac{i\Omega\sigma_v(\omega)}{\rho_0 \omega q^2(\omega)}\right]\xi_2'. \tag{6.48}$$

The definition of the propagation constant in equation (6.24) allows equation (6.48) to be re-written as

$$\frac{\partial p_2'}{\partial r}=\frac{\kappa(\omega)\Gamma}{\Omega}\xi_2'. \tag{6.49}$$

The bulk modulus can be replaced by the bulk modulus for the bulk material by using equation (2.30); the use of equation (3.12) then allows the radial displacement to be written as

$$\xi_2'=\frac{1}{i\omega\Gamma z_a}\frac{\partial p_2'}{\partial r}, \tag{6.50}$$

where z_a is the characteristic impedance of the porous material (see Chapter 2). The displacement impedance for region 2 is now found by substituting equations (6.50) and (6.32) into equation (6.35) to give

$$\varepsilon_2(r_1)=\frac{\Gamma}{k_{r_2}}\frac{z_a}{\rho_0 c_0}\left[\frac{J_0(k_{r_2}r_1)Y_1(k_{r_2}r_2)-Y_0(k_{r_2}r_1)J_1(k_{r_2}r_2)}{J_1(k_{r_2}r_1)Y_1(k_{r_2}r_2)-Y_1(k_{r_2}r_1)J_1(k_{r_2}r_2)}\right]. \tag{6.51}$$

6.2.6 Implementation of the Boundary Conditions at the Perforate

The displacement impedance boundary condition between regions 1 and 2 can now be expressed by using equation (6.37) to give

$$\frac{\Gamma}{k_{r_2}}\frac{z_a}{\rho_0 c_0}\left[\frac{J_0(k_{r_2}r_1)Y_1(k_{r_2}r_2)-Y_0(k_{r_2}r_1)J_1(k_{r_2}r_2)}{J_1(k_{r_2}r_1)Y_1(k_{r_2}r_2)-Y_1(k_{r_2}r_1)J_1(k_{r_2}r_2)}\right]+\zeta=\frac{i[k_0-Mk_x]^2}{k_0 k_{r_1}}\frac{J_0(k_{r_1}r_1)}{J_1(k_{r_1}r_1)}. \tag{6.52}$$

Equation (6.52) is an eigenequation written in terms of k_x, which may be written as

$$\frac{k_{r_2}}{k_0 k_{r_1}\Gamma}\frac{\rho_0 c_0}{z_a}\left[J_1(k_{r_2}r_1)Y_1(k_{r_2}r_2)-Y_1(k_{r_2}r_1)J_1(k_{r_2}r_2)\right]\left\{i[k_0-Mk_x]^2 J_0(k_{r_1}r_1)-\zeta k_0 k_{r_1}J_1(k_{r_1}r_1)\right\}$$

$$-J_1(k_{r_1}r_1)\left[J_0(k_{r_2}r_1)Y_1(k_{r_2}r_2)-Y_0(k_{r_2}r_1)J_1(k_{r_2}r_2)\right]=0. \tag{6.53}$$

Equation (6.53) is identical to the eigenequation found by Cummings and Chang [16] except that the perforate included here introduces an extra term. The eigenequation can be written as a function of the common axial wavenumber k_x by substituting expressions for k_{r_1} and k_{r_2} from equations (6.15) and (6.29) respectively. The eigenequation is valid for any mode present in the assumed solution to equation (6.11). In the paper by Cummings and Chang [23], the eigenequation was solved by using the Newton-Raphson method from which a number of different modes was found, including the fundamental mode, by using an appropriate initial guess for the wavenumber of each individual mode. The problem with this method is that, although the fundamental mode is usually easily found, it is possible that higher order modes might be missed due to an inappropriate initial guess. A more reliable method for finding higher order modes requires a completely different approach to solving the wave equation and this will be discussed later on in the thesis.

The silencer model in this chapter is centred on the fundamental mode solution to equation (6.53). For virtually every practical situation, the lowest eigenvalues ($k_{x_{i,r}}$) are those of the fundamental mode at very low frequencies. An approximate explicit solution to equation (6.53) has been found by Peat [13]. This was done by applying a small argument series expansion to the Bessel and Neumann functions in the eigenequation. The small argument, or low frequency, approximation ensures that only the fundamental mode is found since there are only two eigenvalues that emerge from this approximation, for the positive and negative propagating mode. Peat's fundamental mode method is used here but only for very low frequencies.

In the following analysis separate solutions for the incident and reflected waves appear once the eigenequation in k_x has been solved. A series expansion for Bessel and Neumann functions with small arguments was given in Chapter 2 (see equations (2.51) to (2.54)). If terms of $O((k_{r_1} r_1)^2)$ and $O((k_{r_2} r_2)^2)$ are neglected, the low frequency formulation of equation (6.53) is

$$k_{r_1}^2 + i\frac{k_0}{\Gamma}\frac{\rho_0 c_0}{z_a}\frac{S_2}{S_1}k_{r_2}^2\left\{[1-MK_x]^2 + i\zeta\frac{k_{r_1}^2}{k_0}\frac{r_1}{2}\right\} = 0, \tag{6.54}$$

where $K_x = k_x/k_0$, and $S_1 = \pi r_1^2$, $S_2 = \pi(r_2^2 - r_1^2)$ are the cross sectional areas of the central channel and the absorbent region respectively. So that equation (6.54) may be solved analytically, K_x must be expanded in the form (see Peat [13])

$$K_x = \alpha + \beta M + \gamma M^2 + ... \quad . \tag{6.55}$$

In the expansion of K_x, terms of $O(M^3)$ are neglected since in automotive exhausts M is typically less than 0.3. It is helpful to re-write equation (6.54) to give

$$F_1 k_{r_1}^2 + k_{r_2}^2\left\{[1-MK_x]^2 + i\zeta\frac{r_1}{2}\frac{k_{r_1}^2}{k_0}\right\} = 0, \tag{6.56}$$

where

$$F_1 = \frac{\Gamma}{ik_0}\frac{z_a}{\rho_0 c_0}\frac{S_1}{S_2}, \tag{6.57}$$

and $k_{r_1}^2$ and $k_{r_2}^2$ are given by equations (6.15) and (6.29) respectively, i.e.

$$k_{r_1}^2 = k_0^2\left[1 - 2MK_x - \left(1 - M^2\right)K_x^2\right], \tag{6.58}$$

and

$$k_{r_2}^2 = -k_0^2\left[\frac{\Gamma^2}{k_0^2} + K_x^2\right]. \tag{6.59}$$

Substituting equations (6.58) and (6.59) into equation (6.56) allows the eigenequation to be written in ascending powers of K_x, i.e.

$$F_2 - 2MF_2K_x - \left[\frac{\Gamma^2}{k_0^2} + F_2 + F_3 - M^2F_2\right]K_x^2 + 2MF_3K_x^3 - \left[M^2F_3 - (F_3 - 1)\right]K_x^4 = 0, \tag{6.60}$$

where

$$F_2 = F_1 - \frac{\Gamma^2}{k_0^2}\left(1 + i\zeta\frac{k_0 r_1}{2}\right) \text{ and } F_3 = 1 + i\zeta\frac{k_0 r_1}{2}. \qquad (6.61), (6.62)$$

The assumed form for K_x is

$$K_x = \alpha + \beta M + \gamma M^2, \tag{6.63}$$
$$K_x^2 = \alpha^2 + 2\alpha\beta M + \left(2\alpha\gamma + \beta^2\right)M^2, \tag{6.64}$$
$$K_x^3 = \alpha^3 + 3\alpha^2\beta M + \left(3\alpha^2\gamma + 3\alpha\beta^2\right)M^2, \tag{6.65}$$
$$K_x^4 = \alpha^4 + 4\alpha^3\beta M + \left(4\alpha^3\gamma + 6\alpha^2\beta^2\right)M^2. \tag{6.66}$$

Substitution of equations (6.63) to (6.66) into equation (6.60) gives

$$F_2 - 2\alpha F_2 M - 2\beta F_2 M^2 - \left[\alpha^2 + 2\alpha\beta M + \left(2\alpha\gamma + \beta^2\right)M^2\right]\left\{\frac{\Gamma^2}{k_0^2} + F_2 + F_3\right\} + \alpha^2 F_2 M^2$$
$$+2\alpha^3 F_3 M + 6\alpha^2\beta F_3 M^2 + (F_3 - 1)\left[\alpha^4 + 4\alpha^3\beta M + \left(4\alpha^3\gamma + 6\alpha^2\beta^2\right)M^2\right] - \alpha^4 F_3 M^2 = 0. \tag{6.67}$$

Terms containing similar powers of M, appearing in equation (6.67), are now equated to give values for the coefficients α, β and γ of

$$\alpha=\pm\left\{\left(\left[\frac{\Gamma^2}{k_0^2}+F_2+F_3\right]\pm\sqrt{\left[\frac{\Gamma^2}{k_0^2}+F_2+F\right]^2-4F_2(F_3-1)}\right)\Big/2(F_3-1)\right\}^{\frac{1}{2}}, \tag{6.68}$$

$$\beta=\frac{F_2-\alpha^2F_3}{2(F_3-1)\alpha^2-\left[\frac{\Gamma^2}{k_0^2}+F_2+F_3\right]}, \tag{6.69}$$

$$\gamma=\frac{6\alpha^2\beta^2(1-F_3)+\alpha^2F_3(\alpha^2-6\beta)+F_2(2\beta-\alpha^2)+\beta^2\left[\frac{\Gamma^2}{k_0^2}+F_2+F_3\right]}{4(F_3-1)\alpha^3-2\alpha\left[\frac{\Gamma^2}{k_0^2}+F_2+F_3\right]}. \tag{6.70}$$

If the values for the coefficients given above are compared to those found by Peat [13] it is noticeable that two extra solutions appear for α. It is also evident that equations (6.68) to (6.70) cannot be reduced to those found by Peat simply by setting $\zeta=0$ since the denominator of equation (6.68) is equal to zero when $\zeta=0$. However it is possible to compare solutions with and without the perforate in the model by taking ζ to be very small but non-zero. When this was carried out it was found that solutions for α obtained by taking the negative square root inside the bracket, i.e.

$$\alpha=\pm\left\{\left(\left[\frac{\Gamma^2}{k_0^2}+F_2+F_3\right]-\sqrt{\left[\frac{\Gamma^2}{k_0^2}+F_2+F_3\right]^2-4F_2(F_3-1)}\right)\Big/2(F_3-1)\right\}^{\frac{1}{2}}, \tag{6.71}$$

produced results identical to those found when the perforate is not included in the model (note that the positive root outside the brackets in equation (6.71) corresponds to the incident wave, the negative root to the reflected wave). The two remaining solutions to equation (6.68) are "non-physical", and correspond to taking the positive square root inside the brackets, producing values for α tending towards infinity as $\zeta\rightarrow0$. Consequently only solutions for α given by equation (6.71) are considered here when calculating values for K_x.

6.2.7 Transfer Matrix or Four-pole Formulation

Once values have been calculated for K_x it is necessary to find the transmission loss and insertion loss in order to allow a comparison with the experimental data in Chapter 5. In the introduction to this chapter it was mentioned that it is desirable to formulate solutions in the form of transfer matrices. For each individual component of an exhaust system, such as uniform lengths of pipe, area contractions/expansions and absorption elements, four-pole formulations can be derived. This involves relating the state variables at the input of the component to those at the output, via four-pole parameters. When the four-pole formulation is applied to acoustical problems, the acoustic pressure and particle volume velocity are commonly adopted as the two state variables. Therefore the transfer matrix for and individual element or number of elements can be written as follows

$$\begin{Bmatrix} p_{\text{in}} \\ u_{\text{in}} \end{Bmatrix} = \begin{bmatrix} \text{A} & \text{B} \\ \text{C} & \text{D} \end{bmatrix} \begin{Bmatrix} p_{\text{out}} \\ u_{\text{out}} \end{Bmatrix}. \tag{6.72}$$

where A, B, C and D are the four-pole parameters. It should be noted here that the transfer matrix formulation always assumes a plane wave upstream and downstream of the element. In order to formulate the transfer matrix for an individual silencer such as the one considered in this chapter it is necessary to calculate the sound pressure and axial particle volume velocity at $x = 0$ and $x = l$, i.e.

$$\begin{Bmatrix} p_{x=0} \\ u_{x=0} \end{Bmatrix} = \begin{bmatrix} \text{A} & \text{B} \\ \text{C} & \text{D} \end{bmatrix} \begin{Bmatrix} p_{x=l} \\ u_{x=l} \end{Bmatrix}. \tag{6.73}$$

Once the transfer matrix has been calculated for each individual component in the exhaust it is possible successively to multiply the four-poles to arrive at a final transfer matrix which is a characteristic of the performance of the exhaust system as whole. This method is obviously particularly useful for predicting the insertion loss of a complete exhaust system. A detailed account of the theory behind four-pole formulations is given by Munjal [99].

Since the transfer matrix approach requires a plane wave at the inlet and outlet of the silencer and the fundamental mode in a lined duct is not planar, it is necessary to average the eigenvectors across the radial dimension in order to yield equivalent plane wave quantities. Accordingly, the average sound pressure in regions 1 and 2 is given by

$$\overline{p}'_{1,2} = P_i \overline{\Psi}_{i_1,i_2} e^{-ik_{x_i}x} + P_r \overline{\Psi}_{r_1,r_2} e^{-ik_{x_r}x}, \tag{6.74}$$

where

$$\overline{\Psi}_{1,2} = \frac{2\pi}{S_{1,2}} \int_{S_{1,2}} \Psi_{1,2} r dr. \tag{6.75}$$

The mean values for the eigenvectors are found by substituting equations (6.14) and (6.28) into equation (6.75) to give

$$\overline{\Psi}_1 = \frac{2}{k_{r_1} r_1} J_1\left(k_{r_1} r_1\right), \tag{6.76}$$

and

$$\overline{\Psi}_2 = -\frac{2}{k_{r_2} r_1} \frac{S_1}{S_2} \left[J_1\left(k_{r_2} r_1\right) - \frac{J_1\left(k_{r_2} r_2\right) Y_1\left(k_{r_2} r_1\right)}{Y_1\left(k_{r_2} r_2\right)} \right]. \tag{6.77}$$

The formulation of the transfer matrix proceeds by finding $p_{x=0,l}$ and $u_{x=0,l}$, where

$$p = \frac{1}{S_1 + S_2}\left[S_1 \overline{p}'_1 + S_2 \overline{p}'_2\right] \text{ and } u = S_1 \overline{u}'_1 + S_2 \overline{u}'_2. \qquad (6.78), (6.79)$$

The mean sound pressure in region 1 is given by

$$\overline{p}'_1 = P_i \overline{\Psi}_{i_1} e^{-ik_{x_i}x} + P_r \overline{\Psi}_{r_1} e^{-ik_{x_r}x}, \tag{6.80}$$

and the axial particle velocity in region 1 is found from the momentum equation. Equation (6.1), for propagation in the x direction only, gives

$$-\frac{1}{\rho_0}\frac{\partial \overline{p}_1'}{\partial x}=\frac{\partial \overline{u}_{x_1}'}{\partial t}+U_0\frac{\partial \overline{u}_{x_1}'}{\partial x}, \tag{6.81}$$

therefore, assuming a time dependence of $e^{i\omega t}$ and $\partial/\partial x=-ik_x$, the average acoustic particle velocity in the x direction is given by

$$\overline{u}_{x_1}'=\frac{1}{\rho_0 c_0}\left[P_{\mathrm{i}}\overline{\Psi}_{\mathrm{i}_1}\frac{K_{x_\mathrm{i}}}{\left(1-MK_{x_\mathrm{i}}\right)}e^{-ik_{x_\mathrm{i}}x}+P_{\mathrm{r}}\overline{\Psi}_{\mathrm{r}_1}\frac{K_{x_\mathrm{r}}}{\left(1-MK_{x_\mathrm{r}}\right)}e^{-ik_{x_\mathrm{r}}x}\right]. \tag{6.82}$$

In region 2, the mean sound pressure is given by

$$\overline{p}_2'=P_{\mathrm{i}}\overline{\Psi}_{\mathrm{i}_2}e^{-ik_{x_\mathrm{i}}x}+P_{\mathrm{r}}\overline{\Psi}_{\mathrm{r}_2}e^{-ik_{x_\mathrm{r}}x}, \tag{6.83}$$

and the momentum equation, for propagation in the x direction only, gives (see equation (6.17))

$$-\frac{\partial \overline{p}_2'}{\partial x}=\frac{\rho_0 q^2(\omega)}{\Omega}\frac{\partial \overline{u}_{x_2}'}{\partial t}+\sigma_{\mathrm{v}}(\omega)\overline{u}_{x_2}'. \tag{6.84}$$

Equation (6.84) can be re-written as

$$k_{x_\mathrm{i}}P_{\mathrm{i}}\overline{\Psi}_{\mathrm{i}_2}e^{-ik_{x_\mathrm{i}}x}+k_{x_\mathrm{r}}P_{\mathrm{r}}\overline{\Psi}_{\mathrm{r}_2}e^{-ik_{x_\mathrm{r}}x}=\frac{\rho_0\omega q^2(\omega)}{\Omega}\left[1-\frac{i\Omega\sigma_{\mathrm{v}}(\omega)}{\omega\rho_0 q^2(\omega)}\right]\overline{u}_{x_2}'. \tag{6.85}$$

The right hand side of equation (6.85) can be simplified by substitution from equation (6.24) and re-writing by using equations (2.30) and (3.12), i.e.

$$\frac{\rho_0\omega q^2(\omega)}{\Omega}\left[1-\frac{i\Omega\sigma_{\mathrm{v}}(\omega)}{\rho_0\omega q^2(\omega)}\right]=\frac{\Gamma z_a}{i}. \tag{6.86}$$

The particle velocity in region 2 is therefore given by

$$\overline{u}'_{x_2} = \frac{ik_0}{\Gamma z_a}\left[K_{x_\mathrm{i}} P_\mathrm{i} \overline{\Psi}_{\mathrm{i}_2} e^{-ik_{x_\mathrm{i}} x} + K_{x_\mathrm{r}} P_\mathrm{r} \overline{\Psi}_{\mathrm{r}_2} e^{-ik_{x_\mathrm{r}} x}\right]. \tag{6.87}$$

Expressions for p and u can now be found by substituting equations (6.80) and (6.83) into equation (6.78) and equations (6.82) and (6.87) into equation (6.79) to give

$$p = P_\mathrm{i} \overline{\Psi}_\mathrm{i} e^{-ik_{x_\mathrm{i}} x} + P_\mathrm{r} \overline{\Psi}_\mathrm{r} e^{-ik_{x_\mathrm{r}} x}, \tag{6.88}$$

where

$$\overline{\Psi}_{\mathrm{i,r}} = \frac{1}{S_1 + S_2}\left[S_1 \overline{\Psi}_{\mathrm{i}_1,\mathrm{r}_1} + S_2 \overline{\Psi}_{\mathrm{i}_2,\mathrm{r}_2}\right], \tag{6.89}$$

and

$$u = P_\mathrm{i} f_\mathrm{i} e^{-ik_{x_\mathrm{i}} x} + P_\mathrm{r} f_\mathrm{r} e^{-ik_{x_\mathrm{r}} x}, \tag{6.90}$$

where

$$f_{\mathrm{i,r}} = \frac{K_{x_{\mathrm{i,r}}}}{\rho_0 c_0}\left[\frac{S_1 \overline{\Psi}_{\mathrm{i}_1,\mathrm{r}_1}}{\left(1 - MK_{x_{\mathrm{i,r}}}\right)} + \frac{ik_0}{\Gamma}\frac{\rho_0 c_0}{z_a} S_2 \overline{\Psi}_{\mathrm{i}_2,\mathrm{r}_2}\right]. \tag{6.91}$$

Therefore at $x = 0$ and $x = l$, p and u are given by

$$p(0) = P_\mathrm{i} \overline{\Psi}_\mathrm{i} + P_\mathrm{r} \overline{\Psi}_\mathrm{r}, \tag{6.92}$$

$$p(l) = P_\mathrm{i} \overline{\Psi}_\mathrm{i} e^{-ik_{x_\mathrm{i}} l} + P_\mathrm{r} \overline{\Psi}_\mathrm{r} e^{-ik_{x_\mathrm{r}} l}, \tag{6.93}$$

$$u(0) = P_\mathrm{i} f_\mathrm{i} + P_\mathrm{r} f_\mathrm{r}, \tag{6.94}$$

$$u(l) = P_\mathrm{i} f_\mathrm{i} e^{-ik_{x_\mathrm{i}} l} + P_\mathrm{r} f_\mathrm{r} e^{-ik_{x_\mathrm{r}} l}. \tag{6.95}$$

The transfer matrix for the silencer is found by eliminating P_i and P_r from equations (6.92) to (6.95) to give

$$\begin{bmatrix} p(0) \\ u(0) \end{bmatrix} = \frac{1}{\left[\overline{\Psi}_i f_r - \overline{\Psi}_r f_i\right]} \begin{bmatrix} \overline{\Psi}_i f_r e^{-ik_{x_i} l} - \overline{\Psi}_r f_i e^{-ik_{x_r} l} & \overline{\Psi}_i \overline{\Psi}_r \left(e^{-ik_{x_r} l} - e^{-ik_{x_i} l}\right) \\ f_i f_r \left(e^{-ik_{x_i} l} - e^{-ik_{x_r} l}\right) & \overline{\Psi}_i f_r e^{-ik_{x_r} l} - \overline{\Psi}_r f_i e^{-ik_{x_i} l} \end{bmatrix} \begin{bmatrix} p(l) \\ u(l) \end{bmatrix}. \tag{6.96}$$

The four-pole parameters A, B, C and D are found by comparing equation (6.73) with equation (6.96). The transmission loss (TL) is then calculated from the four-poles (see Munjal [99] and Peat [13]) in the following way:

$$\mathrm{TL} = 10\log_{10}\left|\mathrm{A} + \frac{\mathrm{B}}{z} + \mathrm{C}z + \mathrm{D}\right|, \qquad \text{(dB)} \tag{6.97}$$

where $z = \rho_0 c_0 / S_1$.

Section 6.3

Results and Discussion

There are two different methods available for calculating the transmission loss of silencers using the fundamental mode approach. The first method, used by Peat [13], involves approximating the Bessel and Neumann functions appearing in the eigenequation and also introducing an approximate solution for the axial wavenumber. The approximation to the full eigenequation is given by equation (6.54), and approximating the axial wavenumber allows the solution to be written in the form given by equation (6.67). Peat introduced a further simplification by approximating the Bessel and Neumann functions in the eigenvectors of equations (6.76) and (6.77) and this gives values for $\overline{\Psi}_1$ and $\overline{\Psi}_2$ of unity. The second approach to finding the common axial wavenumber, and hence the transmission loss, is to solve the full eigenequation (equation (6.53)) directly by using an approach such as the Newton-Raphson method, and this approach is termed here the "full fundamental mode solution". This method for solving the eigenequation was used by Cummings and Chang [16] and requires an initial guess for the axial wavenumber in addition to numerical algorithms for the Bessel and

Neumann functions. The full solution also requires the mean values for the eigenvectors $\overline{\Psi}_1$ and $\overline{\Psi}_2$ to be calculated exactly.

The results published by Peat [13] were for a "straight-through" silencer of outside diameter 76mm and inside diameter 39.6mm. Peat found that, for frequencies up to 2.5kHz, the solution remained accurate to within 1.5% of the full fundamental mode solution. However, solutions were not presented for "larger" silencers where it is expected that errors associated with the approximations present in Peat's method will become more apparent at lower frequencies. The validity of the approximate fundamental mode solution can be found by examining the terms involving k_{r_1} and k_{r_2}. These are the terms contained within the Bessel and Neumann functions in the eigenequation, and terms of $O((k_{r_1}r_1)^2)$ and $O((k_{r_2}r_2)^2)$ were ignored in order to formulate equation (6.54). In Figure 6.2, the complex moduli of $k_{r_1}r_1$ and $k_{r_2}r_2$ are shown for both the silencer used by Peat and silencers 1 and 2 that are discussed in Chapter 5. It is evident from Figure 6.2 that the approximations used by Peat were valid for his silencer across the entire frequency range studied, though when larger silencers are used the approximations appear to be in error across a wider frequency range. Therefore, for the silencers measured in Chapter 5 it is necessary to employ the full fundamental mode solution. This does not present any problems since computational Bessel and Neumann routines are readily available. It is also possible to use the approximate method of Peat to find an initial guess for k_x at very low frequencies in the region where Figure 6.2 indicates the method to be valid, and this procedure was adopted here. Once an initial guess has been found, it is used to initiate the Newton-Raphson procedure for solving equation (6.53) at a higher frequency. This procedure is then repeated by using the new solution for k_x as an initial value in the iteration until the desired frequency range has been covered. Consequently, the approximate method of Peat is very useful for ensuring that the fundamental mode is found for every silencer and this is the reason why the method has been discussed in full in this chapter.

The fundamental mode solution is only applicable to axisymmetric silencers and therefore the results for silencers 1, 2 and 3 will be discussed here first. Transmission loss predictions using the full fundamental mode solution, ignoring the perforate, are compared to experimental data for silencers 1, 2 and 3 in Figure 6.3 (M=0) and Figure 6.4 (M=0.15). The results indicate good agreement between theory and experiment, especially for the smaller diameter silencers 1 and 3. The accuracy in the predictions appears to be reduced at higher frequencies, and this is probably because of the neglect of higher order modes, although conclusions based upon experimental data above 1kHz should be treated with caution (see Chapter 5). The predictions for silencer 2 appear to contain the largest errors and again this is probably caused by the neglect of higher order modes, particularly since higher modes begin to be relatively lightly attenuated at lower frequencies in silencers of large outside diameter. However, it is possible that omitting the perforate from the model has also affected the accuracy of the predictions for all three silencers and that errors are not just a result of the omission of higher order modes; this question will be discussed later. A comparison between the full fundamental mode predictions and the approximate solution revealed differences between the solutions of up to 5% for silencer 2. Such a small error is somewhat surprising considering the magnitude of $k_{r_1} r_1$ and $k_{r_2} r_2$ in Figure 6.2. Therefore, especially in the low to middle frequency range, it appears that the approximate method provides predictions comparable in accuracy with those obtained by using the full fundamental mode solution.

The effect of including the perforate in the model will now be examined. The acoustic impedance of perforates subjected to grazing flow was discussed in Chapter 4 and the values obtained for ζ (equal to $z_0/\rho_0 c_0$; see Chapter 4) are included in the model here when $M \neq 0$. For the case of no mean flow, values for the perforate impedance without porous backing (ζ_{np}) are given (see Ingård [75] and Sullivan [107]) by the expression

$$\zeta_{\mathrm{np}} = \frac{1}{\rho_0 c_0}\left(1+\frac{t}{d}\right)\left[8\mu\rho_0\omega\right]^{\frac{1}{2}} + ik_0\left(t+0.75d\right), \tag{6.98}$$

where μ is the dynamic viscosity of the gas, t is the hole depth and d the hole diameter. The effect of the porous material upon the mass end correction can be accounted for in the same manner as for the grazing flow predictions in Chapter 4. Therefore the perforate impedance (ζ) without flow is given by

$$\zeta_{np} = \frac{1}{\rho_0 c_0}\left(1+\frac{t}{d}\right)[8\mu\rho_0\omega]^{\frac{1}{2}} + ik_0(t+0.75d) + 0.425dk_0\left[\frac{z_a}{\rho_0 c_0}\frac{\Gamma}{k_0} - i\right], \qquad (6.99)$$

where z_a is the characteristic impedance and Γ the propagation constant of the porous material. A similar method was used by Bolt [108], who studied the absorption coefficient of a perforate plate backed by a locally reacting porous absorber. Bolt, who neglected the viscous resistance, added the mass reactance of the holes to that of the porous material to predict the combined effect of the perforate plus absorbent. The absorption coefficient of the porous material with a perforate facing is then read directly from a design chart, given a knowledge of the acoustic impedance of the unfaced material. The effect of the porous material on the acoustic impedance of a perforate has been found to be considerable (see Chapter 4). From the results of the experiments on perforates subjected to grazing flow, it was concluded that adding the effect of the porous material to the empirical results obtained in the absence of the porous material (as above) was valid. The empirical prediction of the acoustic impedance of perforates without grazing flow has been widely covered in the literature and hence it was felt unnecessary to perform further experiments, especially in view of the fact that the addition of the porous material dominates the acoustic impedance of a perforate.

The effect of adding the perforate impedance to the full fundamental mode solution is shown in Figure 6.5 for silencers 1 and 3 (note that the same perforate, plate 3, Table 4.1, has been used in all the silencers; for this, $t = 1$mm, $d = 3.5$mm and the porosity of the plate is 27.2%). It is evident from Figure 6.5 that the perforate has a substantial effect upon the predicted transmission loss for silencer 1, but not for silencer 3. The large effect in the case of silencer 1 occurs because the perforate is backed by E glass, which has a high flow resistivity and hence introduces a much larger effect upon the mass end correction. In contrast, silencer 3 is backed by A glass which has a relatively low flow resistivity and therefore contributes a much smaller effect. The qualitative trend in the results found by adding the perforate is similar to that found by Peat [109]; for instance, when the perforate impedance is small the transmission loss is increased only slightly at the higher frequencies, but if the perforate impedance is large then the transmission loss is increased at lower frequencies and reduced at higher frequencies. This comparison appears to indicate that the incorporation of the perforate into the fundamental mode model in this chapter is correct.

A comparison between measurement and prediction for the transmission loss of silencers 1, 2 and 3, with a perforate present, is shown in Figure 6.6 (M=0) and Figure 6.7 (M=0.15). It is evident from a comparison of the results with those in Figures 6.4 and 6.5 that the inclusion of a perforate in the model has increased the accuracy of the predictions, especially at higher frequencies (above 1kHz). However, it is difficult to draw any firm conclusions concerning the higher frequencies because of the uncertainty over the accuracy of the experimental data. At lower frequencies (100-1kHz), the experimental data are more reliable and it appears that predictions are more accurate for silencers 2 and 3, but less accurate for silencer 1. Unfortunately it is difficult to asses thoroughly the accuracy of the predictions made by including the perforate in the model since only the fundamental mode has been used in the modelling. For silencers of a similar size to silencers 1, 2 and 3, higher order modes can have relatively little attenuation at comparatively low frequencies and this is likely to influence the transmission loss. Consequently it is possible that any improvement found in the predictions shown in Figures 6.6 and 6.7 could be fortuitous, especially as it is anticipated that the acoustic impedance of the perforate may have been overestimated because of irregular packing of the absorbent (see the discussion in Chapter 4). Therefore, for definite conclusions to be drawn concerning the modelling of the perforate in the manner described here (and hence the accuracy of the fundamental mode model) a more comprehensive silencer model must be implemented, which at least accounts for the presence of higher order modes. Furthermore, an examination of the results for silencer 2 indicates that, even accounting for possible inaccuracies in prediction of the perforate impedance, higher order modes must be included in the solution since the quality of the predictions is poor. This effect is even more obvious when the fundamental mode solution is applied to silencers of non-circular cross-section, such as ellipses. Obviously, the model described in this chapter can only cope with axisymmetric silencers, and therefore silencers 4 and 5 are treated here as circular cross-section silencers with an outer cross-sectional area equivalent to that contained within the ellipse. The equivalent outer diameter of silencer 4 is 161mm and that of silencer 5 is 139mm. A comparison between prediction and experiment for the transmission loss of silencers 4 and 5 is shown in Figure 6.8 (without a perforate) and Figure 6.9 (with a perforate). It can be seen from Figures 6.8 and 6.9 that the predictions and measurements agree well for frequencies up to approximately 800Hz for silencer 4 and 500Hz for silencer 5. At higher frequencies the three dimensional nature of the silencers causes the predictions to differ considerably from the experimental data. It is evident from a comparison between silencers 4 and 5 that the fundamental mode solution is less accurate for the more "squashed" of the two ellipses (silencer 5). Therefore it appears that at low frequencies the transmission loss of a non-axisymmetrically shaped silencer can be predicted with reasonable accuracy by using the fundamental mode model, but as the silencer departs further from axisymmetry, the upper frequency limit at which acceptable accuracy can be found is reduced.

The fundamental mode model used in this chapter can be seen to perform very well, taking into account its relative simplicity. It is possible that, if models for axisymmetric dissipative silencers are required, which need to be computationally very fast and do not require a high degree of accuracy, then a fundamental mode model (full or approximate) will suffice. However, for silencers of arbitrary cross-sectional shape and/or large outside diameter, then a more complex model is required, which will allow properly for the cross-sectional geometry and account for higher order modes. Moreover, in the context of this thesis, a more accurate model is required in order to examine further the effect of the perforate, and to allow conclusions to be drawn on the possible overprediction of the effects of the porous material on the perforate impedance.

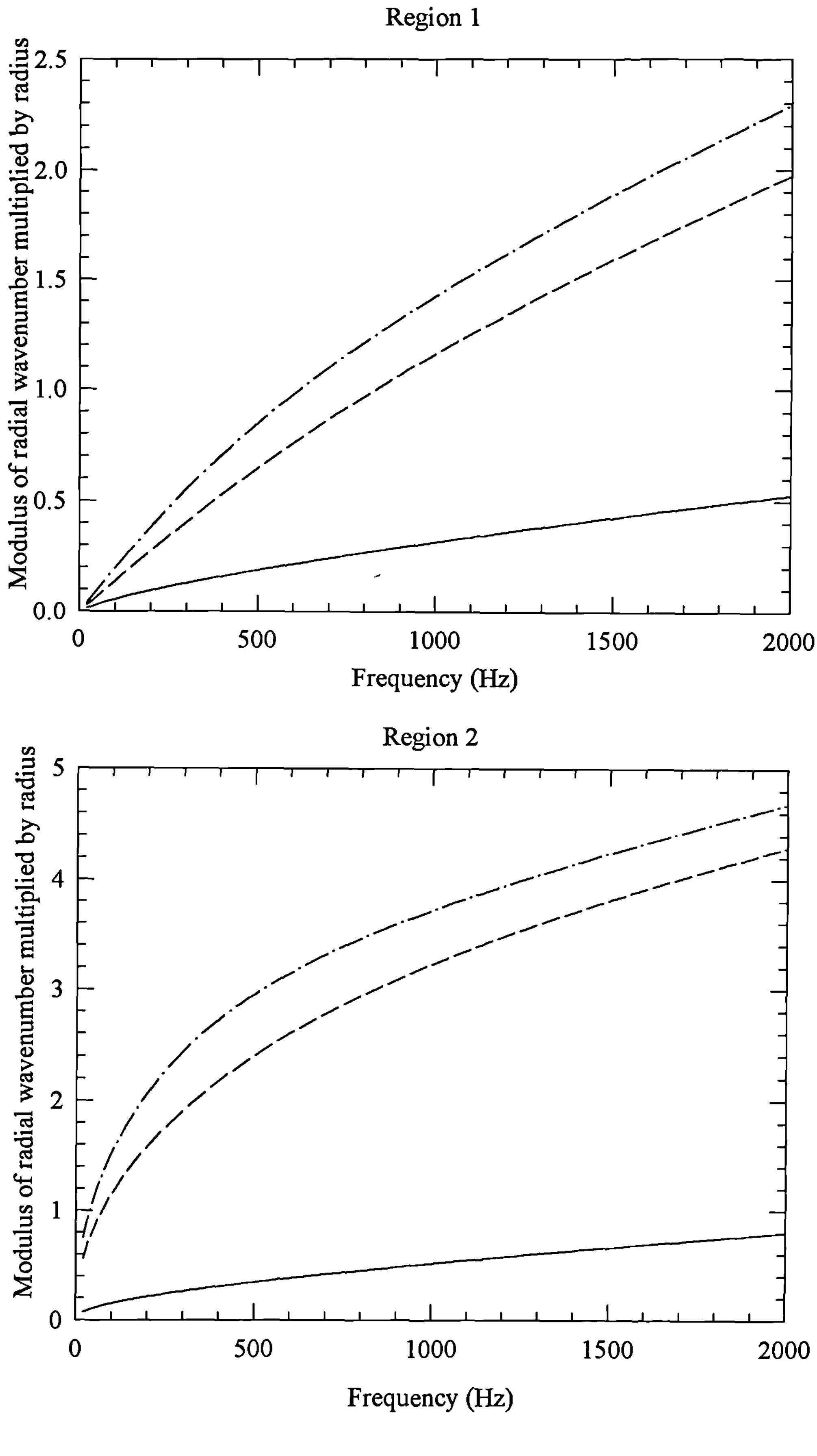

Figure 6.2. Modulus of radial wavenumbers. ——— , Silencer used by Peat [13]; – – – , silencer 1; —·— , silencer 2.

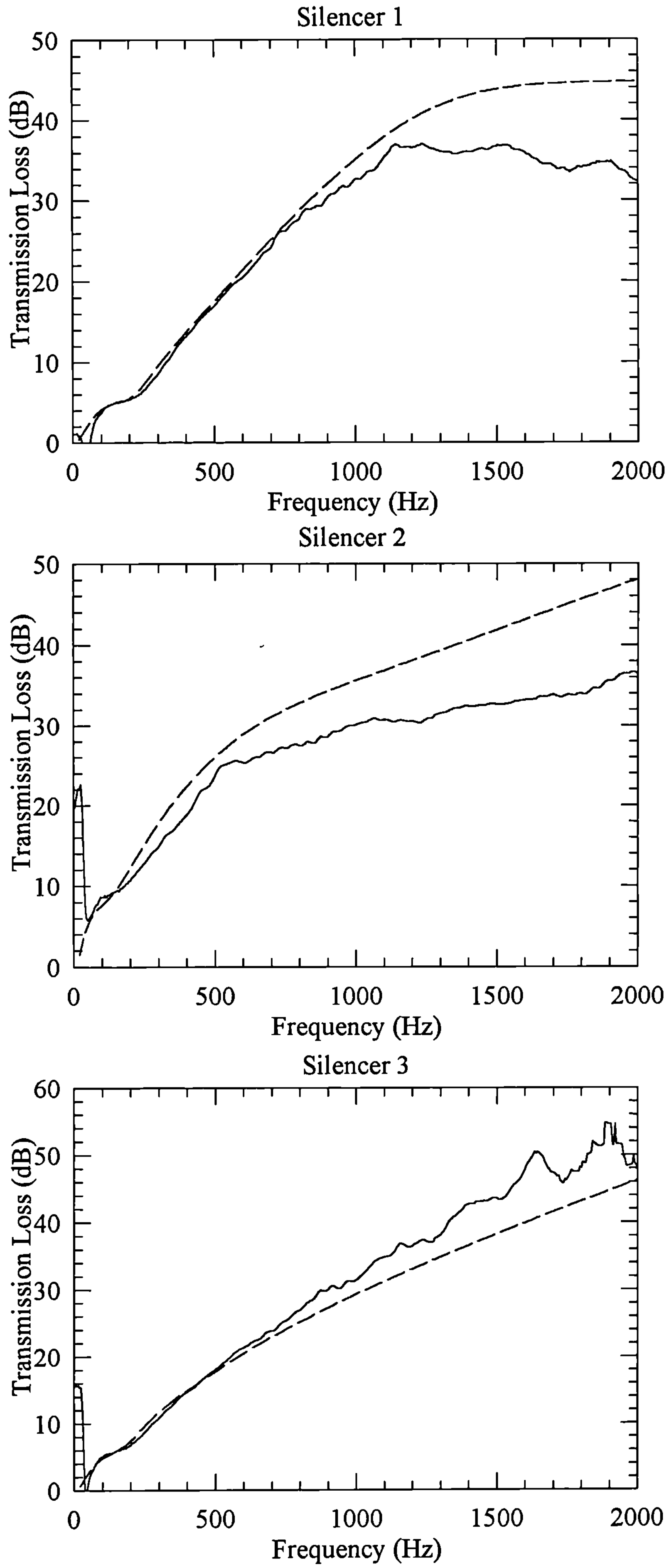

Figure 6.3. Fundamental mode predictions with no perforate and M=0.
——— , Experiment; – – – , Fundamental mode predictions.

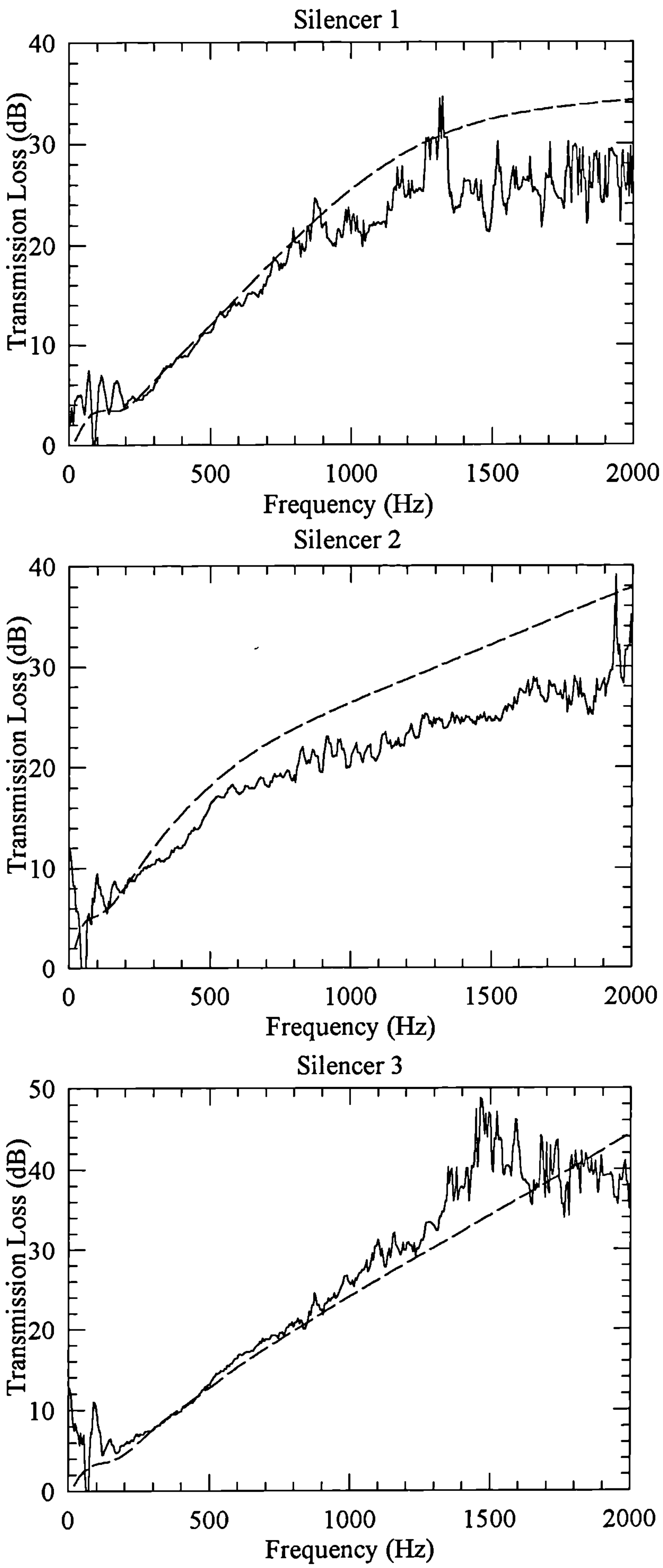

Figure 6.4. Fundamental mode predictions with no perforate and M=0.15.
——— , Experiment; — — — , Fundamental mode predictions.

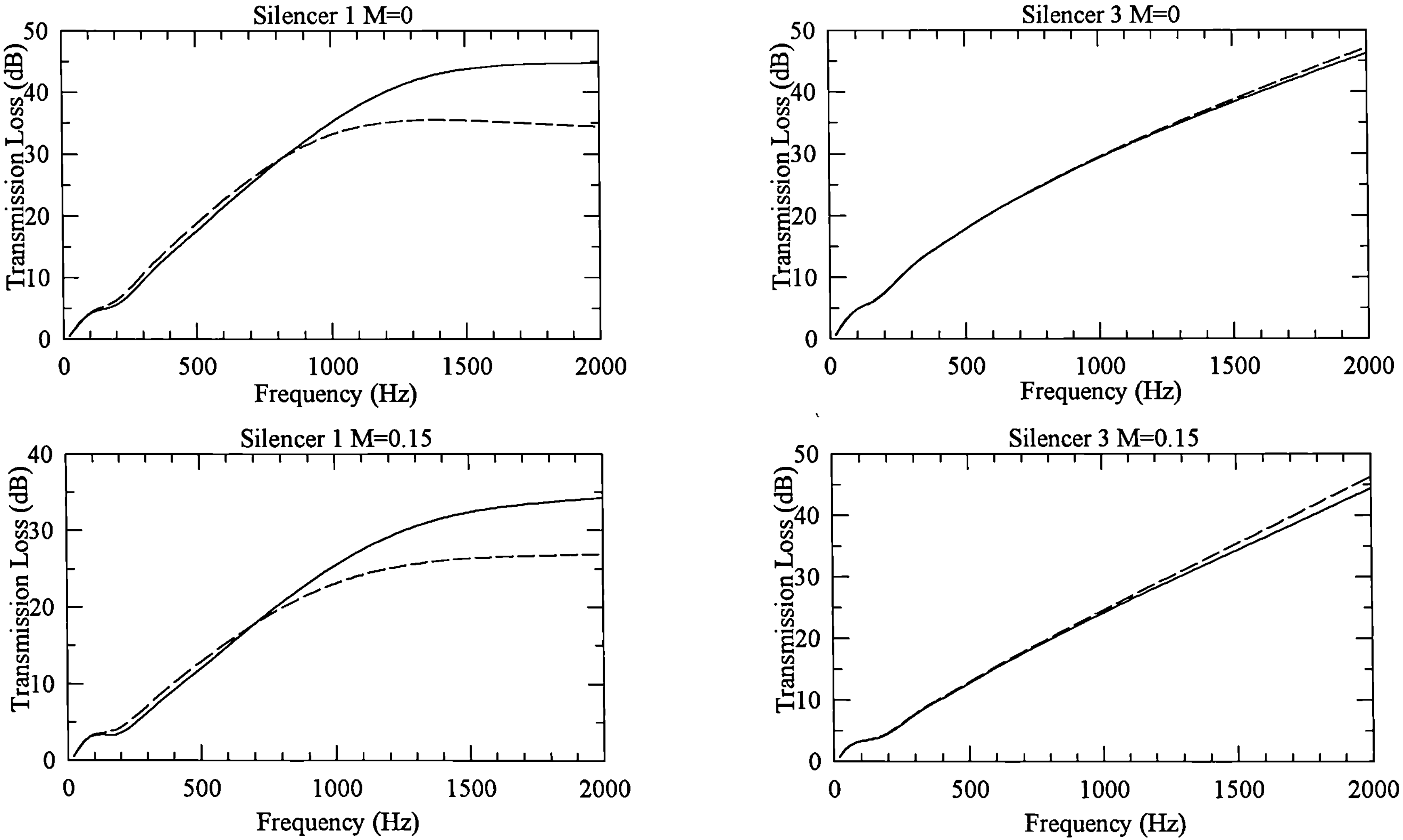

Figure 6.5. Comparison of the fundamental mode solution with and without a perforate. ——— , No perforate present; — — — , Perforate present.

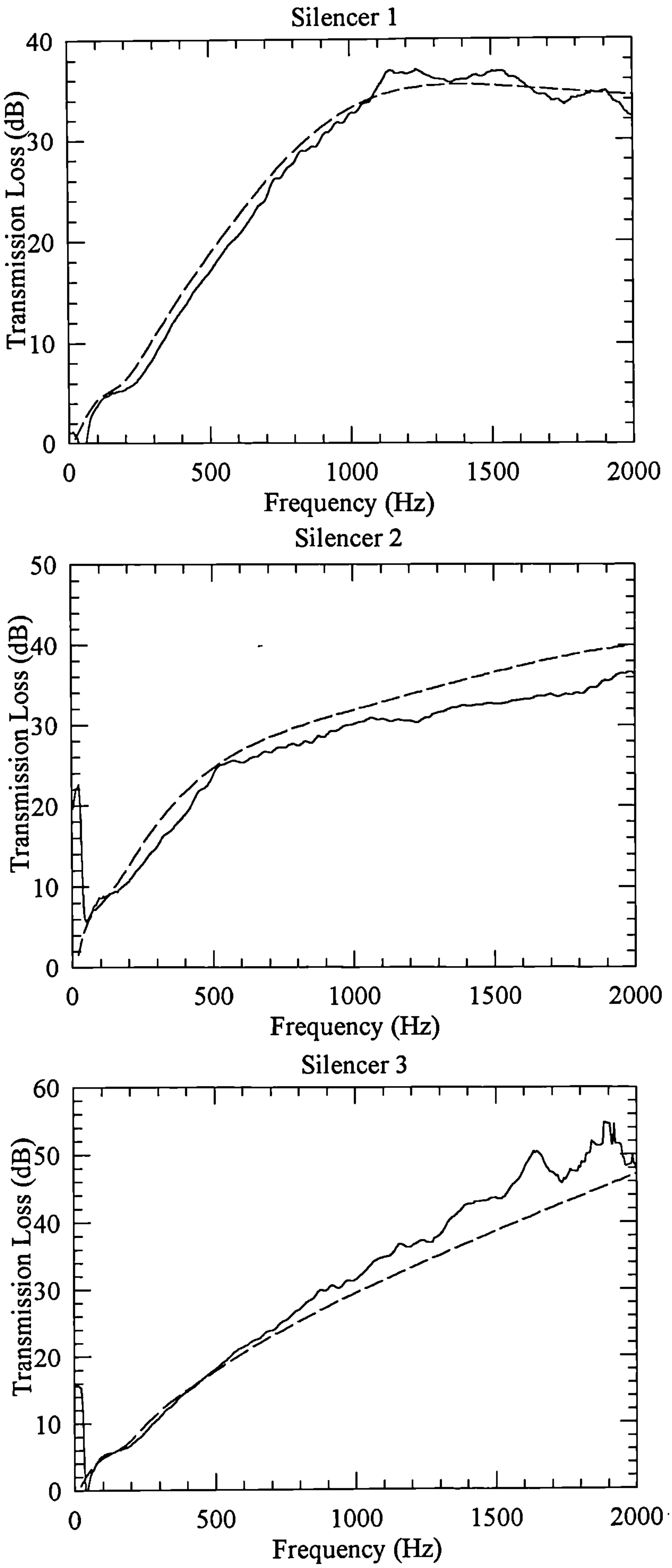

Figure 6.6. Fundamental mode solution with perforate M=0.
——— , Experiment; — — — , Fundamental mode prediction.

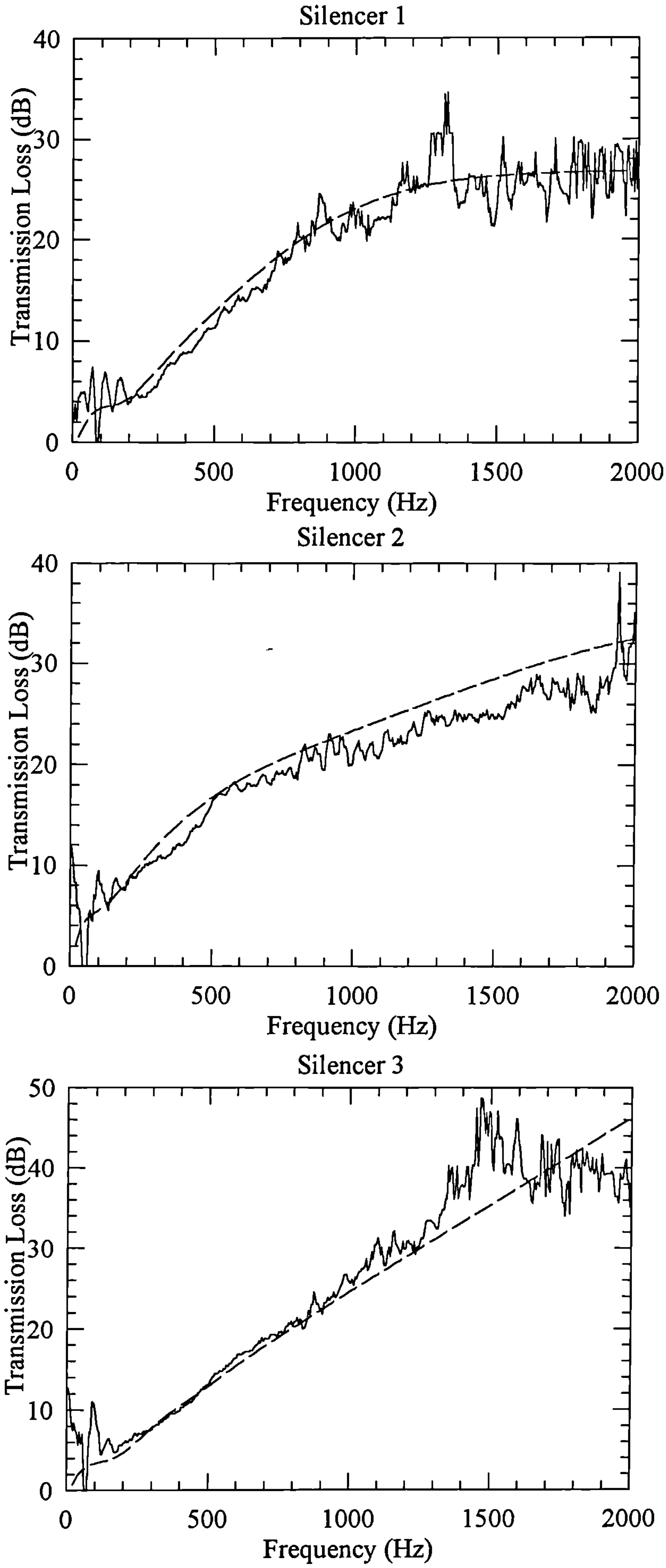

Figure 6.7. Fundamental mode prediction with perforate and M=0.15. ——— , Experiment; – – – , Fundamental mode prediction.

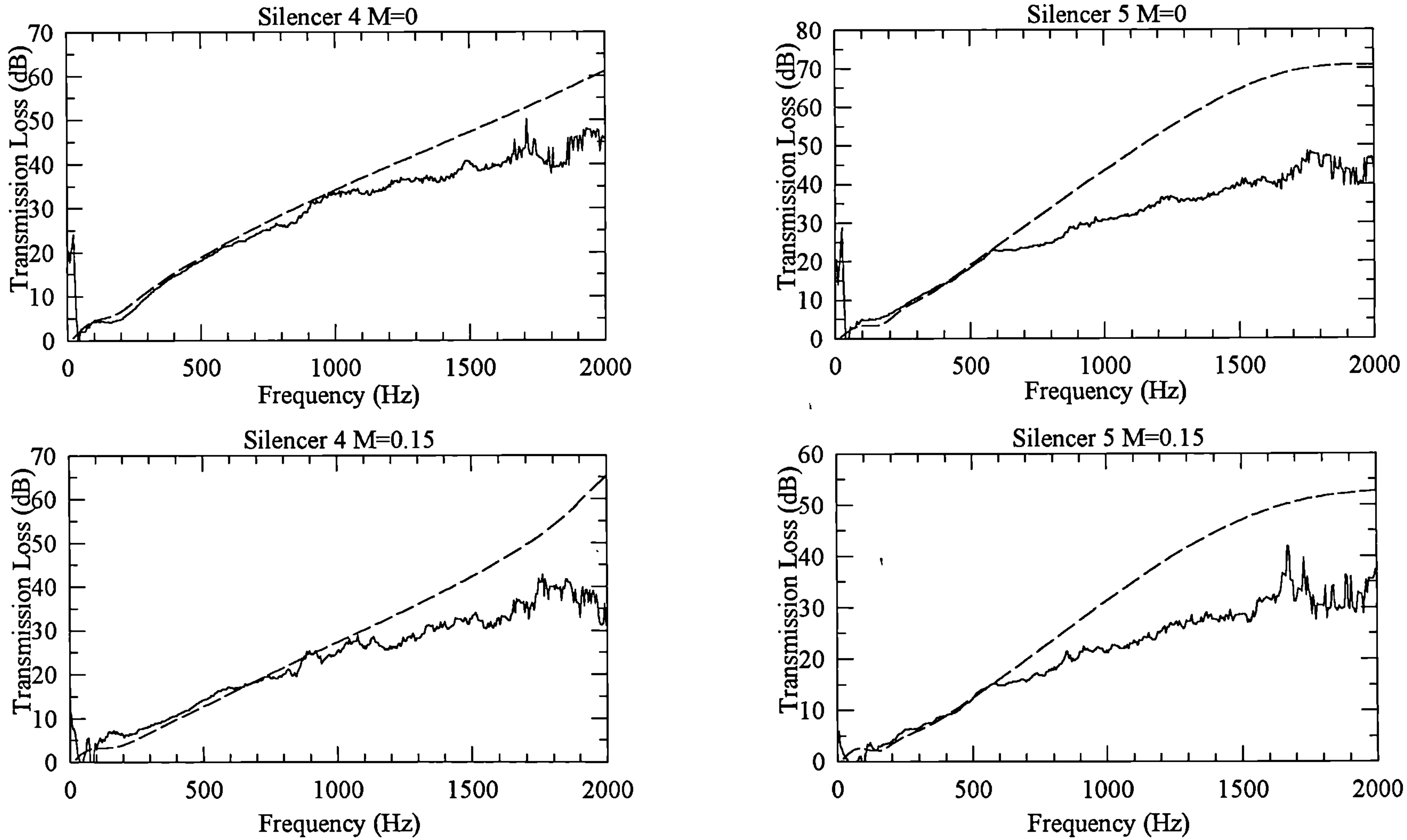

Figure 6.8. Fundamental mode predictions without perforate. ——— , Experiment; – – – , Fundamental mode predictions.

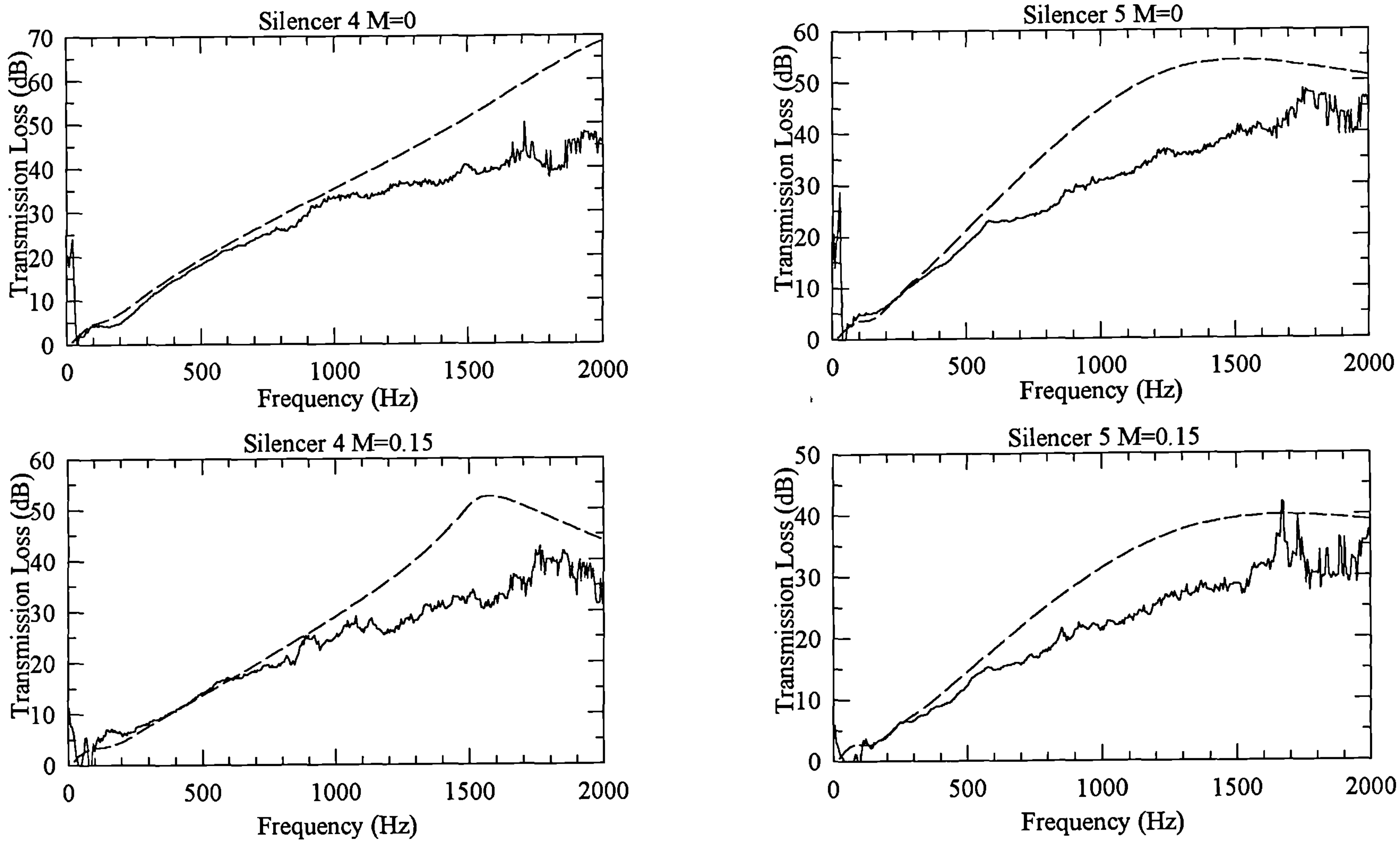

Figure 6.9. Fundamental mode prediction with perforate. ——— , Experiment; – – – , Fundamental mode prediction.

CHAPTER 7

THE FINITE ELEMENT METHOD

APPLIED TO DISSIPATIVE SILENCERS

Section 7.1

Introduction

In the previous chapter theoretical predictions of silencer transmission loss were obtained by using a quasi plane-wave approach, but correlation with experimental data was found to be poor in certain cases, especially for silencers with a large diameter and/or oval cross section. Consequently a more complete approach to modelling dissipative silencers is required, and this must account for effects such as the propagation of higher order modes and the three dimensional nature of a general silencer. The modelling of silencers with an arbitrary cross-sectional shape, such as an oval, inevitably requires the use of numerical techniques which allow irregular shapes to be tackled, though this does require a much higher degree of computational effort as compared to an analytical solution such as the one described in Chapter 6. In a commercial environment a consideration of the computational effort or cost required in modelling exhaust systems may be important and this must be balanced against the accuracy required in the predictions. In this chapter a fully three dimensional finite element numerical solution is described, which is probably the most computationally expensive approach to modelling a dissipative silencer. The model is probably too computationally demanding for use in most commercial design procedures, but as a completely general model it is useful for providing "benchmark" theoretical predictions. Later in this thesis, less complex models are described and the numerical predictions thereby obtained are compared to those presented in this chapter, which allows conclusions to be drawn concerning the required degree of refinement and adaptability that the model must have in order to yield acceptable results. Obviously, with the continual advancement in computer technology, it is possible that in the future the model derived here will become more readily usable in a commercial environment. Finally, the implementation of a completely numerical solution, with its associated improved prediction accuracy permits the further examination of the acoustic behaviour of the perforate, from which definite conclusions on the values used for the acoustic impedance can be made.

Numerical methods for solving the partial differential equations that govern problems such as the one studied here have been widely implemented, especially in recent years with the advancement in computer technology. Perhaps the three most commonly used approaches available for solving partial differential equations numerically are: finite difference, finite element and boundary element methods. The simplest approach is to use a finite difference scheme, which involves splitting up the domain of the problem into a grid in which a differencing approximation is applied to each interior point. Unfortunately finite difference methods are not ideally suited to cope with awkward geometries, and furthermore it is not straightforward to implement a spatially varying grid spacing, and this makes it unsuitable for use with variables that may have locally large gradients. Consequently finite differences are rarely used to study acoustical problems and find wider uses in computational fluid dynamics; finite and boundary element techniques are most commonly used in acoustics and vibration. The finite element method involves dividing the domain into small finite segments, and the behaviour of a variable (in this case sound pressure) is then described by the governing differential equation over each element. The variable distribution across the whole domain is found by combining all the elements that make up the domain. The finite element method is the most general of the aforementioned three numerical techniques since it can be applied directly to the governing differential equations. In addition, the method can cope with complex geometries, locally large gradients in the field variable and linear or non-linear governing equations; additionally, displacement or pressure boundary conditions may be specified at any point within the domain. An alternative to the finite element method is the boundary element method in which, instead of the entire domain being divided into elements, only the boundary of the domain is divided into elements. This obviously has the advantage of reducing the number of elements required and hence provides computationally faster solutions than those obtained by using the finite element method. However the boundary element method requires fundamental solutions to be found for the governing differential equations which are then transformed into integral identities and numerically integrated over each element on the boundary. Like finite element, the boundary element method is capable of coping with complex geometries and rapidly changing variables, but it cannot cope with non-linear variables.

Since the finite element method is the most general of the numerical techniques it has undergone the widest application to engineering problems. The field of duct acoustics reflects most other engineering disciplines in that the finite element method is much more widely established than boundary element methods. Boundary element methods have been successfully developed in duct acoustics, for example Zhenlin et al. [110] modelled a reactive silencer with mean flow, but this has been confined to the study of reactive elements because a fundamental solution to the governing equation in the absorbent region is, at present, unobtainable. Consequently the finite element method provides the only viable numerical technique for examining dissipative silencers with complex shapes.

The foundation for the use of the finite element method in acoustics was laid by Gladwell and Zimmermann [111], who described how acoustic problems could be written in a variational form. Young and Crocker [112] then derived a variational statement for a simple reactive muffler without mean flow in the central channel, they were then able to show how the finite element method could be used to provide an approximate solution to the governing equations. Young and Crocker showed that any degree of accuracy for the solution could be obtained since it converged to the exact solution as the number of elements were increased. Young and Crocker later went on to include flow reversing chambers in their model (see reference [113]) although they again neglected mean flow and used only simple two dimensional rectangular finite elements with variable thicknesses, and this restricted the analysis to rectangular sections. Craggs [114] found that expansion chambers with a circular cross section could be more successfully modelled by using hexahedral elements. Kagawa et al. [115] also studied reactive silencers without mean flow but were able to model silencers of arbitrary non-uniform circular cross section. The effects of uniform mean flow on non-uniform ducts containing locally reacting walls was later studied by Astley and

Eversman [116]. The effect of mean flow on a hard walled reactive silencer was studied by Peat [117], who used finite elements to calculate the four pole parameters for a silencer. The effects of dissipative elements such as porous materials were first studied, with the use of the finite element method, by Kagawa et al. [118], who introduced small amounts of a locally reacting porous absorbent onto the walls of a simple expansion chamber. Craggs [24] also studied the effect of porous materials by using a locally reacting model but varied the thickness of the porous material in the model; the surface impedance of the material was predicted by using the formulae of Delany and Bazley. Neither Kagawa et al. [118] nor Craggs [24] included mean flow in the central channel. The effects of mean flow in the central channel were first incorporated in finite element models of dissipative silencers in the context of cross-sectional eigenvalue problems for infinite silencers. Astley and Eversman [119] studied axisymmetric and two dimensional flow ducts with locally reacting soft walls and found that an acceptable degree of accuracy could be achieved by using quadratic shape functions coupled with a modest number of elements. Later, Astley and Cummings [17] introduced an eigenvalue solution for silencers of arbitrary cross-section that included both mean flow and a bulk reacting liner; they then applied their model to rectangular ducts lined on all four walls. The finite element method was applied to finite length dissipative silencers by Christiansen and Krenk [120], who calculated the insertion loss of a silencer with a bulk reacting liner by using a recursive technique, although mean flow in the central channel was omitted. Mean flow in the central channel was added to finite element models of finite length dissipative silencers by Hobbeling [25] and later by Peat and Rathi [26]. In addition Peat and Rathi accounted for mean flow within the absorbing material itself; they computed this flow field, induced by axial pressure gradients, by using a finite element formulation. Peat and Rathi also accounted for the anisotropy and inhomogeneity brought about in the porous material when non-uniform mean flow is present. The results of Peat and Rathi were incorporated in four-pole parameters, from which predictions for the transmission loss were found. Although the model of Peat and Rathi is completely general, they only found transmission loss solutions for axisymmetric silencers, and a perforate between the central channel and the absorbent was not included. A full description of the model derived by Peat and Rathi is also given by Rathi [18], where a formulation is additionally given for a silencer with a non-uniform central channel.

The approach of Peat and Rathi [26] appears to be the most general method for modelling dissipative silencers to be found in the literature since it accounts for both mean flow in the central channel and the presence of a bulk reacting absorbent. Therefore this method was adopted here and will be described in the following section, although the effects of mean flow in the absorbent are ignored and absorbent material properties such as the propagation constant and characteristic impedance are considered to be independent of material orientation (i.e. the absorbent was assumed to be isotropic). The model will be extended to include a perforate between the central channel and the absorbent since earlier chapters indicate that this can have a significant effect on the final results. Solutions will also be presented for three dimensional silencers, namely the elliptical silencers 4 and 5 from Chapter 5. The results will then be compared to the experimental data presented in Chapter 5 to indicate the limits on the accuracy of predictions made by using numerical techniques.

The finite element computer code implemented in this chapter was modified from a program originally written by Rathi [121]. The program was originally capable of examining only two specific silencers, namely the two circular silencers which appear in the study by Peat and Rathi [26]. The author modified this program to allow any size of two dimensional silencer to be studied and also included a number of different absorbing materials, using the semi empirical model of Chapter 3, into the program. In addition, new coding was introduced to allow for the study of three dimensional silencers and also the inclusion of a perforate.

Section 7.2

Governing Equations

The finite element analysis of dissipative silencers presented in this chapter is based upon the method used by Peat and Rathi [26] (see also Rathi [18]). However mean flow in the absorbent is ignored here and a perforate is included, separating the central channel from the absorbent material. The porous material is assumed to be isotropic, and this permits the simplification of the wave equation in the absorbent region. The inclusion of the perforate in the model has the effect of modifying the continuity of pressure boundary condition at the interface between the central channel and the absorbent. This problem was tackled in the previous chapter by expressing the pressure and particle displacement boundary conditions in terms of a displacement impedance, but for the analysis presented here it is more straightforward to implement the pressure and displacement boundary conditions separately. The general governing wave equations for both the central channel and the absorbent are identical to those used for the fundamental mode solution in the previous chapter, but now, instead of using separation of variables to solve the equations, they are solved directly by using finite elements to provide an approximate solution. This has the benefit of allowing silencers with a general shape to be modelled although it should be noted that the central channel must remain uniform in the following analysis.

The geometry of the dissipative silencer to be studied in this chapter is given in Figure 7.1 below.

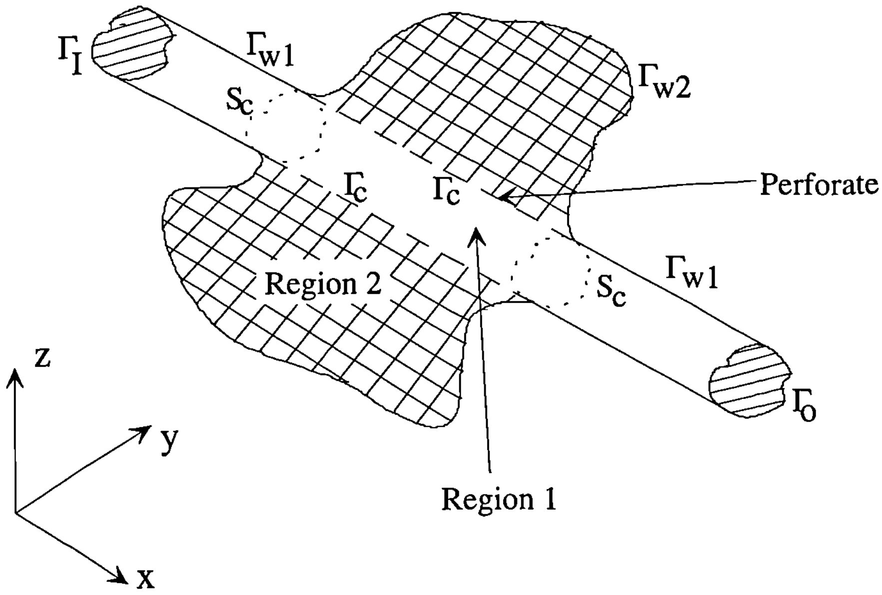

Figure 7.1. Geometry of general silencer.

The silencer is assumed to consist of a uniform central channel (region 1) which carries a uniform mean flow of Mach number M, in the x direction only. The central channel extends beyond the absorbent box in the form of inlet and outlet pipes which are of sufficient length to allow the assumption of plane waves at the boundaries Γ_I and Γ_O. Extended inlet and outlet pipes are important because the problem is eventually formulated into a transfer matrix and this requires plane waves at the input and output. The perforate liner is used to separate the central channel from the surrounding isotropic porous material contained in a box of arbitrary shape (region 2). The perforate lies on the boundary Γ_C in Figure 7.1. The outer walls of both region 1 and 2 are assumed to be rigid and impervious, and are denoted by Γ_{W1} and Γ_{W2} respectively, or collectively by $\Gamma_W (= \Gamma_{W1} + \Gamma_{W2})$.

The solution proceeds by first finding the wave equation for regions 1 and 2. Solutions to the wave equation are then found by using the weak Galerkin formulation, the two governing equations being linked by the pressure and normal particle displacement boundary conditions at the common boundary Γ_C. The assembly of the final stiffness matrix is then carried out by using the gradient evaluation approach described by Peat and Rathi [26]. In Section 7.4, the numerically predicted transmission loss for the axisymmetric and elliptical silencers described in Chapter 5 will be compared to measured data. A description of the finite element meshes that were used to generate the predictions will also be given in Section 7.4.

7.2.1 Acoustic Wave Equation in the Central Channel (Region 1)

The wave equation for the central channel, assuming mean flow in the x direction only, has been derived by combining the linearised Euler and continuity equations (see Chapter 6) to give

$$\nabla^2 p_1' - \frac{1}{c_0^2}\frac{\partial^2 p_1'}{\partial t^2} - \frac{2M}{c_0}\frac{\partial^2 p_1'}{\partial x \partial t} - M^2 \frac{\partial^2 p_1'}{\partial x^2} = 0, \tag{7.1}$$

where p_1' is the acoustic pressure in region 1, t is time, c_0 is the isentropic speed of sound and M is the mean flow Mach number. Taking a time dependence of $e^{i\omega t}$ allows the wave equation to be re-written as

$$\nabla^2 p_1' - 2ik_0 M \frac{\partial p_1'}{\partial x} - M^2 \frac{\partial^2 p_1'}{\partial x^2} + k_0^2 p_1' = 0, \tag{7.2}$$

where $k_0 (= \omega / c_0)$ is the wavenumber in the central channel, ω being the radian frequency.

7.2.2 Acoustic Wave Equation in the Absorbent (Region 2)

The wave equation in region 2, assuming that there is no mean flow in the absorbent and the material is isotropic, is given by (see equation (6.25))

$$\nabla^2 p_2' - \Gamma^2 p_2' = 0, \tag{7.3}$$

where p_2' is the acoustic pressure in region 2 and Γ is the propagation constant of the material, defined in Chapter 2.

7.2.3 Boundary Conditions

In accordance with Peat and Rathi [26], the acoustic particle velocity normal to the impervious boundary Γ_W (where $\Gamma_W = \Gamma_{W1} + \Gamma_{W2}$) is taken to be zero, i.e.

$$\nabla p' \cdot \mathbf{n} = 0 \quad \text{on} \quad \Gamma_W \tag{7.4}$$

for regions R_1 and R_2, where $\mathbf{n}$ is a unit normal vector to the boundary. On the common boundary Γ_C, one must enforce the boundary conditions involving normal particle displacement and continuity of sound pressure.

The acoustic pressure boundary condition on the common boundary is modified from that used by Peat and Rathi [26] because of the presence of the perforate. In the model presented here the perforate is assumed to be infinitesimally thin and hence the perforate links together the pressures on either side of Γ_C in the following manner (see Chapter 6)

$$\zeta = \frac{p_1' - p_2'}{i\omega\rho_0 c_0 \xi_2'} \quad \text{on} \quad \Gamma_C, \tag{7.5}$$

where ζ is the dimensionless acoustic impedance of the perforate (corresponding to $z_0/\rho_0 c_0$ in Chapter 4), ξ_2' is the particle displacement component in region 2 normal to Γ_C and ρ_0 is the mean fluid density. The choice of ξ_2' in equation (7.5) allows for a more convenient implementation of the boundary conditions later in the analysis; identical results could equally be found by choosing ξ_1'. To allow for the straightforward use of equation (7.5) it is convenient to re-write the equation in terms of the acoustic particle velocity vector $\mathbf{u}_2'$, which is given (see equation (6.45)) by

$$\frac{\partial \xi_2'}{\partial t} = \mathbf{u}_2', \tag{7.6}$$

where ξ_2' is the particle displacement vector in region 2. If a time dependence of $e^{i\omega t}$ is assumed then equation (7.5) can be re-written as

$$\mathbf{u}_2' \cdot \mathbf{n}_2 = \frac{1}{\rho_0 c_0 \zeta}\left[p_{C_2}' - p_{C_1}'\right], \tag{7.7}$$

where $\mathbf{n}_2$ is the unit normal vector in region 2 and p_C' is the pressure on boundary Γ_C in either region 1 or 2.

The other boundary condition at the perforate is now formulated, namely the continuity of normal particle displacement, which gives

$$\xi_1' \cdot \mathbf{n}_C = \xi_2' \cdot \mathbf{n}_C \quad \text{on} \quad \Gamma_C, \tag{7.8}$$

where ξ_1' is the particle displacement vector in region 1 and $\mathbf{n}_C$ is the unit normal vector to the boundary Γ_C. An expression for the normal particle displacement in region 1 was given in the previous chapter (see equation (6.39)) and, for a time dependence of $e^{i\omega t}$, this gives

$$\xi_1' = \frac{\mathbf{u}_1'}{i\omega\left[1 - \dfrac{iM}{k_0}\dfrac{\partial}{\partial x}\right]}. \tag{7.9}$$

The substitution of equations (7.6) and (7.9) into equation (7.8) gives

$$\mathbf{u}_1' \cdot \mathbf{n}_1 = \left[1 - \frac{iM}{k_0}\frac{\partial}{\partial x}\right]\mathbf{u}_2' \cdot \mathbf{n}_C, \tag{7.10}$$

where the unit normal vector $\mathbf{n}_C$ on the left hand side of equation (7.8) has been replaced by $\mathbf{n}_1$ and $\mathbf{n}_C = \mathbf{n}_1 = -\mathbf{n}_2$.

In order to formulate the overall solution of the problem in terms of four-pole parameters, Peat [117] showed that it is necessary to solve the entire problem twice. This involves implementing two independent sets of boundary conditions on the inlet and outlet of region 1 (Γ_I and Γ_O). From here, the transmission loss of the overall system can be evaluated. The two different sets of boundary conditions were defined by Peat [117] as

$$\frac{\partial p_1'}{\partial x} = \text{constant on } \Gamma_I, \quad p_1' = 0 \text{ on } \Gamma_O \qquad (7.11), (7.12)$$

and

$$p_1' = \text{constant on } \Gamma_I, \quad \mathbf{u}_1' = 0 \Rightarrow \frac{\partial p_1'}{\partial x} = ik_0 M p_1 \text{ on } \Gamma_O. \qquad (7.13), (7.14)$$

Section 7.3

Finite Element Discretization

In this section, the numerical solution of the wave equations in both the central channel and the absorbent by the finite element method is described. The theory underlying the finite element method has been extensively covered in the literature (see for example Zienkiewicz [122]) and does not therefore require detailed repetition here. However the basic procedure which underlies the finite element method, involves dividing the domain of the problem up into elements which are used to represent the sound pressure by use of an arbitrary interpolation function. The interpolation function or "shape function" is usually chosen to be a low order polynomial, and in general quadratic polynomials are used here (see Section 7.4 for a more complete discussion on the elements used). The shape functions are local, element-based functions and they assume a value of one at the node to which they refer and the value zero at all other nodes on the particular element. Since adjacent elements share common nodes, a single node is associated with the shape functions throughout all the elements which contain that node. One can then define global, nodal-based interpolation functions, which are the sum of all the element based shape functions relating to a single node, and these are known as global basis functions. Therefore, for an individual node, the global basis function is zero over all the elements which do not contain that particular node.

The solution method employed in the present investigation is the method of weighted residuals, in particular the Galerkin approach, since this allows the finite element equations to be derived directly from the governing wave equations. It may be noted that this technique does not require the derivation of a functional, as would be the case in the variational approach. The Galerkin method is a particular form of the weighted residual method, which specifies the global basis functions as the weighting functions. The "weak" Galerkin formulation, which was also used by Peat and Rathi [26], is implemented in order to reduce the maximum order of the derivative terms in the governing differential equations. This is important since it reduces the derivatives to first order only and this allows finite elements to be used which require only the acoustic pressure to be continuous at the interface between each element. If second order derivatives remain in the final equations then one must ensure that the elements also satisfy continuity of the derivative of the acoustic pressure at inter-element boundaries, and this requires the use of a much more complex element. The use of the weak Galerkin formulation thereby allows the use of simple elements which need only satisfy continuity of acoustic pressure and these elements are known as C^0 continuous elements. Elements which are required to satisfy continuity of the first derivative of the acoustic pressure at the inter-element boundaries are known as C^1 continuous elements, and so on.

We can approximate the solution to the wave equation in region 1 by a trial solution,

$$p_1' \approx \sum_{J=1}^{N_1} \psi_J p_{1_J}', \tag{7.15}$$

where $\psi_J(x,y,z)$ are the global basis functions, p_{1_J}' is the value of p_1' at the J^{th} node and N_1 is the number of nodes in region 1. Applying the Galerkin formulation to equation (7.2) gives

$$\int_{R_1} \psi_I \left(\nabla \cdot [\mathrm{M}] \nabla p_1' - 2iMk_0 \frac{\partial p_1'}{\partial x} + k_0^2 p_1' \right) dV = 0, \quad I = 1, \ldots\ldots, N_1, \tag{7.16}$$

where [M] is a diagonal matrix given by

$$[\mathbf{M}] = \begin{bmatrix} (1-M^2) & 0 & 0 \\ 0 & 1 & 0 \\ 0 & 0 & 1 \end{bmatrix}. \tag{7.17}$$

The application of Green's theorem to equation (7.16) gives a weak Galerkin formulation of

$$\int_{R_1} \left(\nabla \psi_I \cdot [\mathbf{M}] \nabla p_1' + 2iMk_0 \psi_I \frac{\partial p_1'}{\partial x} - k_0^2 \psi_I p_1' \right) dV = \int_{\Gamma_1} \psi_I [\mathbf{M}] \nabla p_1' \cdot \mathbf{n}_1 d\Gamma. \tag{7.18}$$

Substituting the assumed trial solution from equation (7.15) into equation (7.18) gives

$$\sum_{J=1}^{N_1} \left[\int_{R_1} \left(\nabla \psi_I \cdot [\mathbf{M}] \nabla \psi_J + 2iMk_0 \psi_I \frac{\partial \psi_J}{\partial x} - k_0^2 \psi_I \psi_J \right) dV \right] p_{1_J}' = \int_{\Gamma_1} \psi_I [\mathbf{M}] \nabla p_1' \cdot \mathbf{n}_1 d\Gamma, \tag{7.19}$$

The wave equation for region 2 is solved in a similar manner, where the approximation to the acoustic pressure is given by

$$p_2' \approx \sum_{J=1}^{N_2} \psi_J p_{2_J}', \tag{7.20}$$

where N_2 is the number of nodes in region 2. Applying the Galerkin formulation to equation (7.3) gives

$$\int_{R_2} \psi_I \left(\nabla^2 p_2' - \Gamma^2 p_2' \right) dV = 0, \quad I = 1, \ldots\ldots, N_2. \tag{7.21}$$

The application of Green's theorem to equation (7.21) gives a weak Galerkin formulation of

$$\int_{R_2}\left(\nabla\psi_I\cdot\nabla p_2'+\Gamma^2\psi_I p_2'\right)dV=\int_{\Gamma_2}\psi_I\nabla p_2'\cdot\mathbf{n}_2 d\Gamma. \tag{7.22}$$

Substituting the assumed trial solution from equation (7.20) into equation (7.22) gives

$$\sum_{J=1}^{N_2}\left[\int_{R_2}\left(\nabla\psi_I\cdot\nabla\psi_J+\Gamma^2\psi_I\psi_J\right)dV\right]p_{2_J}'=\int_{\Gamma_2}\psi_I[\mathbf{G}]\nabla p_2'\cdot\mathbf{n}_2 d\Gamma, \tag{7.23}$$

7.3.1 Matching of the Acoustic Fields

The finite element meshes for regions 1 and 2 must be matched together using continuity of pressure and displacement at each node along the boundary Γ_C. However the inclusion of the (infinitesimally thin) perforate along this boundary means that the two regions do not share a set of common nodes. This is evident in equation (7.7), since p_{C_1}' must contain nodes on the boundary Γ_C in region 1, whereas p_{C_2}' must contain nodes on the boundary Γ_C in region 2. This represents an important difference between the present model and that used by Peat and Rathi [26] since they were able to combine the pressure on either side of the boundary into a common node because $p_{C_1}'=p_{C_2}'=p_C'$. The use of the perforate here requires the finite element mesh to be constructed so that the number of nodes on the common boundary Γ_C is doubled as compared to an equivalent mesh based on the method of Peat and Rathi; half the nodes on Γ_C exist in region 1 and half in region 2. Unfortunately this complicates the generation of the finite element mesh, the consequences of which will be discussed later on in this chapter.

In addition to the boundary conditions at the perforate, the governing equations must be solved subject to the hard-wall boundary condition (equation (7.4)) and the inlet/outlet conditions given by equations (7.11) to (7.14). The hard-wall boundary condition implies that the surface integral in region 2 (right hand side of equation (7.23)) is zero except on the perforate boundary Γ_C, since $\Gamma_2=\Gamma_{W2}+\Gamma_C$. Similarly, the surface integral on the right hand side of equation (7.19) is zero over Γ_{W1}, although, in addition to a contribution along Γ_C, one must also include contributions from the inlet and outlet surfaces Γ_I and Γ_O. The additional inlet/outlet boundary conditions associated with equations (7.11) and (7.14) must also be implemented on Γ_I and Γ_O, Peat and Rathi [26] noted that these are variously Dirichlet, Neumann and Cauchy conditions which can be implemented in the standard way (see Zienkiewicz [122]).

The combination of inlet and outlet boundary conditions on Γ_I and Γ_O are grouped together here to form the forcing vector $\mathbf{f}_1$. If the surface integrals associated with the right hand sides of equations (7.19) and (7.23) form the vectors $\mathbf{f}_C^1$ and $\mathbf{f}_C^2$ respectively then equations (7.19) and (7.23) can be written in matrix form, i.e.

$$\begin{bmatrix} \mathbf{K}_{11} & \mathbf{K}_{1C} \\ \mathbf{K}_{C1} & \mathbf{K}_{CC}^1 \end{bmatrix} \begin{Bmatrix} \mathbf{p}_1 \\ \mathbf{p}_{C_1} \end{Bmatrix} = \begin{Bmatrix} \mathbf{f}_1 \\ \mathbf{f}_C^1 \end{Bmatrix}, \tag{7.24}$$

and

$$\begin{bmatrix} \mathbf{K}_{CC}^2 & \mathbf{K}_{C2} \\ \mathbf{K}_{2C} & \mathbf{K}_{22} \end{bmatrix} \begin{Bmatrix} \mathbf{p}_{C_2} \\ \mathbf{p}_2 \end{Bmatrix} = \begin{Bmatrix} \mathbf{f}_C^2 \\ 0 \end{Bmatrix}, \tag{7.25}$$

where $[\mathbf{K}_{11}]$ is of order $(N_1 - N_C) \times (N_1 - N_C)$, $[\mathbf{K}_{22}]$ is of order $(N_2 - N_C) \times (N_2 - N_C)$, $[\mathbf{K}_{CC}^1]$ and $[\mathbf{K}_{CC}^2]$ are of order $(N_C \times N_C)$, and so on. The vectors $\mathbf{p}_1$ and $\mathbf{p}_2$ are the vectors of p'_{1_J} and p'_{2_J} values which do not lie on Γ_C, $\mathbf{p}_{C_1}$ and $\mathbf{p}_{C2}$ are the vectors of p'_{1_J} and p'_{2_J} which do lie on Γ_C. The vectors $\mathbf{f}_C^1$ and $\mathbf{f}_C^2$, for node I, are given by

$$\mathbf{f}_{C_I}^1 = \int_{\Gamma_C} \psi_I [\mathbf{M}] \nabla p_1' \cdot \mathbf{n}_1 d\Gamma, \tag{7.26}$$

and

$$\mathbf{f}_{C_I}^2 = \int_{\Gamma_C} \psi_I \nabla p_2' \cdot \mathbf{n}_2 d\Gamma. \tag{7.27}$$

The boundary conditions along the boundary Γ_C must now be implemented in the governing equation via vectors $\mathbf{f}_{CI}^1$ and $\mathbf{f}_{CI}^2$. For region 1 this can be done by first examining the linearized Navier-Stokes equation (see equation (6.1)) which gives

$$\nabla p_1' = -i\rho_0 c_0 k_0 \left[1 - \frac{iM}{k_0}\frac{\partial}{\partial x}\right]\mathbf{u}_1'. \tag{7.28}$$

Substituting equation (7.28) into equation (7.26) gives

$$\mathbf{f}_{C_1}^1 = -i\rho_0 c_0 k_0 \int_{\Gamma_C} \psi_I [\mathbf{M}] \left[1 - \frac{iM}{k_0}\frac{\partial}{\partial x}\right]\mathbf{u}_1' \cdot \mathbf{n}_1 d\Gamma. \tag{7.29}$$

Continuity of normal particle displacement on Γ_C (equation (7.10)) can now be introduced into equation (7.29) to give

$$\mathbf{f}_{C_1}^1 = -i\rho_0 c_0 k_0 \int_{\Gamma_C} \psi_I \left[1 - \frac{iM}{k_0}\frac{\partial}{\partial x}\right]^2 \mathbf{u}_2' \cdot \mathbf{n}_C d\Gamma, \tag{7.30}$$

where only the unitary elements of $[\mathbf{M}]$ are relevant since $\mathbf{u}_2' \cdot \mathbf{n}_C$ is perpendicular to x. The gradient evaluation approach described by Peat and Rathi [26] is implemented here since this method was shown to be more computationally efficient than the gradient elimination approach. Consequently the trial solution given by equation (7.15) is substituted directly into equation (7.30) to give

$$\mathbf{f}_C^1 = \left\{ i\rho_0 c_0 k_0 \int_{\Gamma_C} \left(\psi_I - 2i\psi_I \frac{M}{k_0}\frac{\partial}{\partial x} - \psi_I \frac{M^2}{k_0^2}\frac{\partial^2}{\partial x^2} \right) \psi_J d\Gamma \right\} \{\mathbf{u}_2' \cdot \mathbf{n}_2\}. \tag{7.31}$$

Continuity of pressure on Γ_C (see equation (7.7)) allows equation (7.31) to be re-written as

$$\mathbf{f}_C^1 = \left\{ \frac{ik_0}{\zeta} \int_{\Gamma_C} \left(\psi_I \psi_J - 2i\psi_I \frac{M}{k_0}\frac{\partial \psi_J}{\partial x} - \psi_I \frac{M^2}{k_0^2}\frac{\partial^2 \psi_J}{\partial x^2} \right) d\Gamma \right\} \left[\{\mathbf{p}_{C_2}'\} - \{\mathbf{p}_{C_1}'\} \right], \tag{7.32}$$

where $\{\mathbf{P}_C'\}$ is the vector of nodal p_{C_J}' values on the boundary Γ_C in either region 1 or 2. It is convenient to re-write equation (7.32) in matrix form such that

$$\{\mathbf{f}_{\mathrm{C}}^{1}\}=\left[\tilde{\mathbf{F}}_{\mathrm{C}_1}^{1} \quad \tilde{\mathbf{F}}_{\mathrm{C}_2}^{1}\right]\begin{Bmatrix}\mathbf{p}_{\mathrm{C}_1}\\ \mathbf{p}_{\mathrm{C}_2}\end{Bmatrix}, \tag{7.33}$$

where $\left[\tilde{\mathbf{F}}_{\mathrm{C}_1}^{1}\right]$ and $\left[\tilde{\mathbf{F}}_{\mathrm{C}_2}^{1}\right]$ are $(\mathrm{N_C} \times \mathrm{N_C})$ matrices, the $(\mathrm{I,J})^{\text{th}}$ elements of which are given by

$$\tilde{\mathbf{F}}_{\mathrm{C}}^{1}=\frac{ik_0}{\zeta}\int_{\Gamma_{\mathrm{C}}}\left(\psi_{\mathrm{I}}\psi_{\mathrm{J}}-2i\psi_{\mathrm{I}}\frac{M}{k_0}\frac{\partial\psi_{\mathrm{J}}}{\partial x}-\psi_{\mathrm{I}}\frac{M^2}{k_0^2}\frac{\partial^2\psi_{\mathrm{J}}}{\partial x^2}\right)d\Gamma. \tag{7.34}$$

The order of differentiation in equation (7.34) can be reduced through the use of Green's theorem to give, finally,

$$\tilde{\mathbf{F}}_{\mathrm{C}}^{1}=\frac{ik_0}{\zeta}\int_{\Gamma_{\mathrm{C}}}\psi_{\mathrm{I}}\psi_{\mathrm{J}}d\Gamma+\frac{2M}{\zeta}\int_{\Gamma_{\mathrm{C}}}\psi_{\mathrm{I}}\frac{\partial\psi_{\mathrm{J}}}{\partial x}d\Gamma+\frac{iM^2}{\zeta k_0}\int_{\Gamma_{\mathrm{C}}}\frac{\partial\psi_{\mathrm{I}}}{\partial x}\frac{\partial\psi_{\mathrm{J}}}{\partial x}d\Gamma-\frac{iM^2}{\zeta k_0}\int_{\mathrm{S_C}}\psi_{\mathrm{I}}\frac{\partial\psi_{\mathrm{J}}}{\partial x}d\mathrm{S}, \tag{7.35}$$

where $\mathrm{S_C}$ is the pair of circuits which mark the ends of the boundary Γ_{C}, see Figure 7.1.

A similar process of implementing the boundary conditions at the perforate into the governing equation for region 2 can now be used. Therefore the momentum equation in region 2 (see equation (6.17)) gives

$$-\nabla p_2'=\Gamma z_a\mathbf{u}_2', \tag{7.36}$$

where z_a is the characteristic impedance of the porous material (see Chapter 2). The substitution of equation (7.36) into equation (7.27) allows the continuity of pressure boundary condition (equation (7.7)), valid normal to the common boundary only, to be introduced and, following the method used for region 1, this gives

$$\mathbf{f}_{\mathrm{C}}^{2}=-\left\{\frac{\Gamma z_a}{\zeta\rho_0 c_0}\int_{\Gamma_{\mathrm{C}}}\psi_{\mathrm{I}}\psi_{\mathrm{J}}d\Gamma\right\}\left[\{\mathbf{p}_{\mathrm{C}_2}'\}-\{\mathbf{p}_{\mathrm{C}_1}'\}\right], \tag{7.37}$$

Writing equation (7.37) in matrix form gives

$$\{\mathbf{f}_C^2\} = \begin{bmatrix} \tilde{\mathbf{F}}_{C_1}^2 & \tilde{\mathbf{F}}_{C_2}^2 \end{bmatrix} \begin{Bmatrix} \mathbf{p}_{C_1} \\ \mathbf{p}_{C_2} \end{Bmatrix}, \tag{7.38}$$

where

$$\tilde{\mathbf{F}}_C^2 = -\frac{\Gamma z_a}{\zeta \rho_0 c_0} \int_{\Gamma_C} \psi_I \psi_J d\Gamma. \tag{7.39}$$

As before, $\left[\tilde{\mathbf{F}}_{C_1}^2\right]$ and $\left[\tilde{\mathbf{F}}_{C_2}^2\right]$ are matrices of order $(N_C \times N_C)$.

The governing equations (7.24) and (7.25) can now be combined into a final global matrix with the use of equations (7.33) and (7.38) to give

$$\begin{bmatrix} \mathbf{K}_{11} & \mathbf{K}_{1C} & 0 & 0 \\ \mathbf{K}_{C1} & \mathbf{K}_{CC}^1 + \tilde{\mathbf{F}}_C^1 & -\tilde{\mathbf{F}}_C^1 & 0 \\ 0 & \tilde{\mathbf{F}}_C^2 & \mathbf{K}_{CC}^1 - \tilde{\mathbf{F}}_C^2 & \mathbf{K}_{C2} \\ 0 & 0 & \mathbf{K}_{2C} & \mathbf{K}_{22} \end{bmatrix} \begin{Bmatrix} \mathbf{p}_1 \\ \mathbf{p}_{C_1} \\ \mathbf{p}_{C_2} \\ \mathbf{p}_2 \end{Bmatrix} = \begin{Bmatrix} \mathbf{f}_1 \\ \mathbf{0} \\ \mathbf{0} \\ \mathbf{0} \end{Bmatrix}. \tag{7.40}$$

Equation (7.40) can now be solved for the unknown pressures $\mathbf{p}$ at each nodal point on the finite element mesh.

Section 7.4

Results

The problem has now been formulated into the conventional finite element form, $[\mathbf{K}]\{\mathbf{p}\} = \{\mathbf{f}\}$, where $[\mathbf{K}]$ is the square global stiffness matrix, $\{\mathbf{p}\}$ is the vector of (unknown) nodal pressures and $\{\mathbf{f}\}$ is the vector of applied nodal forces. In the finite element method the stiffness matrix always embodies the governing equations for each element, while the forcing vector applies the external boundary conditions. The standard method for finding the unknown pressures $\{\mathbf{p}\}$ in equation (7.40) proceeds by first subdividing the domain of the problem into individual elements which are joined together by common nodes, the subdivision of the domain into elements forming a mesh which completely covers the domain.

The generation of a mesh for each of the dissipative silencers measured in Chapter 5 can be considerably simplified by examining lines of symmetry on the silencers, and this also has the advantage of substantially reducing the number of elements and hence the problem size. Obviously the axisymmetric silencers (silencers 1, 2 and 3) contain an axial line of symmetry and therefore only a two dimensional (2D) mesh is necessary. The elliptical silencers exhibit planar symmetry and therefore only one quarter of the cross section of the silencer needs to be modelled, although a full three dimensional (3D) mesh is still necessary. Once the domain of the problem has been specified it is necessary to choose which individual elements will make up the mesh. The choice of element type and size has a large influence on both the accuracy of the final solution and the size of the problem. Fortunately, the silencers studied here do not involve complex geometries and the generation of a simple regular mesh is straightforward, especially for the axisymmetric silencers. The choice of individual elements used for meshing a domain has been widely covered (see Zienkiewicz [122]) and commercial packages are now available which will, once the type and size of element has been decided upon, automatically mesh the entire domain (a software package called FEMGEN was used for this purpose in the present analysis). The user must choose elements which reflect the anticipated variation of the pressure across the silencer, and in addition, each element must adequately represent any curvature in the geometry of the domain; this will apply particularly to the elliptical silencers. The implementation of problems such as the one studied here can be greatly simplified by choosing elements that approximate the geometry of the domain to the same order as that used for the trial solution, and such elements are called isoparametric. In general, experience has shown that using quadratic elements provides the best balance between accuracy of solution and computational effort. This is because quadratic elements allow curved boundaries to be modelled but are simple enough to prevent an excessive increase in the problem size. Therefore, for the axisymmetric silencers, eight noded quadrilateral isoparametric elements were used. An example of a typical mesh (without a perforate present) generated automatically using FEMGEN is shown in Figure 7.2 for silencer 2. The lengths of the inlet and outlet pipes are three times the radius of the central channel, and this ensures that plane waves are present on the boundaries Γ_I and Γ_O. For the elliptical silencers, fifteen noded wedge elements were used to mesh the central channel and twenty noded brick elements to mesh the absorbent region. The mesh generated by FEMGEN for silencer 5 is shown in Figure 7.3. In order to decide upon the optimum number of elements to be used to mesh each silencer, preliminary transmission loss solutions were found for each axisymmetric silencer using different mesh densities. All the preliminary results were obtained without the presence of a perforate in the model, and this was because of problems encountered in including the perforate in the mesh; these problems will be discussed later in this section. The method of Peat and Rathi [26] was used to establish convergence of the 2D model and also to find preliminary results for the 3D model. Therefore it is necessary to re-formulate the governing equations because of the alteration of the continuity of pressure boundary condition on Γ_C, and hence equations (7.35) and (7.39) are now given by

$$\tilde{\mathbf{F}}_C^1 = \frac{ik_0\rho_0 c_0}{\Gamma z_a}\left(\int_{\Gamma_C}\left[\psi_I\frac{\partial\psi_J}{\partial\mathbf{n}} + \frac{2iM}{k_0}\frac{\partial\psi_I}{\partial x}\frac{\partial\psi_J}{\partial\mathbf{n}} + \frac{M^2}{k_0^2}\frac{\partial\psi_I}{\partial x}\frac{\partial^2\psi_J}{\partial x\partial\mathbf{n}}\right]d\Gamma - \int_{S_C}\left[\frac{2iM}{k_0}\psi_I\frac{\partial\psi_J}{\partial\mathbf{n}} - \frac{M^2}{k_0^2}\frac{\partial\psi_I}{\partial x}\frac{\partial\psi_J}{\partial\mathbf{n}}\right]dS\right) \tag{7.41}$$

and

$$\tilde{\mathbf{F}}_C^2 = -\frac{k_0^2}{\Gamma^2}\int_{\Gamma_C}\psi_I\frac{\partial\psi_J}{\partial\mathbf{n}}d\Gamma. \tag{7.42}$$

The final global matrix must also be re-written to give

$$\begin{bmatrix} \mathbf{K}_{11} & \mathbf{K}_{1C} & 0 \\ \mathbf{K}_{C1} & \left(\mathbf{K}_{CC}^1 - \tilde{\mathbf{F}}_{1C} + \mathbf{K}_{CC}^2 - \tilde{\mathbf{F}}_{2C}\right) & \left(\mathbf{K}_{C2} - \tilde{\mathbf{F}}_{12} - \tilde{\mathbf{F}}_{22}\right) \\ 0 & \mathbf{K}_{2C} & \mathbf{K}_{22} \end{bmatrix}\begin{Bmatrix} \mathbf{p}_1 \\ \mathbf{p}_C \\ \mathbf{p}_2 \end{Bmatrix} = \begin{Bmatrix} \mathbf{f}_1 \\ \mathbf{0} \\ \mathbf{0} \end{Bmatrix}. \tag{7.43}$$

Each node on the boundary Γ_C now shares a common sound pressure $\mathbf{p}_C$, and this allows a simple mesh to be generated in the standard way. The method of Peat and Rathi was used to establish convergence of the solution for 2D silencers and from here the number of elements which gave the best balance between accuracy and computational demands was found. Once the optimum number of elements was established, the size of each element was dictated by the geometry of each silencer. The establishment of convergence for the elliptical silencers proved to be a greater problem than for the axisymmetric silencers because of the considerable effort, both manual and computational, required to provide a 3D solution. When the code for the 3D model was first executed, a 3D mesh for a circular silencer was generated which employed the same mesh density as for the equivalent 2D model, and the results found were then compared with the 2D predictions. The use of a 3D model for the axisymmetric silencers allowed the accuracy of the 3D model to be examined and also established that the code was functioning correctly. The 3D model was found to give results comparable in accuracy to the 2D model and hence the mesh density used to model the ellipses was based upon that used for the circular 3D model. The advantage of this method was that it avoided the generation of numerous 3D meshes. The optimum number of elements and nodes for meshing silencers 1 to 5, without a perforate, is given in Table 7.1 below:

Table 7.1. Dimensions of finite element mesh.

Silencer	Number of elements	Number of nodes
1	92	343
2	114	413
3	120	441
4	352	1497
5	416	1757

Once the type, size and number of elements has been decided, the elements and nodes must be numbered. The numbering of the nodes in each element is very important since this fixes the manner in which the global stiffness matrix is assembled. Generally, in the use of the finite element method, the assembly of the element equations into the global stiffness matrix produces a banded matrix, and this ensures that the computational speed of solution is optimised. The bandwidth of the global stiffness matrix depends upon the way the nodes in each element are numbered. In general, to minimise the bandwidth, the nodes should be labelled across the shortest dimension, and hence the silencers examined here were numbered radially. This method of node numbering was performed automatically using the FEMGEN package and was found to work well for silencers which did not include a perforate in the model. An example of the way in which the mesh for a 2D silencer is numbered by the mesh generator in order to minimise the bandwidth of the stiffness matrix is given in Figure 7.4(a).

When the perforate is present in the model it is necessary to re-number the mesh since the sound pressures $\mathbf{p}_{C_1}$ and $\mathbf{p}_{C_2}$ (see equation (7.40)) on either side of the boundary Γ_C must be calculated. To do this the mesh must be re-numbered in the manner shown in Figure 7.4(b). This involves assigning two nodes to each co-ordinate on the boundary Γ_C, assuming that the perforate is infinitesimally thin. Unfortunately the automatic mesh generator was incapable of performing this, and so the boundary had to be numbered manually by adding extra nodes onto a mesh generated in the standard way. To maintain a banded matrix, the node numbers had to be rearranged and, for the 2D model, this was accomplished by writing a code which automatically realigned the numbering for a general silencer whose mesh was generated using FEMGEN. Unfortunately it proved impossible to write an additional section of code to re-configure the node numbering on the 3D silencers. Therefore the only way to insert the perforate into the 3D model was to number each node manually on Γ_C for each individual silencer, which - in addition to being extremely tedious - also results in an unbanded matrix. Clearly the number of nodes required to mesh a 3D silencer is substantially greater than that required for a 2D silencer and therefore the anticipated solution time for an unbanded 3D matrix was expected to be prohibitive. Consequently the finite element solutions presented here which include a perforate are limited to the 2D models used for the axisymmetric silencers.

One notable consequence of adding the perforate to the model is the modification of the surface integrals in the governing equations. The derivation of the global stiffness matrix both with and without a perforate was performed using the gradient evaluation approach of Peat and Rathi [26] since this provided the most computationally efficient method. However, when no perforate is present it is noticeable that a second order derivative is present in the formulation of Peat and Rathi [26] (equation (7.41)) which implies that C^1 continuous elements must be used to ensure inter-element compatibility. Peat and Rathi pointed out that so long as the element boundaries were aligned to both the axial and radial directions, it was possible to use elements with C^0 continuity. However no such restriction occurs when the gradient evaluation approach is applied to the model with a perforate, since every term in equation (7.35) is of first order. This is perhaps not too important in the present analysis although it could be of consequence in the examination of silencers with non-uniform central channels.

The final assembly of the global stiffness matrix was performed by using the Finite Element NAG Library [123]. The simultaneous linear equations found in equations (7.40) and (7.43) were then solved using standard NAG routines. It should be mentioned here that in all the predictions presented in Figures 7.5 to 7.8 the line integral around the circuits S_C, appearing in equations (7.35) and (7.41), has been ignored; this integral was also omitted by Peat and Rathi [26]. The line integral was omitted because instability problems occurred in the transmission loss predictions when the integral was included; the reasons for this are not clear but it is possible that the problems occurred because the perforate boundary condition is being implemented at nodes on S_C which are also situated on the hard-walled boundary.

The external boundary conditions necessary for calculating the four-pole parameters require two complete solutions of the entire problem, one implementing equations (7.11) and (7.12) and the other equations (7.13) and (7.14). The four pole parameters A, B, C and D are then given (see Peat [117]) by

$$\mathrm{A}=\left(\frac{p'_{\mathrm{in}}}{p'_{\mathrm{out}}}\right)_{u'_{\mathrm{out}}=0}, \quad \mathrm{C}=\left(\frac{u'_{\mathrm{in}}}{p'_{\mathrm{out}}}\right)_{u'_{\mathrm{out}}=0}, \tag{7.44), (7.45}$$

$$\mathrm{B}=\left(\frac{p'_{\mathrm{in}}}{u'_{\mathrm{out}}}\right)_{p'_{\mathrm{out}}=0}, \quad \mathrm{D}=\left(\frac{u'_{\mathrm{in}}}{u'_{\mathrm{out}}}\right)_{p'_{\mathrm{out}}=0}. \tag{7.46), (7.47}$$

The transmission loss (TL) of the silencer is given by

$$\mathrm{TL}=10\log_{10}\left|\mathrm{A}+\mathrm{B}+\mathrm{C}+\mathrm{D}\right|. \tag{7.48}$$

As a partial check on the formulation for a silencer with a perforate, transmission loss predictions made by solving equation (7.40) - with $\zeta=10^{-5}$ - were compared to predictions for a silencer with no perforate. The two sets of data were within 1% of each other indicating that the two dimensional model including the perforate had been implemented correctly.

The results from the 2D model of the axisymmetric silencers are compared to experiment in Figure 7.5 to 7.7 respectively. The results are shown for M=0 and M=0.15, both with and without a perforate. The predictions for the 3D model without a perforate are compared to experiment in Figure 7.8 for silencers 4 and 5. A discussion of the accuracy of the predictions made by using the finite element method is given in the next section and a comparison with other models will be given in Chapter 10.

Section 7.5

Discussion

The finite element theoretical predictions shown in Figures 7.5 to 7.8 were obtained by solving either equation (7.43) for the case of no perforate, or equation (7.40) when a perforate was present, by the use of NAG routines that were run on a mainframe computer system. A comparison between the number of nodes used to mesh the axisymmetric silencers and the number required to mesh the elliptical silencers (see Table 7.1) indicates that there is a large difference in the problem size between the 2D and 3D models. This difference affects the size of the final global stiffness matrix and hence the computational time required to solve the problem. If the size of the global stiffness matrix is $N \times N$, then the computational execution time required in order to find a solution to the set of equations using NAG routines is proportional to N^3. Consequently it can take considerably longer to solve the 3D problem than it does to solve the 2D problem. Obviously, when using a mainframe computer system, the overall time required to find a solution is dependent upon the number of other users on the system, but in general the 2D model took several hours to solve for the required number of frequency intervals, whereas the 3D model took several days. The relatively large amount of computational time required to solve the 3D model influenced the way in which the mesh density was chosen (this was discussed in the previous section). When the perforate was added to the 2D model it was found that the addition of the nodes along the boundary Γ_C had little effect upon the overall time required to solve the problem.

The finite element predictions made without a perforate in the model will be discussed first and these are compared with experiment on the left hand sides of Figures 7.5 to 7.7 for the axisymmetric silencers and Figure 7.8 for the elliptical silencers. Without the presence of a perforate, the model used is identical to that formulated by Peat and Rathi [26], except that mean flow in the absorbent has been ignored here. Therefore, to establish that the code was working correctly, transmission loss predictions were originally obtained for the test silencer studied by Cummings and Chang [16] since this was the silencer for which Peat and Rathi originally published results. Once the code produced results identical to those found by Peat and Rathi with no flow in the absorbent, predictions for silencers 1 to 3 were generated. Peat and Rathi compared their results to the mode matching predictions of Cummings and Chang [23] and they found significant discrepancies between the two models at low frequencies; this problem will be examined further in Chapter 9. In this chapter the finite element predictions are compared to the experimental data of Chapter 5 since this will allow further insight into the accuracy of the finite element method. It is evident that, on the left hand side of Figures 7.5 to 7.7, the predictions shown for the axisymmetric silencers with no perforate are very close to the measured data across a frequency range of 50Hz to 1kHz, both with and without flow. It appears that, within this frequency range, the accuracy of the predictions remain unaffected by the dimensions of the silencer, whereas this was not the case for the fundamental mode solution. Problems are apparent in predicting the transmission loss above 1kHz, especially for silencers 1 and 2 where discrepancies between theory and experiment become larger as the frequency is increased. It is possible that such discrepancies are a result of experimental error since the measured data are only reliable up to 1kHz, although if a comparison is made between experiment and theory for the expansion chamber (see Figure 5.3) it indicates that it should be possible to achieve closer agreement, at least up to 1.6kHz. One possible explanation for the discrepancies at higher frequencies is the omission of the perforate from the model.

The finite element predictions for the elliptical silencers (silencers 4 and 5) are shown in Figure 7.8, both with and without flow. As previously mentioned, predicted data are unavailable for the 3D silencers with a perforate included. A comparison between prediction and experiment in Figure 7.8 indicates very good agreement between the two. For both silencers, the agreement across the frequency range is of similar quality to that found for the 2D model. However one problem apparent with the 3D model which did not occur in the 2D formulation is the prediction of a negative transmission loss at low frequencies (approximately 50Hz). The problem seems to be exacerbated by the introduction of mean flow, for example see silencer 5 with M=0.15 (bottom right hand corner of Figure 7.8). Obviously the prediction of a negative transmission loss does not make physical sense. It is possible that these problems have occurred because of the omission of the line integral around S_C, but it is more likely that numerical problems occurring in the solution of equation (7.43) are responsible. Numerical errors might result from the size of the matrix necessary to solve the 3D problems, and this could result in errors being magnified at low frequencies. The problem of negative transmission loss at low frequencies needs further investigation but, since the finite element model reported in this chapter is to be used only to provide "benchmark" predictions, it was decided that no further investigation was warranted at present.

The finite element predictions obtained with the perforate included in the model are shown, for axisymmetric silencers only, on the right hand side of Figures 7.5 to 7.7. The behaviour of the predicted transmission loss, after the introduction of the perforate, is similar to that noted in the fundamental mode solution. For example, silencers 1 and 2 exhibit a transmission loss that is increased in the lower frequency range but reduced at higher frequencies. The similarity of this behaviour to that of the fundamental mode solution appears to indicate that the perforate has been introduced correctly into the finite element model. The inclusion of the perforate evidently has a significant effect upon the transmission loss predictions, especially for silencers 1 and 2. The reason why the effect of the perforate is large for silencers 1 and 2 is that they contain E glass, whereas silencer 3 contains A glass (see also Chapter 6). The effect of the perforate on the predictions obtained by using the finite element model is greater than the corresponding effect upon the fundamental mode model and this is probably because of the additional effect upon the higher order modes that are implicitly included here. If the predicted and measured data for silencers with and without perforates are compared, it is apparent that including the perforate in the model does not necessarily enhance agreement between prediction and measurement. In particular, at frequencies above 1kHz, over-prediction in the absence of perforates becomes under-prediction with perforates in the cases of silencers 1 and 2, and *vice versa* in the case of silencer 3. This points strongly to the use of incorrect values for the perforate impedance, since errors in the theoretical assumptions have now been minimised by the inclusion of higher order modes. Consequently it is concluded here that the perforate impedance has been over-predicted and that a more accurate value must be found, applicable to randomly packed silencers. This is not surprising given that the random packing of the absorbing material around the perforate can have a large effect upon the impedance of the perforates, for reasons that were discussed in Chapter 4. In Chapter 10, new values will be assigned to the acoustic impedance of the perforates, designed to account for the random nature of the packing in an attempt to obtain better agreement between the predictions presented here and experimental data.

Taking into account the problems found in introducing representative values for the perforate impedance into the model, the agreement between prediction and experiment for both the 2D and 3D finite element models is considered to be good. The predictions presented in this chapter do indicate that, when a perforate is present in the test silencer, it is unnecessary to include mean flow in the absorbent. This appears to validate the simplifications made to Peat and Rathi's model [26] in Section 7.3. The analysis described in this chapter is a completely general approach to finding transmission loss predictions and the results are useful for providing "benchmark" predictions, to which the fundamental mode solution of the previous chapter and also solutions presented later in this thesis can be compared. This was the original purpose of implementing the full finite element method, the practical use of the technique for commercial design purposes being limited because of the large amount of computational effort required. In the following two chapters, attempts to reduce the computational effort and provide a model that is capable of achieving accuracy comparable to that achieved here will be described.

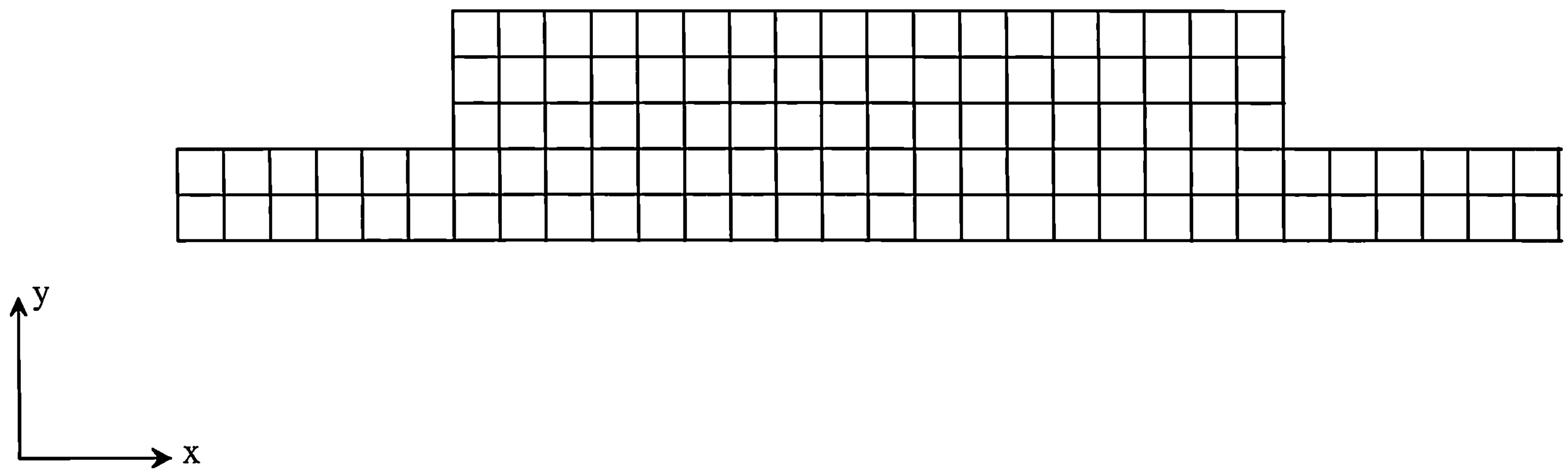

Figure 7.2. Two dimensional mesh for silencer 2.

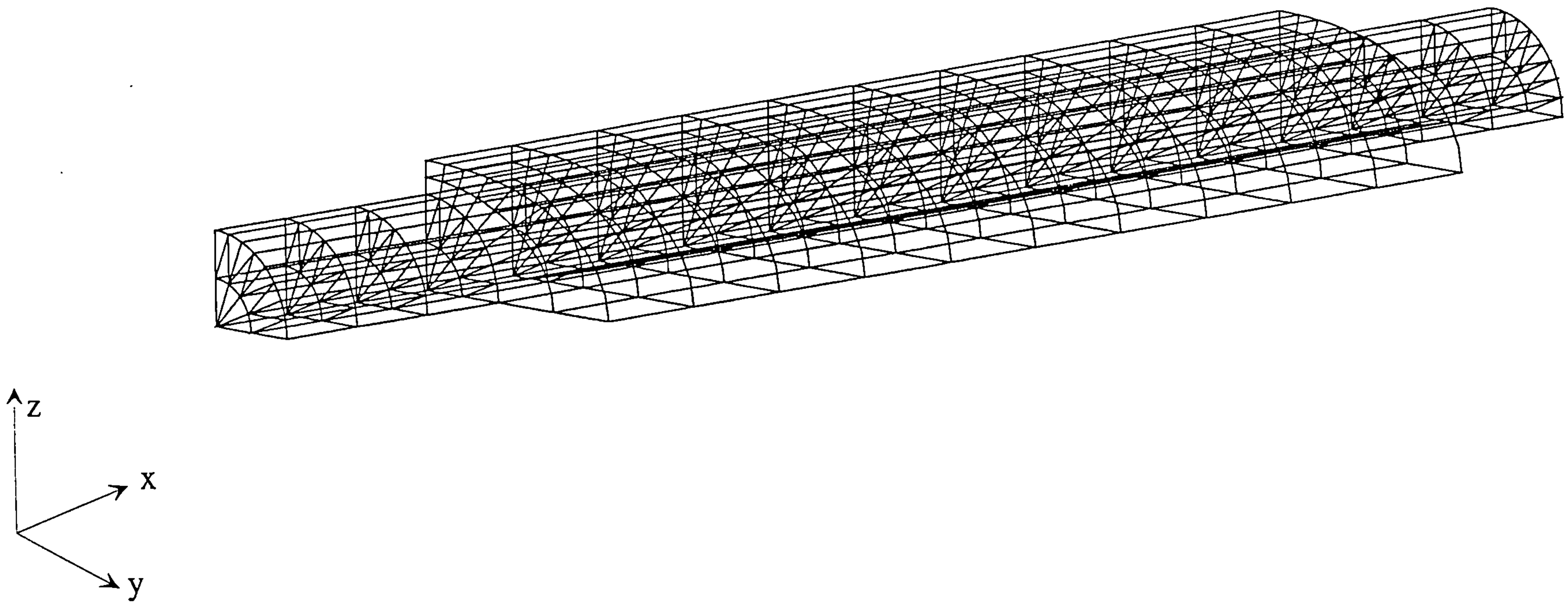

Figure 7.3. Three dimensional mesh for Silencer 5.

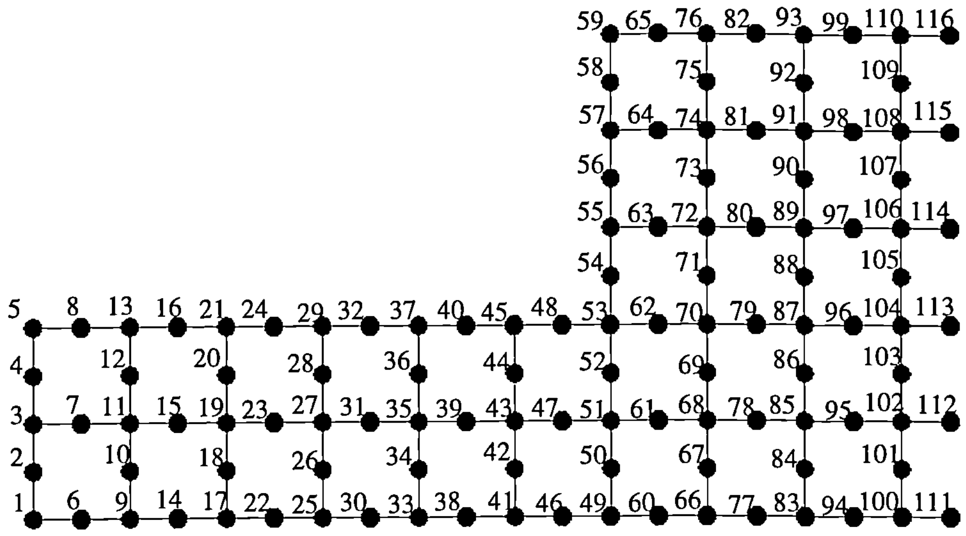

(a)

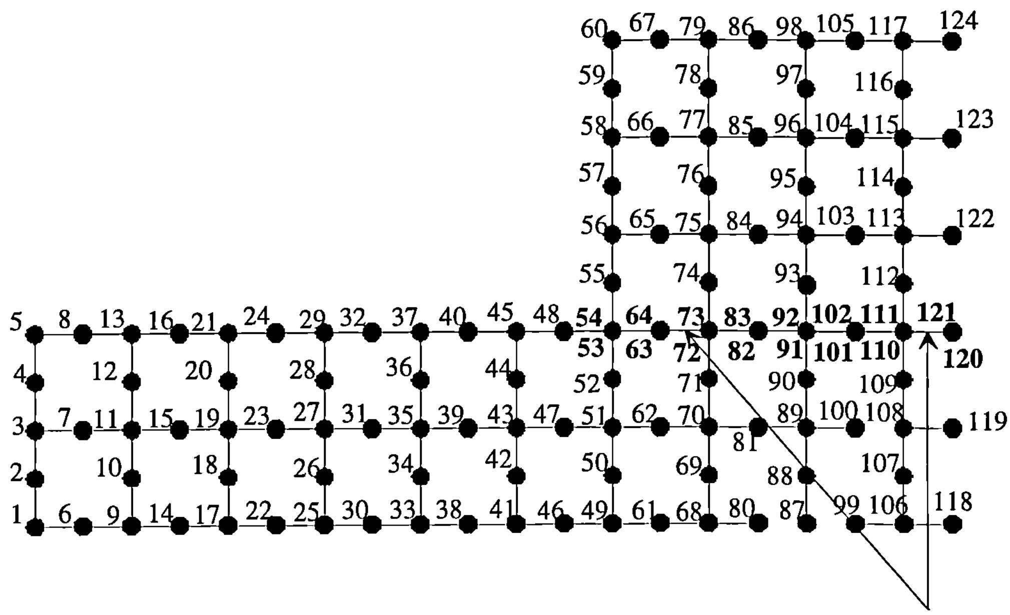

(b)

Figure 7.4. Typical node numbering of elements for 2D mesh. (a) No perforate, (b) Perforate present (bold nodes indicate two nodes with common co-ordinate on perforate boundary)

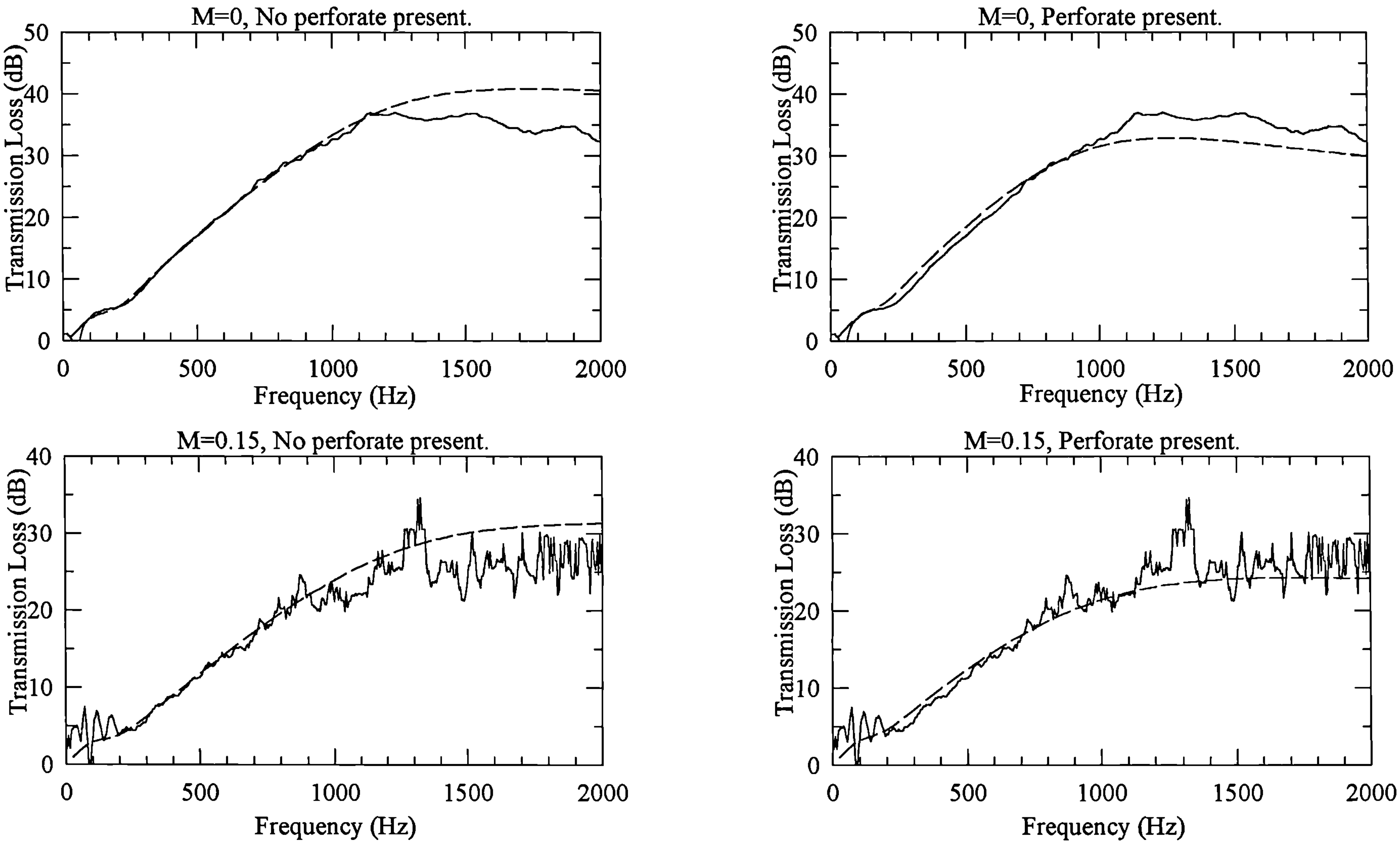

Figure 7.5. Finite element predictions for Silencer 1. ——— , Experiment; – – – , Finite element predictions.

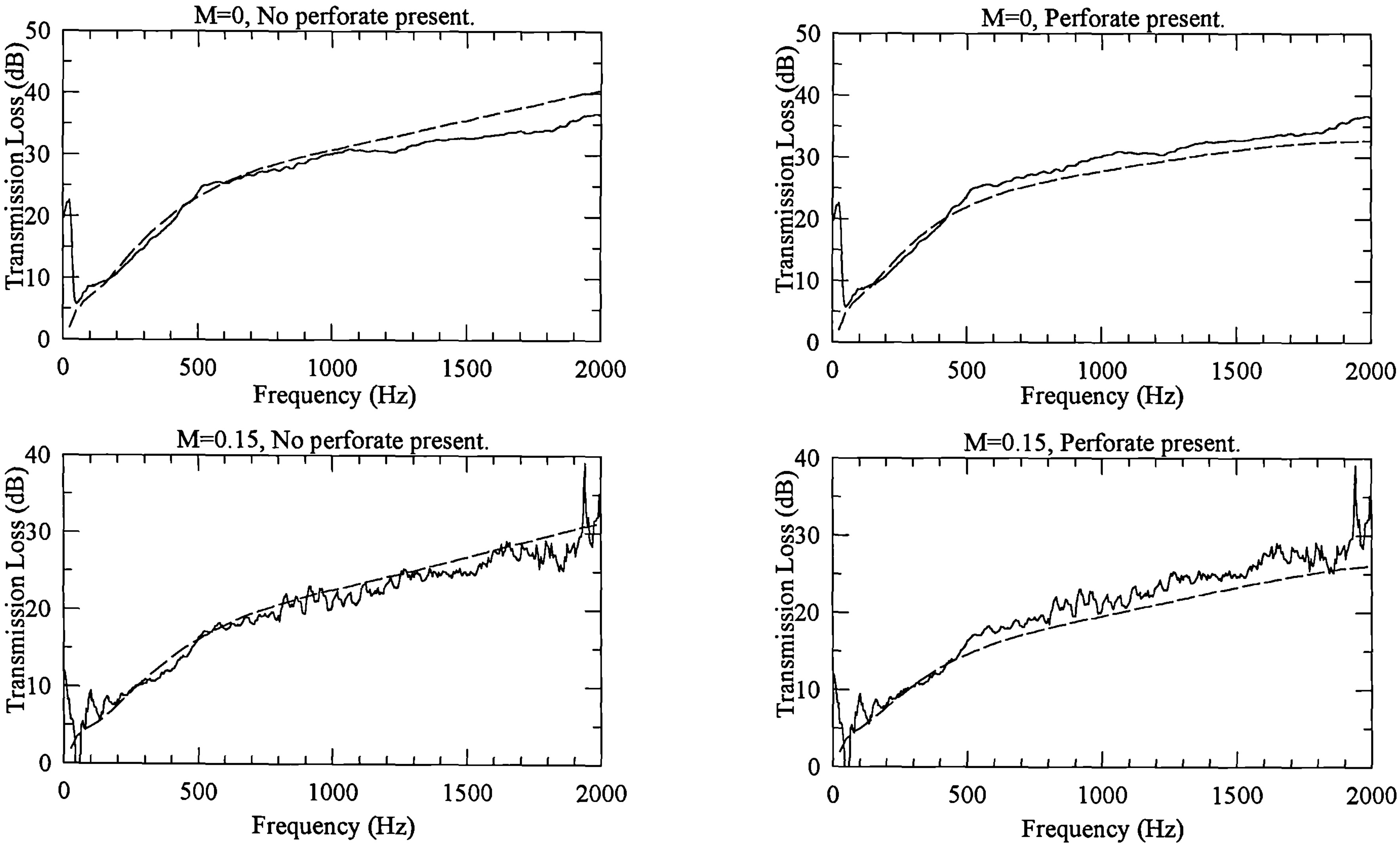

Figure 7.6. Finite element predictions for Silencer 2. —— , Experiment; – – – , Finite element predictions.

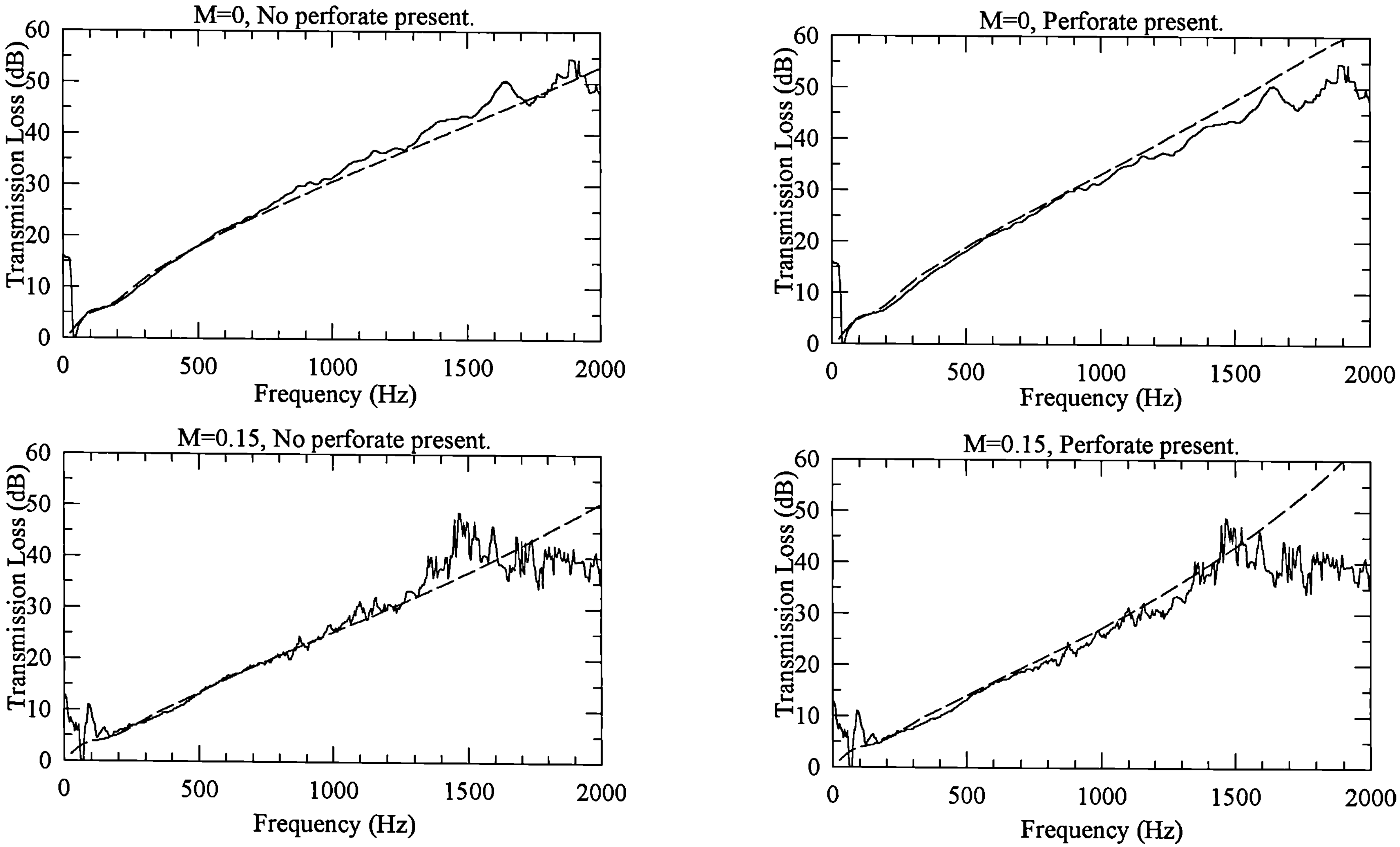

Figure 7.7. Finite element predictions for Silencer 3. —— , Experiment; – – – , Finite element predictions.

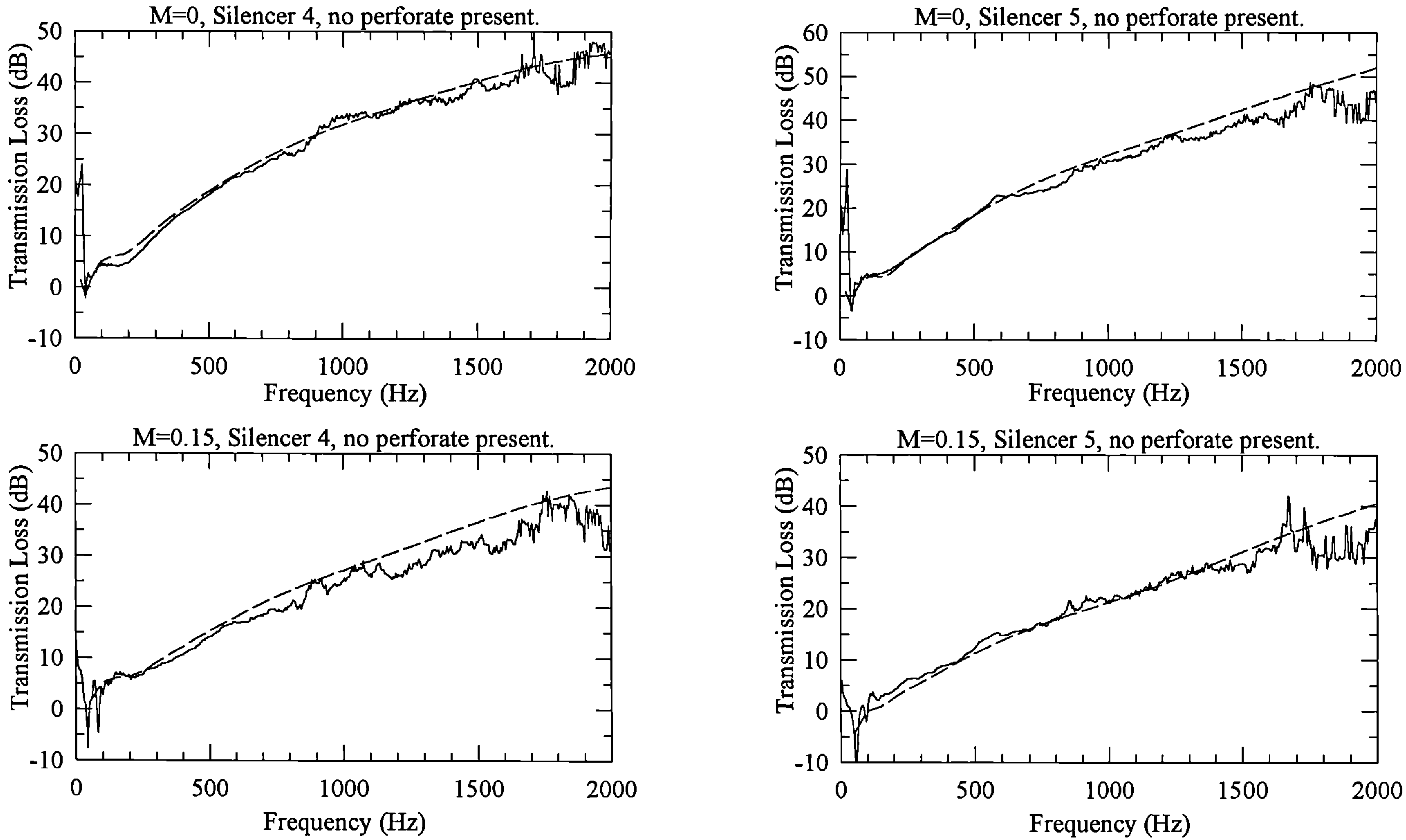

Figure 7.8. Finite element predictions for Silencers 4 and 5. ——— , Experiment; – – – , Finite element predictions.

CHAPTER 8

A FINITE ELEMENT EIGENVALUE SOLUTION FOR DISSIPATIVE SILENCERS WITH IRREGULAR CROSS-SECTIONS

Section 8.1

Introduction

In the previous chapter a full finite element solution for a silencer with arbitrary shape was described, and although good agreement between prediction and experiment was observed, the method proved to be computationally very expensive. Consequently, a method is required which, in addition to accommodating a silencer of arbitrary shape, is also capable of providing solutions in a computationally efficient way. A common method used to reduce the numerical size of a problem, and hence reduce computational expenditure, is to implement an eigenvalue analysis. When an eigenvalue analysis is applied to exhaust silencers the silencer is assumed to be infinite in length, and the equations governing the acoustic behaviour of the silencer are written in the form of an eigenequation by using separation of variables in a manner similar to the method employed in Chapter 6. Treating the silencer as infinite in length has the advantage of reducing the dimensions of the problem by one, and hence an axisymmetric silencer can be represented by a one dimensional model, whilst an elliptical silencer requires only a two dimensional formulation. This has the potential to reduce significantly the computational time required to find solutions compared to those obtained by using a full finite element solution in Chapter 7. This is, however, at the expense of requiring the silencer to be uniform along its length. This is not unduly restrictive since most commercial silencers are uniform in their design, and in any case one cannot expect to model a completely general non-uniform silencer by using a simplified finite element formulation. The eigenvalue formulation presented here is similar in essence to the fundamental mode solution derived in Chapter 6 since separation of variables is again used here in order to find coupled modes for the governing wave equations in the central channel and the absorbent. However a full eigenvalue analysis automatically involves finding some of the higher order modes present in the silencer in addition to the fundamental mode. This has the potential to eliminate some of the problems encountered in the predictions for large silencers using the fundamental mode approach in Chapter 6. The computation of higher order modes does, however, complicate the prediction of the transmission loss for finite length silencers, since mode matching must be performed at the inlet and outlet of the lined section in order to utilise the eigenvalue solutions. Mode matching, employing the eigenvalues and eigenvectors described in this chapter, is covered in detail in Chapter 9. In this chapter a general method is given for finding and ordering modes in an infinite dissipative silencer which includes mean flow in the central channel and also a perforate which separates the central channel from a bulk reacting absorbent.

Because of its apparent simplicity as compared to the modelling of finite length silencers, eigenvalue analysis is a popular method for examining dissipative silencers. The attenuation of modes propagating in circular ducts lined with porous material was examined by Morse [3], who neglected mean flow in his model and also used a locally reacting lining. The simplicity of the model allowed Morse to produce a number of design charts for the ducts studied. Scott [4] extended the model of Morse to include bulk reacting porous media and showed that large errors in Morse's theory can occur if a bulk material is approximated as locally reacting. Unfortunately the inclusion of a bulk reacting absorbent complicated the final eigenequation and the absence of computers meant that is was a laborious task to solve Scott's equation. It was not until the 1960's, with the advent of computers, that these problems were overcome. Bokor [5] was able to solve Scott's equation and find predictions for the fundamental mode of a rectangular duct lined on opposite walls. Kurze and Vér [7], who also studied rectangular ducts lined on opposite walls, derived a more general form of Scott's equation by including a non-isotropic bulk reacting material, and found the attenuation of the fundamental mode by solving the eigenequation with the Newton-Raphson method. The validity of the solutions found by Kurze and Vér was later examined by Wassilieff [8], who found their formulation to contain an error. Wassilieff corrected Kurze and Vér's theory and, in solving the revised equation by using the Newton-Raphson method, found much closer agreement between prediction and experiment. Wassilieff also showed that the corrected expression of Kurze and Vér now reduced to that found by Scott for isotropic linings.

The effect of uniform mean flow in the central channel of a lined duct was first examined by Ingård [10] and later by Cummings [14], who introduced a perforate between the central channel and the bulk reacting liner of a rectangular duct lined on opposite walls. For circular ducts, mean flow in the central channel was included by Nilsson and Brander [15] who also included a perforate and a bulk reacting lining in their model. Nilsson and Brander used both numerical and analytical techniques to solve the governing equations and, in a subsequent set of papers [20,21,22], studied duct discontinuities and their application to finite length silencers. Analytical formulations of the eigenequation were also found by Cummings and Chang [16] for the case of an axisymmetric silencer with mean flow in both the central channel and the absorbent (a perforate was not included) and by Sormaz [124] for splitter silencers with mean flow and a bulk reacting absorbent. The formulation of Cummings and Chang was described in Chapter 6 where modifications to it were described, allowing a perforate to be included, the eigenequation being solved for all but the very lowest frequencies by the use of the Newton-Raphson method. Cummings and Chang found solutions for a number of different modes and later used these to implement a mode matching solution for a finite length silencer [23]. The method used by Cummings and Chang is, however, only of use for modelling axisymmetric silencers, and it is also possible that employing the Newton-Raphson method to find individual modes could result in some modes being missed. A comprehensive range of predictions for the attenuation of both circular ducts and rectangular ducts lined on opposite walls is given by Bies et al. [125]. Although Bies et al. did derive a general theory for ducts with arbitrary cross sections, their design curves were limited to circular and rectangular ducts.

The solution of a general eigenequation for ducts with arbitrary cross sections has, inevitably, been carried out by using numerical techniques. For a locally reacting liner, Astley and Eversman [119] used a Galerkin formulation of the finite element method to solve the governing equations for ducts with mean flow. Astley and Cummings [17], in a general formulation, later introduced a bulk reacting liner and employed a weak Galerkin formulation; a solution was found for a rectangular duct lined on all four walls. Rathi [18] later used this method to investigate silencers with both circular and elliptical cross sections and he also included mean flow in the absorbent though; as in the model of Astley and Cummings, a perforate was neglected. Whilst a full finite element scheme has been shown here to provide accurate predictions for silencers with arbitrary cross sections, simpler approaches have also been tried in an attempt to reduce computational effort. Some of these simplified numerical solutions attempted have themselves been variants of the finite element method. This is because other numerical methods, such as finite difference and the boundary element method, cannot readily be successfully applied to dissipative silencers with arbitrary cross sections (the reasons which lie behind this having been outlined in Chapter 7). A common method used to reduce the computational effort involved in finite element schemes is to re-formulate the governing equations by using a variational formulation. Although this approach is related to the finite element method, it does allow the problem to be simplified and this has the potential to reduce computational demands. A variational approach was developed by Cummings [126] who used a segmented Rayleigh-Ritz formulation to study silencers with oval cross sections. In a later paper, Cummings introduced mean flow into the absorbent [127], but neither models included a perforate. The Rayleigh-Ritz solution used by Cummings was however limited to the fundamental mode. Two different numerical eigenvalue solutions were found for a dissipative silencer of arbitrary cross-sectional shape by Glav, who introduced a null-field approach [128] and a point matching approach [129]. The null-field approach is essentially a semi-analytical method, whilst the point matching (or collocation) is related to the weighted residual finite element approach. Both solutions neglected mean flow, and it appears also that the null field method is unsuitable for the introduction of mean flow and the study of complex shapes. The collocation method was shown to work well with no mean flow but convergence of the solution is very sensitive to the correct selection of points.

The principal requirement of the model described in this chapter is that it should be capable of finding the higher order modes existing in lined ducts and also be valid for silencers with arbitrary cross sections. Consequently the use of numerical methods in the present study is inevitable. Obviously, the computational effort required to arrive at the solution is also an important consideration, although the method must be completely general and provide a "robust" way of finding the eigenvalues. Of the numerical schemes described previously, the largest reduction in computational effort appears to be offered by either the Rayleigh-Ritz formulation of Cummings [127] or the point matching method used by Glav [129]. However, the solution supplied by Cummings is applicable to the fundamental mode only, solutions for higher order modes being dependent upon assigning different trial functions which must resemble the actual mode shapes. Whilst it is possible that trial functions could be found for higher order modes, it does not appear to provide a robust method for tackling silencers of arbitrary shape, especially since the possibility of missing modes also appears likely. The collocation method implemented by Glav [129] was derived for a silencer without mean flow in the central channel and hence it was possible to use continuity of normal acoustic particle velocity as one of the two boundary conditions between the central channel and the absorbent. The introduction of mean flow would require the re-formulation of this boundary condition giving continuity of normal particle displacement on the boundary. Whilst this should not prove to be too difficult, it is anticipated that problems might arise in achieving convergence of the solution, especially given the sensitivity of the collocation method to the selection of points. Therefore the method of collocation does not appear to provide a robust approach to modelling the silencers being studied here. This narrows down the choice of a numerical method to the solution of a finite element eigenvalue problem. Whilst a finite element scheme is the most computationally expensive approach of the eigenvalue formulations discussed here, it does appear to present the only viable method for meeting the criteria demanded in this chapter. However, the finite element method implemented here should still be computationally faster than the approach used in Chapter 7 since the order of the problem has been reduced by one. The appropriate finite element scheme for finding eigenvalues in general dissipative silencers was first implemented by Astley and Cummings [17] and later by Rathi [18]. Therefore the eigenvalue solution derived in this chapter will follow this method, although modifications are introduced here via the introduction of a perforate.

The solution presented in this chapter is concerned solely with the identification of the modes which constitute the sound field in a silencer. A number of modes with attenuations low enough to affect the acoustic performance of a silencer will be identified here and the practical use of these eigenvalues in the design of finite length silencers will be examined in Chapter 9.

In common with Chapter 7, the finite element computer code employed when finding predictions in this chapter was modified from a program originally written by Rathi [121]. The author was again responsible for re-formulating the program to run for any configuration of silencer, employing either a one dimensional or two dimensional mesh in the present analysis. In addition, new code was introduced to allow for the inclusion both of a perforate and the semi-empirical model for a porous material described in Chapter 3.

Section 8.2

Governing Equations

The finite element eigenvalue solution derived in this section proceeds along the same lines as that presented by Astley and Cummings [17] and later, in a slightly modified form, by Rathi [18]. In accordance with the models presented in the two previous chapters, mean flow in the absorbent is ignored, a perforate is included separating the central channel from the surrounding absorbent and the absorbing material is assumed to be isotropic. The formulation of the general eigenvalue problem is based upon principles similar to those associated with the fundamental mode solution presented in Chapter 6, and coupled modes are assumed to exist for the sound fields in both the airway and the absorbent, sharing a common axial wavenumber. Whereas in Chapter 6 the governing wave equations were solved analytically for silencers of circular cross section, the use of numerical techniques in this chapter will allow this restriction to be lifted. The finite element method is used to provide an approximate numerical solution to the governing wave equations and from here a general eigenequation is formulated, valid for silencers of arbitrary cross section. The finite element method also provides a more reliable means of finding the higher order modes in a silencer as compared to analytical solutions, which often rely upon using initial guesses for axial wavenumbers.

The geometry of the dissipative silencer studied in this chapter is given in Figure 8.1 below; note that the silencer is assumed to be of infinite length in the x direction.

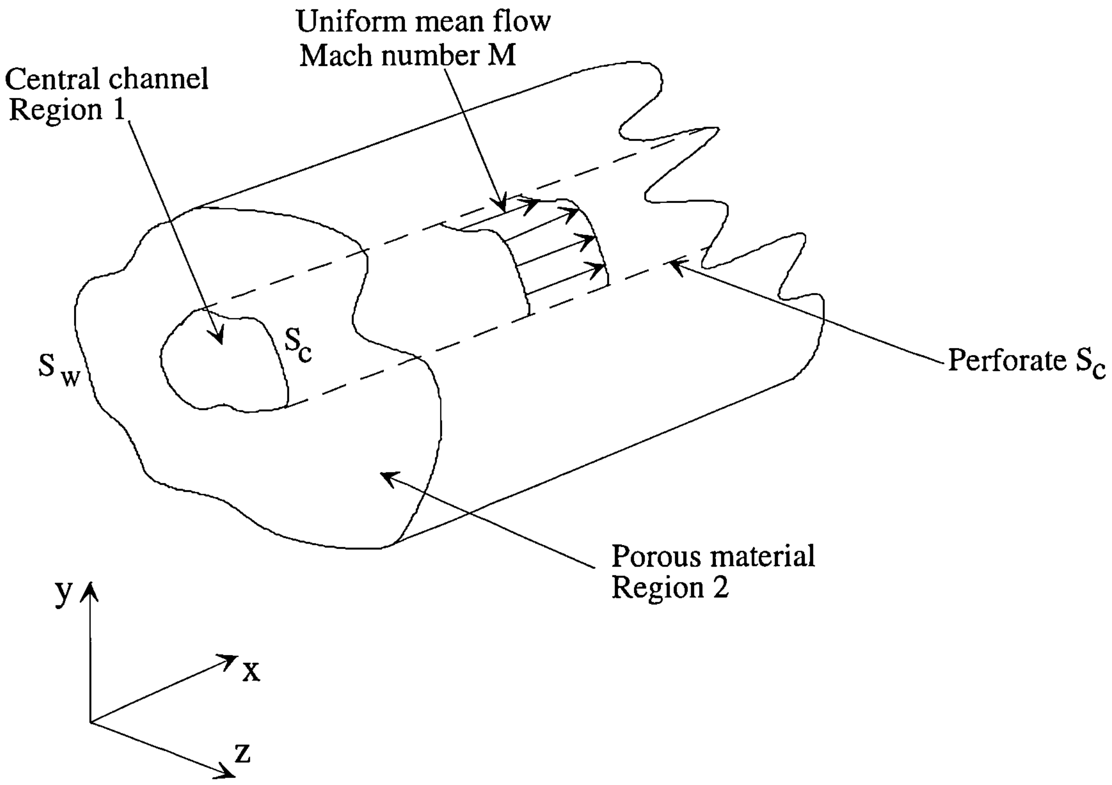

Figure 8.1. Geometry of silencer.

The dissipative silencer in Figure 8.1 has an outer box of arbitrary cross section filled with isotropic porous material which surrounds a central channel, also of arbitrary cross section, that carries uniform mean flow of Mach number M. The central channel is separated from the porous material by a perforated tube. There is assumed to be no mean flow in the absorbent. The central channel is denoted region 1, the absorbent region 2, and the mean flow velocity is assumed to be in the x direction only. The outer wall of region 1 (the perforate) is denoted by S_C, the outer wall of region 2, assumed to be rigid and acoustically non-transmitting, is denoted by S_W, where the total surface of region 2 (S_2) is made up of from both S_C and S_W.

The acoustic wave equations for both region 1 and region 2 are now formulated and the finite element approximations to the governing equations are presented in the next section.

8.2.1 Acoustic Wave Equation in the Central Channel (Region 1)

The acoustic wave equation in region 1 was derived in Chapter 6 and is given by

$$\nabla^2 p_1' - \frac{1}{c_0^2}\frac{\partial^2 p_1'}{\partial t^2} - \frac{2M}{c_0}\frac{\partial^2 p_1'}{\partial x \partial t} - M^2\frac{\partial^2 p_1'}{\partial x^2} = 0, \tag{8.1}$$

where p_1' is the acoustic pressure in region 1, t is time, c_0 is the isentropic speed of sound and M is the mean flow Mach number. An eigenvalue formulation requires a separated solution to equation (8.1) to be found, and therefore the acoustic pressure in region 1 is assumed to have the form

$$p_1'(x,y,z,t) = p_1(y,z)e^{i\omega t - ik_0\lambda x}, \tag{8.2}$$

where ω is the radian frequency and $k_0\lambda$ ($k_0 = \omega/c_0$) is the common (complex) axial wavenumber which links region 1 to region 2. Substituting the assumed form for p_1' into the governing wave equation gives

$$\nabla_{yz}^2 p_1 + k_0^2(1-\lambda M)^2 p_1 - k_0^2\lambda^2 p_1 = 0, \tag{8.3}$$

where ∇_{yz} denotes a two dimensional form of the Laplacian operator (y,z plane).

8.2.2 Acoustic Wave Equation in the Absorbent (Region 2)

The acoustic wave equation in region 2, assuming that no mean flow is present in the absorbent, was given by equation (7.3) as

$$\nabla^2 p_2' - \Gamma^2 p_2' = 0, \tag{8.4}$$

where Γ is the propagation constant of the porous material. A separated solution to equation (8.4) is therefore sought for region 2,

$$p_2'(x,y,z,t) = p_2(y,z)e^{i\omega t - ik_0\lambda x}. \tag{8.5}$$

Substituting the assumed form for p_2' into equation (8.4) gives

$$\nabla_{yz}^2 p_2 - \left(\Gamma^2 + k_0^2\lambda^2\right)p_2 = 0, \tag{8.6}$$

8.2.3 Boundary Conditions

The appropriate boundary conditions are continuity of normal particle displacement and continuity of pressure on the common boundary S_C, and zero normal particle displacement on the boundary S_W. The general equation for continuity of normal particle displacement on S_C was derived in Chapter 7 (see equation (7.13)) and this gives

$$\mathbf{u}_1' \cdot \mathbf{n}_1 = -\left[1 - i\frac{M}{k_0}\frac{\partial}{\partial x}\right]\mathbf{u}_2' \cdot \mathbf{n}_2, \tag{8.7}$$

where $\mathbf{u}'$ is the acoustic velocity vector and $\mathbf{n}$ the outward unit normal vector in either region 1 or region 2 ($\mathbf{n}_1 = -\mathbf{n}_2$). The acoustic particle velocity can be expressed in the same form as the acoustic pressure in equation (8.5), and equation (8.7) may be written

$$\mathbf{u}_1' \cdot \mathbf{n}_1 = -[1 - \lambda M]\mathbf{u}_2' \cdot \mathbf{n}_2. \tag{8.8}$$

The introduction of the perforate modifies the continuity of pressure boundary condition on S_C from that used by Astley and Cummings [17], giving (see equation (7.7))

$$p_{C_2} - p_{C_1} = \rho_0 c_0 \zeta \mathbf{u}_2' \cdot \mathbf{n}_2, \tag{8.9}$$

where p_C is the sound pressure on boundary S_C in either region 1 or region 2 and ζ is the dimensionless acoustic impedance of the perforate (corresponding to $z_0/\rho_0 c_0$; see Chapter 4). Note that it is again assumed here that the perforate is infinitesimally thin. The final boundary condition is the hard-walled boundary condition which gives

$$\nabla p_2 \cdot \mathbf{n}_2 = 0 \quad \text{on} \quad S_W. \tag{8.10}$$

Section 8.3

Finite Element Discretization

A finite element approximation of the governing wave equations is now formulated in order to solve the problem numerically. To do this a weak Galerkin formulation, similar to that found in Chapter 7, is used here.

For the wave equation in region 1, we can approximate the acoustic pressure by a trial solution,

$$p_1 \approx \sum_{J=1}^{N_1} \psi_J p_{1_J}, \tag{8.11}$$

where $\psi_J(y,z)$ are the global basis functions, p_{1_J} is the value of p_1 at the J[th] node and N_1 is the number of nodes in region 1. Applying the Galerkin formulation to equation (8.3) gives

$$\int_{R_1} \psi_I\left(\nabla^2 p_1 + k_0^2[1-\lambda M]^2 p_1 - k_0^2\lambda^2 p_1\right)dR = 0, \qquad I = 1,\ldots\ldots, N_1. \tag{8.12}$$

Since we are to employ a weak Galerkin formulation, the application of Green's theorem gives

$$\int_{R_1}\left(\nabla\psi_I\nabla p_1 + k_0^2\left[\lambda^2 - (1-\lambda M)^2\right]\psi_I p_1\right)dR = \int_{S_{C_1}} \psi_I \nabla p_1 \cdot \mathbf{n}_1 dS, \tag{8.13}$$

where S_{C_1} denotes the boundary S_C in region 1. Substituting the assumed trial solution from equation (8.11) into equation (8.13) gives

$$\left\{\int_{R_1}\left(\nabla\psi_I\nabla\psi_J + k_0^2\left[\lambda^2 - (1-\lambda M)^2\right]\psi_I\psi_J\right)dR\right\}\{\mathbf{p}_1\} = \int_{S_{C_1}} \psi_I \nabla p_1 \cdot \mathbf{n}_1 dS. \tag{8.14}$$

The wave equation for region 2 is solved in a similar manner, and hence the approximation to the acoustic pressure in region 2 is given by

$$p_2 \approx \sum_{J=1}^{N_2} \psi_J p_{2_J}, \tag{8.15}$$

where N_2 is the number of nodes in region 2. Applying the Galerkin formulation to equation (8.6) yields

$$\int_{R_2} \psi_I\left(\nabla^2 p_2 - \left[\left(\Gamma^2 + k_0^2\lambda^2\right)\right]p_2\right)dR = 0, \qquad I = 1,\ldots\ldots\ldots, N_2. \tag{8.16}$$

The application of Green's theorem to equation (8.16) gives

$$\int_{R_2} \left(\nabla \psi_I \nabla p_2 + \left[\Gamma^2 + k_0^2 \lambda^2 \right] \psi_I p_2 \right) dR = \int_{S_2} \psi_I \nabla p_2 \cdot \mathbf{n}_2 dS . \tag{8.17}$$

Substituting the assumed trial solution from equation (8.15) into equation (8.17) finally gives

$$\left\{ \int_{R_2} \left(\nabla \psi_I \nabla \psi_J + \left[\Gamma^2 + k_0^2 \lambda^2 \right] \psi_I \psi_J \right) dR \right\} \{ \mathbf{p}_2 \} = \int_{S_2} \psi_I \nabla p_2 \cdot \mathbf{n}_2 dS . \tag{8.18}$$

8.3.1 Matching of the Acoustic Fields

The boundary conditions are now introduced in a manner similar to that used for the full finite element approach in Chapter 7. The hard-wall boundary condition on S_W (equation (8.10)) implies that the surface integral in equation (8.18) is zero, except over the perforate boundary in region 2 (S_{C_2}), since $S_2 = S_W + S_{C_2}$. It was shown in Chapter 7 that the implementation of the boundary conditions on S_C is simplified with the help of the momentum equations in each region. Therefore, in region 1, the linearized momentum equation is given by (see equation (6.1))

$$\nabla p_1 = -i \rho_0 c_0 k_0 [1 - \lambda M] \mathbf{u}_1 , \tag{8.19}$$

and for region 2 the momentum equation gives (see equation (6.17))

$$-\nabla p_2 = \Gamma z_a \mathbf{u}_2 , \tag{8.20}$$

where z_a is the characteristic impedance of the porous material. Substituting equation (8.19) into the weak Galerkin form of the wave equation for region 1 (equation (8.14)) gives

$$\left\{\int_{R_1}\left(\nabla\psi_I\nabla\psi_J + k_0^2\left[\lambda^2-(1-\lambda M)^2\right]\psi_I\psi_J\right)dR\right\}\{\mathbf{p}_1\} = -\int_{S_{C_1}} i\rho_0 c_0 k_0[1-\lambda M]\psi_I \mathbf{u}_1\cdot\mathbf{n}_1 dS.$$

(8.21)

Equation (8.21) can now be re-written by using equation (8.7) to give

$$\left\{\int_{R_1}\left(\nabla\psi_I\nabla\psi_J + k_0^2\left[\lambda^2-(1-\lambda M)^2\right]\psi_I\psi_J\right)dR\right\}\{\mathbf{p}_1\} = \int_{S_{C_1}} i\rho_0 c_0 k_0[1-\lambda M]^2\psi_I \mathbf{u}_2\cdot\mathbf{n}_2 dS.$$

(8.22)

For region 2, equation (8.20) is simply substituted into equation (8.18) to give

$$\left\{\int_{R_2}\left(\nabla\psi_I\nabla\psi_J + \left(\Gamma^2+k_0^2\lambda^2\right)\psi_I\psi_J\right)dR\right\}\{\mathbf{p}_2\} = -\int_{S_{C_2}} \Gamma z_a \psi_I \mathbf{u}_2\cdot\mathbf{n}_2 dS, \qquad (8.23)$$

where S_{C_2} denotes the line integral around the boundary S_C.

The right hand sides of both wave equations have now been written in a form allowing the introduction of the continuity of pressure boundary condition. Therefore substituting equation (8.9) into the right hand side of both equations (8.22) and (8.23) gives, for region 1

$$\left\{\int_{R_1}\left(\nabla\psi_I\nabla\psi_J + k_0^2\left[\lambda^2-(1-\lambda M)^2\right]\psi_I\psi_J\right)dR\right\}\{\mathbf{p}_1\} = \left\{\int_{S_{C_1}} i\frac{k_0}{\zeta}[1-\lambda M]^2\psi_I\psi_J dS\right\}\left[\{\mathbf{p}_{C_2}\}-\{\mathbf{p}_{C_1}\}\right],$$

(8.24)

and for region 2

$$\left\{\int_{R_2}\left(\nabla\psi_I\nabla\psi_J + \left(\Gamma^2+k_0^2\lambda^2\right)\psi_I\psi_J\right)dR\right\}\{\mathbf{p}_2\} = -\left\{\int_{S_{C_2}} \frac{\Gamma z_a}{\rho_0 c_0 \zeta}\psi_I\psi_J dS\right\}\left[\{\mathbf{p}_{C_2}\}-\{\mathbf{p}_{C_1}\}\right],$$

(8.25)

where $\{\mathbf{p}_C\}$ is the vector of nodal p_{C_J} values on the boundary S_C in either region 1 or 2.

In order to formulate the final eigenequation which is then solved for λ, equations (8.24) and (8.25) are added together, giving

$$\left\{\int_{R_1}\left(\nabla\psi_I\nabla\psi_J + k_0^2\left[\lambda^2-(1-\lambda M)^2\right]\psi_I\psi_J\right)dR\right\}\{\mathbf{p}_1\}+\left\{\int_{R_2}\left(\nabla\psi_I\nabla\psi_J + (\Gamma^2+k_0^2\lambda^2)\psi_I\psi_J\right)dR\right\}\{\mathbf{p}_2\}$$

$$-\left\{\int_{S_{C_1}} i\frac{k_0}{\zeta}[1-\lambda M]^2\,\psi_I\psi_J dS\right\}\left[\{\mathbf{p}_{C_2}\}-\{\mathbf{p}_{C_1}\}\right]+\left\{\int_{S_{C_2}}\frac{\Gamma z_a}{\rho_0 c_0\zeta}\psi_I\psi_J dS\right\}\left[\{\mathbf{p}_{C_2}\}-\{\mathbf{p}_{C_1}\}\right]=0.$$

(8.26)

Equation (8.26) now forms a second order eigenvalue problem in λ. It is noticeable that when this eigenequation is compared with the equivalent eigenequation found by Astley and Cummings [17], the order of the eigenequation in λ has been reduced by two in the present study. This has occurred because of the introduction of the perforate and the subsequent modification of the continuity of pressure boundary condition. It is possible that the reduction in the order of the eigenequation found here will reduce the computational time required to solve the problem.

It is convenient to re-write equation (8.26) in matrix from such that

$$[\mathbf{A}(\lambda)]\{\mathbf{p}\}=\{\mathbf{0}\}, \tag{8.27}$$

where $\mathbf{A}(\lambda)$ can be split up into individual components to give

$$\mathbf{A}(\lambda)=[\mathbf{A}]+\lambda[\mathbf{B}]+\lambda^2[\mathbf{C}]. \tag{8.28}$$

Therefore equating orders of λ in equation (8.26) allows expressions for the individual components of $\mathbf{A}(\lambda)$ to be written, i.e.

$$[\mathbf{A}]\{\mathbf{p}\}=[\mathbf{K}_1]\{\mathbf{p}_1\}-k_0^2[\mathbf{M}_1]\{\mathbf{p}_1\}+[\mathbf{K}_2]\{\mathbf{p}_2\}+\Gamma^2[\mathbf{M}_2]\{\mathbf{p}_2\}-(ik_0/\zeta)[\mathbf{M}_{1C}]\{\mathbf{p}_{C_2}\}$$

$$+(ik_0/\zeta)[\mathbf{M}_{1C}]\{\mathbf{p}_{C_1}\}+(\Gamma z_a/\rho_0 c_0\zeta)[\mathbf{M}_{2C}]\{\mathbf{p}_{C_2}\}-(\Gamma z_a/\rho_0 c_0\zeta)[\mathbf{M}_{2C}]\{\mathbf{p}_{C_1}\}, \tag{8.29}$$

$$[\mathbf{B}]\{\mathbf{p}\} = 2Mk_0^2[\mathbf{M}_1]\{\mathbf{p}_1\} + (2iMk_0/\zeta)[\mathbf{M}_{1\mathrm{C}}]\{\mathbf{p}_{\mathrm{C}_2}\} - (2iMk_0/\zeta)[\mathbf{M}_{1\mathrm{C}}]\{\mathbf{p}_{\mathrm{C}_1}\},$$

(8.30)

$$[\mathbf{C}]\{\mathbf{p}\} = k_0^2(1-M^2)[\mathbf{M}_1]\{\mathbf{p}_1\} + k_0^2[\mathbf{M}_2]\{\mathbf{p}_2\} - (ik_0M^2/\zeta)[\mathbf{M}_{1\mathrm{C}}]\{\mathbf{p}_{\mathrm{C}_2}\} + (ik_0M^2/\zeta)[\mathbf{M}_{1\mathrm{C}}]\{\mathbf{p}_{\mathrm{C}_1}\},$$

(8.31)

where the $(\mathrm{I,J})^{\mathrm{th}}$ elements of the matrices are

$$[\mathbf{K}_1]_{\mathrm{I,J}} = \int_{\mathrm{R}_1} \nabla\psi_{\mathrm{I}}\nabla\psi_{\mathrm{J}}\,dydz, \tag{8.32}$$

$$[\mathbf{K}_2]_{\mathrm{I,J}} = \int_{\mathrm{R}_2} \nabla\psi_{\mathrm{I}}\nabla\psi_{\mathrm{J}}\,dydz, \tag{8.33}$$

$$[\mathbf{M}_1]_{\mathrm{I,J}} = \int_{\mathrm{R}_1} \psi_{\mathrm{I}}\psi_{\mathrm{J}}\,dydz, \tag{8.34}$$

$$[\mathbf{M}_2]_{\mathrm{I,J}} = \int_{\mathrm{R}_2} \psi_{\mathrm{I}}\psi_{\mathrm{J}}\,dydz, \tag{8.35}$$

$$[\mathbf{M}_{1\mathrm{C}}]_{\mathrm{I,J}} = \int_{\mathrm{S}_{\mathrm{C}_1}} \psi_{\mathrm{I}}\psi_{\mathrm{J}}\,dS_{\mathrm{C}}, \tag{8.36}$$

$$[\mathbf{M}_{2\mathrm{C}}]_{\mathrm{I,J}} = \int_{\mathrm{S}_{\mathrm{C}_2}} \psi_{\mathrm{I}}\psi_{\mathrm{J}}\,dS_{\mathrm{C}}. \tag{8.37}$$

A clearer representation of equations(8.29) to (8.31) can be achieved by expanding the matrices to give

$$[\mathbf{A}]\{\mathbf{p}\} = \begin{bmatrix} [\mathbf{K}_1]-k_0^2[\mathbf{M}_1] & [\mathbf{K}_1]-k_0^2[\mathbf{M}_1] & 0 & 0 \\ [\mathbf{K}_1]-k_0^2[\mathbf{M}_1] & [\mathbf{K}_1]-k_0^2[\mathbf{M}_1]+(ik_0/\zeta)[\mathbf{M}_{1\mathrm{C}}] & -(ik_0/\zeta)[\mathbf{M}_{1\mathrm{C}}] & 0 \\ 0 & -(\Gamma z_a/\zeta\rho_0c_0)[\mathbf{M}_{2\mathrm{C}}] & [\mathbf{K}_2]+\Gamma^2[\mathbf{M}_2]+(\Gamma z_a/\zeta\rho_0c_0)[\mathbf{M}_{2\mathrm{C}}] & [\mathbf{K}_2]+\Gamma^2[\mathbf{M}_2] \\ 0 & 0 & [\mathbf{K}_2]+\Gamma^2[\mathbf{M}_2] & [\mathbf{K}_2]+\Gamma^2[\mathbf{M}_2] \end{bmatrix} \begin{Bmatrix} \mathbf{p}_1 \\ \mathbf{p}_{\mathrm{C}_1} \\ \mathbf{p}_{\mathrm{C}_2} \\ \mathbf{p}_2 \end{Bmatrix}$$

(8.38)

$$[\mathbf{B}]\{\mathbf{p}\} = \begin{bmatrix} 2Mk_0^2[\mathbf{M}_1] & 2Mk_0^2[\mathbf{M}_1] & 0 \\ 2Mk_0^2[\mathbf{M}_1] & 2Mk_0^2[\mathbf{M}_1]-(2iMk_0/\zeta)[\mathbf{M}_{1\mathrm{C}}] & (2iMk_0/\zeta)[\mathbf{M}_{1\mathrm{C}}] \end{bmatrix} \begin{Bmatrix} \mathbf{p}_1 \\ \mathbf{p}_{\mathrm{C}_1} \end{Bmatrix}$$

(8.39)

$$
[\mathbf{C}]\{\mathbf{p}\}=\begin{bmatrix} k_0^2(1-M^2)[\mathbf{M}_1] & k_0^2(1-M^2)[\mathbf{M}_1] & 0 & 0 \\ k_0^2(1-M^2)[\mathbf{M}_1] & k_0^2(1-M^2)[\mathbf{M}_1]+(ik_0M^2/\zeta)[\mathbf{M}_{1c}] & -(ik_0M^2/\zeta)[\mathbf{M}_{1c}] & 0 \\ 0 & 0 & k_0^2[\mathbf{M}_2] & k_0^2[\mathbf{M}_2] \\ 0 & 0 & k_0^2[\mathbf{M}_2] & k_0^2[\mathbf{M}_2] \end{bmatrix}\begin{Bmatrix} \mathbf{p}_1 \\ \mathbf{p}_{C_1} \\ \mathbf{p}_{C_2} \\ \mathbf{p}_2 \end{Bmatrix}
$$

(8.40)

In order to solve equation (8.27) in the standard way it is necessary to re-formulate the problem. Hence the eigenequation

$$
\left[[\mathbf{A}]+\lambda[\mathbf{B}]+\lambda^2[\mathbf{C}]\right]\{\mathbf{p}\}=\{\mathbf{0}\}, \tag{8.41}
$$

is re-written in the form

$$
\left[-[\mathbf{C}]^{-1}[\mathbf{A}]-\lambda[\mathbf{C}]^{-1}[\mathbf{B}]\right]\{\mathbf{p}\}=\lambda^2\{\mathbf{p}\}, \tag{8.42}
$$

where $[\mathbf{C}]^{-1}$ is the inverse of matrix $[\mathbf{C}]$. The problem can now be solved for λ in a manner similar to that used by Astley and Cummings [17], hence re-writing equation (8.42) gives

$$
\begin{bmatrix} 0 & \mathbf{I} \\ -[\mathbf{C}]^{-1}[\mathbf{A}] & -[\mathbf{C}]^{-1}[\mathbf{B}] \end{bmatrix}\begin{Bmatrix} \mathbf{p} \\ \lambda\mathbf{p} \end{Bmatrix}=\lambda\begin{Bmatrix} \mathbf{p} \\ \lambda\mathbf{p} \end{Bmatrix}, \tag{8.43}
$$

where $\mathbf{I}$ is an identity matrix.

Equation (8.43) now forms a standard eigenequation of order 2n (n being the total number of nodes) and this can be solved in the usual way (see the next section). The solution to equation (8.43) provides eigenvalues which correspond to the common axial wavenumbers of the modes in the duct and eigenvectors which are equivalent to the transverse modal eigenfunctions. It is worth noting that the matrix partitioning used by Astley and Cummings [17] was not necessary here because of the reduction in the order of the problem, this has the benefit of simplifying the code and also reducing the size of the final matrix, this potentially allows solutions to be found more quickly. An additional reduction in computational effort, common to both the method described here and that of Astley and Cummings, can be found if no mean flow is present since, when $M = 0$, matrix $[\mathbf{B}]$ is identically zero. This reduces equation (8.41) to give

$$[[\mathbf{A}] + \lambda^2[\mathbf{C}]]\{\mathbf{p}\} = \{\mathbf{0}\}, \tag{8.44}$$

which has a problem size of order n. This represents a halving of the problem size when no mean flow is present. Again, the solution to equation (8.44) is achieved in the standard way.

Finally, once the problem has been solved for λ, either with or without mean flow, the results are commonly presented in the form of attenuation per unit length and the phase speed for individual modes. For the i$^{\text{th}}$ mode, the attenuation α and phase speed c are given by [17]

$$\alpha_{\mathrm{i}} = -8.6858\ \Im\mathrm{m}(k_0\lambda_{\mathrm{i}}), \qquad (\mathrm{dB/m}) \tag{8.45}$$

and

$$c_{\mathrm{i}} = c_0 / \Re\mathrm{e}(k_0\lambda_{\mathrm{i}}). \qquad (\mathrm{m/s}) \tag{8.46}$$

It is also of interest to study the shape of each of the individual modes and this can be done by examining the eigenvectors directly. Results of attenuation, phase speed and mode shapes for the silencers measured in Chapter 5 are given in the next section.

Section 8.4

Results and Discussion

Solutions to the eigenvalue problem can be found by solving either equation (8.44), when there is no mean flow in the central channel, or equation (8.43) when mean flow is introduced. As in previous chapters solutions are also presented here both with and without a perforate in the model thus allowing the effect of the perforate to be studied further. To find the eigenvalues in a dissipative silencer without a perforate present one may follow exactly the method used by Astley and Cummings [17] and later by Rathi [18]. This involves re-defining the matching conditions on the boundary Γ_C which in turn alters the final equations. The modified equations for the case without the presence of a perforate are not given here in order to save space.

The solution of the finite element problem, both with and without a perforate, was performed here in a manner similar to that used for the full finite element method in Chapter 7. This involved using the commercial package FEMGEN to generate the finite element mesh, from which the final matrices in equations (8.43) and (8.44) were assembled in the standard way using the NAG finite element library [123]. Finally, the set of linear equations associated with the assembly of equations (8.43) and (8.44) was solved simultaneously by using the standard routines found in the NAG library.

One of the obvious benefits to be found when using an eigenvalue formulation is the reduction in the number of elements and nodes that are required to mesh each silencer when compared to those needed for the full finite element solution. The eigenvalue formulation requires the axisymmetric silencers to modelled using only a one dimensional (1D) mesh, whilst the elliptical silencers require only a two dimensional (2D) mesh. Furthermore, planar symmetry means that it is only necessary to mesh one quarter of the cross section of each ellipse. This has the potential of providing considerable savings in computational effort when compared to the method used in the previous chapter, although it should be noted that equations (8.43) and (8.44) do not provide banded matrices and this will adversely affect the solution time. In addition one must also invert the $[C]$ matrix when mean flow is present, placing additional computational demands.

The type of elements used in this section to mesh each silencer were based upon the elements used in Chapter 7 since these were shown to provide adequate results. Therefore, for the axisymmetric silencers, three noded isoparametric line elements were used and for the elliptical silencers, six noded isoparametric triangular elements were used to mesh the airway and eight noded isoparametric rectangular elements to mesh the absorbent. To determine the optimum number of nodes and elements required for meshing each silencer the perforate was omitted from the model. The attenuation and phase speed were then found for the least attenuated mode of the axisymmetric silencers and convergence of the solution was established after comparison with the analytical solution found in Chapter 6. The number of elements used to mesh the elliptical silencers was then based upon the number of elements used for the axisymmetric silencers. However, it should be noted that the number of elements required to provide accurate solutions for the least attenuated mode is lower than that required for the second least attenuated mode and so on. This is because higher order modes have progressively more complex mode shapes as the mode order increases and hence a larger number of elements is required in order to represent the shapes accurately. Unfortunately this problem cannot be solved simply by using a very large number of elements since this will increase the size of the final matrices, introducing numerical problems into the solution of equations (8.43) and (8.44). The number of modes and elements used for silencers 1 to 5 (without a perforate present) are given in Table 8.1 below; these were chosen to provide the best balance between the accuracy required in the predictions and the minimisation of numerical problems.

Table 8.1. Dimensions of finite element mesh

Silencer	Number of Elements	Number of nodes
1	20	40
2	20	40
3	20	40
4	24	75
5	24	75

An example of the mesh generated for silencer 5 (without a perforate) is shown in Figure 8.2.

Once the optimum number of elements was found for each silencer, the mesh was re-configured to include the perforate. This requires a modification of the mesh in a manner similar to that found when including the perforate in the mesh used in Chapter 7. This involves assigning two different node numbers to each co-ordinate on the common boundary Γ_C, thus allowing the pressures $\mathbf{p}_{C_1}$ and $\mathbf{p}_{C_2}$ to be calculated. Problems were encountered (as outlined in the previous chapter) when including the perforate in a three dimensional mesh, but the reduction in the dimensions of the problem studied here allows these problems to be avoided. This is because it is a straightforward task to write the additional code required to include the perforate in both the 1D and the 2D meshes used here. Consequently it should now be possible to produce transmission loss predictions for the oval section silencers including a perforate, and this will be covered in Chapter 9.

The computer output obtained from the solution of equations (8.43) and (8.44) (and also the equivalent equations when no perforate is present [17]) occurs in the form of an unordered list of eigenvalues and their associated eigenvectors, with the number of eigenvalues obtained being equal to the number of nodes present in the mesh. It should be noted that it is commonly accepted that only half of the eigenvalues calculated when using a numerical scheme such as the one found here are accurate enough for use in future mode matching schemes. From the list of eigenvalues it is necessary to identify the modes required and these must be chosen with a view to the mode matching schemes proposed in Chapter 9. Consequently the least attenuated modes are of principal interest here, but in the following discussion, no attempt is made to order the modes with reference to individual mode shapes. An examination of equation (8.45) indicates that arranging the modes in order of increasing attenuation requires sorting of the eigenvalues according to the size of their imaginary components. However, it is also necessary to examine the sign of the imaginary part, since this describes the direction in which the mode is attenuated. It is only necessary to examine the sign of the eigenvalue when mean flow is present, since without mean flow the eigenvalues occur in complex conjugate pairs. The sign of the real part of the eigenvalue is also significant since this defines the direction in which the mode propagates (though see later comments about apparently anomalous combinations of signs of the real and imaginary parts). The significance of the sign of the real and imaginary components of each eigenvalue can be summarised by the Argand diagram below:

	$\Im m(\lambda)$	
Propagates x^- Attenuates x^-	Propagates x^+ Attenuates x^-	$\Re e(\lambda)$
Propagates x^- Attenuates x^+	Propagates x^+ Attenuates x^+	

In addition to identifying the incident and reflected waves when mean flow is present, it is also necessary to identify the so-called hydrodynamic modes [17]. This can easily be done since hydrodynamic modes have a phase velocity of U_0 and are effectively unattenuated. However hydrodynamic modes do not contribute to the sound field and, once identified, they must be rejected. Hydrodynamic modes were found here in the eigenvalue solution without a perforate; they were also found by both Astley and Cummings [17] and Rathi [18], although no hydrodynamic modes were found in the present work for silencers with perforates. The physical reasons behind the absence of hydrodynamic modes when a perforate is present are not clear although it is probably a result of the change in matching conditions on Γ_C; indeed other eigenvalue solutions which include a perforate, see for example Nilsson and Brander [15], do not exhibit hydrodynamic modes either. The reduction in the order of the eigenvalue problem from quartic to quadratic, as a perforate is introduced, is probably responsible for the disappearance of the hydrodynamic modes.

For each frequency analysed the list of eigenvalues must be ordered, sorted into incident and reflected wave; also, if present, the hydrodynamic modes should be rejected. In general the solutions performed here cover frequencies from 50Hz up to 2kHz. As the frequency increases, the position of each mode *shape* in mode numbering order, based on modal attenuation, can change. For example, the fundamental mode pattern can begin as the least attenuated mode at 50Hz but become the second least attenuated mode at 2kHz. This effect is particularly apparent in higher order modes, especially when mean flow is present and it is possible that a single mode shape can shift through a number of positions in the modal order. This phenomenon means that it is very difficult to track a single mode shape by studying its position in the mode order based on attenuation alone, and one must usually resort to examining the eigenfunction as well to check that the same mode shape is being followed. Consequently any mode matching scheme based solely on mode shapes is very difficult to implement in a robust way. This is the reason why mode shapes themselves are not tracked in this analysis; it does, however, require the assumption that a mode matching scheme will work equally well with a specified number of modes that are ordered on the basis of modal attenuation or on the basis of mode shapes. It will become evident later on in this section that this does not cause any problems for the 1D model, although for the 2D solutions, non-axisymmetric modes can infiltrate into the specified number of least attenuated modes and, since non-axisymmetrical modes are not required in the mode matching schemes (see later on), a larger number of eigenvalues must be used to ensure the retention of a constant number of axisymmetrical modes. This can effect the convergence of the transmission loss predictions formulated in Chapter 9. This problem cannot be rectified by simply using a large number of least attenuated modes in the mode matching scheme since, as previously discussed, numerical problems can appear when a large number of nodes are used to mesh a silencer.

Solutions are presented in this section for the attenuation and phase speed of the four least attenuated modes in silencers 1 to 5 covering frequencies up to 2kHz. In general, the axisymmetric silencers studied here do not exhibit mode shapes jumping position, though this phenomenon does become evident when the two dimensional model is used. The mode shapes which correspond to the four least attenuated modes found in the axisymmetric silencers studied here generally conform to the fundamental mode followed by the three lowest radial modes. This can be seen in Figure 8.3, where the modulus of the eigenfunctions for the four least attenuated modes in silencer 2 are plotted at a frequency of 1kHz for M=0 and M=0.15, both with and without a perforate (r being the radial coordinate and R_2 the outside diameter of the silencer). The number of minima exhibited in the modulus of the eigenfunctions determines the order of each mode (see Cummings and Chang [23]), although the minima are somewhat indistinct for the second least attenuated mode (order 1). It is evident that, for silencer 2, the fundamental mode is far from being a plane wave at 1kHz, the E glass present causing a high degree of non-uniformity in the modal pressure pattern. The individual mode shapes do not appear to be greatly affected by either the introduction of a perforate or mean flow, although this is almost certainly because of the frequency used and the silencer tested. The attenuation and phase speed of the four least attenuated modes present in silencers 1 and 3 are plotted in Figures 8.4 and 8.5 for M=0, both with and without a perforate. The mode shapes for the fundamental mode (least attenuated mode in these silencers) and the next three radial modes for silencers 1 and 3 correspond to the same mode order as those shown for silencer 2 in Figure 8.3. It is noticeable that the mode order corresponding to each modal pressure pattern remains unchanged for silencers 1 to 3, although this will not necessarily be the case at frequencies above 2kHz. The effect of the perforate on both the attenuation and the phase speed will be discussed later. The effect of introducing flow into the axisymmetric silencers is shown for silencer 2 (M=0.15) in Figures 8.6 and 8.7. Both the upstream and downstream propagating waves are shown, both with and without a perforate. It can be seen that the least attenuated mode undergoes a much larger attenuation in the upstream direction as compared to downstream, although this is not generally true for the higher order modes. One interesting phenomenon that often occurs is the reversal in direction of the phase speed for higher order modes. At first sight it appears that, for instance, a mode which is attenuated in the positive direction is propagating in the negative direction. Cummings [130] also observed this phenomenon but pointed out that, whilst there is a small power flow in the negative direction in the central channel, a much larger positive power flow occurs in the liner and this causes a net power flow in the direction of modal attenuation. The phase speed of these modes can be seen to change abruptly from negative to positive as the frequency is increased in Figures 8.6 and 8.7. It should be pointed out, however, that this has not occurred because of a mode jumping position when the eigenvalues were sorted; indeed the corresponding attenuation still exhibits a continuous curve.

The use of a 1D model for the axisymmetric silencers ensures that only axisymmetrical modes are found and, for the silencers studied here, the jumping of position of modes was not observed over the frequency range of interest. This provides an "ideal" set of least attenuated modes: the fundamental mode, the next radial mode and so on; this ordering of modes is important for examining problems that occur in the mode matching schemes of Chapter 9. The importance of establishing a set of axisymmetrical modes using a 1D model is apparent when 2D solutions are studied. In a 2D solution non-axisymmetric modes appear which, although providing a legitimate solution to the eigenvalue problem, effect the accuracy of the mode matching schemes. This is because the mode matching schemes presented in Chapter 9 are designed to find the transmission loss of finite length silencers, which involves matching solutions to a plane wave at the input and output pipes of the silencer. Consequently non-axisymmetric modes cannot effect the final transmission loss predictions and therefore represent undesirable modes in the least attenuated mode order. These modes can often appear very low in the least attenuated mode order and this increases the size of the mode matching matrices since more modes must be used to ensure the retention of a constant number of axisymmetric modes. If the number of non-axisymmetric modes present with low attenuations is large then this causes numerical problems in the mode matching schemes. Clearly it would be desirable to identify each non-axisymmetric mode and remove it before running a mode matching scheme, but the identification of non-axisymmetric modes is not always straightforward from an examination of the attenuation alone and one must usually resort to examining individual mode shapes at each discrete frequency. This problem was best illustrated by studying a 2D model of an axisymmetric silencer since the axisymmetrical modes can be identified by comparing attenuation and phase speed predictions with those found using a 1D solution. A comparison between the 1D and 2D solutions showed a number of non-axisymmetric modes appearing in the 2D solution ranging anywhere from second in the mode order upwards, for each axisymmetric silencer. Furthermore, the non-axisymmetric modes often suddenly appeared with a low attenuation at a certain frequency, and often this was also accompanied by a phase speed which began reducing exponentially from infinity. This phenomenon was also observed by Rathi [18]. It appears that a number of the non-axisymmetric modes are very highly attenuated at low frequencies but, as the frequency is increased, they can undergo an abrupt reduction in attenuation; one also notes a corresponding large jump in the phase speed. This effect, found originally in 2D axisymmetric models, was also observed in the solutions found for the oval silencers, although strictly speaking, axisymmetrical modes do not exist in the oval silencers. For instance, Figure 8.8 indicates that, for silencer 4 without a perforate and no mean flow, behaviour similar to that found in the axisymmetric silencers is observed, indicating the presence of modes in the oval silencers similar to those found in circular silencers. This is particularly apparent in the sudden appearance (at approximately 700Hz) of a phase speed reducing from infinity for the fourth least attenuated mode. The attenuation and phase speed of this mode in Figure 8.8 below 700Hz belong to a different mode *shape* which has simply changed its position in the least attenuated mode order at 700Hz. Indeed one can identify two different modes below 700Hz, the attenuation and phase speed of which would remain continuous if a larger number of modes had been plotted in Figure 8.8. The "non-axisymmetric" mode has therefore jumped from a much higher attenuation to a low attenuation at approximately 700Hz. This phenomenon is obviously dependent upon the silencer studied since it appears to be very difficult to predict, although it does appear that non-axisymmetric modes are responsible for most of the mode jumping that occurs in 2D models. Furthermore, as pointed out by Rathi [18], although only one quarter of the cross section has been utilised as a solution domain in the 2D models used here, it is possible to mesh the entire cross section of the silencer; but this would simply add further non-axisymmetric modes, which would complicate matters even more. It appears that the identification and removal of non-axisymmetric modes is not possible without investigating the mode shape of each individual mode, and this is obviously undesirable. Therefore the consequences of including non-axisymmetric modes in mode matching schemes must be tolerated and these will be discussed further in Chapter 9.

The effect of the perforate on both the attenuation and phase speed of silencers 1, 2, 3 and 4 has been shown in Figures 8.4 to 8.8. A comparison between the attenuation of the least attenuated mode, both with and without a perforate, appears to show trends similar to those observed in the fundamental mode solution, as one would expect, and also the full finite element solutions. For instance, when a perforate is added, silencers 1 and 2 exhibit a small increase in attenuation at lower frequencies but, above approximately 1kHz, a large decrease occurs, especially for silencer 2. When porous material with a low flow resistivity, such as A glass is used, the effect of the perforate (which has previously been shown to be small) is seen to be minimal in the case of silencer 3. Silencer 4 also indicates little difference in the predictions of the least attenuated mode with and without a perforate, and this is probably explained by the use of basalt wool (which has an intermediate flow resistivity) in silencer 4 . The effect of the perforate on higher order modes is less straightforward to quantify, especially for the axisymmetric silencers where only a small change in attenuation and - perhaps more obviously - phase speed, occurs. This does however point to the dominant role of the least attenuated mode in further transmission loss predictions. It is apparent from examining the data for silencer 4 in Figure 8.8 that, when a perforate is present, an non-axisymmetric mode has not appeared at 700Hz for the fourth least attenuated mode. This apparent reduction in the frequency of appearance of non-axisymmetric modes with very large phase speeds can also be observed for silencer 5 (see Figure 8.9). It appears that, even if some of the higher order modes shown, in the presence of a perforate, in Figures 8.8 and 8.9 are non-axisymmetric, they have not undergone the abrupt changes in attenuation and phase speed found without a perforate. It is not known why this has occurred or even if this feature is attributable only to the choice of silencers studied here.

The eigenvalue solution presented in this chapter has been formulated for use in mode matching schemes and these will be discussed in the next chapter. Experimental data were deemed unnecessary since a comparison of the solutions found here with other published data, both theoretical and experimental, appears sufficient for establishing accuracy of the method (to avoid reproducing large amounts of data, such comparisons have not been shown here). Indeed the effect of the perforate on the least attenuated mode appears consistent with previous theoretical predictions and this appears to show that the eigenvalue solution with a perforate is valid. Transmission loss predictions will be presented in the next chapter, utilising the eigenvalue solutions found here, and the relative computational speed and accuracy of the model presented in this chapter will be compared to the other theoretical models in Chapter 10.

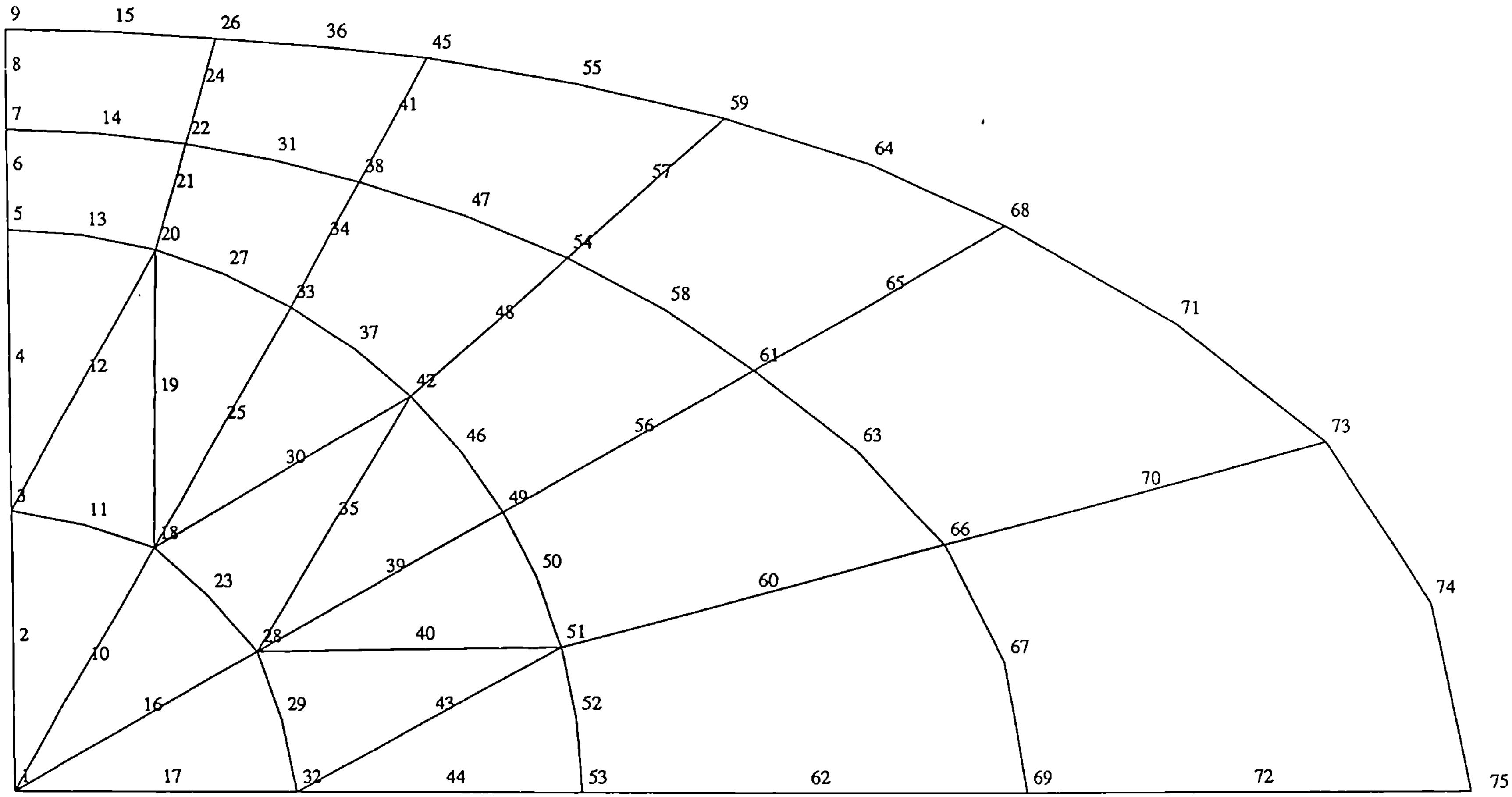

Figure 8.2. Two dimensional mesh for Silencer 5.

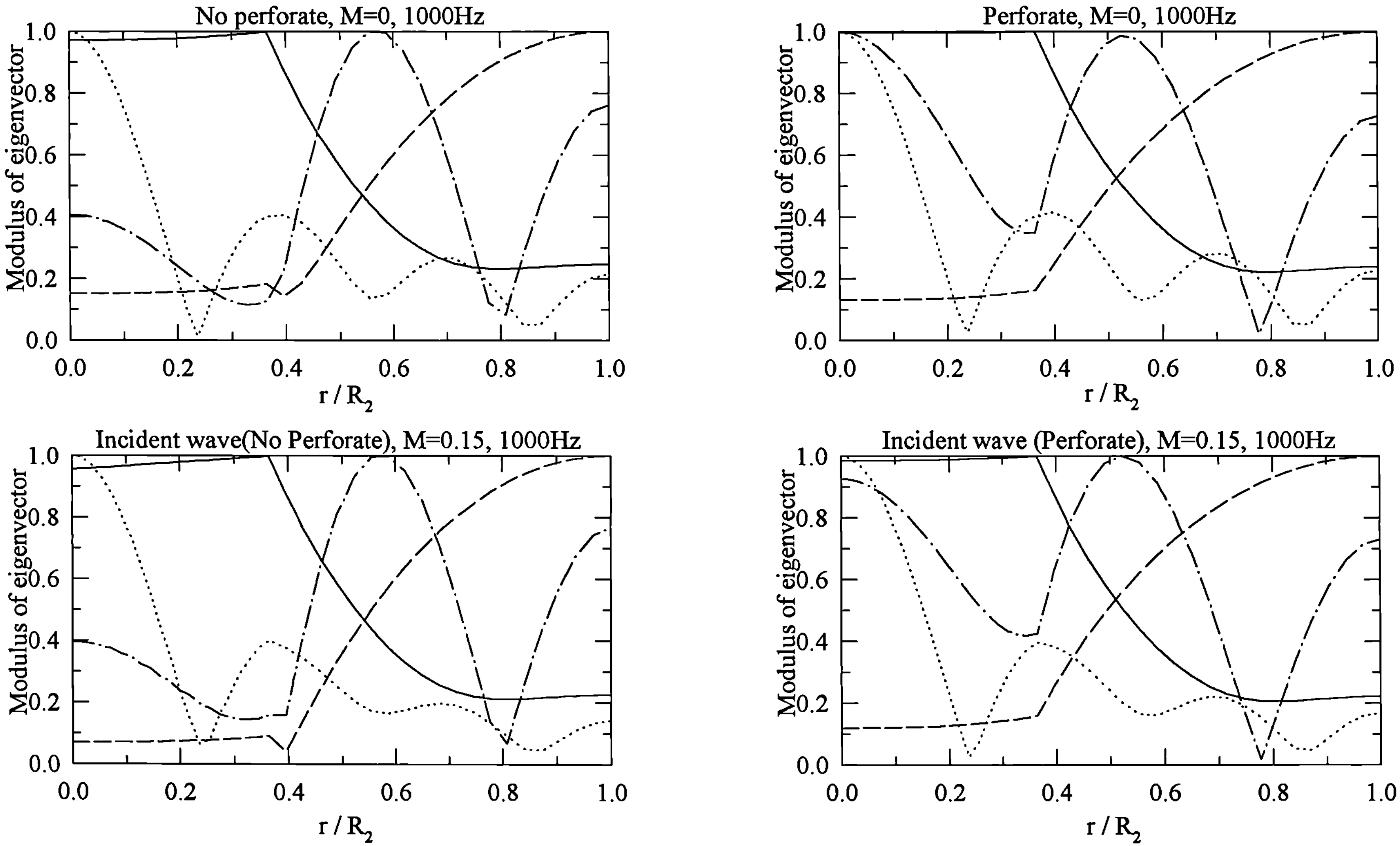

Figure 8.3. Mode shapes for silencer 2. ——— , Least attenuated mode; — — — , Second least attenuated mode; —·— , Third least attenuated mode; ········ , Fourth least attenuated mode.

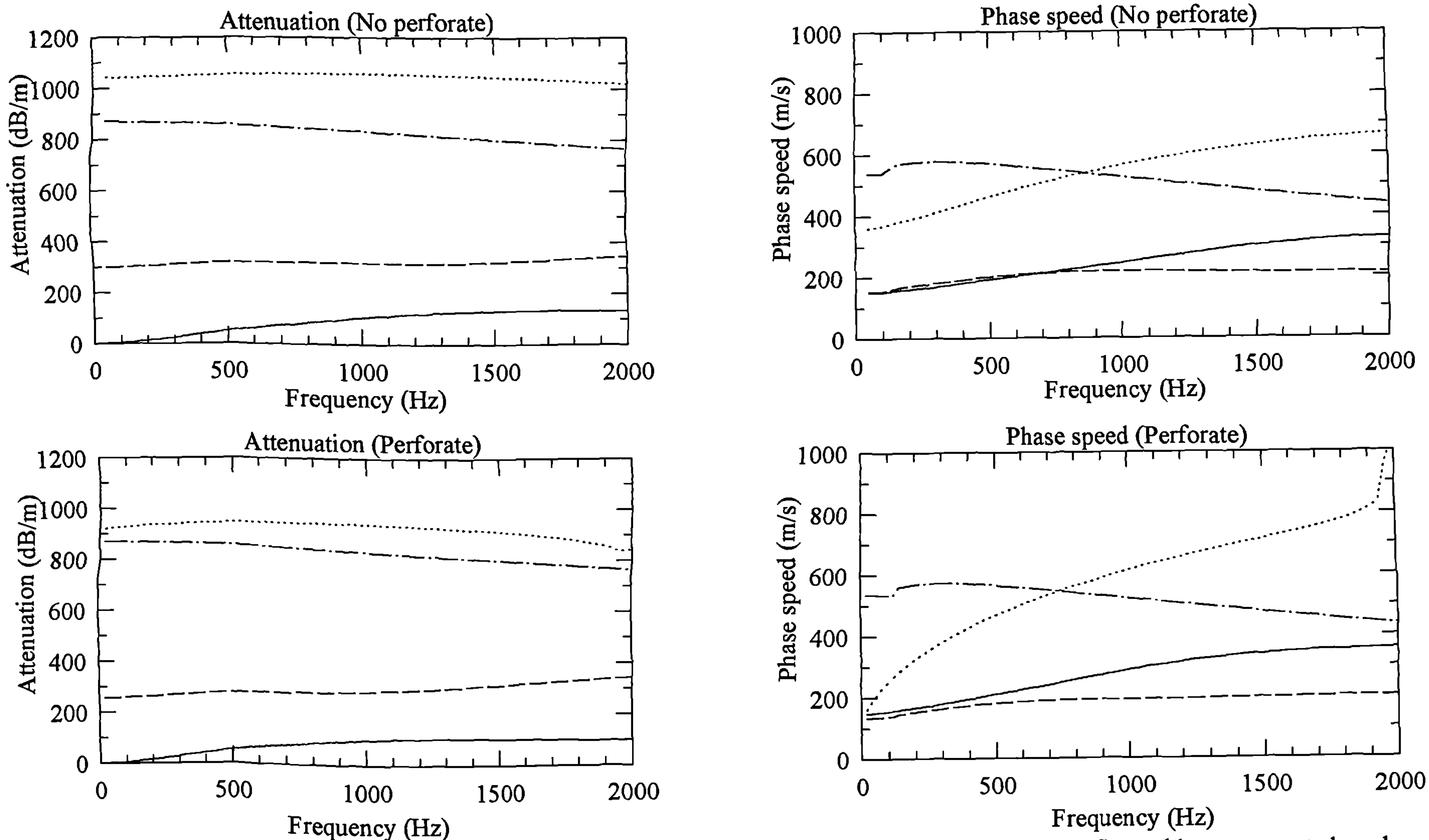

Figure 8.4. Finite element predictions for Silencer 1, M=0. ——— , Least attenuated mode; – – – , Second least attenuated mode; —·— , Third least attenuated mode; ········ , Fourth least attenuated mode.

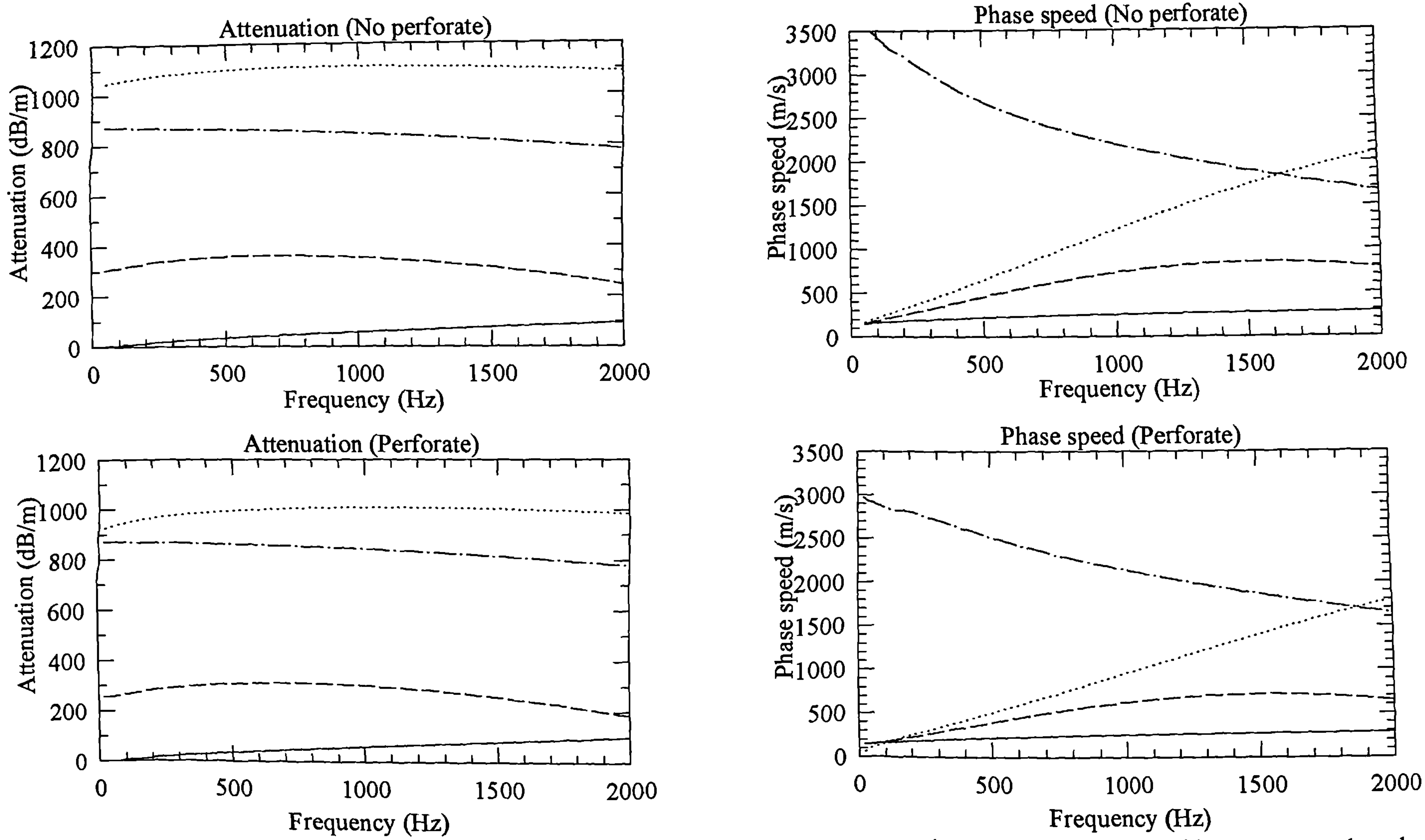

Figure 8.5. Finite element predictions for Silencer 3, M=0. ——— , Least attenuated mode; – – – , Second least attenuated mode; —·— , Third least attenuated mode; ········ , Fourth least attenuated mode.

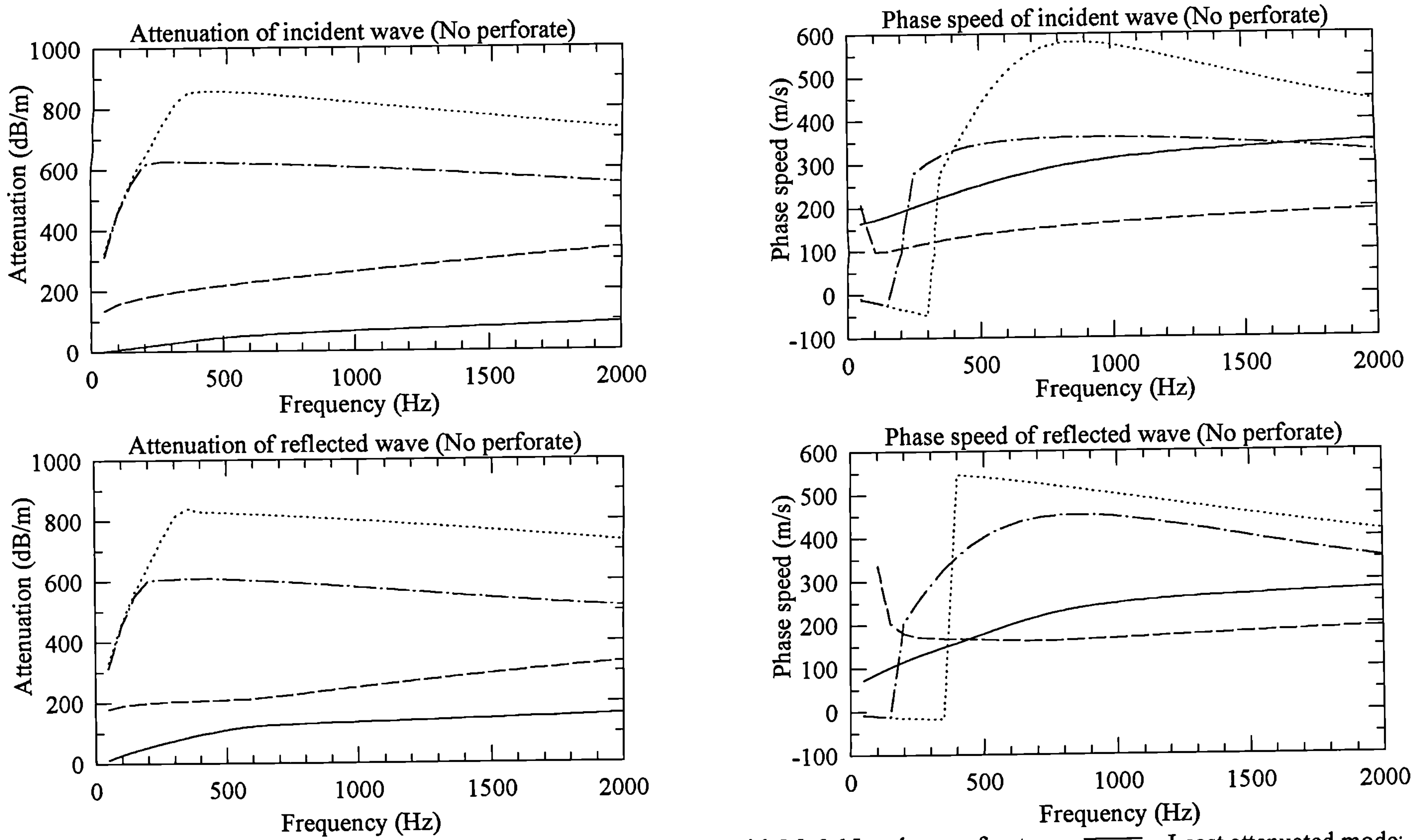

Figure 8.6. Finite element predictions for incident wave in Silencer 2 with M=0.15 and no perforate. ——— , Least attenuated mode; — — — , Second least attenuated mode; —·— , Third least attenuated mode; ········ , Fourth least attenuated mode.

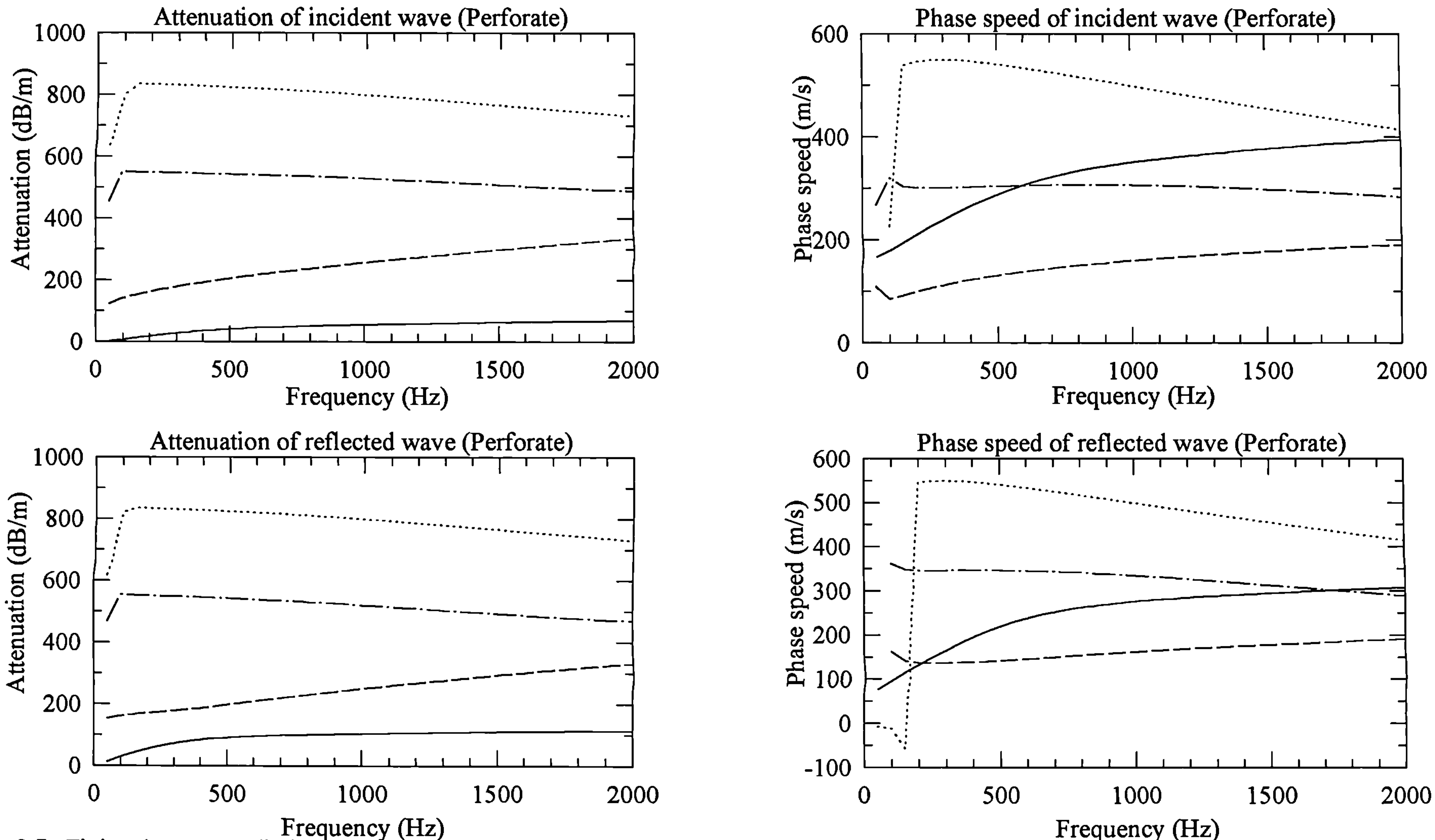

Figure 8.7. Finite element predictions for incident and reflected waves in Silencer 2 with M=0.15 and a perforate. ——— , Least attenuated mode; – – – , Second least attenuated mode; —·— , Third least attenuated mode; ········ , Fourth least attenuated mode.

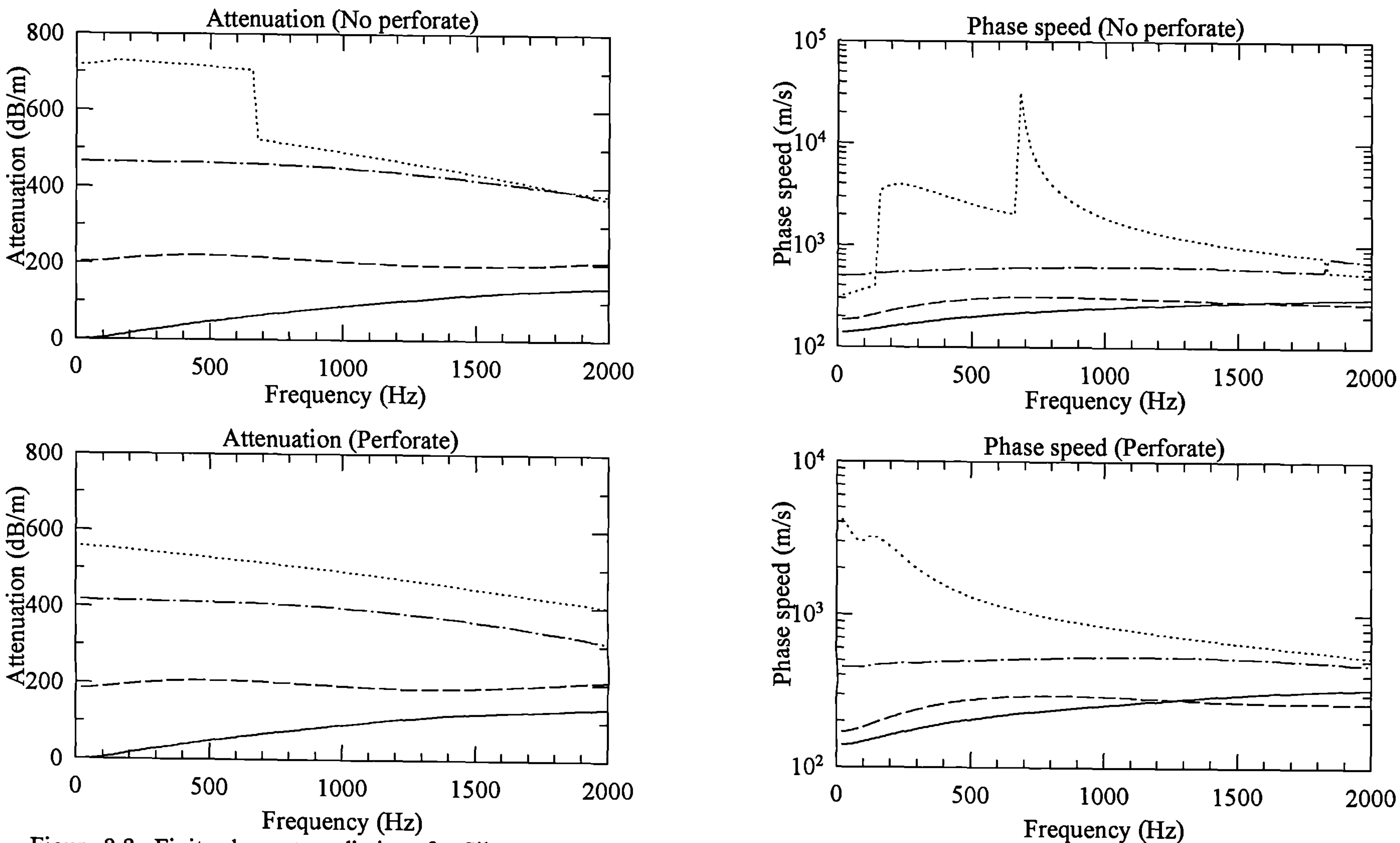

Figure 8.8. Finite element predictions for Silencer 4, M=0. ——— , Least attenuated mode; — — — , Second least attenuated mode; —·— , Third least attenuated mode; ········ , Fourth least attenuated mode.

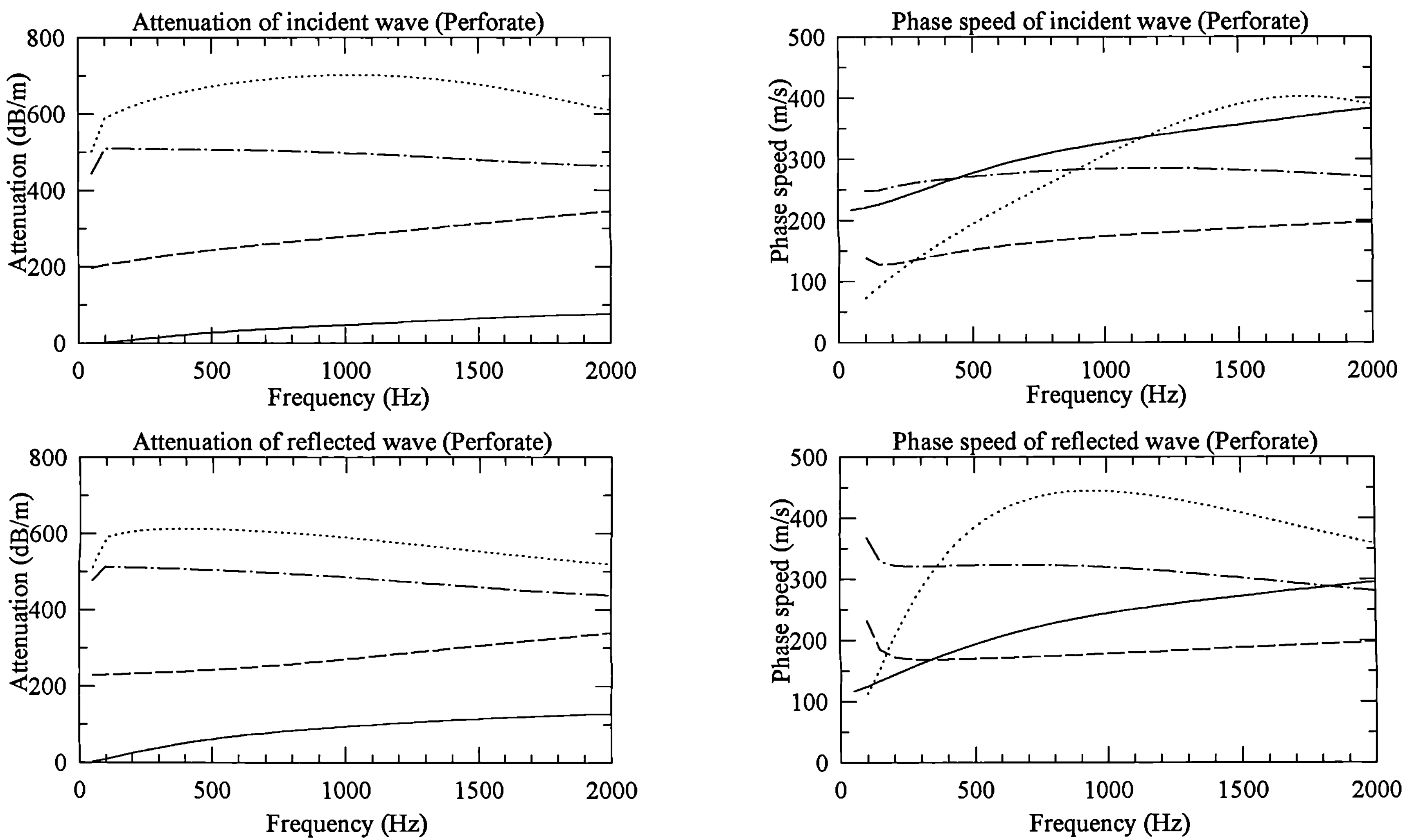

Figure 8.9. Finite element predictions for incident and reflected waves in Silencer 5 with M=0.15 and a perforate. ——— , Least attenuated mode; — — — , Second least attenuated mode; —·— , Third least attenuated mode; ········ , Fourth least attenuated mode.

CHAPTER 9

MODE MATCHING TECHNIQUES FOR DISSIPATIVE SILENCERS WITH IRREGULAR CROSS–SECTIONS

Section 9.1

Introduction

In the previous chapter, eigenvalue solutions were obtained for acoustic modes propagating in an infinite duct, and these are now utilised in order to find the transmission loss of a silencer with finite length. The further study of finite length silencers is necessary because, as discussed in Chapter 5, transmission loss predictions provide a better indication of the acoustic performance of individual silencer elements than the attenuation/unit length of infinite lined ducts. The calculation of the transmission loss of a finite length silencer, described in this chapter, requires the prior knowledge of the eigenvalues and eigenvectors in each section of the silencer. For the silencers studied here this includes the eigenvalues and eigenvectors in both the inlet and outlet pipes and, so long as these are assumed to be rigid walled ducts, the values are well documented (see for example the book by Morse and Ingård [27]). In this chapter the modal representations of the sound field in each section of the duct are matched together on either side of the discontinuities present at each end of the silencer. The matching of the sound pressure fields allows a finite length silencer to be modelled by using the eigenvalue solutions found for an infinite lined duct and, so long as the different pressure fields can be matched efficiently, this approach offers considerable savings in computational time when compared to models such as the one described in Chapter 7.

Discontinuities in ducts were examined by Miles [131], who introduced higher order modes and an abrupt area change into a rigid walled duct of circular cross-section. To do this, Miles enforced continuity of pressure and continuity of volume velocity across the discontinuity. In order to arrive at a series of independent linear equations, Miles multiplied the two matching conditions by weighting functions. Miles employed weighting functions which were orthogonal and this later allowed the solution of the final equations to be simplified. The approach of Miles is a particular method used in the study of discontinuities, which has later become known as "mode matching". The method of mode matching has since become a popular way of examining duct discontinuities because of its apparent simplicity and subsequently a number of variations on the mode matching principle have been implemented. For example, Alfredson [132] used a mode matching method to study small area changes in ducts, and used this to model an exponential horn. Alfredson also introduced higher order modes into the model but showed that this required the alteration of one of the matching conditions used by Miles: matching continuity of particle velocity was employed, rather than continuity of volume velocity. The matching conditions employed by Alfredson have since become universally used, the velocity matching condition implemented by Miles later being shown to be a special case of Alfredson's condition, applicable when only the fundamental mode is present. Alfredson employed the orthogonality properties of Bessel functions in order to supply weighting functions which allowed further simplification of the problem. The study of duct discontinuities was later extended to cover reactive exhaust silencers without mean flow by Cummings [133], who examined a folded annular duct, and El-Sharkawy and Nayfeh [134] who examined a plane expansion chamber. Both authors modelled the discontinuities by using a mode matching formulation, employing Bessel functions as the weighting functions. The introduction of mean flow into an expansion chamber is rather more complex, since the behaviour of the mean flow as it emerges downstream of the first discontinuity is difficult to model accurately and this disrupts the mode matching procedure, see for example Cummings [135]. The problem was, however, tackled by Ih and Lee [136], whose obtained acceptable predictions by including higher order modes and employing a four-pole formulation. Åbom [137] also used four-pole parameters to study higher order mode effects, but added inlet and outlet pipes to the expansion chamber; mean flow effects were, however, neglected. Åbom also employed a mode matching formulation to examine each discontinuity, however the eigenfunctions of each section were used to provide the weighting functions, and these eigenfunctions were shown by Åbom also to be orthogonal.

The study of discontinuities in dissipative silencers is more complex, and less attention has been applied to this problem than the equivalent case in reactive silencers.

One reason for this is, perhaps, the difficulty of finding the eigenvalues in the dissipative section of the silencer. Glav [19] used mode matching to study dissipative silencers with an arbitrary cross section by employing the duct eigenfunctions as the weighting functions. Glav neglected mean flow and used a quasi-orthogonality relationship obtained for the eigenfunctions to simplify the final equations, although a numerical solution was not pursued. Mean flow was introduced into an axisymmetric dissipative silencer by Cummings and Chang [23], who also applied the mode matching method by simply employing the duct eigenfunctions as weighting functions. This method was shown by Cummings and Chang to give good agreement with experimental data despite the fact that when mean flow is present the weighting functions are not orthogonal. Examination of the literature indicates that, to the best of the author's knowledge, the method of Cummings and Chang is the only mode matching method in which dissipative silencers containing both bulk reacting lining and mean flow in the central channel have been studied.

In addition to using mode matching methods to enforce the boundary conditions at each discontinuity in a dissipative silencer, complex alternative methods have also been devised. Sormaz [124], in the belief that non-orthogonal weighting functions should not be used in a mode matching scheme, employed a variational formulation to match conditions at discontinuities in a splitter silencer which was lined with a bulk reacting material. A commonly employed alternative to the mode matching method is the Wiener-Hopf technique, and this approach has been widely developed in the study of electromagnetic waveguides which are, in most cases, analogous to the problem discussed here (see for example, the book by Mittra and Lee [138]). This approach differs from mode matching since instead of expressing the pressure field as a modal sum from which an infinite set of linear equations is obtained, a single equation - known as the Wiener-Hopf equation - is derived by taking a Fourier transform of the governing equations. Nilsson and Brander [21] used a modified Wiener-Hopf technique to study discontinuities in dissipative silencers with mean flow in the central channel and later combined two discontinuities to give predictions for finite length silencers [22]. The advantage of the Wiener-Hopf technique is that it does not depend, as the mode matching method does, on the completeness of the eigenfunctions in the dissipative duct (something which has yet to be proved for dissipative silencers), although the approach is far more complex than the mode matching method.

Of the methods available for enforcing matching conditions onto eigenvalue solutions for infinite dissipative ducts with mean flow in the central channel, the mode matching method appears to be the most straightforward. A study of the alternatives available, namely a variational solution or the Wiener-Hopf method indicates that these introduce too high a degree of complexity for easy implementation in practical design methods. For instance, the variational method of Sormaz [124] requires the separate implementation of both the real and imaginary parts of the matching conditions and this produces a very large number of complex equations, such that implementing this formulation in computer code presents many difficulties. The Wiener-Hopf method is mathematically the most advanced technique, perhaps used most frequently in the study of electromagnetic waveguides, and is beyond the scope of this thesis. One is therefore left with the mode matching method which, at first sight, is a straightforward technique, offering rapid solutions. However, the mode matching method does suffer from a number of problems. For example, the most commonly applied mode matching methods require the use of weighting functions in order to obtain a set of independent linear equations. It appears that some disagreement exists in the literature over whether these weighting functions should be orthogonal. In a number of methods, for example that used by Glav [19], the orthogonality of the eigenfunctions was utilised solely to simplify the final matrices, and this did not imply that the mode matching technique itself depended upon orthogonality to yield the correct results. Sormaz [124], however, asserted that mode matching schemes that employ weighting functions do in fact depend upon orthogonality for the correct results to be obtained. On the other hand, Cummings and Chang [23] did appear to be successful in implementing a mode matching scheme involving the use of non-orthogonal eigenfunctions as weighting functions. Unfortunately it appears that, in the literature, every mode matching method is applied to situations in which the orthogonality of the eigenfunctions is guaranteed, except for the method used by Cummings and Chang. This makes it very difficult to draw definite conclusions about the use of non-orthogonal weighting functions in mode matching schemes. In this chapter the Cummings and Chang method is applied first (see Section 9.3) since this offers the most straightforward method of implementing the matching conditions at the discontinuities. However it will become apparent later that problems were found when applying this method, and that these occur only when mean flow is present, thus coinciding with eigenfunction non-orthogonality. It is difficult to say whether the problems found when implementing the Cummings and Chang method are as a result of the mode matching approach itself requiring modal orthogonality, or simply that orthogonal weighting functions must be used, or even that the weighting functions used by Cummings and Chang are themselves incorrect. In an attempt to tackle this problem, a least squares formulation is applied to the matching conditions in Section 9.4, and this does not require orthogonality from the outset, although weighting functions do appear later in this method and these were found to be similar to those employed by Cummings and Chang. Finally, in Section 9.5, a method is proposed which uses completely different weighting functions from those used in the previous sections and consequently this method is completely independent of the question of orthogonality.

The chapter begins with a listing of the matching conditions necessary for the analysis of dissipative silencers, subsequently the three aforementioned mode matching schemes are presented separately. The mode matching schemes are called here, the "Cummings and Chang method", the "least squares method" and the "integral method". Each method is treated here as a black box, the input being the eigenvalues and eigenvectors obtained in the previous chapter, and the output being transmission loss predictions for a finite length silencer. The results and the problems found in each method are discussed within their individual sections. The performance of each method is independent of the input, and hence the effect of the perforate is irrelevant in the initial testing of each matching scheme. Therefore the perforate is only included in the final transmission loss predictions and these are given in Section 9.6.

Section 9.2

Governing Equations

The implementations of two of the three mode matching schemes presented later in this chapter begin with the same modal representation of the sound pressure in each element of the silencer, and in addition they also involve the application of the same matching conditions to each discontinuity. This section outlines the basic modal representation and matching conditions used in Sections 9.3 and 9.4; a completely different formulation is used in Section 9.5.

The silencer is divided into four sections: the inlet and outlet pipes, which are denoted by regions 3 and 4 respectively, the central channel, denoted by region 1 and the absorbent which is denoted by region 2, see Figure 9.1 below.

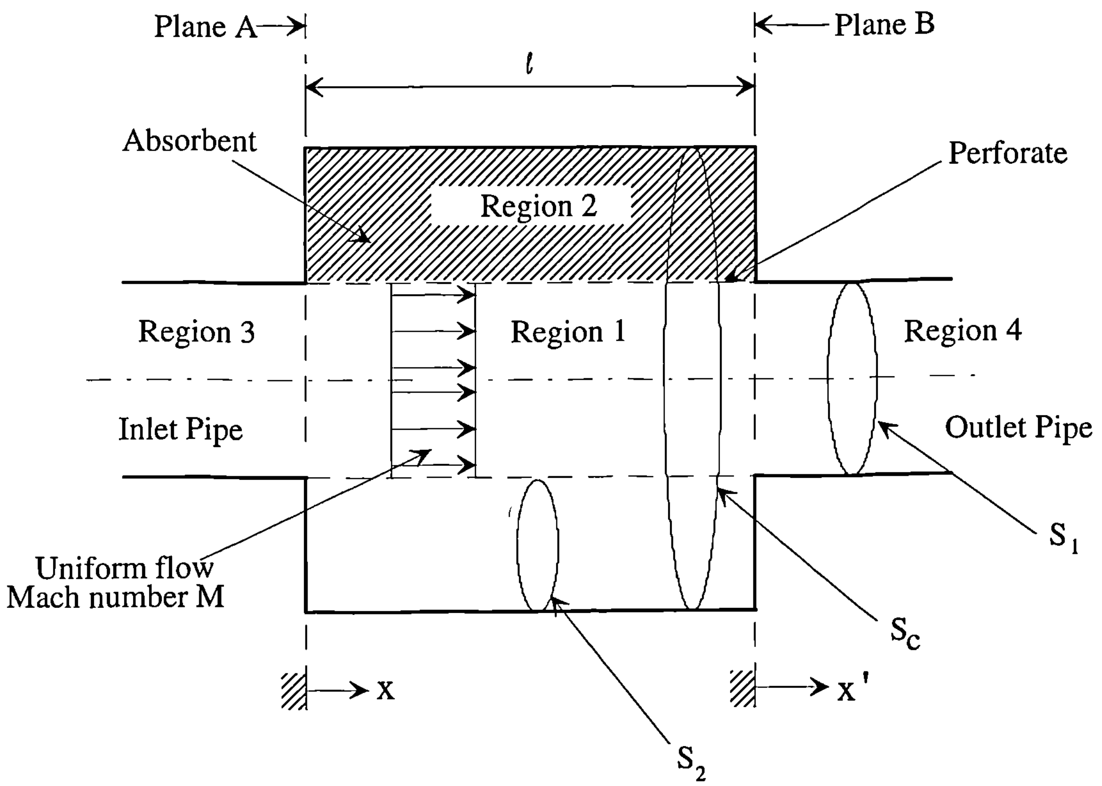

Figure 9.1. Geometry of dissipative silencer.

The silencer, of length l , has discontinuities in planes A and B and a uniform mean flow of Mach number M in the central channel. A section through the silencer is shown in Figure 9.1, and it must be stressed that the cross section of the silencer can assume any shape, according to the model used in Chapter 8, although it must remain uniform along its length. Each section of the silencer has been numbered in the manner shown to avoid confusion with previous chapters. In the three mode matching methods outlined in this chapter, it is assumed that the eigenvalues and eigenfunctions are known for regions 3 and 4 and also for the combination of regions 1 and 2 (denoted collectively as region c).

A modal expansion for both the acoustic pressure and the acoustic particle velocity is now employed, and this has a form similar to that used in Chapter 6. Therefore the acoustic pressure in regions 1 and 2 is given by

$$p_{\mathrm{c}}' = \sum_{n=0}^{\infty} P_{\mathrm{i_c}}^{n} \Psi_{\mathrm{i}}^{n} e^{-ik_0 \lambda_{\mathrm{i}}^{n} x} + \sum_{n=0}^{\infty} P_{\mathrm{r_c}}^{n} \Psi_{\mathrm{r}}^{n} e^{-ik_0 \lambda_{\mathrm{r}}^{n} x}, \tag{9.1}$$

where k_0 is the wavenumber in the central channel, p_{c}' is the acoustic pressure in the chamber (regions 1 and 2), P^n is the modal coefficient, Ψ^n is the transverse modal eigenfunction, λ^n is the dimensionless axial wavenumber (or eigenvalue) and i refers to an incident wave, r to a reflected wave. For the inlet pipe (region 3) the acoustic pressure is given by

$$p_3' = P_{\mathrm{i_3}}^{0} e^{-ik_0 x/(1+M)} + P_{\mathrm{r_3}}^{0} e^{ik_0 x/(1-M)} + \sum_{n=1}^{\infty} P_{\mathrm{r_3}}^{n} R_{\mathrm{r}}^{n} e^{-ik_0 \gamma_{\mathrm{r}}^{n} x} \tag{9.2}$$

and for the outlet pipe (region 4) by

$$p_4' = P_{\mathrm{i_4}}^{0} e^{-ik_0 x'/(1+M)} + \sum_{n=1}^{\infty} P_{\mathrm{i_4}}^{n} R_{\mathrm{i}}^{n} e^{-ik_0 \gamma_{\mathrm{i}}^{n} x'}, \tag{9.3}$$

where $x' = x + l$, P^0 is the modal coefficient for the fundamental mode, R^n is the transverse modal eigenfunction and γ^n is the dimensionless eigenvalue for a hard-walled circular duct (see Morse and Ingård [27]). The fundamental mode ($n = 0$) has been separated from the modal sum in regions 3 and 4 since it can be readily shown that

$\gamma_{\mathrm{i}}^{0}=1/(1+M)$, $\gamma_{\mathrm{r}}^{0}=-1/(1-M)$ and $R_{\mathrm{i,r}}^{0}=1$. In equation (9.2) it is assumed that a plane wave is incident upon the silencer, hence $P_{\mathrm{i}_3}^{n}(n=1,....,\infty)$ is zero, whilst in equation (9.3) it is assumed that the outlet pipe is anechoically terminated, therefore $P_{\mathrm{r}_4}^{n}(n=0,....,\infty)$ is zero.

Use of the Euler equation allows the axial component of the particle velocity in region 1, u'_{x_1}, to be written as

$$\rho_0 c_0 u'_{x_1}=\sum_{n=0}^{\infty}\frac{\lambda_{\mathrm{i}}^{n}}{\left(1-M\lambda_{\mathrm{i}}^{n}\right)}P_{\mathrm{i_c}}^{n}\Psi_{\mathrm{i}}'^{n}e^{-ik_0\lambda_{\mathrm{i}}^{n}x}+\sum_{n=0}^{\infty}\frac{\lambda_{\mathrm{r}}^{n}}{\left(1-M\lambda_{\mathrm{r}}^{n}\right)}P_{\mathrm{r_c}}^{n}\Psi_{\mathrm{r}}'^{n}e^{-ik_0\lambda_{\mathrm{r}}^{n}x} \tag{9.4}$$

and in region 2 as

$$\rho_0 c_0 u'_{x_2}=\sum_{n=0}^{\infty}\frac{\lambda_{\mathrm{i}}^{n}}{\Gamma z_a}P_{\mathrm{i_c}}^{n}\Psi_{\mathrm{i}}''^{n}e^{-ik_0\lambda_{\mathrm{i}}^{n}x}+\sum_{n=0}^{\infty}\frac{\lambda_{\mathrm{r}}^{n}}{\Gamma z_a}P_{\mathrm{r_c}}^{n}\Psi_{\mathrm{r}}''^{n}e^{-ik_0\lambda_{\mathrm{r}}^{n}x}, \tag{9.5}$$

where ρ_0 is the mean fluid density, c_0 is the isentropic speed of sound, u'_x is the acoustic particle velocity in the x direction, Γ is the propagation constant and z_a the characteristic impedance of the bulk porous material. In regions 3 and 4, the axial particle velocity is given by

$$\rho_0 c_0 u'_{x_3}=P_{\mathrm{i}_3}^{0}e^{-ik_0x/(1+M)}-P_{\mathrm{r}_3}^{0}e^{ik_0x/(1-M)}+\sum_{n=1}^{\infty}\frac{\gamma_{\mathrm{r}}^{n}}{\left(1-M\gamma_{\mathrm{r}}^{n}\right)}P_{\mathrm{r}_3}^{n}R_{\mathrm{r}}^{n}e^{-ik_0\gamma_{\mathrm{r}}^{n}x} \tag{9.6}$$

and

$$\rho_0 c_0 u'_{x_4}=P_{\mathrm{i}_4}^{0}e^{-ik_0x'/(1+M)}+\sum_{n=1}^{\infty}\frac{\gamma_{\mathrm{i}}^{n}}{\left(1-M\gamma_{\mathrm{i}}^{n}\right)}P_{\mathrm{i}_4}^{n}R_{\mathrm{i}}^{n}e^{-ik_0\gamma_{\mathrm{i}}^{n}x'}. \tag{9.7}$$

Matching conditions must now be applied to the sound fields at the discontinuities (planes A and B) in order to represent a finite length silencer. The matching conditions to be applied at each discontinuity (according to Cummings and

Chang [23]) are continuity of pressure and continuity of axial particle velocity, so that on plane A,

$$p_3' = p_c', \quad \text{over area } S_1 \text{ on plane A}, \tag{9.8}$$

$$u_3' = u_1', \quad \text{over area } S_1 \text{ on plane A}, \tag{9.9}$$

$$u_2' = 0, \quad \text{over area } S_2 \text{ on plane A}, \tag{9.10}$$

and for plane B

$$p_c' = p_4', \quad \text{over area } S_1 \text{ on plane B}, \tag{9.11}$$

$$u_1' = u_4', \quad \text{over area } S_1 \text{ on plane B}, \tag{9.12}$$

$$u_2' = 0, \quad \text{over area } S_2 \text{ on plane B}. \tag{9.13}$$

The implementation of matching conditions (9.8) to (9.13), using the modal representations given by equations (9.1) to (9.7), is discussed in the context of the Cummings and Chang method and the least squares method in the following two sections.

Section 9.3

Mode Matching using the Cummings and Chang Method

In the introduction to this chapter it was noted that, in the literature, the only mode matching scheme to be applied to discontinuities in dissipative silencers containing mean flow was the method implemented by Cummings and Chang [23]. Fortunately this method is straightforward to apply, and transmission loss predictions can be found in a computationally efficient manner. The method described here follows exactly the formulation used by Cummings and Chang, and so only a brief description is given here. Solutions obtained by the use of this method will be discussed later in this section, in addition to an examination of some of the problems encountered when implementing the method.

The method applied by Cummings and Chang is essentially the standard mode matching technique in which duct eigenfunctions are employed as the weighting functions in order to form a set of linearly independent equations. The formulation used by Cummings and Chang ignores higher order modes in the inlet and outlet pipes since, for applications such as automotive exhausts, the effect of higher order modes, in what are usually small pipes, can reasonably be assumed to be negligible provided these modes are evanescent. Incidentally, the introduction of higher order modes into the inlet and outlet pipes in the method described here is by no means straightforward.

The method proceeds by the multiplication of the pressure and velocity matching conditions by the duct eigenfunctions, integration then being carried out over each region. Therefore the rejection of higher order modes in regions 3 and 4 (see Figure 9.1) allows the continuity of pressure in plane A (equation (9.8) to be written as

$$S_1\left(P_{i_3}^0 + P_{r_3}^0\right) = \sum_{n=0}^{\infty}\left(P_{i_c}^n \int_{S_1} \Psi_i^n dS_1 + P_{r_c}^n \int_{S_1} \Psi_r^n dS_1\right), \tag{9.14}$$

where S_1 is the area of region 1. The implementation of continuity of axial particle velocity in plane A involves grouping together equations (9.9) and (9.10) to give a single matching condition for the velocity. To form a set of linearly independent equations the matching condition is multiplied by Ψ_i^m and integrated, i.e.

$$\int_{S_1} u'_{x_3} \Psi_i^m dS_1 = \int_{S_c} u'_{x_c} \Psi_i^m dS_c. \tag{9.15}$$

The use of equations (9.4) to (9.6) allows equation (9.15) to be written as

$$\left(P_{i_3}^0 + P_{r_3}^0\right)\int_{S_1} \Psi_i^m dS_1 = \sum_{n=0}^{\infty}\left(P_{i_c}^n \int_{S_c} A_i^n \Psi_i^n \Psi_i^m dS_c + P_{r_c}^n \int_{S_c} A_r^n \Psi_r^n \Psi_i^m dS_c\right), \tag{9.16}$$

where

$$A_{\mathrm{i,r}}^{n}=\left\{\begin{array}{ll}\dfrac{\lambda_{\mathrm{i,r}}^{n}}{\left(1-M\lambda_{\mathrm{i,r}}^{n}\right)}, & \text{region 1}\\ \dfrac{\lambda_{\mathrm{i,r}}^{n}}{\Gamma z_{a}}\quad , & \text{region 2}\end{array}\right\}. \tag{9.17}$$

The same procedure is applied to plane B and this gives a continuity of pressure matching condition of

$$S_1 P_{\mathrm{i}_4}^{0}=\sum_{n=0}^{\infty}\left(P_{\mathrm{i_c}}^{n} e^{-ik_0\lambda_{\mathrm{i}}^{n} l}\int_{S_1}\Psi_{\mathrm{i}}^{n} dS_1 + P_{\mathrm{r_c}}^{n} e^{-ik_0\lambda_{\mathrm{r}}^{n} l}\int_{S_1}\Psi_{\mathrm{r}}^{n} dS_1\right) \tag{9.18}$$

and continuity of axial particle velocity of

$$P_{\mathrm{i}_4}^{0}\int_{S_1}\Psi_{\mathrm{i}}^{m} dS_1=\sum_{n=0}^{\infty}\left(P_{\mathrm{i_c}}^{n} e^{-ik_0\lambda_{\mathrm{i}}^{n} l}\int_{S_\mathrm{c}} A_{\mathrm{i}}^{n}\Psi_{\mathrm{i}}^{n}\Psi_{\mathrm{i}}^{m} dS_\mathrm{c} + P_{\mathrm{r_c}}^{n} e^{-ik_0\lambda_{\mathrm{r}}^{n} l}\int_{S_\mathrm{c}} A_{\mathrm{r}}^{n}\Psi_{\mathrm{r}}^{n}\Psi_{\mathrm{i}}^{m} dS_\mathrm{c}\right). \tag{9.19}$$

The problem has now been written as a doubly infinite set of linear equations. To find a solution, equations (9.14), (9.16), (9.18) and (9.19) must be truncated at a suitable point in order to form a set of equations which can be solved simultaneously. In the method used by Cummings and Chang both the modal sums were truncated at the same number of modes (N). The solution was split up by Cummings and Chang who, in an attempt to increase computational accuracy, adopted an iterative method as follows.

Initially, $P_{\mathrm{i}_3}^{0}$ is arbitrarily put equal to unity (real), and the $P_{\mathrm{r_c}}^{n}$ (for $n=0,1,\ldots\ldots,N$) are put equal to zero in plane A. The equations (9.14) and (9.16) (with $m=0,1,\ldots\ldots,N$) are solved for $P_{\mathrm{i_c}}^{n}$ (for $n=0,1,\ldots\ldots,N$) and $P_{\mathrm{r}_3}^{0}$. Next, equations (9.18) and (9.19) (with $m=0,1,\ldots\ldots,N$) are solved for $P_{\mathrm{r_c}}^{n}$ ($n=0,1,\ldots\ldots,N$) and $P_{\mathrm{i}_4}^{0}$, using these $P_{\mathrm{i_c}}^{n}$ values. Then, the $P_{\mathrm{r_c}}^{n}$ values thus obtained are used in the solution to equations (9.14) and (9.16) as before (still with $P_{\mathrm{i}_3}^{0}=1+i0$) to find a new set of $P_{\mathrm{i_c}}^{n}$ values. This process is repeated until the modal amplitudes show an insignificantly small change in successive iteration cycles. The transmission loss of the silencer is then given by

$$\mathrm{TL}=-20\log\left|P_{\mathrm{i}_4}^{0}\right|. \tag{9.20}$$

9.3.1 Results and Discussion

In this section, transmission loss predictions are presented, which were obtained by using exactly the same method as that employed by Cummings and Chang [23]. The values used for Ψ_m and λ_m were supplied from the solution of the eigenvalue problem in Chapter 8, allowing an extension of the method to include silencers with irregular cross sections. The use of the finite element method, described in Chapter 8, also means that the eigenfunctions are supplied in the form of pressure values at individual nodes, relevant to a finite element mesh which, for the individual silencers studied here, were given in Chapter 8. In order to assess the accuracy of the mode matching routine, transmission loss predictions were originally sought using eigenfunctions obtained for the axisymmetric silencers only (without a perforate), since the one dimensional finite element predictions for the eigenfunctions in Chapter 8 provide a set of axisymmetrical modes. It is therefore reasonable to assume here that any problems encountered when applying the mode matching scheme to axisymmetric silencers is not a direct result of numerical problems occurring due to the eigenfunction solutions, such as those associated with the non-axisymmetric modes found in the two dimensional solution.

An examination of both the predictions and the experimental results obtained by Cummings and Chang [23], when neglecting mean flow in the absorbent, appears to show some anomalies. For instance, a study of the experimental transmission loss results found for a positive Mach number, indicate that a rising transmission loss occurs at low frequencies, as the frequency falls (below approximately 200Hz). This is unlikely to reflect the true performance of the silencer, although such measurements are not uncommon. For instance, if one examines the experimental data measured for silencers 1 to 5 with mean flow present in Chapter 5, one finds that, at such frequencies, a similar trend occurs. Such trends in experimental data at very low frequencies are almost certainly caused by experimental error and this is usually exacerbated by flow noise when mean flow is present. One would therefore naturally question the experimental data measured by Cummings and Chang in the same frequency range but with a negative Mach number. Indeed the transmission loss data measured by

Cummings and Chang with M=-0.196 do show the expected trend down to approximately 200Hz, although this trend is reversed over the final number of data points below 200Hz indicating experimental error. Furthermore, for a Mach number of -0.163, Cummings and Chang have measured a transmission loss of approximately 12dB at frequencies as low as 100Hz, a behaviour that, based on other published data for silencers of a similar size, does appear to be unlikely and is, again, probably caused by experimental error. As discussed previously, the discrepancies which have been found in the experimental data of Cummings and Chang are not unexpected, but it is surprising that, when mean flow is present, the mode matching predictions seem to indicate good agreement with experiment, even below 200Hz. For a Mach number of 0.163, the mode matching predictions computed by Cummings and Chang rise at very low frequencies; furthermore when M=-0.163, a transmission loss of approximately 12dB is predicted below 200Hz. This behaviour is surprising since one would intuitively expect the transmission loss of the silencer to tend towards zero as the frequency approached zero, regardless of the direction of mean flow and this behaviour has indeed been predicted by others (see for example Peat [13] and Peat and Rathi [26]). These apparent discrepancies observed in the predictions of Cummings and Chang were also noted by Peat and Rathi [26], who compared their full finite element predictions with Cummings' and Chang's mode matching method. Peat and Rathi observed significant differences between their finite element predictions and the predicted data of Cummings and Chang, and they tentatively proposed that the differences between the two models were caused by errors occurring in the Delany and Bazley formulae used by Cummings and Chang at very low frequencies. However it does appear unlikely that this can be the sole cause of the discrepancies observed at low frequencies and therefore it is worthwhile re-examining the predictions found by Cummings and Chang.

In light of the above discussion, the Cummings and Chang method was first used here to generate numerical predictions for the particular silencer measured by Cummings and Chang. For consistency with their method, the Delany and Bazley formulae were used to predict the bulk properties of the absorbent, rather than the semi-empirical model described in Chapter 3. Figure 9.2 shows the mode matching predictions obtained for Cummings' and Chang's silencer, first without mean flow in the central channel (using 6 modes), then with a Mach number of 0.197 and -0.197 using only 1 mode, and finally with a Mach number of 0.197 using 6 modes. It is immediately obvious that there are some significant differences between the predictions obtained here and those found by Cummings and Chang, although the predictions found without mean flow do appear to be identical. When mean flow is introduced, and when only 1 mode is present, the predictions obtained here now exhibit the correct limiting behaviour at low frequencies. This sheds further doubt upon the numerical predictions of Cummings and Chang, especially since the higher order modes should have little effect upon the transmission loss at very low frequencies. To check the mode matching method used here further, the predictions obtained using only one mode were compared to those obtained by using the full finite element method described in Chapter 7. Both models were observed to be in good agreement across the frequency range but especially, as one would expect, at low frequencies. Therefore one can conclude that differences between Cummings' and Chang's predictions and the finite element predictions obtained by Peat and Rathi [26] are not the result of different applications of porous material data. The most significant discrepancies between the mode matching predictions found here and those obtained by Cummings and Chang appear when higher order modes are introduced into a solution which also contains mean flow. The predictions shown for M=0.197 in Figure 9.2, using 6 modes, are substantially different from those obtained for a single mode and also the multi-mode solutions of Cummings and Chang, especially at low frequencies where the multi-mode solution implemented here predicts a negative transmission loss below 100Hz. At very low frequencies, predictions found using 1 mode and 6 modes should be similar, or at least the differences should be similar to those observed between a single mode solution and a full finite element solution. Consequently the results obtained indicate that problems have also occurred when implementing the mode matching scheme here. The reasons behind the differences observed between the results published here and those obtained by Cummings and Chang are unknown, but the author is led to conclude here that errors must be present in the predictions obtained by Cummings and Chang, especially considering their poor correlation with the finite element method. Unfortunately one must also conclude that the mode matching method itself is flawed, since problems are now evident when higher order modes are introduced into solutions which contain mean flow. These predictions, shown in Figure 9.2, indicate a large difference between the single mode and multi-mode solution, and this occurs no matter how many higher order modes are used. Furthermore, the convergence of the solution when mean flow was present also caused problems, since the results often fluctuated significantly, making identification of convergence difficult. This problem could not be solved by simply using a large number of modes since if more than 12 modes were used numerical problems became apparent.

In order to investigate Cummings' and Chang's method further, predictions were also made (without a perforate) for silencers 1 to 5, both with and without mean flow, and these are shown in Figures 9.3 to 9.5. It is evident that, when no mean flow is present, the correlation between the multi-mode predictions and experimental data is good and is at least comparable to the accuracy found when using the full finite element method in Chapter 7. Indeed when studying the elliptical silencers, the problems observed at low frequencies when using the full finite element method are no longer encountered here. When mean flow is introduced, the mode matching predictions still appear to be good when only one mode is used. Again, in most cases, the mode matching predictions provide accuracy comparable to that found using the full finite element method, although the correlation is not as good as that found for no mean flow. However problems are again observed when higher order modes are introduced with mean flow and these are at their most obvious in the low frequency range. Although a negative transmission loss is not found in Figures 9.3 to 9.5, there is still a significant difference between the single and multi-mode predictions at low frequencies. It appears that the largest discrepancies are found for the silencers which contain absorbent materials with a low flow resistivity, see for example the predictions found for silencers 3 and 4 (Figure 9.4), which contain A glass and basalt wool respectively. This observation correlates with the somewhat larger discrepancies found for the Cummings and Chang silencer, since this silencer contained a material with an even lower flow resistivity than those studied here. Therefore it appears that the size of the errors encountered when implementing the multi-mode solution are linked to the flow resistivity of the absorbent. However, after the study of an additional five silencers here, one must still conclude that the mode matching predictions obtained by using the Cummings and Chang mode matching method are unreliable, principally when mean flow is used in conjunction with higher order modes.

The exact reasons which lie behind the failure of the Cummings and Chang method when mean flow is introduced are difficult to pinpoint; however, it is perhaps more than coincidental that the problems have occurred when the eigenfunctions are known to be non-orthogonal. The use of non-orthogonal eigenfunctions in this analysis merely has the effect of introducing non zero contributions to off-diagonal elements in the matrices obtained from equation (9.16) and (9.19). It is not clear why the inclusion of off-diagonal contributions should cause any problems to the solution of the matrices, although it is possible that they build instabilities into the final numerical solutions.

Despite the problems found with Cummings and Chang's method it does appear to provide satisfactory predictions when the modes are orthogonal. This is the case when no mean flow is present (for any number of modes) and when 1 mode is used in the presence of mean flow (where the question of orthogonality is irrelevant). In fact, the predictions found when only one mode is present appear to provide good correlation with experimental data for the silencers studied here. Furthermore, when mean flow is present, the predictions are, in most cases, within 1 or 2 dB of those found using the full finite element method. However, it is intended in this chapter to provide a more general mode matching model, one which can be used in the study of much larger silencers and this inevitably requires the introduction of the higher order modes. Consequently, a new method is tried in the next section which attempts to resolve the problems found here.

Section 9.4

A Least Squares Approach to Mode Matching

The problems apparent when applying the mode matching method of Cummings and Chang [23] mean that it is necessary to examine other methods. A well known alternative to the Galerkin type of approach used in the previous section is the least squares method. The least squares method simply requires that the sum of the square of the errors over the entire range of the independent variable be reduced to zero. Therefore applying the least squares formulation to the mode matching method requires that the sum of the square of the errors found in each matching condition (equations (9.8) to (9.13)) must be reduced to zero. The original motivation behind employing this method was the desire to remove the question of orthogonality which arose in the mode matching formulation described in Section 9.3. However it will become apparent later in this section that a form of weighting function is still required in the least squares method studied here. Consequently, although the method itself should not depend upon orthogonality, if these weighting functions are indeed "incorrect" for use in this type of problem, then the solutions found in this section may behave in the same way as those found previously. One advantage that is gained by using a least squares formulation is that the introduction of the higher order modes into the inlet and outlet ducts is relatively straightforward. Consequently these higher order modes are included here for completeness.

The basic principles behind the least squares approach are very simple. For instance, the continuity of pressure matching condition on plane A (equation (9.8)) requires that $p_3' = p_c'$ over area S_1. In the least squares approach it is assumed that an error is present in this matching condition and this is called the error function where

$$\varepsilon_1 = p_c' - p_3', \tag{9.21}$$

and ε_1 is the error function associated with equation (9.8). The mean square sum of the errors over area S_1 is now minimised. Therefore, if the sum of the mean square errors is called the deviation function, then

$$D_1 = \int_{S_1} \varepsilon_1^2 dS_1, \tag{9.22}$$

where D_1 is the deviation function associated with equation (9.8). To ensure that the deviation function is a minimum, one must equate the partial derivative of D_1, with respect to the unknown variables in equation (9.21), to zero. Therefore, if the modal representations for p_c' and p_3' (equations (9.1) and (9.2)) are substituted into equation (9.21),

$$\varepsilon_1 = \sum_{n=0}^{\infty}\left(P_{i_c}^n \Psi_i^n + P_{r_c}^n \Psi_r^n\right) - \left(P_{i_3}^0 + P_{r_3}^0 + \sum_{n=1}^{\infty} P_{r_3}^n R_r^n\right), \tag{9.23}$$

and taking the partial derivatives of the deviation function with respect to $P_{r_3}^m$ and P_{i_c,r_c}^m gives

$$\frac{\partial D_1}{\partial P_{r_3}^m} = -2\int_{S_1}\left\{\sum_{n=0}^{\infty}\left(P_{i_c}^n \Psi_i^n + P_{r_c}^n \Psi_r^n\right) - \left(P_{i_3}^0 + P_{r_3}^0 + \sum_{n=1}^{\infty} P_{r_3}^n R_r^n\right)\right\} R_r^m dS_1 = 0, \tag{9.24}$$

and

$$\frac{\partial D_1}{\partial P_{i_c,r_c}^m} = 2\int_{S_1}\left\{\sum_{n=0}^{\infty}\left(P_{i_c}^n \Psi_i^n + P_{r_c}^n \Psi_r^n\right) - \left(P_{i_3}^0 + P_{r_3}^0 + \sum_{n=1}^{\infty} P_{r_3}^n R_r^n\right)\right\} \Psi_{i,r}^m dS_1 = 0. \tag{9.25}$$

Two independent equations have now been formulated from the continuity of pressure matching condition over plane A; it is, however, noticeable that "weighting functions" similar to those found in the previous section are now present.

The least squares process must now be repeated for the other five matching conditions. For continuity of axial particle velocity over plane A, equations (9.9) and (9.10) give error functions of

$$\varepsilon_2 = \rho_0 c_0 \left(u'_{x_c} - u'_{x_1} \right) \quad \text{and} \quad \varepsilon_3 = \rho_0 c_0 u'_{x_c}, \tag{9.26), (9.27}$$

where ε_2 is the error function associated with equation (9.9) and ε_3 the error function associated with equation (9.10). For the particle velocity matching condition the two error functions are combined, giving

$$D_2 = \int_{S_1} \varepsilon_2^2 dS_1 + \int_{S_2} \varepsilon_3^2 dS_2. \tag{9.28}$$

Substituting equations (9.4), (9.5) and (9.6) into equations (9.26) and (9.27) allows the partial derivative of D_2 to be taken with respect to $P_{\mathrm{r}_3}^m$ and $P_{\mathrm{i_c,r_c}}^m$, giving

$$\frac{\partial D_2}{\partial P_{\mathrm{r}_3}^m} = -2 \int_{S_1} \left\{ \sum_{n=0}^{\infty} \left(P_{\mathrm{i_c}}^n A_{\mathrm{i}}^n \Psi_{\mathrm{i}}^n + P_{\mathrm{r_c}}^n A_{\mathrm{r}}^n \Psi_{\mathrm{r}}^n \right) - \left(P_{\mathrm{i}_3}^0 - P_{\mathrm{r}_3}^0 + \sum_{n=1}^{\infty} P_{\mathrm{r}_3}^n Y_{\mathrm{r}}^n R_{\mathrm{r}}^n \right) \right\} Y_{\mathrm{r}}^m R_{\mathrm{r}}^m dS_1 = 0 \tag{9.29}$$

and

$$\frac{\partial D_2}{\partial P_{\mathrm{i_c,r_c}}^m} = 2 \int_{S_1} \left\{ \sum_{n=0}^{\infty} \left(P_{\mathrm{i_c}}^n A_{\mathrm{i}}^n \Psi_{\mathrm{i}}^n + P_{\mathrm{r_c}}^n A_{\mathrm{r}}^n \Psi_{\mathrm{r}}^n \right) - \left(P_{\mathrm{i}_3}^0 - P_{\mathrm{r}_3}^0 + \sum_{n=1}^{\infty} P_{\mathrm{r}_3}^n Y_{\mathrm{r}}^n R_{\mathrm{r}}^n \right) \right\} A_{\mathrm{i,r}}^m \Psi_{\mathrm{i,r}}^m dS_1$$

$$+ 2 \int_{S_2} \left\{ \sum_{n=0}^{\infty} \left(P_{\mathrm{i_c}}^n A_{\mathrm{i}}^n \Psi_{\mathrm{i}}^n + P_{\mathrm{r_c}}^n A_{\mathrm{r}}^n \Psi_{\mathrm{r}}^n \right) \right\} A_{\mathrm{i,r}}^m \Psi_{\mathrm{i,r}}^m dS_2 = 0, \tag{9.30}$$

where

$$Y_{\mathrm{i,r}}^n = \gamma_{\mathrm{i,r}}^n / \left(1 - M \gamma_{\mathrm{i,r}}^n \right). \tag{9.31}$$

The same procedure is now repeated for plane B, where the error functions ε_4, ε_5 and ε_6 are given by

$$\varepsilon_4 = p'_c - p'_4, \quad \varepsilon_5 = \rho_0 c_0 \left(u'_{x_c} - u'_{x_4}\right) \text{ and } \varepsilon_6 = \rho_0 c_0 u'_{x_c}. \qquad (9.32), (9.33), (9.34)$$

The deviation functions for plane B are then defined as

$$D_3 = \int_{S_1} \varepsilon_4^2 dS_1 \text{ and } D_4 = \int_{S_1} \varepsilon_5^2 dS_1 + \int_{S_2} \varepsilon_6^2 dS_2. \qquad (9.35), (9.36)$$

The substitution of equations (9.1) and (9.3) into equation (9.32) and equations (9.4), (9.5) and (9.7) into equations (9.33) and (9.34), allows the partial derivatives of the deviation functions to be taken, and for the continuity of pressure matching condition this gives

$$\frac{\partial D_3}{\partial P^m_{\mathrm{i}_4}} = -2\int_{S_1} \left\{ \sum_{n=0}^{\infty} \left(P^n_{\mathrm{i}_c} \Psi^n_{\mathrm{i}} e^{-ik_0\lambda^n_{\mathrm{i}} l} + P^n_{\mathrm{r}_c} \Psi^n_{\mathrm{r}} e^{-ik_0\lambda^n_{\mathrm{r}} l} \right) - \left(P^0_{\mathrm{i}_4} + \sum\nolimits_{n=1}^{\infty} P^n_{\mathrm{i}_4} R^n_{\mathrm{i}} \right) \right\} R^m_{\mathrm{i}} dS_1 = 0 \qquad (9.37)$$

and

$$\frac{\partial D_3}{\partial P^m_{\mathrm{i}_c,\mathrm{r}_c}} = 2\int_{S_1} \left\{ \sum_{n=0}^{\infty} \left(P^n_{\mathrm{i}_c} \Psi^n_{\mathrm{i}} e^{-ik_0\lambda^n_{\mathrm{i}} l} + P^n_{\mathrm{r}_c} \Psi^n_{\mathrm{r}} e^{-ik_0\lambda^n_{\mathrm{r}} l} \right) - \left(P^0_{\mathrm{i}_4} + \sum\nolimits_{n=1}^{\infty} P^n_{\mathrm{i}_4} R^n_{\mathrm{i}} \right) \right\} \Psi^m_{\mathrm{i,r}} e^{-ik_0\lambda^m_{\mathrm{i,r}} l} dS_1 = 0. \qquad (9.38)$$

For the continuity of axial particle velocity matching condition over plane B,

$$\frac{\partial D_4}{\partial P^m_{\mathrm{i}_4}} = -2\int_{S_1} \left\{ \sum_{n=0}^{\infty} \left(P^n_{\mathrm{i}_c} A^n_{\mathrm{i}} \Psi^n_{\mathrm{i}} e^{-ik_0\lambda^n_{\mathrm{i}} l} + P^n_{\mathrm{r}_c} A^n_{\mathrm{r}} \Psi^n_{\mathrm{r}} e^{-ik_0\lambda^n_{\mathrm{r}} l} \right) - \left(P^0_{\mathrm{i}_4} + \sum\nolimits_{n=1}^{\infty} P^n_{\mathrm{i}_4} Y^n_{\mathrm{i}} R^n_{\mathrm{i}} \right) \right\} Y^m_{\mathrm{i}} R^m_{\mathrm{i}} dS_1 = 0 \qquad (9.39)$$

and

$$\frac{\partial D_4}{\partial P^m_{\mathrm{i}_c,\mathrm{r}_c}} = 2\int_{S_1} \left\{ \sum_{n=0}^{\infty} \left(P^n_{\mathrm{i}_c} A^n_{\mathrm{i}} \Psi^n_{\mathrm{i}} e^{-ik_0\lambda^n_{\mathrm{i}} l} + P^n_{\mathrm{r}_c} A^n_{\mathrm{r}} \Psi^n_{\mathrm{r}} e^{-ik_0\lambda^n_{\mathrm{r}} l} \right) - \left(P^0_{\mathrm{i}_4} + \sum\nolimits_{n=1}^{\infty} P^n_{\mathrm{i}_4} Y^n_{\mathrm{i}} R^n_{\mathrm{i}} \right) \right\} A^m_{\mathrm{i,r}} \Psi^m_{\mathrm{i,r}} e^{-ik_0\lambda^m_{\mathrm{i,r}} l} dS_1$$

$$+2\int_{S_2} \left\{ \sum_{n=0}^{\infty} \left(P^n_{\mathrm{i}_c} A^n_{\mathrm{i}} \Psi^n_{\mathrm{i}} e^{-ik_0\lambda^n_{\mathrm{i}} l} + P^n_{\mathrm{r}_c} A^n_{\mathrm{r}} \Psi^n_{\mathrm{r}} e^{-ik_0\lambda^n_{\mathrm{r}} l} \right) \right\} A^m_{\mathrm{i,r}} \Psi^m_{\mathrm{i,r}} e^{-ik_0\lambda^m_{\mathrm{i,r}} l} dS_2 = 0. \qquad (9.40)$$

A set of eight independent equations has resulted from enforcing the matching conditions on planes A and B using the least squares method. To find the transmission loss of the silencer it is now necessary to solve these eight equations to find $P^0_{\mathrm{i}_4}$. To do this it is first necessary to eliminate $P^0_{\mathrm{r}_3}$ and $P^0_{\mathrm{i}_4}$ from the eight equations. For plane A, this can be done by first adding equation (9.24) to equation (9.29), and this gives

$$\int_{S_1}\left\{\sum_{n=0}^{\infty}\left(\left[1+A_{\mathrm{i}}^n\right]P_{\mathrm{i_c}}^n\Psi_{\mathrm{i}}^n+\left[1+A_{\mathrm{r}}^n\right]P_{\mathrm{r_c}}^n\Psi_{\mathrm{r}}^n\right)-\sum\nolimits_{n=1}^{\infty}\left[1+Y_{\mathrm{r}}^n\right]P_{\mathrm{r_3}}^n R_{\mathrm{r}}^n\right\}R_{\mathrm{r}}^m dS_1=2P_{\mathrm{i_3}}^0\int_{S_1}R_{\mathrm{r}}^m dS_1 .$$

$$(m=1,2,.....,\infty) \qquad (9.41)$$

To eliminate $P^0_{\mathrm{r}_3}$ from equations (9.25) and (9.30), one must first multiply equation (9.25) by $A^m_{\mathrm{i,r}}$ and then add this to equation (9.30), which gives

$$\int_{S_1}\left\{\sum_{n=0}^{\infty}\left(\left[1+A_{\mathrm{i}}^n\right]P_{\mathrm{i_c}}^n\Psi_{\mathrm{i}}^n+\left[1+A_{\mathrm{r}}^n\right]P_{\mathrm{r_c}}^n\Psi_{\mathrm{r}}^n\right)-\sum\nolimits_{n=1}^{\infty}\left[1+Y_{\mathrm{r}}^n\right]P_{\mathrm{r_3}}^n R_{\mathrm{r}}^n\right\}A_{\mathrm{i}}^m\Psi_{\mathrm{i}}^m dS_1$$

$$+\int_{S_2}\left\{\sum_{n=0}^{\infty}\left(P_{\mathrm{i_c}}^n A_{\mathrm{i}}^n\Psi_{\mathrm{i}}^n+P_{\mathrm{r_c}}^n A_{\mathrm{r}}^n\Psi_{\mathrm{r}}^n\right)\right\}A_{\mathrm{i}}^m\Psi_{\mathrm{i}}^m dS_2=2P_{\mathrm{i_3}}^0\int_{S_1}A_{\mathrm{i}}^m\Psi_{\mathrm{i}}^m dS_1 .$$

$$(m=0,1,.....,\infty) \qquad (9.42)$$

The same procedure is now applied to the equations found for plane B, and here equation (9.39) is subtracted from equation (9.37) to give

$$\int_{S_1}\left\{\sum_{n=0}^{\infty}\left(\left[1-A_{\mathrm{i}}^n\right]P_{\mathrm{i_c}}^n\Psi_{\mathrm{i}}^n e^{-ik_0\lambda_{\mathrm{i}}^n l}+\left[1-A_{\mathrm{r}}^n\right]P_{\mathrm{r_c}}^n\Psi_{\mathrm{r}}^n e^{-ik_0\lambda_{\mathrm{r}}^n l}\right)-\sum\nolimits_{n=1}^{\infty}\left[1-Y_{\mathrm{i}}^n\right]P_{\mathrm{i_4}}^n R_{\mathrm{i}}^n\right\}R_{\mathrm{i}}^m dS_1=0,$$

$$(m=1,2,.....,\infty) \qquad (9.43)$$

and multiplying equation (9.38) by $A^m_{\mathrm{i,r}}$ and subtracting from it equation (9.40) gives

$$\int_{S_1}\left\{\sum_{n=0}^{\infty}\left(\left[1-A_{\mathrm{i}}^{n}\right]P_{\mathrm{i_c}}^{n}\Psi_{\mathrm{i}}^{n}e^{-ik_0\lambda_{\mathrm{i}}^{n}l}+\left[1-A_{\mathrm{r}}^{n}\right]P_{\mathrm{r_c}}^{n}\Psi_{\mathrm{r}}^{n}e^{-ik_0\lambda_{\mathrm{r}}^{n}l}\right)-\sum_{n=1}^{\infty}\left[1-Y_{\mathrm{i}}^{n}\right]P_{\mathrm{i_4}}^{n}R_{\mathrm{i}}^{n}\right\}A_{\mathrm{r}}^{m}\Psi_{\mathrm{r}}^{m}dS_1$$

$$-\int_{S_2}\left\{\sum_{n=0}^{\infty}\left(P_{\mathrm{i_c}}^{n}A_{\mathrm{i}}^{n}\Psi_{\mathrm{i}}^{n}e^{-ik_0\lambda_{\mathrm{i}}^{n}l}+P_{\mathrm{r_c}}^{n}A_{\mathrm{r}}^{n}\Psi_{\mathrm{r}}^{n}e^{-ik_0\lambda_{\mathrm{r}}^{n}l}\right)\right\}A_{\mathrm{r}}^{m}\Psi_{\mathrm{r}}^{m}dS_2=0.$$

$$(m=0,1,.....,\infty) \qquad (9.44)$$

Equations (9.41) to (9.44) can be combined into a single matrix equation which can then be solved directly for $P_{\mathrm{i_c}}^{n}$, $P_{\mathrm{r_c}}^{n}$, $P_{\mathrm{r_3}}^{n}$ and $P_{\mathrm{i_4}}^{n}$ once the incident plane wave has been assigned unit amplitude (i.e. $P_{\mathrm{i_3}}^{0}=(1+i0)$). First, however, the infinite series must be truncated and this is carried out at the same point for m and n, denoted here by N. In order to show how equations (9.41) to (9.44) are combined into a single matrix equation, it is convenient to write each equation in matrix form. Accordingly, defining the following matrices as

$$[\mathbf{K}_1]_{\mathrm{i}}^{\mathrm{A}}=\int_{S_1}\left[1+A_{\mathrm{i}}^{n}\right]R_{\mathrm{r}}^{m}\Psi_{\mathrm{i}}^{n}dS_1 \qquad (n=0,1,.....,N),\ (m=1,2,.....,N) \qquad (9.45)$$

$$[\mathbf{K}_1]_{\mathrm{r}}^{\mathrm{A}}=\int_{S_1}\left[1+A_{\mathrm{r}}^{n}\right]R_{\mathrm{r}}^{m}\Psi_{\mathrm{r}}^{n}dS_1 \qquad (n=0,1,.....,N),\ (m=1,2,.....,N) \qquad (9.46)$$

$$[\mathbf{K}_2]_{\mathrm{i}}^{\mathrm{A}}=\int_{S_1}\left[1+A_{\mathrm{i}}^{n}\right]A_{\mathrm{i}}^{m}\Psi_{\mathrm{i}}^{n}\Psi_{\mathrm{i}}^{m}dS_1+\int_{S_2}A_{\mathrm{i}}^{n}A_{\mathrm{i}}^{m}\Psi_{\mathrm{i}}^{n}\Psi_{\mathrm{i}}^{m}dS_2$$

$$(n=0,1,.....,N),\ (m=0,1,.....,N) \qquad (9.47)$$

$$[\mathbf{K}_2]_{\mathrm{r}}^{\mathrm{A}}=\int_{S_1}\left[1+A_{\mathrm{r}}^{n}\right]A_{\mathrm{i}}^{m}\Psi_{\mathrm{r}}^{n}\Psi_{\mathrm{i}}^{m}dS_1+\int_{S_2}A_{\mathrm{r}}^{n}A_{\mathrm{i}}^{m}\Psi_{\mathrm{r}}^{n}\Psi_{\mathrm{i}}^{m}dS_2$$

$$(n=0,1,.....,N),\ (m=0,1,.....,N) \qquad (9.48)$$

$$[\mathbf{M}_1]^{\mathrm{A}}=-\int_{S_1}\left[1+Y_{\mathrm{r}}^{n}\right]R_{\mathrm{r}}^{n}R_{\mathrm{r}}^{m}dS_1 \qquad (n=1,2,.....,N),\ (m=1,2,.....,N) \qquad (9.49)$$

$$[\mathbf{M}_2]^{\mathrm{A}}=-\int_{S_1}\left[1+Y_{\mathrm{r}}^{n}\right]A_{\mathrm{i}}^{m}R_{\mathrm{r}}^{n}\Psi_{\mathrm{i}}^{m}dS_1 \qquad (n=1,2,.....,N),\ (m=0,1,.....,N) \qquad (9.50)$$

$$[\mathbf{K}_1]_{\mathrm{i}}^{\mathrm{B}}=\int_{S_1}\left[1-A_{\mathrm{i}}^{n}\right]R_{\mathrm{i}}^{m}\Psi_{\mathrm{i}}^{n}e^{-ik_0\lambda_{\mathrm{i}}^{n}l}dS_1 \qquad (n=0,1,.....,N),\ (m=1,2,.....,N) \qquad (9.51)$$

$$[\mathbf{K}_1]_{\mathrm{r}}^{\mathrm{B}}=\int_{S_1}\left[1-A_{\mathrm{r}}^{n}\right]R_{\mathrm{i}}^{m}\Psi_{\mathrm{r}}^{n}e^{-ik_0\lambda_{\mathrm{r}}^{n}l}dS_1 \qquad (n=0,1,.....,N),\ (m=1,2,.....,N) \qquad (9.52)$$

$$[\mathbf{K}_2]_{\mathrm{i}}^{\mathrm{A}}=\int_{S_1}\left[1-A_{\mathrm{i}}^{n}\right]A_{\mathrm{r}}^{m}\Psi_{\mathrm{i}}^{n}\Psi_{\mathrm{r}}^{m}e^{-ik_0\lambda_{\mathrm{i}}^{n}l}dS_1-\int_{S_2}A_{\mathrm{i}}^{n}A_{\mathrm{r}}^{m}\Psi_{\mathrm{i}}^{n}\Psi_{\mathrm{r}}^{m}e^{-ik_0\lambda_{\mathrm{i}}^{n}l}dS_2$$

$$(n=0,1,.....,N),\ (m=0,1,.....,N) \qquad (9.53)$$

$$[\mathbf{K}_2]_{\mathrm{r}}^{\mathrm{B}} = \int_{S_1} [1 - A_{\mathrm{r}}^n] A_{\mathrm{r}}^m \Psi_{\mathrm{r}}^n \Psi_{\mathrm{r}}^m e^{-ik_0\lambda_{\mathrm{r}}^n l} dS_1 - \int_{S_2} A_{\mathrm{r}}^n A_{\mathrm{r}}^m \Psi_{\mathrm{r}}^n \Psi_{\mathrm{r}}^m e^{-ik_0\lambda_{\mathrm{r}}^n l} dS_2$$

$$(n = 0,1,\ldots\ldots,N),\ (m = 0,1,\ldots\ldots,N) \tag{9.54}$$

$$[\mathbf{M}_1]^{\mathrm{B}} = \int_{S_1} [1 - Y_{\mathrm{i}}^n] R_{\mathrm{i}}^n R_{\mathrm{i}}^m dS_1 \qquad (n = 1,2,\ldots\ldots,N),\ (m = 1,2,\ldots\ldots,N) \tag{9.55}$$

$$[\mathbf{M}_2]^{\mathrm{B}} = \int_{S_1} [1 - Y_{\mathrm{i}}^n] A_{\mathrm{r}}^m R_{\mathrm{i}}^n \Psi_{\mathrm{r}}^m dS_1 \qquad (n = 1,2,\ldots\ldots,N),\ (m = 0,1,\ldots\ldots,N) \tag{9.56}$$

$$[\mathbf{R}_1] = 2\int_{S_1} R_{\mathrm{r}}^m dS_1 \qquad (m = 1,2,\ldots\ldots,N) \tag{9.57}$$

$$[\mathbf{R}_2] = 2\int_{S_1} A_{\mathrm{i}}^m \Psi_{\mathrm{i}}^m dS_1 \qquad (m = 0,1,\ldots\ldots,N) \tag{9.58}$$

allows equation (9.41) to (9.44) to be written in the form

$$\begin{bmatrix} [\mathbf{K}_1]_{\mathrm{i}}^{\mathrm{A}} & [\mathbf{K}_1]_{\mathrm{r}}^{\mathrm{A}} & [\mathbf{M}_1]^{\mathrm{A}} & 0 \\ [\mathbf{K}_2]_{\mathrm{i}}^{\mathrm{A}} & [\mathbf{K}_2]_{\mathrm{r}}^{\mathrm{A}} & [\mathbf{M}_2]^{\mathrm{A}} & 0 \\ [\mathbf{K}_1]_{\mathrm{i}}^{\mathrm{B}} & [\mathbf{K}_1]_{\mathrm{r}}^{\mathrm{B}} & 0 & [\mathbf{M}_1]^{\mathrm{B}} \\ [\mathbf{K}_2]_{\mathrm{i}}^{\mathrm{B}} & [\mathbf{K}_2]_{\mathrm{r}}^{\mathrm{B}} & 0 & [\mathbf{M}_2]^{\mathrm{B}} \end{bmatrix} \begin{Bmatrix} \mathbf{p}_{\mathrm{i_c}} \\ \mathbf{p}_{\mathrm{r_c}} \\ \mathbf{p}_{\mathrm{r_3}} \\ \mathbf{p}_{\mathrm{i_4}} \end{Bmatrix} = \begin{Bmatrix} [\mathbf{R}_1] \\ [\mathbf{R}_2] \\ \mathbf{0} \\ \mathbf{0} \end{Bmatrix}. \tag{9.59}$$

Equation (9.59) provides solutions for $P_{\mathrm{i_c}}^n(n = 0, N)$, $P_{\mathrm{r_c}}^n(n = 0, N)$, $P_{\mathrm{r_3}}^n(n = 1, N)$ and $P_{\mathrm{i_4}}^n(n = 1, N)$. These solutions are then substituted back into equation (6.37) to find a value for $P_{\mathrm{i_4}}^0$. The transmission loss (TL) is then given by

$$\mathrm{TL} = -20\log\left|P_{\mathrm{i_4}}^0\right|. \tag{9.60}$$

9.4.1 Results and Discussion

It was mentioned at the beginning of this section that, although the derivation of the least squares method does not rely on eigenfunction orthogonality, problems do begin to appear. This is evident after examination of the matrices which make up equation (9.59). For example, the $[\mathbf{K}_2]$ matrices contain integration of products of the duct eigenfunctions similar to those appearing in the Cummings and Chang method. Therefore if this non-orthogonality relationship is the root cause of the problems found in Section 9.3, one would also expect to encounter problems in this section too.

In the previous section, the problems associated with the mode matching scheme were at their most obvious when studying the silencer used by Cummings and Chang [23], and therefore this silencer is modelled first in this section. Transmission loss predictions obtained by using the least squares method for Cummings' and Chang's silencer are shown at the top of Figure 9.6, both with and without mean flow. The solutions shown in Figure 9.6 were both found using 8 modes, i.e. $N = 8$ in equation (9.59). When no mean flow is present, the least squares formulation provides predictions very close to those found using the Cummings and Chang method (see Figure 9.2). Incidentally, when mean flow was not present, the least squares approach took longer to converge than the Cummings and Chang method, hence the use of more modes in Figure 9.6. Also, slight differences between the predictions of the two models are evident at higher frequencies, though this is probably attributable to the inclusion of higher order modes in the inlet and outlet pipes in this section. When mean flow is introduced, problems similar to those found in the previous section are apparent. For instance, a negative transmission loss is once again predicted below 100Hz. The least squares predictions, including mean flow, are shown in Figure 9.6 for 8 modes only. No comparison with the single mode solution is shown since it was only for 8 modes that the solution was found to converge. Indeed the convergence of the least squares method proved to be somewhat erratic and, as with the Cummings and Chang method, numerical instabilities appeared for more than 12 modes. In fact the least squares method provided very inaccurate predictions when using only one mode. The reasons behind this are not clear, although it is possible that it was caused by solving the whole problem in a single step, in contrast to the iterative procedure employed in the Cummings and Chang method.

Transmission loss predictions were also obtained for the axisymmetric silencers of Chapter 5 (silencers 1, 2 and 3) in order to confirm the trends shown in the top of Figure 9.6. The least squares predictions for silencers 1, 2 and 3 are shown in Figures 9.6 and 9.7, both with and without flow. Further predictions were not obtained for the oval silencers since these were not expected to provide any additional information about the accuracy of the model. Figures 9.6 and 9.7 indicate that, for silencers 1 to 3, the least squares method predicts results similar to that found using the Cummings and Chang method. For instance, when no mean flow is present, the predictions correlate well with experimental data and they are also very similar to those found using the Cummings and Chang method. However, the problems found with the convergence of the least squares solutions are apparent when no mean flow is present, and these can be observed for silencer 2 ($M = 0$, top left of Figure 9.7) where a slight kink in the predictions is apparent around 1400Hz. When mean flow is introduced, the problems with convergence are more obvious, for example see silencer 3 (Figure 9.7), where the predictions can be seen to undulate at the lower frequencies. When mean flow is present the predictions obtained by using the least squares method are again similar to that from the Cummings and Chang method, though unfortunately this also extends to under-predicting the transmission loss below approximately 200Hz.

The comparison between prediction and experiment for silencers 1 to 3 using the least squares method, and also the predictions found for Cummings' and Chang's silencer, indicate that the problem of non-orthogonality has not been eradicated by the use of the present solution. Problems identical to those found in the previous section have been observed and this means that non-orthogonality is not a problem linked solely to a single method. This points to a fundamental problem, common to both methods, which warns against the use of non-orthogonal eigenfunctions in mode matching techniques.

It is concluded here that the non-orthogonality of the eigenfunctions is responsible for the problems found both in this section and also the previous section. While the reasons behind this observation are unknown, it is worthwhile pursuing another mode matching scheme in which the orthogonality question is removed completely. In the next section a new mode matching method is presented, which does exactly this.

Section 9.5

Mode Matching Using a Direct Integration Method

The implementation of continuity conditions at a discontinuity in a dissipative silencer by the use of a mode matching method has been found to be fraught with unforeseen difficulties. Problems have been found in the use of both the Cummings and Chang method [23] and a least squares formulation. Whilst the application of these methods should not, in itself, depend upon orthogonality of the eigenfunctions, problems have undoubtedly occurred which do appear to be linked to the orthogonality question. In this section a completely different approach is implemented, which has the advantage of eliminating any uncertainties about the orthogonality of the eigenfunctions. The approach applied in this section is based upon a method employed by Smith [139, 140] in the study of fluid flow in rivers. The method is called here - for want of a better name - the integral method, since integration is applied directly to the governing wave equations. This method does not initially require modal expansion of the pressure fields, since the governing wave equations are multiplied by weighting functions which are then integrated. Instead of originally assuming a modal expansion for the sound pressure fields in regions 1 and 2, it is necessary, at a later stage in the method, to define a modal pressure distribution upon the walls of each discontinuity, i.e. upon planes A and B in region 2. This pressure distribution is required to fit the relevant boundary conditions along these walls and, whilst this does not present any problems for axisymmetric silencers, defining pressure distributions along the wall of silencers which have a an arbitrary cross sectional shape, including ellipses, was found to be impossible. Nevertheless, the method is useful for providing a comparison with the two previous mode matching formulations, since it does appear to show that orthogonality problems can be avoided. The integral method is the final mode matching scheme implemented in this chapter and, whilst is does not provide a completely general solution to the problem, it does perhaps point a way in which future work can proceed.

The method implemented in this section begins by first integrating the wave equations found in regions 1 and 2 (see Chapter 6). The wave equation in region 1, for an axisymmetric silencer (see Figure 6.1), is given (see equation (6.10)) by

$$\frac{1}{r}\frac{\partial}{\partial r}\left(r\frac{\partial p_1'}{\partial r}\right)+\left(1-M^2\right)\frac{\partial^2 p_1'}{\partial x^2}-2iMk_0\frac{\partial p_1'}{\partial x}+k_0^2 p_1'=0, \tag{9.61}$$

where p' is the acoustic pressure, M is the mean flow Mach number and k_0 is the wavenumber in the central channel. For region 2, the wave equation is given (see equation (6.25)) by

$$\frac{1}{r}\frac{\partial}{\partial r}\left(r\frac{\partial p_2'}{\partial r}\right)+\frac{\partial^2 p_2'}{\partial x^2}-\Gamma^2 p_2'=0, \tag{9.62}$$

where Γ is the propagation constant of the porous material in region 2. The two wave equations are subject to the same boundary conditions as those found in Chapter 6 (see also Figure 6.1 for the notation used here), hence for the hard walled boundary

$$\frac{\partial p_2'}{\partial r}=0, \qquad \text{at } r=r_2, \tag{9.63}$$

and

$$\frac{\partial p_2'}{\partial x}=0, \qquad r_1\le r\le r_2 \text{ at } x=0 \text{ and } x=l. \tag{9.64}$$

Finally, continuity of normal particle displacement on the common boundary gives

$$\left(\frac{\partial p_1'}{\partial r}\right)_{a_-}=R\left[1-i\frac{M}{k_0}\frac{\partial}{\partial x}\right]^2\left(\frac{\partial p_2'}{\partial r}\right)_{a_+}, \tag{9.65}$$

where a_- refers to dimension r_1 in region 1, a_+ refers to dimension r_1 in region 2 and $R = ik_0\rho_0 c_0/\Gamma z_a$, z_a being the characteristic impedance of the porous material in region 2.

The method now proceeds by multiplying each wave equation by the same weighting function and then integrating each equation over its domain. Therefore for region 1,

$$\int_0^l \int_0^{a_-} \Psi_m e^{-ik_0\lambda_m x}\left\{\frac{1}{r}\frac{\partial}{\partial r}\left(r\frac{\partial p_1'}{\partial r}\right) + \left(1-M^2\right)\frac{\partial^2 p_1'}{\partial x^2} - 2iMk_0\frac{\partial p_1'}{\partial x} + k_0^2 p_1'\right\} r dr dx = 0,$$
$$(m = 1,2,\ldots\ldots,\infty) \qquad (9.66)$$

where Ψ_m is the transverse modal eigenfunction and λ_m the axial wavenumber for the dissipative silencer (found in Chapter 8). Integrating equation (9.66) by parts gives

$$\int_0^l e^{-ik_0\lambda_m x}\left\{\left[\Psi_m r\frac{\partial p_1'}{\partial r}\right]_0^{a_-} - \left[r\frac{\partial \Psi_m}{\partial r} p_1'\right]_0^{a_-} + \int_0^{a_-}\frac{1}{r}\frac{\partial}{\partial r}\left(r\frac{\partial \Psi_m}{\partial r}\right) p_1' r dr\right\} dx$$
$$+\left(1-M^2\right)\int_0^{a_-}\Psi_m\left\{\left[e^{-ik_0\lambda_m x}\frac{\partial p_1'}{\partial x}\right]_0^l + ik_0\lambda_m\left[e^{-ik_0\lambda_m x}p_1'\right]_0^l - k_0^2\lambda_m^2\int_0^l e^{-ik_0\lambda_m x}p_1' dx\right\} r dr$$
$$-2iMk_0\int_0^{a_-}\Psi_m\left\{\left[e^{-ik_0\lambda_m x}p_1'\right]_0^l + ik_0\lambda_m\int_0^l e^{-ik_0\lambda_m x}p_1' dx\right\} r dr + k_0^2\int_0^l\int_0^{a_-}\Psi_m e^{-ik_0\lambda_m x}p_1' r dr dx = 0.$$
$$(9.67)$$

Simplifying equation (9.67) then gives

$$\int_0^l e^{-ik_0\lambda_m x}\left\{\Psi_m(r_1) r_1\left(\frac{\partial p_1'}{\partial r}\right)_{a_-} - r_1\left(\frac{\partial \Psi_m}{\partial r}\right)_{a_-} p_1'(r_1)\right\} dx$$
$$+\int_0^{a_-}\Psi_m\left\{\left(1-M^2\right)\left[e^{-ik_0\lambda_m x}\frac{\partial p_1'}{\partial x}\right]_0^l + \left(\left[1-M^2\right]ik_0\lambda_m - 2iMk_0\right)\left[e^{-ik_0\lambda_m x}p_1'\right]_0^l\right\} r dr$$
$$+\int_0^l e^{-ik_0\lambda_m x}\int_0^{a_-} p_1'\left\{\frac{1}{r}\frac{\partial}{\partial r}\left(r\frac{\partial \Psi_m}{\partial r}\right) + \Psi_m k_0^2\left[\left(1+\lambda_m M\right)^2 - \lambda_m^2\right]\right\} r dr dx = 0. \qquad (9.68)$$

The same procedure is now applied to the wave equation in region 2, and multiplying equation (9.62) by the weighting function and integrating over the domain gives

$$\int_0^l \int_{a_+}^{r_2} \Psi_m e^{-ik_0\lambda_m x}\left\{\frac{1}{r}\frac{\partial}{\partial r}\left(r\frac{\partial p_2'}{\partial r}\right)+\frac{\partial^2 p_2'}{\partial x^2}-\Gamma^2 p_2'\right\} r dr dx=0. \tag{9.69}$$

Integrating equation (9.69) by parts gives

$$\int_0^l e^{-ik_0\lambda_m x}\left\{\left[\Psi_m r\frac{\partial p_2'}{\partial r}\right]_{a_+}^{r_2}-\left[r\frac{\partial \Psi_m}{\partial r}p_2'\right]_{a_+}^{r_2}+\int_{a_+}^{r_2}\frac{1}{r}\frac{\partial}{\partial r}\left(r\frac{\partial \Psi_m}{\partial r}\right)p_2' r dr\right\}dx$$

$$+\int_{a_+}^{r_2}\Psi_m\left\{\left[e^{-ik_0\lambda_m x}\frac{\partial p_2'}{\partial x}\right]_0^l+ik_0\lambda_m\left[e^{-ik_0\lambda_m x}p_2'\right]_0^l-k_0^2\lambda_m^2\int_0^l e^{-ik_0\lambda_m x}p_2' dx\right\}rdr$$

$$-\Gamma^2\int_0^l e^{-ik_0\lambda_m x}\left\{\int_{a_+}^{r_2}\Psi_m p_2' r dr\right\}dx=0. \tag{9.70}$$

Equation (9.70) can be simplified with the use of the hard wall boundary conditions given by equations (9.63) and (9.64), to yield

$$\int_0^l e^{-ik_0\lambda_m x}\left\{-\Psi_m(r_1)r_1\left(\frac{\partial p_2'}{\partial r}\right)_{a_+}-r_2\left(\frac{\partial \Psi_m}{\partial r}\right)_{r_2}p_2'(r_2)+r_1\left(\frac{\partial \Psi_m}{\partial r}\right)_{a_+}p_2'(r_1)\right\}dx$$

$$ik_0\lambda_m\int_{a_+}^{r_2}\Psi_m\left\{p_2'(l)e^{-ik_0\lambda_m l}-p_2'(0)\right\}rdr$$

$$+\int_0^l e^{-ik_0\lambda_m l}\int_{a_+}^{r_2}p_2'\left\{\frac{1}{r}\frac{\partial}{\partial r}\left(r\frac{\partial \Psi_m}{\partial r}\right)-\Psi_m\left(\Gamma^2+k_0^2\lambda_m^2\right)\right\}rdrdx=0. \tag{9.71}$$

The procedure used for the two wave equations is also applied to the boundary condition along the common boundary. Since the domain of this boundary covers a length l only, then

$$\int_0^l e^{-ik_0\lambda_m x}\left\{R\left[1-i\frac{M}{k_0}\frac{\partial}{\partial x}\right]^2\left(\frac{\partial p_2'}{\partial r}\right)_{a_+}-\left(\frac{\partial p_1'}{\partial r}\right)_{a_-}\right\}dx=0. \tag{9.72}$$

Integration by parts gives

$$\int_0^l e^{-ik_0\lambda_m x}\left\{R\left(\frac{\partial p_2'}{\partial r}\right)_{a_+}-\left(\frac{\partial p_1'}{\partial r}\right)_{a_-}\right\}dx$$

$$-\frac{M^2R}{k_0^2}\left\{\left[e^{-ik_0\lambda_m x}\frac{\partial}{\partial x}\left(\frac{\partial p_2'}{\partial r}\right)_{a_+}\right]_0^l+ik_0\lambda_m\left[e^{-ik_0\lambda_m x}\left(\frac{\partial p_2'}{\partial r}\right)_{a_+}\right]_0^l-k_0^2\lambda_m^2\int_0^l e^{-ik_0\lambda_m x}\left(\frac{\partial p_2'}{\partial r}\right)_{a_+}dx\right\}$$

$$-\frac{2iMR}{k_0}\left\{\left[e^{-ik_0\lambda_m x}\left(\frac{\partial p_2'}{\partial r}\right)_{a_+}\right]_0^l+ik_0\lambda_m\int_0^l e^{-ik_0\lambda_m x}\left(\frac{\partial p_2'}{\partial r}\right)_{a_+}dx\right\}=0. \tag{9.73}$$

Simplifying equation (9.73) gives

$$\int_0^l e^{-ik_0\lambda_m x}\left\{R[1+\lambda_m M]^2\left(\frac{\partial p_2'}{\partial r}\right)_{a_+}-\left(\frac{\partial p_1'}{\partial r}\right)_{a_-}\right\}dx$$

$$-\frac{iMR}{k_0}(2+\lambda_m M)\left[e^{-ik_0\lambda_m x}\left(\frac{\partial p_2'}{\partial r}\right)_{a_+}\right]_0^l-\frac{M^2R}{k_0^2}\left[e^{-ik_0\lambda_m x}\frac{\partial}{\partial x}\left(\frac{\partial p_2'}{\partial r}\right)_{a_+}\right]_0^l=0. \tag{9.74}$$

Now, if the weighting function $\Psi_m e^{-ik_0\lambda_m x}$ is taken to be the spatial factor for a mode of propagation that satisfies the governing wave equations, substitution of $\Psi_m e^{-ik_0\lambda_m x}$ into equations (9.61) and (9.62) yields

$$\frac{1}{r}\frac{\partial}{\partial r}\left(r\frac{\partial\Psi_m}{\partial r}\right)+\Psi_m k_0^2\left[(1-\lambda_m M)^2-\lambda_m^2\right]=0 \tag{9.75}$$

and

$$\frac{1}{r}\frac{\partial}{\partial r}\left(r\frac{\partial\Psi_m}{\partial r}\right)-\Psi_m\left[\Gamma^2+k_0^2\lambda_m^2\right]=0. \tag{9.76}$$

Similarly the boundary condition given by equation (9.65) results in

$$R(1-\lambda_m M)^2\left(\frac{\partial \Psi_m}{\partial r}\right)_{a_+} = \left(\frac{\partial \Psi_m}{\partial r}\right)_{a_-} . \tag{9.77}$$

The relationships given by equations (9.75) to (9.77) have been derived previously (see Chapter 6). It is evident that equations (9.75), (9.76) and (9.77) can be used to eliminate terms from equations (9.68), (9.71) and (9.74) respectively, so long as the Mach number used in equations (9.75) to (9.77) is reversed. Therefore provided that the solutions found for the eigenfunction Ψ_m and the eigenvalue λ_m are calculated using a Mach number of sign opposite to that used in the present derivation, equations (9.75) to (9.77) can be successfully used to simplify equations (9.68), (9.71) and (9.74). Note that the derivation assumes that, for a single propagating mode, $m=1$ denotes an incident wave and $m=2$ a reflected wave. Therefore carrying out this simplification gives

$$\int_0^l e^{-ik_0\lambda_m x}\left\{\Psi_m(r_1) r_1\left(\frac{\partial p_1'}{\partial r}\right)_{a_-} - r_1\left(\frac{\partial \Psi_m}{\partial r}\right)_{a_-} p_1'(r_1)\right\}dx$$

$$+\int_0^{a_-}\Psi_m\left\{(1-M^2)\left[e^{-ik_0\lambda_m x}\frac{\partial p_1'}{\partial x}\right]_0^l + \left([1-M^2]ik_0\lambda_m - 2iMk_0\right)\left[e^{-ik_0\lambda_m x}p_1'\right]_0^l\right\}rdr = 0, \tag{9.78}$$

$$\int_0^l e^{-ik_0\lambda_m x}\left\{-\Psi_m(r_1) r_1\left(\frac{\partial p_2'}{\partial r}\right)_{a_+} + r_1\left(\frac{\partial \Psi_m}{\partial r}\right)_{a_+} p_2'(r_1)\right\}dx$$

$$ik_0\lambda_m\int_{a_+}^{r_2}\Psi_m\left\{p_2'(l)e^{-ik_0\lambda_m l} - p_2'(0)\right\}rdr = 0 \tag{9.79}$$

and

$$\int_0^l e^{-ik_0\lambda_m x}\left\{R[1+\lambda_m M]^2\left(\frac{\partial p_2'}{\partial r}\right)_{a_+} - \left(\frac{\partial p_1'}{\partial r}\right)_{a_-}\right\}dx$$

$$-\frac{iMR}{k_0}(2+\lambda_m M)\left[e^{-ik_0\lambda_m x}\left(\frac{\partial p_2'}{\partial r}\right)_{a_+}\right]_0^l - \frac{M^2 R}{k_0^2}\left[e^{-ik_0\lambda_m x}\frac{\partial}{\partial x}\left(\frac{\partial p_2'}{\partial r}\right)_{a_+}\right]_0^l = 0. \tag{9.80}$$

The solution now proceeds by combining equations (9.78), (9.79) and (9.80) to form a final, single equation, which can then be solved. It is convenient here to add $R(1+\lambda_m M)^2 \times (9.79)$ to both (9.78) and (9.80) and this gives

$$\int_0^l e^{-ik_0\lambda_m x}\left\{\Psi_m(r_1)r_1\left(\frac{\partial p_1'}{\partial r}\right)_{a_-} - r_1\left(\frac{\partial \Psi_m}{\partial r}\right)_{a_-} p_1'(r_1)\right\}dx$$

$$+\int_0^{a_-}\Psi_m\left\{\left(1-M^2\right)\left[e^{-ik_0\lambda_m x}\frac{\partial p_1'}{\partial x}\right]_0^l + \left(\left[1-M^2\right]ik_0\lambda_m - 2iMk_0\right)\left[e^{-ik_0\lambda_m x}p_1'\right]_0^l\right\}rdr$$

$$+R(1+\lambda_m M)^2\int_0^l e^{-ik_0\lambda_m x}\left\{-\Psi_m(r_1)r_1\left(\frac{\partial p_2'}{\partial r}\right)_{a_+} + r_1\left(\frac{\partial \Psi_m}{\partial r}\right)_{a_+} p_2'(r_1)\right\}dx$$

$$+R(1+\lambda_m M)^2 ik_0\lambda_m\int_{a_+}^{r_2}\Psi_m\left\{p_2'(l)e^{-ik_0\lambda_m l} - p_2'(0)\right\}rdr$$

$$+\int_0^l e^{-ik_0\lambda_m x}\left\{R\left[1+\lambda_m M\right]^2\left(\frac{\partial p_2'}{\partial r}\right)_{a_+} - \left(\frac{\partial p_1'}{\partial r}\right)_{a_-}\right\}dx$$

$$-\frac{iMR}{k_0}(2+\lambda_m M)\left[e^{-ik_0\lambda_m x}\left(\frac{\partial p_2'}{\partial r}\right)_{a_+}\right]_0^l - \frac{M^2 R}{k_0^2}\left[e^{-ik_0\lambda_m x}\frac{\partial}{\partial x}\left(\frac{\partial p_2'}{\partial r}\right)_{a_+}\right]_0^l = 0. \qquad (9.81)$$

Equation (9.81) can be simplified by use of the boundary condition imposed at the common boundary between regions 1 and 2 (equations (9.65) and (9.77)), allowing equation (9.81) to be re-written as

$$\left(1-M^2\right)\int_0^{a_-}\Psi_m\left[e^{-ik_0\lambda_m x}\frac{\partial p_1'}{\partial x}\right]_0^l rdr + ik_0\left(\left[1-M^2\right]\lambda_m - 2M\right)\int_0^{a_-}\Psi_m\left[e^{-ik_0\lambda_m x}p_1'\right]_0^l rdr$$

$$+ik_0\lambda_m R(1+\lambda_m M)^2\int_{a_+}^{r_2}\Psi_m\left\{p_2'(l)e^{-ik_0\lambda_m l} - p_2'(0)\right\}rdr$$

$$-\frac{iMR}{k_0}(2+\lambda_m M)\left[e^{-ik_0\lambda_m x}\left(\frac{\partial p_2'}{\partial r}\right)_{a_+}\right]_0^l - \frac{M^2 R}{k_0^2}\left[e^{-ik_0\lambda_m x}\frac{\partial}{\partial x}\left(\frac{\partial p_2'}{\partial r}\right)_{a_+}\right]_0^l = 0. \qquad (9.82)$$

Now, if p_2' in plane A is denoted by p_{A}, p_2' in plane B by p_{B}, p_1' in plane A by p_0 and p_1' in plane B by p_l, then equation (9.82) can be re-written to give

$$\left(1-M^2\right)\int_0^{a_-}\Psi_m\left[e^{-ik_0\lambda_m l}\left.\frac{\partial p_1'}{\partial x}\right|_l-\left.\frac{\partial p_1'}{\partial x}\right|_0\right]rdr+ik_0\left(\left[1-M^2\right]\lambda_m-2M\right)\int_0^{a_-}\Psi_m\left[e^{-ik_0\lambda_m l}p_l-p_0\right]rdr$$

$$+ik_0\lambda_m R\left(1+\lambda_m M\right)^2\int_{a_+}^{r_2}\Psi_m\left\{p_{\mathrm{B}}e^{-ik_0\lambda_m l}-p_{\mathrm{A}}\right\}rdr$$

$$-\frac{iMR}{k_0}\left(2+\lambda_m M\right)\left[e^{-ik_0\lambda_m l}\left.\frac{\partial p_{\mathrm{B}}}{\partial r}\right|_{a_+}-\left.\frac{\partial p_{\mathrm{A}}}{\partial r}\right|_{a_+}\right]=0. \tag{9.83}$$

At this point it is necessary to assume a modal pressure distribution for both p_{A} and p_{B}. Both pressure distributions are assumed to have the same form and they are both subject to the hard wall boundary condition $\partial p_{\mathrm{A,B}}/\partial r=0$ at $r=r_2$. Both the pressure distributions are also chosen to give $\partial p_{\mathrm{A,B}}/\partial r=0$ at $r=r_1$, since when this restriction was relaxed, the final numerical solution proved to be very unstable. An arbitrary function is chosen here which fits both these boundary conditions and it is given by

$$p_{\mathrm{A,B}}=p_0+\sum_{n=1}^{\infty}C_n^{\mathrm{A,B}}\left(r-r_1\right)^2\left[\left(r-r_1\right)-\left(r_2-r_1\right)\left(1-n/2\right)\right]^n, \tag{9.84}$$

where C_n is the modal coefficient in either plane A or plane B. The use of the relationship

$$\left.\frac{\partial p_1'}{\partial x}\right|_l=-\frac{ik_0}{\left(1+M\right)}p_l, \tag{9.85}$$

and the substitution of the assumed pressure distribution for p_{A} and p_{B}, allows equation (9.83) to be re-written as

$$-\left(1-M^2\right)\int_0^{r_1}\Psi_m\left[\frac{ik_0}{(1+M)}e^{-ik_0\lambda_m l}p_l+\left.\frac{\partial p_1'}{\partial x}\right|_0\right]rdr$$

$$+ik_0\left(\left[1-M^2\right]\lambda_m-2M\right)\int_0^{r_1}\Psi_m\left[e^{-ik_0\lambda_m l}p_l-p_0\right]rdr$$

$$+ik_0\lambda_m R(1+\lambda_m M)^2\int_{r_1}^{r_2}\left\{e^{-ik_0\lambda_m l}\left[p_0+C_n^{\mathrm{B}}(r-r_1)^2\left[(r-r_1)-(r_2-r_1)(1-n/2)\right]^n\right]\right.$$

$$\left.-\left[p_0+C_n^{\mathrm{A}}(r-r_1)^2\left[(r-r_1)-(r_2-r_1)(1-n/2)\right]^n\right]\right\}\Psi_m rdr=0.$$

(9.86)

Grouping together the unknowns in equation (9.86) gives

$$p_l\left\{ik_0e^{-ik_0\lambda_m l}\left(\lambda_m\left[1-M^2\right]-M-1\right)\int_0^{r_1}\Psi_m rdr\right\}-\left.\frac{\partial p_1'}{\partial x}\right|_0\left\{\left(1-M^2\right)\int_0^{r_1}\Psi_m rdr\right\}$$

$$-C_n^{\mathrm{A}}\left\{ik_0\lambda_m R(1+\lambda_m M)^2\int_{r_1}^{r_2}\Psi_m(r-r_1)^2\left[(r-r_1)-(r_2-r_1)(1-n/2)\right]^n rdr\right\}$$

$$+C_n^{\mathrm{B}}\left\{ik_0\lambda_m R(1+\lambda_m M)^2e^{-ik_0\lambda_m l}\int_{r_1}^{r_2}\Psi_m(r-r_1)^2\left[(r-r_1)-(r_2-r_1)(1-n/2)\right]^n rdr\right\}$$

$$=p_0\left\{ik_0\left(\left[1-M^2\right]\lambda_m-2M\right)\int_0^{r_1}\Psi_m rdr+ik_0\lambda_m R(1+\lambda_m M)^2\left[1-e^{-ik_0\lambda_m l}\right]\int_{r_1}^{r_2}\Psi_m rdr\right\}.$$

$$(m=1,2,\ldots\ldots,N),\ (n=1,2,\ldots\ldots,N-1) \qquad (9.87)$$

Equation (9.87) is the final equation which must be solved for p_l, $\partial p_1'/\partial x|_0$, C_n^{A} and C_n^{B}, once p_0 has been set equal to unity (real). The left hand side of equation (9.87) forms a matrix of size $(N\times N)$, from which values for Ψ_m and λ_m must be supplied from the eigenvalue solution performed in Chapter 8 (with the Mach number reversed). The eigenvalues and eigenfunctions are supplied in groups of incident and reflected modes so that, in equation (9.87), $m=1$ refers to the incident least attenuated mode, $m=2$ refers to the reflected least attenuated mode, and so on.

Finally, the transmission loss (TL) of the silencer is given by

$$\mathrm{TL}=20\log\left\{\frac{(1+M)}{2}\left|\frac{1+\dfrac{i(1-M)}{k_0}\left.\dfrac{\partial p_1'}{\partial x}\right|_0}{p_I}\right|\right\}. \tag{9.88}$$

9.5.1 Results and Discussion

The purpose behind the mode matching method employed in this section was the avoidance of integrals which contained products of the duct eigenfunctions. An examination of the final equation (equation (9.87)) shows that the integrals are now only performed on a single eigenfunction. Therefore any question about the orthogonality of the eigenfunctions has been removed. The final solution of equation (9.87) appears to be straightforward, especially when $N=1$, which allows the elimination of C_n^{A} and C_n^{B}. However the inclusion of higher order modes does require a function for the pressure to be found at the end plates of the silencer, and this must satisfy the appropriate boundary conditions. Equation (9.87) gives one possible formulation for p_{A} and p_{B} for use in axisymmetric silencers from which the modal coefficients C_n^{A} and C_n^{B} can then be found. Unfortunately it was found to be impossible to find an equivalent modal pressure distribution for the oval silencers. Consequently, all the multi-mode predictions obtained from the integral method are limited to axisymmetric silencers. However one can still find predictions for the oval silencers so long as only one mode is used. This does however require the integration of the eigenfunctions over the equivalent area denoted in the integral signs in equation (9.87).

In the previous two sections the silencer studied by Cummings and Chang [23] was modelled first. Therefore the predictions obtained for the Cummings and Chang silencer by using the integral method are shown in Figure 9.8, for M=0 and M=0.197. These were obtained using 8 modes, since this was the point at which the transmission loss predictions converged. Predictions are also shown in Figure 9.8 for a single mode when mean flow is present, since this shows the effect of adding higher order modes to the model. The accuracy of the solutions found when only one mode was present (with M=0.197) was comparable to that found when using the Cummings and Chang method.

Once higher order modes were introduced here, the solutions were very unstable for small numbers of modes, only stabilising when more than about 6 modes were included. Indeed, the solutions found for between 2 and 4 modes were very inaccurate, far more so than those derived from the previous two methods. This effect is perhaps attributable to the addition of the assumed pressure distribution at the end plates, and the convergence of the solution might be improved by a better choice of function for p_A and p_B. The solution was found to begin diverging when more than about 12 modes were included, which is again attributable to numerical problems. When no mean flow is present, the integral method provides predictions comparable to those found by using the two previous methods. However, when mean flow is included, in addition to higher order modes, a negative transmission loss is no longer predicted (see Figure 9.8). A comparison between the predictions found by using 1 mode and those found by using 8 modes shows almost identical results at low frequencies. This appears to indicate that the integral method works correctly when higher order modes are present. At higher frequencies only a small difference is observed because of the presence of higher order modes, although this difference will be minor because of the relatively small dimensions of the silencer studied by Cummings and Chang.

Multi-mode solutions were also found for silencers 1, 2 and 3, and these are shown in the bottom of Figure 9.8 and Figure 9.9, both with and without mean flow. Again, it is evident that, when no mean flow is present, the predictions found using the integral method are close to the experimental data and also similar to those found in the two previous sections. When mean flow is present, the accuracy of the prediction has improved slightly over the previous methods, and this is especially true at low frequencies where under-prediction is no longer a problem. Unfortunately, for the reasons mentioned earlier, predictions for the ellipses could only be obtained using one mode, and these are shown in Figure 9.10. However, for a single mode, the predictions found using the integral method are very similar to those obtained using the Cummings and Chang method. Actually the predictions for the elliptical silencers in Figure 9.10 are surprisingly good considering only one mode has been used and, as in the case of the Cummings and Chang method, no problems appear at low frequencies, an area where numerical problems had previously occurred with the full three dimensional finite element solution.

The results obtained using the integral method show good agreement with experiment and the method has been shown to be capable of eradicating the problems associated with the non-orthogonality of modes which are apparent in the previous two sections. Indeed, the solutions obtained here appear to reinforce the observation that one must avoid using non-orthogonal eigenfunctions in mode matching schemes. Unfortunately the model derived in this section cannot be applied to the study of higher order modes in silencers with arbitrary cross sections. Since the original intention of this chapter was to find a scheme by which transmission loss predictions could be computed for silencers of arbitrary cross-sectional shape, the method does not satisfy this criterion. Therefore, in the future, further modification of this method is needed in order to find a way of examining arbitrary cross-sectional shapes, although such a task is beyond the scope of this thesis.

Section 9.6

Evaluation of the Mode Matching Techniques

In this chapter, three different mode matching techniques have been implemented in order to model a finite length silencer using only the eigenvalue solutions found in Chapter 8. It was found here that the implementation of a mode matching scheme for dissipative silencers which also contain mean flow in the central channel is far more difficult than at first appeared. Of the three methods investigated, the first two methods (the Cummings and Chang and least squares methods) gave virtually identical predictions, both exhibiting problems when mean flow in addition to higher order modes were present. It was tentatively concluded that these problems were caused by the non-orthogonality of the eigenfunctions - something which was common to both methods - although no proof of this was given. The integral method, implemented last, appears to reinforce this observation since when the non-orthogonality question was removed, acceptable results were obtained. However the integral method suffers from its own problems, limiting solutions for silencers with arbitrary cross-sectional shape to one mode only. Consequently problems have occurred with all three mode matching schemes and not one of them fully fits the initial criterion. The method of mode matching requires further examination, which is beyond the scope of this thesis, although the author suggests that the integral method of Section 9.5 appears to provide the best hope for providing a stable mode matching scheme in the future. Also, it is by no means certain that non-orthogonality was solely responsible for the problems found in the first two methods and therefore this question also requires further investigation. However it is possible that one might have to resort to more complex ways of matching the continuity conditions over the discontinuities. Two alternative methods were mentioned in the introduction and these are the variational method used by Sormaz [124] and the Wiener-Hopf method implemented by Nilsson and Brander [22].

Although the mode matching schemes were not successful in every situation, most of the predictions made for the silencers studied here appear to be reasonably satisfactory. The three methods can still be useful for design purposes, despite their limitations, and therefore in view of this it is useful to study further the relative performance of each method. Both the Cummings and Chang method and the least squares method gave similar transmission loss predictions, both with and without mean flow, although the least squares method converged less readily than the Cummings and Chang method. Obtaining convergence for the integral method proved to be difficult, even when mean flow was not present. This cautions against the use of the integral method in its current form, since convergence cannot be assumed to have occurred for a given number of modes; and so, at present, one must manually examine the convergence of each solution for individual silencers. Consequently it is concluded here that, of the three mode matching schemes implemented in this chapter, the Cummings and Chang method is currently the most useful for design purposes since, in most cases, it provides solution of accuracy comparable to the other two methods but provides a stable convergence of solution. Therefore, although the Cummings and Chang method must be employed without the inclusion of higher order modes when mean flow is present, the result are sufficiently good to allow its use in silencer design, and subsequently this method will be used to provide the mode matching predictions further on in this thesis.

A problem common to all three mode matching schemes was the divergence of the solution once more than about 12 modes had been included. This problem is thought to be caused by numerical instabilities occurring when executing the code and this is why it is largely unrelated to the mode matching method used. It is possible that this effect could cause serious problems when studying two dimensional eigenvalue problems. This is because mode matching with one dimensional modes required the use of at least 8 axisymmetrical modes in order to achieve convergence. Now, the transmission loss solution requires only axisymmetrical modes, but in two dimensional problems non-axisymmetric modes exist (see Chapter 8), and these modes make no contribution to the convergence of a solution. Therefore if, for example, 8 axisymmetrical modes are required for convergence but 6 non-axisymmetric modes already exist before 8 modes are reached, then the numerical problems associated with the solution of large matrices will occur before all the necessary axisymmetrical modes have appeared unless the non-axisymmetric modes can be eliminated from the mode matching procedure. This has the potential to inhibit convergence, especially if a large number of axisymmetrical modes are needed in two dimensional solutions. This effect could not be studied here because of the problems encountered when introducing higher order modes into the two dimensional solutions. However it does have the potential to cause large problems in mode matching solutions, although it is anticipated that this effect will only be apparent in extreme cases, such as in the study of large silencers with cross sections of arbitrary shape.

Finally it is interesting to study the effect of the perforate on the mode matching predictions. Since it has been decided that only the Cummings and Chang method will be employed further, predictions obtained for silencers containing perforates are given here for the Cummings and Chang method only. Indeed it is only necessary to study the effect of the perforate on one method, because the same trends ought to be common to the other methods since they have a common input. The mode matching predictions obtained for silencers 1, 2, 4 and 5, including perforates, are given in Figures 9.11 and 9.12. It is evident from Figure 9.11 that the effect of the perforate on the transmission loss of the axisymmetric silencers is similar to that observed in the full finite element predictions in Chapter 7. Again it can be observed that at lower frequencies, the predictions are slightly higher than those found without a perforate (see Figures 9.3-9.5), whilst above approximately 1kHz the predictions are rather lower. It was mentioned in Chapter 7 that the perforate impedance has probably been over-predicted, and this effect will be discussed further in the context of the mode matching method in Chapter 10. It is interesting also to examine the effect of the perforate upon the oval silencers, and this is shown in Figure 9.12. For silencer 4 there appears to be very little difference between the predictions with and without a perforate at low frequencies, whilst only a small difference (of the order of 5dB) occurs at 2kHz. The effects of the perforate on the transmission loss predictions for silencer 4 are smaller than those found for silencers 1 and 2 and this is to be expected because the porous material present in silencer 4 (basalt wool) has a much lower flow resistivity than E glass, which is present in silencers 1 and 2. Silencer 5 does contain E glass, and the effect of the perforate is indeed larger than that found for silencer 4, although in view of the results obtained for silencers 1 and 2, one might have expected the effect of the perforate to have been greater. It is possible that the smaller effect of the perforate upon the elliptical silencers, compared to that found for the axisymmetric silencers, might be caused by their difference in shape, although this is by no means certain. A fuller discussion of the effect of the perforate in mode matching solutions for both axisymmetric and elliptical silencers will be given in Chapter 10.

One may conclude that applying the mode matching method to dissipative silencers is by no means straightforward and requires further investigation. However the results presented in this chapter do appear to be acceptable for design purposes in the cases of the silencers studied and it is possible, even with the use of only one mode, that the Cummings and Chang method would provide sufficiently good predictions for use in commercial silencer design software. In addition, this method has the potential to reduce CPU costs compared to the full finite element method described in Chapter 7.

The relative merits of the Cummings and Chang mode matching model, the fundamental mode model and the finite element model are discussed in the next chapter.

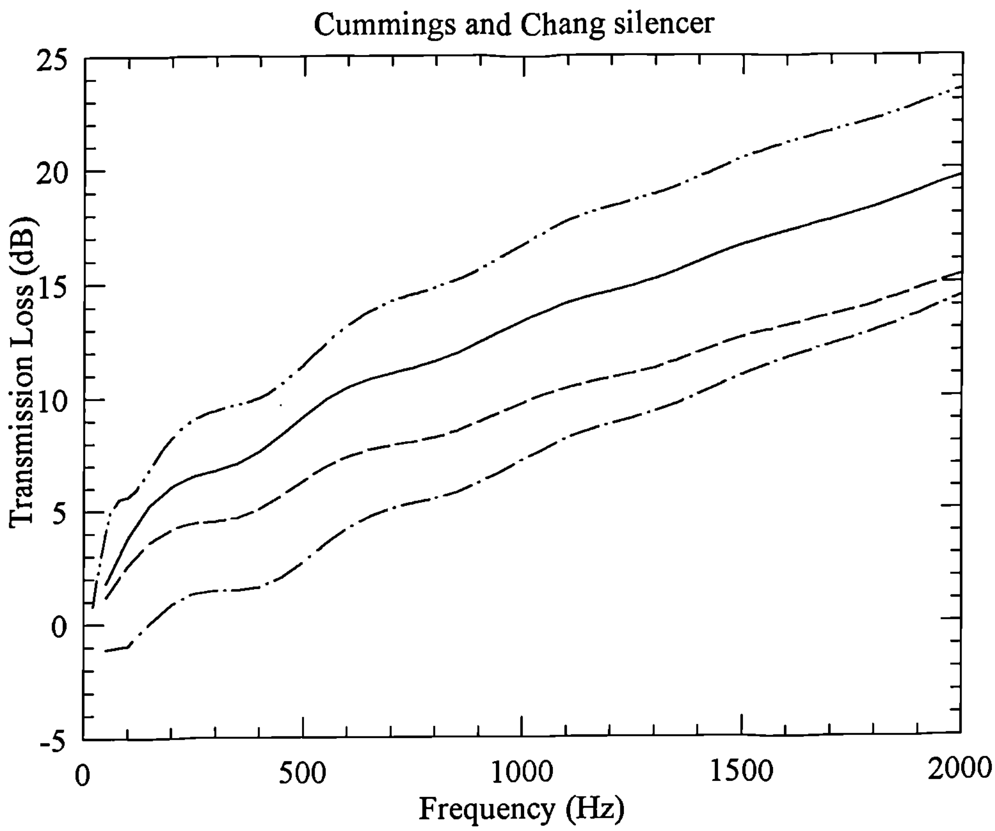

Figure 9.2. Mode matching predictions using Cummings and Chang method.
——— , M=0 (6modes); – – – , M=0.197 (1 mode);
—·— , M=0.197 (6 modes); —··— , M= −0.197 (1 mode).

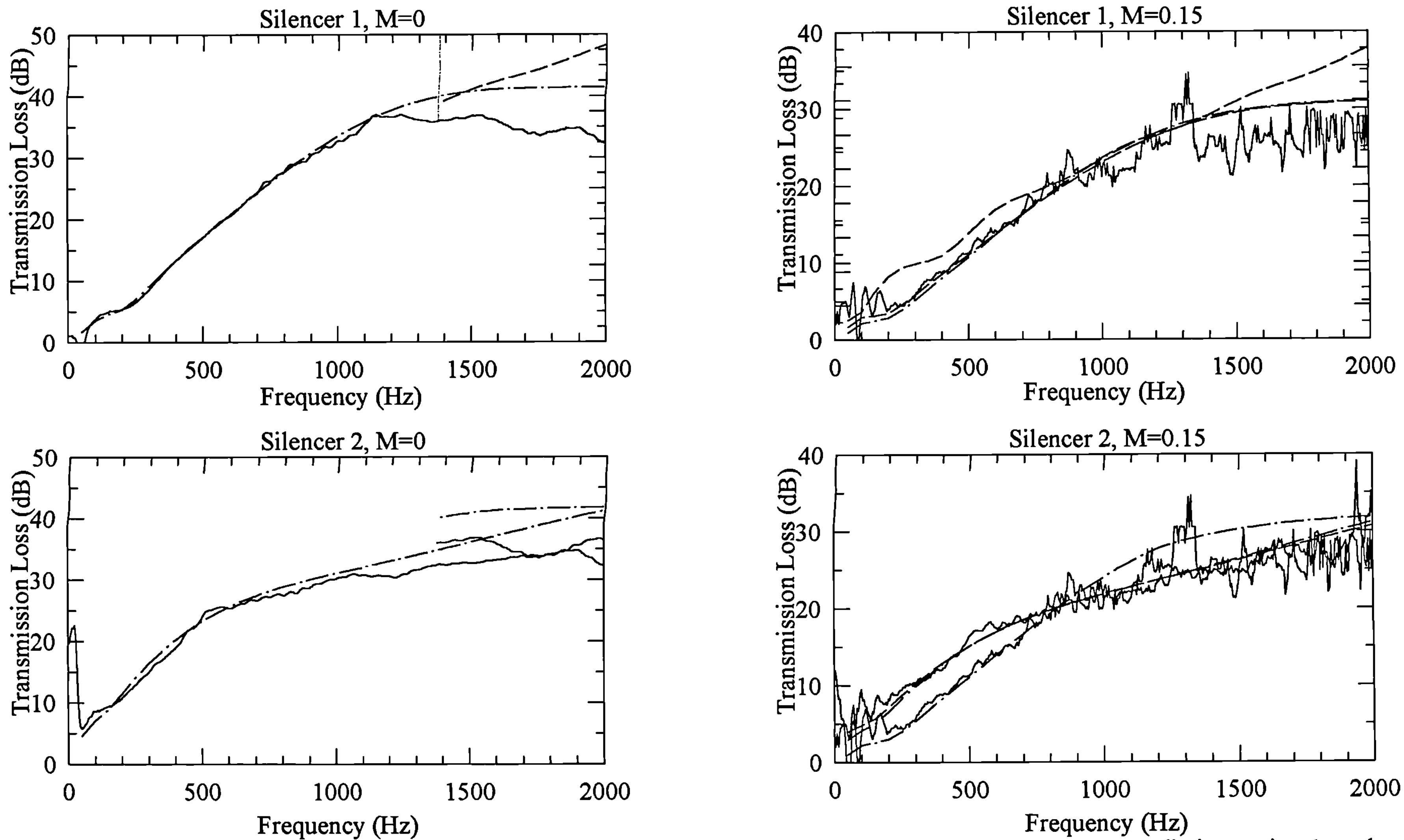

Figure 9.3. Mode matching predictions using Cummings and Chang method. ——— , Experiment; —·—·— , Predictions using 1 mode; —·— , Predictions using 6 modes.

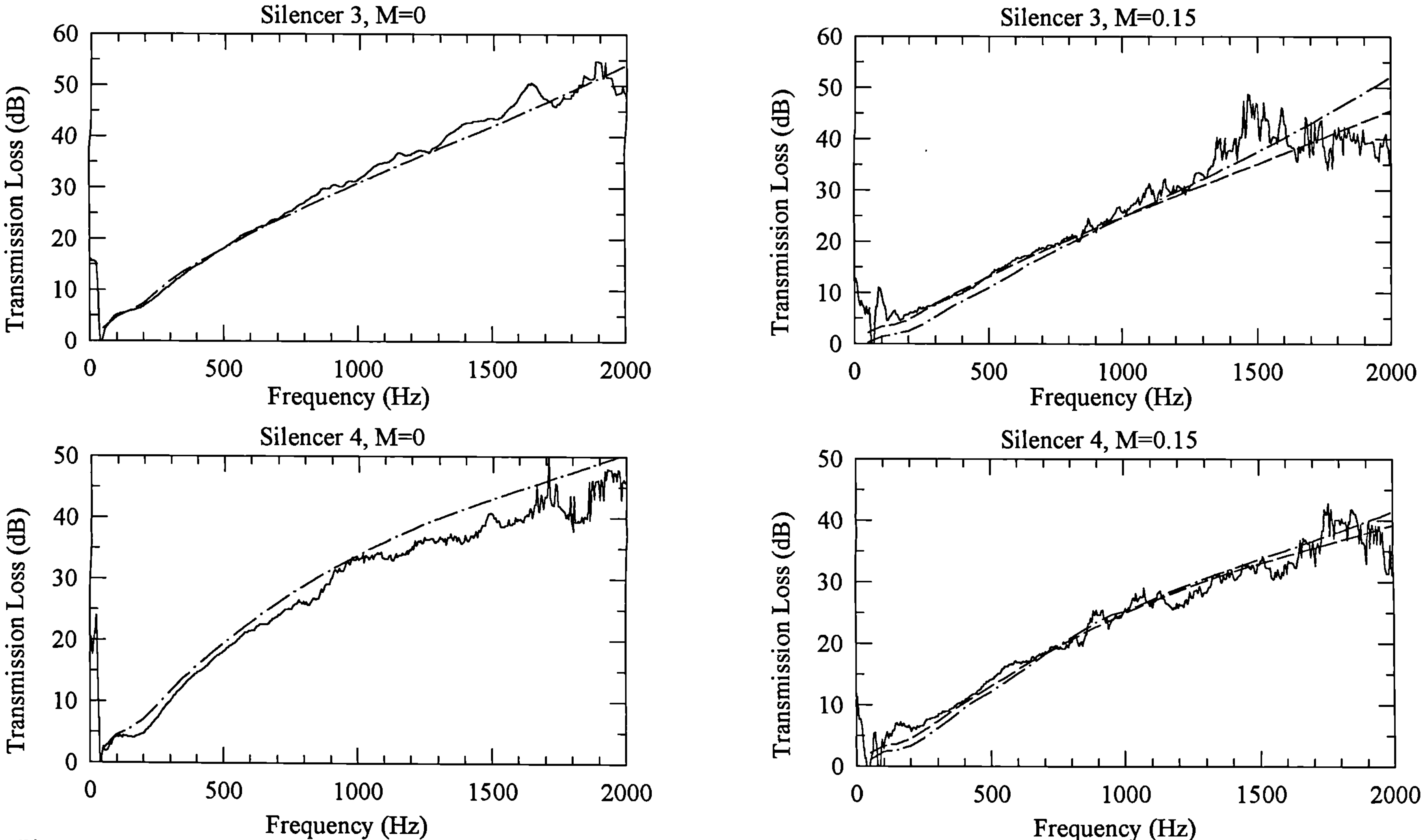

Figure 9.4. Mode matching predictions using Cummings and Chang method. ——— , Experiment; — — — , Predictions using 1 mode; —·— , Predictions using 6 modes.

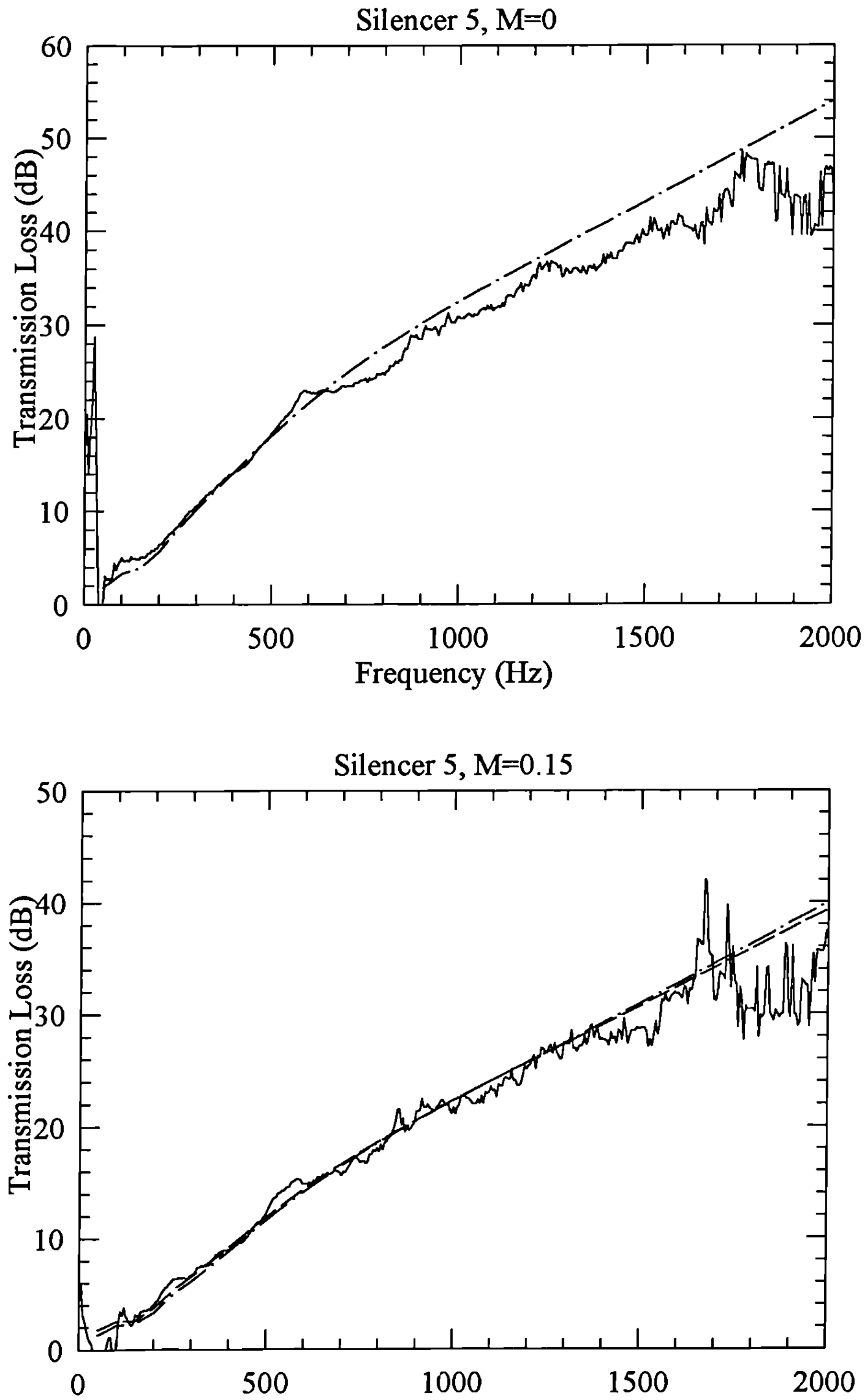

Figure 9.5. Mode matching predictions using Cummings and Chang method.
——— , Experiment; – – – , Predictions using 1 mode;
—·— , Predictions using 6 modes.

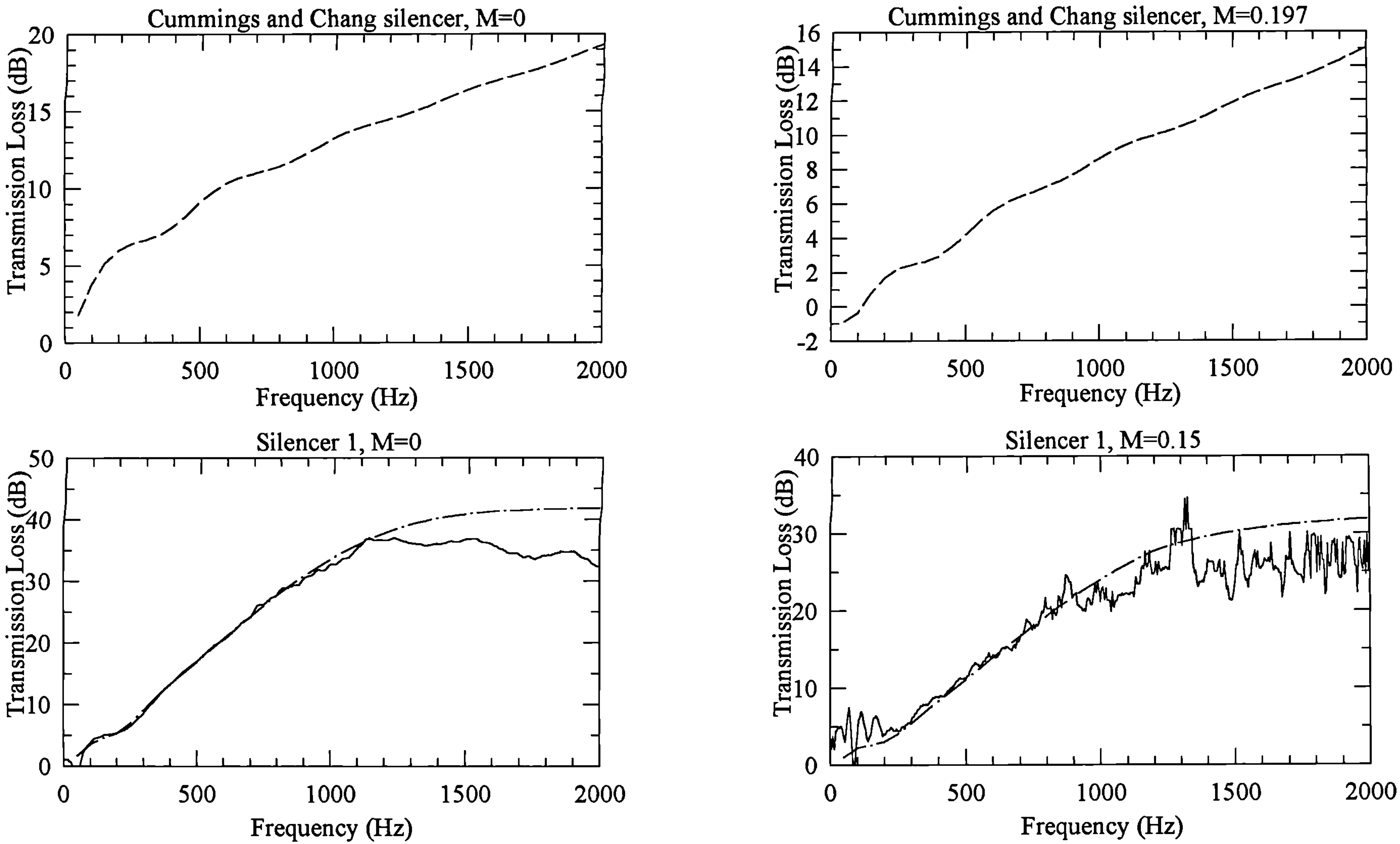

Figure 9.6. Mode matching predictions using least squares method. ——— , Experiment; —·— , Predictions using 6 modes; – – – , Predictions using 8 modes.

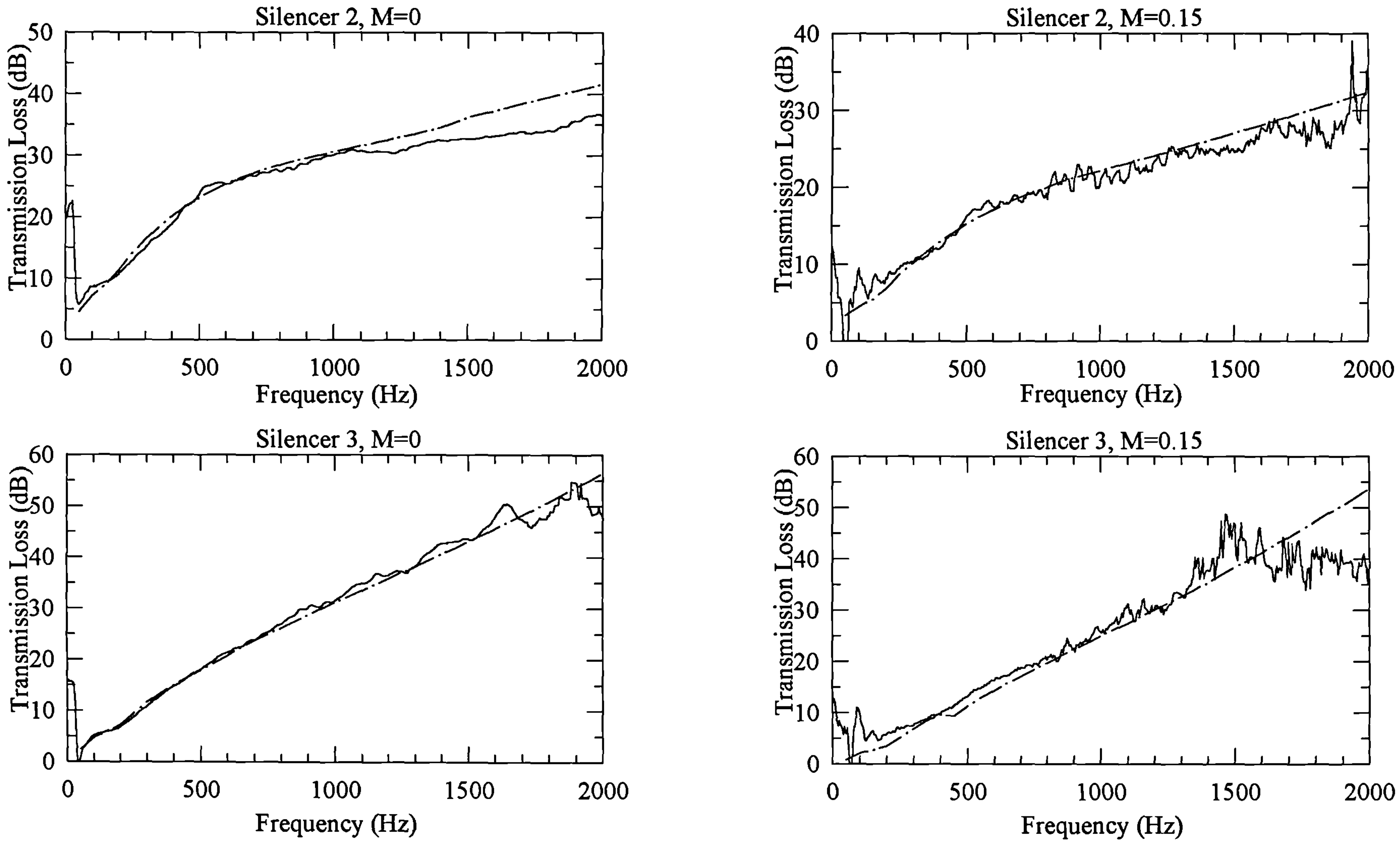

Figure 9.7. Mode matching preditcions using least squares method. ——— , Experiment; —·— , Predictions using 8 modes.

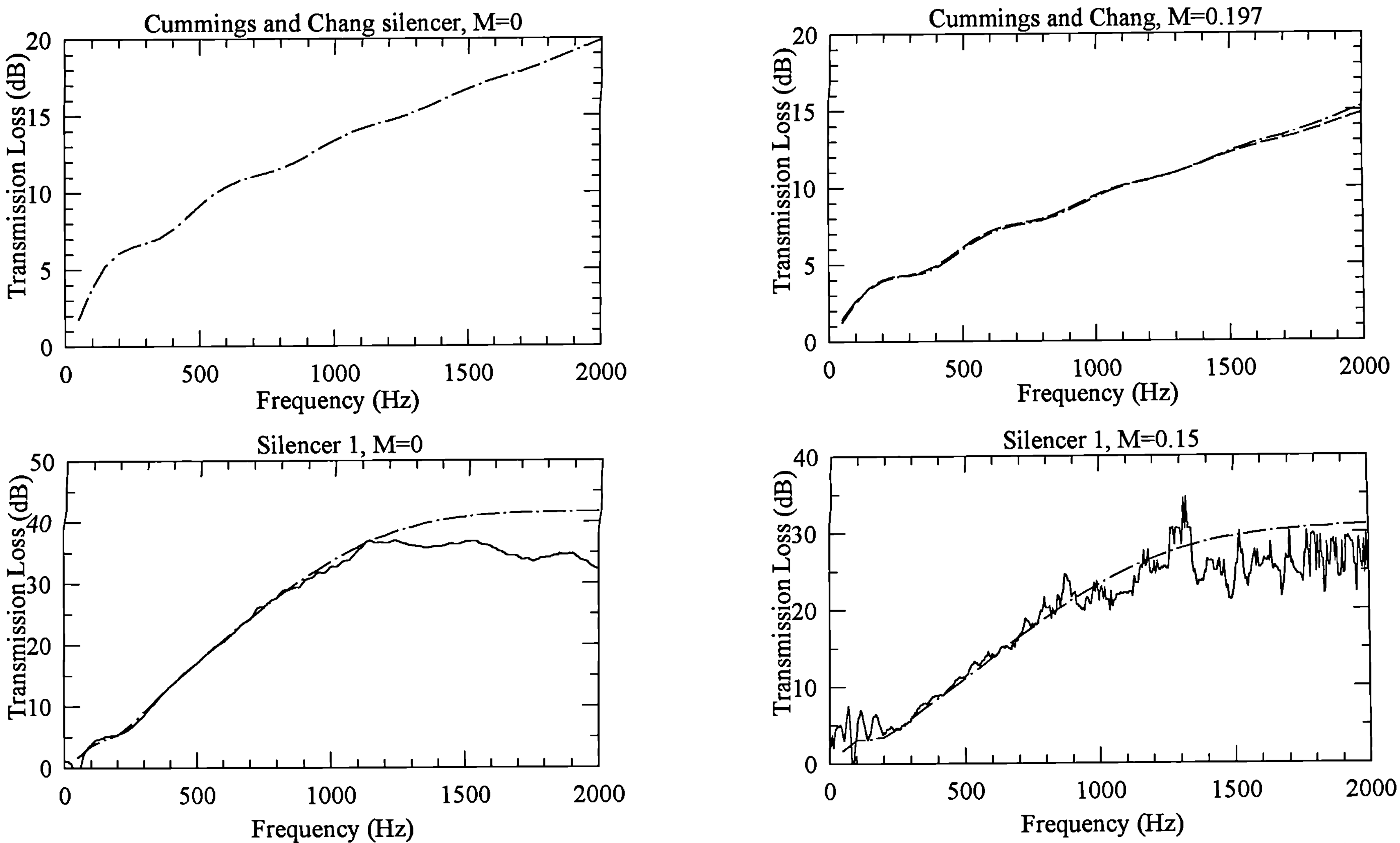

Figure 9.8. Mode matching predictions using the integral method. ——— , Experiment; — — — , Predictions using 1 mode; —·— , Predictions using 10 modes.

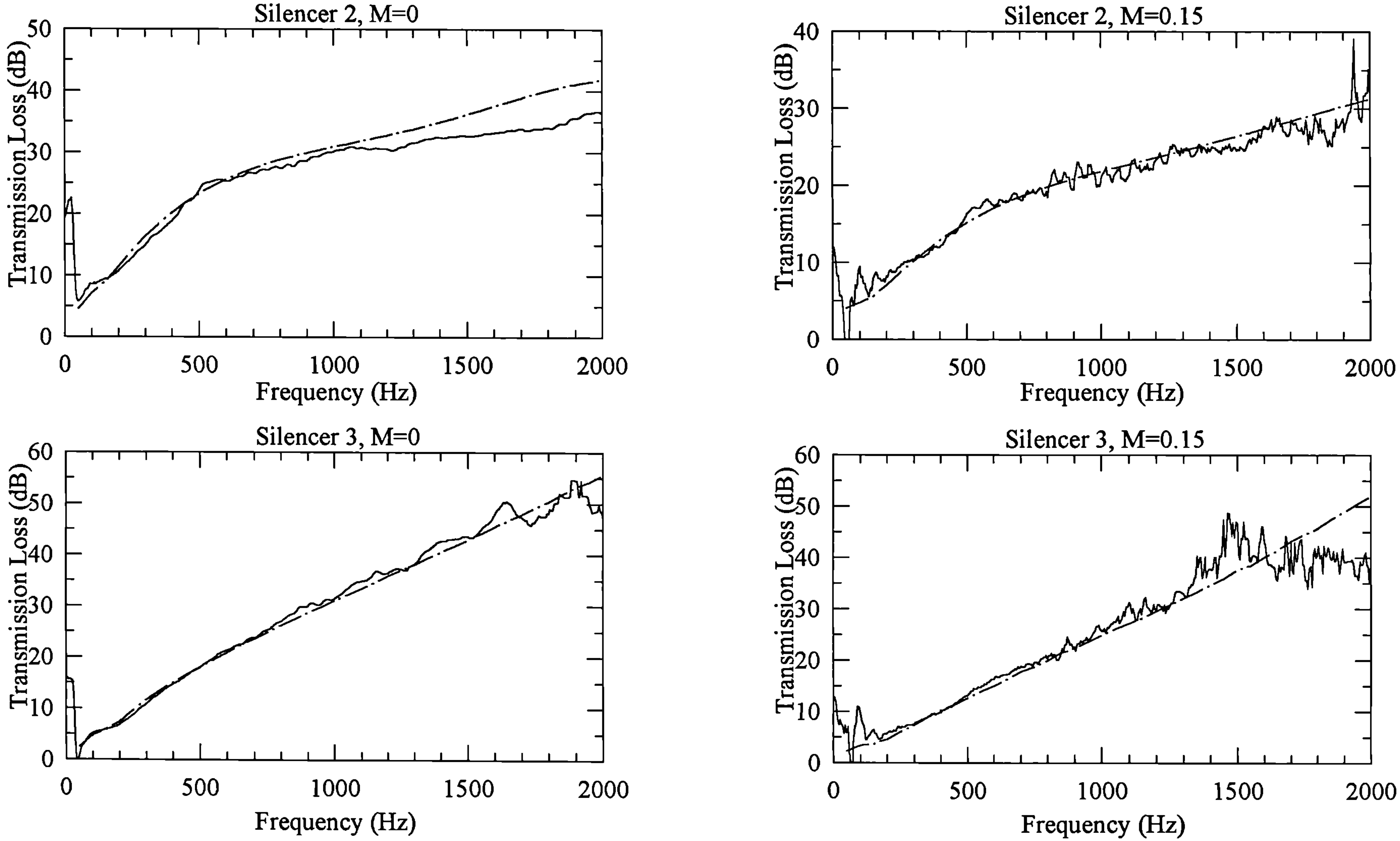

Figure 9.9. Mode matching predictions using integral method. ——— , Experiment; —·— , Predictions using 10 modes.

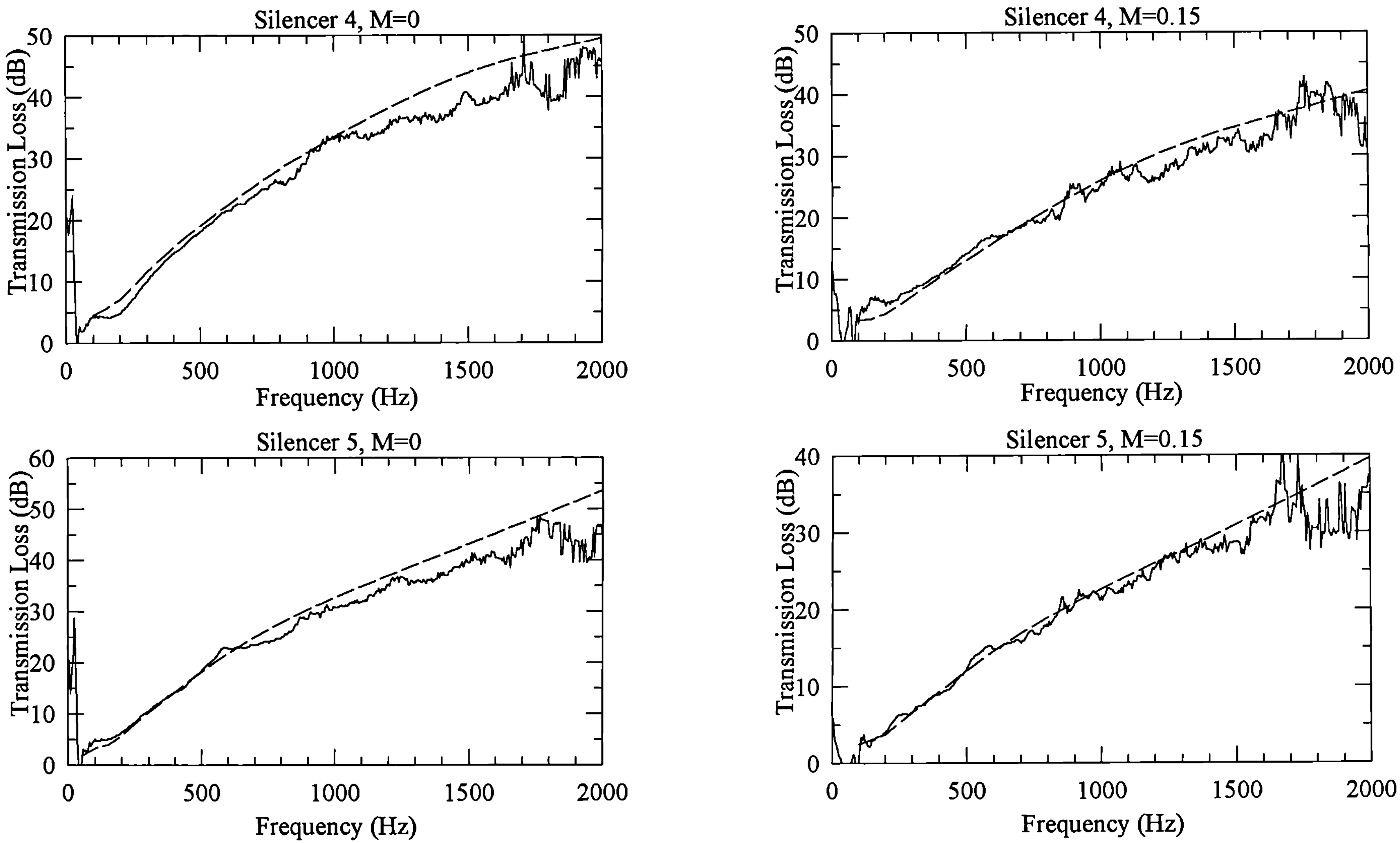

Figure 9.10. Mode matching predictions using integral method. ——— , Experiment; – – – , Predictions using 1 mode.

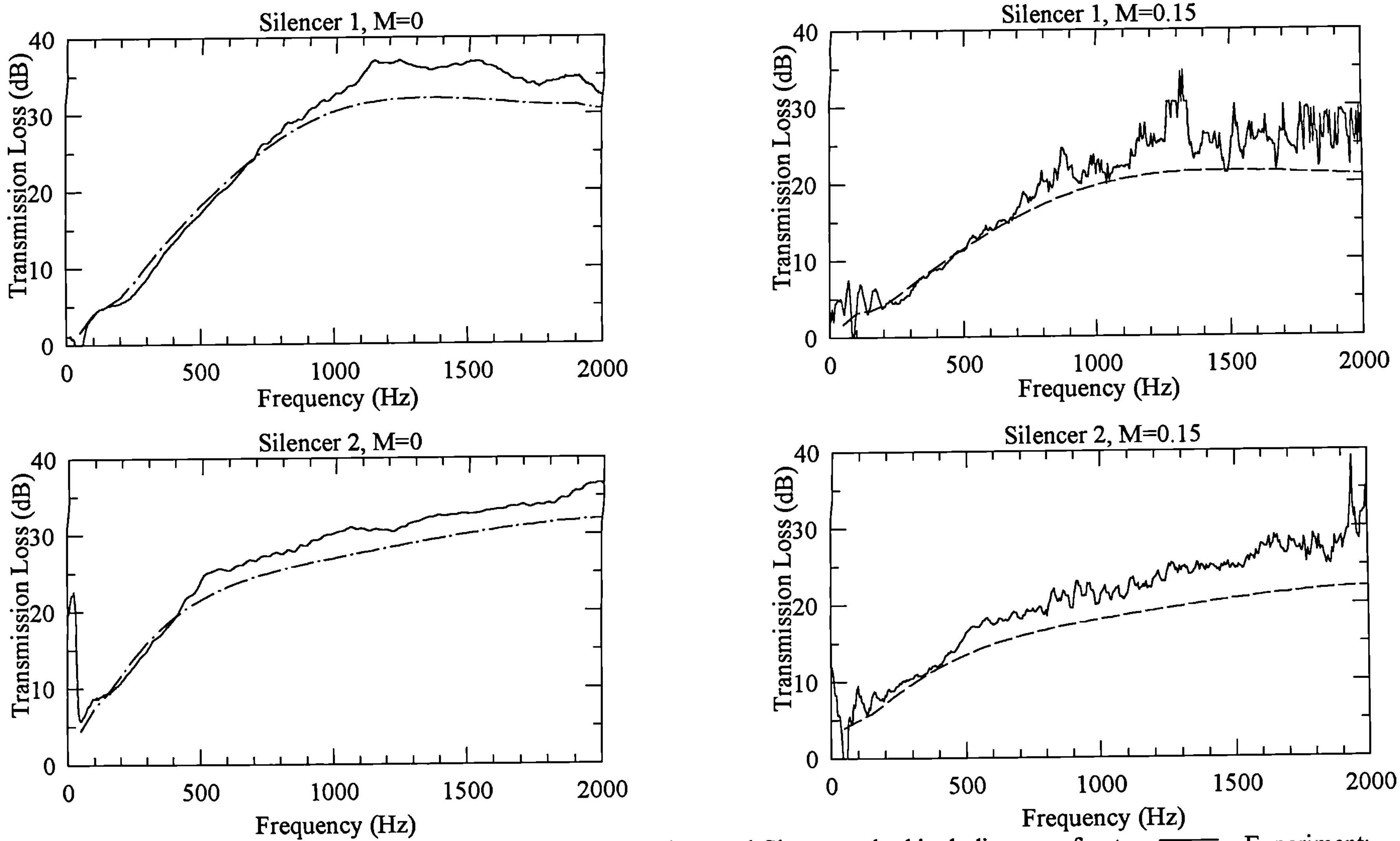

Figure 9.11. Mode matching predictions using Cummings and Chang method including a perforate. ——— , Experiment; — — — , Predictions using 1 mode; —·— , Predictions using 6 modes.

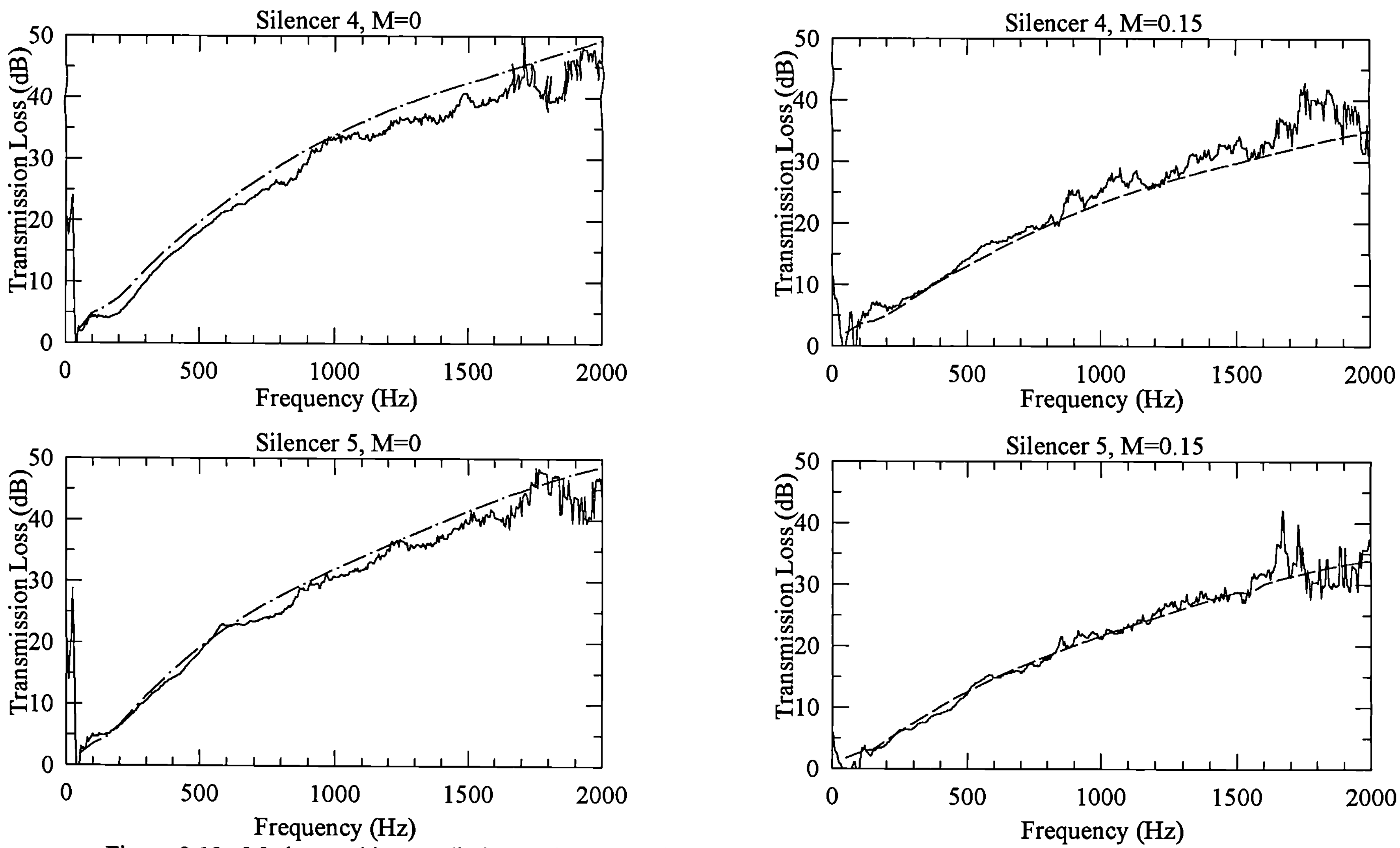

Figure 9.12. Mode matching predictions using Cummings and Chang method including a perforate. ——— , Experiment; — — — , Predictions using 1 mode; —·— , Predictions using 6 modes.

CHAPTER 10

EVALUATION OF THE MODELLING TECHNIQUES FOR DISSIPATIVE SILENCERS

Section 10.1

Introduction

In this thesis, three different theoretical approaches to predicting the behaviour of finite length exhaust silencers have been examined. The fundamental mode model (see Chapter 6) was examined first in view of its relative simplicity and because the model proved capable of providing transmission loss predictions with minimal computational effort. However correlation between the fundamental mode predictions and experimental data was poor, especially for large silencers and those with a non-circular arbitrary cross sectional shape. Therefore a more complete approach was implemented in Chapter 7, and this involved applying a full finite element analysis to the dissipative silencer. The finite element model provided a much better correlation between prediction and experiment for both the axisymmetric and the oval silencers. Unfortunately the improvement in prediction accuracy obtained by using the finite element method was gained at the expense of a large increase in computational effort. Finally, a mode matching model was implemented (see Chapter 9) which utilised eigenvalue solutions obtained by using a finite element method (see Chapter 8). The mode matching approach provided better correlation with experimental data than the fundamental mode method but, as with the full finite element method, this was at the expense of an increase in computational effort. However the mode matching predictions did offer some saving in computational effort when compared to the full finite element method, whilst maintaining good correlation with experimental data. The question which arises from the three models studied is: which model best fits the initial design criteria? In this chapter, the three different theoretical models are compared to one another, from which recommendations are made concerning the future usefulness of each model as a design tool. To avoid confusion, the model implemented in Chapter 7 is called here the finite element model and the model implemented in Chapter 9 is termed the mode matching model, despite the use of finite elements being common to both methods.

In this chapter the comparison between the three models is based upon predictions obtained for the five silencers described in Chapter 5. The silencers were designed differently in order to asses the capability of each theoretical model in relation to aspects such as size, shape and absorbent material. In previous chapters, the experimental data obtained in Chapter 5 were used as the sole basis for estimating the accuracy of each model, and from here decisions were made concerning the direction in which future modelling should go. However, to avoid constant duplication of results, the different theoretical models were not directly compared to one another. Accordingly, in this chapter the relative merits of each model are assessed by direct comparisons between the models. It is assumed here that the finite element model provides the best theoretical predictions available and that these can be used, in addition to the experimental data, as a basis for examining the accuracy of both the fundamental mode and mode matching predictions which both contain simplifications. This is particularly useful at higher frequencies, where doubts about the accuracy of the experimental data exists. From here conclusions can be drawn about the degree of complexity that one must incorporate in the model to obtain acceptable predictions.

The relative suitability of each of the theoretical models for use in silencer design is evaluated in the next section, and this is based upon criteria laid out in the introduction to this thesis (Chapter 1). To re-cap, the criteria require that the theoretical model must be capable of predicting the performance of a dissipative silencer over a nominal frequency range of 0-2kHz. The model must also account for a silencer of arbitrary cross-sectional shape which also includes mean flow in a central channel separated from the absorbent by a perforated plate. Finally the model must also be capable of providing an iterative design tool which can be used on a PC. This final point places some restrictions upon the degree of complexity which can be included in the model. In the next section, the performance of each model against each of these criteria, and also against each other, is examined. Initially, this is to be done without the inclusion of a perforate because, as was mention in previous chapters, some doubt still exists about the values being used for the perforate impedance. The effect of the perforate on transmission loss predictions is examined separately in Section 10.3, in which an attempt is made to find corrected values for the perforate impedance. Finally, in Section 10.4, insertion loss predictions are compared to the experimental data obtained in Chapter 5 in order to provide an alternative test upon the accuracy of the predictions found using the theoretical models studied here. Also, a brief discussion is given on the consequences of the transmission loss results found for the silencers studied here, and also the future design of exhaust silencers.

Section 10.2

Evaluation of Theoretical Models

The relative merits of each of the three theoretical models are discussed in this section, based upon the criteria mentioned in the introduction to this chapter. Transmission loss predictions obtained using the fundamental mode, finite element and mode matching models are compared with experimental data in Figures 10.1, 10.2 and 10.3, for silencers 1 to 5 (without a perforate). It is evident from these figures that all three models give similar predictions at low frequencies (below approximately 200Hz), especially for the axisymmetric silencers. This is to be expected since only the fundamental mode should affect the transmission loss at such frequencies. However, when one examines frequencies above 200Hz, a progressive difference between the three predictions occurs. For the fundamental mode solution it is obvious, from a comparison between prediction and experiment, that relatively poor correlation is achieved at higher frequencies, especially above 750Hz. This is particularly true for the oval silencers since the fundamental mode model is capable of predictions for circular silencers only, and therefore an equivalent area prediction must be used. At higher frequencies the experimental data are potentially inaccurate above 1kHz, and therefore it is more informative to compare the fundamental mode predictions to those found by using the finite element method. Above 1kHz, the fundamental mode model provides relatively poor correlation with both the mode matching and the finite element predictions for each of the silencers studied. It is perhaps surprising that the fundamental mode model is in such poor agreement with the mode matching predictions since, when mean flow is present, only a single mode has been used to find the mode matching predictions. It is thought that these discrepancies are caused by the use of different weighting functions in each model since, when only the least attenuated mode is assumed to propagate, the matching of volume velocity in the fundamental mode solution is equivalent to matching particle velocity in the mode matching solution. For instance, the fundamental mode model applies an area weighting to the matching conditions whereas the mode matching method employs the duct eigenfunctions as the weighting functions. This implies that the mode matching method places a greater weighting on matching the continuity conditions in the central channel, but the reasons behind why this improves the overall transmission loss predictions obtained using the mode matching method when compared to the fundamental mode model are, at present, unclear. The fundamental mode model does, however, offer one advantage over the other two methods since transmission loss predictions can be computed quickly and easily on a PC. In addition there is no need to resort to finite element packages such as the finite element NAG routines required here for use in the other two methods. However, in producing a very fast and simple solution, accuracy is inevitably sacrificed and, unless one only requires a model accurate up to approximately 500Hz, the predictions are not good enough to allow the method to be used as a design tool.

One is now left with a choice between the two numerical formulations. This is, perhaps, inevitable in view of the need to account for arbitrary cross-sectional shapes. Since the full finite element model described in Chapter 7 provides a completely general approach to modelling silencers it has been assumed here that this method provides the most accurate numerical results of the three methods studied. This allows the mode matching model to be compared to these "benchmark" finite element predictions to ascertain its accuracy A comparison between the finite element and mode matching predictions shows that, in most cases, the predictions agree remarkably well. This is particularly true for the axisymmetric silencers when no mean flow is present, the correlation no doubt being helped by the introduction of higher order modes in the mode matching predictions. When mean flow is introduced, only a single mode is used in the application of the mode matching method and the predictions differ to a greater extent, especially at higher frequencies, although the correlation between the two still remains good. For the oval silencers the correlation between the two methods is again good for silencer 5 (see Figure 10.3), although a larger difference between the two methods is observed for silencer 4. The reasons behind the increase in the discrepancies between the two models for silencer 4 are not clear although the effect cannot be caused by the neglect of higher order modes in the mode matching solution, since similar behaviour is also observed when no mean flow is present and higher order modes are included. One rather surprising aspect observed in the present results is the apparently small effect of the higher order modes on the correlation between the mode matching predictions and those found using the finite element method. Indeed, whilst the higher order modes do offer a slight improvement in predictions when no mean flow is present, the additional difference between the mode matching and finite element predictions caused by the neglect of higher order modes when mean flow is present is small and amounts to no more than about 2dB. While one would expect these differences to increase above 2kHz, within the frequency range of 0-2kHz studied here, the effect of the higher order modes does seem to be relatively small. This confirms that the discrepancies found when applying the fundamental mode model to axisymmetric silencers are caused principally by the use of different weighting functions. If it is assumed that the finite element predictions are the most accurate of those discussed here, then a comparison between the mode matching and the finite element predictions indicates that the mode matching method retains enough accuracy potentially to replace the full finite element method. However, before a recommendation of the most effective theoretical model is made, one must also examine the relative CPU time required to solve the finite element and the mode matching model.

A major reason behind implementing the mode matching method was the need to reduce the computational time demanded by the full finite element model. For the Cummings and Chang mode matching scheme (see Section 9.3), the time taken to solve the problem is dominated by the finite element solution of the eigenvalue problem. Since the eigenvalue problem requires only the cross section of the silencer to be meshed it offers a large reduction in the number of nodes required when compared to the full finite element solution. This appears to offer the benefit of faster solution times, but unfortunately this is not always the case. It is certainly true that in the modelling of the oval silencers, in which a full three dimensional mesh is required by the finite element model, the jump in problem size from the two dimensional to the three dimensional induces a very large increase in computational effort. Consequently, the use of a two dimensional eigenvalue solution will always lead to computationally faster transmission loss predictions. However for the axisymmetric silencers, the difference between the time required to solve a two dimensional full finite element problem and a one dimensional mode matching problem is not as large as one would expect. Part of the reason for this is that the formulation of the full finite element problem automatically results in a banded matrix, whereas this is not the case for the eigenvalue matrices. This problem is exacerbated when mean flow is present, since the eigenvalue matrix is doubled in size compared to its zero mean flow matrix. In addition, it is also necessary to invert a matrix when computing the eigenvalues. Indeed when mean flow was present, transmission loss predictions obtained using the mode matching method could take even longer to solve than those obtained using the full finite element method. This observation obviously depends upon the number of nodes used to mesh each problem. In Chapter 8, the mesh sizes used for the eigenvalue problem were chosen in order to find accurate solutions for a number of higher order modes in addition to the least attenuated mode, and this required a relatively high mesh density. If the mode matching model implemented in Chapter 9 is run with similar mesh densities to those in Chapter 8 then, especially when mean flow is present, the mode matching solutions take longer to compute than the finite element solutions obtained using the mesh sizes listed in Chapter 7. This is a surprising result, although the solution times for the eigenvalue matrices do appear to be very sensitive to the number of nodes used. Fortunately, transmission loss solutions found by using the mode matching method do not require the higher order modes to be predicted to such a high degree of accuracy, and therefore one can reduce the number of nodes used. The reduction in the number of nodes then allows a faster solution to be obtained by using the mode matching method than that for the finite element method. However, one must caution against reducing the number of nodes too far since, especially if other mode matching schemes are used which require a large number of modes in order to achieve convergence, a sufficient number of nodes must be retained in order to calculate even the second and third least attenuated modes accurately. Fortunately this is not a problem in the present case, since the Cummings and Chang mode matching method only works adequately for a single mode when mean flow is present and therefore a relatively coarse mesh is possible. Consequently, in general, the Cummings and Chang mode matching predictions can be obtained more rapidly than the equivalent finite element predictions, something which is always true for the elliptical silencers. Therefore the mode matching method does appear to be successful at reducing CPU time in addition to retaining a high degree of accuracy.

Since the finite element and mode matching models both use numerical approaches relying upon finite element formulations, the amount of input required from the user at the start of the problem is important. Clearly, if either model is to be used for design purposes, then it is necessary to generate a completely new mesh for each silencer studied. For the axisymmetric silencers this does not present too much of a problem. For instance a one dimensional mode matching mesh is very simple to produce and does not even require the use of a specialised mesh generator. A two dimensional finite element mesh is not quite so straightforward but it is, nevertheless, not too time consuming to generate, especially considering the simple rectangular elements which can be used. Significant problems only occur in modelling oval silencers using a full finite element model. This requires the use of a full three dimensional finite element mesh such as the one shown in Figure 7.3, and hence considerably more effort on the part of the user is necessary, even with the aid of a commercial mesh generator. In contrast, only a simple two dimensional mesh is required by the mode matching model in order to study silencers with arbitrary cross sectional shapes. Therefore, if ease of use is a consideration, then the mode matching method appears to be more practicable to use than the full finite element model.

Apart form the computational expense associated with the finite element predictions, problems have also occurred in the predictions themselves. This only came to light in the case of the oval silencers which required three dimensional modelling. At very low frequencies (below 100Hz) the predictions become unstable and, in some cases, even become negative (see Figure 10.3 and also Figure 7.8). This effect was discussed in Chapter 7 and it was concluded that this is caused by numerical problems, but it is obviously an undesirable effect, especially if a robust silencer model is required. In contrast, the mode matching predictions obtained for silencers 4 and 5 at low frequencies seem to be stable and produce reasonable answers, and thus one would expect fewer problems to occur with the mode matching model. However, the author is by no means certain that the mode matching method, in the form implemented here, is free from problems. This is because various fundamental aspects of the mode matching approach - particularly stability and convergence criteria - are far from fully understood, and the Cummings and Chang method probably needs further testing in order to establish its robustness. However, so long as only a single mode is used when mean flow is present, the author is confident that the mode matching method will be free from problems for silencers of the type studied here.

It may be concluded from this assessment of the three theoretical models that a mode matching formulation, based upon the approach used by Cummings and Chang [23], offers the best balance between accuracy of predictions, speed of solutions, ease of use and robustness.

Section 10.3

The Influence of the Perforate on Transmission Loss Predictions

A perforated plate is often employed in silencers, to separate the absorbent material from the central channel of the silencer, and this has been introduced into each of the theoretical models examined in this thesis. At present it is common practice to ignore the effect of the perforate, indeed the number of models in the literature that include a perforate is small; examples of the few investigations including perforates are those of Cummings [14], and Nilsson and Brander [15]. Evidence justifying the neglect of the perforate was cited by Peat [109], who studied the effect of perforate porosity on plane wave transmission loss predictions obtained for a silencer identical to that examined by Cummings and Chang [23]. Peat concluded that, unless a perforate of low porosity was used (below approximately 10%), the additional effect of the perforate on transmission loss predictions was negligible. Consequently, most theoretical models of automotive dissipative silencers ignore the effect of the perforate and this was the case in the original formulation of the models studied here. The perforate was introduced into the theoretical models discussed in this thesis in the belief that its behaviour had not yet been investigated comprehensively enough to permit its complete omission. Furthermore, in Chapter 4, it was found that when a porous material was backing a perforate it could significantly increase the impedance of the perforate, an effect which had not been considered before. In this section the effect of the perforate is studied further, and conclusions are drawn concerning its future use in theoretical modelling.

The acoustic impedance of the perforate alters the pressure boundary condition between the central channel and the absorbent. Semi-empirical expressions for the perforate impedance are given in Chapter 4, for the case when mean flow is present. When mean flow is not present, perforate impedance values given in the literature are used [107] since different attenuation mechanisms are now present and one cannot simply employ the semi-empirical predictions given in Chapter 4 with the friction velocity set equal to zero. The additional effect of the absorbent material is added to the predictions without mean flow in the same way as that carried out for the semi-empirical model in Chapter 4. The introduction of these impedance values into the three completely independent theoretical models showed that the qualitative effect of the perforate on each silencer was similar, indicating that the impedance of the perforate has been introduced correctly into the three models. This is particularly noticeable for silencers 1 and 2, both with and without flow, since all three models predict an increase in transmission loss at lower frequencies and a reduction at higher frequencies. Indeed, the finite element method and mode matching predictions are very similar, although one would expect this from the similarity observed in the predictions found without a perforate. However the effect of the perforate on the fundamental mode solution is much smaller than that in the two numerical methods, especially at high frequencies. The reasons for this are, at present, not entirely clear, although the effect is probably linked to the choice of weighting functions in the fundamental mode model. In addition, the effect of the perforate on transmission loss predictions can be observed to depend upon the type of silencer modelled; for instance the predictions for silencers 3 and 4, which contain materials with a relatively low flow resistivity, indicate that for these silencers, the perforate has a much smaller influence on the transmission loss than that when a high flow resistivity material is employed. This indicates that the effect of the perforate on transmission loss predictions depends upon which type of theoretical modelling has been used and the details of the silencer. Consequently, one cannot draw definite conclusions about the influence of the perforate until predictions have been obtained for a number of different silencers using an accurate and versatile theoretical model such as the finite element model described in Chapter 7.

The author is confident that, for the models implemented in this thesis, the perforate impedance has been introduced correctly. However, when one examines the transmission loss predictions obtained with a perforate included, given in the previous chapters, one finds that an improvement in correlation with experimental data does not necessarily occur as the perforate is introduced. Consequently the values used for the perforate impedance must be questioned. It has been discussed in previous chapters that the additional effect of the porous material on the perforate impedance has a substantial influence upon the transmission loss predictions. For absorbent materials with high flow resistivities, such as E glass, this effect has been shown to produce differences in the transmission loss as high as 10dB at the higher frequencies. The additional effect of the absorbent depends heavily upon the localised influence of the porous material on the acoustic streamlines adjacent to the holes in the perforate. In Chapter 4, the semi-empirical predictions obtained for the acoustic impedance of the perforate were made with the assumption that a uniform density of material was present immediately adjacent to the perforate. This is, however, unlikely to be the case in silencers such as the ones studied here, in which the absorbent materials have not been uniformly packed and will contain "voids" adjacent to the perforate holes. Consequently it is suggested here that the influence of the absorbing material on the acoustic impedance of the perforate is reduced in a randomly packed silencer, since the density of the absorbent material adjacent to the holes is not uniform. To account for this "random" effect it is proposed here to use an empirical constant in order to reduce the effective average density of the absorbent material adjacent to the holes. Obviously, it is not practicable to measure the bulk density of the material adjacent to the holes in each silencer, and therefore the constant must be obtained by trial and error, once comparisons have been made between predictions and experimental data. Unfortunately this method relies upon assuming that the experimental data found in Chapter 5 are accurate over the entire frequency range of interest. In Chapter 5, transmission loss measurements were presented over a frequency range of 0-2kHz, but the method used to find this data is such that only frequencies lying in the range 100Hz-1kHz were reliable. An area of uncertainty therefore exists between 1kHz and 2kHz, in which one cannot be sure of the accuracy of the experimental data. This frequency range also represents the region in which the effect of the perforate is at its greatest. However, as described in Chapter 5, a measurement technique identical to that used for the dissipative silencers was also applied to a plain expansion chamber and a comparison between prediction and experiment indicated good agreement up to approximately 1600Hz. Therefore it is possible that the measurements found for the dissipative silencers may be sufficiently reliable up to approximately 1600Hz. Whilst it is not expected that the values measured between 1kHz and 2kHz are quantitatively very accurate, it is nevertheless hoped that the qualitative trends observed provide a good indication of the silencers' actual performance. Therefore the acoustic impedance of the perforate is to be altered here through the use of an adjustable constant which is changed by trial and error until a value is obtained which provides the "best fit" between prediction and experiment over a frequency range of 0-1600Hz. The question which now arises is: how should this constant be defined? The author believes that the impedance of the perforate depends upon the local density of the absorbent material, adjacent to the holes. In a randomly packed silencer, one would expect a range of material densities adjacent to each hole and, after examining the problem experimentally, it became evident that the area of lowest material density provided the greatest influence on the impedance of the perforate. For example, small areas in which no material was present often occurred adjacent to the holes, and this had the effect of significantly reducing the overall acoustic impedance of the perforate. Also it appears that the manner in which the silencers studied here were manufactured has, to some extent, caused the voids to appear adjacent to the perforate. Consequently, the *effective* density of the material adjacent to the perforate is less than the overall bulk density of the material in the silencer box. Therefore it is proposed here that the random packing of the material adjacent to each hole should be quantified by an adjustable parameter which is related to the localised density of this material. The constant will be called here the "perforate coefficient" and is less than or equal to unity, the effective localised density of the material adjacent to each hole being made equal to the average bulk density of the material in the silencer box multiplied by the perforate coefficient. Values for the perforate coefficient should be unique to each silencer, although it is anticipated that a value can be found, characteristic of individual materials so that it is unnecessary to find experimental data for every silencer studied. For the silencers studied here values for the perforate coefficient were obtained by trial and error after making a number of different numerical predictions by using the full finite element method. The process involves "fitting" the finite element predictions to the experimental data across the entire frequency range of 0-2kHz, although the biggest differences occur at higher frequencies and so this area tended to dominate the procedure. It was observed that, when the perforate coefficient was reduced below unity, the finite element transmission loss predictions for silencers 1 and 2 reduced slightly at the lower frequencies and increased at higher frequencies. Unfortunately, the influence of the perforate coefficient was much greater on the predictions at high frequencies so that, whilst good correlation could be obtained above 1kHz, no significant improvement was observed at lower frequencies. This behaviour can be observed for silencers 1 and 2, both of which contain E glass, in Figure 10.4. Transmission loss curves for a perforate coefficient of 0.55 are shown in Figure 10.4 and one can observe no significant improvement at the lower frequencies over those predictions for the same silencer with a perforate, that are given in Chapter 7. The same perforate coefficient was also applied to the mode matching model and the transmission loss predictions for silencers 1 and 2 are shown in Figure 10.5. It is evident from both Figures 10.4 and 10.5 that introducing the perforate coefficient has improved predictions at the higher frequencies, both with and without mean flow. Unfortunately this benefit is not universally observed at lower frequencies. This is particularly true for the finite element predictions when no mean flow is present since, especially for silencer 1, the predictions are consistently higher than experiment up to about 1kHz. This is rather disappointing since the corresponding predictions found without a perforate were very good for this particular silencer. The predictions obtained using the mode matching method do appear to offer a small improvement on the finite element predictions when no mean flow is present although, when mean flow is present, this improvement is not maintained at higher frequencies. It is perhaps tempting here still to explain the discrepancies between prediction and experiment at the lower frequencies in terms of an overprediction of the influence of the porous material on the perforate, suggesting that one should use still lower values for the perforate coefficient. However, it was observed that, even if the additional effect of the absorbent material was totally removed from the model when no mean flow was present, differences of approximately 1dB were still observed for silencers 1 and 2. This means that the perforate impedance on its own, without the additional effect of the absorbent, can still cause differences between the transmission loss predictions with and without a perforate. This behaviour is in contrast to that observed by Peat [109]. However, the difference between the results found here and the observations of Peat might be explained by the fact that, in addition to the use of a different theoretical model here, different values for the perforate impedance have also been used. This is apparent if one examines the values used for the imaginary part of the perforate impedance, since Peat [109] used a value of 0.25 inside the bracket (see equation (6.98)) whereas in the present analysis, a value of 0.75 has been used. At low frequencies, the imaginary component of the impedance dominates the influence of the perforate upon the transmission loss, and consequently it is not surprising that an increase in the effect of the perforate has been observed here. Subsequently it was found that, no matter how small the value for the perforate coefficient was, the predictions still did not agree well with experimental data at low frequencies. Indeed this effect was particularly noticeable in the case of silencer 3, since the additional effect of the A glass present in silencer 3 is small because of its low flow resistivity, and so any changes in the transmission loss predictions are caused principally by the effects of the perforate itself. Therefore, the application of the perforate coefficient only caused significant differences in the transmission loss predictions for silencer 3 at higher frequencies and hence this is not shown here. Consequently, whilst it is possible to use the perforate coefficient to obtain better correlation between prediction and experiment over the entire frequency range, one is still left with a slight overprediction of the transmission loss at low frequencies.

In addition to altering the transmission loss predictions, the perforate changes the theoretical formulations of each of the models and also other aspects of the physical behaviour of the silencer. One significant consequence of including a perforate in a dissipative silencer is the influence it exerts over the mean flow in the absorbent. The author believes that the presence of a perforate prevents significant levels of mean flow from being induced in the absorbent, and therefore in each of the theoretical models implemented in this thesis, mean flow in the absorbent has been neglected. This observation was confirmed by measuring the pressure drop along the length of the absorbent in the silencer box, from which mean flow values can be inferred. For each of the dissipative silencers studied here, the mean flow values inferred from pressure drop measurements were extremely small, indicating a virtual absence of mean flow in the absorbent which is thought to be caused by the presence of the perforate; the solid part of the perforated tube largely preventing the penetration of the mean flow, in the flow passage of the silencer, into the porous absorbent. A similar observation was also made by Peat [109]. Consequently the presence of the perforate allows the theoretical models to be simplified, and this is especially true for the finite element formulation described in Chapter 7, where it is now unnecessary to include the non-linear mean flow field in the absorbent (see the investigation of Peat and Rathi [26]). The perforate has been found to effect the formulation of the theoretical models in other ways; for instance, both the finite element model of Chapter 7 and the eigenvalue model of

Chapter 8 have been simplified. For the finite element model, the perforate now allows the use of C^0 continuous elements in the finite element mesh (see Chapter 7), whereas for the eigenvalue solution, the final matrices have been significantly reduced in size. Indeed this introduction of the perforate into the eigenvalue problem has introduced a slight saving in the computational time required to solve the problem. The underlying reasons why the perforate has had such an effect upon the problem formulations is linked to the new matching conditions at the boundary, although why this should cause a simplification of the problem is not fully understood. Unfortunately the inclusion of the perforate does place additional demands upon the formulation of the finite element mesh. For instance an extra set of nodes must be included along the boundary in which the perforate lies. Since the commercial package used to generate each mesh in this thesis could not cope with the addition of these extra nodes, the mesh had to be reformulated manually. This process was found to present no problem for the one and two dimensional solutions, although it could not be performed for three dimensional solutions. Therefore if the perforate is to be included in a full finite element formulation in the future, the model will probably require the use of a specialised mesh generator.

The inclusion of a perforate has been shown in this section to improve the correlation between prediction and experiment at higher frequencies, so long as one accepts the experimental data obtained in this frequency range as being of adequate accuracy. The predictions at low frequencies do, however, cause concern. Even if one ignores the additional effect of the porous material on the perforate impedance, the transmission loss predictions including a perforate are still too high. The discrepancy at low frequencies is particularly significant because, when one implements the finite element model without a perforate, the predictions in this low frequency range are very good. It is not known why the perforate induces a deterioration in the predictions at low frequencies, or indeed if there are any other problems with the modelling not associated with the perforate which could be affecting these predictions. Since the largest problems seem to occur only for silencer 1, it is perhaps possible that problems unique to this silencer have caused the discrepancies. However the author would doubt this and it is probably necessary to investigate the behaviour of the perforate more closely in the future. What cannot be disputed is that, if the perforate impedance values reported in Chapter 4, or at least those of Ingård [75], are correct, then for plate porosity values such as those used here (approximately 26%), the perforate cannot be ignored. However at the moment it is perhaps sensible to omit the perforate from the theoretical formulations until a more complete understanding has been obtained, although the author believes that this omission will lead to an overprediction of the transmission loss at high frequencies.

Section 10.4

Dissipative Silencer Design

A review of the three different theoretical approaches to designing dissipative silencers, described earlier in this thesis, has been given in this chapter. The usefulness of each of these models depends ultimately upon the design environment in which they are to be used. It is assumed that most detailed mathematical models such as those investigated here, are used as a replacement for either an experimental trial and error design procedure, or extremely simplified theoretical models. The models developed here will be useful for providing accurate predictions as a part of an iterative design procedure, from which a final silencer prototype can be obtained. Only then will it be necessary to fabricate a silencer and test it "on-engine". The usefulness of each theoretical model depends, to a large extent, on the computing capacity at the disposal of the designer. It is entirely possible to use the full finite element method implemented in Chapter 7, if one has a large amount of CPU time available. This approach will provide the best predictions in addition to permitting the modelling of silencer boxes which have a completely arbitrary shape. However, dialogue with the industrial sponsors involved in this project has revealed that most of them felt that the full finite element model was probably too complex for use as an everyday design tool. Therefore, since the fundamental mode model provides predictions which are regarded as insufficiently accurate, one is left with the Cummings and Chang mode matching method. The mode matching method probably offers the best balance between computational expense and accuracy of predictions, and it does appear perfectly possible to implement this model on a PC. It should be noted, however, that to allow use of the mode matching formulation the silencer studied must be uniform along its length. The principal advantages offered by the mode matching method are the ease with which one can initiate solutions, since only a simple one dimensional or two dimensional mesh is required, and also the speed of solution available. However, if one requires the mode matching scheme to provide numerical predictions with an accuracy comparable to that of the measured data for the silencers studied here, then the number of elements used in the finite element mesh cannot be reduced too far. This was especially true for the two dimensional models; for example a two dimensional study of silencer 1, which involved the use of only four elements, introduced an error of 2dB at 2kHz. Consequently one must balance speed and accuracy and the choice is left to the designer. However it must be stressed here that the Cummings and Chang mode matching model, as currently implemented, has a number of limitations and, in addition, various fundamental aspects of the formulation are still not fully understood. At present, this means that the model should preferably be restricted to silencers of sizes roughly similar to those in the current investigation. Such restrictions should not cause difficulties in the design of automotive silencers in general, but the author would not recommend the use of this method in the design of large air conditioning ducts, for example.

So far in this chapter, the relative merits of each of the theoretical models have been discussed. It is also of interest to examine how the results presented at the beginning of this thesis (in Chapters 2 to 4) affect the final predictions; this principally concerns the values of parameters calculated for the absorbent materials and the perforate. The effects of one of the perforates studied here was discussed in the previous section, and unfortunately these are still not fully understood. For instance, the perforate coefficient improved predictions at high frequencies but not a low frequencies. Furthermore, if one must define a perforate coefficient for each individual silencer, then the models cannot be used without reference to experimental data and this defeats the object of using a predictive theoretical model for design purposes. It is possible, however, that a perforate coefficient can be assigned to a particular material, and that this can then be applied to any silencers containing the same material. This does appear feasible in view of the predictions for silencers 1 and 2 shown in Figure 10.4. In formulating transmission loss predictions in Chapters 6 to 9, the effects of a single perforate on the transmission loss are examined. However, in view of the results obtained for a number of different perforate plates in Chapter 4, it appears possible to alter the acoustic performance of a silencer simply by changing the perforate. For example, the other flat perforates studied in Chapter 4 have lower porosities than that discussed in Section 10.3, and hence it is likely that they will have a larger influence on the transmission loss. This should manifest itself as a slight increase in the transmission loss at lower frequencies (below about 700Hz), and a reduction in the transmission loss at higher frequencies. It is therefore possible to change the type of perforate used in the silencer so as to increase the transmission loss in a given frequency range. From the results reported in this thesis, it would appear that, if a flat perforate is used, a perforate with a large percentage open area will induce an increase in the transmission loss at high frequencies and only a small decrease in transmission loss at lower frequencies, whilst a perforate of low porosity (around 5%) might increase the transmission loss at low frequencies, but reduce the transmission loss at high frequencies. Another design possibility is to use louvres which, unlike the flat perforates, do not allow the absorbent material to introduce an additional effect in the acoustic impedance of the perforate. It is expected that this will cause an increase in the transmission loss at frequencies above 1kHz. Only a rough, qualitative guide to the potential advantages to be gained from changing the perforate has been given here, although the author is certain that the careful design of a perforate can provide considerable benefits to the performance of dissipative silencers.

The relative behaviour of each of the porous materials in the context of the theoretical models reported in the previous chapters also deserves a mention here. First, it is worthwhile to recall how the propagation constant (Γ) and the characteristic impedance (z_a) of the materials are introduced into each theoretical model. If one examines the formulations in Chapters 6 to 9, it is clear that, in every case, the product Γz_a appears. This is important since equation (3.13) indicates that Γz_a is equal to the bulk complex density of the material multiplied by $i\omega$. The principal reason behind the implementation of the semi-empirical model discussed in Chapter 3 was that physically implausible values for the bulk complex density were obtained at low frequencies when experimental data, expressed in the form of Delany and Bazley coefficients (see Figure 3.6), were extrapolated to frequencies below the range of Delany's and Bazley's data [54]. Since the complex density appears in every theoretical formulation, potential errors could be introduced if these "non-physical" values are used, especially in iterative schemes such as those discussed in Chapters 6 and 9. Consequently the benefits bestowed by the semi empirical model are important, at least for the elimination of non-physical predictions. It is also interesting to examine the relative performance of each of the materials used in the dissipative silencers. Obviously one cannot do this by examining the results obtained for the silencers measured in Chapter 5, since different shapes and sizes of silencer have been used. However, if one runs a number of solutions with different materials in a single silencer, distinct differences are observed in the behaviour of the three materials. In general, at low frequencies (below 500Hz), materials with a low flow resistivity provide the best sound attenuation. This is because the high flow resistivity materials offer a much higher resistance (and impedance mismatch) to the penetration of sound waves with long wavelengths into the material. Therefore - as one would expect - in this region, A glass provides the best sound attenuation. However, even at frequencies around 500Hz, the low flow resistivity of A glass introduces a relatively poor performance in comparison to other materials. This is because it is no longer capable of dissipating the progressively shorter wavelengths (with increasing frequency) to the same degree as the materials with a higher flow resistivity. Consequently in the intermediate frequency range (approximately 500Hz to 1200Hz) the higher flow resistivity materials tend to yield the higher sound attenuation. Of the materials examined here, E glass, which has the highest flow resistivity, offered the greatest sound attenuation in the middle frequency range. At the higher frequencies (above 1200Hz), A glass still performed poorly, but basalt wool, somewhat unexpectedly, produced higher attenuations than E glass. This effect has probably been caused by the extremely high flow resistivity of E glass, since for this particular material there is still - even at these relatively high frequencies - a significantly greater impedance mismatch than is the case with materials having a lower flow resistivity, such as basalt wool. It appears that the greatest benefits to be found when choosing a porous material are to be gained at higher frequencies, since at low frequencies there is little to choose between the three materials (a maximum of approximately 1dB in transmission loss for the silencers studied here). Consequently the material which provided the best balance between sound attenuation at both low and high frequencies, was found to be basalt wool. Basalt wool is also, ironically, the cheapest of the three materials examined here. Furthermore, basalt wool has a low enough flow resistivity to prevent a significant increase in the acoustic impedance of the perforate, and this offers further benefits at higher frequencies. These are, however, only preliminary observations, made after the examination of only a few of the silencers studied here. The real purpose of this thesis is to provide design tools that enable these observations to be investigated in more detail.

In Chapter 3, four porous materials were studied; however only three, A glass, E glass and basalt wool, have been included in silencer models. Steel wool was omitted because it is usually only included as a "sock" which fits around the perforate. The purpose of the steel wool is to protect the main sound absorbing material from the erosive effects of the gas flow. The inclusion of a steel wool sock complicates the theoretical modelling since, for the finite element models, a large increase in mesh density is required in order to model the steel wool effectively. Consequently, in view of the relatively small influence that steel wool imparts upon the acoustic properties of a typical silencer it has been ignored in the present investigation. However in view of the results found for the other materials, it appears that steel wool does have the potential to provide a small increase in the sound attenuation at very low frequencies. At high frequencies steel wool reduces the effective diameter of the silencer, becoming effectively acoustically transparent. The steel wool will however provide some advantages, since its additional effect on the impedance of the perforate will be negligible, thus increasing the transmission loss at higher frequencies.

One final point concerning the bulk acoustic properties of the porous materials in this investigation is the question of anisotropy. The experimental data measured, and the modelling performed, in this thesis have been based on the assumption that the porous material encased in the silencer box behaves in an isotropic manner. For the silencers studied here, each porous material was originally packed in an essentially random fashion, and so the *local* distribution of the material would clearly not be isotropic. However it has been assumed here that the bulk acoustic properties of the material can be averaged over the entire volume of the silencer, thus allowing the bulk behaviour of the material to be treated as isotropic. Indeed, for randomly packed silencers, the designer is left with no other option, since it would be impossible either to measure the detailed packing characteristics of the silencer, or to proceed to represent them in a finite element based model such as the mode matching solution. The author acknowledges that some manufacturers do use manufacturing techniques such as the winding of the absorbent around a perforate tube - which will render the bulk acoustic properties equal in the radial and axial directions, but not the circumferential direction - although such methods are uncommon because of the expense involved. If the effects of anisotropy were required to be included, it is not too difficult to introduce them in the models presented previously, since the formulations upon which these models were based already include anisotropy (see for example Rathi [18]). However, an examination of the correlation between prediction and experiment for the silencers studied here, particularly without a perforate, indicate that the inclusion of material anisotropy is unnecessary for randomly packed silencers.

Eventually, the theoretical models developed in this thesis will be incorporated into a more general model which will account for the performance of the exhaust system as a whole. The modelling of a complete exhaust system requires a knowledge of the acoustic behaviour of components such as the exhaust and tail pipes. One also requires a knowledge of the impedance of the sound source and the performance of other dissipative elements such as catalytic converters. The integration of dissipative silencer elements into a complete exhaust system is beyond the scope of this thesis, although a number of experimental insertion loss results for a simple exhaust system which included an exhaust pipe and a tail pipe, were given in Chapter 5. It is interesting to include the theoretical predictions from previous chapters in a model from which the insertion loss can be calculated for comparison with experimental data. Insertion loss predictions are calculated by combining the four pole data for each section of the exhaust system in the manner described in Chapter 6. Since the experimental insertion loss data were taken under laboratory conditions (see Chapter 5), comparisons between prediction and experiment will provide little further insight into the quality of the theoretical prediction for the exhaust systems of internal combustion engines. Also, the mode matching solution has yet to be formulated into a four pole matrix and therefore this cannot be integrated into insertion loss predictions at present. Consequently only insertion loss predictions obtained by the use of the full finite element of Chapter 7 are included here, although this does offer an insight into the closest available correlation between theory and experiment. In addition, the perforate is not included in the following insertion loss predictions because of the uncertainty about the values used for the perforate impedance. A comparison between the full finite element predictions and the insertion loss measurements is shown, for no mean flow only, in Figures 10.6 and 10.7, for silencers 1 to 5. It is evident from Figures 10.6 and 10.7 that the trend shown in the correlation between prediction and experiment is similar to that found for the transmission loss predictions, namely that the correlation is generally good up to approximately 1kHz, but begins to deteriorate at higher frequencies. However, some discrepancies do occur at the lower frequencies and these are almost certainly caused by the incorrect modelling of components in the experimental apparatus other than the dissipative silencer. This uncertainty about the accuracy of the predictions for these additional components is the reason why experimental transmission loss data were used for comparison purposes in previous chapters. Nevertheless the insertion loss predictions do provide good correlation with experiment and the model appears capable of offering accuracy at least comparable to that found for the expansion chamber described in Chapter 5 (see Figure 5.7).

The ultimate test of the theoretical modelling carried out in this research is a comparison of predictions with insertion loss measurement obtained "on-engine". Clearly with a silencer situated on-engine, it is necessary to make predictions for high temperatures (up to 700°C in some cases). However, the absence of experimental insertion loss data at higher temperatures in the present work precludes the evaluation of high temperature theoretical predictions at present. However, including the effects of high temperatures on the absorbent material should cause no difficulties so long as one uses the semi empirical model of Chapter 3. This is because this model contains all relevant gas properties and it also provides the correct limiting behaviour as the frequency tends to zero. Christie [70] found that at higher temperatures the flow resistivity of fibrous materials changes, increasing with temperature up to approximately 500°C. Consequently at higher temperatures, the flow resistivity for the materials studied here would be increased, and this is equivalent to a lowering of frequency at room temperature. Therefore, the semi empirical model would be even more important for providing the correct limiting predictions below the frequency range of data measured at room temperature. The amount of work carried out on the behaviour of porous material at high temperatures is small and therefore further work needs to be carried out to confirm the observations of Christie, although at present the actual inclusion of high temperature effects in the models studied here does not present any problems.

In this chapter the author has made some observations based upon the results obtained from three theoretical models. These are only intended to provide a rough guide to future silencer design. The real purpose of the work presented in this thesis is the provision of tools with which the designers can decide for themselves what combination of parameters must be used to give the required silencer performance. It is hoped that in the future, the theoretical models described here can be successfully incorporated into a more complete model of the whole exhaust system, from which the designer will eventually be able to predict the "drive-by" performance of an exhaust system fitted to an engine. Such models are still a long way from completion, although the results presented in this thesis do indicate that the performance of dissipative silencers can, at least, be modelled accurately.

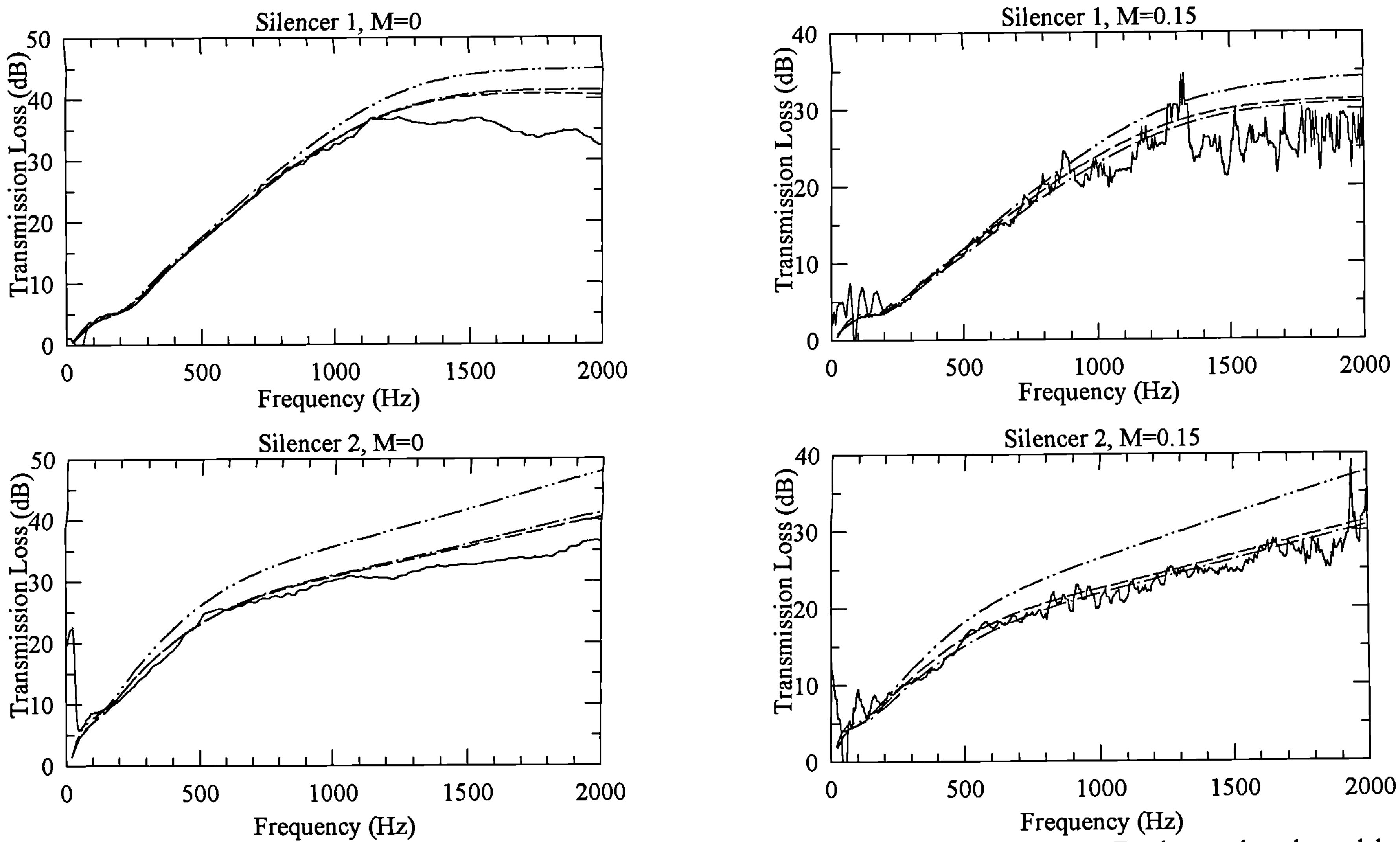

Figure 10.1. Comparison of theoretical predictions with experiment. ——, Experiment; —··—, Fundamental mode model; —·—, Mode matching model; – – –, Finite element model.

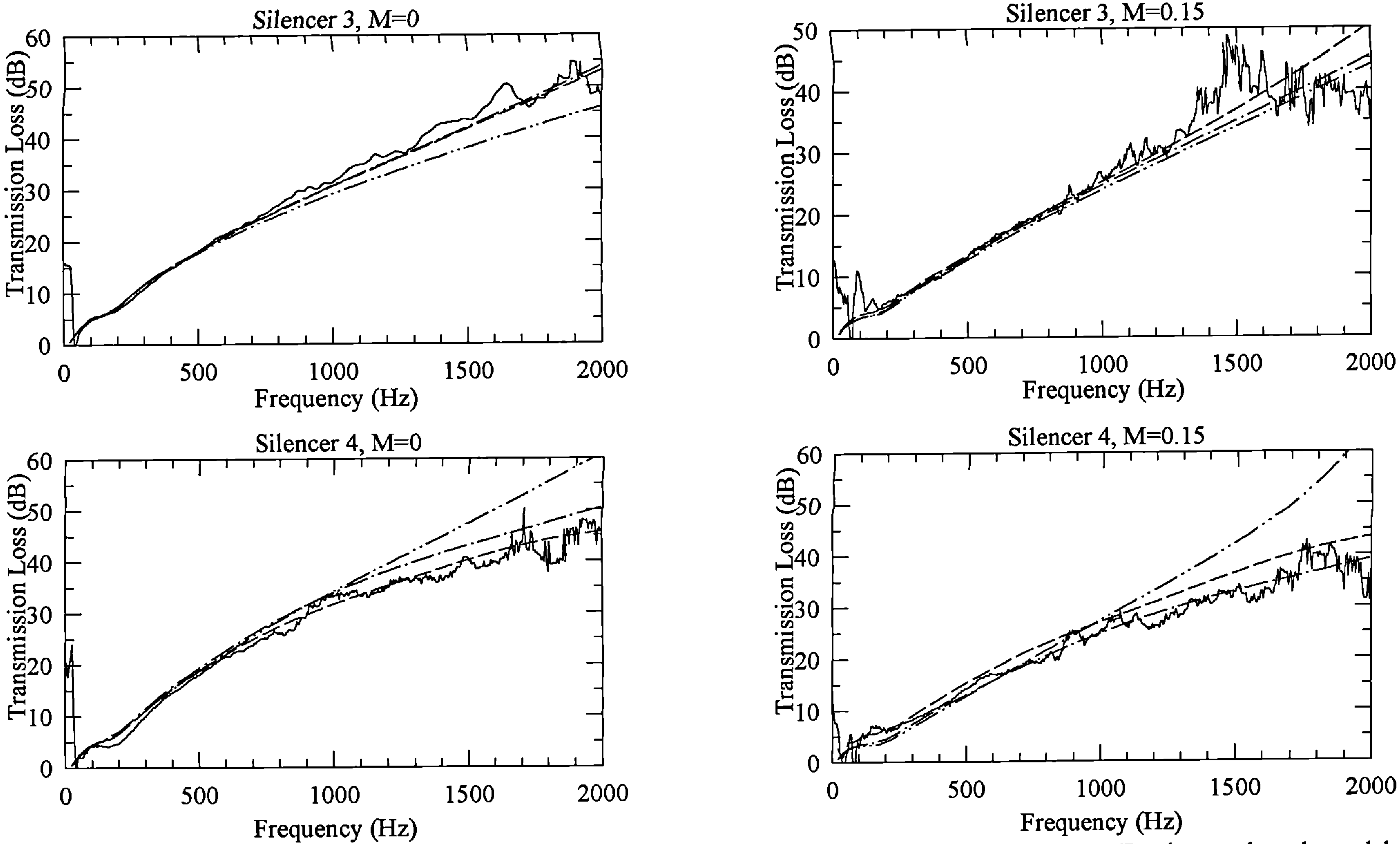

Figure 10.2. Comparison of theoretical predictions with experiment. ——— , Experiment; —··— , Fundamental mode model; —·— , Mode matching model; — — — , Finite element model.

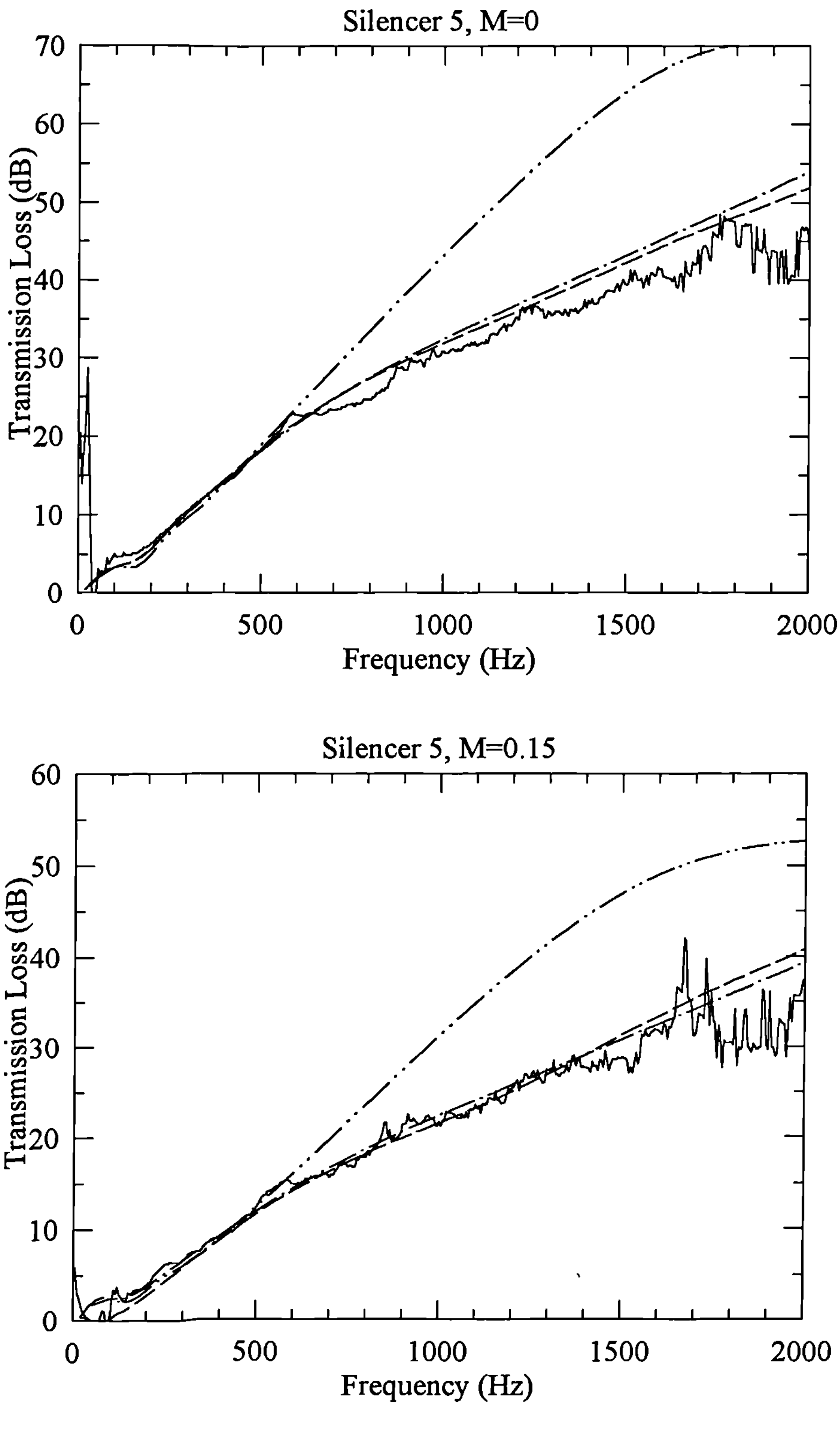

Figure 10.3. Comparison of theoretical predictions with experiment.
——— , Experiment; —··— , Fundamental mode model;
—·— , Mode matching model; – – – , Finite element model.

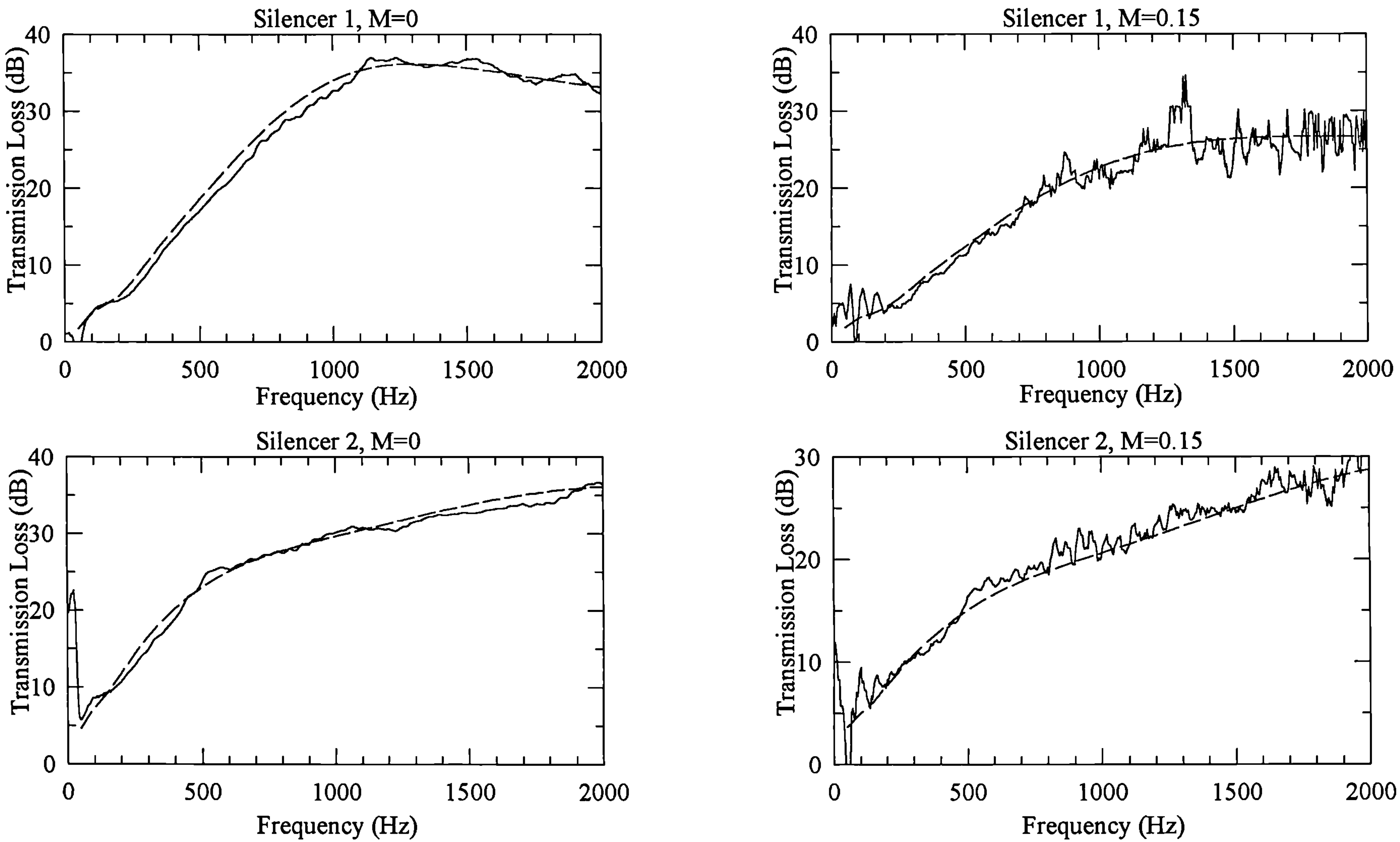

Figure 10.4. Finite element predictions with a perforate coefficient of 0.55. ——— , Experiment; – – – , Finite element predictions.

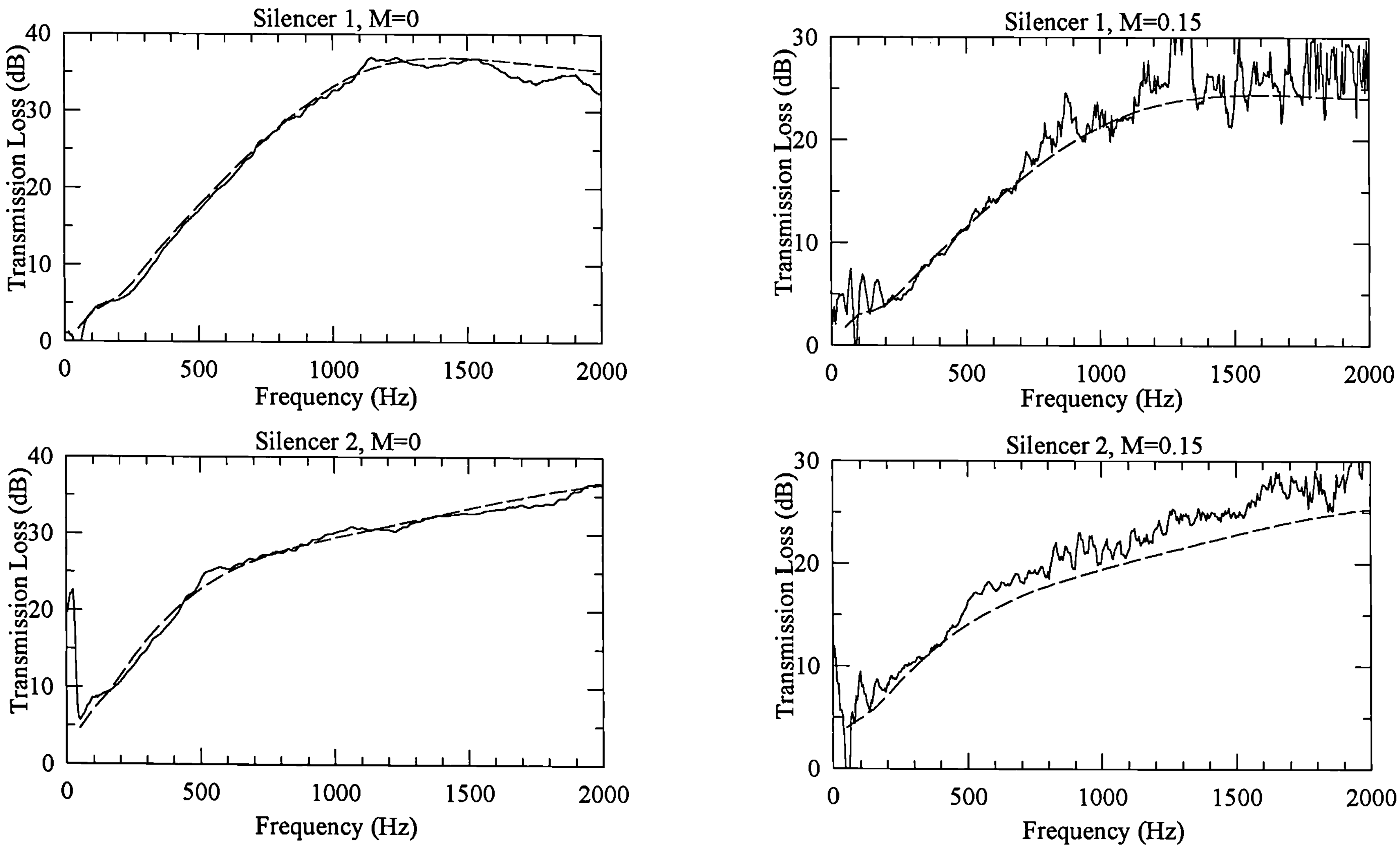

Figure 10.5. Mode matching predictions with a perforate coefficient of 0.55. ——— , Experiment; – – – , Mode matching predictions.

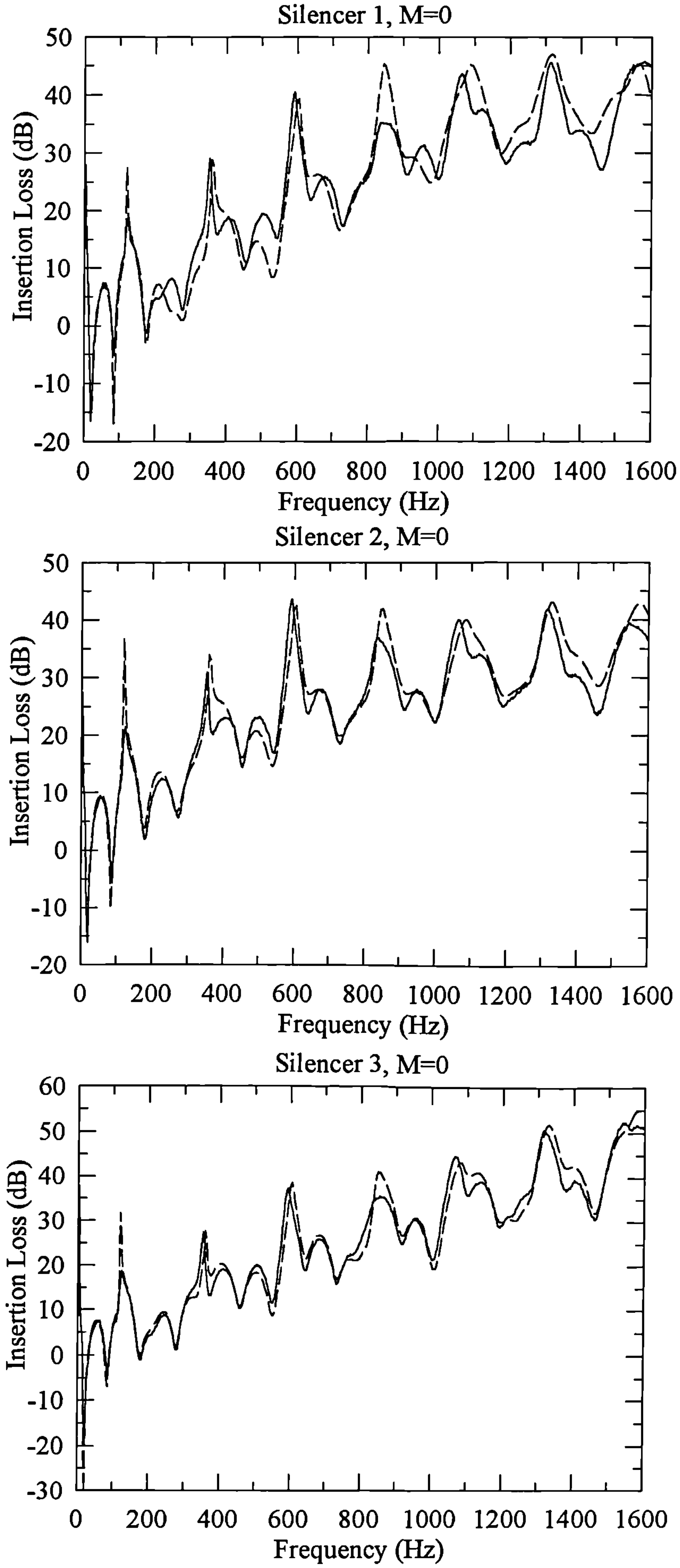

Figure 10.6. Comparison between prediction and experiment for the insertion loss.
——— , Experiment; – – – , Finite element predictions.

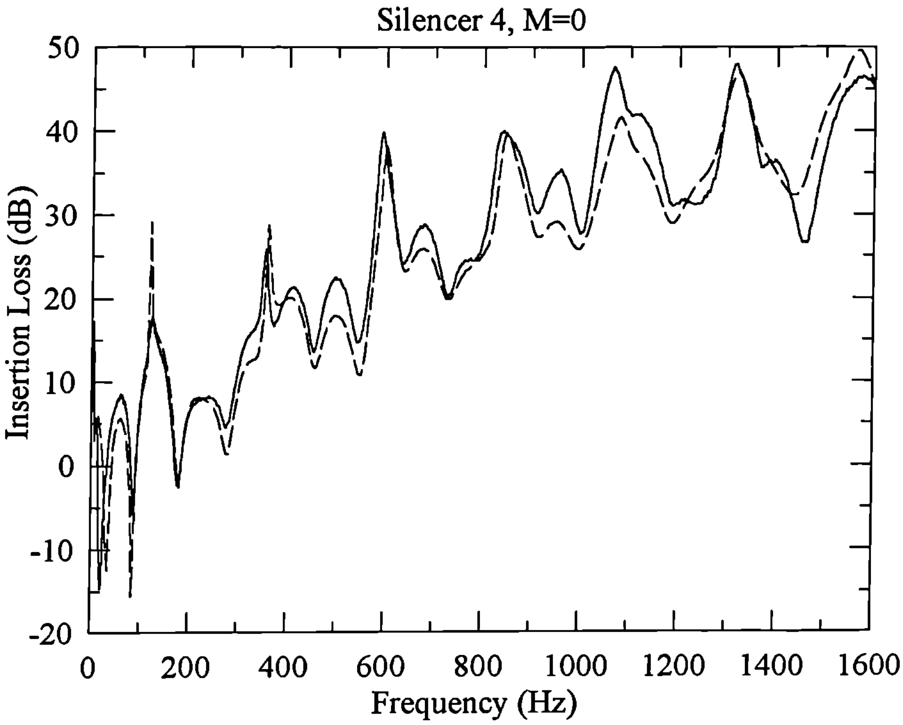

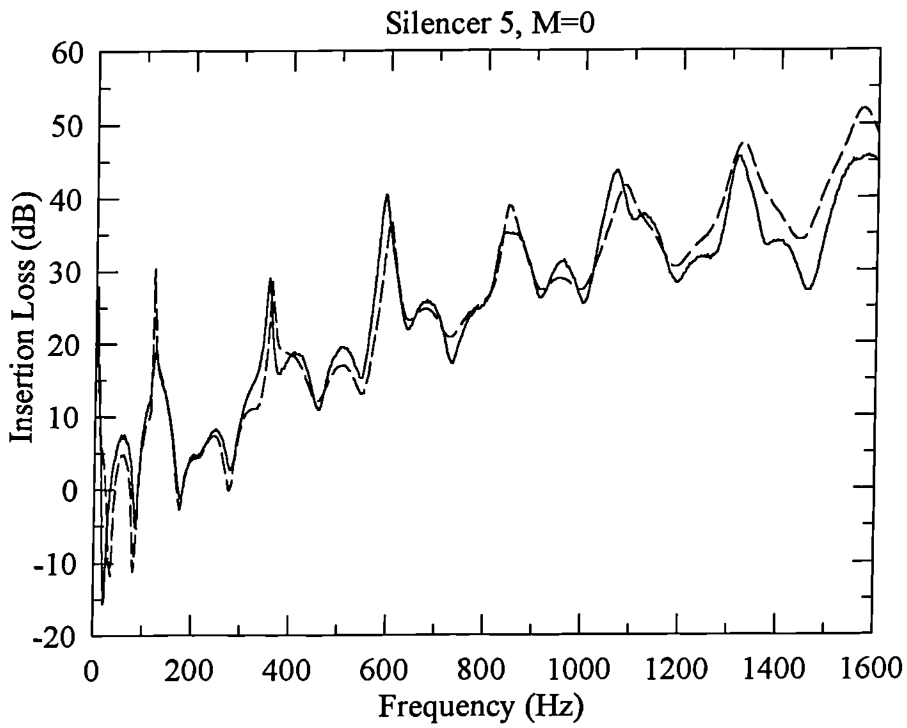

Figure 10.7. Comparison between prediction and experiment for the insertion loss.
——— , Experiment; – – – , Finite element predictions.

CHAPTER 11

WAVE PROPAGATION IN CATALYTIC CONVERTERS WITH AXIAL TEMPERATURE GRADIENTS

Section 11.1

Introduction

This thesis is concerned with the modelling of dissipative elements which go to make up the typical exhaust system of an automotive engine. So far, attention has concentrated on those elements which have been inserted into the exhaust specifically to reduce sound emissions from the engine. However, in recent years, an additional dissipative element in the form of a catalytic converter, inserted upstream of the silencer boxes, has become commonplace in automotive exhaust systems. The primary function of the catalytic converter is, of course, to reduce emissions of harmful exhaust gases, such as carbon monoxide and nitrous oxides, but it is known that they are also capable of dissipating sound energy. When compared to the silencer boxes studied in previous chapters, the catalytic converter only provides a small contribution to the acoustic performance of the exhaust system as a whole, although this effect is still significant enough to require its inclusion in the acoustic analysis of a complete exhaust system.

The active part of a typical catalytic converter consists of a uniform honeycomb of small, parallel, open pores which run axially along the length of the catalytic converter "brick" or "monolith". Usually, the catalytic converter substrate is formed from a ceramic which has pores that are approximately square in cross-section although in recent years metallic substrates have also been used, and these contain pores which are approximately triangular in cross-section. For both the metallic and ceramic bricks, a porous "washcoat" is applied to the substrate and this later facilitates the introduction of the catalyst itself. The washcoat has very small pores and consequently has a high total surface area and this increases the effective surface area of the brick, allowing the amount of catalyst applied to the brick to be increased. In the case of the ceramic bricks, the washcoat is commonly made largely from aluminium oxide, onto which the catalytic layer (for example platinum) is applied. An electron micrograph showing the juxtaposition of the washcoat and the ceramic substrate is given in the paper by Astley and Cummings [141].

Catalytic converters are commonly arranged in the form of two bricks, one downstream of the other (see for example Glav et al. [142]). The bricks are situated close to the exhaust manifold where temperatures in the region of 1000K exist. At such temperatures, an exothermic reaction between the exhaust gas and the catalyst occurs and this induces a temperature rise in the brick of the order of 100K. Experiments have shown that the majority of this temperature rise occurs within the first 20mm of axial distance along the first brick, which is usually approximately 150mm long. The temperature in any subsequent bricks remains approximately constant.

The pores in the catalytic converter, once the washcoat has been applied, typically have a width of the order of 1mm, and therefore, in light of the studies in Chapters 2 and 3, one would expect significant viscous and thermal boundary layers to be present, which in turn cause the dissipation of sound energy. Accordingly, in this chapter, the dissipation of acoustic energy in catalytic converters is examined, with particular reference to the influence of temperature gradients upon the sound propagation. In order to provide a meaningful comparison with previous chapters, the dissipative characteristics of catalytic converters are quantified here by transmission loss predictions, and these are later compared to experimentally measured data.

Since catalytic converters consist of small capillary tubes, the modelling of their acoustic behaviour has been based upon parallel-tube idealisations of sound propagation in porous materials, such as those implemented by Zwikker and Kosten [31] and Tijdeman [32]. For instance, Roh et al. [143] found the propagation constant and characteristic impedance for a porous material with straight rectangular tubes as a series expansion. The study by Roh et al. was undoubtedly aimed at catalytic converters, although this was not explicitly stated in their paper. The predictions obtained by Roh et al. did, however, require the use of an anomalous tortuosity factor (see Chapter 2) greater than unity - even though all the tubes were straight and parallel to the direction of sound propagation - in order to agree well with experimental measurements performed on a ceramic catalyst. Arnott et al. [144] later showed that the tortuosity factor was linked to the additional acoustic effect of wall porosity (the tests were carried out on a ceramic substrate with no washcoat applied to it). The model was reformulated by introducing a locally reacting wall impedance (considered to be purely reactive) to account for the wall porosity, and good agreement was then observed with experiment without the need to resort to the use of a tortuosity factor other than unity. The investigations by both Roh et al. and Arnott et al. were the first in which the acoustic effects of the small pores located in the substrate of ceramic bricks were reported. However, both models were essentially porous material models similar to those described in Chapters 2 and 3, in which the effects of mean flow were ignored.

In actual engine exhaust systems, the capillary tubes in catalytic converters contain a mean gas flow emanating from the engine, and this can induce a Mach number in the tubes of between 0.2 and 0.3. The introduction of mean flow into the porous material models described earlier complicates the problem and, because catalytic converters have only recently become commonplace in exhaust systems, current understanding of the mean flow effects in catalytic converters is relatively limited. The effects of mean flow were first examined by Glav et al. [142], who modified the basic zero flow porous material theory of Morse and Ingård [27] by use of Ingård and Singhal's [145] work concerning sound attenuation in turbulent pipe flow. Glav et al. found good agreement between prediction and experiment at low frequencies when no mean flow was present, but they did not make predictions when mean flow was present and therefore it is unclear how accurate these predictions might have been. However in view of the rather heuristic nature of the work of Ingård and Singhal it is unlikely that this method provides sufficient accuracy when mean flow is present. Peat [146] used an approximate variational solution to obtain analytical expressions for the attenuation and phase speed in cylindrical capillary tubes with mean flow. He used parabolic forms for the velocity and temperature profiles, and this limited the validity of the model to shear wavenumbers (s) of less than four (where $s = R\sqrt{\rho_0\omega/\mu}$, R being the tube radius, ρ_0 the mean fluid density, ω the radian frequency and μ the dynamic viscosity). It was shown by Peat that the variational formulation could be simplified by assuming that the disturbances occur isentropically, although in view of the viscous effects occurring in the pores this is perhaps an unrealistic representation of the physics of the problem. However this assumption did allow Peat to find solutions both with and without a radial velocity component, from which it was concluded that the effects of the radial velocity were negligible. This observation then allowed Peat to formulate a non-isentropic solution. Astley and Cummings [141] later used finite elements to examine mean flow effects in capillary tubes with non-circular cross sections. They computed the attenuation and phase speed for both circular and square cross sectioned tubes using a non-isentropic formulation, both with and without mean flow. The use of finite elements permitted Astley and Cummings to disregard the assumptions made about the shape of the velocity and temperature waveforms by Peat [146], and this subsequently allowed the model to be extended to higher values of the shear wave number. Ih et al. [147] also relaxed Peat's shear wave number restriction and this was done by using transverse functional variations for the velocity and temperature, from which the governing equations were reduced to a form such that the solutions could be expressed in terms of confluent hypergeometric functions. Recently, Jeong and Ih [148] obtained non-isentropic solutions for capillary tubes with internal mean flow by using numerical methods. This involved applying Runge-Kutta and shooting methods to initiate a recursive solution to the governing equations, and it also allowed the effects of the radial velocity to be included in a non-isentropic solution. Jeong and Ih did however omit radial and axial temperature gradients. They were, however, the first authors to compute transmission loss predictions for a catalytic converter with mean flow in the pores. This was accomplished by equating the acoustic pressure and mass velocity at the inlet and outlet of the brick in order to obtain a transfer matrix from which the four-pole parameters were then calculated. Jeong and Ih compared their transmission loss predictions to experimental data obtained for several bricks placed end to end and they found good agreement between prediction and experiment.

The first treatment of temperature gradients in catalytic converters has only very recently been reported by Peat [149]. He assumed that a linear axial temperature gradient was present and ignored radial velocity components. An analytical solution was developed by using low-order expansions for both the Mach number and the temperature change parameter, although this restricted the final solution to Mach numbers below 0.1. The analysis in this chapter is intended to extend the work of Peat to include higher order terms in the expansion of the problem, so that Mach numbers of up to 0.3 can be examined. This does, however, require the introduction of numerical methods. In this chapter, numerical formulations for both isentropic and non-isentropic acoustic disturbances are given in a formulation that includes the effects of the temperature gradient in the catalyst pores. It will, however, become obvious later on in this chapter that employing a treatment which will allow the Mach numbers to be as high as 0.3 presents a number of new problems and, at present, no solution to these has been found. However, the development of theoretical models for predicting the acoustic behaviour of catalytic converters is still at an early stage, and the models presented here await further development before they can become fully integrated into the design of a complete exhaust system.

Section 11.2

Governing Equations

The analysis of the acoustic behaviour of a catalytic converter can be reduced to that of a single capillary duct, the dimensions of the catalyst brick only being inserted when the transmission loss is to be calculated. The equations of continuity, momentum and energy for axisymmetric flow through a uniform capillary duct were given by Peat [146], and in this section, these equations are modified in order to introduce a linear axial temperature gradient into the problem.

If the radial velocity component in the capillary duct is neglected, then the continuity equation is given by

$$\frac{\partial \rho}{\partial t}+u\frac{\partial \rho}{\partial x}+\rho\frac{\partial u}{\partial x}=0, \tag{11.1}$$

where ρ is the density, u is the axial velocity component, t is time and x is the axial co-ordinate. The components of the momentum equation, in the axial and radial direction, are given by

$$\rho\left(\frac{\partial u}{\partial t}+u\frac{\partial u}{\partial x}\right)=-\frac{\partial p}{\partial x}+\mu\left(\frac{\partial^2 u}{\partial r^2}+\frac{1}{r}\frac{\partial u}{\partial r}\right) \tag{11.2}$$

and

$$\frac{\partial p}{\partial r}=0, \tag{11.3}$$

subject to the usual boundary layer approximations [146], where p is the pressure, μ is the dynamic viscosity and r is the radial co-ordinate. Finally, the energy equation is given by

$$\rho C_p\left(\frac{\partial T}{\partial t}+u\frac{\partial T}{\partial x}\right)=\frac{\partial p}{\partial t}+K\left(\frac{\partial^2 T}{\partial r^2}+\frac{1}{r}\frac{\partial T}{\partial r}\right)+u\frac{\partial p}{\partial x}+\mu\left(\frac{\partial u}{\partial r}\right)^2+Q(x,r), \tag{11.4}$$

where C_p is the specific heat at constant pressure, T is the temperature, K is the thermal conductivity and Q denotes a steady state heat generation per unit volume of fluid. The fluid in the capillary duct is assumed to behave in the manner of a perfect gas, so that the equation of state is given by

$$p=\rho R_0 T, \tag{11.5}$$

where R_0 is the gas constant.

In accordance with Peat [146], it is now assumed that the mean flow through the capillary duct is a superposition of laminar steady flow and a small harmonic acoustic disturbance of radian frequency ω. A linear axial temperature dependence is also added to the problem and this is introduced in the manner recently suggested by Peat [149]. Therefore, if a linear temperature change is assumed to occur over a duct length of $2L$, then

$$T_s(\xi)=T_0(1+\tau\xi), \qquad -1\le\xi\le 1, \tag{11.6}$$

where $\xi = x/L$, T_0 denoting the mean temperature in the centre of the duct $(\xi = 0)$, T_s denoting the local value of the steady state temperature and τ being a constant, called here the "temperature change parameter". The fluid variables are now expanded in the form [149]

$$\rho = \rho_0\left[(1-\tau\xi) + \alpha\rho'(\xi)e^{i\omega t}\right] \tag{11.7}$$
$$u = c_0\left[M(1+\tau\xi)f(\eta) + \alpha u'(\xi,\eta)e^{i\omega t}\right] \tag{11.8}$$
$$p = p_0\left[1 + M^2 g(\xi) + \alpha p'(\xi)e^{i\omega t}\right] \tag{11.9}$$
$$T = T_0\left[(1+\tau\xi) + \alpha T'(\xi)e^{i\omega t}\right], \tag{11.10}$$

where $\alpha << 1$, M is the steady flow Mach number, c_0 is the isentropic speed of sound and $g(\xi)$ and $f(\eta)$ are steady flow variables. The variables M, ρ_0, c_0, p_0 and T_0 are mean values relating to the centre of the duct $(\xi = 0)$, whilst ρ', u', p' and T' denote dimensionless acoustic perturbations. The normalised radius $\eta = r/R$, where R is the radius of the capillary duct. The complex propagation constant of the duct, which was originally included in the expansion of the fluid variables by Peat [146], is included later on in this analysis.

The substitution of the expanded form of the variables into equations (11.1) to (11.5) allows an expansion in α to be obtained; the zeroth order relates to the steady flow solution, whilst higher order terms relate to "acoustic" perturbations (though this term should, strictly speaking, be reserved for isentropic disturbances). In the present analysis $\alpha << 1$, and therefore the acoustic perturbations are to be limited to the first order in α.

11.2.1 Steady Flow Solution

The steady flow solution is obtained after substituting equations (11.7) to (11.10) into the governing equations and equating zeroth orders in α; therefore for the continuity equation this gives

$$\frac{d}{d\xi}\left(1-\tau^2\xi^2\right)=0, \tag{11.11}$$

and for the equation of state

$$1+M^2 g(\xi)=1-\tau^2\xi^2. \tag{11.12}$$

The equations of continuity and state are satisfied only if terms of both $O[\tau^2]<<1$ and $O[M^2 g(\xi)]<<1$. The radial momentum equation (11.3) is clearly satisfied, whilst the axial momentum equation simplifies to give

$$\tau f^2=-\frac{1}{\gamma}\frac{dg}{d\xi}+\frac{(1+\tau\xi)}{\mathrm{Re}(R/L)}\frac{1}{\eta}\frac{d}{d\eta}\left(\eta\frac{df}{d\eta}\right), \tag{11.13}$$

where $\mathrm{Re}=\rho_0 c_0 MR/\mu$, the mean flow Reynolds number based upon the duct radius, and γ is the ratio of specific heats. Equations (11.11) to (11.13) are sufficient to allow expressions for $g(\xi)$ and $f(\eta)$ to be obtained, and these are later used in the solution of the acoustic equations (first order in α). However, in order to obtain solutions for $g(\xi)$ and $f(\eta)$, it is first necessary to consider a series solution to equation (11.13). Consequently $g(\xi)$ and $f(\eta)$ are expanded in terms of the temperature change parameter τ, hence

$$g(\xi)=g_0(\xi)+\tau g_1(\xi)+\tau^2 g_2(\xi)+\ldots., \tag{11.14}$$

and

$$f(\eta)=f_0(\eta)+\tau f_1(\eta)+\tau^2 f_2(\eta)+\ldots.. \tag{11.15}$$

Substituting the assumed forms for $g(\xi)$ and $f(\eta)$ into equation (11.13) for zeroth order in τ yields the equations

$$\frac{\mathrm{Re}(R/L)}{\gamma}\frac{dg_0}{d\xi}=\frac{1}{\eta}\frac{d}{d\eta}\left(\eta\frac{df_0}{d\eta}\right)=\text{constant}. \tag{11.16a,b}$$

The solutions to equations (11.16), which satisfy the no-slip condition at the wall, are simply those of Poiseuille flow, i.e.

$$f_0(\eta) = 2(1-\eta^2) \tag{11.17}$$

and

$$\frac{dg_0}{d\xi} = -\frac{8\gamma}{\mathrm{Re}(R/L)}. \tag{11.18}$$

Peat [146] pointed out that this solution to the axial momentum equation does not fully satisfy the energy and state equations, but, in accordance with other authors, this imbalance is ignored here. In the paper by Peat [149], $g_1(\xi)$ and $f_1(\eta)$ were not found since the equations for perturbations were only developed to first order in M and τ and it turned out that this did not require the knowledge of $g_1(\xi)$ and $f_1(\eta)$. However, in the present analysis, orders of $M\tau$ are retained and this requires solutions for $g_1(\xi)$ and $f_1(\eta)$ to be obtained. Therefore, retaining first order terms in τ gives

$$\frac{\mathrm{Re}(R/L)}{\gamma}\frac{dg_1}{d\xi} + 8\xi = \frac{1}{\eta}\frac{d}{d\eta}\left(\eta\frac{df_1}{d\eta}\right) - 4\,\mathrm{Re}(R/L)(1-\eta^2)^2 = \text{constant}. \tag{11.19a,b}$$

Solving equations (11.19), subject to the same boundary conditions as before, gives

$$f_1 = -\mathrm{Re}(R/L)\left[\frac{\eta^2}{2}(\eta^2-1) + \frac{1}{9}(1-\eta^6)\right] \tag{11.20}$$

and

$$\frac{dg_1}{d\xi} = -2\gamma - \frac{8\gamma\xi}{\mathrm{Re}(R/L)}. \tag{11.21}$$

Solutions have now been obtained for $dg_1/d\xi$ and $f_1(\eta)$, neglecting $O(\tau^2)$, and these are now employed in the equations for perturbations derived in the following analysis.

11.2.2 Equations for Perturbations

Equating the first order terms in α in equations 11.1 to 11.5, gives a continuity equation,

$$ik\rho' + Mf(\eta)\left[(1+\tau\xi)\frac{\partial\rho'}{\partial\xi} + \tau\rho'\right] - \tau u' + (1-\tau\xi)\frac{\partial u'}{\partial\xi} = 0, \tag{11.22}$$

where k is a non-dimensional wavenumber $(k = \omega L/c_0)$. The momentum equations in the axial and radial directions are given by

$$ik(1-\tau\xi)u' + Mf(\eta)\frac{\partial u'}{\partial\xi} + M\tau f(\eta)u' = -\frac{1}{\gamma}\frac{\partial p'}{\partial\xi} + \frac{k}{s^2}\frac{1}{\eta}\frac{\partial}{\partial\eta}\left(\eta\frac{\partial u'}{\partial\eta}\right) \tag{11.23}$$

and

$$\frac{dp'}{d\eta} = 0, \tag{11.24}$$

where s is the shear wavenumber $\left(s = R\sqrt{\rho_0\omega/\mu}\right)$. In the following section both isentropic and non-isentropic disturbances are examined. If one assumes that the disturbances are isentropic then for the first order in α, the equation of state gives

$$p' = \rho'\gamma(1+\tau\xi). \tag{11.25}$$

When non-isentropic disturbances are examined, one must also employ the energy equation which for the first order in α, is given by

$$ik(1-\tau\xi)T' + Mf(\eta)\frac{\partial T'}{\partial\xi} + \tau u' + \tau Mf(\eta)\rho' = \frac{k}{\sigma^2 s^2}\frac{1}{\eta}\frac{\partial}{\partial\eta}\left(\eta\frac{\partial T'}{\partial\eta}\right) + ik\left(\frac{\gamma-1}{\gamma}\right)p'$$

$$+M\left(\frac{\gamma-1}{\gamma}\right)(1+\tau\xi)f(\eta)\frac{\partial p'}{\partial\xi} + \frac{kM}{s^2}(\gamma-1)(1+\tau\xi)\left[2\frac{\partial f}{\partial\eta}\frac{\partial u'}{\partial\eta} + \frac{u'}{\eta}\frac{\partial}{\partial\eta}\left(\eta\frac{\partial f}{\partial\eta}\right)\right], \tag{11.26}$$

where σ is the square root of the Prandtl number $\left(\sigma=\sqrt{\mu C_p/K}\right)$. Finally the equation of state gives

$$p' = (1-\tau\xi)T' + (1+\tau\xi)\rho'. \tag{11.27}$$

It is now necessary to write the acoustic variables as a series expansion in τ. This also involves introducing the propagation constant as defined by Peat [146]. The acoustic variables are now expanded in the forms

$$\rho' = e^{k\Gamma\xi}\left[\rho'_{\mathrm{A}} + \tau\rho'_{\mathrm{B}}(\xi) + \;.....\right] \tag{11.28}$$
$$u' = e^{k\Gamma\xi}\left[u'_{\mathrm{A}}(\eta) + \tau u'_{\mathrm{B}}(\xi,\eta) + \;.....\right] \tag{11.29}$$
$$p' = e^{k\Gamma\xi}\left[p'_{\mathrm{A}} + \tau p'_{\mathrm{B}}(\xi) + \;.....\right] \tag{11.30}$$
$$T' = e^{k\Gamma\xi}\left[T'_{\mathrm{A}} + \tau T'_{\mathrm{B}}(\xi) + \;.....\right], \tag{11.31}$$

for positive travelling waves, where Γ is the complex propagation constant for the capillary duct and terms of $O\left(\tau^2\right)$ have been neglected. One can now substitute the expanded acoustic variables back into the acoustic equations, and an order expansion in τ is obtained. Therefore, substituting equations (11.28) to (11.31) into equations (11.22), (11.23) and (11.26) gives, for zeroth order in τ,

$$i\rho'_{\mathrm{A}} + Mf_0\Gamma\rho'_{\mathrm{A}} + \Gamma u'_{\mathrm{A}} = 0, \tag{11.32}$$

$$iu'_{\mathrm{A}} + Mf_0\Gamma u'_{\mathrm{A}} = -\frac{\Gamma p'_{\mathrm{A}}}{\gamma} + \frac{1}{s^2}\frac{1}{\eta}\frac{d}{d\eta}\left(\eta\frac{du'_{\mathrm{A}}}{d\eta}\right), \tag{11.33}$$

$$(i+Mf_0\Gamma)T'_{\mathrm{A}} = \frac{1}{\sigma^2 s^2}\frac{1}{\eta}\frac{\partial}{\partial\eta}\left(\eta\frac{\partial T'_{\mathrm{A}}}{\partial\eta}\right) + \left(\frac{\gamma-1}{\gamma}\right)\left[i+Mf_0\Gamma\right]p'_{\mathrm{A}} - 8(\gamma-1)\frac{M}{s^2}\frac{\partial}{\partial\eta}(u'_{\mathrm{A}}\eta), \tag{11.34}$$

for the continuity, axial momentum and energy equations respectively. The zeroth order expansion in τ for the equation of state gives

$$p'_{\mathrm{A}} = \rho'_{\mathrm{A}} + T'_{\mathrm{A}}. \tag{11.35}$$

The first order expansion in τ for the continuity, axial momentum and energy equations then gives

$$ik\rho'_{\mathrm{B}} + Mf_0\left[\rho'_{\mathrm{A}} + k\Gamma\rho'_{\mathrm{B}} + \xi k\Gamma\rho'_{\mathrm{A}} + \partial\rho'_{\mathrm{B}}/\partial\xi\right] + Mf_1 k\Gamma\rho'_{\mathrm{A}}$$

$$+k\Gamma u'_{\mathrm{B}} + \partial u'_{\mathrm{B}}/\partial\xi - \xi k\Gamma u'_{\mathrm{A}} - u'_{\mathrm{A}} = 0, \tag{11.36}$$

$$ik\left(u'_{\mathrm{B}} - \xi u'_{\mathrm{A}}\right) + Mf_0\left[u'_{\mathrm{A}} + k\Gamma u'_{\mathrm{B}} + \partial u'_{\mathrm{B}}/\partial\xi\right] + Mf_1 k\Gamma u'_{\mathrm{A}}$$

$$= -\frac{1}{\gamma}\left[k\Gamma p'_{\mathrm{B}} + \frac{\partial p'_{\mathrm{B}}}{\partial\xi}\right] + \frac{k}{s^2}\frac{1}{\eta}\frac{\partial}{\partial\eta}\left(\eta\frac{\partial u'_{\mathrm{B}}}{\partial\eta}\right) \tag{11.37}$$

and

$$ik\left(T'_{\mathrm{B}} - \xi T'_{\mathrm{A}}\right) + Mf_0\left[\rho'_{\mathrm{A}} + k\Gamma T'_{\mathrm{B}} + \frac{\partial T'_{\mathrm{B}}}{\partial\xi}\right] + Mf_1 k\Gamma T'_{\mathrm{A}} + u'_{\mathrm{A}} = \frac{k}{\sigma^2 s^2}\frac{1}{\eta}\frac{\partial}{\partial\eta}\left(\eta\frac{\partial T'_{\mathrm{B}}}{\partial\eta}\right)$$

$$+ik\left(\frac{\gamma-1}{\gamma}\right)p'_{\mathrm{B}} + Mf_0\left(\frac{\gamma-1}{\gamma}\right)\left[k\Gamma p'_{\mathrm{B}} + k\Gamma\xi p'_{\mathrm{A}} + \frac{\partial p'_{\mathrm{B}}}{\partial\xi}\right] + Mf_1\left(\frac{\gamma-1}{\gamma}\right)k\Gamma p'_{\mathrm{A}}$$

$$-\frac{8kM}{s^2}(\gamma-1)\left[\frac{\partial}{\partial\eta}\left(\eta u'_{\mathrm{A}}\right) + \frac{\partial}{\partial\eta}\left(\eta u'_{\mathrm{B}}\right)\right]. \tag{11.38}$$

The first order expansion in τ for the equation of state is given by

$$p'_{\mathrm{B}} = \rho'_{\mathrm{B}} + T'_{\mathrm{B}} - \xi\left(T'_{\mathrm{A}} - \rho'_{\mathrm{A}}\right). \tag{11.39}$$

Equations (11.32) to (11.39) represent the zeroth and first order expansions in τ for the acoustic equations (first order in α), and these will be solved in the next two sections. Two different approaches to solving these equations can be applied. First, one can assume isentropic disturbances and this simplifies the equations derived here since it allows the energy equation to be decoupled from the continuity and momentum equations. The assumption of isentropic disturbances allows one to write

$$p'_{\mathrm{A}} = \gamma \rho'_{\mathrm{A}} \qquad (11.40)$$

for the zeroth order in τ, and

$$p'_{\mathrm{B}} = \gamma\left(\xi \rho'_{\mathrm{A}} + \rho'_{\mathrm{B}}\right) \qquad (11.41)$$

for the first order in τ. Unfortunately, this assumption rather oversimplifies the problem and the benefits of employing equations (11.40) and (11.41) can be outweighed by the subsequent reduction in the accuracy of the predictions.

Section 11.3

Equations of Zeroth Order in τ

An examination of equations (11.32) to (11.41) indicates that, as one would expect, it is possible to separate the zeroth order solution from the first order solution. The equations for zeroth order in τ are given by equations (11.32) to (11.34), coupled with equation (11.35) for non-isentropic disturbances and equation (11.40) for isentropic disturbances. A comparison between the equations obtained in the previous section and those derived by Peat [149], indicates that the inclusion of $O(\tau M)$ terms has complicated the problem and one can no longer employ an analytical solution. Instead, it is necessary to resort to the use of numerical methods.

The zeroth order equations obtained in the previous section are identical to those derived by Jeong and Ih [148], if one takes into account the omission of the radial velocity component in the present analysis. Jeong and Ih computed non-isentropic solutions by using Runge-Kutta and shooting methods, from which a recursive solution was proposed. The method implemented by Jeong and Ih is followed here in order to provide the zeroth order solution. To do this it is necessary to rewrite the velocity and temperature perturbations as

$$u_A' = \Gamma s^2 p_A' u_A / \gamma \qquad \text{and} \qquad T_A' = t_A p_A', \tag{11.42), (11.43}$$

where u_A and t_A are defined by these equations. Equations (11.32) to (11.34) are now be re-written and, employing equation (11.35) to eliminate the density terms, one arrives at a non-isentropic formulation for the continuity, momentum and energy equations of

$$\Gamma^2 s^2 u_A / \gamma + i + Mf_0\Gamma - (it_A + Mf_0\Gamma t_A) = 0, \tag{11.44}$$

$$\frac{1}{\eta}\frac{d}{d\eta}\left(\eta \frac{du_A}{d\eta}\right) - s^2(i + Mf_0\Gamma)u_A = 1 \tag{11.45}$$

and

$$\frac{1}{\eta}\frac{d}{d\eta}\left(\eta \frac{dt_A}{d\eta}\right) - \sigma^2 s^2(i + Mf_0\Gamma)t_A = -\left(\frac{\gamma-1}{\gamma}\right)\sigma^2 s^2(i + Mf_0\Gamma)$$

$$+8\left(\frac{\gamma-1}{\gamma}\right)\sigma^2 s^2 \Gamma M \frac{d}{d\eta}(u_A \eta). \tag{11.46}$$

The continuity equation can only be satisfied in the integral sense, hence

$$\Gamma^2 s^2 \langle u_A \rangle / \gamma + i + M\Gamma - i\langle t_A \rangle - M\Gamma\langle f_0 t_A \rangle = 0, \tag{11.47}$$

where $\langle\ \rangle$ denotes an average value on the duct cross-section.

Equations (11.45) to (11.47) must be solved subject to the relevant boundary conditions. It is assumed here that the walls of the duct are rigid and that they have a much greater thermal conductivity than the fluid, so

$$u_A = t_A = 0 \qquad \text{at} \qquad \eta = 1, \tag{11.48}$$

and symmetry yields

$$\frac{du_A}{d\eta} = \frac{dt_A}{d\eta} = 0 \qquad \text{at} \qquad \eta = 0. \tag{11.49}$$

The method used by Jeong and Ih for solving equations (11.45), (11.46) and (11.47) is as follows. First, one must make an initial guess for Γ, which is then substituted into the momentum equation (11.45). Finding an initial guess for Γ is not a problem since, if one initiates the solution at a very low frequency (and hence low shear wave number), one can use the analytical method of Peat [146] to provide the initial guess. The solution of equation (11.45) provides values for $u_A(\eta)$, which can then be substituted into the energy equation (11.46). This equation is then solved for values of $t_A(\eta)$ (again with the same initial guess for Γ). One can now compute the cross-sectionally averaged values $\langle u_A \rangle$ and $\langle t_A \rangle$ which, when substituted into equation (11.47), allow a new value for Γ to be calculated. This new value for Γ is then substituted back into equation (11.45) and the whole process is repeated until convergence in Γ is obtained.

The solution of both equation (11.45) and (11.46) was carried out by using Runge-Kutta and shooting methods. The values calculated for Γ were found to converge to within $O(10^{-5})$ in percentage error after 5 iterations for the incident wave and 9 iterations for the reflected wave. The solution procedure was then repeated at a higher frequency by using the value found for Γ at the previous frequency as the initial guess, and so on until the desired frequency range has been covered.

The solution described in this section has been for the non-isentropic case since this is the most accurate solution (requiring the fewest approximations) and predictions can readily be computed both with and without mean flow. However, if computations for the isentropic case are to be made, one simply eliminates the density from equation (11.32) by using equation (11.40) and it is no longer necessary to calculate values for $t_A(\eta)$. The isentropic solution has been described previously in the literature and is therefore not included here. The solutions obtained by using the non-isentropic method described in this section are formulated into transmission loss predictions in Section 11.5, where comparisons are also made with experimental measurement.

Section 11.4

Equations of First Order in τ

The equations for the first order in τ are given by equations (11.36) to (11.38) in Section 11.2, and these are combined with either equation (11.39), for non-isentropic disturbances, or equation (11.41) for isentropic disturbances. In this section, both isentropic and non-isentropic solutions are examined, since the non-isentropic solution for the first order in τ is considerably more complicated than the zeroth order solution described previously. In accordance with the equations of zeroth order in τ, the temperature and particle velocity variables are re-defined here (see equations (11.42) and (11.43)) as

$$u_{\mathrm{B}}' = \Gamma s^2 p_{\mathrm{A}}' u_{\mathrm{B}} / \gamma \quad \text{and} \quad T_{\mathrm{B}}' = t_{\mathrm{B}} p_{\mathrm{A}}'. \qquad (11.50), (11.51)$$

11.4.1 Isentropic Solution

The assumption of isentropic disturbances allows the energy equation to be decoupled from both the continuity and momentum equations. Consequently equations (11.40) and (11.41) can be used to eliminate the density terms from the continuity equation (11.36). This has the advantage of simplifying the continuity equation, when compared to the non-isentropic formulation, and in addition the energy equation can be discarded. Therefore, by substituting equations (11.40) and (11.41) into (11.36), and introducing the re-defined velocity and temperature variables, the continuity equation for first order in τ can be re-written as

$$\frac{ik}{\Gamma s^2}\left[\frac{p_{\mathrm{B}}'}{p_{\mathrm{A}}'} - \xi\right] + \frac{Mf_0}{\Gamma s^2}\left[k\Gamma \frac{p_{\mathrm{B}}'}{p_{\mathrm{A}}'} + \frac{\partial (p_{\mathrm{B}}'/p_{\mathrm{A}}')}{\partial \xi}\right] + \frac{Mf_1 k}{s^2} + k\Gamma u_{\mathrm{B}} + \frac{\partial u_{\mathrm{B}}}{\partial \xi} - \xi k \Gamma u_{\mathrm{A}} - u_{\mathrm{A}} = 0.$$

(11.52)

Similarly, the axial momentum equation (11.37) can be re-written as

$$is^2(u_B - \xi u_A) + \frac{Mf_0 s^2}{k}\left(u_A + k\Gamma u_B + \frac{\partial u_B}{\partial \xi}\right) + Mf_1\Gamma s^2 u_A =$$

$$-\left[\frac{p'_B}{p'_A} + \frac{1}{k\Gamma}\frac{\partial(p'_B/p'_A)}{\partial \xi}\right] + \frac{1}{\eta}\frac{\partial}{\partial \eta}\left(\eta\frac{\partial u_B}{\partial \eta}\right). \tag{11.53}$$

The problem has now been written in terms of two equations, (11.52) and (11.53), and two unknowns, u_B and p'_B. Unfortunately, first derivatives with respect to ξ appear for both unknowns in each equation which means that one cannot solve the two equations directly. Therefore it is necessary to expand the unknowns further in orders of ξ. Peat [149] also applied this approach to solving the continuity and momentum equations and suggested that the unknowns be expanded in the forms

$$\frac{p'_B}{p'_A} = B_0 + B_1\xi + B_2\xi^2 \tag{11.54}$$

and

$$u_B = u_{B_0}(\eta) + u_{B_1}(\eta)\xi + u_{B_2}(\eta)\xi^2. \tag{11.55}$$

He pointed out that B_0 serves only to adjust the absolute value of the acoustic pressure at $\xi = 0$ and may be taken to be zero if p'_A is regarded as $p|_{\xi=0}$ in all cases. Therefore, substituting the assumed forms for p'_B/p'_A and u_B into both the continuity and momentum equations (setting $B_0 = 0$) gives an expansion for the zeroth, first and second order terms in ξ. For the continuity equation this gives

$$\frac{M\langle f_0\rangle B_1}{\Gamma s^2} + \frac{M\langle f_1\rangle k}{s^2} + k\Gamma\langle u_{B_0}\rangle + \langle u_{B_1}\rangle - \langle u_A\rangle = 0, \tag{11.56}$$

$$\frac{ik}{\Gamma s^2}(B_1 - 1) + \frac{M\langle f_0\rangle}{\Gamma s^2}(k\Gamma B_1 + 2B_2) + k\Gamma\langle u_{B_1}\rangle + 2\langle u_{B_2}\rangle - k\Gamma\langle u_A\rangle = 0 \tag{11.57}$$

and

$$\left(i+Mf_0\Gamma\right)\mathrm{B}_2+\Gamma^2 s^2\left\langle u_{\mathrm{B}_2}\right\rangle=0, \tag{11.58}$$

where $\langle\ \rangle$ denotes a cross-sectionally averaged value. In accordance with the solution for zeroth order in τ, the continuity equation can again only be satisfied in the integral sense. The momentum equation for the zeroth, first and second order terms in ξ respectively is given by

$$is^2 u_{\mathrm{B}_0}+\frac{Mf_0 s^2}{k}\left(u_{\mathrm{A}}+u_{\mathrm{B}_1}+k\Gamma u_{\mathrm{B}_0}\right)+Mf_1\Gamma s^2 u_{\mathrm{A}}+\frac{\mathrm{B}_1}{k\Gamma}=\frac{1}{\eta}\frac{d}{d\eta}\left(\eta\frac{du_{\mathrm{B}_0}}{d\eta}\right), \tag{11.59}$$

$$is^2\left(u_{\mathrm{B}_1}-u_{\mathrm{A}}\right)+\frac{Mf_0 s^2}{k}\left(k\Gamma u_{\mathrm{B}_1}+2u_{\mathrm{B}_2}\right)+\mathrm{B}_1+\frac{2\mathrm{B}_2}{k\Gamma}=\frac{1}{\eta}\frac{d}{d\eta}\left(\eta\frac{du_{\mathrm{B}_1}}{d\eta}\right) \tag{11.60}$$

and

$$\left(i+Mf_0\Gamma\right)s^2 u_{\mathrm{B}_2}+\mathrm{B}_2=\frac{1}{\eta}\frac{d}{d\eta}\left(\eta\frac{du_{\mathrm{B}_2}}{d\eta}\right). \tag{11.61}$$

If one examines the similarity between equations (11.61) and (11.45), in addition to the fact that all the velocity components are subject to the same no-slip boundary conditions at the wall, it follows that

$$u_{\mathrm{B}_2}=\mathrm{B}_2 u_{\mathrm{A}}. \tag{11.62}$$

If this relationship is substituted into equation (11.58), it is found that equation (11.58) is now redundant. Therefore one is left with five equations and five unknowns.

The isentropic problem can now be solved either with or without mean flow. Neglecting mean flow is obviously undesirable when examining a catalyst "on-engine", although this approximation does simplify the continuity and momentum equations considerably and the subsequent solution is useful for providing an indication of the likely influence of temperature gradients when mean flow is introduced. Therefore, setting $M=0$, and making use of equation (11.62), one arrives at two momentum and two continuity equations which have the forms

$$is^2 u_{B_0} + \frac{B_1}{k\Gamma} = \frac{1}{\eta}\frac{d}{d\eta}\left(\eta \frac{du_{B_0}}{d\eta}\right) \tag{11.63}$$

$$is^2\left(u_{B_1} - u_A\right) + B_1 + \frac{2B_2}{k\Gamma} = \frac{1}{\eta}\frac{d}{d\eta}\left(\eta \frac{du_{B_1}}{d\eta}\right) \tag{11.64}$$

$$k\Gamma\left\langle u_{B_0}\right\rangle + \left\langle u_{B_1}\right\rangle - \left\langle u_A\right\rangle = 0 \tag{11.65}$$

$$\frac{ik}{\Gamma s^2}\left(B_1 - 1\right) + k\Gamma\left\langle u_{B_1}\right\rangle + 2\left\langle u_{B_2}\right\rangle - k\Gamma\left\langle u_A\right\rangle = 0. \tag{11.66}$$

Equations (11.63) to (11.66) can now be solved for B_1, B_2, $u_{B_0}(\eta)$ and $u_{B_1}(\eta)$. The solution proceeds by first guessing a value for B_1 and solving equation (11.63) for $u_{B_0}(\eta)$. Next, if equation (11.65) is substituted into equation (11.66), one finds that

$$\frac{2B_2}{k\Gamma} = k\Gamma\frac{\left\langle u_{B_0}\right\rangle}{\left\langle u_A\right\rangle} + B_1 - 1. \tag{11.67}$$

Substituting equation (11.67) into equation (11.64) therefore allows a solution to be found for $u_{B_1}(\eta)$. Once values for $\left\langle u_{B_0}\right\rangle$ and $\left\langle u_{B_1}\right\rangle$ have been calculated they are substituted into equation (11.65), from which an error in the equation is obtained. A new guess for B_1 is then chosen, based upon the error found in equation (11.65), and this guess is substituted back into equation (11.63). The process is repeated until the error in equation (11.65) has been minimised. For the capillary ducts studied here, the modulus of the left hand side of equation (11.65) was required to be of the order of 10^{-5} in order to obtain a "converged" solution. The predictions obtained using the method outlined above are presented in Section 11.5.

The introduction of mean flow does not, at first sight, appear to alter the problem as compared to that without mean flow. For instance, one can combine equations (11.56) and (11.57) to give

$$\frac{2B_2}{k\Gamma} = \left[k\Gamma \frac{\langle u_{B_0} \rangle}{\langle u_A \rangle} + B_1 - 1 \right] \Big/ (1 + iM\Gamma). \tag{11.68}$$

It is then possible to guess values for B_1 and $\langle u_{B_0} \rangle$, and substitute equation (11.68) into equation (11.60), from which one can calculate $u_{B_1}(\eta)$. This then allows equation (11.59) to be solved for $u_{B_0}(\eta)$. If one then substitutes the computed values for $\langle u_{B_0} \rangle$ and $\langle u_{B_1} \rangle$ into equation (11.56), new values for B_1 can be calculated directly. Converged values for B_1 could not, however, be obtained using this method. The problems with convergence appear to be linked to the calculation of a new value for B_1, using equation (11.56), since one must divide by M to obtain B_1. At vanishingly small values of M it is apparent that large values of B_1 will occur and this will undoubtedly influence the convergence of the solution. This appears to indicate that, at present, the problem has not be well posed and that the set of equations need to be solved by using a different technique. The development of such a method is, however, beyond the scope of this thesis.

11.4.2 Non-isentropic Solution

The non-isentropic solution is more complicated than the isentropic solution since the energy equation can no longer be de-coupled from the continuity and momentum equations. Consequently, one must solve the energy equation, in addition to employing equations (11.35) and (11.39) to eliminate the density terms from the continuity equation. Accordingly, the continuity equation (11.36) now assumes the non-isentropic form

$$ik\left[\frac{p'_{\rm B}}{p'_{\rm A}}-t_{\rm B}+\xi(t_{\rm A}-1)\right]+Mf_0\left[t_{\rm A}+k\Gamma\left(\frac{p'_{\rm B}}{p'_{\rm A}}-t_{\rm B}\right)+\xi k\Gamma t_{\rm A}\right]+Mf_1k\Gamma(1-t_{\rm A})$$

$$+\frac{k\Gamma^2s^2}{\gamma}u_{\rm B}+\frac{\Gamma s^2}{\gamma}\frac{\partial u_{\rm B}}{\partial\xi}-\frac{k\Gamma^2s^2}{\gamma}\xi u_{\rm A}-\frac{\Gamma s^2}{\gamma}u_{\rm A}=0, \tag{11.69}$$

and the energy equation assumes the form

$$ik(t_{\rm B}-\xi t_{\rm A})+Mf_0\left[(1-t_{\rm A})+k\Gamma t_{\rm B}+\left(\frac{\partial t_{\rm B}}{\partial\xi}\right)\right]+Mf_1k\Gamma t_{\rm A}+\frac{\Gamma s^2}{\gamma}u_{\rm A}=$$

$$ik\left(\frac{\gamma-1}{\gamma}\right)\frac{p'_{\rm B}}{p'_A}+Mf_0\left(\frac{\gamma-1}{\gamma}\right)\left[k\Gamma\frac{p'_{\rm B}}{p'_A}+k\Gamma\xi+\frac{\partial(p'_{\rm B}/p'_{\rm A})}{\partial\xi}\right]+Mf_1k\Gamma\left(\frac{\gamma-1}{\gamma}\right)$$

$$-8k\Gamma M\left(\frac{\gamma-1}{\gamma}\right)\left[\frac{\partial(\eta u_{\rm A})}{\partial\eta}+\frac{\partial(\eta u_{\rm B})}{\partial\eta}\right]+\frac{k}{\sigma^2s^2}\frac{1}{\eta}\frac{\partial}{\partial\eta}\left(\eta\frac{\partial t_{\rm B}}{\partial\eta}\right). \tag{11.70}$$

The momentum equation remains unchanged from that used in the isentropic solution (see equation (11.53)). The unknowns in the continuity, momentum and energy equations must now be expanded in the same manner as that implemented in the case of the isentropic solution, hence $p'_{\rm B}/p'_{\rm A}$ and $u_{\rm B}$ are defined by equations (11.54) and (11.55) respectively, whilst the temperature is expanded in the form

$$\frac{T'_{\rm B}}{p'_{\rm A}}=t_{{\rm B}_0}(\eta)+t_{{\rm B}_1}(\eta)\xi+t_{{\rm B}_2}(\eta)\xi^2. \tag{11.71}$$

Substituting the expanded form of the unknowns into equations (11.69) and (11.70) gives zeroth, first and second order expansions in ξ. The continuity equation gives, respectively, the zeroth, first and second order integral forms in perturbations

$$-ik\gamma\langle t_{{\rm B}_0}\rangle+M\gamma\left[\langle f_0t_{\rm A}\rangle-k\Gamma\langle f_0t_{{\rm B}_0}\rangle\right]+Mk\Gamma\gamma\left[\langle f_1\rangle-\langle f_0t_{\rm A}\rangle\right]$$

$$+k\Gamma^2s^2\langle u_{{\rm B}_0}\rangle+\Gamma s^2\left[\langle u_{{\rm B}_1}\rangle-\langle u_{\rm A}\rangle\right]=0, \tag{11.72}$$

$$-ik\gamma\left[\mathrm{B}_1\left\langle t_{\mathrm{B}_1}\right\rangle+2\langle t_{\mathrm{A}}\rangle-1\right]+Mk\Gamma\gamma\left[\mathrm{B}_1\langle f_0\rangle-\left\langle f_0 t_{\mathrm{B}_1}\right\rangle+\langle f_0 t_{\mathrm{A}}\rangle\right]$$

$$+k\Gamma^2 s^2\left[\left\langle u_{\mathrm{B}_1}\right\rangle-\langle u_{\mathrm{A}}\rangle\right]+2\Gamma S^2\left\langle u_{\mathrm{B}_2}\right\rangle=0 \tag{11.73}$$

and

$$i\gamma\left[\mathrm{B}_2-\left\langle t_{\mathrm{B}_2}\right\rangle\right]+M\Gamma\gamma\left[\mathrm{B}_2\langle f_0\rangle-\left\langle f_0 t_{\mathrm{B}_2}\right\rangle\right]+\Gamma^2 s^2\left\langle u_{\mathrm{B}_2}\right\rangle=0. \tag{11.74}$$

The energy equation yields the zeroth, first and second order perturbation equations

$$ikt_{\mathrm{B}_0}+Mf_0\left[(1-t_{\mathrm{A}})+k\Gamma t_{\mathrm{B}_0}+t_{\mathrm{B}_1}\right]+Mf_1 k\Gamma t_{\mathrm{A}}+\frac{\Gamma s^2}{\gamma}u_{\mathrm{A}}=Mf_0\left(\frac{\gamma-1}{\gamma}\right)\mathrm{B}_1+Mf_1 k\Gamma\left(\frac{\gamma-1}{\gamma}\right)$$

$$-8k\Gamma M\left(\frac{\gamma-1}{\gamma}\right)\left[\frac{\partial}{\partial\eta}(\eta u_{\mathrm{A}})+\frac{\partial}{\partial\eta}\left(\eta u_{\mathrm{B}_0}\right)\right]+\frac{k}{\sigma^2 s^2}\frac{1}{\eta}\frac{\partial}{\partial\eta}\left(\eta\frac{\partial t_{\mathrm{B}_0}}{\partial\eta}\right), \tag{11.75}$$

$$i\left(t_{\mathrm{B}_1}-t_{\mathrm{A}}\right)+Mf_0\Gamma\left(t_{\mathrm{B}_1}+\frac{2t_{\mathrm{B}_2}}{k\Gamma}\right)=i\left(\frac{\gamma-1}{\gamma}\right)\mathrm{B}_1+Mf_0\Gamma\left(\frac{\gamma-1}{\gamma}\right)\left[\mathrm{B}_1+1+\frac{2\mathrm{B}_2}{k\Gamma}\right]$$

$$-8\Gamma M\left(\frac{\gamma-1}{\gamma}\right)\frac{\partial}{\partial\eta}\left(\eta u_{\mathrm{B}_1}\right)+\frac{1}{\sigma^2 s^2}\frac{1}{\eta}\frac{\partial}{\partial\eta}\left(\eta\frac{\partial t_{\mathrm{B}_1}}{\partial\eta}\right) \tag{11.76}$$

and

$$(i+Mf_0\Gamma)t_{\mathrm{B}_2}=\left(\frac{\gamma-1}{\gamma}\right)[i+Mf_0\Gamma]\mathrm{B}_2-8\Gamma M\left(\frac{\gamma-1}{\gamma}\right)\frac{\partial}{\partial\eta}\left(\eta u_{\mathrm{B}_2}\right)+\frac{1}{\sigma^2 s^2}\frac{1}{\eta}\frac{\partial}{\partial\eta}\left(\eta\frac{\partial t_{\mathrm{B}_2}}{\partial\eta}\right). \tag{11.77}$$

The expanded forms of the momentum equation are identical to those obtained for the isentropic case (see equations (11.59) to (11.61)). Consequently, equation (11.62) is also valid for the non-isentropic case. In addition, if one compares equation (11.77) to equation (11.46), it follows that

$$t_{\mathrm{B}_2}=\mathrm{B}_2 t_{\mathrm{A}}. \tag{11.78}$$

If equations (11.62) and (11.78) are substituted into equations (11.74), one finds that equation (11.74) is redundant. This means that six equations are now left, containing six unknowns.

A solution for the case with no mean flow is, as with the isentropic case, obtained first here because of its simplicity. Setting $M = 0$ allows the momentum, continuity and energy equations in zeroth and first order perturbations respectively, to be written as

Momentum

$$is^2 u_{\mathrm{B}_0} + \frac{\mathrm{B}_1}{k\Gamma} = \frac{1}{\eta}\frac{d}{d\eta}\left(\eta \frac{du_{\mathrm{B}_0}}{d\eta}\right) \tag{11.79}$$

$$is^2\left(u_{\mathrm{B}_1} - u_{\mathrm{A}}\right) + \mathrm{B}_1 + \frac{2\mathrm{B}_2}{k\Gamma} = \frac{1}{\eta}\frac{d}{d\eta}\left(\eta \frac{du_{\mathrm{B}_1}}{d\eta}\right) \tag{11.80}$$

Continuity

$$-ik\gamma\left\langle t_{\mathrm{B}_0}\right\rangle + k\Gamma^2 s^2\left\langle u_{\mathrm{B}_0}\right\rangle + \Gamma^2 s^2\left[\left\langle u_{\mathrm{B}_1}\right\rangle - \left\langle u_{\mathrm{A}}\right\rangle\right] = 0 \tag{11.81}$$

$$ik\gamma\left[\mathrm{B}_1 - \left\langle t_{\mathrm{B}_1}\right\rangle + 2\left\langle t_{\mathrm{A}}\right\rangle - 1\right] + 2\Gamma s^2 \mathrm{B}_2\left\langle u_{\mathrm{A}}\right\rangle + k\Gamma^2 s^2\left[\left\langle u_{\mathrm{B}_1}\right\rangle - \left\langle u_{\mathrm{A}}\right\rangle\right] = 0 \tag{11.82}$$

Energy

$$ikt_{\mathrm{B}_0} + \frac{\Gamma s^2}{\gamma}u_{\mathrm{A}} = \frac{k}{\sigma^2 s^2}\frac{1}{\eta}\frac{d}{d\eta}\left(\eta\frac{dt_{\mathrm{B}_0}}{d\eta}\right) \tag{11.83}$$

$$i\left(t_{\mathrm{B}_1} - t_{\mathrm{A}}\right) - i\left(\frac{\gamma - 1}{\gamma}\right)\mathrm{B}_1 = \frac{1}{\sigma^2 s^2}\frac{1}{\eta}\frac{d}{d\eta}\left(\eta\frac{dt_{\mathrm{B}_1}}{d\eta}\right). \tag{11.84}$$

It is now possible to solve equations (11.79) to (11.84) for B_1, B_2, $u_{\mathrm{B}_0}(\eta)$, $u_{\mathrm{B}_1}(\eta)$, $t_{\mathrm{B}_0}(\eta)$ and $t_{\mathrm{B}_1}(\eta)$ in a manner similar to that employed for the isentropic case.

Guessing an initial value for B_1 allows $u_{B_0}(\eta)$ to be calculated in equation (11.79) and $t_{B_1}(\eta)$ in equation (11.84). Substituting equation (11.81) into equation (11.82) gives

$$\frac{2B_2}{k\Gamma} = k\Gamma\frac{\langle u_{B_0}\rangle}{\langle u_A\rangle} + \gamma(B_1 - 1) + \gamma k\Gamma\langle t_{B_0}\rangle - \gamma\langle t_{B_1}\rangle + 2\gamma\langle t_A\rangle. \tag{11.85}$$

Once equation (11.83) has been solved for values of $t_{B_0}(\eta)$, one can substitute equation (11.85) into equation (11.80), from which values for $u_{B_1}(\eta)$ can be obtained. The values calculated for $\langle t_{B_0}\rangle$, $\langle u_{B_0}\rangle$ and $\langle u_{B_1}\rangle$ are then substituted into equation (11.81), from which an error is found. A new guess for B_1 is then chosen and the process is repeated until the error in equation (11.81) is minimised. Adequate convergence of the non-isentropic solution was found to occur once the modulus of the error in equation (11.81) was of the order of 10^{-4}. The non-isentropic predictions obtained using this method are given in the next section.

The method used for finding the non-isentropic predictions without mean flow shares many similarities with that used for the isentropic disturbances. In light of the problems found when introducing mean flow into the isentropic case, the author anticipates that the inclusion of mean flow into the non-isentropic case will give rise to similar difficulties. Consequently, the inclusion of mean flow in the non-isentropic solution awaits the formulation of a successful method for solving the isentropic case.

Section 11.5

Results

The majority of the theoretical studies conducted on sound propagation in capillary tubes has concentrated on calculating the attenuation and phase speed of the forward and backward propagating acoustic waves. In fact, Jeong and Ih [148] are the only authors so far to have extended this approach to cover the transmission loss of a finite length catalytic converter. It is attractive to study the characteristics of the catalytic converter in the form of transmission loss predictions since, in previous chapters, dissipative silencers were also represented in this way. This therefore allows the relative influences of the catalytic converter and dissipative silencer on the dissipation of sound in an exhaust system to be readily examined.

To determine the transmission loss of a catalytic converter, Jeong and Ih [148] found the acoustic pressure and the mass particle velocity at each end of the catalyst brick. From here, a transfer matrix relating the sound pressure and mass velocity between these two end points was obtained, each component of the transfer matrix corresponding to a four-pole parameter (see Chapter 6). The transfer matrix method of calculating the transmission loss employed by Jeong and Ih is also followed here. Therefore, the acoustic pressure in the capillary tube is given by equation (11.30), i.e.

$$p' = e^{k\Gamma\xi}\left[p'_{\mathrm{A}} + \tau p'_{\mathrm{B}}\right], \tag{11.86}$$

whilst the mass velocity is given by

$$w' = \rho_0 S u' = \rho_0 c_0 S e^{k\Gamma\xi}\left[u'_{\mathrm{A}}(\eta) + \tau u'_{\mathrm{B}}(\eta)\right], \tag{11.87}$$

where w' is the mass velocity in the capillary duct and S is the cross-sectional area of the duct. In accordance with Jeong and Ih, equation (11.86) is divided by p'_{A} (see Sections 11.3 and 11.4) and, after substitution from equation (11.54), this gives

$$\frac{p'}{p'_{\mathrm{A}}} = 1 + \tau\left(\mathrm{B}_0 + \mathrm{B}_1\xi + \mathrm{B}_2\xi^2\right). \tag{11.88}$$

The mass velocity is divided here by $p'_{\mathrm{A}}p_0$, and, after use of equations (11.42), (11.50) and (11.55), equation (11.87) yields

$$\frac{w'}{p'_{\mathrm{A}}p_0} = S\frac{\Gamma s^2}{c_0}\left[u_{\mathrm{A}}(\eta) + \tau\left(u_{\mathrm{B}_0}(\eta) + u_{\mathrm{B}_1}(\eta)\xi + u_{\mathrm{B}_2}(\eta)\xi^2\right)\right]. \tag{11.89}$$

To satisfy equation (11.89) fully, one must take the cross-sectionally averaged values for the particle velocity, hence

$$\frac{w'}{p'_A p_0} = \frac{\Gamma s^2}{c_0}\left[\langle u_A \rangle + \tau\left(\langle u_{B_0} \rangle + \langle u_{B_1} \rangle \xi + \langle u_{B_2} \rangle \xi^2\right)\right]. \tag{11.90}$$

To obtain a transfer matrix it is necessary to calculate the pressure and mass velocity for both the incident and reflected waves at each end of the capillary duct. Therefore at $\xi = -1$,

$$\frac{p'}{p'_A} = \left[1 + \tau\left(-B_1^{i,r} + B_2^{i,r}\right)\right] \tag{11.91}$$

and

$$\frac{w'}{p'_A p_0} = \frac{\Gamma_{i,r} s^2}{c_0}\left[\langle u_A \rangle^{i,r} + \tau\left(\langle u_{B_0} \rangle^{i,r} - \langle u_{B_1} \rangle^{i,r} + \langle u_{B_2} \rangle^{i,r}\right)\right], \tag{11.92}$$

where superscript i refers to an incident wave, r to a reflected wave (note that $B_0 = 0$ - see Section 11.4). Similarly at $\xi = +1$,

$$\frac{p'}{p'_A} = \left[1 + \tau\left(B_1^{i,r} + B_2^{i,r}\right)\right] \tag{11.93}$$

and

$$\frac{w'}{p'_A p_0} = \frac{\Gamma_{i,r} s^2}{c_0}\left[\langle u_A \rangle^{i,r} + \tau\left(\langle u_{B_0} \rangle^{i,r} + \langle u_{B_1} \rangle^{i,r} + \langle u_{B_2} \rangle^{i,r}\right)\right]. \tag{11.94}$$

Now, if we define

$$F_1^{i,r} = 1 + \tau\left(-B_1^{i,r} + B_2^{i,r}\right), \tag{11.95}$$

$$F_2^{i,r} = 1 + \tau\left(B_1^{i,r} + B_2^{i,r}\right), \tag{11.96}$$

$$G_1^{i,r} = \frac{\Gamma_{i,r} s^2}{c_0}\left[\langle u_A \rangle^{i,r} + \tau\left(\langle u_{B_0} \rangle^{i,r} - \langle u_{B_1} \rangle^{i,r} + \langle u_{B_2} \rangle^{i,r}\right)\right], \tag{11.97}$$

$$G_2^{i,r} = \frac{\Gamma_{i,r} s^2}{c_0}\left[\langle u_A \rangle^{i,r} + \tau\left(\langle u_{B_0} \rangle^{i,r} + \langle u_{B_1} \rangle^{i,r} + \langle u_{B_2} \rangle^{i,r}\right)\right], \tag{11.98}$$

then at $x = -L$, the pressure can be written as

$$P^0 = \mathrm{A}F_1^i e^{-ik_0\Gamma_i L} + \mathrm{B}F_1^r e^{-ik_0\Gamma_r L} \tag{11.99}$$

and the mass velocity as

$$W^0 = \mathrm{A}G_1^i e^{-ik_0\Gamma_i L} + \mathrm{B}G_1^r e^{-ik_0\Gamma_r L}, \tag{11.100}$$

where A and B are constants and $k_0 = \omega/c_0$. Similarly at $x = L$,

$$P^L = \mathrm{A}F_2^i e^{-ik_0\Gamma_i L} + \mathrm{B}F_2^r e^{-ik_0\Gamma_r L} \tag{11.101}$$

and

$$W^L = \mathrm{A}G_2^i e^{-ik_0\Gamma_i L} + \mathrm{B}G_2^r e^{-ik_0\Gamma_r L}. \tag{11.102}$$

The transfer matrix for the capillary duct is now given by

$$\begin{Bmatrix} P^0 \\ W^0 \end{Bmatrix} = \begin{bmatrix} a_{11} & a_{12} \\ a_{21} & a_{22} \end{bmatrix} \begin{Bmatrix} P^L \\ W^L \end{Bmatrix}, \tag{11.103}$$

where a_{11}, a_{12}, a_{21} and a_{22} are the four pole parameters. One can obtain expressions for the four-pole parameters by eliminating the constants A and B from equations (11.99) to (11.102), giving

$$a_{11} = \frac{1}{\mathrm{D}}\left[G_2^r F_1^i e^{-2k_0\Gamma_i L} - G_2^i F_1^r e^{-2k_0\Gamma_r L}\right] \tag{11.104}$$

$$a_{12} = \frac{1}{\mathrm{D}}\left[F_1^r F_2^i e^{-2k_0\Gamma_r L} - F_1^i F_2^r e^{-2k_0\Gamma_i L}\right] \tag{11.105}$$

$$a_{21} = \frac{1}{\mathrm{D}}\left[\mathrm{G}_1^{\mathrm{i}}\mathrm{G}_2^{\mathrm{r}}e^{-2k_0\Gamma_{\mathrm{i}}L} - \mathrm{G}_1^{\mathrm{r}}\mathrm{G}_2^{\mathrm{i}}e^{-2k_0\Gamma_{\mathrm{r}}L}\right] \tag{11.106}$$

$$a_{22} = \frac{1}{\mathrm{D}}\left[\mathrm{G}_2^{\mathrm{r}}\mathrm{F}_2^{\mathrm{i}}e^{-2k_0\Gamma_{\mathrm{r}}L} - \mathrm{G}_1^{\mathrm{i}}\mathrm{F}_2^{\mathrm{r}}e^{-2k_0\Gamma_{\mathrm{i}}L}\right], \tag{11.107}$$

where

$$\mathrm{D} = \left[\mathrm{G}_2^{\mathrm{r}}\mathrm{F}_2^{\mathrm{i}} - \mathrm{G}_2^{\mathrm{i}}\mathrm{F}_2^{\mathrm{r}}\right]. \tag{11.108}$$

The transmission loss (TL) of the catalytic converter is then given by

$$\mathrm{TL} = 20\log_{10}\left\{\left|a_{11} + a_{12}/\Omega c_0 + \Omega c_0 a_{21} + a_{22}\right|/2\right\}, \tag{11.109}$$

where Ω is the percentage open area, or porosity, normal to the cross section of the catalyst brick.

11.5.1 Transmission Loss Predictions for Zeroth Order in τ

The theoretical predictions obtained for the zeroth order in τ solution obviously do not include a temperature gradient. It is therefore appropriate for numerical predictions to be compared with experimental data obtained at room temperature and standard measurement techniques such as those discussed in Chapter 5 can be used. The measurement of the acoustic performance of a catalytic converter at much higher temperatures presents a number of problems and it is assumed here that, for the zeroth order in τ predictions, observations concerning the comparison between predicted and measured data made at room temperature are also applicable at high temperatures.

In this section, a comparison between prediction and experiment is given for two very different types of catalytic converter. The first type is the common ceramic brick, supplied here by Johnson Matthey. Two ceramic bricks will be examined; the first had a length of 133mm and a diameter of 99mm, whilst the second was 150mm long and 77mm in diameter. Both ceramic bricks contain the same substrate, denoted by the manufacturer as CGW/400/6, the figure 400 representing the number of cells per square inch. Each of these cells, or capillary ducts, has a square cross-section. A side of each cell is approximately 1mm long and the walls are typically 0.16mm thick. The ceramic bricks also have a washcoat applied to them which increases the thickness of each wall by approximately 60μm. The washcoat also tends to migrate towards the corners of each cell causing them to fill in slightly, and this has the effect of rounding the corners of the cells, typically with a radius of the order of one-fifth of the wall thickness (see also Astley and Cummings [141]). Once the washcoat has been applied, the porosity (Ω) of both ceramic bricks was measured to be approximately 64%. The second type of catalytic converter to be studied here is a metallic brick and this was also supplied by Johnson Matthey. The metallic catalytic converters are produced in much smaller lengths than the ceramic ones, the brick studied here being 75mm in length with a diameter of 98mm. The substrate in the metallic brick used here is called by the manufacturer "interatom". The metallic bricks are typically constructed by sandwiching together alternating corrugated and non-corrugated sheets of substrate material, and this means that the capillary pores are no longer square in cross-section. Once a washcoat has been added to the metallic substrate, the pore typically assumes an approximately polygonal shape. However, the pores in the metallic catalysts are similar in size to those in the ceramic catalyst, the largest dimensions being of the order of 1mm. The use of a metallic substrate allows the cell walls to be made much thinner than in the case of the ceramic catalyst. For the metallic brick studied here, a wall thickness of approximately 40μm was typical prior to the application of the washcoat. The layer of washcoat added to the metallic brick is also much thinner and this typically increased the width of the cell by approximately 20μm. The use of thinner walls means that the metallic catalyst has a higher porosity than a ceramic one, which, for the brick studied here, was measured to be 76%.

In the theoretical analysis presented earlier on in this chapter it was assumed that a capillary tube was of a cylindrical cross section. This is obviously not the case for either the ceramic or metallic catalytic converters. Astley and Cummings [141] have studied non-circular cross-sectional geometries, such as those encountered here, by using a finite element formulation. In the present modelling procedure, taking into account the cross-sectional shape in detail would prove complicated and the introduction of such a method into the first order in τ solutions would present many problems. Instead, the author believes that sufficient accuracy can be achieved simply by determining the hydraulic radius for each pore and then implementing the cylindrical model discussed in the previous sections, for a circular pore radius equal to the hydraulic radius of the actual pore. Consequently, an average value for the hydraulic radius (R_h) was calculated from the measured pore geometry for each brick and this gave values of $R_h = 0.517\text{mm}$ for the metallic brick, and $R_h = 0.562\text{mm}$ for both types of ceramic brick. The effect of using the hydraulic radius to represent non-circular cross-sections was examined by employing a simple variational model to compute transmission loss predictions for a capillary pore with a square cross-section and with a circular cross-section. A comparison between the transmission loss predictions obtained for a square cross-section and those obtained employing the hydraulic radius showed little difference, indicating that accuracy has not been sacrificed in the present analysis by using the hydraulic radius to represent non-circular cross-sections.

In order to asses the accuracy of transmission loss predictions to zeroth order in τ, experimental data were obtained at room temperature. The transmission loss measurements on the catalytic converters were performed in exactly the same way as the tests carried out on the dissipative silencers in Chapter 5. Transmission loss tests on several catalytic converters were carried out, beginning with the measurement of individual ceramic and metallic bricks. Since each brick is rather short in length, it can produce only small levels of sound attenuation and consequently problems in accuracy can occur when attempts are made to measure this. This was particularly noticeable when measuring the metallic catalyst since it is only 75mm long and hence the transmission loss is very small. When a small transmission loss is being measured, experimental error is particularly noticeable, especially when mean flow is present and such small sound attenuations can often become swamped by the effects of flow noise. In an attempt to overcome this problem, four ceramic catalysts were joined together so as to produce a much higher transmission loss. Following a method suggested by Jeong

[150], the individual capillary tubes in the four catalyst bricks were lined up by using wires, and the bricks were then taped together to form one large brick. This allowed an effective brick length of 0.6m to be measured, which would provide a transmission loss similar in magnitude to that measured by Jeong and Ih [148], who combined six ceramic catalysts to achieve a length of 0.66m.

In view of the experimental difficulties prevailing when mean flow is present, the measurements for the individual ceramic catalyst (length 0.133m) and the metallic catalyst are compared to non-isentropic predictions without the presence of mean flow in Figure 11.1. In Figure 11.2, non-isentropic transmission loss predictions are compared with experiment for the combination of four ceramic catalysts, both with and without flow. It is evident from Figures 11.1 and 11.2 that the transmission loss measured for a single brick is small, especially for the metallic catalyst, and that it is desirable to increase the effective length of the bricks in order to measure a more substantial effect. However, the most striking feature of both Figure 11.1 and 11.2 is the large discrepancy between prediction and experiment for the ceramic catalysts. Indeed, for the 0.6m length, the measured transmission loss is more than double that predicted by the non-isentropic formulation of Section 11.3. It is possible that a part of the underprediction in Figure 11.2 is caused by the incorrect alignment of holes when forming the 0.6m length of brick although, in view of the results obtained for the single ceramic brick in Figure 11.1, this is unlikely to be the major cause. The discrepancies in Figures 11.1 and 11.2 were not, however, observed by Jeong and Ih [148], who obtained very good agreement between prediction and experiment using the same non-isentropic formulation as that implemented here. One must therefore conclude that, either large errors have occurred in the present experimental investigation, or a different ceramic catalyst has been measured here, as compared to that used by Jeong and Ih. In view of the quality of experimental data obtained for the dissipative silencers in Chapter 5, it is very likely that the discrepancies are caused by differences in the type of ceramic catalyst between the present study and that of Jeong and Ih, and indeed this was later confirmed by Jeong [150]. One is still left, however, with the large discrepancies in Figures 11.1 and 11.2, although if one examines Figure 11.1, it appears that no such problems occur in the case of the metallic catalyst. It is possible that the porosity of the walls of the capillary tubes in the ceramic catalysts was influencing the propagation of sound in the tubes. Indeed, such an effect had already been identified by Arnott et al. [144], who found it necessary to introduce a reactive wall impedance into their theoretical model to take account of the acoustic effect of the very small pores in the walls of the substrate. However, Arnott et al. restricted their analysis to ceramic bricks without a washcoat, and it was originally thought that the introduction of a washcoat would reduce the acoustic effect of the walls, especially as the washcoat has much smaller pores (see Astley and Cummings [141]). However, the predictions obtained here appear to indicate that the pores in the washcoat, in addition to those in the substrate, are influencing sound attenuation.

In order to investigate the effects of wall porosity, the normal impedance of one end of a washcoated ceramic brick was measured parallel to the capillary tubes, with the opposite end being terminated in a rigid metal plate. Figure 11.3 shows a comparison between values predicted for the normal impedance of the ceramic catalyst, using a non-isentropic formulation, and those measured experimentally by the use of a standing wave tube (see Chapter 3). It is evident from Figure 11.3 that large discrepancies between prediction and experiment also occur for the normal impedance measurements and one can therefore conclude that a wall porosity effect must be present. Clearly, to model the ceramic catalysts studied here one must therefore include the wall porosity effects, but it is important first to establish the accuracy of the model implemented in Section 11.3. To do this, the wall porosity effect can be removed by blocking the small pores in the walls of the capillary tubes. This was done by soaking the ceramic catalyst, which included a washcoat, in dilute varnish and allowing the solvent to evaporate. This method was also employed, concurrent to the work performed here, by Bernard et al. [151]. A number of surface impedance tests was performed on the varnished brick, using an increasing number of coats, until the addition of a further coat of varnish produced a negligible effect. In Figure 11.3, the surface impedance data obtained after the application of four coats of varnish is compared, both with the theoretical predictions and the data obtained without varnish. It was observed that, after each additional coat of varnish, the measured impedance values moved progressively closer to those predicted, finally converging to the values shown for four coats of varnish in Figure 11.3. It is evident from Figure 11.3 that the addition of the varnish has produced a significant improvement in the correlation between prediction and experiment. This effect was also apparent when transmission loss measurements were performed on a varnished brick. For example Figure 11.4 shows much closer agreement between prediction and experiment for the ceramic catalyst brick (0.15m long) with four coats of varnish applied, than for the unvarnished brick (the latter results are not shown here, but the data for M=0 are similar to those in Figure 11.1 for a brick 0.133m long).

From an examination of the results presented in Figures 11.1 to 11.3, one must conclude that, to the zeroth order in τ, the combined effects of porosity of both the substrate and the washcoat have a significant influence upon the acoustic performance of a ceramic catalyst. If one removes this effect, either by examining a metallic brick or by applying varnish to a ceramic brick, one finds very good agreement between the non-isentropic predictions of Section 11.3 and measured data. Also, the quality of these predictions does not seem to be affected by the assumption that the capillary tubes are circular in cross-section; the use of the hydraulic radius appears to be sufficient for examining cells with arbitrary cross-sections. It does, however, appear that, in order to characterise the acoustic performance of the ceramic bricks studied here accurately, one must include wall porosity effects in the model. A method for achieving this was suggested by Arnott et al. [144], although they did not examine the additional effects of the washcoat. The application of a washcoat would probably require the addition of both reactive and resistive terms to the impedance values used by Arnott et al., and values for these must be measured experimentally. Furthermore one must also include the radial velocity in the theoretical model if the wall porosity is being included and, whilst this does not present too many problems for the zeroth order in τ solution (see Jeong and Ih [148]), it does appear to complicate the first order in τ solution. Predicting the effects of wall porosity on the performance of a ceramic catalytic converter and including them in a model which also accounts for an axial temperature gradient is beyond the scope of the work presented in this thesis.

11.5.2 Transmission Loss Predictions for First Order in τ

The study of the predictions obtained in Section 11.4 for the first order in τ solution are limited to a comparison with zeroth order theoretical predictions only. This is because measuring the effects of a temperature gradient on a catalytic converter experimentally requires exothermic reactions in the catalyst to be induced, and to do this the catalyst must be subjected to a temperature of the order of 1000K. Performing such an experiment is difficult at present, especially since, in addition to raising the temperature to 1000K, one must then measure the acoustic characteristics at this temperature.

For a ceramic catalytic converter of the type examined in the zeroth order solution previously described, the exothermic reaction induces a temperature rise in the order of 100K over a distance of approximately 20mm. If this temperature rise is assumed to be linear then, substituting a mean temperature of 1000K back into equation (11.6), one obtains a value for the temperature change parameter τ of 0.05. In order to simplify the calculations here, the temperature gradient is assumed to exist over the complete length of the capillary duct, with the same value of τ=0.05. The predictions obtained for the ceramic catalyst (0.15m in length), with a hydraulic radius of 0.56mm and a porosity of 0.639, are given in Figure 11.5, for a mean temperature of 1000K. Both the isentropic and non-isentropic solutions are given, with τ=0 and τ=0.05. Mean flow has not been included since, as discussed in Sections 11.3 and 11.4, the solutions including mean flow are at present unobtainable. It is evident from Figure 11.5 that, regardless of the temperature gradient, the increase in mean temperature increases the transmission loss of the catalytic converter. However it is apparent that the introduction of a temperature gradient does reduce this effect slightly. For the isentropic case, the temperature gradient causes a constant reduction in the transmission loss, of the order of 0.5dB over the entire frequency range. For the non-isentropic case, a reduction in transmission loss is also predicted, although this is no longer constant over the frequency range. At very low frequencies, the non-isentropic case appears - as one would expect - to give similar predictions to those obtained by using the isentropic solution. However, as the frequency increases, the difference between the solutions for

$\tau=0$ and $\tau=0.05$ decreases. It appears that as the frequency tends towards infinity, the two solutions converge. If one compares the isentropic and non-isentropic solutions, it is evident that, especially when a temperature gradient is present, the isentropic solution provides a serious underprediction of the transmission loss as the frequency is increased. For the particular catalyst in Figure 11.5, the isentropic solution is of the order of 1.8dB lower at 2kHz. This gives some indication of the size of error involved when assuming isentropic disturbances and, for catalytic converters such as those studied here, cautions against the use of isentropic solutions. Unfortunately, the effects of mean flow cannot be included in the present study, although it is probably safe to assume that the effect of the temperature gradient, when mean flow is present, is similar to that observed in Figure 11.5. This observation does, however, remain to be proved and, in the light of the discrepancies between the isentropic and non-isentropic predictions in Figure 11.5, to do this one must solve the non-isentropic problem with mean flow. This presents a number of problems since, as discussed in Section 11.4, the non-isentropic solution with mean flow is complex and a solution awaits further work. However, from the result with $\tau=0.05$ presented in Figure 11.5, it does seem that the effect of the temperature gradient is relatively small and it is possible that it can be ignored in most situations. This is particularly true if one is including the catalytic converter in a complete model of the exhaust system, since the additional effect of the temperature gradient will be minimal and probably impossible to measure when the catalytic converter is incorporated with other dissipative elements such as the silencers studied in previous chapters. However, when subjected to the high temperatures prevailing close to the exhaust manifold, the catalytic converter itself does appear to have a significant influence on the dissipation of sound in an exhaust system and, although this influence is small compared with dissipative silencers, it should nevertheless be included. This is particularly true at very low frequencies where the dissipation of sound by the catalytic converter is of a similar order to that found for the dissipative silencers, and it is at these frequencies where the catalyst will provide the most beneficial influence.

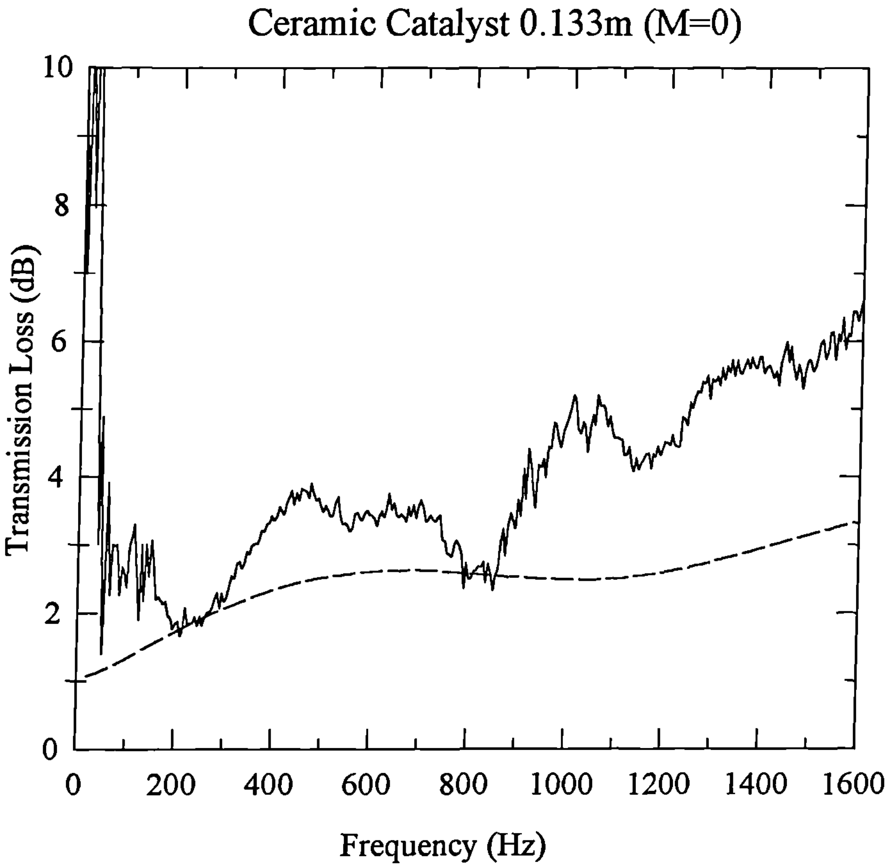

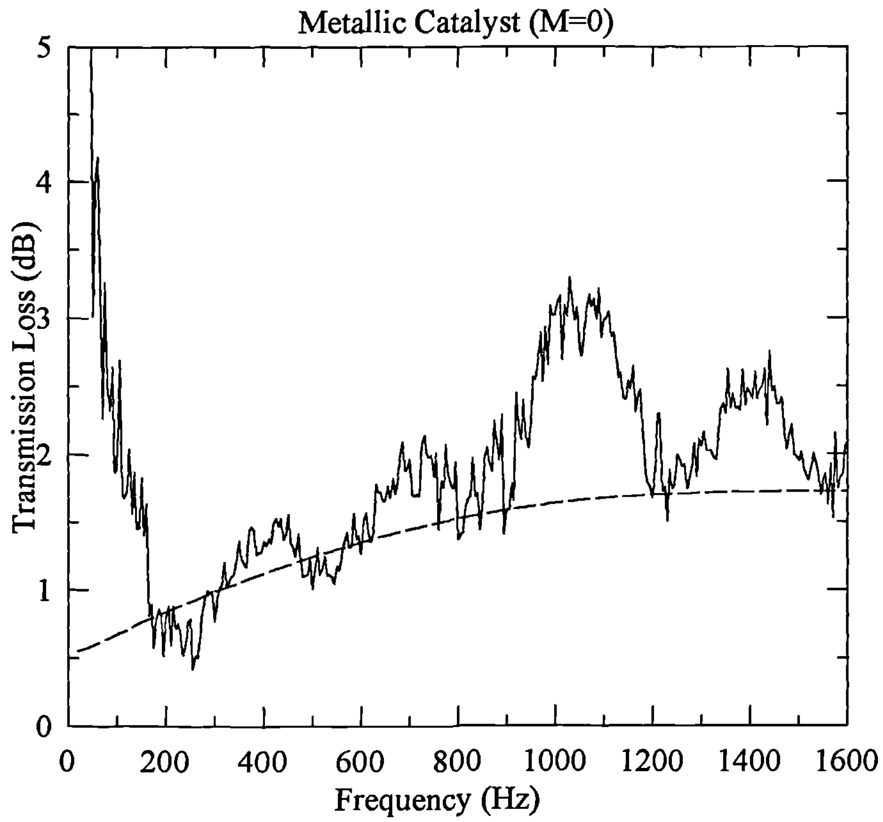

Figure 11.1. Comparison between prediction and experiment for catalytic converters.
—— , Experiment; – – – , Prediction, non-isentropic, zeroth order in τ.

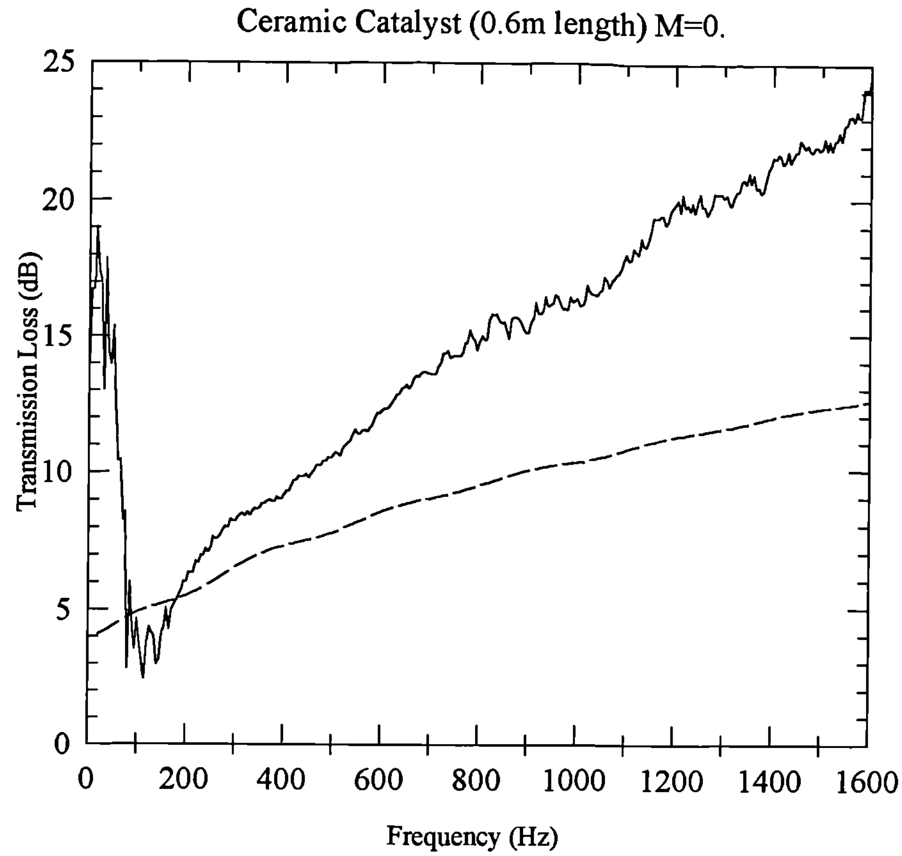

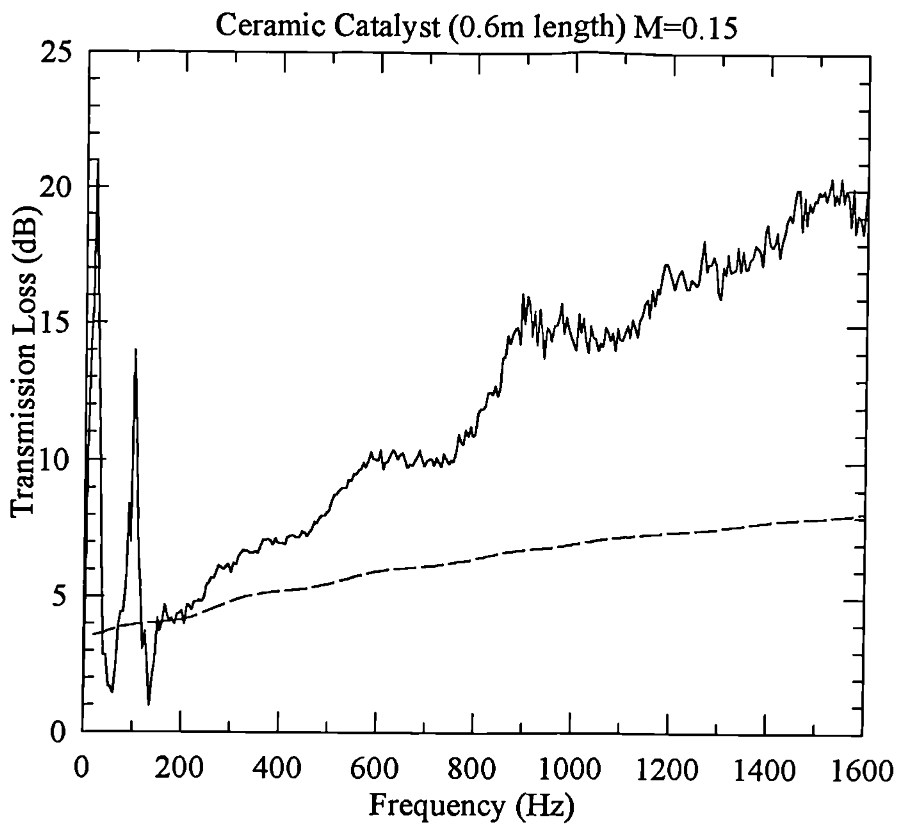

Figure 11.2. Comparison between prediction and experiment for ceramic catalyst.
——— , Experiment; — — , Prediction, non-isentropic, zeroth order in τ.

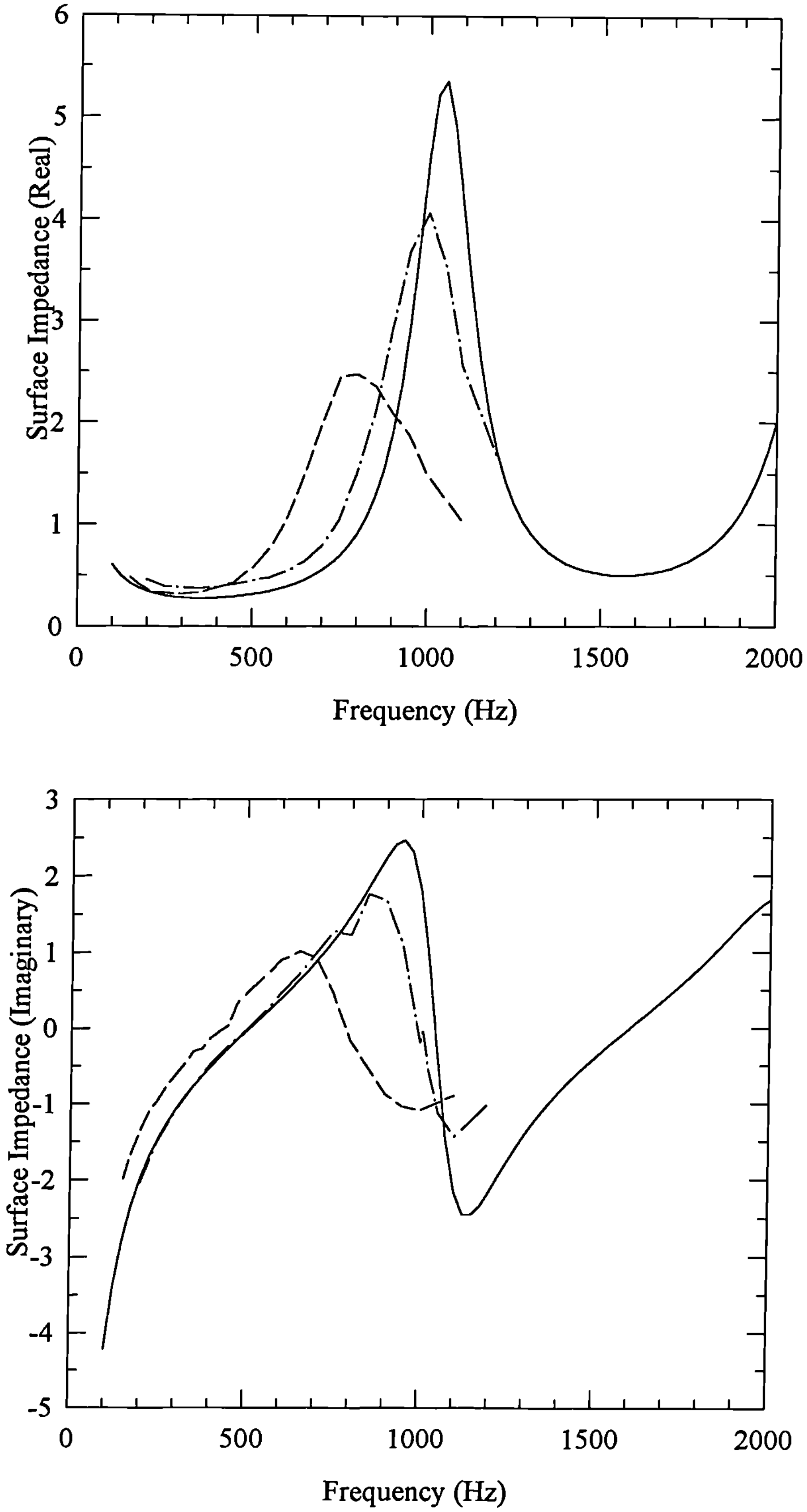

Figure 11.3. Surface impedance of ceramic catalyst (0.15m long) with a rigid backing.
——— , Prediction; — — — , Experiment - Washcoat Only;
—·— , Experiment - 4 coats of varnish.

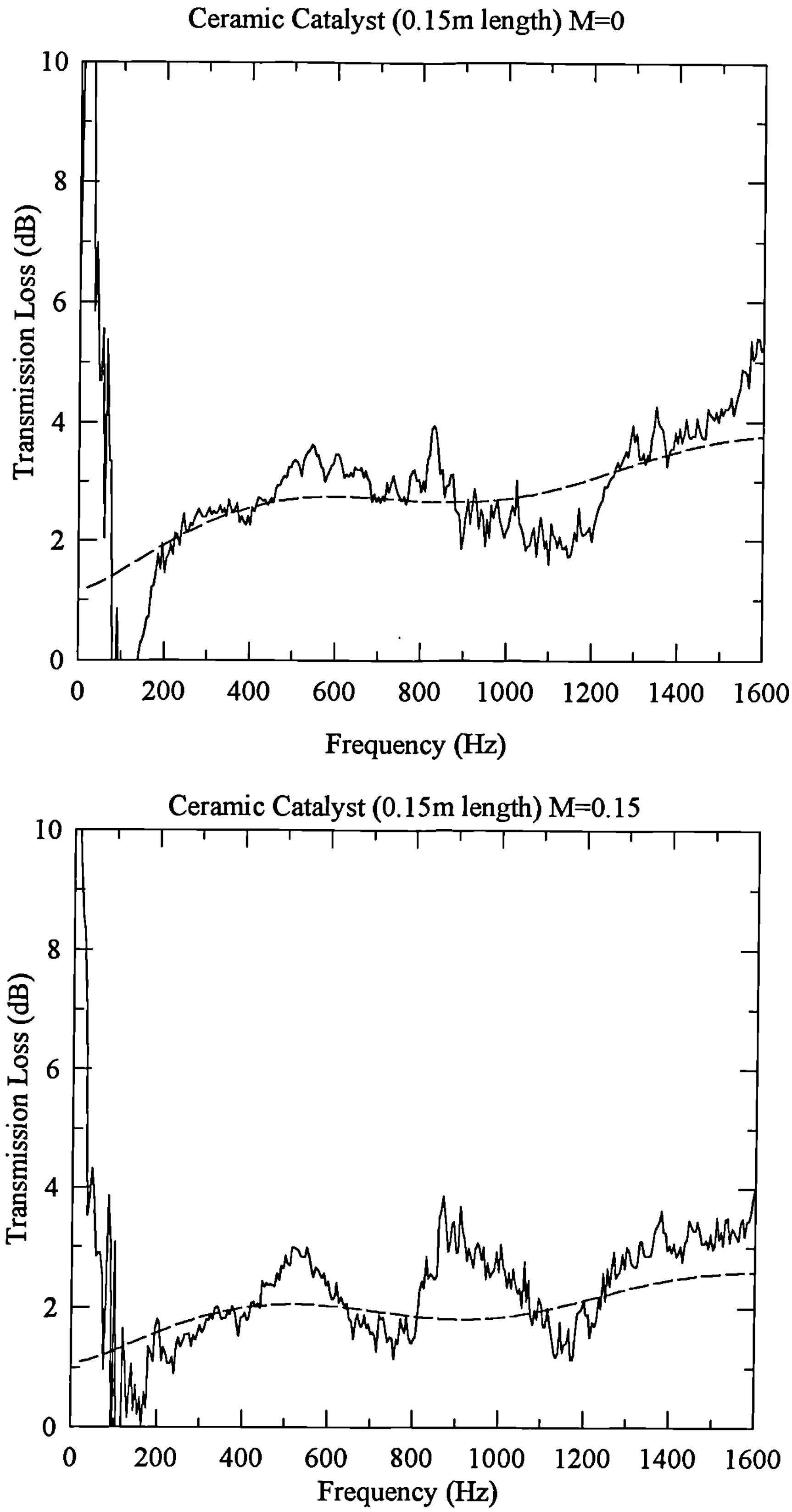

Figure 11.4. Comparison between prediction and experiment for varnished catalyst.
——— , Experiment; – – – , Prediction, non-isentropic, zeroth order in τ.

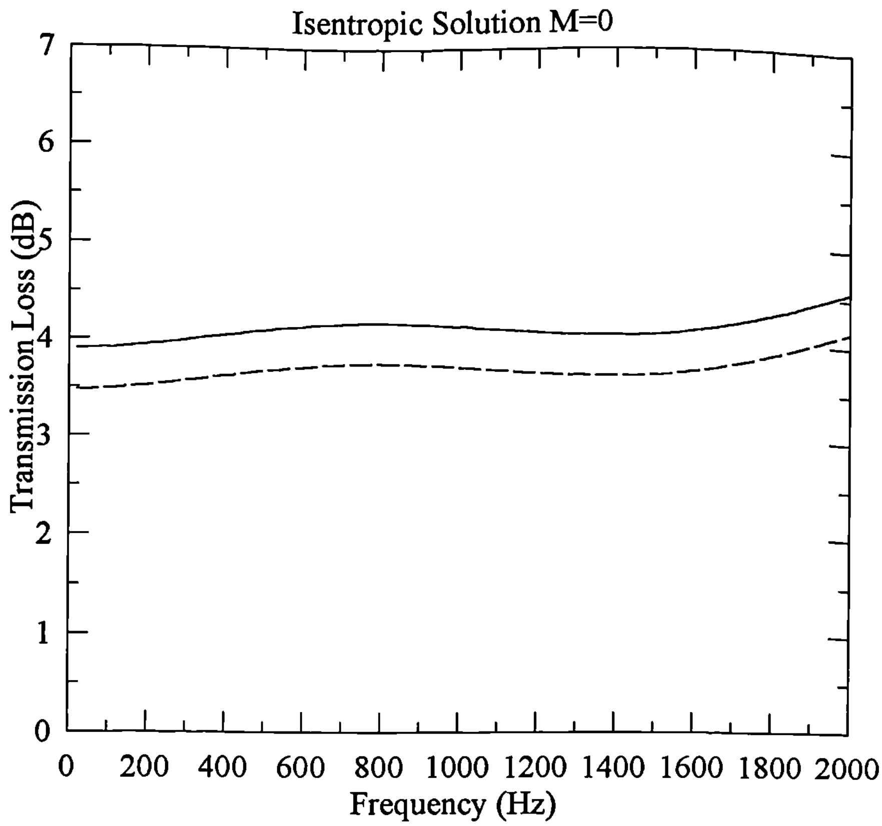

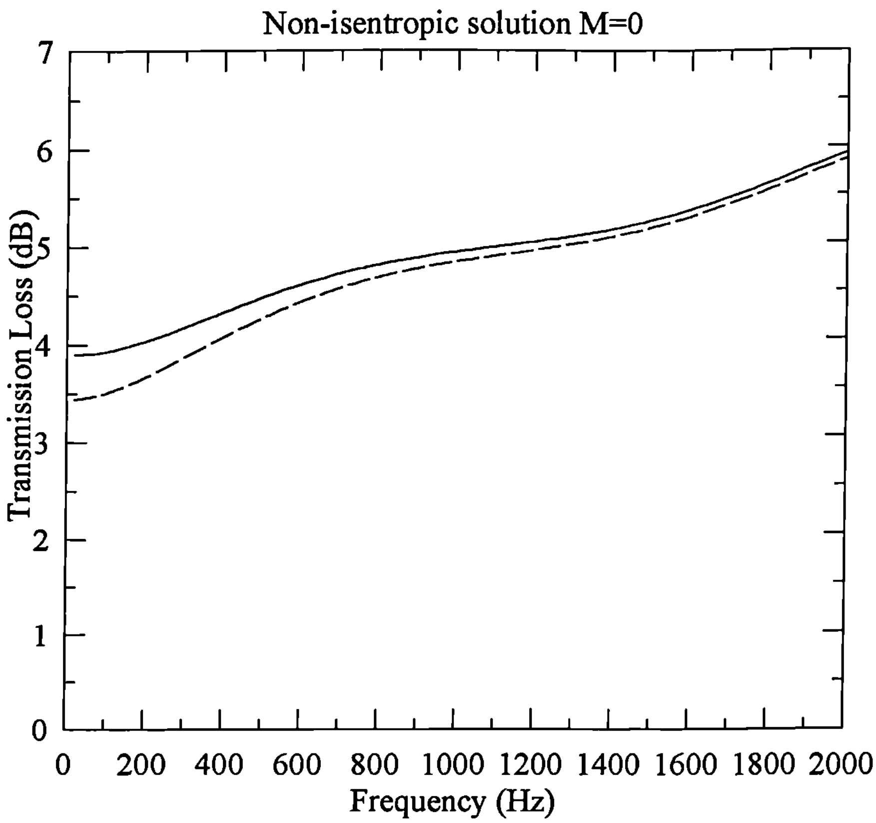

Figure 11.5. Comparison between predictions with and without a temperature gradient. ——— , Prediction τ=0; – – – , Prediction τ=0.05.

CHAPTER 12

CONCLUSIONS

The research reported in this thesis has included an examination of the acoustic design of dissipative elements commonly found in automotive exhaust systems, namely dissipative silencers and catalytic converters. The study of dissipative silencers has formed the bulk of the thesis because - as expected - these attenuate sound energy to a far greater extent than do catalytic converters. Work has concentrated here on formulating methods for modelling dissipative silencers mathematically, with a view to employing such models in future commercial design software. This has involved examining a number of different theoretical approaches, which have varied in their relative complexity. The models were compared both with one another and with an extensive range of experimental data taken prior to modelling, and final conclusions were drawn concerning the mathematical model which was best suited to the requirements of the industrial sponsors. The procedure employed in this thesis has involved examining existing modelling techniques and then modifying these to suit the specific requirements. In general this has required the extension of previous modelling techniques to include a perforate between the central channel and the absorbent, and the introduction of a new semi-empirical model describing the acoustic properties of the absorbent.

Of primary importance to the performance of dissipative silencers is the behaviour of the porous material. In Chapters 2 and 3 a new semi-empirical method was introduced for predicting the bulk acoustic properties of the porous materials used in subsequent silencer modelling. This was accomplished first by theoretically modelling the absorbent by the use of a parallel fibre microstructure model, and then approximating this model to low frequencies only. From here, new values for a frequency dependent tortuosity and pore shape factor were inferred by employing experimental data measured using the standard impedance tube method. The model allows predictions for the bulk acoustic properties to remain accurate in the region in which experimental data is available, but provides a seamless transition to theoretical predictions at frequencies below those obtainable via experiment, thus ensuring that the correct limiting behaviour is observed. The semi-empirical model was shown to work well for materials of medium to high flow resistivity such as those employed in the present study (A glass, E glass and basalt wool). For materials with a much lower flow resistivity, such as steel wool, the semi-empirical model does not work quite so well, principally because the high frequency limit of the approximations inherent in the microstructure model is approached at lower frequencies than for the medium to high flow resistivity materials. Therefore if one is to employ this model with low flow resistivity materials, further examination is necessary to establish the range of validity of this model. Nevertheless, for materials typically present in bulk form inside automotive dissipative silencers, the new semi-empirical method was seen to work well.

A feature of the majority of the dissipative silencer models reported in the Literature is the omission of the perforate. It was commonly thought that perforates with a high porosity, such as those studied here, had very little influence on the acoustic properties of dissipative silencers. Whilst it was known that the introduction of grazing flow substantially changes the acoustic impedance of a perforate, the additional effect of a porous material backing the perforate had not previously been studied. In Chapter 4 the effect of a porous material on the acoustic impedance of a perforate subjected to grazing flow was discussed and a semi-empirical model was proposed, employing data found for perforates without a porous backing and combining these with theoretical predictions of the effect of the absorbent backing. The validity of the semi-empirical predictions was assessed by taking experimental data for a number of perforates backed by porous materials, and good agreement between prediction and experiment was observed. It was concluded that the porous material causes a large increase in the acoustic impedance of a perforate and one can no longer ignore the effect of perforates in the modelling of dissipative silencers. The size of this increase in impedance was also found to depend upon the flow resistivity of the backing material, the largest increase occurring with high flow resistivity materials. In addition, the effect of the porous material was found to be very localised and to depend heavily upon the density of the material immediately adjacent to the holes. This later had consequences in the prediction of the impedance of perforates situated in a randomly packed silencer, since one cannot fully describe the behaviour of the perforate without a detailed knowledge of the packing density adjacent to the perforated tube. The study in Chapter 4 also includes, for the first time, an examination of the acoustic impedance of louvred plates. Louvres were found to behave in a significantly different way from flat plates and one can no longer obtain universal formulae for the acoustic impedance of a louvre without a porous backing. In addition, the presence of a porous material backing a louvre was found to produce no additional increase in the acoustic impedance of the perforate.

The semi-empirical models for absorbents and perforates, described in Chapters 2, 3 and 4, were later introduced into the theoretical modelling of the dissipative silencers themselves. This presented no additional problems associated with the bulk acoustic properties, but the introduction of a perforate required a re-formulation of each theoretical model in order to account for the change in the boundary conditions between the central channel and the absorbent. The fundamental mode model was studied first because of its apparent simplicity and this model was extended here to include the perforate. In addition, the low frequency approximations introduced by Peat [13] were removed to allow larger silencers to be examined. Indeed, the experimental data obtained in Chapter 5 allowed the performance of the fundamental mode model to be studied far more closely than before, and it was observed that, whilst the model performed relatively well for "small" silencers, the prediction accuracy for larger axisymmetric silencers and oval shaped silencers was poor. It also later became apparent that the area weighting functions employed by Peat introduced further approximations into the model and that, in the future, better results may be achieved by employing the duct eigenfunctions as the weighting functions. However, even accounting for this improvement, one cannot expect the fundamental mode model to yield accurate predictions for a full range of dissipative silencers and in particular the oval shaped silencers that are commonly employed in automotive exhausts.

It became clear after examining the fundamental mode predictions in Chapter 6 that if one requires a model for dissipative silencers which have an arbitrary cross-sectional shape, then numerical methods must be used and this is best performed by using finite elements. In Chapter 7 the fully general finite element model of Peat and Rathi [26] was examined. The model was modified here to omit mean flow in the absorbent and also to include a perforate. Unfortunately the inclusion of a perforate required the re-configuration of the finite element mesh and this prevented the inclusion of a perforate in three dimensional solutions. However results were still obtained using a three dimensional mesh for oval shaped silencers without a perforate for the first time. The accuracy of the predictions using the full finite element method was found to be very good, and this was unaffected by either the size or shape of the silencer. Indeed, of all the theoretical predictions examined in this thesis, the highest degree of accuracy obtainable when comparing prediction to experiment was provided by the full finite element method. However, penalties are associated with the use of the full finite element method since one must employ large amounts of CPU time to find solutions and for this particular method the demand on CPU time proved to be prohibitive. Also, the full finite element method itself was not without its problems although these were limited to the three dimensional solutions. For example, at very low frequencies, a number of "non-physical" predictions were obtained and the reasons behind this need further investigation. Also, in future, a more specialised mesh generator is required in order to allow a perforate to be included in three dimensional predictions.

In Chapters 8 and 9, work concentrated on reducing the CPU time necessary to implement a finite element scheme. This involved assuming the silencer to be infinite in length and employing an eigenvalue solution (see Chapter 8) which was then coupled with a mode matching solution in Chapter 9 in order to obtain predictions for a silencer of finite length. Whilst this method does require the cross-section of the silencer to be uniform along its length, it did allow the dimensions of the problem to be reduced by one as compared to the full finite element approach. The eigenvalue solution employed in Chapter 8 was based upon the method of Astley and Cummings [17], but was re-formulated here to include a perforate. The reduction in the dimensions of the eigenvalue solution allowed a two dimensional mesh to be formulated for the oval shaped silencers and this allowed the perforate to be included for the first time in predictions for oval shaped silencers. The eigenvalue formulation in Chapter 8 was shown to provide a "robust" method for finding the least attenuated modes, and did not suffer from the problems, such as missing modes, which can often occur in iterative schemes. The eigenvalue solution was formulated with the intention of providing data for the mode matching schemes of Chapter 9, and hence no attention was paid to mode shapes, the modes simply being ordered on the basis of attenuation alone. This approach worked well for the silencers of the size and shape studied here, although when a two dimensional mesh was used, non-axisymmetric modes appeared in the solution; these could be a potential source of problems in predictions for larger silencers or those with a greater area expansion ratio. Therefore in future a closer examination of the eigenvalue solution is probably necessary in order to ascertain the range of validity of the model when using this in conjunction with a mode matching scheme.

The eigenvalue solutions described in Chapter 8 were employed in the three separate mode matching solutions discussed in Chapter 9. It was originally intended to employ the straightforward mode matching method of Cummings and Chang [23], but after a detailed examination of the method, it was found to give non-physical predictions when higher order modes were introduced in the presence of mean flow. The reasons why this problem occurred are still not entirely clear, although the problems are thought to be caused by the use of non-orthogonal weighting functions. In an attempt to overcome this problem a least squares mode matching approach was attempted, but similar problems to those encountered in the Cummings and Chang method were observed. To overcome this, a new mode matching method was employed, and this involved integrating the governing equations directly, thus removing the orthogonality question. The non-physical predictions of the previous two mode matching schemes were eliminated and good agreement between prediction and experiment was observed, although the convergence of the solution was erratic and higher order modes could not be introduced into solutions for oval shaped silencers. It became apparent after studying the three different mode matching schemes that the implementation of continuity conditions at an abrupt area change in a dissipative silencer using a mode matching formulation is fraught with difficulty and the problem is still not fully understood. It appears that one should not employ non-orthogonal weighting functions in mode matching solutions, although the reasons behind this are not clear. In future the mode matching approach requires further investigation, although it might eventually be necessary to abandon a mode matching formulation altogether and employ alternative methods such as the Wiener-Hopf method. However, for the type and size of silencer studied here, it was shown in Chapter 10 that the Cummings and Chang mode matching method employing only one mode works well and does not undergo too large a reduction in accuracy when compared to the full finite element model described in Chapter 7. Indeed, since only one mode is sufficient, it is possible to employ a relatively coarse finite element mesh in the eigenvalue solution and this has the potential to reduce CPU time significantly. However, this method does require further investigation, especially if it is to be used in the design of much larger silencers such as those found in air conditioning ducts.

Finally, in Chapter 11, catalytic converters were studied, and these were shown to provide only a small contribution to the overall sound transmission loss in a dissipative exhaust silencer. If one compares the predictions obtained for both the "straight-through" dissipative silencers and the catalytic converters studied here, then it would appear that at medium to high frequencies, the relative effect of the catalyst is small, although at very low frequencies the catalyst is capable of producing significant levels of sound attenuation. In Chapter 11, a model was formulated which - for the first time - incorporated a temperature gradient, together with a mean flow Mach number of between 0.2 and 0.3. When no mean flow was present, the temperature gradient was observed to reduce the overall transmission loss slightly, although the effect did depend upon whether an isentropic or non-isentropic formulation was employed. Indeed significant differences between the isentropic and non-isentropic solutions were observed, especially at high frequencies, and it appears that if a catalytic converter is to be modelled accurately then one must employ a non-isentropic formulation. Unfortunately, numerical solutions to the problem including both mean flow and a temperature gradient have yet to be realised and therefore in future different methods need to be found for solving the final equations. Furthermore, a comparison between prediction and experiment without a temperature gradient indicated, for the catalysts studied here, the presence of a substantial wall porosity effect. It is apparent that this effect must be included in the future modelling of catalytic converters in order to obtain accurate prediction of attenuation. Nevertheless, when one removes the wall porosity effect, a comparison between experiment and prediction indicated that the model without a temperature gradient provides quite accurate predictions. The difficulty in obtaining experimental data for a catalyst with a temperature gradient means that the accuracy of the temperature gradient model remains as yet unspecified. Further research is required in order to resolve this question.

Of the research reported in this thesis, the author believes that the results indicating the influence of the perforate are the most significant. It appears that the perforate can substantially alter the performance of a dissipative silencer, particularly at high frequencies, even with perforate porosities as high as 27%. The design of the perforate potentially offers significant further scope for improvement in dissipative silencer design and this should be reflected in further investigations into the physics of the behaviour of the perforate, which at present is still not fully understood.

In general, the mathematical modelling presented in this thesis has shown good agreement with experimental data, both for the dissipative silencers and the catalytic converters. It appears that one can successfully predict the behaviour of dissipative silencers to a high degree of accuracy, at least over a frequency range of 0-1kHz. The problems associated with the demands upon CPU time appear to have been solved - as far as possible - by use of the Cummings and Chang mode matching method employing one mode. It therefore appears perfectly possible to formulate predictive software for dissipative elements in automotive exhausts which is both accurate and relatively fast in execution. It has also been shown here that it is possible to achieve modelling accuracy for dissipative silencers that is comparable to that presently available in the design of reactive silencers, although the modelling of dissipative silencers is inevitably more complex than that of reactive silencers and it remains to be seen how the relative computational times for numerical solution compare. It is hoped that, in future, the dissipative silencers models examined here can be combined with models for reactive elements, such that complex multi-pass silencers can be modelled. Ultimately, such software will play an integral role in predicting the external noise radiated from an exhaust system as a whole, and allow for the more efficient acoustic design of automotive exhausts.

REFERENCES

1. K.S. Peat 1995 *Proceedings of Euro-Noise '95*, 791-796. LAMPS software for the acoustic analysis of silencers.

2. L.J. Sivian 1937 *Journal of the Acoustical Society of America* **9**, 135-140. Sound propagation in ducts lined with absorbing materials.

3. P.M. Morse 1939 *Journal of the Acoustical Society of America* **11**, 205-210. The transmission of sound inside pipes.

4. R.A. Scott 1946 *Proceedings of the Physical Society* **58**, 165-183. The absorption of sound in a homogeneous porous medium.

5. A. Bokor 1969 *Journal of Sound and Vibration* **10**, 390-403. Attenuation of sound in lined ducts.

6. A. Bokor 1971 *Journal of Sound and Vibration* **14**, 367-373. A comparison of some acoustic duct lining materials according to Scott's theory.

7. U.J. Kurze and I.L. Vér 1972 *Journal of Sound and Vibration* **24**, 177-187. Sound attenuation in ducts lined with non-isotropic material.

8. C. Wassilieff 1987 *Journal of Sound and Vibration* **114**, 239-251. Experimental verification of duct attenuation models with bulk reacting linings.

9. E. Meyer, F. Mechel and G. Kurtze 1958 *Journal of the Acoustical Society of America* **30**, 165-174. Experiments on the influence of flow on sound attenuation in absorbing ducts.

10. U. Ingård 1959 *Journal of the Acoustical Society of America* **31**, 1035-1036. Influence of a fluid motion past a plane boundary on sound reflection, absorption and transmission.

11. D.H. Tack and R.F. Lambert 1965 *Journal of the Acoustical Society of America* **38**, 655-666. Influence of shear flow on sound attenuation in a lined duct.

12. S.-H. Ko 1972 *Journal of Sound and Vibration* **22**, 193-210. Sound attenuation in acoustically lined circular ducts in the presence of uniform flow and shear flow.

13. K.S. Peat 1991 *Journal of Sound and Vibration* **146**, 353-360. A transfer matrix for an absorption silencer element.

14. A. Cummings 1976 *Journal of Sound and Vibration* **49**, 9-35. Sound attenuation in ducts lined on two opposite walls with porous material, with some applications to splitters.

15. B. Nilsson and O. Brander 1980 *IMA Journal of Applied Mathematics* **26**, 269-298. The propagation of sound in cylindrical ducts with mean flow and bulk reacting lining. I. Modes in an infinite duct.

16. A. Cummings and I.J. Chang 1987 *Acustica* **64**, 170-178. Internal mean flow effects on the characteristics of bulk-reacting liners in circular ducts.

17. R.J. Astley and A. Cummings 1987 *Journal of Sound and Vibration* **116**, 239-263. A finite element scheme for attenuation in ducts lined with porous material: comparison with experiment.

18. K.L. Rathi 1994 *Loughborough University* Ph.D. Thesis. Finite element acoustic analysis of absorption silencers with mean flow.

19. R. Glav 1994 *Royal Institute of Technology, Stockholm, Sweden* Ph.D. Thesis. On acoustic modelling of silencers.

20. B. Nilsson and O. Brander 1980 *IMA Journal of Applied Mathematics* **26**, 381-410. The propagation of sound in cylindrical ducts with mean flow and bulk reacting lining. II. Bifurcated ducts.

21. B. Nilsson and O. Brander 1980 *IMA Journal of Applied Mathematics* **27**, 105-131. The propagation of sound in cylindrical ducts with mean flow and bulk reacting lining. III. Step discontinuities.

22. B. Nilsson and O. Brander 1980 *IMA Journal of Applied Mathematics* **27**, 263-289. The propagation of sound in cylindrical ducts with mean flow and bulk reacting lining. IV. Several interacting discontinuities.

23. A. Cummings and I.J. Chang 1988 *Journal of Sound and Vibration* **127**, 1-17. Sound attenuation of a finite length dissipative flow duct silencer with internal mean flow in the absorbent.

24. A. Craggs 1977 *Journal of Sound and Vibration* **54**, 285-296. A finite element method for modelling dissipative mufflers with a locally reactive lining.

25. H.S. Hobbeling 1989 *Acustica* **67**, 275-283. Calculation of complex absorption and reflection silencers using a finite element method.

26. K.S. Peat and K.L. Rathi 1995 *Journal of Sound and Vibration* **184**, 529-545. A finite element analysis of the convected wave motion in dissipative silencers.

27. P.M. Morse and K.U. Ingård 1968 *Theoretical Acoustics*, McGraw Hill, London.

28. J.W. Strutt (Lord Rayleigh) 1896 *Theory of Sound (Volume II)*, Macmillan, London.

29. G. Kirchhoff 1868 *Poggendorfer Annalen* **134**, 177-193. Ueber den einfluss der wärmeleitung in einem gase auf die schallbewegung.

30. P.C. Carman 1956 *Flow of Gases Through Porous Media*, Butterworth, London.

31 C. Zwikker and C.W. Kosten 1949 *Sound Absorbing Materials*, Elsevier, Amsterdam.

32. H. Tijdeman 1975 *Journal of Sound and Vibration* **39**, 1-33. On the propagation of sound waves in cylindrical tubes.

33. M.R. Stinson 1991 *Journal of the Acoustical Society of America* **89**, 550-558. The propagation of plane sound waves in narrow and wide circular tubes, and generalisation to uniform tubes of arbitrary cross-sectional shape.

34. M.A. Biot 1956 *Journal of the Acoustical Society of America* **28**, 168-178. Theory of propagation of elastic waves in a fluid-saturated porous solid. I. Low frequency range.

35. P.G. Smith and R.A. Greenkorn 1971 *Journal of the Acoustical Society of America* **51**, 247-253. Theory of acoustical wave propagation in porous media.

36. K. Attenborough and L.A. Walker 1971 *Journal of the Acoustical Society of America* **49**, 1331-1338. Scattering theory for the absorption of sound in fibrous media.

37. S.H. Burns 1971 *Journal of the Acoustical Society of America* **49**, 1-8. Propagation constant and specific impedance of airborne sound in metal wool.

38. F.P. Mechel 1976/77 *Acustica* **36**, 53-64. Eine modelltheorie zum faserabsorber Teil I: Reguläre faseranordnung.

39. F.P. Mechel 1976/77 *Acustica* **36**, 65-89. Eine modelltheorie zum faserabsorber Teil II: Absorbermodell aus elementarzellen und numerische ergebnisse.

40. A. Cummings and I.J. Chang 1987 *Journal of Sound and Vibration* **114**, 565-581. Acoustic propagation in porous media with internal mean flow.

41. K. Attenborough 1982 *Physics Report* **82**, 179-227. Acoustical characteristics of porous materials.

42. D.L. Johnson, J. Koplik and R. Dashen 1987 *Journal of Fluid Mechanics* **176**, 379-402. Theory of dynamic permeability and tortuosity in fluid saturated porous media.

43. J.F. Allard, B. Castagnede, M. Henry and W. Lauriks 1994 *Review of Scientific Instruments* **65**, 754-755. Evaluation of tortuosity in acoustic porous materials saturated by air.

44. J.F. Allard and Y. Champoux 1992 *Journal of the Acoustical Society of America* **91**, 3346-3353. New empirical equations for sound propagation in rigid frame fibrous materials.

45. M.R. Stinson and Y. Champoux 1992 *Journal of the Acoustical Society of America* **91**, 685-695. Propagation of sound and the assignment of shape factors in model porous materials having simple pore geometries.

46. K. Attenborough 1983 *Journal of the Acoustical Society of America* **73**, 785-799. Acoustical characteristics of rigid fibrous absorbents and granular materials.

47. Y. Champoux and M.R. Stinson 1992 *Journal of the Acoustical Society of America* **92**, 1120-1131. On acoustical models for the sound propagation in rigid frame porous materials and the influence of shape factors.

48. F.P. Mechel 1988 *Journal of the Acoustical Society of America* **83**, 1002-1013. Design charts for sound absorber layers.

49. S.N. Chandler-Wilde and K.V. Horoshenkov 1995 *Journal of the Acoustical Society of America* **98**, 1119-1129. Padé approximants for the acoustical characteristics of rigid frame porous media.

50. K.S. Peat 1994 *Journal of Sound and Vibration* **174**, 475-489. A first approximation to the effects of mean flow on sound propagation through capillary tubes.

51. F.M. White 1979 *Fluid Mechanics*, McGraw Hill, London.

52. M. Abramowitz and I.A. Stegun 1964 *Handbook of Mathematical Functions*, National Bureau of Standards, Washington D.C.

53. A. Craggs and J.G. Hildebrandt 1984 *Journal of Sound and Vibration* **92**, 321-331. Effective densities and resistivities for acoustic propagation in narrow tubes.

54. M.E. Delany and E.N. Bazley 1970 *Applied Acoustics* **3**, 105-116. Acoustic properties of fibrous materials.

55. F.P. Mechel 1982 *IBP Report*. Akustishe kennwerte von faserabsorben.

56. L.L. Beranek 1940 *Journal of the Acoustical Society of America* **12**, 3-13. Precision measurement of acoustic impedance.

57. R.A. Scott 1946 *Proceedings of the Physical Society* **58**, 253-265. An apparatus for accurate measurement of the acoustic impedance of sound-absorbing materials.

58. L.L. Beranek 1949 *Acoustic Measurements*, Wiley, London.

59. D.A. Bies 1963 *Journal of the Acoustical Society of America* **35**, 495-499. Acoustic properties of steel wool.

60. S.L. Yaniv 1973 *Journal of the Acoustical Society of America* **54**, 1138-1142. Impedance tube measurement of propagation constant and characteristic impedance of porous acoustical material.

61. C.D. Smith and T.L. Parrott 1983 *Journal of the Acoustical Society of America* **74**, 1577-1582. Comparison of three methods for measuring acoustic properties of bulk materials.

62. H. Utsuno, T. Tunaka, T. Fujikawa and A.F. Seybert 1989 *Journal of the Acoustical Society of America* **86**, 637-643. Transfer function method for measuring characteristic impedance and propagation constant of porous materials.

63. A.F. Seybert and D.F. Ross 1977 *Journal of the Acoustical Society of America* **61**, 1362-1370. Experimental determination of acoustic properties using a two-microphone random-excitation technique.

64. J.Y. Chung and D.A. Blazer 1980 *Journal of the Acoustical Society of America* **68**, 907-913. Transfer function method of measuring in-duct acoustic properties. I Theory.

65. J.Y. Chung and D.A. Blazer 1980 *Journal of the Acoustical Society of America* **68**, 914-921. Transfer function method of measuring in-duct acoustic properties. II Experiment.

66. F.J. Fahy 1984 *Journal of the Acoustical Society of America* **97**, 168-170. Rapid method for the measurement of sample acoustic impedance in a standing wave tube.

67. D.A. Bies and C.H. Hansen 1980 *Applied Acoustics* **13**, 357-391. Flow resistance information for acoustical design.

68. Data supplied by Lancaster Glass Fibre.

69. A.W. Al-Khafaji and J.R. Tooley 1986 *Numerical Methods in Engineering Practice*, HRW, London.

70. D.R.A. Christie 1976 *Journal of Sound and Vibration* **46**, 347-355. Measurement of the acoustic properties of a sound absorbing material at high temperatures.

71. K. Attenborough 1971 *Journal of Sound and Vibration* **16**, 419-442. The influence of microstructure on propagation in porous fibrous absorbents.

72. L.L. Beranek 1960 *Noise Reduction*, McGraw Hill, London.

73. F.P Mechel 1976 *Acustica* **35**, 210-213. Ausweitung der absorberformel von Delany und Bazley zu tiefen frequenzen.

74. P.M. Morse 1936 *Vibration and Sound*, McGraw Hill, London.

75. U. Ingård 1953 *Journal of the Acoustical Society of America* **25**, 1037-1061. On the theory and design of acoustic resonators.

76. T.H. Melling 1973 *Journal of Sound and Vibration* **29**, 1-65. The acoustic impedance of perforates at medium and high sound pressure levels.

77. D. Ronneberger 1972 *Journal of Sound and Vibration* **24**, 133-150. The acoustic impedance of holes in the wall of flow ducts.

78. K.J. Baumeister and E.J. Rice 1978 *American Institute of Aeronautics and Astronautics Journal* **16**, 233-236. Flow visualization in long-neck Helmholtz resonators with grazing flow.

79. P.A. Nelson, N.A. Halliwell and P.E. Doak 1981 *Journal of Sound and Vibration* **78**, 15-38. Fluid dynamics of a flow excited resonance, Part I: Experiment.

80. P.A. Nelson, N.A. Halliwell and P.E. Doak 1983 *Journal of Sound and Vibration* **91**, 375-402. Fluid dynamics of a flow excited resonance, Part II: Flow acoustic interaction.

81. M.S. Howe 1979 *Journal of Sound and Vibration* **67**, 533-544. The influence of a grazing flow on the acoustic impedance of a cylindrical wall cavity.

82. D. Ronneberger 1980 *Journal of Sound and Vibration* **71**, 565-581. The dynamics of shearing flow over a cavity - a visual study related to the acoustic impedance of small orifices.

83. B.E. Walker and A.F. Charwat 1982 *Journal of the Acoustical Society of America* **72**, 550-555. Correlation of the effects of grazing flow on the impedance of Helmholtz resonators.

84. S. Kaji, M. Hiramoto and T. Okazaki 1984 *Bulletin of the Japan Society of Mechanical Engineers* **27**, 2388-2396. Acoustic characteristics of orifice holes exposed to grazing flow.

85. A.S. Hersh, B. Walker and M. Bucka 1978 *American Institute of Aeronautics and Astronautics* Paper 78-1124. Effect of grazing flow on the acoustic impedance of Helmholtz resonators consisting of single and clustered orifices.

86. K. Narayana Rao and M.L. Munjal 1986 *Journal of Sound and Vibration* **108**, 283-295. Experimental evaluation of impedance of perforates with grazing flow.

87. A. Goldman and R.L. Panton 1976 *Journal of the Acoustical Society of America* **60**, 1397-1404. Measurement of the acoustic impedance of an orifice under a turbulent boundary layer.

88. D. Coles 1956 *Journal of fluid mechanics* **1**, 191-226. The law of the wake in the turbulent boundary layer.

89. A. Goldman and C.H. Chung 1982 *Journal of the Acoustical Society of America* **71**, 573-579. Impedance of an orifice under a turbulent boundary layer with pressure gradient.

90. J.W. Kooi and S.L. Sarin 1981 *American Institute of Aeronautics and Astronautics* Paper 81-1998. An experimental study of the acoustic impedance of Helmholtz resonator arrays under a turbulent boundary layer.

91. A. Cummings 1986 *Acustica* **61**, 233-242. The effects of grazing turbulent pipe-flow on the impedance of an orifice.

92. K.P. Flynn and R.L. Panton 1990 *Journal of the Acoustical Society of America* **87**, 1482-1488. The interaction of Helmholtz resonators in a row when excited by a turbulent boundary layer.

93. U. Ingård and R.H. Bolt 1951 *Journal of the Acoustical Society of America* **23**, 533-540. Absorption characteristics of acoustic material with perforated facings.

94. W.A. Davern 1977 *Applied Acoustics* **10**, 85-112. Perforated facings backed with porous materials as sound absorbers - and experimental study.

95. R.L. Panton 1984 *Incompressible Flow*, Wiley, New York.

96. F.B. Gessener and J.B. Jones 1965 *Journal of Fluid Mechanics* **23**, 689-713. On some aspects of fully developed turbulent flow in rectangular channels.

97. H. Fujita 1979 *Transactions of the Japan Society of Mechanical Engineers* **B45**, 197-207. Turbulent flow in smooth and rough-walled square ducts.

98. V.C. Patel 1965 *Journal of Fluid Mechanics* **23**, 185-208. Calibration of the Preston tube and limitations on its use in pressure gradients.

99. M.L. Munjal 1987 *Acoustics of ducts and Mufflers*, Wiley, New York.

100. B.S. Sridhara and M.J. Crocker 1994 *Journal of the Acoustical Society of America* **95**, 2363-2370. Review of theoretical and experimental aspects of acoustical modelling of engine exhaust systems.

101. M.G. Prasad and M.J. Crocker 1981 *Journal of the Acoustical Society of America* **70**, 1339-1344. Insertion loss studies on models of automotive exhaust systems.

102. W.S. Gatley and R. Cohen 1969 *Journal of the Acoustical Society of America* **46**, 6-16. Methods for evaluating the performance of small acoustic filters.

103. R. Singh and T. Katra 1978 *Journal of Sound and Vibration* **56**, 279-298. Development of an impulse technique for measurement of muffler characteristics.

104. R. Singh and T. Katra 1978 *Journal of Sound and Vibration* **58**, 459-462. On the digital generation of an acoustic excitation impulse.

105. M. Salikuddin, K.K Ahuja and W.H. Brown 1984 *Journal of Sound and Vibration* **94**, 33-61. An improved impulse method for studies of acoustic transmission in flow ducts with use of signal synthesis and averaging of acoustic pulses.

106. K.S. Peat 1993. Personal communication.

107. J.W. Sullivan 1979 *Journal of the Acoustical Society of America* **66**, 779-788. A method for modelling perforated tube muffler components. II. Applications.

108. R.H. Bolt 1947 *Journal of the Acoustical Society of America* **19**, 917-921. On the design of perforated facings for acoustic materials.

109. K.S. Peat 1990 *Proceedings of Inter-Noise 90* **1**, 579-582. A numerical decoupling analysis of absorption silencer elements.

110. J. Zhenlin, M. Qiang and Z. Zhihua 1994 *Journal of Sound and Vibration* **173**, 57-71. Application of the boundary element method to predicting acoustic performance of expansion chamber mufflers with mean flow.

111. G.M.L. Gladwell and G. Zimmermann 1966 *Journal of Sound and Vibration* **3**, 233-241. On energy and complementary energy formulations of acoustic and structural vibration problems.

112. C-I.J. Young and M.J.Crocker 1975 *Journal of the Acoustical Society of America* **57**, 144-148. Prediction of transmission loss in mufflers by the finite element method.

113. C-I.J. Young and M.J.Crocker 1976 *Journal of the Acoustical Society of America* **60**, 1111-1118. Acoustical analysis, testing, and design of flow reversing muffler chambers.

114. A. Craggs 1976 *Journal of Sound and Vibration* **48**, 377-392. A finite element method for damped acoustic systems: an application to evaluate the performance of reactive mufflers.

115. Y. Kagawa and T. Omote 1976 *Journal of the Acoustical Society of America* **60**, 1003-1013. Finite-element simulation of acoustic filters of arbitrary profile with circular cross section.

116. R.J. Astley and W. Eversman 1981 *Journal of Sound and Vibration* **74**, 103-121. Acoustic transmission in non-uniform ducts with mean flow, Part II: The finite element method.

117. K.S. Peat 1982 *Journal of Sound and Vibration* **84**, 389-395. Evaluation of four-pole parameters for ducts with flow by the finite element method.

118. Y. Kagawa, T. Yamabuchi and A. Mori 1977 *Journal of Sound and Vibration* **53**, 357-374. Finite element simulation of an axisymmetric acoustic transmission system with a sound absorbing wall.

119. R.J. Astley and W. Eversman 1979 *Journal of Sound and Vibration* **65**, 61-74. A finite element formulation of the eigenvalue problem in lined ducts with flow.

120. P.S. Christiansen and S. Krenk 1988 *Journal of Sound and Vibration* **112**, 107-118. A recursive finite element technique for acoustic fields in pipes with absorption.

121. K.L. Rathi 1994. Personal communication.

122. O.C. Zienkiewicz 1977 *The finite element method*, McGraw-Hill, London.

123. Science and Engineering Research Council 1991 NAG finite element library, Release 3.0.

124. N. Sormaz 1994 *Hull University* Ph.D. Thesis. Acoustic attenuation of dissipative splitter silencers.

125. D.A. Bies, C.H. Hansen and G.E. Bridges 1991 *Journal of Sound and Vibration* **146**, 47-80. Sound attenuation in rectangular and circular cross-section ducts with flow and bulk-reacting liner.

126. A. Cummings 1992 *Proceedings of the Second International Conference on Recent Developments in Air and Structure Borne Sound and Vibration, Auburn University, Auburn, Alabama, U.S.A.*, 689-696. Sound absorbing ducts.

127. A. Cummings 1995 *Journal of Sound and Vibration* **187**, 23-37. A segmented Rayleigh-Ritz method for predicting sound transmission in a dissipative exhaust silencer of arbitrary cross-section.

128. R. Glav 1996 *Journal of Sound and Vibration* **189**, 489-509. The null field approach to dissipative silencers of arbitrary cross-section.

129. R. Glav 1996 *Journal of Sound and Vibration* **189**, 123-135. The point-matching method on dissipative silencers of arbitrary cross-section.

130. A. Cummings 1989 *Proceedings of the Institute of Acoustics* **11**, 643-650. Sound generation in a duct with a bulk-reacting liner.

131. J.W. Miles 1944 *Journal of the Acoustical Society of America* **16**, 14-19. The reflection of sound due to a change in cross section of a circular tube.

132. R.J. Alfredson 1972 *Journal of Sound and Vibration* **23**, 433-442. The propagation of sound in a circular duct of continuously varying cross sectional area.

133. A. Cummings 1975 *Journal of Sound and Vibration* **41**, 375-379. Sound transmission in a folded annular duct.

134. A.I. El-Sharkawy and A.H. Nayfeh 1978 *Journal of the Acoustical Society of America* **63**, 667-674. Effect of an expansion chamber on the propagation of sound in circular pipes.

135. A. Cummings 1975 *Journal of Sound and Vibration* **38**, 149-155. Sound transmission at sudden area expansion in circular ducts, with superimposed mean flow.

136. J.G. Ih and B.H. Lee 1985 *Journal of the Acoustical Society of America* **77**, 1377-1388. Analysis of higher order mode effects in the circular expansion chamber with mean flow.

137. M. Åbom 1990 *Journal of Sound and Vibration* **137**, 403-418. Derivation of four-pole parameters including higher order mode effects for expansion chamber mufflers with extended inlet and outlet.

138. R. Mittra and S.W. Lee 1971 *Analytical Techniques in the Theory of Guided Waves*, Macmillan, London.

139. R. Smith 1988 *Journal of Fluid Mechanics* **187**, 589-597. Minimizing shoreline pollution in rivers with tributaries.

140. R. Smith 1989 *Journal of Fluid Mechanics* **208**, 25-43. Loss of frequency response along sampling tubes for the measurements of gaseous composition at high temperature and pressures.

141. R.J. Astley and A. Cummings 1995 *Journal of Sound and Vibration* **188**, 635-657. Wave propagation in catalytic converters: Formulation of the problem and finite element solution scheme.

142. R. Glav, H. Bodén and M. Åbom 1988 *Proceedings of Inter-Noise 88*, 1261-1266. An acoustic model for automobile catalytic converters.

143. H.-S. Roh, W.P. Arnott, J.M. Sabatier and R. Raspet 1991 *Journal of the Acoustical Society of America* **89**, 2617-2624. Measurement and calculation of acoustic propagation constants in arrays of small air-filled rectangular tubes.

144. W.P. Arnott, J.M. Sabatier and R. Raspet 1991 *Journal of the Acoustical Society of America* **90**, 3299-3306. Sound propagation in capillary-tube type porous media with small pores in the capillary walls.

145. U. Ingård and U.K. Singhal 1974 *Journal of the Acoustical Society of America* **55**, 535-538. Sound attenuation in turbulent pipe flow.

146. K.S. Peat 1994 *Journal of Sound and Vibration* **175**, 475-489. A first approximation to the effects of mean flow on sound propagation through cylindrical capillary tubes.

147. J.-G. Ih, C.-M. Park and H.-J. Kim 1996 *Journal of Sound and Vibration* **190**, 163-173. A model for sound propagation in capillary ducts with mean flow.

148. K.-W. Jeong and J.-G. Ih 1996 *Journal of Sound and Vibration* (to appear). A numerical study on the propagation of sound through capillary tubes with mean flow.

149. K.S. Peat 1996 *Journal of Sound and Vibration* (to appear). Convected acoustic wave motion along a capillary duct with a temperature gradient.

150. K.-W. Jeong 1995. Personal communication.

151. M. Bernard, D. Velea and J.M. Sabatier 1996 *Journal of the Acoustical Society of America* **99**, 2430-2432. Permanent removal of the wall porosity in monolithic catalyst support ceramics.